UNIVERSIDAD NACIONAL DEL LITORAL


DOCTORADO EN INGENIERÍA

# Diseño Computacional de Metamateriales Mecánicos en Régimen Lineal y No Lineal

Nestor Oscar Rossi Cabral

FICH

FACULTAD DE INGENIERÍA

Y CIENCIAS HÍDRICAS

INTEC

INSTITUTO DE DESARROLLO TECNOLÓGICO

PARA LA INDUSTRIA QUÍMICA

CIMEC

CENTRO DE INVESTIGACIÓN

DE MÉTODOS COMPUTACIONALES

sinc($i$)

INSTITUTO DE INVESTIGACIÓN EN SEÑALES,

SISTEMAS E INTELIGENCIA COMPUTACIONAL

Tesis de Doctorado **2024**

**Doctorado en Ingeniería**

**Mención mecánica computacional**

Título de la obra:

# Diseño Computacional de Metamateriales Mecánicos en Régimen Lineal y No Lineal

Autor: Nestor Oscar Rossi Cabral

Lugar: Santa Fe, Argentina

Palabras Claves:

Mecánica computacional, metamateriales mecánicos,
homogeneización inversa, optimización topológica,
simetrías cristalográficas, propiedades elásticas extremas,
G-clausura, microarquitecutras parametrizadas,
energías no convexas, transiciones de fase,
inestabilidades elásticas, pozos de energía,
histerón, modelos reducido, relajación
modelo generalizado estándar, inestabilidades volumétricas.


UNIVERSIDAD NACIONAL DEL LITORAL

Facultad de Ingeniería y Ciencias Hídricas

Instituto de Desarrollo Tecnológico para la Industria Química

Centro de Investigación de Métodos Computacionales

Instituto de Investigación en Señales, Sistemas e Inteligencia Computacional

# Diseño Computacional de Metamateriales Mecánicos en Régimen Lineal y No Lineal

**Nestor Oscar Rossi Cabral**

Tesis remitida al Comité Académico del Doctorado
como parte de los requisitos para la obtención
del grado de
DOCTOR EN INGENIERÍA
Mención Mecánica Computacional
de la
UNIVERSIDAD NACIONAL DEL LITORAL

**2024**

Secretaría de Posgrado, Facultad de Ingeniería y Ciencias Hídricas, Ciudad Universitaria,
Paraje “El Pozo”, S3000, Santa Fe, Argentina.

UNIVERSIDAD NACIONAL DEL LITORAL

Facultad de Ingeniería y Ciencias Hídricas

Instituto de Desarrollo Tecnológico para la Industria Química

Centro de Investigación de Métodos Computacionales

Instituto de Investigación en Señales, Sistemas e Inteligencia Computacional

# Diseño Computacional de Metamateriales Mecánicos en Régimen Lineal y No Lineal

**Nestor Oscar Rossi Cabral**

**Lugar de trabajo:**
CIMEC
Centro de Investigación de Métodos Computacionales
Facultad de Ingeniería y Ciencias Hídricas
Universidad Nacional del Litoral

**Director:**
Dr. Alfredo E. Huespe CIMEC (CONICET) / Universidad Nacional del Litoral

**Co-director:**
Dr. Pablo J. Sánchez CIMEC (CONICET) / Universidad Tecnológica Nacional

**Jurado Evaluador:**
Dr. Pablo Zavattieri Lyles School of Civil Engineering - Purdue University
Dr. Martín Ignacio Idiart CONICET / Universidad Nacional de La Plata
Dr. Juan Carlos Cante CIMNE / Universitat Politècnica de Catalunya

**2024**

(1994–2024) 30 años de la Consagración Constitucional de la Autonomía y Autarquía Universitaria en Argentina.

**UNIVERSIDAD NACIONAL DEL LITORAL**
**Facultad de Ingeniería y Ciencias Hídricas**

Santa Fe, 02 de Agosto de 2024.

Como miembros del Jurado Evaluador de la Tesis de Doctorado en Ingeniería titulada ***"Diseño Computacional de Metamateriales Mecánicos en Régimen Lineal y No Lineal"***, desarrollada por el Ing. Néstor Oscar ROSSI CABRAL, en el marco de la Mención "Mecánica Computacional", certificamos que hemos evaluado la Tesis y recomendamos que sea aceptada como parte de los requisitos para la obtención del título de Doctor en Ingeniería.

La aprobación final de esta disertación estará condicionada a la presentación de dos copias encuadernadas de la versión final de la Tesis ante el Comité Académico del Doctorado en Ingeniería.

| | | |
|---|---|---|
| Dr. Pablo Zavatieri | Dr. Martín Indiart | Dr. Juan Carlos Cante |

Santa Fe, 02 de Agosto de 2024.

Certifico haber leído la Tesis, preparada bajo mi dirección en el marco de la Mención "Mecánica Computacional" y recomiendo que sea aceptada como parte de los requisitos para la obtención del título de Doctor en Ingeniería.

| | |
|---|---|
| Dr. Pablo Sánchez<br>Codirector de Tesis | Dr. Alfredo Huespe<br>Director de Tesis |

Mg. Virginia Margenet
Subsecretaria de Posgrado FICH
Coordinadora Académica
EGA - MGA - FICH - UNL

Secretaría de Posgrado
Ruta Nacional N° 168, S/N
3000, Santa Fe, Argentina
0342-4575234 (Int 7(
posgrado@fich.unl.edu.ar

# Declaración legal del autor

Esta Tesis ha sido remitida como parte de los requisitos para la obtención del grado de Doctor ante la Universidad Nacional del Litoral y ha sido depositada en la Biblioteca de la Facultad de Ingeniería y Ciencias Hídricas para que esté disponible a sus lectores bajo las condiciones estipuladas por el Reglamento de la mencionada Biblioteca.

Citaciones breves de esta disertación son permitidas sin la necesidad de un permiso especial, en la suposición de que la fuente sea correctamente citada. Solicitudes de permiso para una citación extendida o para la reproducción de este manuscrito en un todo o en parte serán exigidas por el portador legal del derecho de propiedad intelectual de la misma.

Nestor Oscar Rossi Cabral

*Dedicado a mi alentador incansable Toto,*
*y a la memoria de Alba y Oscar.*

# Agradecimientos

Agradezco en primer lugar a las instituciones que me dieron la oportunidad de formarme e hicieron posible la realización de esta tesis. Al Consejo Nacional de Investigaciones Científicas y Técnicas (CONICET), la Facultad de Ingeniería y Ciencias Hídricas de la Universidad Nacional del Litoral (FICH-UNL) y al Centro de Investigación de Métodos Computacionales (CIMEC). A la Facultad de Ingeniería de la Universidad Nacional del Nordeste (UNNE) y a mis compañeros de la cátedra Estabilidad II, por la confianza y el apoyo para que pueda realizar el doctorado. A todos los argentinos y argentinas que día a día trabajan para que la educación en Argentina sea pública.

Agradezco a Ignacio Iturrioz, por ser el primero en mostrarme de qué se trata hacer investigación y por entusiasmarme para que realice un doctorado.

Agradezco a los doctores Juan Carlos Cante e Ignacio Romero, por abrirme las puertas de sus grupos y tratarme como uno más de sus alumnos durante mis visitas. Asimismo, agradezco a la Asociación Universitaria Iberoamericana de Postgrado por el apoyo recibido en mi visita al CIMNE, y a la Fundación Carolina y el (en aquel momento) Ministerio de Educación de la República Argentina por el apoyo recibido en mi visita a IMDEA Materials.

Agradezco a todos aquellos con los que tuve el gusto de colaborar durante este doctorado: Rolando, Carlos, Sebastián, Juan Manuel, Facundo, Ignacio, y mi co-Director Pablo. De todos ellos he aprendido mucho y me quedo con el grato recuerdo de trabajar juntos.

Agradezco especialmente a mi Director, Alfredo. Por enseñarme tanto durante estos años, por la paciencia, la confianza y la generosidad inagotables. Por compartirme ese entusiasmo y pasión con el que aprendí a mirar la ciencia, y por trabajar siempre codo a codo conmigo.

Agradezco a mis compañeros de CIMEC, en especial a aquellos con los que comparto la oficina 48, por hacer el día a día más fácil.

Agradezco a mi familia, en especial a la santafecina, por el apoyo y el aliento incondicional. A mis padres , María Ester y Néstor, por soportar la distancia y estar siempre dispuestos a ayudarme, sin importar si la ayuda es grande o chica.

Agradezco a Celeste, por compartir este desafío conmigo y por sostenerme cada vez que se hizo difícil seguir.

# Resumen

En esta tesis se aborda el problema de diseño computacional de metamateriales mecánicos en régimen elástico lineal y no lineal, orientados a diversas propiedades efectivas. Los metamateriales son un tipo especial de materiales compuestos que se conciben en dos escalas de longitud bien diferenciadas. Una escala superior o macroescala, donde se manifiestan las respuestas aparentes sobresalientes y donde el material puede ser explotado para aplicaciones específicas, y una escala inferior o microescala, donde es apreciable una distribución geométrica de sus constituyentes y donde se comporta como una estructura. El estudio y diseño de metamateriales comprende, por lo tanto, el análisis de ambas escalas.

En esta tesis se desarrollan diversas herramientas y estrategias numéricas que asisten al diseño topológico computacional de metamateriales mecánicos. Para demostrar la validez de estas técnicas se eligen problemas de máxima exigencia para el desempeño en la macroescala, lo que se entiende como comportamiento extremo de los metamateriales. En primer lugar, se propone una metodología basada en emparentar los metamateriales con cristales. Esto permite asistir la metodología de homogeneización inversa, es decir diseño de compuestos con propiedades objetivo mediante optimización topológica, con propiedades fundamentales de la física de cristales. Sobresale en este sentido la conexión entre la simetría de la microarquitectura y la simetría de la respuesta efectiva. Esta metodología es aplicada al diseño de metamateriales elásticos lineales con propiedades extremas, lo que se entiende como materiales cuyas propiedades se ubican en la frontera de lo realizable. Los resultados logrados, permiten la identificación de características geométricas clave en el desempeño. Este aprendizaje conlleva a la propuesta de microarquitecturas parametrizadas basadas en las topologías optimizadas. Estos nuevos metamateriales son mas simples que los originales y logran un mejor desempeño efectivo. Posteriormente, se aborda el diseño de metamateriales elásticos no lineales capaces de liberar energía extrínsecamente. El objetivo buscado es encontrar microarquitecturas que maximicen la capacidad de liberar energía. El comportamiento efectivo de estos materiales es no convexo en términos de energía de deformación, por lo que no es aceptable utilizar técnicas de homogeneización tradicionales. Como primera solución, se propone un modelo subrogado que reduce considerablemente el costo computacional de la evaluación de volúmenes de muestreo que incluyen un alto número de celdas unidad. Además, se expone una concepción novedosa del análisis multiescala necesario para este tipo de metamateriales, el cual involucra la relajación de funciones de energía no convexas y establecer variables internas, y está concebido como un modelo generalizado estándar en la macroescala. Se muestran también los pasos dados en la dirección de optimizar topológicamente estos compuestos y las dificultades encontradas.

Seis trabajos completos surgen como resultado de los estudios de esta tesis, cinco de ellos publicaciones en revistas y una publicación en un congreso internacional.

# Abstract

This thesis addresses the problem of the computational design of mechanical metamaterials in linear and nonlinear elastic regimes, oriented to various effective properties. Metamaterials are a special composite material type, conceived in two distinct length scales. A higher scale or macroscale, where the outstanding apparent responses are manifested and where the material can be exploited for specific applications, and a lower scale or microscale, where the geometric distribution of its constituents can be seen and where it behaves like a structure. The study and design of metamaterials therefore includes the analysis of both scales.

In this thesis, various numerical tools and strategies are developed that assist the computational topological design of mechanical metamaterials. To demonstrate the validity of these techniques, highly demanding problems are chosen for performance on the macroscale, which is understood as extreme behavior of metamaterials. Firstly, a methodology based on matching metamaterials with crystals is proposed. This assists the inverse homogenization methodology, that is, the design of compounds with target properties through topology optimization, through fundamental properties of crystal physics. In this sense, the connection between the symmetry of microarchitecture and the symmetry of effective response stands out. This methodology is applied to the design of linear elastic metamaterials with extreme properties, which are understood as materials whose properties are located on the boundary of what is feasible. The achieved results allow the identification of key geometric features in performance. This learning leads to the proposal of parameterized microarchitectures based on optimized topologies. These new metamaterials are simpler than the originals and achieve better effective performance. Subsequently, the design of nonlinear elastic metamaterials capable of extrinsically releasing energy is addressed. The objective is to find microarchitectures that maximize the capacity to release energy. The effective behavior of these materials is non-convex in terms of strain energy, so it is not acceptable to use traditional homogenization techniques. As a first solution, a surrogate model is proposed that considerably reduces the computational cost of evaluating sampling volumes that include a high number of unit cells. In addition, a novel conception of the multiscale analysis necessary for this type of metamaterials is presented, which involves the relaxation of non-convex energy functions and establishing internal variables, and it is conceived as a standard generalized model on the macroscale. The steps taken in the direction of topologically optimizing these compounds and the difficulties encountered are also shown.

Six complete works emerge as a result of the studies of this thesis, five of them publications in journals and one publication in an international conference.

# Índice general

# Índice de figuras

# Índice de tablas

# Parte I

# Introducción

# Capítulo 1

# Introducción

## 1.1. De qué trata esta tesis

A lo largo del tiempo, el progreso de la humanidad ha estado fuertemente ligado a la disponibilidad de materiales para llevar a cabo funciones específicas a cada momento histórico. Tal es así, que nuestro nivel de vida actual necesita del entendimiento de una variedad inmensa de materiales como metales, cerámicos, y plásticos, sólo para nombrar algunos. Como señalan Ashby y Jones [1], la innovación en ingeniería usualmente significa el uso inteligente de un nuevo material, donde la novedad puede deberse al uso de un material conocido en una aplicación original, como al desarrollo de materiales no existentes previamente. En este sentido, la ingeniería y ciencia de materiales se centran en la búsqueda de mejorar el desempeño de los materiales actuales y en el desarrollo de nuevos materiales. En este contexto, el concepto de material compuesto aparece en las últimas décadas como una estrategia exitosa de combinar dos o más constituyentes, explotando las propiedades individuales de cada uno, de manera de lograr un comportamiento conjunto de características superadoras. Particularizando en compuestos donde la interacción entre sus constituyentes ocurre de forma mecánica, se pueden mencionar el hormigón armado que combina la resistencia a compresión y durabilidad del hormigon con la resistencia a tracción y ductilidad del acero, los cermets que son capaces de soportar altas temperaturas y abrasión como los cerámicos pero gozan de la maleabilidad de los metales que lo conforman, o los polímeros reforzados con fibras de vidrio que constituyen un material liviano, resistente y de buena resistencia a la corrosión. Es por esto que, el actual y constante requerimiento de la sociedad en conseguir nuevos estándares de bienestar y confort en todos los órdenes de la vida (transporte, vivienda, comunicación, ocio, salud), establece el desafío de concebir materiales con nuevas propiedades, muchos de ellos dentro del ámbito de los materiales de alta tecnología.

De la mano del enorme avance tecnológico en los procesos de manufactura aditiva tridimensional, a partir de técnicas como litografía óptica, sintetizado láser, polimerización, impresión por chorro de tinta o impresión por fusión en caliente, entre tantas otras (ver las revisiones hechas por Truby y Lewis [2], Kadic et al. [3]), cobra importancia el concepto de metamateriales como una nueva filosofía de concepción de compuestos para la obtención de propiedades sobresalientes. La idea de metamaterial alude a materiales que se analizan en dos escalas de longitud bien diferenciadas. De manera muy intuitiva, se puede mencionar que la escala superior o macroescala, refiere al material "visto lo suficientemente lejos" para que parezca homogéneo. Es en esta escala donde se manifiestan las respuestas aparentes excepcionales de estos compuestos y donde el material puede ser explotado para aplicaciones específicas necesarias de un alto desempeño. Por otra parte, la escala inferior o microescala, alude al material "visto lo suficientemente cerca" para notar la distribución geométrica, típicamente periódica, de sus constituyentes, lo que se denomina como microarquitectura. En esta escala, la microarquitectura del metamaterial se comporta básicamente como una estructura sometida a un sistema apropiado de cargas. El diseño por metamateriales se basa, por lo tanto, en un diseño meticuloso de la microarquitectura en

la microescala, de manera que el material en la macroescala exhiba las propiedades deseadas[1]. Lo destacable de esta estrategia es que permite lograr respuestas aparentes inusuales y en casos contraintuitivas si se las compara con lo disponible en la naturaleza o en los compuestos tradicionales. Limitándose al campo de los metamateriales mecánicos, dentro de la muy extensa lista de propiedades conseguidas se destacan: módulo de Poisson negativo o auxeticidad en régimen lineal y no lineal [4–6], módulo de corte nulo [7, 8], compresibilidad lineal negativa [9, 10], rigidez negativa incremental [11], formación de patrones y cambios en la morfología de la microarquitectura [12, 13], liberación de energía extrínseca en materiales hiperelásticos [14, 15], manipulación de ondas elásticas en diferentes tipos de estructuras [16]. Revisiones muy completas sobre distintos tipos de metamateriales fueron hechas por Kochmann y Bertoldi [17], Yu et al. [18], Li et al. [19].

Dada la naturaleza de los metamateriales de existir en distintas longitudes de escala, su estudio requiere de técnicas específicas que permitan la conexión entre ellas. No sería computacionalmente posible resolver la respuesta de una estructura constituida por un metamaterial si se tienen que considerar todos los detalles de la microarquitectura en la escala superior. Esto implica determinar la respuesta constitutiva efectiva del material en la macroescala (o una aproximación), a partir de conocer la microarquitectura en la microescala. Las estrategias de análisis multiescala, mucho más generales que el campo de metamateriales, se centran en realizar este enlace entre escalas, y constituyen un área de estudio todavía en desarrollo, con más de 60 años de progreso. Estos métodos han evolucionado desde los aportes fundacionales de Eshelby [20] basado en la aproximación de campos de tensiones y deformaciones constantes de a tramos en cada constituyente del compuesto, y Hill [21], Hashin y Shtrikman [22] direccionados a la obtención de cotas a los módulos elásticos a partir de principios generales para comportamiento lineal elástico, pasando por las cotas variacionales para compuestos no lineales como las propuestas por Castañeda [23], y por los métodos computacionales basados en la identificación de volúmenes representativos como el de Michel et al. [24], hasta los métodos actuales de homogeneización computacional de alto orden o aquellos basados en datos (data-driven) y aprendizaje de máquina (machine learning), revisados, por ejemplo, en los trabajos de Matouš et al. [25], Bishara et al. [26]. Siendo que las propiedades sobresalientes de los metamateriales se deben, en general, a microarquitecturas complejas, su análisis multiescala queda restringido a los métodos de homogeneización computacional que toleren una descripción precisa de la geometría en la microescala. Asimismo, la estrategia particular a utilizar depende de la naturaleza del fenómeno a resolver. A modo de ejemplo, el método para homogeneizar la respuesta de un material con fractura en la microescala, como el propuesto por Toro et al. [27], difiere de la estrategia seguida para homogeneizar un medio poroso saturado, como el presentado por Anonis et al. [28]. En este sentido, no todos los comportamientos microescala cuentan con técnicas de homogeneización unificadas. Como regla general para materiales periódicos, se puede notar que técnicas de homogeneización basadas en el promediado de volúmenes representativos coincidentes con las celdas unitarias del material son aceptables mientras el comportameinto efectivo tenga una respuesta convexa en términos de energía de deformación vs. deformación. Si esta premisa no se satisface, entonces este tipo de técnicas dejan de ser válidas y se debe recurrir a metodologías donde el numero de celdas unitarias comprendidas en el volúmen representativo a considerar en el análisis de homogeneización pasa a constituir una nueva variable del problema.

Por otra parte, la disponibilidad conjunta de las diversas técnicas de manufacturabilidad y de las estrategias de análisis multiescala impone una alta exigencia en las técnicas de diseño de la microarquitectura para lograr los desempeños esperados. Si bien el diseño basado en la imaginación o la intuición suele ser el primer paso en la propuesta de nuevas funcionalidades y ha sido el responsable de una enorme cantidad de propuestas, este enfoque tiene una evidente limitación. Esto denota la importancia de contar con procedimientos, reglas o estrategias, que guíen el proceso de diseño de estos compuestos. Una estrategia muy utilizada y de gran versatilidad es la optimización topológica, la cual consiste en

[1] Existen metamateriales denominados jerárquicos, en los cuales se extiende la idea de las longitudes de escalas a más de dos. A pesar de la validez del marco teórico, llevar estos materiales a la realidad implica un salto tecnológico aún más desafiante.

encontrar la mejor distribución posible de dos o más materiales para mejorar algún aspecto de una estructura. Revisiones muy completas de esta técnica fueron hechas por Bendsoe y Sigmund [29], Sigmund y Maute [30], Van Dijk et al. [31], Liu et al. [32]. Similarmente a los métodos multiescala, los enfoques de optimización topológica son mucho más generales que su uso en el campo de metamateriales, donde la "estructura" que se optimiza es precisamente la microarquitectura del metamaterial. La optimización topológica ha sido utilizada extensamente como herramienta de asistencia para el diseño de materiales, logrando comportamientos tan variados como máxima resistencia a cargas de compresión con consideraciones de pandeo en la microescala [33], manipulación del ancho de banda en materiales fonónicos [34], y respuesta tensión-deformación prestablecida con desformaciones finitas incorporando autocontacto de la microarquitectura [35], e incluso abriendo la posibilidad a diseños con una multiplicidad de constituyentes en la microescala de acuerdo a lo desarrollado por Onco y Giusti [36]. El acople con los métodos multiescala reside en que son estos últimos los que proporcionan la información necesaria para el cálculo de funciones objetivo (es decir, la propiedad efectiva deseada) y las sensibilidades, ambas necesarias para todo problema de optimización basado en gradientes. Esto implica que no contar con estrategias de homogeneización adecuadas para el problema a analizar, invalida la posibilidad de la optimización topológica.

Esta tesis se orienta a contribuir al desarrollo de herramientas numéricas que faciliten el diseño computacional de metamateriales mecánicos y el entendimiento de su comportamiento en la macroescala. En particular, se estudian metamateriales elásticos de comportamiento lineal y no lineal, donde el objetivo en ambos casos es lograr un comportamiento tan extremo como sea posible.[2] De acuerdo a los objetivos de diseño elegidos, se verá que en el caso del problema de metamateriales lineales, la técnica de homogeneización multiescala está bien establecida y es posible formular un problema de optimización topológica. Por el contrario, en el caso no lineal, no se cuenta con estrategias multiescala adecuadas, por lo cual el enfoque por optimización topológica está limitado y se orienta el diseño desde distintas perspectivas. En ambos casos, la imposición de simetrías a la microarquitectura funcionará como factor fundamental de orden en la distribución de los constituyentes en la microescala, con implicancias físicas relevantes.

## 1.2. Objetivos

### 1.2.1. Objetivo general

A partir del desarrollo e implementación de técnicas matemáticas y herramientas computacionales, se busca diseñar de manera óptima la microarquitectura de materiales compuestos avanzados (metamateriales) con el fin de alcanzar comportamientos mecánicos lineal y no lineal sobresalientes. Estos comportamientos son evaluados en la macroescala a partir de técnicas apropiadas a cada problema.

### 1.2.2. Objetivos particulares

- Desarrollar una técnica de diseño basada en optimización topológica asistida por simetrías para la obtención de microarquitecuras de metamateriales elásticos actuantes en régimen lineal.

- Aplicar esta técnica de optimización al problema de G-clausura de materiales isotrópicos compuestos por dos fases elásticas lineales, es decir a la obtención de metamateriales cuya respuesta efectiva aproxime los límites de las propiedades alcanzables.

- Desarrollar una metodología computacional para el análisis de la microescala de metamateriales mecánicos con transiciones de fase elásticas generadas por inestabilidades geométricas del tipo

[2] Cómo debe entenderse la noción de extremo en cada caso se explica oportunamente en el cuerpo de la tesis.

snap-through. El estudio de la microescala incluye fenómenos como la formación de patrones, falta de unicidad de la solución y la liberación de energía elástica extrínseca.

- Contribuir al entendimiento de un análisis multiescala adecuado para metamateriales con inestabilidades en la microescala a partir de la formulación de modelos materiales macroescala con dos potenciales.

- Lograr diseños de microarquitecturas parametrizadas simples, aptas para manufactura, en los casos de comportamiento lineal y no lineal.

## 1.3. Estructura de la tesis

Esta tesis está escrita dentro del formato de *tesis por compilación*, en la cual se busca lograr un vínculo asociativo sólido con los trabajos publicados. El cuerpo de la tesis se escribió con la intención de presentar brevemente al lector la secuencia de aprendizajes realizados durante el doctorado, plasmando lo más fielmente posible las dificultades encontradas en el proceso de investigación y el porqué de las soluciones propuestas. Se espera que esto facilite la posterior lectura de las publicaciones logradas, las cuales presentan los aportes concretos conseguidos y son replicadas en los Apéndices. En general, se buscó evitar repetir la explicación de metodologías o la exposición de resultados ya presentados en los artículos publicados. Es por esto que, con el propósito de apuntalar los conceptos principales, algunos capítulos cuentan con material no publicado. Un caso especial de esto ocurre en el último capítulo destinado a la exposición de los aportes de la tesis, donde se presenta trabajo aún en desarrollo.

La estructura general de la tesis está conformada por cinco partes: (I) Introducción, (II) Preliminares, (III) Aportes al diseño computacional de metamateriales mecánicos, (IV) Conclusiones, y (V) Apéndices, las cuales se explican a continuación:

- La “Parte I: Introducción” expone el contexto general de esta tesis, estableciendo los objetivos planteados. Incluye un único capítulo.

- La “Parte II: Preliminares” se incorpora a la tesis con el propósito de hacerla razonablemente autocontenida, pero sin necesariamente modificar el estilo de tesis por compilación. El objetivo de su único capítulo es abarcar una suma de conceptos establecidos en la literatura, los cuales no son aportes de esta tesis, y que sumados constituyen la teoría en la que se sostiene la misma, pero que mayormente no se incluyen en las publicaciones debido a su carácter de conocimiento general. Se presentan distintos campos y tópicos estudiados durante el doctorado, que incluyen: restricciones a los modelos constitutivos, teoría multiescala basada en RVE, fundamentos de simetrías de cristales, fundamentos de optimización topológica, y nociones del modelo generalizado estándar de materiales. Aunque durante la tesis se hace referencia a este material, el lector familiarizado con estos conceptos puede perfectamente obviar este capítulo.

- La “Parte III: Aportes al diseño computacional de metamateriales mecánicos” contiene los cuatro capítulos que refieren a los aportes propiamente dichos de esta tesis. Los capítulos 3 y 4 están destinados al problema de metamateriales en régimen lineal, mientras que los capítulos 5 y 6 al problema de metamateriales en régimen no lineal.

- La “Parte IV: Conclusiones” esta constituida por un breve capítulo que resume las contribuciones de este trabajo.

- La “Parte V: Apéndices” replica los seis trabajos publicados que conforman esta tesis, cinco de ellos publicaciones en revistas internacionales y el restante un trabajo en la edición 2022 del Congreso Mundial de Mecánica Computacional.

Finalmente, se presenta en la Figura 1.1 una secuencia de lectura sugerida en función del contenido de los capítulos en relación a las publicaciones.

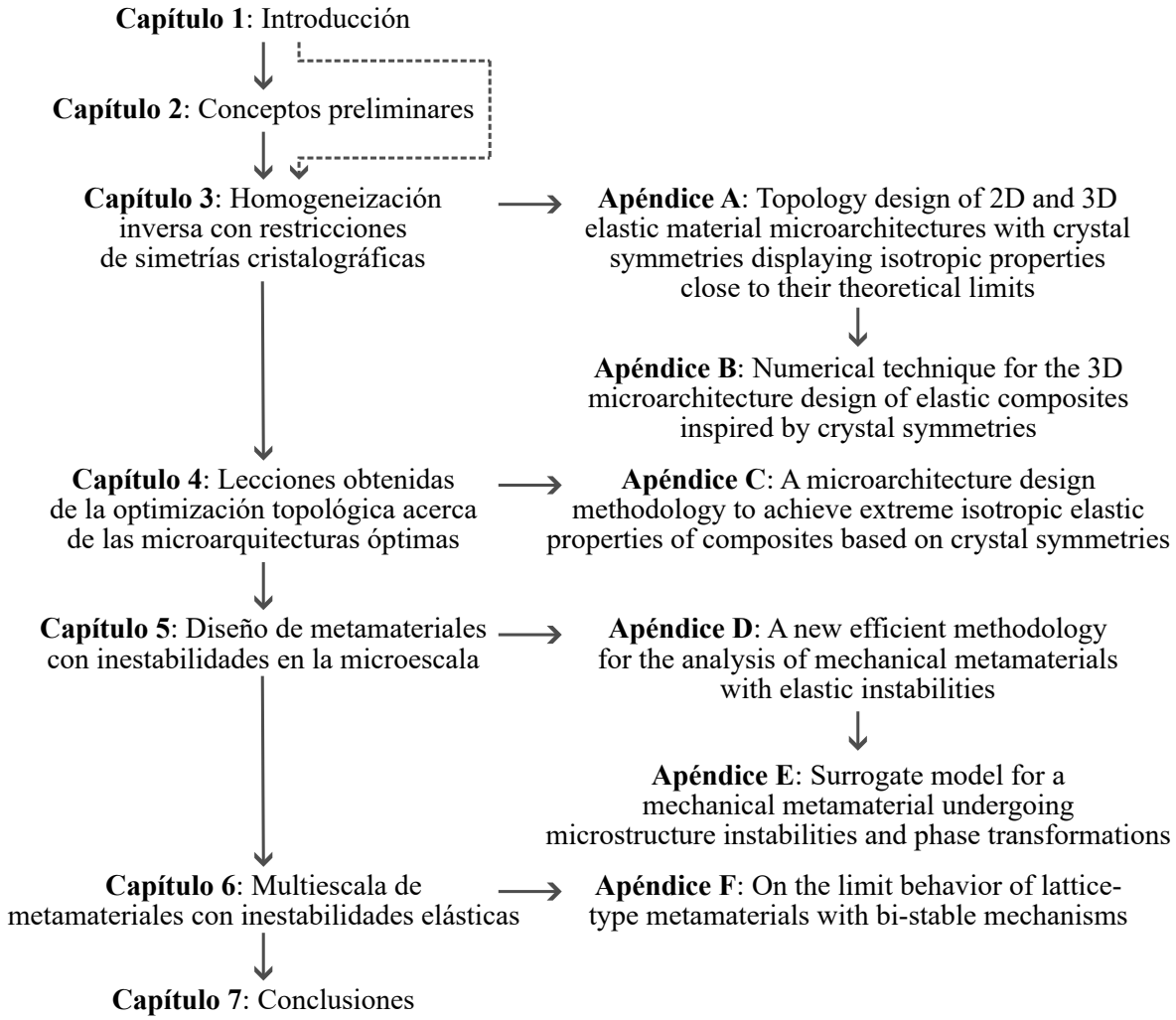


**Figura 1.1:** Estructura de la tesis, con secuencia de lectura sugerida.

# Parte II

# Preliminares

# Capítulo 2

# Conceptos preliminares

## 2.1. Introducción

El propósito de este capítulo es presentar de manera resumida distintas temáticas y herramientas que fueron utilizadas para generar los aportes de esta tesis y son necesarias para su comprensión. Siendo que estos temas están bien establecidos en la literatura, la mayor parte de este contenido no es replicada en los artículos, por lo cual la lectura de este capítulo facilita el entendimiento de las publicaciones sin necesariamente recurrir a trabajos anteriores de otros autores. Sin embargo, no se pretende de ninguna manera hacer una descripción abarcativa, y para mayores detalles si debe recurrirse a la bibliografía. Los tópicos presentados en este capítulo están ordenados de la siguiente manera. La Sección 2.2 está dedicada a restricciones a los modelos constitutivos para cumplir con criterios de estabilidad y existencia. La Sección 2.3 presenta un resumen de la teoría multiescala basada en RVE. La Sección 2.4 muestra fundamentos mínimos de la física de cristales apuntando al rol de las simetrías. La Sección 2.5 aborda nociones básicas de optimización topológica, haciendo foco en el algoritmo utilizado en esta tesis y el problema de diseño de metamateriales. Por último, la Sección 2.6 está destinada a un planteo mínimo del modelo generalizado estándar de materiales.

## 2.2. Breve repaso sobre restricciones constitutivas

La formulación de relaciones contitutivas en el marco de materiales hiperelásticos (elasticidad de Green) esta condicionada por varias restricciones sobre la función de energía $W(\mathbf{F})$, siendo $\mathbf{F}$ el tensor gradiente de deformación, el cual pertenece al espacio $\mathbb{M}^3_+$ de tensores reales de orden 3 con determinante positivo. En este sentido, los módulos tangente de la relación constitutiva resultan determinantes en la naturaleza de la solución a las ecuaciones diferenciales de equilibrio. En esta sección se revisan brevemente las restricciones relevantes a esta tesis con las que deben cumplir los modelos constitutivos de manera que resulten físicamente admisibles. Los conceptos que aquí se repasan resultan luego la base de la discusión en la búsqueda de un desempeño extremo de los materiales diseñados en esta tesis bajo el concepto multiescala. El desarrollo que se presenta sigue mayormente el texto de Ogden [37].

### 2.2.1. Nociones de estabilidad

Dado un cuerpo con configuración de referencia $\mathcal{B}_0 \subset \mathbb{R}^3$ y configuración actual (deformation en inglés) $\mathbf{x} = \boldsymbol{\chi}(\mathbf{X})$, siendo $\mathbf{X} \in \mathcal{B}_0$ las posiciones de los puntos materiales en la configuración de referencia, el criterio clásico para definir la estabilidad de $\boldsymbol{\chi}$, consiste en que dicha configuración de equilibrio es estable si el funcional de energía $E$ (energía potencial total) es minimizado dentro del

espacio de configuraciones cinemáticamente admisibles $\boldsymbol{\chi}'$, es decir:

$$E\{\boldsymbol{\chi}'\} \geq E\{\boldsymbol{\chi}\} \quad \forall \boldsymbol{\chi}' \text{ cinemáticamente admisible.} \tag{2.1}$$

En general, no existe una correspondencia entre estabilidad y unicidad (soluciones estables pueden no ser únicas, y soluciones únicas pueden no ser estables). La condicion (2.1) es, en general, muy restrictiva como una condición necesaria de estabilidad global de $\boldsymbol{\chi}$. Un ejemplo de esto que resulta de especial interés para el desarrollo de esta tesis consiste en que existen ocasiones en que un cuerpo, para determinadas condiciones de borde, puede presentar varias configuraciones de equilibrio metaestables (esta idea se explota en el marco de metamateriales en los Capítulos 5 y 6). Desde el punto de vista del funcional de energía, esto se corresponde a mas de un mínimo (local) del funcional, donde una de estas configuraciones suele ser energéticamente favorable a las demás. Sin embargo, la condición (2.1) sigue siendo válida como un criterio de estabilidad local, si se limita a $\boldsymbol{\chi}'$ a una vecindad de $\boldsymbol{\chi}$. De esta manera se la utiliza como criterio de estabilidad infinitesimal o local.

Para un problema de equilibrio incremental, con condiciones de borde mixtas y cargas muertas, el criterio (2.1) puede rescribirse como:

$$\int_{\mathcal{B}_0} tr\{(\mathcal{C}\ \delta\mathbf{F})\delta\mathbf{F}\}dV \geq 0 \quad \forall \delta\boldsymbol{\chi} \text{ cinemáticamente admisible} \quad , \tag{2.2}$$

donde $\mathcal{C} = \partial^2 W/\partial \mathbf{F}^2$ es el tensor de módulos elásticos tangente, $\delta\mathbf{F} = Grad\ \delta\boldsymbol{\chi}$, y $\delta\boldsymbol{\chi} = \boldsymbol{\chi}' - \boldsymbol{\chi}$ es un incremento admisible desde la configuración de equilibrio. Esta forma de la condición de equilibrio infinitesimal refleja mas claramente la imposición sobre el tensor $\mathcal{C}$. Esta restricción es integral en el sentido de que asegura la estabilidad del cuerpo $\mathcal{B}_0$ en su totalidad, por lo cual se la denomina condición de estabilidad integral. Para el caso particular de un cuerpo de material y deformación homogéneos, al considerar una deformación incremental con gradiente uniforme, la condición de estabilidad local deriva en:

$$tr\{(\mathcal{C}\ \delta\mathbf{F})\delta\mathbf{F}\} \geq 0 \quad , \tag{2.3}$$

lo cual establece que $\mathcal{C}$ debe ser semi-definido positivo, condición suficiente para lograr localmente estabilidad integral. Al contrario de la condición (2.2), la restricción de estabilidad (2.3) tiene naturaleza local en el dominio, y se conoce como condición de estabilidad puntual.

Si se considera $\delta\mathbf{F}$ proporcional a un tensor de rango uno $\mathbf{m} \otimes \mathbf{N}$, donde $\mathbf{m}$ y $\mathbf{N}$ son vectores Euleriano y Lagrangiano arbitrarios, la condición (2.3) toma la forma:

$$tr\{[\mathcal{C}\ (\mathbf{m} \otimes \mathbf{N})]\ (\mathbf{m} \otimes \mathbf{N})\} \geq 0 \quad , \tag{2.4}$$

conocida como condición de Legendre-Hadamard y se cumple cuando vale para todo $\mathbf{m} \otimes \mathbf{N} \neq \mathbf{0}$. En caso que la desigualdad (2.4) se verifique de manera estricta, se denomina condición de elipticidad fuerte, y tanto la función de energía de deformación $W(\mathbf{F})$ como las ecuaciones de gobierno se denominan fuertemente elípticas si $\mathcal{C}$ la satisface para todo $\mathbf{F}$. La condición de elipticidad fuerte es otra medida de la estabilidad del material ya que impone en el material velocidades de propagación reales para ondas planas infinitesimales (estas velocidades surgen como autovalores del tensor acústico). Como se presenta a continuación para el caso de materiales elásticos en régimen lineal, la condición de estabilidad fuerte es menos restrictiva que la condición de definido positivo.

La estabilidad de los cuerpos y los materiales es una característica central a esta tesis. En los Capítulos 5 y 6 se aprovecha la pérdida de estabilidad para lograr características sobresalientes como disipación de energía en compuestos elásticos. Además, resulta iluminador particularizar las restricciones de definido positivo y de elipticidad al caso de elasticidad lineal isotrópica. Esto permite ganar una noción intuitiva de las diferentes implicancias de ambas condiciones, las cuales serán exploradas oportunamente en los próximos capítulos.

**Régimen lineal elástico isotrópico**

Al analizar el comportamiento lineal del material, se hace coincidir la configuración actual con la configuración de referencia (sin tensiones) del material. En este escenario, las componentes de $\mathcal{C}$ son constantes materiales, independientes de la deformacion. Si además se asume un material isotrópico, las componentes de este tensor resultan:

$$C_{ijkl} = \lambda\delta_{ij}\delta_{kl} + \mu(\delta_{ik}\delta_{jl} + \delta_{il}\delta_{jk}) \quad , \tag{2.5}$$

donde $\lambda$ y $\mu$ son las constantes de Lamé. De mayor utilidad para esta tesis será considerar el par ($\kappa$, $\mu$), donde $\kappa = \lambda + 2\mu/3$ es el módulo de compresibilidad, y $\mu$ es el módulo de corte. Siguiendo estas definiciones, la condición de definido positivo (2.3) (estabilidad puntual) puede reescribirse como:

$$\mu > 0 \quad , \quad \kappa > 0 \quad . \tag{2.6}$$

Es posible, además, expresar estas restricciones en el par ($\nu$, $E$), donde $\nu = [3\kappa - 2\mu]/[2(3\kappa + \mu)]$ es el coeficiente de Poisson, y $E = [9\kappa\mu]/[3\kappa + \mu]$ es el módulo de elasticidad. En este caso la condición de definido positivo establece los límites:

$$E > 0 \quad , \quad -1 \leq \nu \leq 0.5 \quad . \tag{2.7}$$

Las cotas (2.6) y (2.7) establecen que, un cuerpo de material homogéneo necesita que los tres módulos materiales sean positivos para ser estable, lo cual es físicamente razonable. Como comportamiento peculiar, nótese que un material sólido con $\mu \to 0$ se comporta aproximadamente como un fluido. Asimismo, también es lógica la cota superior de $\nu \leq 0.5$, que en caso de ser superada permitiría que un material se encoja volumétricamente ante un alargamiento longitudinal. Por el contrario, menos intuitiva resulta la cota inferior, que habilita la posibilidad de coeficientes de Poisson negativos, es decir, materiales que ante un estiramiento longitudinal, se ensanchen transversalmente. Esta característica se conoce como auxeticidad. En los Capítulos 3 y 4 se explora el diseño de materiales que aproximen este tipo de comportamiento límite, y sus análogos bidimensionales.

Complementariamente, la condición de elipticidad fuerte (2.4) se reduce a:

$$\mu > 0 \quad , \quad \kappa + 4/3\mu > 0 \quad , \tag{2.8}$$

la cual en el espacio ($\nu$, $E$), amplia el conjunto admisible (2.7) con:

$$E > 0 \quad , \quad \nu > 1 \quad , \tag{2.9}$$
$$E < 0 \quad , \quad \nu < -1 \quad . \tag{2.10}$$

Es claro que la condición de definido positivo (2.6) es más restrictiva que la condición de elipticidad fuerte (2.8). La Figura 2.1 muestra los espacios de módulos admisibles de acuerdo a los criterios de positivo definido y de elipticidad fuerte.

La condición de elipticidad fuerte amplía, en ciertas circunstancias, el abanico de propiedades materiales factibles. Tanto para la situación en que un cuerpo homogéneo sea rígidamente restringido en todo su contorno, o en el caso de inclusiones dentro de un cuerpo heterogéneo que pueda ser integralmente estable de acuerdo con la restricción (2.2), la elipticidad fuerte se vuelve la condición suficiente para la estabilidad puntual. Esto admite, por ejemplo, en el caso de elasticidad isotrópica lineal, módulos de compresibilidad y de Young negativos (es decir, un material que al estirarlo, interiormente desarrolle esfuerzos de compresión). La posibilidad de materiales con rigidez (incremental) negativa se explora en los Capítulos 5 y 6.

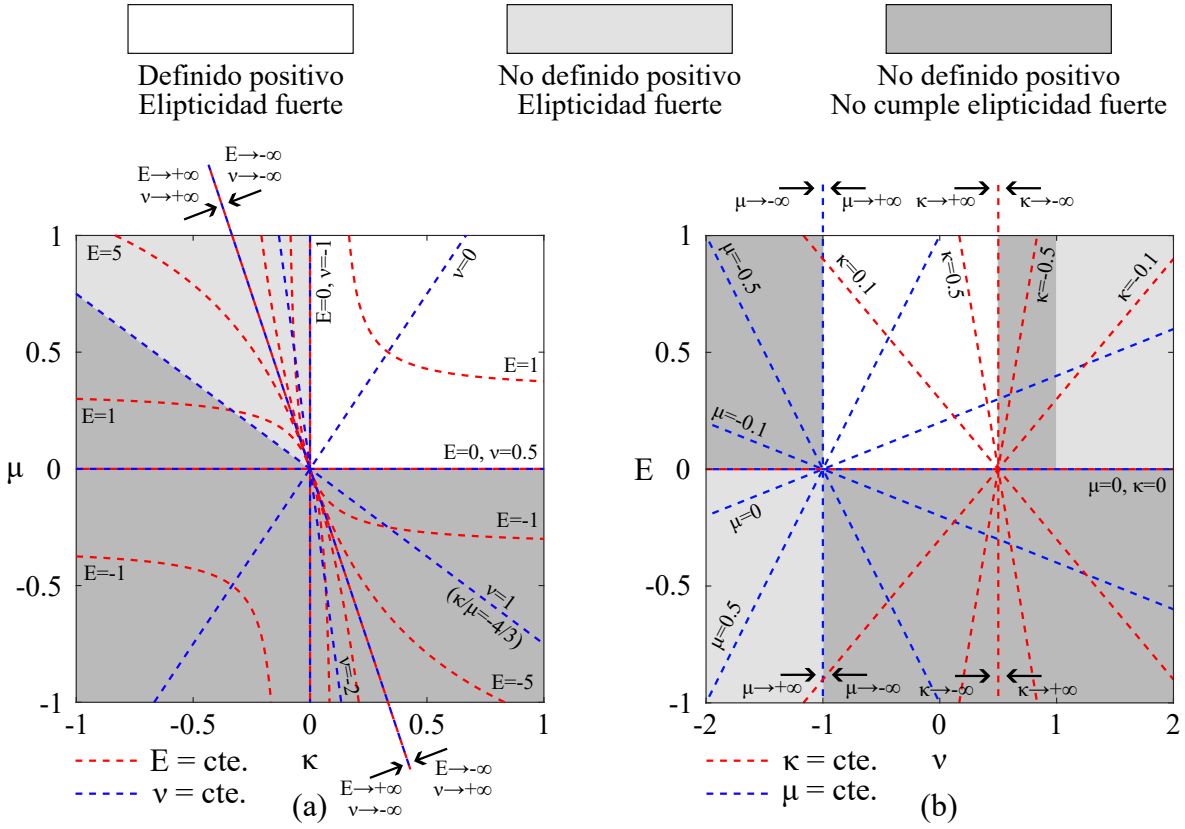


**Figura 2.1:** Espacio de módulos admisbles por restricciones de estabilidad en sólidos elásticos isotrópicos en deformaciones infinitesimales. El color del sombreado indica los diferentes criterios de estabilidad. (a) Espacio ($\kappa$, $\mu$), con cotas (2.6) y (2.7). Se muestran isocurvas de $E$ y $\nu$. (b) Espacio ($\nu$, $E$), con cotas (2.8) y (2.10). Se muestran isocurvas de $\kappa$ y $\mu$.

### 2.2.2. Nociones de existencia

La existencia de soluciones en elasticidad para problemas con condiciones de contorno está íntimamente relacionada con desigualdades constitutivas que caracterizan el grado de convexidad de la función de energía que caracteriza el modelo material [38]. La condición de convexidad ordinaria viene dada por:

$$W(\lambda \mathbf{F}_1 + (1-\lambda)\mathbf{F}_2) \leq \lambda W(\mathbf{F}_1) + (1-\lambda) W(\mathbf{F}_2) \quad , \quad \forall \mathbf{F}_1, \mathbf{F}_2 \in \mathbb{M}^3_+, \forall \lambda \in [0,1] \quad . \tag{2.11}$$

Si bien se han formulado teoremas de existencia basados en esta condición, la misma es incompatible con la condición de invariancia de observador (ver Gurtin et al. [39]) y con la propiedad de que $W(\mathbf{F}) \to +\infty$ cuando $\det \mathbf{F} \to 0^+$ (ver Ciarlet [40]). La noción menos restrictiva de cuasiconvexidad, introducida por Morrey [41], resulta apropiada para garantizar existencia de minimizadores en la siguiente expresión integral en $\mathcal{B}$ de la energía de deformación:

$$\int_{\mathcal{B}} W(\mathbf{F}) dV = |\mathcal{B}| W(\mathbf{F}) \leq \int_{\mathcal{B}} W(\mathbf{F} + \nabla \mathbf{v}) dV \quad , \quad \forall \mathbf{F} \in \mathbb{M}^3_+, \forall \mathbf{v} = \mathbf{0} \text{ en } \partial\mathcal{B} \quad , \tag{2.12}$$

donde $\mathcal{B}$ es arbitrario y $\mathbf{F}$ es constante en $\mathcal{B}$. Esta condición puede interpretarse de la siguiente manera: para un cuerpo homogéneo (compuesto de un material que cumple cuasiconvexidad) sometido a condiciones de borde $\mathbf{x} = \mathbf{F}\mathbf{X}$ en la frontera $\partial\mathcal{B}$, el estado de deformación (strain) homogénea tiene menor energía que un estado perturbado, es decir, el estádo homogéneo es minimizador absoluto de la energía total. La dificultad de considerar la condición de cuasiconvexidad reside en que está formulada como una expresión integral. La condición mas restrictiva de policonvexidad fue introducida por Ball [42], como

solución a esta dificultad. Se tiene que $W(\mathbf{F})$ es policonvexa si existe una función $\tilde{W}$ tal que:

$$W(\mathbf{F}) = \tilde{W}(\mathbf{F}, \text{adj}\mathbf{F}, \det \mathbf{F}) \quad , \tag{2.13}$$

siendo $\tilde{W}$ convexa en el conjunto $\{(\mathbf{F}, \text{adj}\mathbf{F}, \det \mathbf{F}) \in (\mathbb{M}^3 \times \mathbb{M}^3 \times \mathbb{R}), \mathbf{F} \in \mathbb{M}^3_+\}$. A modo de ejemplo, una interpretación gráfica de la policonvexidad se presenta en la Figura 2.2, para el caso particular de la función de energía correspondiente a un material hiperelástico NeoHookeano, dada por:

$$W(\mathbf{F}) = \frac{1}{2}\lambda_0(\ln(\det \mathbf{F}))^2 - \mu_0 \ln(\det \mathbf{F}) + \frac{1}{2}\mu_0(\,\text{tr}\,(\mathbf{F}^T\mathbf{F}) - 3) \quad , \tag{2.14}$$

siendo $\lambda_0$ y $\mu_0$ las constantes de Lamé iniciales del material, las cuales en este ejemplo se eligieron como unitarias. Se analizan las condiciones de convexidad y policonvexidad para una familia de tensores $\mathbf{F}$ dados por:

$$\mathbf{F} = \begin{bmatrix} 1+\alpha & \alpha & 0 \\ -\alpha & 1+\alpha & 0 \\ 0 & 0 & 1 \end{bmatrix} \quad , \tag{2.15}$$

los cuales tienen siempre determinante positivo. Para comparar los requerimientos de convexidad y policonvexidad se elijen dos tensores $\mathbf{F}_A$ y $\mathbf{F}_B$, caracterizados respectivamente por coeficientes $\alpha_A$ y $\alpha_B$. Además, el tensor de combinación convexa $\mathbf{F}_\lambda = \lambda\mathbf{F}_A + (1-\lambda)\mathbf{F}_B$ también pertenece a esta familia, siendo $\alpha_\lambda = \lambda\alpha_A + (1-\lambda)\alpha_B$. Para este ejemplo se elije $\alpha_A = 0$ y $\alpha_B = -1$. Los efectos de los tensores $\mathbf{F}_A$ y $\mathbf{F}_B$ sobre un elemento cúbico se esquematizan en la Figura 2.2(a), donde $\mathbf{F}_A$ corresponde al elemento sin deformar, y $\mathbf{F}_B$ al elemento rotado $90^o$ en sentido antihorario. La Figura 2.2(b) muestra curvas de valor constante en $W$, en un espacio $\alpha$ vs. $\det \mathbf{F}$. Estas dos variables estan naturalmente enlazadas, por lo cual solo una curva de este espacio es efectivamente admisible para los estados de deformación dados por la familia (2.15), y coincide con la sucesión de tensores a verificar para el control de la condición de convexidad (2.11) (recordar que la combinación convexa también pertence a esta familia). Esta curva se presenta en color azul entre los extremos $\mathbf{F}_A$ y $\mathbf{F}_B$, y se observa en la Figura 2.2(c) que la energía a lo largo del mismo es no convexa, por lo cual no cumple con la condición de convexidad.

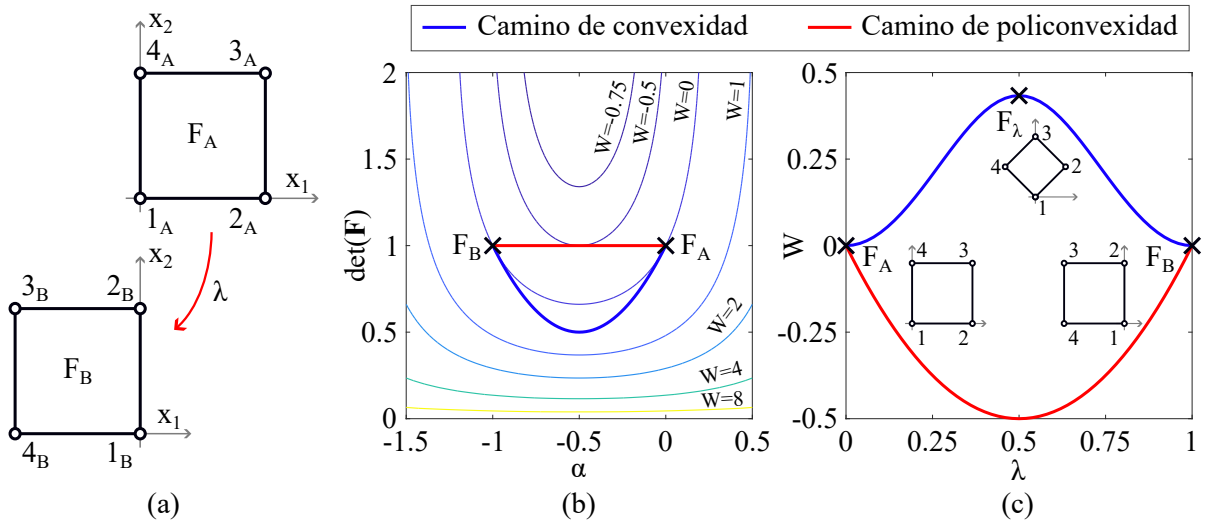


**Figura 2.2:** Ejemplo de policonvexidad. (a) Configuraciones de un elemento cúbico (en una vista 2D, y con sus vértices numerados) de acuerdo a la acción de los tensores $\mathbf{F}_A$ y $\mathbf{F}_B$. (b) Caminos recorridos de acuerdo a las condiciones de convexidad y policonvexidad. (c) Función de energía $W$ a lo largo de ambos caminos.

Por el contrario, la condición de policonvexidad exige convexidad en el espacio expandido (considerando los argumentos como variables desacopladas). El camino recorrido en este caso corresponde a la

curva roja, y la energía si es convexa a lo largo de este, verificando de esta manera la policonvexidad de la energía (al menos para esta familia de $\mathbf{F}$)

***Observación**: El camino de energía no convexo y sus correspondientes configuraciones para la serie de tensores $\mathbf{F}_\lambda$, es el mecanismo subyacente para la propuesta de metamateriales con inestabilidades elásticas en el Capítulo 6.*

Para completar las nociones de convexidad, se tiene que una condición más débil que cuasiconvexidad es la convexidad de rango uno, la cual consiste en la convexidad de la función a lo largo de un incremento en $\mathbf{F}$ con la forma de un tensor de rango uno $\mathbf{a} \otimes \mathbf{b}$ :

$$W(\mathbf{F} + \lambda \mathbf{a} \otimes \mathbf{b}) \leq \lambda W(\mathbf{F} + \mathbf{a} \otimes \mathbf{b}) + (1 - \lambda) W(\mathbf{F}) \quad , \quad \forall \mathbf{a}, \mathbf{b} \in \mathbb{R}^3, \forall \lambda \in [0, 1] \quad . \tag{2.16}$$

La convexidad de rango uno es equivalente a la condición de Legendre-Hadamard (2.4). Teniendo en cuenta las definiciones, valen las siguientes implicancias:

$$\text{convexidad} \Rightarrow \text{policonvexidad} \Rightarrow \text{cuasiconvexidad} \Rightarrow \text{convexidad de rango uno}$$

Para funciones definidas en una dimensión, las cuatro definiciones se reducen a la convexidad ordinaria. Existe una estrecha relación entre este concepto y el de estabilidad discutido en la subsección anterior. Ejemplo de esto es que, para un material elástico en régimen lineal, que el tensor constitutivo cumpla con la condición de definido positivo es equivalente a la convexidad de la función de energía. En los Capítulos 5 y 6 se presentan materiales cuya función de energía en la microescala no respeta la condición mínima de cuasiconvexidad, y se analizan las implicancias de esto en la macroescala. Además, el concepto de cuasiconvexidad resulta clave en el proceso de homogeneización de la función de energía de estos materiales para lograr el modelo macroescala propuesto en el Capítulo 6.

## 2.3. Teoría constitutiva multiescala basada en homogeneización del RVE

El propósito general del análisis multiescala es la estimación de las propiedades efectivas macroscópicas a partir del conocimiento de la microarquitectura, es decir, la distribución geométrica de las fases constituyentes en la microescala y sus propiedades materiales. En esta sección se presentan los fundamentos centrales a la teoría multiescala basada en RVE, herramienta recurrente a todo el desarrollo de esta tesis.

### 2.3.1. Elemento de volumen representativo: RVE

La idea principal detrás de esta teoría es la hipótesis de que existen dos longitudes de escala bien diferenciadas, ver Figura 2.3. Por un lado la escala superior o macroescala, donde el cuerpo $\Omega$ tiene una longitud característica $L$. Todo punto $x$ del cuerpo en la macroescala está asociado con un RVE local en la escala inferior o microescala, caracterizado por un dominio $\Omega_\mu$, con una longitud característica $L_\mu$, y se cumple que $L \gg L_\mu$.

Desde un punto de vista mecánico, el RVE puede entenderse como la mínima muestra del compuesto que contiene suficientes mecanísmos de deformación como para ser considerada estadísticamente típica de la combinación de fases, y cuya respuesta efectiva promedio no cambia ante un aumento en el tamaño de dicha muestra. Es decir, un RVE debe ser lo suficientemente grande como para incluir toda la información relevante de la microestructura, y, sin embargo, no mas grande que lo estrictamente necesario. Esta idea de que el tamaño del RVE debe tener una cota superior cobra importancia para asegurar la separación de escalas. Al mismo tiempo, en los análisis multiescala basados en métodos numéricos, considerar el mínimo volumen posible tiene un beneficio evidente desde el costo de cálculo implicado. Siguiendo la idea original de Hill [21], se está en presencia de un RVE cuando se obtiene la misma propiedad efectiva

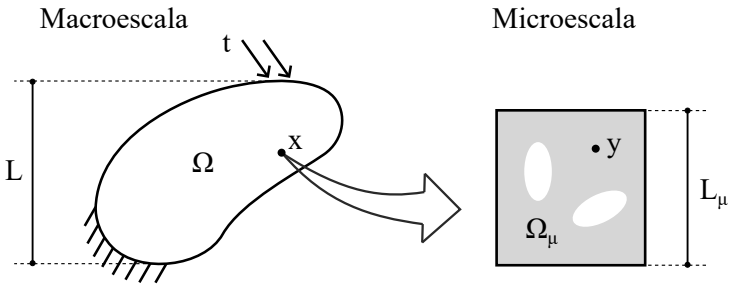


**Figura 2.3:** Cuerpo macroscópico con material aparente, con una geometría asociada en una longitud de escala inferior.

indistintamente si se aplica un estado de tracción uniforme o desplazamiento lineal sobre la frontera del volumen.

### 2.3.2. Marco axiomático de la teoría variacional multiescala clásica

La teoría multiescala referida como la teoría clásica, ha sido desarrollada de manera abarcativa en los trabajos de De Souza Neto y Feijóo [43, 44], Perić et al. [45]. En esta sección se repasan los conceptos mas fundamentales necesarios para el entendimiento de esta tesis. Generalizaciones de esta teoría se han presentado, por ejemplo, en Sánchez et al. [46], De Souza Neto et al. [47], Blanco et al. [48]. Asimismo el reporte de Taroco et al. [49] presenta una explicación profunda y detallada de los principios aquí discutidos. Los desarrollos que se presentan a continuación asumen la ausencia de fuerzas de inercia y de cuerpo.

El tratamiento formal de la formulación multiescala se sustenta en tres pasos: (i) postulado de la descripción cinemática a nivel micro; (ii) imposición de las restricciones de admisibilidad cinemática; y (iii) postulado del Principio Variacional de Hill-Mandel para establecer la equivalencia energética en términos de potencias virtuales entre micro y macro escalas. Estos pasos fundamentales son discutidos a continuación en el contexto simplificado de desplazamientos infinitesimales.

#### (i) Descripción cinemática en la microescala

Se asume en primer lugar, que el campo de desplazamientos en la microescala $\boldsymbol{u_\mu}(\boldsymbol{y})$, siendo $\boldsymbol{y} \in \Omega_\mu$ las coordenadas a nivel micro, puede descomponerse como:

$$\boldsymbol{u_\mu}(\boldsymbol{y}) = \boldsymbol{u} + \bar{\boldsymbol{u}}_{\boldsymbol{\mu}}(\boldsymbol{y}) + \tilde{\boldsymbol{u}}_{\boldsymbol{\mu}}(\boldsymbol{y}) \quad , \tag{2.17}$$

donde $\boldsymbol{u}$ es un desplazamiento de cuerpo rígido constante del RVE coincidente con el desplazamiento del punto macro $\boldsymbol{x}$ asociado, $\bar{\boldsymbol{u}}_{\boldsymbol{\mu}}(\boldsymbol{y}) := \boldsymbol{\varepsilon y}$ es un campo lineal dependiente de la deformación macro $\boldsymbol{\varepsilon}$, y $\tilde{\boldsymbol{u}}_{\boldsymbol{\mu}}(\boldsymbol{y})$ es el campo de fluctuaciones de desplazamientos.

Siendo que el campo de deformaciones (strains) en la microescala surge de:

$$\boldsymbol{\varepsilon_\mu} = \nabla^s \boldsymbol{u_\mu} \quad , \tag{2.18}$$

donde $\nabla^s$ es el operador gradiente simétrico respecto de las coordenadas micro $\boldsymbol{y}$, el campo de deformaciones en la microescala toma la forma:

$$\boldsymbol{\varepsilon_\mu}(\boldsymbol{y}) = \nabla^s \bar{\boldsymbol{u}}_{\boldsymbol{\mu}} + \nabla^s \tilde{\boldsymbol{u}}_{\boldsymbol{\mu}} = \boldsymbol{\varepsilon} + \tilde{\boldsymbol{\varepsilon}}_{\boldsymbol{\mu}}(\boldsymbol{y}) \tag{2.19}$$

De aquí se interpreta que el campo de deformaciones micro es la suma de la deformación macro $\boldsymbol{\varepsilon}$ uniforme, que sería el campo de deformaciones presente en caso que el RVE fuera homogéneo, y un

campo de fluctuaciones en deformaciones $\tilde{\boldsymbol{\varepsilon}}_{\boldsymbol{\mu}}(\boldsymbol{y})$, que oscila alrededor de este valor medio, y aparece debido a la presencia de las heterogeneidades existentes.

Además, se asume por conveniencia para el próximo paso, pero sin pérdida de generalidad, que el origen del sistema de coordenadas en la microescala esta ubicado en el baricentro del RVE, es decir:

$$\int_{\Omega_\mu} \boldsymbol{y}\, dV = \mathbf{0} \tag{2.20}$$

**(ii) Admisibilidad cinemática**

Se postula que la conexión entre los desplazamientos y deformaciones en la microescala con sus correspondientes contrapartes en la macroescala surge de una homogeneización o promediado volumétrico en el RVE:

$$\boldsymbol{u} := \frac{1}{|\Omega_\mu|} \int_{\Omega_\mu} \boldsymbol{u}_{\boldsymbol{\mu}}\, dV \quad , \tag{2.21}$$

y

$$\boldsymbol{\varepsilon} := \frac{1}{|\Omega_\mu|} \int_{\Omega_\mu} \boldsymbol{\varepsilon}_{\boldsymbol{\mu}}\, dV \quad , \tag{2.22}$$

donde $|\Omega_\mu|$ denota la medida del dominio micro. Las ecuaciones (2.21) y (2.22) constituyen restricciones que debe cumplir el campo de desplazamientos en la microescala $\boldsymbol{u}_{\boldsymbol{\mu}}$. Es decir, representan condiciones de admisibilidad cinemática del espacio de búsqueda de la solución.

Reemplazando la expansión (2.17) junto con la condición (2.20) en la restricción (2.21), se logra una condición alternativa sobre el campo de las fluctuaciones de desplazamiento:

$$\int_{\Omega_\mu} \tilde{\boldsymbol{u}}_{\boldsymbol{\mu}}\, dV = \mathbf{0} \quad . \tag{2.23}$$

Análogamente, introduciendo la descomposición (2.19) en la restricción (2.22) sobre el campo de deformaciones es posible lograr, luego de integrar por partes, la siguiente restricción adicional:

$$\int_{\Omega_\mu} \tilde{\boldsymbol{\varepsilon}}_{\boldsymbol{\mu}}\, dV = \int_{\Omega_\mu} \nabla^s \tilde{\boldsymbol{u}}_{\boldsymbol{\mu}}\, dV = \int_{\partial\Omega_\mu} \tilde{\boldsymbol{u}}_{\boldsymbol{\mu}} \otimes_s \boldsymbol{n}\, dA = \mathbf{0} \quad , \tag{2.24}$$

donde $\boldsymbol{n}$ es la normal unitaria al contorno $\partial\Omega_\mu$, y $\otimes_s$ es el producto tensor simétrico. Es posible entonces definir, a partir de las restricciones cinemáticas (2.23) y (2.24), el espacio mínimamente restringido de fluctuaciones de desplazamiento cinemáticamente admisibles $\tilde{\boldsymbol{\mathcal{U}}}^*_\mu$ como:

$$\tilde{\boldsymbol{\mathcal{U}}}^*_\mu := \left\{ \boldsymbol{v} : \boldsymbol{v} \in \mathbf{H}^1(\Omega_\mu)\,;\, \int_{\Omega_\mu} \boldsymbol{v}\, dV = \mathbf{0}\,;\, \int_{\partial\Omega_\mu} \boldsymbol{v} \otimes_s \boldsymbol{n}\, dA = \mathbf{0} \right\} \quad . \tag{2.25}$$

El espacio $\tilde{\boldsymbol{\mathcal{U}}}^*_\mu$ reúne las restricciones mínimas que debe cumplir un campo de fluctuación de desplazamientos para respetar las relaciones promedio fundamentales (2.21) y (2.22). Sin embargo, es posible imponer restricciones mas exigentes compatibles con este espacio de acuerdo al problema que se pretende resolver. De esta manera, el espacio de búsqueda, denominado espacio real de fluctuaciones de desplazamiento cinemáticamente admisibles $\tilde{\boldsymbol{\mathcal{U}}}_\mu$, es un subespacio:

$$\tilde{\boldsymbol{\mathcal{U}}}_\mu \subseteq \tilde{\boldsymbol{\mathcal{U}}}^*_\mu. \tag{2.26}$$

La definición precisa de este espacio para los desarrollos de esta tesis se realiza en la Sección 2.3.4. De aquí es posible definir el correspondiente espacio de fluctuaciones de desplazamiento virtuales ci-

nemáticamente admisibles $\tilde{\boldsymbol{\mathcal{V}}}_\mu$ , el cual coincide con $\tilde{\boldsymbol{\mathcal{U}}}_\mu$:

$$\tilde{\boldsymbol{\mathcal{V}}}_\mu := \left\{ \boldsymbol{v} = \boldsymbol{v}_1 - \boldsymbol{v}_2 : \boldsymbol{v}_1, \boldsymbol{v}_2 \in \tilde{\boldsymbol{\mathcal{U}}}_\mu \right\} = \tilde{\boldsymbol{\mathcal{U}}}_\mu \quad . \tag{2.27}$$

**(iii) Principio de trabajos virtuales multiescala (Hill-Mandel)**

Se reformula la forma original del Principio de Hill-Mandel (Hill [21], Mandel [50]), el cual establece la consistencia energética entre las dos escalas de longitud, como un principio variacional. Este principio es referido como Principio de trabajos virtuales multiescala, y el mismo requiere que el trabajo virtual de las tensiones $\boldsymbol{\sigma}$ en la macroescala coincida con el promedio volumétrico de su contraparte a nivel micro-escala debido a las tensiones micro $\boldsymbol{\sigma_\mu}$, para todo campo de deformaciones virtuales cinemáticamente admisibles en el sentido de (2.22) y para toda deformación virtual macro. Esto es:

$$\boldsymbol{\sigma} : \delta\boldsymbol{\varepsilon} = \frac{1}{|\Omega_\mu|} \int_{\Omega_\mu} \boldsymbol{\sigma_\mu} : \delta\boldsymbol{\varepsilon_\mu} \, dV \quad ; \quad \forall \delta\boldsymbol{\varepsilon} \text{ y } \forall \delta\boldsymbol{\varepsilon_\mu} \text{ cinemáticamente admisible.} \tag{2.28}$$

Tomando en cuenta la expansión (2.19), el principio variacional se puede reescribir, luego de un poco de algebra, como:

$$\left[ \boldsymbol{\sigma} - \frac{1}{|\Omega_\mu|} \int_{\Omega_\mu} \boldsymbol{\sigma_\mu} \, dV \right] : \delta\boldsymbol{\varepsilon} \; - \; \frac{1}{|\Omega_\mu|} \int_{\Omega_\mu} \boldsymbol{\sigma_\mu} : \nabla^s \delta\tilde{\boldsymbol{u}}_{\boldsymbol{\mu}} \, dV = 0 \quad ; \quad \forall \delta\boldsymbol{\varepsilon} \text{ y } \forall \delta\tilde{\boldsymbol{u}}_{\boldsymbol{\mu}} \in \tilde{\boldsymbol{\mathcal{V}}}_\mu \, . \tag{2.29}$$

Del principio variacional (2.29) se pueden extraer dos consecuencias fundamentales. En primer lugar, eligiendo $\delta\tilde{\boldsymbol{u}}_{\boldsymbol{\mu}} = \boldsymbol{0}$, y permitiendo variaciones $\delta\boldsymbol{\varepsilon}$ arbitrarias, surge la definición de la homogeneización en tensiones:

$$\boldsymbol{\sigma} = \frac{1}{|\Omega_\mu|} \int_{\Omega_\mu} \boldsymbol{\sigma_\mu} \, dV \quad , \tag{2.30}$$

es decir, que las tensiones macro $\boldsymbol{\sigma}$ se obtienen como el promedio volumétrico en el RVE de las tensiones micro $\boldsymbol{\sigma_\mu}$. Por otra parte, eligiendo $\delta\boldsymbol{\varepsilon} = \boldsymbol{0}$, y permitiendo variaciones $\delta\tilde{\boldsymbol{u}}_{\boldsymbol{\mu}}$ cinemáticamente admisibles, surge la ecuación de equilibrio (en forma débil) de la microescala:

$$\int_{\Omega_\mu} \boldsymbol{\sigma_\mu} : \nabla^s \delta\tilde{\boldsymbol{u}}_{\boldsymbol{\mu}} \, dV = 0 \quad ; \quad \forall \delta\tilde{\boldsymbol{u}}_{\boldsymbol{\mu}} \in \tilde{\boldsymbol{\mathcal{V}}}_\mu \, . \tag{2.31}$$

Lo destacable de este marco teórico es que no es necesario postular la definición de la homogeneización de tensiones, ni el equilibrio mecánico del RVE, sino que estos surgen como consecuencias de argumentos variacionales que derivan del Principio de Hill-Mandel.

### 2.3.3. Modelo constitutivo en la microescala

El problema multiescala se completa a partir de la relación de dependencia entre tensiones y deformaciones micro. Siendo que para los desarrollos de esta tesis se trabaja con constituyentes de la microescala dentro de los límites de la elasticidad, el campo de tensiones micro en el RVE $\boldsymbol{\sigma_\mu}$ depende de las deformaciones micro $\boldsymbol{\varepsilon_\mu}$ a través de un funcional constitutivo:

$$\boldsymbol{\sigma_\mu}(\boldsymbol{y}) = \boldsymbol{\Sigma}(\boldsymbol{\varepsilon_\mu}(\boldsymbol{y})) \tag{2.32}$$

el cual surge, en un marco de cinemática lineal en este caso, de un potencial elástico. Incluyendo la coordenada de la microescala $\boldsymbol{y}$, se enfatiza en esta expresión que la respuesta del material no es necesariamente uniforme a lo largo del dominio $\Omega_\mu$. En general esto se manifiesta debido a la existencia de distintas fases constituyentes del mismo.

### 2.3.4. Análisis multiescala en el contexto de los metamateriales

El hecho de que los metamateriales sean concebidos a partir de una microarquitectura periódica a nivel microescala simplifica, en cierto modo, algunos puntos necesarios de definición dentro de la teoría multiescala. Esto se debe principalemente a que, en general, es esperable que el campo de fluctuaciones de desplazamiento acompañe la periodicidad de la microarquitectura.

De esta manera es posible, en primer lugar, identificar un RVE que respete la periodicidad de la solución simplemente como una muestra que respete la periodicidad de la microarquitectura, y que, por lo tanto, contiene toda la información de la configuración geométrica del mismo [24]. La elección de este RVE se encuentra representado en la Figura 2.4 para un caso de arreglo bidimensional. La repetición periódica de este RVE a lo largo de direcciones específicas permite recuperar el continuo en la macroescala.

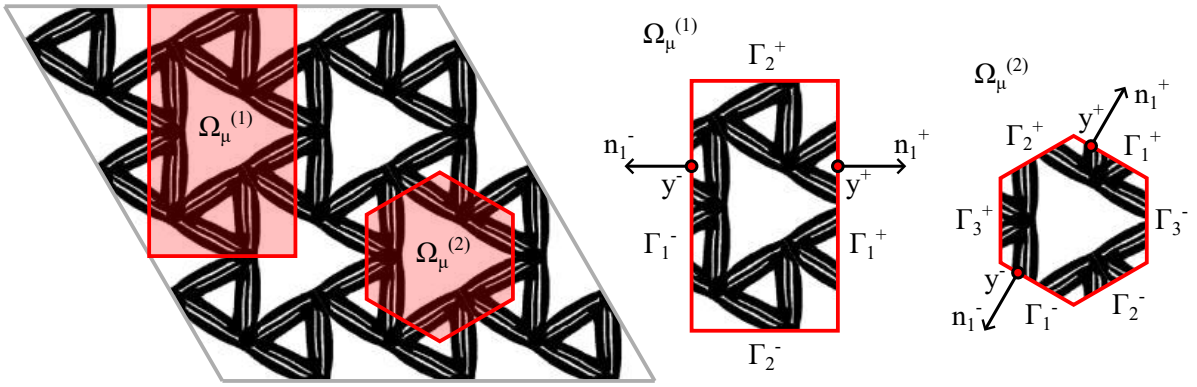


**Figura 2.4:** Identificación de RVEs para geometrías microescala periódicas.

***Observación**: En este punto de la presentación de conceptos preliminares, se hace notar que la identificación del RVE tanto para los trabajos en campo lineal como en campo no lineal constituye un punto central de este trabajo y ha resultado un tema de discusión a lo largo del desarrollo de esta tesis. En el caso de los aportes logrados en el campo del diseño de materiales en régimen lineal (ver Capítulos 3 y 4), la elección del dominio de diseño ha incorporado conceptos de la rama de la Cristalografía, presentados en la Sección 2.4. Con respecto a los aportes en el campo de diseño de materiales en régimen no lineal con inestabilidades (ver Capítulos 5 y 6), el comportamiento intuitivo de periodicidad en las fluctuaciones de desplazamiento acompañando la periodicidad de la microarquitectura deja de ser válido, por lo que se rediscute la identificación de RVE en microarquitecturas periódicas.*

Por otra parte, la periodicidad en el campo de fluctuaciones de desplazamiento permite la definición del espacio $\tilde{\boldsymbol{\mathcal{U}}}_\mu$ adecuado de acuerdo a:

$$\tilde{\boldsymbol{\mathcal{U}}}_\mu := \left\{ \boldsymbol{v} : \boldsymbol{v} \in \tilde{\boldsymbol{\mathcal{U}}}_\mu^* ; \boldsymbol{v}(\boldsymbol{y}^+) = \boldsymbol{v}(\boldsymbol{y}^-) \quad \forall \,\text{par}\,(\boldsymbol{y}^+, \boldsymbol{y}^-) \right\} \quad , \tag{2.33}$$

donde el par $(\boldsymbol{y}^+, \boldsymbol{y}^-)$ indica puntos ubicados en bordes opuestos del contorno del RVE, denominados como $\Gamma^+$ y $\Gamma^-$, que respetan una correspondencia de periodicidad uno a uno. Esta correspondencia se esquematiza en la Figura 2.4. Además, siendo que la repetición del RVE debe completar el espacio se cumple que:

$$\boldsymbol{n}^- = -\boldsymbol{n}^+ \quad . \tag{2.34}$$

Notar que la condición $\boldsymbol{v}(\boldsymbol{y}^+) = \boldsymbol{v}(\boldsymbol{y}^-)$, es mas restrictiva y asegura que $\int_{\partial\Omega_\mu} \boldsymbol{v} \otimes_s \boldsymbol{n}\, dA = \boldsymbol{0}$

correspondiente a la definición (2.25):

$$\int_{\partial\Omega_\mu} \boldsymbol{v} \otimes_s \boldsymbol{n}\, dA = \int_{\Gamma^-} \boldsymbol{v}(\boldsymbol{y}^-) \otimes_s \boldsymbol{n}^-\, dA + \int_{\Gamma^+} \boldsymbol{v}(\boldsymbol{y}^+) \otimes_s \boldsymbol{n}^+\, dA = \int_{\Gamma^-} \boldsymbol{v}(\boldsymbol{y}^-) \otimes_s \boldsymbol{n}^-\, dA - \int_{\Gamma^+} \boldsymbol{v}(\boldsymbol{y}^-) \otimes_s \boldsymbol{n}^-\, dA = \boldsymbol{0}\,. \quad (2.35)$$

Conocido el espacio $\tilde{\boldsymbol{\mathcal{V}}}_\mu = \tilde{\boldsymbol{\mathcal{U}}}_\mu$, es posible estudiar las consecuencias que surgen del principio variacional (2.31). Para ello se relajan las restricciones cinemáticas del espacio a partir de dos multiplicadores de Lagrange $\boldsymbol{\tau}$ y $\boldsymbol{\lambda}$, que representan las reacciones del sistema a las restricciones. De esta manera se obtiene la expresión alternativa[1]:

$$\int_{\Omega_\mu} \boldsymbol{\sigma_\mu} : \nabla^s \delta\tilde{\boldsymbol{u}}_{\boldsymbol{\mu}}\, dV + \boldsymbol{\tau}\cdot\int_{\Omega_\mu} \delta\tilde{\boldsymbol{u}}_{\boldsymbol{\mu}}\, dV + \delta\boldsymbol{\tau}\cdot\int_{\Omega_\mu} \tilde{\boldsymbol{u}}_{\boldsymbol{\mu}}\, dV + \int_{\Gamma^+} \boldsymbol{\lambda}\cdot\delta\tilde{\boldsymbol{u}}_{\boldsymbol{\mu}}(\boldsymbol{y}^+)\, dA - \int_{\Gamma^-} \boldsymbol{\lambda}\cdot\delta\tilde{\boldsymbol{u}}_{\boldsymbol{\mu}}(\boldsymbol{y}^-)\, dA + \int_{\Gamma^+} \delta\boldsymbol{\lambda}\cdot\tilde{\boldsymbol{u}}_{\boldsymbol{\mu}}(\boldsymbol{y}^+)\, dA - \int_{\Gamma^-} \delta\boldsymbol{\lambda}\cdot\tilde{\boldsymbol{u}}_{\boldsymbol{\mu}}(\boldsymbol{y}^-)\, dA = 0 \quad ; \quad \forall(\delta\tilde{\boldsymbol{u}}_{\boldsymbol{\mu}}, \delta\boldsymbol{\tau}, \delta\boldsymbol{\lambda})\,. \quad (2.36)$$

En primer lugar, eligiendo $\delta\tilde{\boldsymbol{u}}_{\boldsymbol{\mu}} = \boldsymbol{0}$ se obtienen las restricciones de admisibilidad cinemática del espacio $\tilde{\boldsymbol{\mathcal{U}}}_\mu$. Mas interesante resulta sacar conclusiones respecto del equilibrio en la microescala haciendo $\delta\boldsymbol{\tau} = \delta\boldsymbol{\lambda} = \boldsymbol{0}$. En este caso la expresión (2.36) se reduce a:

$$\int_{\Omega_\mu} \boldsymbol{\sigma_\mu} : \nabla^s \delta\tilde{\boldsymbol{u}}_{\boldsymbol{\mu}}\, dV + \boldsymbol{\tau}\cdot\int_{\Omega_\mu} \delta\tilde{\boldsymbol{u}}_{\boldsymbol{\mu}}\, dV + \int_{\Gamma^+} \boldsymbol{\lambda}\cdot\delta\tilde{\boldsymbol{u}}_{\boldsymbol{\mu}}(\boldsymbol{y}^+)\, dA - \int_{\Gamma^-} \boldsymbol{\lambda}\cdot\delta\tilde{\boldsymbol{u}}_{\boldsymbol{\mu}}(\boldsymbol{y}^-)\, dA = 0 \quad ; \quad \forall\delta\tilde{\boldsymbol{u}}_{\boldsymbol{\mu}}\,. \quad (2.37)$$

Adoptando $\delta\tilde{\boldsymbol{u}}_{\boldsymbol{\mu}}$ igual un campo constante arbitrario, la ecuación (2.37) se reduce a:

$$\boldsymbol{\tau}\cdot\delta\tilde{\boldsymbol{u}}_{\boldsymbol{\mu}}\,|\Omega_\mu| = 0 \quad , \quad (2.38)$$

de donde se desprende que $\boldsymbol{\tau} = \boldsymbol{0}$. Esto se interpreta como que la restricción de promedio de fluctuaciones de desplazamientos nulo no impone fuerzas reactivas asociadas. Reemplazando ahora este resultado en la ecuación (2.37) e integrando por partes el primer término del lado izquierdo se obtiene para condiciones de borde periódicas:

$$\begin{aligned} &-\int_{\Omega_\mu} (\nabla\cdot\boldsymbol{\sigma_\mu})\cdot\delta\tilde{\boldsymbol{u}}_{\boldsymbol{\mu}}\, dV + \int_{\partial\Omega_\mu} \boldsymbol{\sigma_\mu}\boldsymbol{n}\cdot\delta\tilde{\boldsymbol{u}}_{\boldsymbol{\mu}}\, dA + \int_{\Gamma^+} \boldsymbol{\lambda}\cdot\delta\tilde{\boldsymbol{u}}_{\boldsymbol{\mu}}(\boldsymbol{y}^+)\, dA - \int_{\Gamma^-} \boldsymbol{\lambda}\cdot\delta\tilde{\boldsymbol{u}}_{\boldsymbol{\mu}}(\boldsymbol{y}^-)\, dA \\ &= -\int_{\Omega_\mu} (\nabla\cdot\boldsymbol{\sigma_\mu})\cdot\delta\tilde{\boldsymbol{u}}_{\boldsymbol{\mu}}\, dV + \int_{\Gamma^+} (\boldsymbol{\sigma_\mu}\boldsymbol{n}^+ + \boldsymbol{\lambda})\cdot\delta\tilde{\boldsymbol{u}}_{\boldsymbol{\mu}}(\boldsymbol{y}^+)\, dA + \int_{\Gamma^-} (\boldsymbol{\sigma_\mu}\boldsymbol{n}^- - \boldsymbol{\lambda})\cdot\delta\tilde{\boldsymbol{u}}_{\boldsymbol{\mu}}(\boldsymbol{y}^-)\, dA \\ &= 0 \quad ; \quad \forall\delta\tilde{\boldsymbol{u}}_{\boldsymbol{\mu}}\,, \end{aligned} \quad (2.39)$$

donde $\nabla\cdot$ es el operador divergencia. Eligiendo en turnos que $\delta\tilde{\boldsymbol{u}}_{\boldsymbol{\mu}}$ se anule en el interior del RVE o en alguno de los bordes y eliminando el multiplicador de Lagrange, se obtiene la versión fuerte de las ecuaciones de equilibrio en la microescala:

$$\begin{aligned} \nabla\cdot\boldsymbol{\sigma_\mu} &= \boldsymbol{0} && \text{en} \quad \Omega_\mu \\ \boldsymbol{\sigma_\mu}(\boldsymbol{y}^+)\boldsymbol{n}^+ &= -\boldsymbol{\sigma_\mu}(\boldsymbol{y}^-)\boldsymbol{n}^- && \forall\,\text{par}\,(\boldsymbol{y}^+, \boldsymbol{y}^-)\,\text{de}\;\partial\Omega_\mu \end{aligned} \quad (2.40)$$

lo que se interpreta como el autoequilibrio del RVE, con tracciones antiperiódicas en el contorno, pro-

[1] Note que la restricción de periodicidad ha sido integrada en el contorno, teniendo en cuenta que $|\Gamma^+| = |\Gamma^-|$. Además, al ser una restricción punto a punto, el multiplicador de Lagrange $\boldsymbol{\lambda}$ no es constante en el dominio de integración, a diferencia del multiplicador $\boldsymbol{\tau}$ correspondiente a la restricción de la media del campo de fluctuaciones de desplazamiento.

ducto de la imposición de la periodicidad del campo $\tilde{\boldsymbol{u}}_{\boldsymbol{\mu}}$.

### 2.3.5. Tensor constitutivo homogeneizado

Resulta necesario para los desarrollos de esta tesis utilizar las herramientas de la teoría de multiescala para la obtención del tensor consitutivo efectivo en el caso de compuestos en régimen lineal elástico. Es decir, para elasticidad lineal el funcional constitutivo (2.32) se reduce a:

$$\boldsymbol{\sigma}_{\boldsymbol{\mu}} = \mathbb{C}_{\mu}\boldsymbol{\varepsilon}_{\boldsymbol{\mu}} \quad , \tag{2.41}$$

donde para los fines de esta tesis es suficiente con considerar que el RVE está compuesto por dos fases. Esto es:

$$\mathbb{C}_{\mu}(y) = \begin{cases} {\mathbb{C}_{\mu}}^{1}(y) & \text{si} \quad y \in {\Omega_{\mu}}^{1} \\ {\mathbb{C}_{\mu}}^{2}(y) & \text{si} \quad y \in {\Omega_{\mu}}^{2} \end{cases} \quad , \tag{2.42}$$

donde los supraíndices 1 y 2 indican la fase o consituyente de la microescala. La metodología para obtener el tensor elástico homogeneizado fue presentada por Michel et al. [24], y surge de la idea que tensiones y deformaciones en la macroescala están relacionadas por:

$$\boldsymbol{\sigma} = \mathbb{C}^{h}\boldsymbol{\varepsilon} \quad . \tag{2.43}$$

Por lo tanto, las componentes del tensor constitutivo homogeneizado pueden obtenerse a partir de la superposición de estados de deformación macro elementales asociados a la base canónica: $\boldsymbol{\varepsilon}^{ij} = \boldsymbol{e}_i \otimes_s \boldsymbol{e}_j$, expresados en la base $\{\boldsymbol{e}_i\}$.[2] Esto es:

$$\left[\mathbb{C}^{h}\right]_{ijkl} = \boldsymbol{\sigma}(\boldsymbol{\varepsilon}^{ij}) : \boldsymbol{\varepsilon}^{kl} = \frac{1}{|\Omega_{\mu}|}\int_{\Omega_{\mu}} \left[\boldsymbol{\sigma}_{\boldsymbol{\mu}}(\boldsymbol{\varepsilon}^{ij})\right]_{kl}\, dV \quad , \tag{2.44}$$

donde la nomenclatura $[\cdot]_{ij}$ indica los componentes $ij$ del tensor de segundo orden entre corchetes (análogo para el caso de cuatro subíndices), y la igualdad de la derecha surge de utilizar la homogeneización (2.30). La expresión (2.44) trasluce una dependencia implícita del tensor homogeneizado $\mathbb{C}^h$ con la respuesta constitutiva de los constituyentes ${\mathbb{C}_{\mu}}^{1}$ y ${\mathbb{C}_{\mu}}^{2}$, y con los dominios ocupados por cada uno ${\Omega_{\mu}}^{1}$ y ${\Omega_{\mu}}^{2}$ respectivamente. Es razonable esperar, además, que dados ${\mathbb{C}_{\mu}}^{1}$, ${\mathbb{C}_{\mu}}^{2}$, $|{\Omega_{\mu}}^{1}|$ y $|{\Omega_{\mu}}^{2}|$, la respuesta homogeneizada tiene que estar de alguna manera acotada, mas allá de la distribución geométrica interior al RVE de las fases. El cálculo del tensor elástico homogeneizado es una herramienta utilizada constantemente en los Capítulos 3 y 4.

#### Límites teóricos de compuestos isotrópicos bifásicos

Se discuten en este apartado los límites a la respuesta homogeneizada $\mathbb{C}^h$, para el caso en que tanto la respuesta efectiva macroescala como la respuesta de los materiales constituyentes de la microescala es isotrópica. Que la respuesta efectiva macroescala sea isotrópica es en este contexto una restricción que será buscada mediante optimización topológica de los constituyentes en el Capítulo 3. Esto implica que el comportamiento tanto micro como macro puede describirse a partir de los módulos de compresibilidad $\kappa$ ($K$ para el estado plano) y de corte $G$. Además se asume que el compuesto es bien ordenado, es decir $\kappa_2 < \kappa_1$ y $G_2 < G_1$, donde el subíndice indica la fase (para no sobrecargar la nomenclatura en esta sección los módulos sin índices corresponden a módulos homogeneizados). Asimismo, por conveniencia, se denomina $f_1 = |{\Omega_{\mu}}^{1}|/|\Omega_{\mu}|$ y $f_2 = |{\Omega_{\mu}}^{2}|/|\Omega_{\mu}|$ (con $f_1 + f_2 = 1$) a las fracciones de volumen de cada constituyente.

[2] Se remarca que la notación $\boldsymbol{\varepsilon}^{ij}$ no indica los componentes $ij$ de $\boldsymbol{\varepsilon}$, sino un estado de deformación canónico.

Para el problema 2D, los límites analíticos mas ajustados que se conocen fueron desarrollados por Cherkaev y Gibiansky [51], mientras que en el caso 3D son los conocidos como límites de Berryman–Milton–Phan–Thien (ver Berryman y Milton [52]). En ambos casos, estas cotas degeneran a los conocidos límites de Hashin y Shtrikman [22] cuando la fase blanda tiende al vacío. Se presentan, a modo de ejemplo, los límites de Cherkaev y Gibiansky para el caso bidimensional en el espacio $(K, G)$. La cota superior $G^u(K)$ está definida por:

$$G^u(K) = \frac{\omega^u(f_1G_1 + f_2G_2) + G_1G_2}{G_2f_1 + G_1f_2 + \omega^u} \quad ; \quad \omega^u = -G_1 + \frac{\alpha^u y_K}{\beta^u y_K - \gamma^u}, \tag{2.45}$$

y la cota inferior $G^l(K)$ por:

$$G^l(K) = \frac{\omega^l(f_1G_1 + f_2G_2) + G_1G_2}{f_1G_2 + f_2G_1 + \omega^l} \quad ; \quad \omega^l = -G_1 + \frac{\alpha^l(\frac{1}{y_K} + \frac{1}{K_1})}{\beta^l(\frac{1}{y_K} + \frac{1}{K_1}) - \gamma^l}, \tag{2.46}$$

donde

$$y_K = -K_1K_2\frac{K - \frac{1}{(\frac{f_1}{K_1} + \frac{f_2}{K_2})}}{K - (f_1K_1 + f_2K_2)}\left(\frac{f_1}{K_1} + \frac{f_2}{K_2}\right), \tag{2.47}$$

y los coeficientes $\alpha$, $\beta$, $\gamma$ dependen de $K_1$, $G_1$, $K_2$, y $G_2$. Además, las cotas superior e inferior en el módulo de compresibilidad coinciden con las de Hashin-Shtrikman:

$$K^u_{HS} = K_1 + \frac{f_2}{\frac{1}{K_2 - K_1} + \frac{f_1}{K_1 + G_1}} \quad , \tag{2.48}$$

$$K^l_{HS} = K_2 + \frac{f_1}{\frac{1}{K_1 - K_2} + \frac{f_2}{K_2 + G_2}} \quad . \tag{2.49}$$

Estas cotas delimitan el espacio admisible de propiedades efectivas realizables por los compuestos. Por comodidad para el problema de optimización donde estos límites serán utilizados, se asume también que los módulos materiales de las fases están relacionados por un factor de contraste $c = K_1/K_2 = G_1/G_2$. La Figura 2.5 muestra los límites de Cherkaev-Gibiansky normalizados, para el caso de un compuesto cuyas fases están caracterizadas por los parámetros elásticos: $K_1 = 5/7$, $G_1 = 5/13$, $f_1 = 0.5$, y $c = 200$; para los cuales los coeficientes $\alpha$, $\beta$, $\gamma$ resultan: $\alpha^l = 0.4107$, $\beta^l = 1.0653$, $\gamma^l = 0.0110$, $\alpha^u = -0.1256$, $\beta^u = -0.2200$ y $\gamma^u = 2.0 \times 10^{-4}$. Alternativamente, los límites pueden transformarse al espacio $(E, \nu)$, siendo $E$ el módulo de elasticidad y $\nu$ el coeficiente de Poisson.

Estos límites serán utilizados en los Capítulos 3 y 4 como objetivos de diseño para la obtención de materiales con propiedades elásticas lineales extremas.

## 2.4. Nociones fundamentales de simetría de cristales

Se hace una descripción de nociones básicas fundamentales de Cristalografía, necesarias para el entendimiento de los aportes de la tesis. La información presentada sigue el texto de Giacovazzo [53], y mayor claridad sobre varios puntos puede obtenerse de las figuras del mismo. Otros libros de consulta son Nye [54], Vainshtein [55].

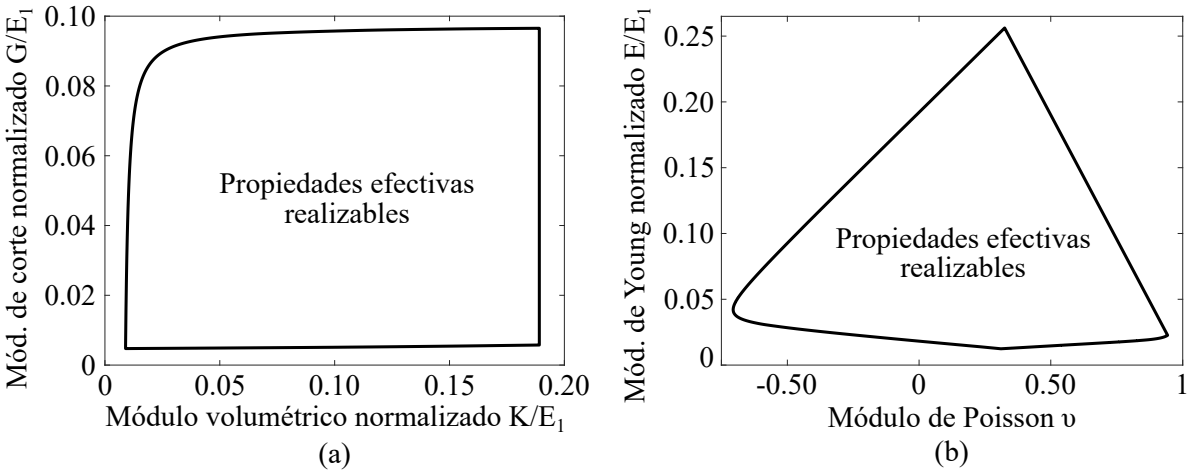


**Figura 2.5:** Límites Cherkaev-Gibiansky de propiedades efectivas realizables por compuestos bifásicos isotrópicos en (a) espacio $(K, G)$, (b) espacio $(E, \nu)$.

### 2.4.1. El estado cristalino

El concepto de estado cristalino hace referencia a la disposición ordenada de las moléculas en un cuerpo sólido. Una característica distintiva del estado cristalino es la repetición regular en el espacio de un motivo (motif en inglés), entendido como un objeto conformado por una molécula o grupo de moléculas, a lo largo de distancias muy superiores al tamaño de las mismas. El estado cristalino es entendido a partir de conocer qué operaciones de repetición son necesarias de realizar para superponer dos objetos idénticos ubicados en posiciones y orientaciones aleatorias. A modo de idea general, se denomina transformación isométrica al conjunto de operaciones necesarias para lograr esta correspondencia entre dos objetos idénticos (estrictamente denominados congruentes).

Estos conceptos son utilizados en el contexto de esta tesis entendiendo al motivo no como un conjunto de moléculas sino como una disposición geométrica de dos materiales.

### 2.4.2. Redes

La periodicidad traslacional de los cristales se comprende a partir de la geometría en la repetición del motivo. En este sentido, se denomina red a la colección de puntos que describen completamente la geometría de la repetición. Estos puntos resultan separados a intervalos $\boldsymbol{a}, \boldsymbol{b}, \boldsymbol{c}$ a lo largo de tres direcciones no coplanares en cristales tri-dimensionales, los cuales coinciden con las direcciones de repetición periódica del motivo. En la Figura 2.6(a) se ilustra un motivo (que será luego abordado como metamaterial en la Parte III) con un cierto patrón de periodicidad traslacional. La red de este motivo se representa en la Figura 2.6(b), donde cada punto corresponde al centro de uno de los triángulos negros. Es importante notar que las características de la red son invariantes a su ubicación respecto del motivo. La misma red se obtiene si se ubican los puntos en uno de los lados de los hexágonos blancos, como se aprecia en la red de puntos verdes.

Tomando como origen de coordenadas a un punto cualquiera de la red, la posición de cualquier otro punto surge de manera única como la combinación lineal de los vectores $\boldsymbol{a}, \boldsymbol{b}, \boldsymbol{c}$, denominados vectores base. Estos vectores definen un parelelepípedo (paralelogramo en 2D) denominado celda unidad, que corresponde a una porción del cristal que contiene toda la información del motivo, y que recupera el cristal completo si se lo replica por translación en dichos vectores. Algunos ejemplos se indican en la Figura 2.6(b) como áreas sombreadas. Las direcciones especificadas por los vectores base se denominan ejes cristalográficos, y los ángulos entre ellos se conocen como ángulos cristalográficos (donde $\alpha$ es el

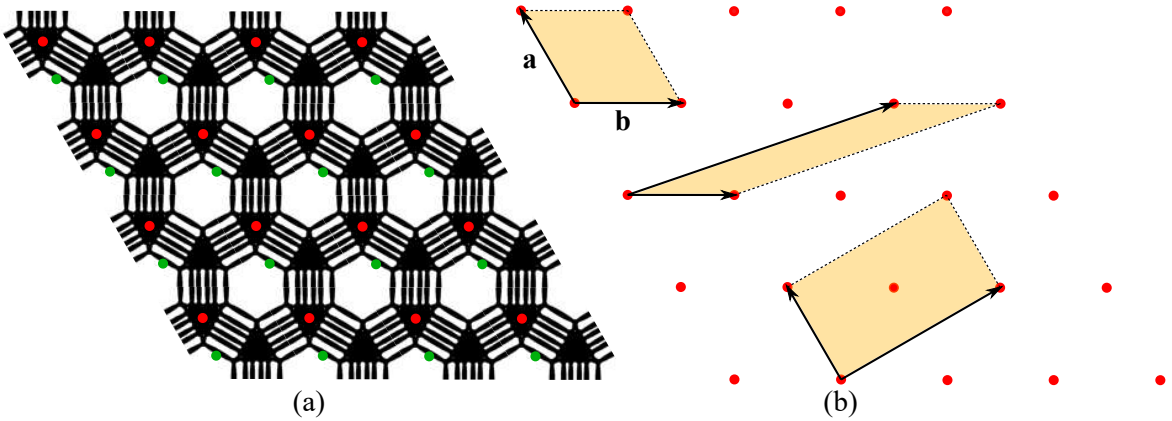


**Figura 2.6:** (a) Periodicidad traslacional de un motivo e identificación de puntos equivalentes. (b) Red correspondiente y ejemplos de celdas primitivas y centrada.

opuesto a $\boldsymbol{a}$, $\beta$ es el opuesto a $\boldsymbol{b}$, y $\gamma$ es el opuesto a $\boldsymbol{c}$). Como la elección de estos vectores base admite cierta arbitrariedad, distintas celdas unidad son posibles para la misma red. Para los propósitos de esta tesis resultará útil distinguir o clasificar las celdas en función del número de puntos que incluyen. De esta manera se denomina celda primitiva a aquella que incluye un único punto de la red, como es el caso de las dos celdas superiores (cada punto de esquina contribuye en $1/4$ a la celda). Por otra parte, las celdas que contienen dos (celda sombreada inferior) o mas puntos se denominan celdas múltiples o centradas.

#### Propiedades racionales de las redes

Dos puntos cualquiera de una red definen una dirección cristalográfica, mientras que tres puntos no colineales cualquiera definen un plano cristalográfico. Las características o propiedades de la red asociadas a estas direcciones y planos se denominan propiedades racionales. La distinción entre los distintas direcciones y planos se hace a través de los índices de Miller.

### 2.4.3. Elementos de simetría

Una *operación de simetría* es una operación isométrica que actúa en todo el espacio y lo hace permanecer inalterable. Los *elementos de simetría* son puntos, ejes y planos con respecto a los cuales estas operaciones son realizadas. Los elementos de simetría son:

- Ejes de rotación: un eje de rotación de orden $n$ mantiene inalteradas las propiedades del espacio luego de una rotación de $2\pi/n$ alrededor del eje. Esto es, existen $n$ posiciones equivalentes alrededor del eje. Se puede demostrar que los únicos casos de interés en cristales ideales son los ejes con $n = 1, 2, 3, 4, 6$. El símbolo escrito es el número $n$.

- Ejes de rototraslación (ejes hélice): un eje de hélice de orden $n$ y componente traslacional relativa $p$ mantiene inalteradas las propiedades del espacio luego de una rotación de $2\pi/n$ alrededor del eje y una traslación $p/n\boldsymbol{T}$ a lo largo del eje, donde $\boldsymbol{T}$ es el vector que une dos puntos equivalentes por traslación. Los valores $n$ de interés en este caso coinciden con los del eje rotacional, siendo además $0 < p < n$ un entero. El símbolo escrito de este elemento es $n_p$.

- Ejes de inversión: un eje de inversión de orden $n$ mantiene inalteradas las propiedades del espacio luego de ejecutar una rotación de $2\pi/n$ alrededor del eje, seguida de una inversión con respecto a un punto ubicado en dicho eje. Nuevamente se tienen las mismas rotaciones válidas mencionadas anteriormente. El símbolo escrito en este caso es $\bar{n}$.

- Planos de reflexión (planos espejo): la transformación lograda por el eje de inversión $\bar{2}$ corresponde a reflejar un semi-espacio a través de un plano perpendicular a dicho eje. Por conveniencia se individualiza este efecto de los ejes de inversión, denominándolo con el símbolo $m$.

- Planos de reflexión con componente traslacional (planos de deslizamiento): un plano de deslizamiento mantiene las propiedades de un semi-espacio de un lado del plano inalteradas luego de una reflexión a través del plano, seguida de una traslación paralela al mismo. La magnitud de la traslación sólo puede corresponder a $1/2\boldsymbol{T}$. Estos elementos se simbolizan con las letras $a, b, c, n, d$ de acuerdo a la dirección de la traslación en la red.

Los símbolos gráficos de los elementos de simetría mencionados (y de la combinación de algunos) se muestran en la Figura 2.7(a). Algunos de estos símbolos son indicados sobre el motivo mostrado en la Figura 2.6(a), que se repite en la Figura 2.7(b). Además de la simbología mencionada, se incluye una diferenciación por color en los planos de flexión y de deslizamiento, para denotar que existen dos sistemas de cada uno de ellos. Representaciones gráficas de los efectos espaciales de estos elementos no incluidas aquí, pueden encontrarse en el texto de Giacovazzo [53].

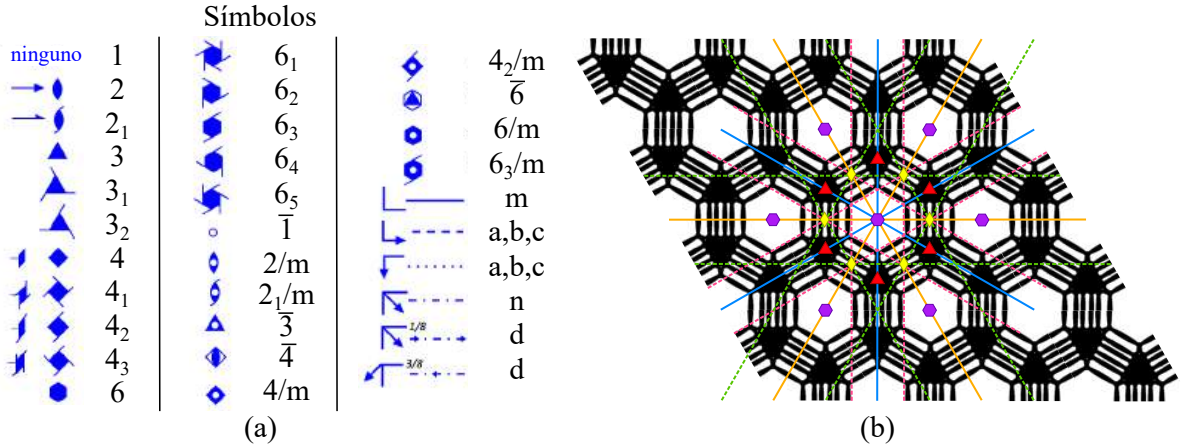


**Figura 2.7:** (a) Símbolos gráficos y escritos de los elementos de simetría. (b) Ejemplo de ubicación de algunos elementos de simetría en un arreglo periódico.

### 2.4.4. Grupos de punto

Los cristales admiten que coexistan mas de un elemento de simetría. En este sentido, se denomina grupo de punto a la combinación de elementos de simetría que no incluyen traslaciones, es decir a la operación conjunta de ejes de rotación y de inversión. Los grupos de punto dejan, al menos, un punto del espacio fijo. El conjunto de cristales que comparten el mismo grupo de punto se denomina clase del cristal y comparte el símbolo del grupo de punto.

Para cristales tridimensionales existen 32 grupos de puntos, de los cuales 13 se obtienen a partir de la existencia de un único eje como elemento de simetría (el cual puede ser de rotación, inversión, o ambos), y 19 surgen a partir de la combinación de tres ejes. Estas combinaciones incluyen (i) tres ejes de rotación, (ii) dos ejes de inversión y uno de rotación, y (iii) tres ejes de rotación e inversión simultáneamente. De acuerdo a las simetrías impuestas por los ejes simultáneos, mas elementos de simetría son necesariamente involucrados. Las Figuras 2.8(a) y (b) presentan dos ejemplos de la coexistencia de tres ejes referidos a un cubo, cuyo centro es el punto fijo de las operaciones de simetría. En estas figuras se indica el nombre del grupo de punto siguiendo la notación internacional acompañado entre paréntesis de los tres ejes que los constituyen. La Tabla 2.1 ordena los 32 grupos de punto tridimensionales.

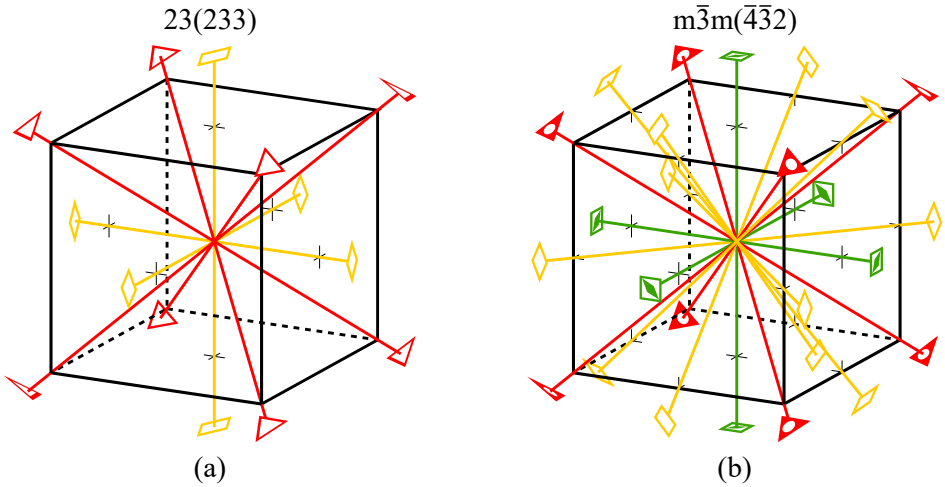


**Figura 2.8:** Coexistencia de elementos de simetría en grupos de punto. (a) Grupo 23. (b) Grupo $m\bar{3}m$

En el espacio bidimensional las únicas operaciones que dejan un punto fijo son los ejes de rotación y la reflexión respecto de una línea. De aquí que sólo se cuentan, en este caso, con 10 grupos de punto, los cuales se enumeran en la Tabla 2.2.

*Observación:* el concepto de grupo de punto resulta clave para los aportes de los Capítulos 3 y 4.

### 2.4.5. Sistemas de cristal

La presencia de ejes de simetría impone restricciones en los parámetros de la red (ejes y ángulos cristalográficos). Los sistemas de cristal agrupan los grupos de punto que restringen las redes de igual manera. De esta forma, los cristales pertenecientes a un mismo sistema pueden ser descritos por celdas unidad del mismo tipo. En esta discusión, estas celdas unidad se asumen primitivas, y definidas por los vectores base con las restricciones mencionadas.

En el espacio 3D, este procedimiento da lugar a siete sistemas de cristal, los cuales están listados en la Tabla 2.1, relacionándolos con los grupos de punto compatibles y las restricciones impuestas en la red. La misma metodología permite obtener cuatro sistemas de cristal en el espacio 2D, los cuales se presentan en la Tabla 2.2.

### 2.4.6. Redes de Bravais

Las redes de Bravais, complementariamente a la descripción de los sistemas de cristal, son tipos de redes basadas tanto en celdas primitivas como no primitivas. En este sentido se consideran redes distintas a aquellas que no pueden ser descritas por la misma celda unidad, a pesar de ser compatibles con los mismos grupos de punto. De esta manera, la definición de redes de Bravais amplía la gama de celdas posibles, y al mismo tiempo limita la arbitrariedad mencionada previamente. Las celdas asociadas a distintas redes de Bravais se denominan celdas convencionales, pudiendo ser las mismas primitivas o no. Para celdas tridimensionales los tipos de celdas incluyen:

- Primitivas (P): puntos de la red en las esquinas.
- Centradas en una cara (A, B o C): puntos de la red en las esquinas y en el centro de una de las caras. A partir de transformaciones siempre es posible reducir la celda a una del tipo centrada en la cara C, es decir, la cara normal al vector base $\boldsymbol{c}$.
- Centrada en todas las caras (F): puntos de la red en las esquinas y en el centro de todas las caras.

- Centrada en el cuerpo (I): puntos de la red en las esquinas y en el centro de la celda.
- Centrada romboédricamente (R): puntos de la red en las esquinas y en dos posiciones interiores a la celda que permiten adaptarla a una celda primitiva de forma romboédrica.

La combinacón de estos tipos con los sistemas de cristal, permite definir 14 redes de Bravais posibles en 3D, las cuales están listadas en la Tabla 2.1.

| Sistema de cristal | Grupos de punto | Parámetros de la red | | Redes de Bravais |
|---|---|---|---|---|
| | | Magnitudes $a, b, c$ | Ángulos $\alpha, \beta, \gamma$ | |
| Triclínico | $1, \bar{1}$ | irrestricto | irrestricto | P |
| Monoclínico | $2, m, 2/m$ | irrestricto | $\alpha = \gamma = 90^o$, $\beta$ irrestricto | P, C |
| Ortorómbico | $222, mm2, mmm$ | irrestricto | $\alpha = \beta = \gamma = 90^o$ | P, C, F, I |
| Tetragonal | $4, \bar{4}, 4/m, 422, 4mm,$ $\bar{4}2m, 4/mmm$ | $a = b$, $c$ irrestricto | $\alpha = \beta = \gamma = 90^o$ | P, I |
| Trigonal | $3, \bar{3}$ $32, 3m, \bar{3}m$ | $a = b$, $c$ irrestricto | $\alpha = \beta = 90^o$, $\gamma = 120^o$ | R |
| Hexagonal | $6, \bar{6}, 6/m, 622, 6mm,$ $\bar{6}2m, 6/mmm$ | $a = b$, $c$ irrestricto | $\alpha = \beta = 90^o$, $\gamma = 120^o$ | P |
| Cúbico | $23, m\bar{3}$ $432, \bar{4}3m, m\bar{3}m$ | $a = b = c$ | $\alpha = \beta = \gamma = 90^o$ | P, F, I |

**Tabla 2.1:** Principales características de cristales tridimensionales. P: primitiva, C: centrada en una cara (normal a $\boldsymbol{c}$), F: centrada en todas las caras, I: centrada en el cuerpo, R: centrada romboédricamente.

Para celdas bidimensionales los tipos de celdas pueden ser del tipo primitivas (P) o centradas (C). Esto da lugar a las 5 redes de Bravais en 2D, ordenadas en la Tabla 2.2. En la Figura 2.9, se esquematizan las redes de Bravais y sus correspondientes celdas convencionales para los casos de una red tridimensional cúbica centrada en el cuerpo -cI- (también denominada BCC en inglés), y a una red bidimensional hexagonal. Note que las propiedades de la red presentada en la Figura 2.6 corresponden a una red hexagonal, lo cual concuerda con la existencia de los ejes de rotación 6.

| Sistema de cristal | Grupos de punto | Parámetros de la red | | Redes de Bravais |
|---|---|---|---|---|
| | | Magnitudes $a, b$ | Ángulo $\gamma$ | |
| Oblicua | $1, 2$ | irrestricto | irrestricto | P |
| Rectangular | $m, 2mm$ | irrestricto | $\gamma = 90^o$ | P, C |
| Cuadrada | $4, 4mm,$ | $a = b$ | $\gamma = 90^o$ | P |
| Hexagonal | $3, 3m, 6, 6mm$ | $a = b$ | $\gamma = 120^o$ | P |

**Tabla 2.2:** Principales características de cristales bidimensionales. P: primitiva, C: centrada.

### Celdas Wigner-Seitz

Las celdas Wigner-Seitz se obtienen a partir de la construcción de Dirichlet o teselación de Voronoi. En primer lugar se une con una recta cada punto de la red con sus vecinos mas cercanos. Luego se trazan planos normarles a estas rectas por sus puntos medios. La región del espacio delimitada por estos planos constituye la celda Wigner-Seitz.

Esta construcción asocia un tipo de celda a cada una de las redes de Bravais existentes. Además tienen la característica de ser, en general, poliedros distintos de los paralelepípedos de las celdas convencionales. Cuentan también con la propiedad de ser siempre celdas primitivas. En la Figura 2.9, se presentan las celdas Wigner-Seitz compatibles con dos redes de Bravais particulares.

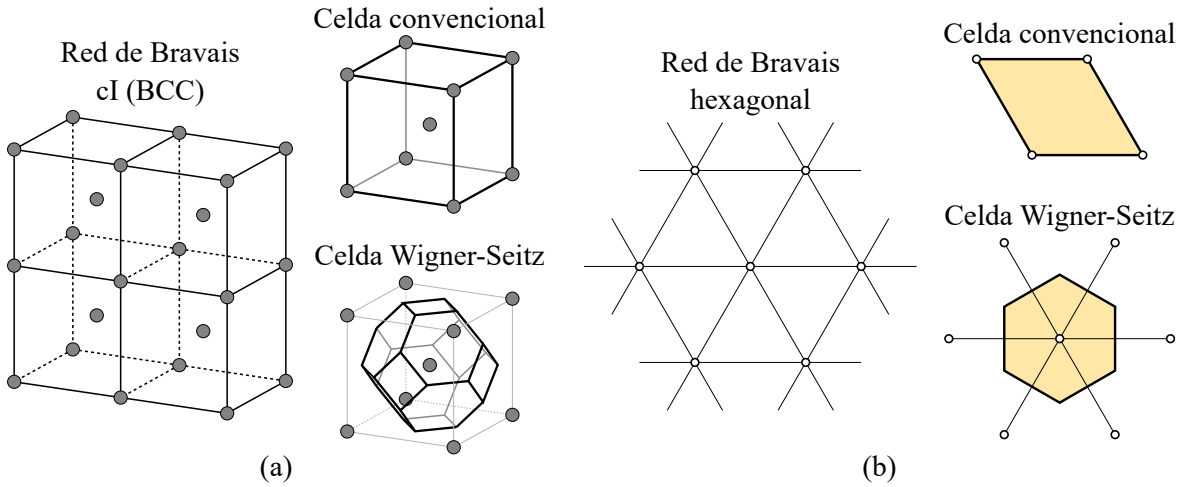


**Figura 2.9:** Redes de Bravais y tipos de celdas en (a) red tridimensional cúbica centrada en el cuerpo, y (b) red bidimensional hexagonal.

### 2.4.7. Grupos de espacio y de plano

Se entiende como grupo de espacio (plano) cristalográfico al conjunto de operaciones de simetría que proyectan un objeto tridimensional (bidimensional) en si mismo. Los grupos de espacio surgen de agregar la periodicidad por traslación a los grupos de punto. Parte de los grupos de espacio surgen de combinar los 32 grupos de punto con las 14 redes de Bravais. Otras variantes surgen de reemplazar los ejes de rotación e inversión de los grupos de punto por ejes hélice, y los planos de reflexión por planos de deslizamiento. En este último caso deja de valer la regla de que al menos un punto del espacio se mantiene fijo antes operaciones de simetría. Siguiendo este procedimiento se determina la existencia de 230 grupos de espacio, y de manera análoga 17 grupos de plano.

Retomando el concepto de propiedades racionales presentado en la Sección 2.4.2, se señala que los grupos de espacio proyectan distintos grupos de plano de acuerdo al plano cristalográfico de la red elegido. Esta característica es utilizada para el análisis de resultados en los aportes del Capítulo 3.

#### Unidad asimétrica

Debido a la presencia de los elementos de simetría, una celda primitiva incluye varios objetos simétricamente equivalentes. Se denomina entonces unidad asimétrica a la parte mas pequeña de la celda unidad que puede recuperar la celda unidad completa mediante la aplicación de las operaciones de simetría. La Figura 2.10(a) replica el motivo de la Figura 2.6(a) indicando las celdas convencional y Wigner-Seitz (contrastar con Figura 2.9(b)). Este motivo corresponde a una red hexagonal con grupo de plano $p6mm$. La Figura 2.10(b) muestra sombreada la unidad asimétrica ubicada en ambas celdas, junto con la ubicación de los elementos de simetría en cada caso.

Mayores detalles acerca de la lista completa de grupos de plano y de espacio, notación, y totalidad de elementos de simetría pertenecientes a cada caso resultan excesivos para los propósitos de este resumen. Los mismos pueden encontrarse tanto en la bibliografía mencionada como en las Tablas Internacionales de Cristalografía [56]. Cabe aclarar, sin embargo, que en las publicaciones que forman esta tesis se especifica oportunamente la información necesaria para el entendimiento de los aportes realizados.

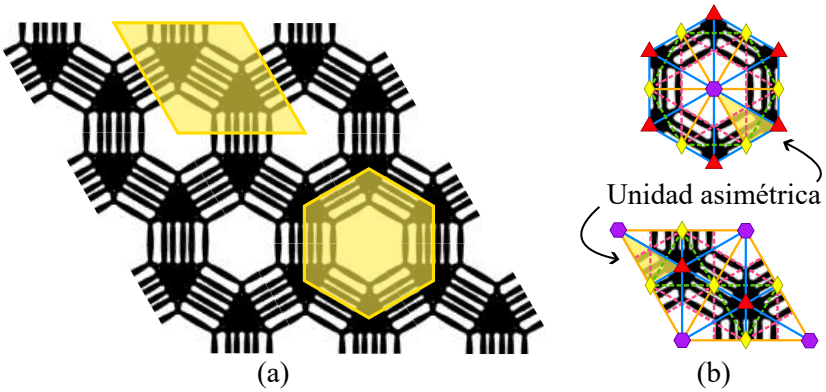


**Figura 2.10:** (a) Identificación de celdas unidad primitivas convencional y Wigner-Seitz en motivo con grupo de plano $p6mm$. (b) Unidad asimétrica y elementos de simetría.

## 2.5. Fundamentos de optimización topológica

El éxito para conseguir metamateriales con un alto desempeño en la macroescala depende fuertemente de la disponibilidad de técnicas que asistan el diseño de las microarquitecturas. En esta sección se presentan muy brevemente las nociones más fundamentales en lo que respecta a la optimización topológica, herramienta central para conseguir los aportes logrados en esta tesis.

### 2.5.1. Topología

La Topología es la rama de la matemática que estudia las propiedades de un objeto que se preservan ante deformaciones continuas. Desde el punto de vista de la topología, dos objetos se consideran equivalentes si es posible consitituir uno de esos objetos a partir de deformar continuamente el otro (como si de una goma se tratase), a partir de acciones como estirar, torcer, arrugar y doblar; es decir, sin cerrar o abrir agujeros, rasgarse o atravesarse. La Figura 2.11 ejemplifica esta idea, mostrando que la tapa de una birome (si tiene el hueco de seguridad) es un objeto topológicamente equivalente a una taza, mientras que un vaso es un objeto diferente.

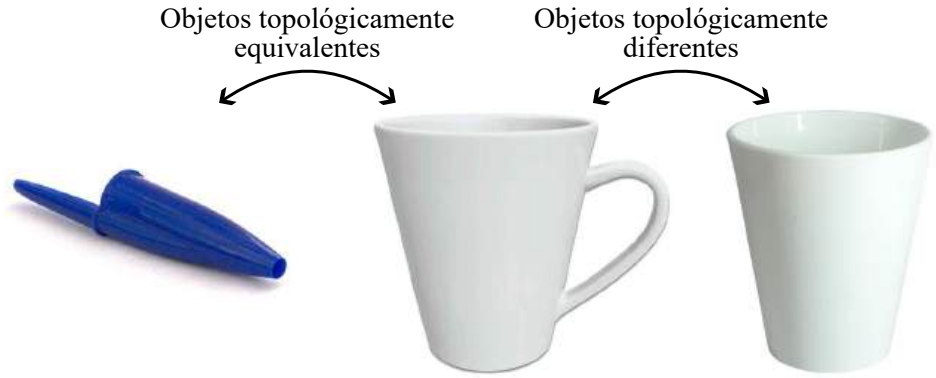


**Figura 2.11:** Equivalencia topológica de los objetos.

### 2.5.2. Optimización topológica

Se conoce como optimización topológica a la técnica matemática y numérica por la cual se busca conocer el número, ubicación y tamaño óptimos de los agujeros en un dominio de diseño de manera

de lograr el mejor comportamiento posible del objeto geométrico en un determinado aspecto. Históricamente, la optimización topológica surge como metodología para generar estructuras que minimicen su flexibilidad ante un sistema de cargas exteriores prestablecido, respetando una proporción de volumen entre la estructura final y el dominio de diseño. Una recopilación completa de la evolución de esta técnica desde su inicio es presentada por Bendsoe y Sigmund [29].

Desde un punto de vista práctico, de aquí en adelante debe entenderse el término "agujero" como "inclusión", la cual puede ser de material vacío o de un segundo material. De esta manera, como todo esquema de optimización, la optimización topológica resulta en un proceso iterativo, en el cual en cada iteración se evalúa la conveniencia de introducir o eliminar estas inclusiones con el propósito de mejorar una función objetivo, mientras se respeta un conjunto de restricciones. Cabe aclarar que, a pesar de ciertas dificultades que son discutidas más adelante, estos métodos han demostrado ser mas exitosos cuando se los incluye en un esquema de optimización por gradientes.

Es importante además que, si bien el concepto de objeto topológicamente equivalente involucra únicamente el número de agujeros o inclusiones, los métodos de optimización topológica atienden no solamente este aspecto, sino también la forma y el tamaño de dicho objeto. Volviendo al ejemplo de la sección anterior, si el objetivo es lograr un objeto que permita tomar café, por más que la topología sea la misma, la experiencia puede ser muy frustrante si se utiliza la tapa de una birome.

Siguiendo la nomenclatura convencional del área, en lo que resta de esta tesis se utiliza la palabra topología para referirse al objeto geométrico (estructura), cuyas inclusiones, forma y tamaño buscan hacerse óptimas.

Existen diferentes técnicas de optimización topológica, entre ellas posiblemente la más difundida sea la denominada SIMP. La misma cuenta con una estrategia para la parametrización de la topología a través de un campo de densidades que consituyen las variables de diseño, y el cáculo de sensibilidades vinculando estas densidades con la rigidez puntoa punto de la estructura. Las ventajas, dificultades y aspectos de implementación de esta metodología son también expuestas en el libro de Bendsoe y Sigmund [29]. Si bien la técnica SIMP se utilizó en parte de esta tesis (ver Capítulo 5), los principales aportes vinculados a optimización topológica se obtuvieron a partir de una estrategia basada en la derivada topológica, concepto del cual se presentan a continuación las nociones mas fundamentales. Detalles específicos del proceso de optimización topológica son presentados en los Capítulos 3 y 5, y en las publicaciones logradas (ver Apéndices).

### Expansión asintótica topológica y derivada topológica

Los conceptos de expansión asintótica y derivada topológica proveen el marco matemático para el tratamiento de perturbaciones singulares en la topología a partir de extender la idea de diferenciabilidad. Una descripción abarcativa de estos conceptos puede encontrarse en el libro de Novotny y Sokołowski [57]. Se parte de asumir la existencia de un funcional $\phi$ que depende de la topología en un cierto dominio, a través de una variable escalar no negativa $\rho$, que representa una inclusión pequeña que perturba la topología. Debido a esto, el valor $\rho = 0$ implica un dominio no perturbado. De aquí se desprende la expansión asintótica topológica (nótese el paralelismo con una expansión por series de Taylor de la función $\phi(\rho)$):

$$\phi(\rho) = \phi(0) + f(\rho) D_T \phi + o(f(\rho)) \quad , \tag{2.50}$$

donde $\phi(\rho)$ es el funcional perturbado topológicamente, $f(\rho)$ es una función no negativa que tiende a 0 si $\rho$ tiende a 0, y $o(f(\rho))$ es una función que contiene los términos de alto orden. El término $D_T\phi$ es la derivada topológica de $\phi$ en el dominio no perturbado.

El concepto de derivada topológica puede combinarse con una representación por una función level-set de la topología para generar un algoritmo de optimización topológica. Los desarrollos de esta tesis siguen los trabajos de Amstutz y Andrä [58], Amstutz et al. [59], y detalles específicos se presentan en el Capítulo 3 y en las publicaciones de Yera et al. [60], Rossi et al. [61]. Como característica a destacar, se

menciona que, a diferencia de otras técnicas de optimización topológica, la estrategia de optimización por level-set y derivada topológica es naturalmente libre de parámetros algorítmicos artificales que fuercen la eliminación de zonas con propiedades intermedias a las de las fases. Por ejemplo, en SIMP es usual penalizar rigideces intermedias aplicando un exponente a la densidad (variable de diseño). Esto simplifica en gran medida la implementación de estos algoritmos y favorece para la obtención de metodologías robustas. La mayor dificultad en este caso reside en contar con la derivada $D_T\phi$ para el problema a abordar.

### No convexidad y falta de existencia

Un aspecto importante a considerar en problemas de optimización topológica es que las funciones objetivo son, en general, no convexas, y cuentan con multiplicidad de mínimos locales. Similarmente a las restricciones de convexidad para los modelos constitutivos planteadas en la Sección 2.2.2, y asumiendo un problema correctamente restringido en el sentido de que existe un espacio de soluciones admisibles no vacío, la falta de convexidad en la función objetivo implica que no se puede asegurar la existencia de una solución mínima global. Además, este tipo de problemas presenta multiplicidad de mínimos locales, los cuales son muy sensibles a la discretización del dominio (diferentes mallas de elementos finitos implican diferentes espacios de búsqueda) y al punto inicial de la optimización.

Si bien es un problema mas general que el del diseño de materiales, la Figura 2.12 ejemplifica el problema de existencia de soluciones equivalentes a través de resultados obtenidos durante el desarrollo de esta tesis (además de este tipo de no unicidad, existen soluciones locales mas favorables que otras). La figura muestra dos microarquitecturas que incluyen una repetición periódica de 3x3 dominios de diseño con forma de paralelogramo, y en cada caso se sombrea uno de estos. Si bien la coincidencia no es perfecta, es claro que el tipo de microarquitectura es el mismo: triángulos del material de mayor rigidez (en color negro) conectados por barras perpendiculares a las caras. En el caso de la solución (a) el dominio de diseño coincide con la celda unidad primitiva (comparar con la Figura 2.10 donde esta celda fue identificada), mientras que en el caso (b) el optimizador tiende a generar una celda múltiple triple en el dominio de diseño. Las respuestas homogeneizadas en ambos casos es (aproximadamente) la misma. El mismo efecto ocurre si se busca maximizar la rigidez unidireccional en una estructura. La estructura óptima consiste en una barra alineada con la dirección de la carga, sin embargo, la misma respuesta se obtiene si en lugar de una se tienen diez barras, siempre y cuando la sección transversal total sea la misma. Este fenómeno puede incluso observarse en la Figura 2.12, donde en las zonas que conectan los triángulos de material rígido, el caso (a) muestra seis barras finas, mientras que en el caso (b) se observan zonas de cuatro y zonas de tres barras.

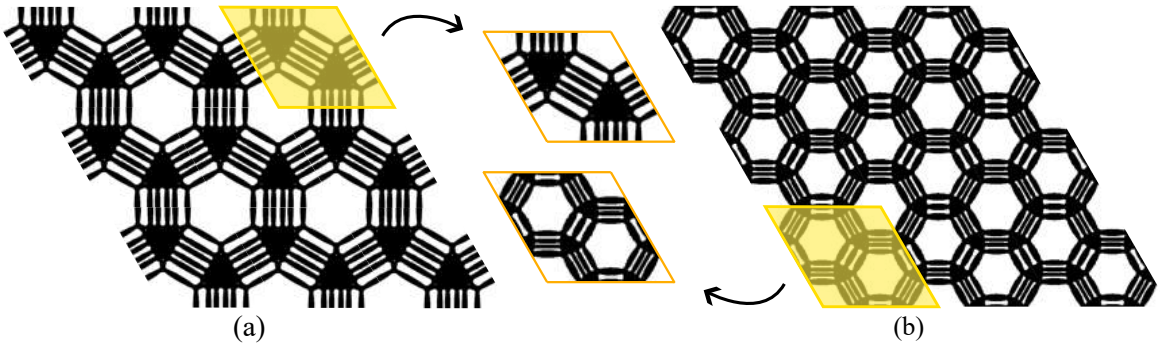


**Figura 2.12:** Mínimos locales equivalentes debido a la no convexidad de la función objetivo. (a) Dominio de diseño capturando una celda unidad. (b) Dominio de diseño capturando una (aproximadamente) celda múltiple triple.

Si bien la formación de múltiples mínimos locales genera una dificultad al momento de lograr un algoritmo de optimización robusto, es interesante remarcar que el análisis de los distintos mínimos deja

traslucir características importantes acerca de las estructuras óptimas. Este tipo de estudio se presenta en el Capítulo 4.

***Observación**: Caracterísitcas como la falta de mínimos globales, la multiplicidad de mínimos locales, y la dependencia con la malla, debido a la no convexidad de la función objetivo, también fueron observadas en metamateriales cuya función de energía de deformación no respeta cuasiconvexidad (ver definición en la Sección 2.2.2). Una discusión al respecto se presenta en el Capítulo 5.*

### 2.5.3. Homogeneización inversa de materiales

Partiendo de la idea de que un metamaterial es básicamente una estructura en la microescala, Sigmund [62] estableció el problema de homogeneización inversa, que consiste en utilizar la metodología de optimización topológica (originalmente pensada para estructuras) para el diseño de la microarquitectura de metamateriales. La homogeneización inversa consiste, por lo tanto, en un problema de optimización topológica donde el objetivo es alcanzar respuestas macroescala prestablecidas o extremas a partir del diseño de topologías de la microarquitectura.

En este contexto, el dominio de diseño es elegido como el RVE del metamaterial. Además, las funciones objetivo planteadas para este tipo de problemas se escriben en términos del tensor elástico homogeneizado $\mathbb{C}^h$, por lo cual el proceso iterativo de la optimización involucra procesos de homogeneización como el descripto en la Sección 2.3.5. Detalles acerca de la formulación de los problemas de optimización topológica, incluyendo distintas funciones objetivo y restricciones, se discuten en el Capítulo 3.

### 2.5.4. La derivada topológica del tensor elástico homogeneizado

Amstutz et al. [59] presentan el concepto de la derivada topológica del tensor de elasticidad homogenizado. Es decir, la sensibilidad de la respuesta efectiva a la nucleación de una inclusión circular dentro del RVE. Para llegar a expresiones cerradas, se asume en la ecuación (2.42) que los tensores constitutivos en la microescala son tensores elásticos isotrópicos:

$$\mathbb{C}_\mu{}^i = \lambda_\mu{}^i(\mathbf{I}\otimes\mathbf{I}) + 2\mu_\mu{}^i\mathbb{I} \quad , \tag{2.51}$$

donde $i$ indica la fase, $\mathbf{I}$ y $\mathbb{I}$ son los tensores unidad de segundo y cuarto orden, y $\lambda_\mu{}^i$ y $\mu_\mu{}^i$ son las constantes de Lamé de cada fase.

Identificando el funcional $\phi$ como el tensor elástico homogeneizado $\mathbb{C}^h$ en la expresión (2.50), la expansión asintótica topológica resulta:

$$\mathbb{C}^h(\rho) = \mathbb{C}^h(0) + f(\rho)D_T\mathbb{C}^h + o(f(\rho)) \quad , \tag{2.52}$$

donde $f(\rho)$ es la fracción volumétrica de la inclusión insertada, y $D_T\mathbb{C}^h$ es la derivada topológica del tensor de elasticidad homogeneizado, la cual constituye un campo tensorial de cuarto orden en $\Omega_\mu$. Esta expansión es demostrada por Amstutz et al. [59] para el problema 2D. Para el problema 3D, la expresión analítica en componentes Cartesianas es (ver Apéndice A en Rossi et al. [61]):

$$D_T\mathbb{C}^h{}_{ijkl}(\boldsymbol{y}) = \boldsymbol{\varepsilon}^{ij}_{\boldsymbol{\mu}}(\boldsymbol{y}) : \mathbb{P} : \boldsymbol{\varepsilon}^{kl}_{\boldsymbol{\mu}}(\boldsymbol{y}) \qquad ; \qquad i,j,k,l = 1,2,3 \tag{2.53}$$

donde, análogamente a lo presentado en la Sección 2.3.5, $\boldsymbol{\varepsilon}^{ij}_{\boldsymbol{\mu}} = \boldsymbol{e}_i \otimes_s \boldsymbol{e}_j$, y $\mathbb{P}$ es el tensor de cuarto orden de polarización (las propiedades de este tensor se encuentran en el trabajo de Ammari et al. [63]):

$$\mathbb{P} = \alpha_1\left(\alpha_2(\mathbf{I}\otimes\mathbf{I}) + 2\mathbb{I}\right) \; ; \tag{2.54}$$

donde los coeficientes $\alpha_1$ y $\alpha_2$ se calculan de acuerdo a:

$$\begin{aligned}\alpha_1 &= \frac{15\mu\delta_\mu(\nu-1)}{15\mu(1-\nu)+2\delta_\mu(5\nu-4)};\\ \alpha_2 &= \frac{\delta_\lambda\left[15\mu\lambda(1-\nu)+2\lambda\delta_\mu(5\nu-4)\right]-2\delta_\mu(\lambda\delta_\mu-5\mu\nu\delta_\lambda)}{5\delta_\mu\left[3\mu\lambda(1-\nu)-3\mu\nu\delta_\lambda-\lambda\delta_\mu(1-2\nu)\right]};\end{aligned} \tag{2.55}$$

con $\delta_\lambda = \lambda - \lambda_0$; $\delta_\mu = \mu - \mu_0$. En la expresión (2.55) $\lambda$, $\mu$ y $\nu$ (coeficiente de Poisson) son las propiedades materiales existentes en el punto $\boldsymbol{y}$, mientras que $\lambda_0$ y $\mu_0$ son las propiedades materiales de la perturbación.

La derivada topológica $D_T\mathbb{C}^h$ permite el cálculo de cualquier función diferenciable respecto de $\mathbb{C}^h$ (o sus componentes) por medio de la regla de la cadena en cálculo diferencial. Esta propiedad es utilizada en los aportes del Capítulo 3.

## 2.6. Sistemas disipativos estándar

Se presentan en esta sección las ecuaciones básicas que describen un material generalizado estándar, en particular las que resultaron de utilidad para el desarrollo de modelos multiescala de metamateriales con transiciones de fase en la microescala en el Capítulo 6, aunque no se hace referencia explícita a dicho problema en este capítulo. La información presentada sigue el texto de Nguyen [64], y se toma en partes la notación de este libro.

### 2.6.1. Modelo generalizado estándar

Un modelo generalizado estándar es un modelo de comportamiento material definido a partir de dos potenciales, un potencial de energía $\mathcal{W}$, y un potencial disipativo $\mathcal{D}$. El potencial de energía es una función que depende de las variables de estado, mientras que el potencial disipativo es una función convexa de flujos (tasas) y puede eventualmente depender del estado actual.

Este marco termodinámico es lo suficientemente versátil para describir un abanico de comportamientos materiales de naturaleza reversible e irreversible. En general, la construcción de un modelo estándar requiere abordar los siguientes pasos: (i) definición de las variables de estado, lo cual implica un conocimiento profundo de la física del material, (ii) identificación de la expresión de la energía libre, (iii) definición de los flujos y fuerzas disipativas, dentro de un análisis de disipación, y (iv) identificación de la expresión del potencial disipativo, el cual provee de relaciones complementarias entre fuerzas y flujos.

Para procesos isotérmicos, el material generalizado estándar admite las variables de estado $\boldsymbol{q} = (\boldsymbol{\varepsilon}, \boldsymbol{\alpha})$ donde $\boldsymbol{\varepsilon}$ es el campo de deformaciones, y $\boldsymbol{\alpha}$ es un vector de variables internas, por lo que se tiene un potencial elástico $\mathcal{W}(\boldsymbol{\varepsilon}, \boldsymbol{\alpha})$. De aquí que la disipación intrínseca por unidad de volumen es

$$d_{in} = \boldsymbol{\sigma}\cdot\dot{\boldsymbol{\varepsilon}} - \dot{\mathcal{W}} = \left(\boldsymbol{\sigma} - \frac{\partial\mathcal{W}}{\partial\boldsymbol{\varepsilon}}\right)\cdot\dot{\boldsymbol{\varepsilon}} - \frac{\partial\mathcal{W}}{\partial\boldsymbol{\alpha}}\cdot\dot{\boldsymbol{\alpha}} = \boldsymbol{A}\cdot\dot{\boldsymbol{\alpha}} \quad , \tag{2.56}$$

donde la última igualdad surge de definir las fuerzas conjugadas $\boldsymbol{A} = -\partial\mathcal{W}/\partial\boldsymbol{\alpha}$, y considerar que las variables internas son el único mecanismo irreversible del material. Además, se asume la existencia del potencial disipativo $\mathcal{D}(\dot{\boldsymbol{\alpha}}, \boldsymbol{\alpha})$, convexo respecto de los flujos $\dot{\boldsymbol{\alpha}}$ (y posiblemente dependiente en el estado actual a partir de $\boldsymbol{\alpha}$). Este potencial permite introducir las leyes de complementariedad que relacionan las fuerzas conjugadas y sus tasas estableciendo que $\boldsymbol{A} = \partial\mathcal{D}/\partial\dot{\boldsymbol{\alpha}}$.

La función dual de $\mathcal{D}$, se obtiene a partir de la transformada de Legendre-Fenchel como

$$\mathcal{D}^*(\boldsymbol{A}, \boldsymbol{\alpha}) = \max_{\dot{\boldsymbol{\alpha}}}\left(\boldsymbol{A}\cdot\dot{\boldsymbol{\alpha}} - \mathcal{D}(\dot{\boldsymbol{\alpha}}, \boldsymbol{\alpha})\right) \quad , \tag{2.57}$$

a partir de la cual se obtiene una expresión alternativa de las leyes de complementariedad como $\dot{\boldsymbol{\alpha}} = \partial \mathcal{D}^* / \partial \boldsymbol{A}$. Luego, dada una historia de las deformaciones $\boldsymbol{\varepsilon}(t)$, el modelo constitutivo consiste en resolver el sistema de ecuaciones con condición inicial

$$\boldsymbol{\sigma} = \frac{\partial \mathcal{W}}{\partial \boldsymbol{\varepsilon}} \quad , \quad \boldsymbol{A} = -\frac{\partial \mathcal{W}}{\partial \boldsymbol{\alpha}} \quad , \quad \dot{\boldsymbol{\alpha}} = \frac{\partial \mathcal{D}^*}{\partial \boldsymbol{A}} \quad , \quad \boldsymbol{\alpha}(0) = \boldsymbol{\alpha}^0 \quad , \tag{2.58}$$

o alternativamente

$$\boldsymbol{\sigma} = \frac{\partial \mathcal{W}}{\partial \boldsymbol{\varepsilon}} \quad , \quad \frac{\partial \mathcal{W}}{\partial \boldsymbol{\alpha}} + \frac{\partial \mathcal{D}}{\partial \dot{\boldsymbol{\alpha}}} = 0 \quad , \quad \boldsymbol{\alpha}(0) = \boldsymbol{\alpha}^0 \quad , \tag{2.59}$$

donde la expresión del centro es conocida como la ecuación de Biot.

### 2.6.2. Respuesta independiente del tiempo

En caso que la respuesta del material incluya mecanismos disipativos independientes del tiempo o no viscosos (rate-independent), el potencial disipativo cumple con la característica de ser convexo y positivamente homogéneo de grado 1 respecto de $\dot{\boldsymbol{\alpha}}$:

$$\mathcal{D}(m\dot{\boldsymbol{\alpha}}, \boldsymbol{\alpha}) = m\mathcal{D}(\dot{\boldsymbol{\alpha}}, \boldsymbol{\alpha}) \qquad \forall\, m > 0 \quad . \tag{2.60}$$

En este caso el potencial $\mathcal{D}$ es sub-diferenciable en $\dot{\boldsymbol{\alpha}} = \boldsymbol{0}$, denominando $\partial_{\dot{\boldsymbol{\alpha}}}\mathcal{D}$ a dicho sub-diferencial. El conjunto $\boldsymbol{P}$ de sub-gradientes en $\dot{\boldsymbol{\alpha}} = \boldsymbol{0}$

$$\boldsymbol{P}(\boldsymbol{\alpha}) = \partial_{\dot{\boldsymbol{\alpha}}}\mathcal{D}(\boldsymbol{0}, \boldsymbol{\alpha}) = \{\boldsymbol{A} \mid \boldsymbol{A} \cdot \delta\dot{\boldsymbol{\alpha}} \leq \mathcal{D}(\delta\dot{\boldsymbol{\alpha}}, \boldsymbol{\alpha}) \quad \forall\, \delta\dot{\boldsymbol{\alpha}}\} \tag{2.61}$$

es el dominio convexo de fuerzas $\boldsymbol{A}$ admisibles. En esta situación, el potencial disipativo dual $\mathcal{D}^*$ es la función indicatriz de este dominio. En este caso la ley de complementariedad que relaciona fuerzas y flujos puede escribirse en la forma $\dot{\boldsymbol{\alpha}} = \boldsymbol{N}_{\boldsymbol{P}}$, que establece que la tasa de las variables internas equivale a la normal $\boldsymbol{N}$ externa al dominio admisible $\boldsymbol{P}$. Es bien establecido que esta ley de evolución de las variables internas es equivalente al principio de máxima disipación clásico en teoría de plasticidad. En este caso la ley de evolución de las fuerzas disipativas se reescribe como $\boldsymbol{A} \in \partial_{\dot{\boldsymbol{\alpha}}}\mathcal{D}$, y la ecuación de Biot resulta

$$\frac{\partial \mathcal{W}}{\partial \boldsymbol{\alpha}} + \partial_{\dot{\boldsymbol{\alpha}}}\mathcal{D} \ni 0. \tag{2.62}$$

Este tipo de pontenciales disipativos no viscosos son utilizados en el Capítulo 6 para la descripción macroescala de metamateriales con transiciones de fase elásticas en la microescala. En dicho capítulo de especializan las entidades a la descripción física del material. En particular se muestra que las variables $\boldsymbol{\alpha}$ se reducen a un escalar, que representa la cantidad de material en cada fase en la microescala.

# Parte III

# Aportes al diseño computacional de metamateriales mecánicos

# Capítulo 3

# Homogeneización inversa con restricciones de simetrías cristalográficas

## 3.1. Introducción

El propósito de este capítulo es servir como lectura complementaria a los primeros dos artículos que constituyen esta tesis, publicados por Yera et al. [60] y Rossi et al. [61], replicados en los Apéndices A y B. El objetivo de estos trabajos es proponer una metodología de diseño topológico mediante homogenización inversa basada en la asociación de los metamateriales con cristales como factor ordenador del proceso. Esta asociación implica la imposición de simetrías de cristales que garantiza una simetría mínima de la respuesta efectiva, la identificación del dominio de diseño como celdas unitarias, y el conocimiento preciso de todas las alternativas de cristales existentes.

La efectividad de la estrategia se demuestra al abordar el problema de G-clausura para materiales isotrópicos definidos en una escala. El problema de G-clausura plantea determinar cuales son las propiedades efectivas alcanzables por un compuesto de características elásticas dadas. En este sentido, los límites presentados en la Sección 2.3.5 constituyen una cota superior, de los cuales sólo algunos puntos se saben alcanzables. Con esta propuesta, se busca lograr una cota inferior de propiedades alcanzables por microarquitecturas en una escala, es decir, con mayor factibilidad para manufacturación. El enfoque consiste en una extensión de la propuesta original de Podestá et al. [65]. El problema se abordó mediante la técnica de level-set y derivada topológica (ver Capítulo 2.5). Los detalles de implementación respecto a esta metodología se encuentran volcados en las publicaciones mencionadas.

El resto de este capítulo está ordenado de la siguiente manera. En la Sección 3.2 se realizan comentarios preliminares sobre la formulación adecuada del problema de optimización para alcanzar propiedades extremas. En la Sección 3.3 se describen los fundamentos que sostienen la propuesta de imposición de simetrías de cristales, y las implicancias que tienen en distintos aspectos del problema de optimización. En la Sección 3.4 se mencionan algunos aspectos puntuales de relevancia al algoritmo de optimización, que surgieron como problemas a resolver en el desarrollo de la tesis. Finalmente, en la Sección 3.5 se presentan las conclusiones del capítulo, para proceder a la lectura de los Apéndices A y B.

## 3.2. Comentarios sobre el diseño de materiales isotrópicos extremos

### 3.2.1. El rol de los límites analíticos de propiedades efectivas

Un metamaterial mecánico se considera extremo cuando sus módulos efectivos elásticos se ubican en la frontera de las propiedades alcanzables. En este sentido, si bien no está demostrado que los límites analíticos existentes (presentados en la Sección 2.3.5) son ajustados, el planteo de la homogeneización inversa buscando aproximar estos límites logra metamateriales con caracteristicas cercanas a lo extremo.

Estos límites dependen de las propiedades y fracciones de volumen de las fases constitutivas del compuesto. Corresponde entonces remarcar un concepto: una propiedad no es extrema en sí misma, sino que depende de las características del compuesto con el cual se la quiere conseguir. La Figura 3.1 ejemplifica esta idea. En ella se muestran los límites de Cherkaev-Gibiansky para tres combinaciones de fracción de fase rígida $f_1$ y contraste entre fases $c$. En la figura se marcan dos puntos del espacio $G/E_1$ vs. $K/E_1$, que presentan caracterísitcas extremas o no según el compuesto analizado ($K$ y $G$ son los módulos de compresibilidad y corte efectivos del compuesto y $E_1$ es el módulo de elasticidad de la fase de mayor rigidez). El punto A identifica una propiedad extrema para los compuestos con límites azul (compuesto 1) y verde (compuesto 2). Para el compuesto 1 esta propiedad corresponde a un mínimo $G$, mientras que para el compuesto 2 corresponde a un máximo $K$. Por otra parte el punto A no es siquiera factible para el compuesto 3. Por el contrario, el punto B representa propiedades efectivas extremas de los compuestos con límites azul y rojo (compuesto 3), nuevamente ubicadas en distintas zonas de los límites de los compuestos 1 y 3. En este caso esta propiedad no es extrema para el compuesto 2. Mas aún, cualquier propiedad efectiva del compuesto 3 no es extrema para el compuesto 2.

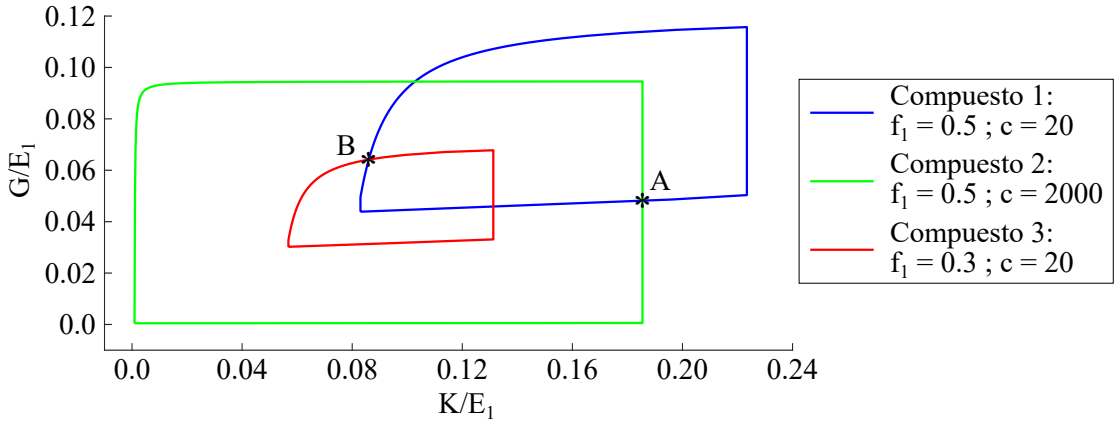


**Figura 3.1:** Límites de Cherkaev y Gibiansky [51] para propiedades efectivas isotrópicas 2D en compuestos con tres combinaciones de parámetros $f_1$ (fracción de volumen de la fase rígida) y $c$ (contraste entre fases). Las propiedades mecánicas de la fase rígida son $E_1 = 1$ y $\nu_1 = 0.3$.

Esta relación entre propiedad extrema y las características del compuesto son fundamentales al momento de plantear el problema de optimización topológica. Buscar obtener la propiedad B con las características del compuesto 3 representa un problema desafiante, mientras que buscarla con las características del compuesto 2 no presenta gran complejidad.

### 3.2.2. Formulación del problema de homogeneización inversa

Se analizan ahora las implicancias de la discusión anterior en la formulación del problema de optimización topológica para 2D y 3D. Las variables denotadas como $\hat{(\cdot)}$ indican características efectivas homogeneizadas, mientras que las nombradas como $(\cdot)^*$ indican propiedades efectivas objetivo, las cuales se toman de los límites analíticos de propiedades efectivas. La formulación original del problema de homogeneización inversa usada por Sigmund [62, 66] tiene la forma:

$$\begin{aligned} &\min\ f_1; \\ &\text{tal que:} \quad ||\hat{\mathbf{C}} - \mathbf{C}^*|| = 0\ . \end{aligned} \tag{3.1}$$

Esta formulación tiene sentido desde el punto de vista de ahorro de material al minimizar $f_1$. Sin embargo, el inconveniente de la misma al buscar características extremas es, precisamente, que la fracción

de volumen $f_1$ está libre, y variaciones de la misma implican variaciones de los límites efectivos, por lo cual no se garantiza en general una respuesta extrema. Se puede observar en la Figura 3.1 que minimizar la fracción de volumen no siempre resulta en una condición más demandante para la optimización. Propiedades extremas de la región izquierda inferior del compuesto 1 (esto incluye compuestos de baja rigidez bimodales y auxéticos), coinciden con propiedades no extremas del compuesto rojo, de menor fracción de volumen. Reemplazar la función objetivo $f_1$ por $|f_1 - f_1^*|$ mejora la formulación pero no elimina por completo el problema. Mas aún, el planteo (3.1) es extremadamente exigente en la realización de la propiedad efectiva. Usualmente este problema resulta en un material cuyas propiedades efectivas no cumplen la restricción, o con una fracción $f_1$ alejada de lo esperado.

Una alternativa natural que soluciona estos inconvenientes es invertir función objetivo y restricción:

$$\begin{aligned} &\min\ ||\hat{\mathbf{C}} - \mathbf{C}^*||; \\ &\quad \text{tal que:} \qquad f_1 - f_1^* = 0\ . \end{aligned} \tag{3.2}$$

Si bien el problema (3.2) está mejor colocado, ya que no se espera igualar el tensor objetivo, sino sólamente aproximarlo (recuerde que no está demostrado que los límites analíticos sean alcanzables en su totalidad), cuenta con la desventaja de no asegurar isotropía de la respuesta (o, en un caso más general, el grado de simetría de $\mathbf{C}^*$). En general, la imposición de simetrías de la respuesta efectiva se logra adicionando restricciones entre las componentes de $\hat{\mathbf{C}}$.

Siendo que para esta tesis sólo se buscan comportamientos isotrópicos, se puede formular el problema a partir de los dos módulos independientes que caracterizan el tensor homogeneizado, por ejemplo:

$$\begin{aligned} &\min\ \hat{G}; \\ &\text{tal que:} \qquad \hat{\kappa} - \kappa^* = 0 \\ &\qquad\qquad\ \ \hat{\mathbf{C}} \text{ isotrópico} \\ &\qquad\qquad\ \ f_1 - f_1^* = 0 \end{aligned} \tag{3.3}$$

El planteo (3.3) fue el utilizado por Yera et al. [60], Rossi et al. [61] (contribuciones replicadas en los Apéndices A y B), y es análogo al usado por Sigmund [67]. Se logra recorrer la totalidad de los límites intercambiando $\hat{G}$ y $\hat{\kappa}$ entre objetivo y restricción, cambiando el problema de minimización por maximización, y variando los valores objetivo. En la sección 3.3.2 se dan especificaciones sobre la forma de imponer la restricción $\hat{\mathbf{C}}$ isotrópico.

Finalmente, cabe preguntarse por qué optimizar $\hat{G}$ y $\hat{\kappa}$, y no $\hat{E}$ y $\hat{\nu}$. Siendo que la formulación (3.3) debe reescribirse en términos de las componentes del tensor elástico (ver detalles en Rossi et al. [61]), la experiencia propia en el desarrollo de esta tesis muestra que resulta más eficiente trabajar con sumas de estos coeficientes que con cocientes entre los mismos.

## 3.3. Imposición de simetrías cristalográficas

Esta sección está dedicada a presentar las implicancias y beneficios de incorporar simetrías de cristales de manera sistemática como parte del proceso de diseño de microarquitecturas en metamateriales mecánicos elásticos de respuesta extrema. Las ideas que se desarrollan son originales a esta tesis y son la base de una gran parte de los aportes logrados.

### 3.3.1. El principio de Neumann como idea fundamental

El patrón periódico de los metamateriales, permite pensar en sus microarquitecturas como cristales. De aquí que es posible enlazar el cuerpo de conocimiento de la rama de la Cristalografía (resumido en la Sección 2.4) con el diseño topológico.

En este sentido, el punto de partida es el principio de Neumann [53, 54]. Este postulado fundamental de la física de cristales enuncia que: *los elementos de simetría de cualquier propiedad física efectiva del cristal deben incluir los elementos de simetría del grupo de punto*. Dicho de otra manera, la propiedad física del cristal tiene **como mínimo** la simetría del grupo de punto. La importancia de este principio, a los fines del diseño de metamateriales mecánicos, reside en que actúa como nexo entre la simetría de la microarquitectura y la simetría del tensor constitutivo elástico homogeneizado.

Dicho esto, es posible extender las Tablas 2.1 y 2.2, incorporando la correspondencia entre los grupos de punto y la simetría del tensor constitutivo. Las Tablas 3.1 y 3.2 muestran de manera genérica los componentes de estos tensores para 3D y 2D respectivamente, cuando se los expresa en su base normal [65]. El procedimiento matemático de imposición de simetrías al tensor constitutivo está presentado, entre otros, por Newnham [68].

### 3.3.2. Implicancias en la formulación del problema de optimización

La metodología de homogeneización inversa restringida por simetrías cristalográficas consiste entonces en imponer a la topología un grupo de espacio en 3D o de plano en 2D, para garantizar, a partir del grupo de punto asociado, un nivel de simetría deseado en la respuesta efectiva. Al imaginar la microarquitectura como un cristal, se cuenta con la ventaja de conocer la totalidad de simetrías que la misma puede tener, ordenando de esta manera el problema de diseño. Existen, de manera general, dos alternativas al momento de elegir que grupo de espacio o de plano imponer, y que evidencian las dos formas de lograr la simetría esperada del tensor $\hat{\mathbf{C}}$ en el planteo (3.3). A continuación se ejemplifican ambos enfoques para el caso de isotropía 2D (contrastar con la información de la Tabla 3.2).

Por un lado, se puede optar por garantizar la simetría de la respuesta objetivo, con un grupo de punto apropiado:

$$\begin{aligned} &\min \hat{G}; \\ \text{tal que:}\quad &\hat{\kappa} - \kappa^* = 0 \\ &f_1 - f_1^* = 0 \\ &\text{topología con grupo } 3m \text{ (sistema hexagonal)} \end{aligned} \tag{3.4}$$

Por el contrario, se puede imponer una simetría topológica inferior que garantice una simetría de la respuesta efectiva menor a la esperada, y adicionar al problema restricciones explícitas que restrinjan los coeficientes del tensor homogeneizado:

$$\begin{aligned} &\min \hat{G}; \\ \text{tal que:}\quad &\hat{\kappa} - \kappa^* = 0 \\ &f_1 - f_1^* = 0 \\ &\text{topología con grupo } 2mm \text{ (sistema rectangular)} \\ &\hat{c}_{1111} - \hat{c}_{2222} = 0 \\ &2\hat{c}_{1212} - \hat{c}_{1111} + \hat{c}_{1122} = 0 \end{aligned} \tag{3.5}$$

En el segundo enfoque, la aproximación a la simetría deseada (en este caso isotropía) se basa en la efectividad del algoritmo de optimización topológica. Ambas alternativas se utilizaron en las publicaciones de Yera et al. [60], Rossi et al. [61] (Apéndices A y B).

### 3.3.3. Implicancias en el RVE

En el problema de homogeneización inversa, una decisión implícita que muchas veces es pasada por alto al definir el problema de optimización topológica es la elección del dominio de diseño. De manera

| Sistema de cristal (Grupos de punto) | Tensor de elasticidad | Constantes independientes |
|---|---|---|
| Triclínico $1, \bar{1}$ | $\begin{bmatrix} c_{1111} & c_{1122} & c_{1133} & c_{1123} & c_{1113} & c_{1112} \\ & c_{2222} & c_{2233} & c_{2223} & c_{2213} & c_{2212} \\ & & c_{3333} & c_{3323} & c_{3313} & c_{3312} \\ & & & c_{2323} & c_{2313} & c_{2312} \\ & \text{Sim} & & & c_{1313} & c_{1312} \\ & & & & & c_{1212} \end{bmatrix}$ | 21 |
| Monoclínico $2, m, 2/m$ | $\begin{bmatrix} c_{1111} & c_{1122} & c_{1133} & 0 & c_{1113} & 0 \\ & c_{2222} & c_{2233} & 0 & c_{2213} & 0 \\ & & c_{3333} & 0 & c_{3313} & 0 \\ & & & c_{2323} & 0 & c_{2312} \\ & \text{Sim} & & & c_{1313} & 0 \\ & & & & & c_{1212} \end{bmatrix}$ | 13 |
| Ortorómbico $222, mm2, mmm$ | $\begin{bmatrix} c_{1111} & c_{1122} & c_{1133} & 0 & 0 & 0 \\ & c_{2222} & c_{2233} & 0 & 0 & 0 \\ & & c_{3333} & 0 & 0 & 0 \\ & & & c_{2323} & 0 & 0 \\ & \text{Sim} & & & c_{1313} & 0 \\ & & & & & c_{1212} \end{bmatrix}$ | 9 |
| Tetragonal $4, \bar{4}, 4/m$ | $\begin{bmatrix} c_{1111} & c_{1122} & c_{1133} & 0 & 0 & c_{1112} \\ & c_{1111} & c_{1133} & 0 & 0 & -c_{1112} \\ & & c_{3333} & 0 & 0 & 0 \\ & & & c_{2323} & 0 & 0 \\ & \text{Sim} & & & c_{2323} & 0 \\ & & & & & c_{1212} \end{bmatrix}$ | 7 |
| Tetragonal $422, 4mm, \bar{4}2m, 4/mmm$ | $\begin{bmatrix} c_{1111} & c_{1122} & c_{1133} & 0 & 0 & 0 \\ & c_{1111} & c_{1133} & 0 & 0 & 0 \\ & & c_{3333} & 0 & 0 & 0 \\ & & & c_{2323} & 0 & 0 \\ & \text{Sim} & & & c_{2323} & 0 \\ & & & & & c_{1212} \end{bmatrix}$ | 6 |
| Trigonal $3, \bar{3}$ | $\begin{bmatrix} c_{1111} & c_{1122} & c_{1133} & c_{1123} & -c_{2213} & 0 \\ & c_{1111} & c_{1133} & -c_{1123} & c_{2213} & 0 \\ & & c_{3333} & 0 & 0 & 0 \\ & & & c_{2323} & 0 & c_{2213} \\ & \text{Sim} & & & c_{2323} & c_{1123} \\ & & & & & \frac{1}{2}(c_{1111} - c_{1122}) \end{bmatrix}$ | 7 |
| Trigonal $32, 3m, \bar{3}m$ | $\begin{bmatrix} c_{1111} & c_{1122} & c_{1133} & c_{1123} & 0 & 0 \\ & c_{1111} & c_{1133} & -c_{1123} & 0 & 0 \\ & & c_{3333} & 0 & 0 & 0 \\ & & & c_{2323} & 0 & 0 \\ & \text{Sim} & & & c_{2323} & c_{1123} \\ & & & & & \frac{1}{2}(c_{1111} - c_{1122}) \end{bmatrix}$ | 6 |
| Hexagonal $6, \bar{6}, 6/m, 622, 6mm, \bar{6}2m, 6/mmm$ | $\begin{bmatrix} c_{1111} & c_{1122} & c_{1133} & 0 & 0 & 0 \\ & c_{1111} & c_{1133} & 0 & 0 & 0 \\ & & c_{3333} & 0 & 0 & 0 \\ & & & c_{2323} & 0 & 0 \\ & \text{Sim} & & & c_{2323} & 0 \\ & & & & & \frac{1}{2}(c_{1111} - c_{1122}) \end{bmatrix}$ | 5 |
| Cúbico $23, m\bar{3}$, $432, \bar{4}3m, m\bar{3}m$ | $\begin{bmatrix} c_{1111} & c_{1122} & c_{1122} & 0 & 0 & 0 \\ & c_{1111} & c_{1122} & 0 & 0 & 0 \\ & & c_{1111} & 0 & 0 & 0 \\ & & & c_{1212} & 0 & 0 \\ & \text{Sim} & & & c_{1212} & 0 \\ & & & & & c_{1212} \end{bmatrix}$ | 3 |

**Tabla 3.1:** Tensores de constantes elásticas para los 32 grupos de punto y los 7 sistemas de cristal tridimensionales.

| Sistema de cristal (Grupos de punto) | Tensor de elasticidad | Constantes independientes |
|---|---|---|
| Oblicua $1, 2$ | $\begin{bmatrix} c_{1111} & c_{1122} & c_{1112} \\ & c_{2222} & -c_{1112} \\ \text{Sim} & & c_{1212} \end{bmatrix}$ | 5 |
| Rectangular $m, 2mm$ | $\begin{bmatrix} c_{1111} & c_{1122} & 0 \\ & c_{2222} & 0 \\ \text{Sim} & & c_{1212} \end{bmatrix}$ | 4 |
| Cuadrada $4, 4mm$ | $\begin{bmatrix} c_{1111} & c_{1122} & 0 \\ & c_{1111} & 0 \\ \text{Sim} & & c_{1212} \end{bmatrix}$ | 3 |
| Hexagonal $3, 3m, 6, 6mm$ | $\begin{bmatrix} c_{1111} & c_{1122} & 0 \\ & c_{1111} & 0 \\ \text{Sim} & & \frac{1}{2}(c_{1111} - c_{1122}) \end{bmatrix}$ | 2 |

**Tabla 3.2:** Tensores de constantes elásticas para los 10 grupos de punto y los 4 sistemas de cristal bidimensionales.

muy intuitiva, el dominio de diseño es la *ventana* por la cual se quiere observar la topología, y si esta ventana no es adecuada, no es posible obtener toda la información relevante.

Un primer punto de encuentro entre la geometría de cristales y la optimización topológica de microarquitecturas es la analogía entre la celda unidad del cristal y el dominio de diseño. Sin embargo, siendo que se desconoce la topología solución al problema, se desconoce también la red del cristal, y, por lo tanto, la celda unidad y el dominio de diseño.

Se presenta en la Figura 3.2 un ejemplo 2D que esboza la significancia de este problema. Anticipando los resultados presentados en el Apéndice A, la microarquitectura mostrada en la figura constituye, no de manera exacta pero si en su esencia, la solución conocida más próxima al punto de Walpole.[1] De acuerdo a lo discutido en la Sección 2.4, esta topología es compatible con una red hexagonal, y puede ser descripta por tres tipos de celda unidad, las cuales se indican en color naranja en la Figura 3.2(a): primitiva de mínima distorsión (acorde a los parámetros de la Tabla 2.2), Wigner-Seitz hexagonal y centrada rectangular. Las primeras dos cuentan con la ventaja de ser primitivas (de mínimo volumen), y la tercera con la simpleza de su forma.[2]

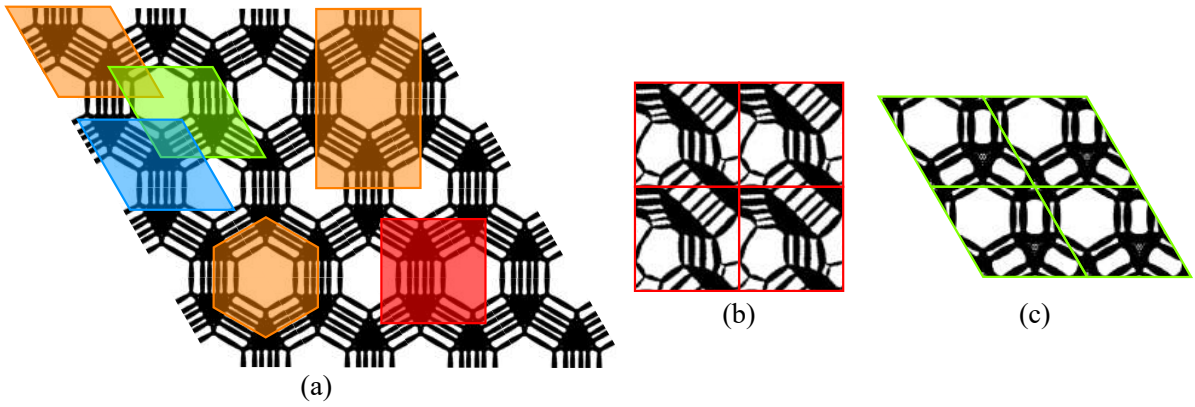


**Figura 3.2:** Implicancias de la imposición de simetrías en el RVE. Ejemplo en solución al problema de Walpole 2D. (a) Compatibilidad de celdas unidad. En naranja celdas primitiva, Wigner-Seitz y centrada. En rojo celda cuadrada no compatible. En verde y celeste, celdas compatibles desplazadas. (b) Resultado de la homogeneización inversa en dominio cuadrado. (c) Resultado de la homogeneización inversa imponiendo grupo de plano $p3m1$, con desplazamiento del dominio de diseño respecto de la microarquitectura.

[1] Una discusión más profunda acerca de las características geométricas de esta topología se presenta en el siguiente capítulo.
[2] Utilizar celdas de mínimo volumen eficientiza los cálculos computacionales y permite discretizar con mallas mas finas.

Por lo tanto, en la búsqueda de una topología solución al punto de Walpole 2D, si se impone un grupo de plano compatible con una red hexagonal, queda determinado de manera inequívoca el dominio de diseño como una celda unidad para una red hexagonal. La solución mostrada en la Figura 3.2(a) se obtuvo imponiendo un grupo $p6mm$, que es apropiado para esta microarquitectura.

Por el contrario, resolver el mismo problema asumiendo otra red limita de gran manera la calidad del resultado logrado. Un ejemplo de esto se ve en la Figura 3.2(a), donde la celda cuadrada sombreada en rojo no es una celda unidad y no replica por periodicidad esta geometría. La Figura 3.2(b) muestra el resultado logrado al resolver el problema con un dominio de diseño cuadrado sin imposición de simetrías (o grupo plano $p1$). En este caso el optimizador solo logra aproximar las formas hexagonales esperadas, y existe un detrimento en las propiedades efectivas obtenidas.

Adicionalmente, la metodología propuesta elimina el problema de desplazamientos relativos entre el dominio de diseño respecto de la microarquitectura. Este fenómeno, representado por la posición de las celdas color verde y celeste respecto de su equivalente naranja en la Figura 3.2(a), dificulta la convergencia de la optimización y no representa beneficio en las propiedades efectivas ya que sólo implica un movimiento de traslación de la *ventana* por la cual se observa la topología. Este comportamiendo puede verse en los resultados de la Figura 11 reportados por Podestá et al. [65]. En las instancias 2, 3 y 5 de la quinta fila, se observa un corrimiento en horizontal de la celda unidad debido a la imposición de un grupo $pm$. Este comportamiento desaparecería si se impusiera el grupo de plano $p2mg$, que es el apropiado para esta solución.

De manera general, la imposición de un grupo de plano o de espacio con suficientes elementos de simetría elimina este efecto, ya que la posición de dichos elementos respecto de la celda es fija. Por ejemplo, el grupo $p6mm$ ubica los ejes de rotación $n = 6$ en los vértices de la celda primitiva, imposibilitando las posiciones de celda como las verde y celeste. Cabe aclarar que, grupos con menores elementos de simetría pueden habilitar a mas de una posición de celda admisible, aunque estas posiciones no son continuas, por lo cual el problema mencionado sigue estando resuelto. Ejemplo de esto se muestra en la Figura 3.2(c), que muestra el resultado al mismo problema al imponer una simetría $p3m1$. Este grupo solo cuenta con ejes de rotación $n = 3$, ubicados en las esquinas de la celda y en los baricentros de los triángulos equiláteros que definen cada media celda. En este caso, uno de estos ejes (de vértice o interior) intenta aproximar el eje $n = 6$. De esta manera surgen configuraciones desplazadas, como la correspondiente a la celda verde.

### 3.3.4. Implicancias en el espacio de soluciones admisibles

La imposición de grupos de espacio y de plano a la topología restringe el espacio de soluciones admisibles. Por un lado, esto beneficia en la robustez y velocidad de convergencia del proceso de optimización, fomentando la aparición de resultados repetitivos, independientes del punto inicial. Por el contrario, si no se revisan todas las simetrías disponibles, se excluyen posibles soluciones satisfactorias. Este efecto es especialmente importante si las simetrías impuestas son de alto orden, ya que prohiben configuraciones con menor cantidad de elementos de simetría. En general, el proceso de selección de simetrías a evaluar requiere del criterio del diseñador en función del problema a resolver.

### 3.3.5. Implicancias en la correlación 3D-2D

De acuerdo a lo discutido en la Sección 2.4.2, un plano intersectando una red 3D captura una red 2D. Asimismo, la intersección de un plano con un grupo de espacio, genera un grupo de plano (ver Sección 2.4.7). En el proceso de diseño inverso de metamateriales 3D, resulta interesante ver las distribuciones geométricas que se forman en planos específicos, en particular aquellos que incluyen varios elementos de simetría. Este análisis fue presentado por Yera et al. [60] (Apéndice A) y revela que la aparición de grupos de plano a través de la imposición de grupos de espacio, genera topologías 2D con el mismo

tipo de respuesta efectiva (por ejemplo auxético, de máxima rigidez, o de bajo módulo de corte) que la buscada en el metamaterial 3D.

Esta correspondencia entre microarquitecturas 3D, que incluyen cortes con microarquitecturas 2D de igual comportamiento, puede explotarse para la búsqueda de nuevas topologías en ambos sentidos. Por un lado al optimizar metamateriales en 3D, la exploración de estos planos puede revelar metamateriales 2D no descubiertos. Por otra parte, el conocimiento de la simetría de topologías 2D de buen desempeño, resulta un indicador de cuales simetrías conviene explorar en 3D, las cuales deberían de incluir el grupo plano de la topología 2D en alguno de sus planos cristalográficos.

## 3.4. Comentarios sobre la optimización topológica

### 3.4.1. Simetrización de la función level-set y derivada topológica

Operativamente, la restricciones de simetrías cristalográficas sobre la topología se consiguen aplicando las operaciones de simetría que conforman los grupos sobre la función level-set. El proceso consiste en identificar puntos equivalentes por simetría y asignarles un único valor de level-set. Esto es sencillo de lograr si se utilizan mallas cuyos nodos preservan la misma simetría que la topología objetivo, permitiendo así realizar las operaciones correspondientes de manera exacta. El mismo proceso de simetrización se aplica sobre la derivada topológica por consistencia. Mayores detalles se brindan en el trabajo de Rossi et al. [61] (Apéndice B).

### 3.4.2. Importancia de elementos de interfase

Las propiedades elásticas asignadas cada elemento finito dependen de una función característica $\chi$. Esta función característica toma, idealmente, valores 0 o 1 de acuerdo con el valor de la función level-set en el elemento (ver Rossi et al. [61]). Cuando todos los nodos pertenecientes a un elemento tienen valores de level-set de igual signo (correspondientes a la misma fase constitutiva), el cálculo de la variable $\chi$ es trivial. Por el contrario, menos clara es la asignación de $\chi$ cuando el elemento es intersectado por la curva de nivel cero de la level-set. Un ejemplo de un caso conflictivo para un elemento finito bidimensional cuadrado se muestra en la Figura 3.3. El color de los nodos de esquina implica el signo de la función level-set, donde el negro indica la fase rígida y el blanco la fase blanda. La figura muestra dos posibilidades de interpretación de la curva de nivel 0, indicada en rojo. En el caso (a) la topología obtenida corresponde a zonas de fase rígida desconectadas, mientras que el caso (b) implica un encuentro fino o articulación. La rigidez a asignar al elemento en cada caso es muy distinta, asumiendo un contraste entre fases alto. En el problema 3D, las posibilidades de combinaciones de este tipo se incrementan. Se muestra en el siguiente capítulo que este tipo de encuentros finos son recurrentes en las topologías.

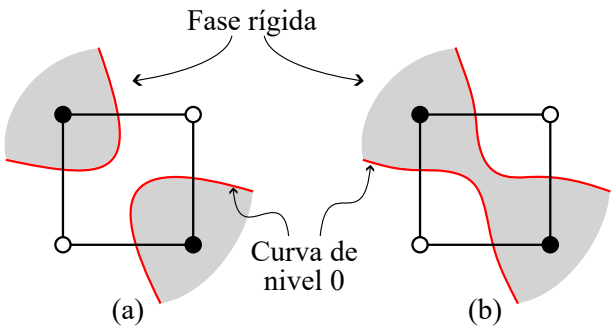


**Figura 3.3:** Caracterización de elementos de interfase. Misma configuración de función level-set nodal (indicada por colores blanco y negro) generando diferentes topologías: (a) zonas de material rígido desconectadas, (b) encuentro fino o articulación.

La experiencia obtenida durante el mejoramiento del algoritmo de optimización indica que el valor $\chi$ asignado a estos elementos de *rigidez intermedia* tiene un rol preponderante en la calidad de la solución final. El valor $\chi$ debe, por un lado, capturar lo mejor posible el comportamiento de mezcla del elemento de interfase en función de los valores de la level-set para prescindir de discretizaciones excesivamente finas, y, además, debe capturar la sensibilidad de la topología a los cambios en la level-set.

Se analizaron distintos esquemas para la determinación de $\chi$. Entre los mas simples se consideró un promedio de valores 0 o 1 asignado a cada nodo, de acuerdo al signo de la función level-set. Esta estrategia tiene las desventajas de mostrar nula sensibilidad a cambios pequeños de los valores nodales sin cambio de signo, y de no considerar la posición relativa de nodos de igual signo. Como técnica mas sofisticada (especialmente orientada a 3D) se probó con el algoritmo de "marching cubes" para la extracción de isosuperficies, muy extendido en el campo de visualización por computadora. Esta estrategia presenta 15 combinaciones posibles de posiciones relativas de los valores nodales en 3D, determinando en cada caso la posición de la superficie de nivel 0. Si bien este esquema tiene la ventaja de ganar sensibilidad según las posiciones relativas de los valores nodales, no elimina todas las indeterminaciones. Más aún, sigue siendo (al menos en su versión mas básica) insensible al valor nodal mas allá del signo. Desde el punto de vista de la implementación, la evaluación de los 15 casos posibles para cada elemento en mallas finas, y en procesos iterativos propios de la optimización, resulta en un gasto de tiempo considerable, que no se corresponde con un beneficio significativo. En el trabajo de Rossi et al. [61] (Apéndice B) se presenta la estrategia con mejores resultados, balanceando eficiencia en el cálculo y sensibilidad a cambios pequeños en la función level-set.

### 3.4.3. Dependencia con la topología inicial

Como es bien sabido, la no convexidad de la función objetivo respecto de la topología genera una fuerte dependencia con el punto de partida del proceso de optimización. Para contrarrestar este inconveniente y encontrar mínimos locales preponderantes, se resolvieron múltiples instancias de cada problema de optimización planteado, partiendo de puntos iniciales diferentes, y se buscaron soluciones topológicas recurrentes. El éxito de esta técnica se discute en el siguiente capítulo.

## 3.5. Conclusiones

Este capítulo se enfoca en el proceso de generación de un algoritmo de diseño inverso de materiales enfocado en lograr propiedades efectivas extremas. La metodología se sustenta en la imposición de grupos de simetrías de cristales al diseño topológico como elemento coordinador del proceso de optimización.

Los resultados expuestos por Yera et al. [60] y Rossi et al. [61], demuestran que la imposición de simetrías resulta en una herramienta útil para lograr aproximar los límites de propiedades efectivas, además de que existe una fuerte relación entre las propiedades alcanzables y la simetría de la microarquitectura.

Para concluir, se remarca que la metodología aquí propuesta es mucho más general que la aplicación abordada en esta tesis. No sólo es posible la búsqueda de respuestas efectivas elásticas con simetrías menores a la isotrópica, sino que es fácilmente extensible a otro tipo respuestas de los materiales, como ser térmica, acústica o fotónica. Esto se debe a que el principio de Neumann respalda la coherencia entre simetrías de la topología y respuesta efectiva.

# Capítulo 4

# Lecciones obtenidas de la optimización topológica acerca de las microarquitecturas óptimas

## 4.1. Introducción

El propósito de este capítulo es servir como nexo entre los primeros dos artículos de esta tesis (Apéndices A y B), y la publicación realizada por Rossi et al. [69] (Apéndice C). Se realiza una exposición del entendimiento logrado sobre la conexión existente entre microarquitectura y comportamiento efectivo elástico. Este aprendizaje resulta de una inspección exhasutiva de los resultados logrados a partir de la técnica de diseño inverso introducida en el capítulo anterior y explicada de manera abarcativa en los trabajos de Yera et al. [60], Rossi et al. [61].

Como continuación del trabajo previo, el objetivo aquí es lograr simplificar las microarquitecturas conseguidas, traduciéndolas en pocos parámetros geométricos pero sin perder el funcionamiento mecánico subyacente. Para esto, las simetrías de cristales mantienen un rol predominante en la interpretación de las topologías. El motivador de este trabajo es la formación de geometrías que aparecen repetitivamente en los resultados, y que constituyen un indicio de que ciertos mínimos locales de la función objetivo son mas convenientes que otros.

El resto de este capítulo está ordenado de la siguiente manera. En la Sección 4.2 se presenta una discusión acerca de los mecanismos subyacentes identificados para los distintos comportamientos efectivos y de ciertos aprendizajes logrados a partir de los resultados de optimización topológica. En la Sección 4.3 se muestra el camino para traducir estos mecanismos en estructuras parametrizadas, para dos topologías 2D. La Sección 4.4 cierra este capítulo presentando las principales conclusiones.

## 4.2. Discusión de las topologías obtenidas

### 4.2.1. Formación de estructura en una escala inferior

La inspección sistemática de las microarquitecturas obtenidas revela que, en muchos casos, la optimización topológica genera formas o estructuras de la fase rígida, acompañadas de huecos o inclusiones de la fase blanda que parecen tender a formar una subestructura caracterizada en una escala de longitud inferior a la del tamaño del RVE.

Este comportamiento se visualiza en la Figura 4.1. En ella se muestran dos pares de microarquitecturas correspondientes a los problemas 8 (máximo $\hat{K}$) y 10 (mínimo $\hat{G}$) en la Figura 7 de Yera et al. [60]. Las microarquitecturas que conforman una misma subfigura comparten la misma forma subyacente de

la fase rígida[1]. En el caso (a) la microarquitectura consiste en una red de hexágonos, mientras que en el caso (b) se identifican figuras aproximadamente hexagonales conectadas por elementos de tres barras. Es notable cómo en ambos casos, el cambio de objetivo del problema 8 al problema 10 induce al optimizador a generar una estructura fina en las barras, manteniendo la forma general de la microarquitectura. Esta subestructura asemeja un material laminado 2D. En la figura se mencionan los grupos de plano impuestos en cada caso.

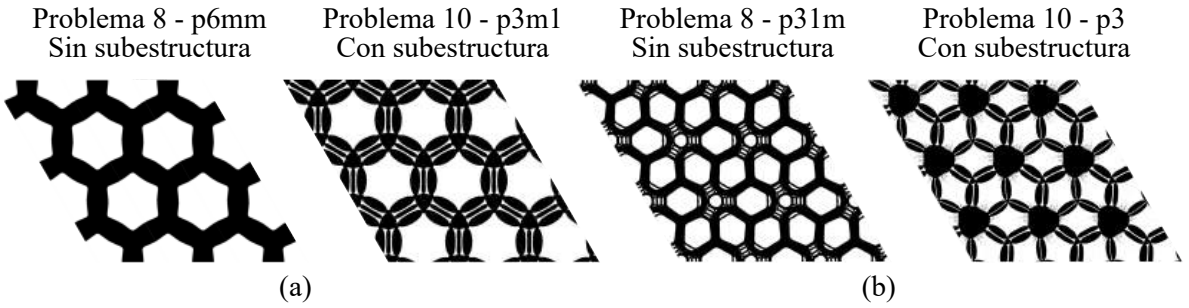


**Figura 4.1:** Formación de subestructuras 2D de acuerdo a las propiedades objetivo. El problema 8 corresponde a máximo $\hat{K}$ mientras que el problema 10 a mínimo $\hat{G}$. (a) Forma subyacente hexagonal. (b) Forma subyacente constituida por tríos de barras conectando nodos.

En problemas 3D es más difícil que se manifiesten estas subestructuras, debido a que por cuestiones de capacidad de cálculo la malla es inicialmente gruesa y es progresivamente refinada a medida que avanza la optimización. Esto genera una fuerte dependencia de la solución final de la malla fina con la primera solución parcial obtenida con malla gruesa. En el caso 2D, por el contrario, es factible realizar la optimización completa en una malla fina. Sin embargo, ciertas propiedades específicas, como máxima rigidez, o mínimo módulo de corte simultáneamente con alto módulo de compresibilidad, tienen una preferencia notable para encontrar este tipo de topologías.

En la Figura 4.2 se muestran tres topologías tridimensionales obtenidas con formación de subestructura, referidas a la numeración de la Figura 12 de Yera et al. [60]. Las primeras dos, Subfiguras (a) y (b), tienden a formar láminas paralelas que conectan cáscaras cerradas de la fase rígida. El caso (c), por el contrario, forma una subestructura que asemeja a fibras paralelas úniendo marcos abiertos.

Desde un punto de vista estructural, la importancia de las subestructuras para transportar carga es ya conocida de la concepción de las denominadas estructuras de Michell. En el caso del diseño de metamateriales extremos, su rol resulta más evidente en algunos casos que en otros. De manera general, si se asume que una sucesión de mallas más finas consiguen subestructuras cada vez más finas, se puede concluir que la optimización topológica busca introducir zonas de material compuesto en una longitud de escala inferior. En los casos (a) y (b) de la Figura 4.2 la tendencia indica un material compuesto reforzado por láminas, mientras que en el caso (c) se tiene un compuesto reforzado por fibras. La característica común a ambos casos es tener modos de deformación de alta y baja rigidez. La combinación de estos modos en direcciones apropiadas logra las propiedades efectivas buscadas.[2]

### 4.2.2. ¿Cómo obtener materiales con algunos modos flexibles?

Siguiendo las ideas presentadas por Milton y Cherkaev [70], el concepto de modos flexibles de un material hace referencia a los modos de deformación en los que el material presenta una muy baja o nula rigidez. En concordancia con los trabajos de Yera et al. [60], Rossi et al. [61], limitando la discusión

[1] Se remarca en este punto que al hablar de forma subyacente no se está refiriendo al concepto de topología, el cual distingue el número de inclusiones de fase blanda, sino una idea mas intuitiva, una "apariencia" general.

[2] Es sabido de la capacidad de los laminados de alto rango para obtener propiedades extremas. Sin embargo, las topologías aquí planteadas solo utilizan este tipos de compuestos de escala inferior en determinadas ubicaciones de la celda unidad.

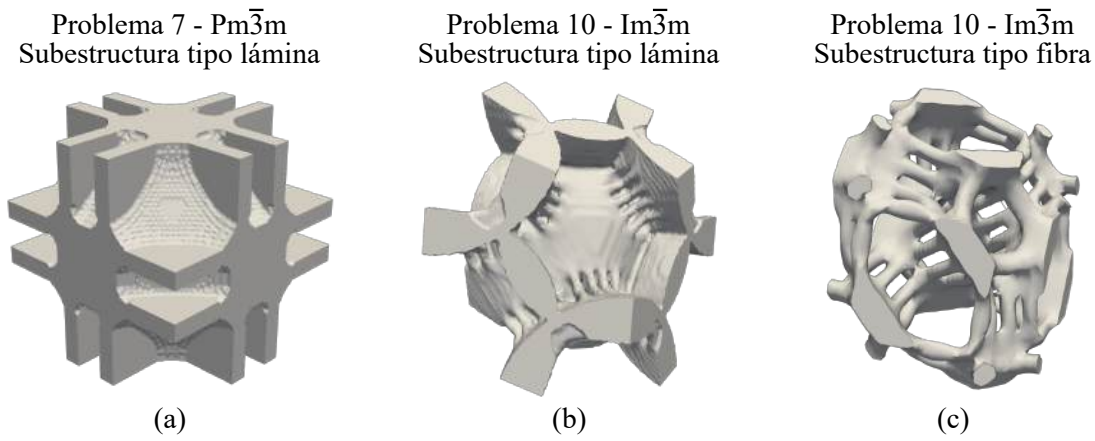


**Figura 4.2:** Formación de subestructuras 3D de acuerdo a las propiedades objetivo. El problema 7 corresponde a máxima rigidez mientras que el problema 10 a mínimo $\hat{G}$. (a) Formación de láminas en estructura de máxima rigidez. (b) Formación de láminas en estructura de bajo $\hat{G}$. (c) Formación de fibras paralelas en estructura de bajo $\hat{G}$.

a materiales con respuesta efectiva isotrópica, los modos de deformación se vinculan naturalmente a un modo esférico y a modos desviadores. De esta manera, al hablar de *algunos* (pero no todos) modos flexibles, resultan de interés dos casos: materiales unimodales y materiales pentamodales (o bimodales en el caso 2D). Los materiales unimodales o auxéticos, presentan un bajo o nulo módulo de compresibilidad, mientras que los pentamodales presentan un bajo o nulo módulo de corte.

Notablemente, los resultados logrados a través de la metodología utilizada respaldan la afirmación de Milton y Cherkaev [70] referida a que para lograr microarquitecturas en una única escala (los autores lo discuten referido a microestructuras posibles de manufacturar), son necesarios vínculos finos, tendiendo a rótulas, entre zonas de la fase rígida.

En la Figura 4.3 se muestran topologías obtenidas que respetan esta lógica. Acompañando las microarquitecturas bidimensionales se presentan esquemas que muestran el rol de estos encuentros (casi) rotulados en los modos flexibles. En el caso de la Subfigura (a), el material auxético está compuesto por hexágonos conectados por barras a través de encuentros finos. La rotación de los hexágonos es compatible con el giro de estas barras con muy poco aporte de energía que se acumula casi por completo en las uniones, generando así una expansión volumétrica sin oposición. Por otro lado, en el caso de la Subfigura (b), el material bimodal presenta planos que son sólo atravesados por este tipo de barras rotuladas, y que permiten, nuevamente con muy poco aporte de energía, un deslizamiento en forma de cizalla entre los elementos triangulares que conectan. Este tipo de comportamiento también explica el funcionamiento de las microarquitecturas 2D publicadas por Yera et al. [60] (Apéndice A).

Se observó, como mecanismo general, que los auxéticos 2D basan su comportamiento en el giro relativo de sus partes. Existen dos posibilidades, la chiralidad, donde todos los polígonos giran en un mismo sentido (caso del hexágono de la Subfigura (a)), o la antichiralidad, donde los giros se dan en ambos sentidos (ver la estructura correspondiente al problema 1 de la Figura 11 en [60]). La chiralidad es compatible con los grupos de plano que no presentan planos de reflexión, es decir $p3$ y $p6$, mientras que, por el contrario, aquellas que si los presentan, $p31m$, $p3m1$ y $p6mm$ son compatibles con la antichiralidad. En la práctica solo se encuentran topologías sencillas antichirales con el grupo plano $p31m$. Esto posiblemente se debe a que es la única de las tres disponibles con ejes de rotación no coincidentes con planos de reflexión. Esto explica las conclusiones presentadas por Yera et al. [60] (Apéndice A) relativas al rol de los distintos grupos de punto para lograr comportamiento auxético.

Para el caso de microarquitecturas 3D, la interpretación de los mecanismos de deformación no siempre es tan evidente, aunque son válidas algunas analogías. En el caso del material auxético de la Subfigura (c), visto desde orientaciones opuestas, se observa que en el centro el espesor del material tiende a es-

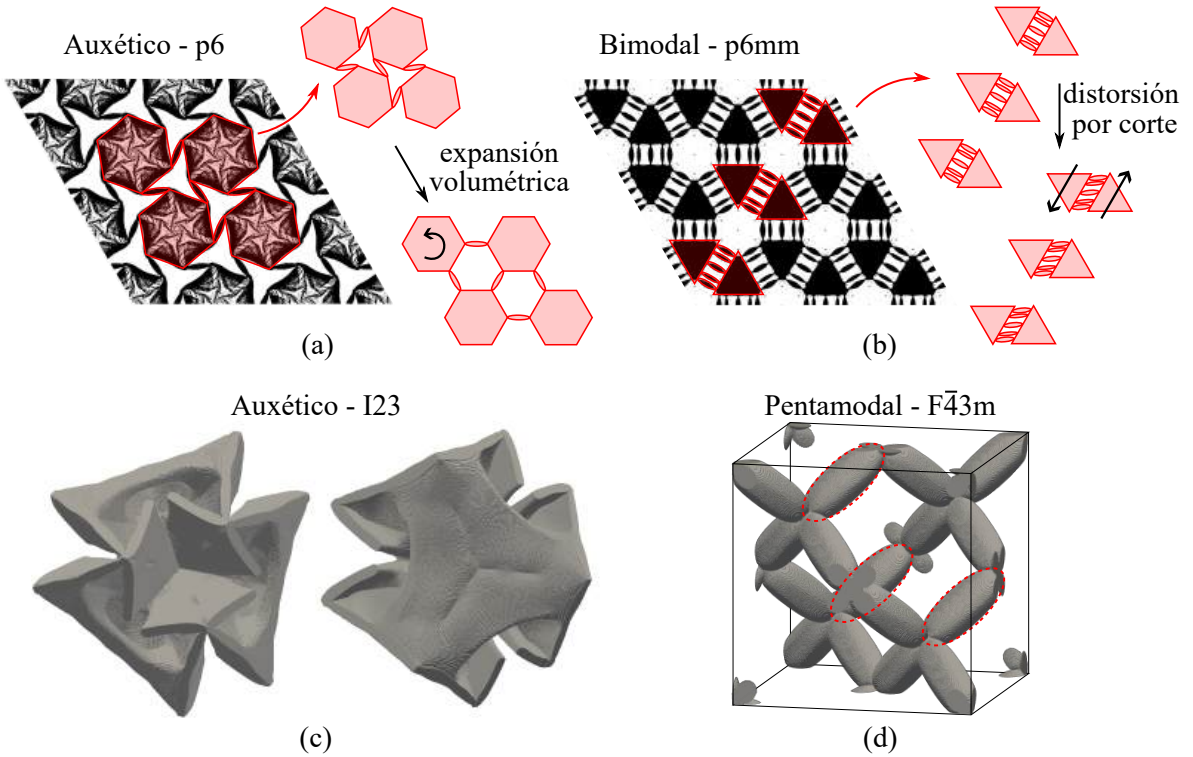


**Figura 4.3:** Encuentros finos en materiales unimodales (auxéticos) y penta/bimodales. (a) Auxético con grupo de plano $p6$. (b) Bimodal con grupo de plano $p6mm$. (a) Auxético con grupo de espacio $I23$. (a) Pentamodal con grupo de espacio $F\bar{4}3m$.

trecharse formando tres surcos. En el caso del material pentamodal de la Subfigura (d) se identifica el mismo comportamiento que el caso bidimensional, donde se forman planos que intersectan de manera normal los elipsoides, generando una debilidad para resistir al corte (en la figura se remarcaron los tres elipsoides correspondientes a uno de estos planos). Estas topologías fueron presentadas por Rossi et al. [61] (Apéndice B). En ese trabajo se profundiza en la explicación del mecanismo de deformación de una topología auxética similar a la mostrada en la Figura 4.3(c).

### 4.2.3. ¿Cómo obtener altas rigideces?

Un material de alta rigidez refiere a una respuesta sin modos blandos. En el caso 3D, se observa que las microarquitecturas optimizadas del problema de máximo módulo de compresibilidad se constituyen como paredes delgadas de la fase mas rígida que encierran "burbujas" de la fase blanda, donde estas burbujas están desconectadas entre sí. Esto puede observarse en la Figura 12 de Rossi et al. [61] (Apéndice B). Se observa también que las topologías con propiedades efectivas cercanas a las máximas rigideces (tanto módulo de compresibilidad como de corte), siempre tienden a una simetría máxima, independientemente del grupo impuesto. Este fenómeno es luego tenido en cuenta para generar las estructuras parametrizadas.

### 4.2.4. Formación de topologías óptimas teóricas

Ante la imposición de los grupos de plano y espacio adecuados, el esquema de homogeneización inversa con restricciones de simetría es capaz de encontrar soluciones que se han demostrado óptimas desde un punto de vista teórico. Ejemplo de esto son la topología de la izquierda de la Figura 4.1(a), la cual corresponde a una estructura de Vigdergauz [71] que maximiza el módulo de compresibilidad en 2D, y la topología de la Figura 4.3(d), la cual fue propuesta por Milton y Cherkaev [70] como minimizadora

del módulo de corte en 3D.

### 4.2.5. Mínimos preferenciales y la identificación de sus topologías

Para ciertas propiedades efectivas objetivo, los resultados del proceso de optimización son recurrentes, aún partiendo de topologías iniciales distintas. Esto indica que la función objetivo para estas propiedades efectivas presenta mínimos locales fuertemente preferenciales. Más aún, se observa que, en la búsqueda de estos mínimos locales preferenciales, la simetría de la topología obtenida aproxima un grupo de plano o de espacio superior al impuesto (entendiéndose como grupo superior a uno que incluye elementos de simetría adicionales a los ya contenidos por el grupo inferior). La Figura 8 de Yera et al. [60] presenta un ejemplo de este comportamiento para la solución del punto de Walpole en 2D. La solución a dicho problema pertenece al grupo de plano de máxima simetría $p6mm$, la cual es superior al resto de los examinados. Para los cuatro grupos de plano menores, las soluciones logradas intentan, de manera natural, adicionar elementos de simetría no impuestos. Por otra parte, la Figura 13 del mismo trabajo muestra el mismo comportamiento para el caso de un auxético 3D. Todas las topologías mostradas se obtuvieron de imponer un grupo de espacio $I23$. Este grupo no incluye planos de reflexión, que sí son obtenidos por este conjunto de microarquitecturas, alcanzando un grupo de espacio $I\bar{4}3m$, superior al impuesto. El paso natural de una simetría inferior a una superior es un gran indicador del grupo de plano o de espacio correcto para ser impuesto en el problema analizado.

Asimismo, habiendo identificado una simetría apropiada, es de esperar que una pequeña perturbación en la propiedad objetivo no afecte en gran medida las conclusiones logradas. Dicho de otra forma, se espera un grado de continuidad entre las simetrías (y las topologías) óptimas entre propiedades extremas próximas a lo largo de los límites teóricos. Esta conclusión es muy relevante para los aportes de esta tesis, y surge de la experiencia propia en la evaluación sistemática de los problemas de optimización topológica modificando los valores objetivo. No se ha encontrado en la literatura un análisis de este tipo. La Figura 4.4 muestra tres resultados, dos en 2D y uno en 3D, que confirman este razonamiento. Las microarquitecturas mostradas en esta figura se obtuvieron a partir de esta metodología, pero en su mayoría no fueron reportadas en las publicaciones.

En primer lugar, el panel (a) muestra una secuencia de topologías obtenidas para propiedades a lo largo de los límites de propiedades extremas inferior y derecho. La numeración señalada corresponde a la Figura 7 en [60]. La microarquitectura subyacente en todos los casos corresponde a la discutida en la Sección 4.2.1 respecto de la Figura 4.1(b). La diferencia entre topologías para obtener distintas propiedades efectivas consiste en la rigidez de los brazos conectores, determinada por el número y espesor de las barras que tienden a una subestructura.

En el panel (b) se muestra una secuencua de topologías del tipo chiral, que aproximan bien los límites izquierdo y superior (ver numeración). En este caso se observan hexágonos de un material *gris*, conectados con mayor o menor inclinación por barras en tendencia a una subestructura. Este material gris se explica a partir de que, con ese nivel de densificación, el hexágono ya es lo suficientemente rígido en relación a las uniones con los brazos conectores. Además de que se deben cumplir restricciones de volumen. En este caso, la rigidez de los brazos y el ángulo relativo entre hexágonos son las características que condicionan la respuesta efectiva.

Por último, en el panel (c) se muestran dos vistas de un material auxético 3D, con el mismo tipo de microarquitectura mostrada en la Figura 4.3(c). En este caso se resolvieron una serie de problemas con propiedades efectivas objetivo más próximas a las propuestas en [60]. En cada microarquitectura se indica la relación entre la restricción del módulo de corte efectivo $G^*$ y el límite analítico superior $G^u$. El mecanismo por el cual esta topología logra auxeticidad fue descripto por Rossi et al. [61]. Solamente se señala aquí como, a medida que aumenta el módulo objetivo $G^*$, se incrementa la apertura entre las *alas* de la topología, y se obtienen tambien mayores espesores de las cáscaras.

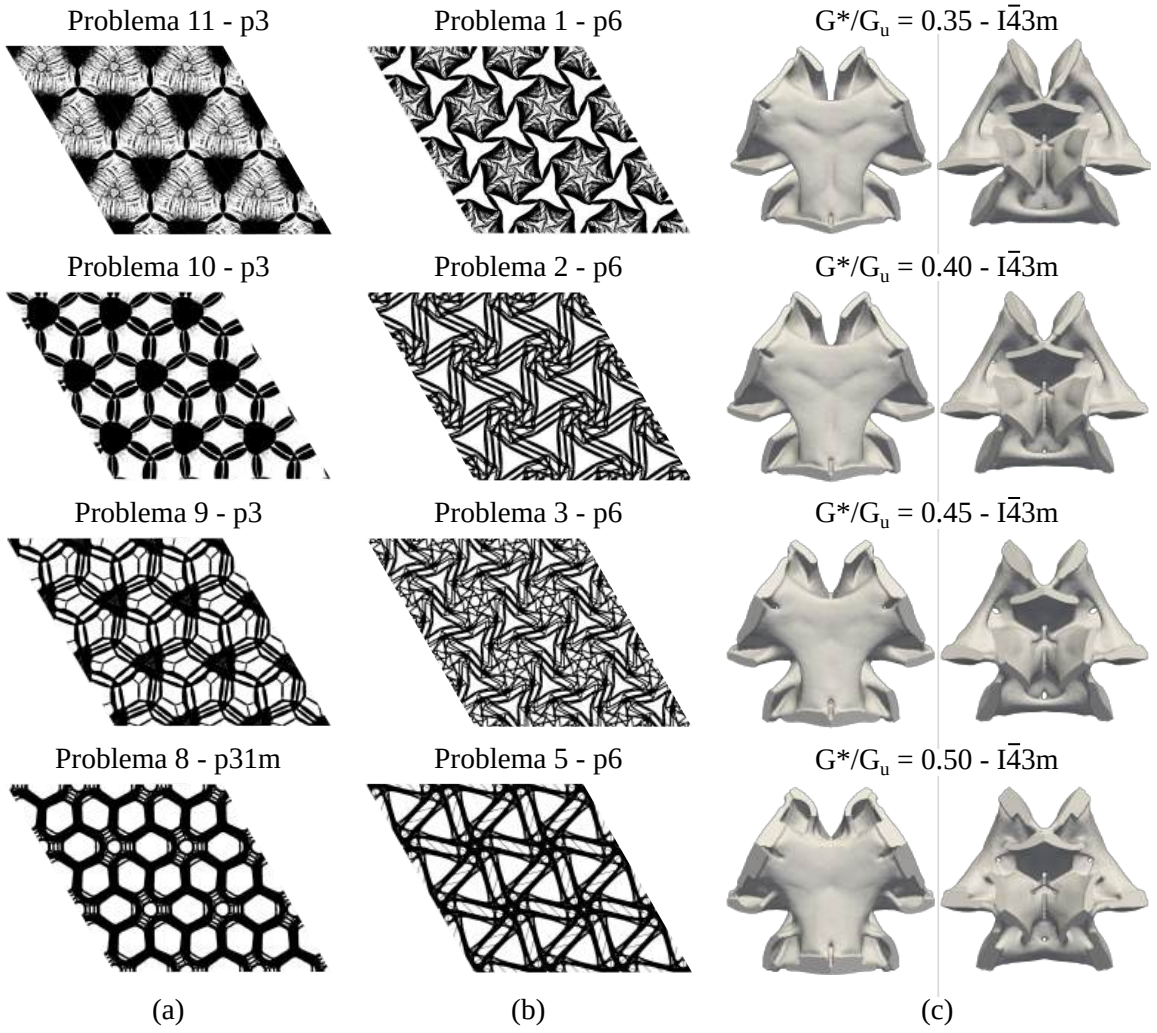


**Figura 4.4:** Transiciones suaves en la microarquitectura de materiales con propiedades efectiva similares. (a) Transición entre materiales 2D de bajo $\hat{G}$ hacia alto $\hat{K}$. (b) Transición de materiales 2D auxéticos hacia materiales de alta rigidez. (c) Transición de materiales 3D auxéticos con creciente $\hat{G}$.

## 4.3. Búsqueda de microarquitecturas parametrizadas

Habiendo identificado relaciones entre las respuestas efectivas y las topologías, surge naturalmente el interés en lograr microarquitecturas parametrizadas que involucren estas características. Al mismo tiempo, resulta de interés simplificar la topología sin ir en detrimento de la propiedad efectiva, o incluso haciéndola aún mas extrema. Para que resulten de mayor utilidad, y basándose en la discusión 4.2.5, las microarquitecturas deben ser capaces de abarcar, ante cambios de parámetros, un amplio rango de propiedades efectivas.

Asimismo, las estructuras parametrizadas deben respetar en todo momento, los grupos de plano y espacio de las estructuras que las inspiraron. Esto garantiza la simetría de la respuesta efectiva independientemente de las propiedades individuales de las fases constituyentes. Esta característica es en absoluto trivial, como fue mencionado por Milton [4].

Un punto clave de las parametrizaciones buscadas consiste en la inclusión de subestructura en una escala inferior, de acuerdo a la discusión 4.2.1. Estas subestructuras se constituyen a partir de las mismas dos fases que conforman el metamaterial. En el caso 2D, el límite de las estructuras finas corresponde

a compuestos laminados (ver Figura 4.1). Mientras que en el caso 3D, el límite de las estructuras finas puede definir tanto compuestos laminados como compuestos matriz-fibra (ver Figura 4.2). Además, de acuerdo a la discusión 4.2.5 concerniente a las regiones hexagonales, es posible también considerar un material isotrópico de rigidez intermedia entre ambas fases.

En el caso 2D, se pudieron formular diversas microarquitecturas periódicas parametrizadas. Las de mejor desempeño fueron publicadas por Rossi et al. [69]. Como anticipación a dicho trabajo, se presentan brevemente dos parametrizaciones no publicadas, que esquematizan el razonamiento seguido para lograr dichas topologías simplificadas.

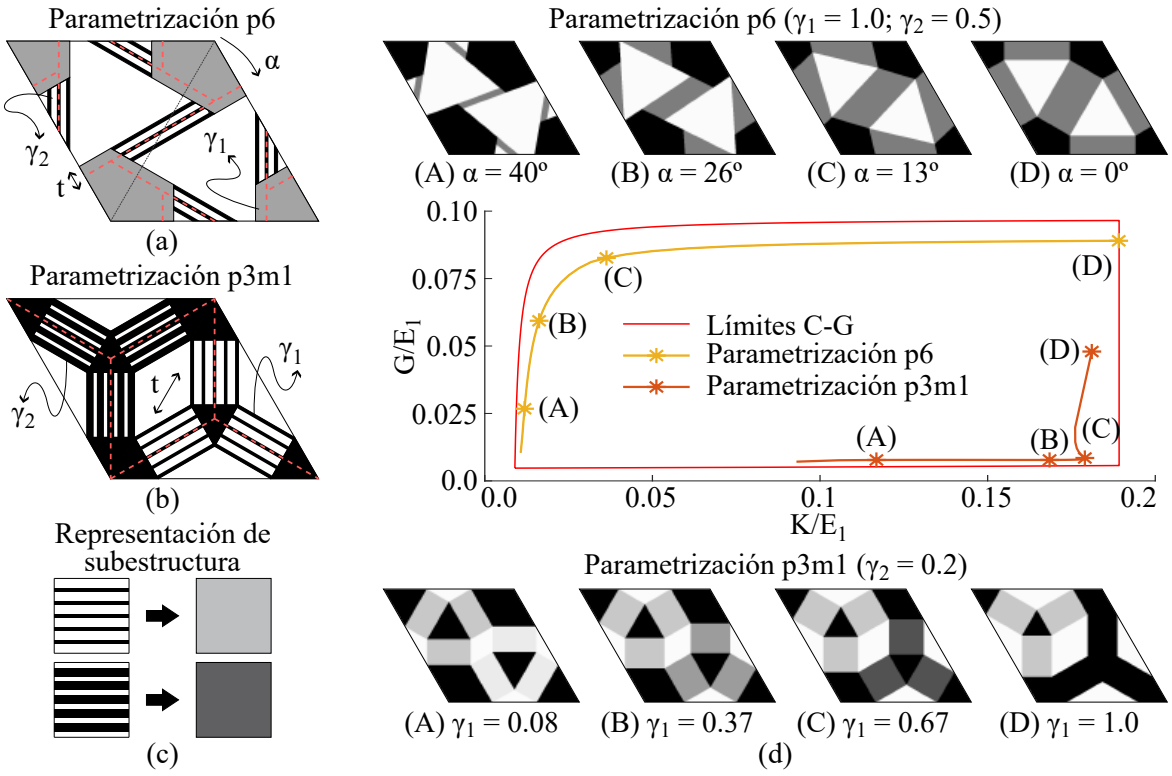


**Figura 4.5:** Microarquitecturas parametrizadas 2D. (a) Parametrización con simetría $p6$ que consigue respuestas auxéticas y de alto módulo $\hat{G}$. (b) Parametrización con simetría $p3m1$ que consigue respuestas bimodales y de alto módulo $\hat{K}$. (c) Esquema de representación en escala de grises del material laminado. (d) Resultados para un barrido en un único parámetro en ambas parametrizaciones.

En primer lugar, la Figura 4.5(a) muestra una microarquitectura chiral inspirada por las topologías de la Figura 4.4(b). La misma posee un grupo de plano $p6$, y esta compuesta por zonas hexagonales de un material isotrópico definido en subestructura (en gris), conectadas entre sí por brazos de material laminado ortotrópico (zonas rayadas). Existen además zonas triangulares de la fase blanda (en blanco). Los parámetros que definen el diseño son: (i) la orientación de los brazos $\alpha$, (ii) la fracción de volumen del material isotrópico $\gamma_1$, (iii) la fracción de volumen del material laminado $\gamma_2$, y (iv) el espesor de los brazos $t$. Esta microarquitectura se genera con el propósito de abarcar las propiedades de la zona superior izquierda en el espacio $K - G$ de propiedades efectivas.

Por otra parte, la Figura 4.5(b) muestra una microarquitectura de simetría $p3m1$ inspirada en los resultados mostrados en la Figura 4.4(a). La topología se constituye de zonas triangulares y hexagonales de de la fase rígida (en negro), conectadas por brazos de material laminado con distintas densidades (zonas rayadas), además de las zonas romboidales de material blando (en blanco). En este caso sólo se necesitan tres parámetros: (i) y (ii) las fracciones de volumen de las zonas de material laminado $\gamma_1$ y $\gamma_2$, y (iii) el espesor de los brazos $t$. Se espera que las propiedades efectivas se aproximen para esta

microarquitectura a los límites en la zona inferior y derecha.

Para ambas parametrizaciones, la dirección de laminación es normal a la dirección de los brazos (indicada en líneas rojas a trazos). Además, el conjunto de valores que tomen los parámetros debe ser tal que se verifique la restricción de volumen general impuesta sobre el metamaterial. En la Figura 4.5(d) se muestran algunas propiedades obtenidas por ambas estructuras parametrizadas dentro del espacio de propiedades alcanzables definido los límites Cherkaev-Gibiansky. En las ilustraciónes, la intensidad del color gris denota las distintas fracciones de volumen de las zonas laminadas, de acuerdo al esquema de la Figura 4.5(c).

En los dos casos el compuesto está constituido por fases con un contraste $c = 200$ y una fracción global de fase rígida $f_1 = 0.5$. Los resultados mostrados para la parametrización $p6$ correponden a un barrido en $\alpha$, fijando $\gamma_1 = 1$ (material de los hexágonos coincide con fase rígida) y $\gamma_2 = 0.5$. Los resultados de la parametrización $p3m1$ corresponden a un barrido en $\gamma_1$, con $\gamma_2 = 0.2$. En ambos casos el espesor $t$ se ajusta para cumplir la restricción de $f_1$. Se observa que las dos parametrizaciones generan un amplio abanico de propiedades efectivas alcanzables, variando únicamente un parámetro. Como estructuras mas interesantes entre las mostradas se menciona que la topología $p6$-(B) es la de menor coeficiente de Poisson $\nu$, la topología $p6$-(D) es la de mayor rigidez, mientras que la topología $p3m1$-(C) es la más próxima al punto de Walpole (máximo $\hat{K}$ con mínimo $\hat{G}$).

Un análisis más profundo, que incluye la variación en todos los parámetros, y un proceso de optimización para aproximar los límites teóricos es presentado por Rossi et al. [69] (Apéndice C).

En el caso 3D, la complejidad de las topologías obtenidas sólo permite interpretar la geometría de microarquitecturas particulares. Un ejemplo de esto es la celda mostrada en la Figura 4.2(a). La misma consiste en una cáscara cerrada de forma aproximadamente octaédrica, vinculada a sus celdas vecinas por un compuesto laminado (la Figura 12 de Rossi et al. [61] muestra un corte que revela el interior de la microarquitectura). Sin embargo, no fue posible lograr en este caso parametrizaciones que incluyan un espectro de propiedades efectivas que aproximen los límites teóricos. Cabe señalar también que es un gran desafío garantizar una respuesta isotrópica a partir de una estructura parametrizada que, como máximo, tiene simetría cúbica.

## 4.4. Conclusiones

El principal objetivo de este capítulo consiste en exponer la validez de la metodología de homogeneización inversa con restricciones de simetrías cristalográficas como fuente de inspiración y aprendizaje para el diseño de microarquitecturas elásticas. En particular, se estudió el problema de topologías con propiedades efectivas isotrópicas que aproximan los límites teóricos. Se lograron identificar mecanismos de deformación subyacentes y soluciones recurrentes, de las cuales algunas fueron reinterpretadas en microarquitecturas simples definidas por un número reducido de parámetros.

Algunas líneas de investigación futuras interesantes que no fueron abordadas en esta tesis incluyen:

- Explorar simetrías no isotrópicas de la respuesta efectiva abordando necesidades específicas. Un ejemplo de esto es la búsqueda de microarquitecturas 3D con propiedades ortotrópicas que repliquen la de los huesos. Esto permitiría la generación de topologías que puedan ser incorporables a prótesis.

- Implementar un proceso de reconocimiento automático de simetrías superior al impuesto durante la optimización topológica. Esto permitiría iniciar el proceso de optimización imponiendo simetrías bajas (incluso que no verifiquen la simetría esperada de la respuesta) y aumentar el número de elementos de simetría impuestos (es decir, pasar a un grupo de plano/espacio) sólo si el optimizador así lo requiere, acompañado esto de la liberación de restricciones pertinente. Esta propuesta requiere de un ordenamiento en secuencia de grupos de plano/espacio posibles de alcanzar al adi-

cionar elementos de simetría. Por ejemplo, un grupo plano $p2$ es compatible tanto con un $p4$ como un $p6$ (según la red elegida), pero estos no son compatibles entre ellos.

- Parametrizar las microarquitecturas 3D. Esto requiere, en primera instancia, de un proceso más exhaustivo de resolución de problemas que incluyan un mayor número de grupos de espacio, para identificar tantos patrones como sea posible. La interpretación de estructuras tridimensionales en un número acotado de parámetros es sin dudas un desafío, sobre todo para respuestas como la auxética. Sin embargo, lograr este objetivo permitiría facilitar la manufacturabilidad de estos compuestos.

# Capítulo 5

# Diseño de metamateriales con inestabilidades en la microescala

## 5.1. Introducción

El propósito de este capítulo es motivar el trabajo realizado durante la tesis en dirección al diseño de metamateriales con transiciones de fase elásticas en la microescala. Este tipo de comportamiento, derivado de funciones de energía de deformación que no cumplen los criterios de convexidad convencionales, posibilita, entre otras cosas, la disipación de energía en materiales elásticos. El objetivo es lograr metamateriales que maximicen la liberación de energía. Los resultados logrados a partir de lo que aquí se expone fueron publicados por Rossi et al. [72, 73, 74], trabajos replicados en los Apéndices D, E, y F.

Para ello se inicia este capítulo exponiendo en la Sección 5.2 los aspectos mas fundamentales detrás de las funciones de energía no convexas y los cambios de fase en la microescala, sin necesidad de hacer referencia a una microarquitectura en particular. Sobre el final de la sección se discute el rol que juega el concepto de metamaterial como un medio para materializar los comportamientos a partir de un diseño de microarquitectura. La propuesta original consistió en mantener la línea de la optimización topológica mostrada hasta el momento, aplicada en este caso a materiales en régimen no lineal. En la Sección 5.3 se presenta el trabajo realizado, incluyendo las dificultades encontradas que interrumpieron este enfoque. Finalmente, en las Secciones 5.4 y 5.5 se presenta el camino alternativo encontrado para contribuir al diseño y el entendimiento de estos materiales.

## 5.2. Generalidades sobre los materiales con cambios de fase elásticos

A modo de primer acercamiento al comportamiento de este tipo de materiales en la microescala, se propone el análisis de la respuesta de un RVE unidimensional $\Omega_\mu$, constituido por un material con dos fases. Este ejemplo fue adaptado del trabajo de Carstensen [75]. Se asume que la densidad de energía de deformación en la microescala tiene la forma:[1]

$$\psi(\varepsilon_\mu) = \left({\varepsilon_\mu}^2 - 1\right)^2 \ , \tag{5.1}$$

donde $\varepsilon_\mu = du_\mu/dy$, siendo $y$ las coordenadas y $u_\mu$ los desplazamientos en la microescala. La Figura 5.1 muestra esta función de energía, así como la función tensión $\sigma_\mu(\varepsilon_\mu) = d\psi/d\varepsilon_\mu$, la cual es no monótona. De acuerdo con los desarrollos de la Sección 2.3, es posible descomponer el campo de deformaciones de

[1] Con el fin de mantener la simplicidad en las expresiones involucradas, la definición de la función de energía (5.1) involucra ciertas incoherencias desde un punto de vista estrictamente físico. El análisis no se limita a pequeños valores de $\varepsilon_\mu$, ni $\psi \to \infty$ cuando $\varepsilon_\mu \to -1$. Esto de ninguna manera afecta los argumentos puramente matemáticos, ni la discusión fundamental subyacente que se pretende realizar.

la microescala en un campo medio macroescala sumado a una fluctuación $\varepsilon_\mu = \varepsilon + \tilde{\varepsilon}_\mu$. La condición de equilibrio surge de la minimización de la energía de deformación total en $\Omega_\mu$:

$$\min_{\tilde{u}_\mu} \int_{\Omega_\mu} \psi\left(\varepsilon + \frac{d\tilde{u}_\mu}{dy}\right) d\Omega_\mu \qquad , \qquad \text{con } \tilde{u}_\mu \in \tilde{\boldsymbol{\mathcal{U}}}_\mu \ , \tag{5.2}$$

y $\tilde{\boldsymbol{\mathcal{U}}}_\mu$ definido de acuerdo a la expresión (2.33). Nótese que en este contexto 1D, la minimización (5.2) implica un campo de tensiones $\sigma_\mu(\varepsilon + \tilde{\varepsilon}_\mu)$ constante. Encontrado el campo de fluctuaciones óptimo $\tilde{u}^*_\mu$, la densidad de energía en la macroescala $\hat{\psi}$ se calcula siguiendo los procedimientos de homogeneización presentados en la Sección 2.3:

$$\hat{\psi}\left(\varepsilon\right) = \frac{1}{|\Omega_\mu|} \int_{\Omega_\mu} \psi\left(\varepsilon + \frac{d\tilde{u}^*_\mu}{dy}\right) d\Omega_\mu \ . \tag{5.3}$$

Para ejemplificar las implicancias de considerar una energía de deformación de la forma (5.1) en la solución al problema (5.2), se analiza el caso particular de una deformación macro $\varepsilon = 0$, lo cual es equivalente a imponer desplazamientos nulos en los extremos del RVE unidimensional.

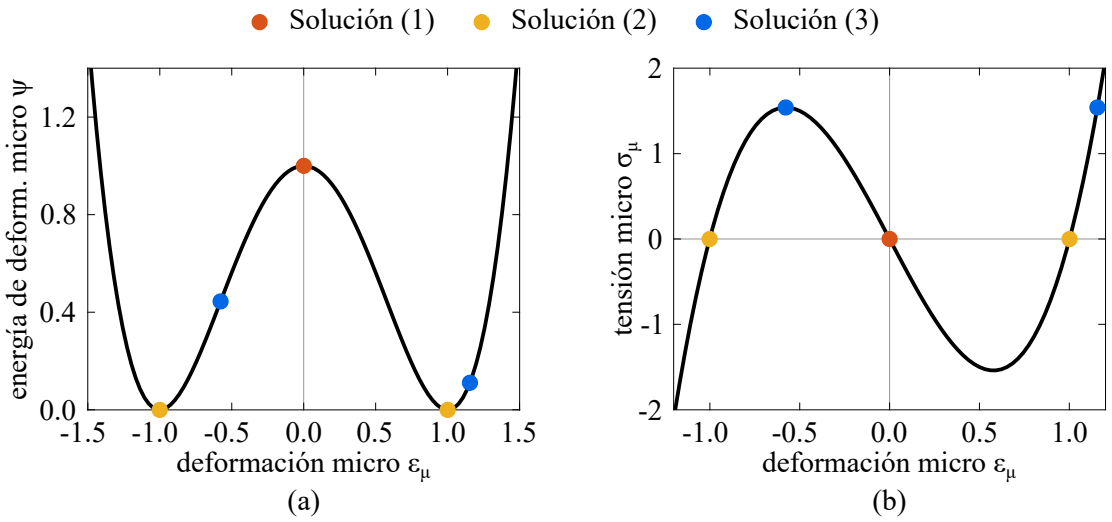


**Figura 5.1:** Equilibrio en material con dos fases. (a) Relación energía - deformación. (b) Relación tensión - deformación.

La solución clásica al problema (5.2), señalada como solución (1) en la Figura 5.1, implica un campo deformaciones homogéneo $\varepsilon_\mu(y) = 0$. Esto implica además un campo de tensiones $\sigma_\mu(y) = 0$ y una energía macro $\hat{\psi}\left(0\right) = 1$. Esta situación, sin embargo, constituye un estado de equilibrio inestable, ya que el material en el RVE se encuentra punto a punto en un máximo de energía.

Se considera ahora la posibilidad de que el campo de deformaciones solución, esté dado por una mezcla de fases. Es decir, que en ciertas zonas del RVE el material presente una deformación $\varepsilon_{\mu_I}$ correspondiente a la rama convexa izquierda de la energía (material en fase I), y en otros presente una deformación $\varepsilon_{\mu_{II}}$ correspondiente a la rama convexa derecha (material en fase II). Para el problema 1D planteado, las condiciones de equilibrio y admisibilidad cinemática dada por el espacio $\tilde{\boldsymbol{\mathcal{U}}}_\mu$ implican:

$$\sigma_\mu(\varepsilon_{\mu_I}) = \sigma_\mu(\varepsilon_{\mu_{II}}) \ , \tag{5.4}$$

$$\varepsilon = (1-c)\, \varepsilon_{\mu_I} + c\, \varepsilon_{\mu_{II}} \ , \tag{5.5}$$

donde $c$ representa una concentración de fase que indica la cantidad de material en fase II, independientemente de la distribución espacial a lo largo del RVE . Partiendo del hecho de que la solución tendrá como

máximo dos fases y siendo que la ecuación (5.5) admite una multiplicidad de soluciones dependientes de la concentración de fases, resulta conveniente reducir la homogeneización (5.3) a:[2]

$$\hat{\psi}\left(\varepsilon, c\right) = \left(1 - c\right) \psi(\varepsilon_{\mu_I}) + c\, \psi(\varepsilon_{\mu_{II}}) \; . \tag{5.6}$$

Esta solución viola la regla de Cauchy-Born, la cual afirma para el caso de un material homogéneo que la deformación es microscópicamente homogénea [76]. Esta característica es típica de problemas con potenciales no convexos, como se muestra a continuación.

Una segunda instancia, representada como solución (2) en la Figura 5.1, es un campo de deformaciones dado por una mezcla de fases que cumple $\varepsilon_\mu(y) = \pm 1$. La solución cumple con la condición de equilibrio (5.4), definiendo un campo de tensiones $\sigma_\mu(y) = 0$. Para cumplir con la condición de compatibilidad (5.5) se tiene $c = 0.5$, por lo que la energía macro es $\hat{\psi}\left(0, 0.5\right) = 0.5\, \psi(-1) + 0.5\, \psi(+1) = 0$. Esta energía es menor a la obtenida por la solución (1), y constituye naturalemente el mínimo global del problema ya que no es posible lograr menores valores de energía. Es decir, resulta energéticamente favorable una solución con campo de deformaciones heterogénea a una homogénea.

Es central señalar en este punto que la descripción hecha hasta el momento ignora por completo el arreglo de las fases en el RVE. Siempre y cuando se respete la medida integral dada por la concentración de fases $c$, el resultado es el mismo. Para entender esto, se presenta en la Figura 5.2(a) una grilla a partir de la cual pueden construirse funciones que representan la solución (2). Se presentan en la misma figura tres soluciones alternativas tipo serrucho a modo de ejemplo (en colores rojo, azul y verde). La amplitud de estas funciones es arbitraria (siempre es posible contruir un serrucho de menor altura), por lo que el problema no posee una escala característica [75]. Las distintas funciones serrucho constituyen lo que se conoce como patrones de microestructura, definidos como campos de deformación (strain) con oscilaciones espaciales de escala corta en relación al RVE. Estas ideas permiten realizar una primera conclusión fundamental de los materiales con energías no convexas:

**Observación.** Dado $\varepsilon$, existen infinitos mínimos energéticamente equivalentes caracterizados por la misma variable macroescala $c$. Estos mínimos equivalentes involucran formación de microestructura, y difieren entre sí en la distribución geométrica de las fases en el interior del RVE.

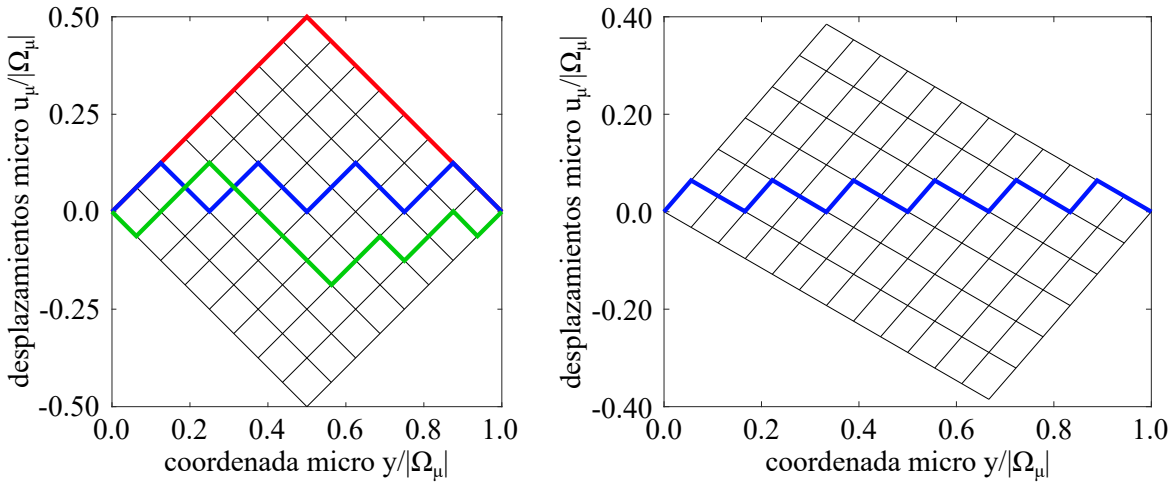


(a) Solución (2) (b) Solución (3)

**Figura 5.2:** Multiplicidad de soluciones en la respuesta macroescala de materiales con dos fases en la microescala. Grillas esquemáticas de configuraciones alternativas para (a) Solución (2), y (b) Solución (3). Cada color indica un campo de desplazamientos micro posible.

Finalmente, se presenta una tercera instancia denominada solución (3) en la Figura 5.1. es un cam-

[2] Nótese la dependencia de la energía de deformación macroescala con la concentración de fases.

po de deformaciones dado por una mezcla de fases que involucra $\varepsilon_{\mu I} = -\sqrt{1/3}$, y $\varepsilon_{\mu II} = 2\sqrt{1/3}$. El equilibrio ocurre para la tensión máxima de fase I, es decir $\sigma_\mu(y) = 8/3\ \sqrt{1/3}$. La condición de compatibilidad requiere $c = 1/3$. A diferencia de los casos anteriores, las energías de los puntos materiales en cada fase es distinta, siendo $\psi(\varepsilon_{\mu I}) = 4/9$, y $\psi(\varepsilon_{\mu II}) = 1/9$, por lo que la energía macro es $\hat{\psi}\,(0, 1/3) = 1/3$. Lo interesante de esta solución es que constituye un mínimo local estable. Al igual que para la solución (2), existen infinitos arreglos de fase compatibles, los cuales se representan en la grilla de la Figura 5.2(b). Siendo que la elección de las deformaciones micro fue arbitraria, se desprende una segunda conclusión fundamental:

***Observación.*** *Dado $\varepsilon$, existen infinitos mínimos locales caracterizados en macroescala por un rango de valores de concentración de fase $c$. Estos mínimos generan distintos niveles energéticos en la macroescala.*

Finalmente, se discute de manera simple el concepto denominado como transición o transformación de fase y las implicancias del mismo. Siendo que para una misma variable macro $\varepsilon$ existen distintas soluciones admisibles, es factible que el sistema cambie espontáneamente entre estas configuraciones estables. Estos cambios involucran un reacomodamiento de la distribución interna de fases, proceso que se conoce como evolución del patrón de deformación o patrón de fases. Asumiendo que en la transición hubo un cambio en la concentración de fases $c$ (es decir excluyendo el reacomodamiento de fases a $c$ constante), este fenómeno implica alteraciones en el nivel de energía, los cuales en el contexto de esta tesis se asumen como energía disipada por el sistema. Para entender esto, se parte de la definición de la tasa de disipación de energía mecánica en la macroescala:

$$\mathcal{D} = \sigma\ \dot{\varepsilon} - \dot{\hat{\psi}}\ . \tag{5.7}$$

En el ejemplo analizado, si el sistema transformara de la solución (3) a la (2), con $\varepsilon$ constante, la tasa de disipación coincide con el negativo de la tasa de variación de la energía interna. Es decir, a lo largo del proceso de transición de la configuración (3) a la (2), la disipación de energía es:

$$D_{mech} = \hat{\psi}_{sol(3)} - \hat{\psi}_{sol(2)} = 1/3\ . \tag{5.8}$$

Notablemente, esta disipación de energía ocurre en el material a nivel de la macroescala, siendo a nivel microescala un material puramente elástico, definido constitutivamente por una función (no convexa) de energía. Por otra parte, el balance energético de un único punto material dentro del RVE puede estudiarse (al menos en el caso 1D) a partir un modelo de resorte con ley constitutiva definida por una energía no convexa. Este análisis está detallado en los trabajos de Rossi et al. [73, 74] (ver Apéndices E y F).

### 5.2.1. Discretización, dependencia de la malla y existencia del RVE

En el contexto de la mecánica computacional, donde se enmarca esta tesis, el problema (5.2) debe resolverse por un método de discretización espacial, típicamente el método de los elementos finitos. Esto agrega al problema una dependecia de la respuesta con la malla utilizada, debido al espacio de soluciones admisibles que cada malla asume implícitamente. Por ejemplo, asumiento funciones de forma lineales, para obtener la solución roja en la Figura 5.2(a) es suficiente con contar con dos elementos finitos. Sin embargo, la solución azul en la misma figura requiere de al menos ocho elementos. Si bien en este caso ambas soluciones son equivalentes desde un punto de vista energético, en general el estado de deformación macro genera que un mayor número de elementos permita mínimos locales energéticamente más convenientes. Esto es fácilmente observable para la solución (3) mostrada en la Figura 5.2(b). No existe un número finito de intervalos de discretización que logren de manera exacta la concentración de fases adecuada de $c = 1/3$.

Imaginando para este ejemplo a un elemento finito como *celda unitaria* de un arreglo periódico 1D,

el razonamiento anterior indica que para el caso del problema discreto, se pierde la noción de RVE presentada en la Sección 2.3.1. Esto sucede ya que la inclusión de nuevos elementos como parte del RVE permite una periodicidad distinta de los campos fluctuantes (los cuales, se insiste, no son homogéneos a pesar de que el material es único), y esto modifica la respuesta global del conjunto, el cual está lejos de caracterizarse a partir de la respuesta de una única celda. En el mejor de los casos, solo puede aproximarse el comportamiento macroescala a partir del estudio de un elemento de volumen de muestreo (en inglés sampling volume element o SVE), el cual contiene alto número de celdas unidad. Este es el enfoque seguido en este capítulo. La discusión respecto de la respuesta macroescala de los materiales con energías no convexas en la microescala se continúa en el Capítulo 6.

### 5.2.2. El rol de los metamateriales

La filosofía de diseño de los metamateriales es una estrategia válida para la realización de materiales caracterizados por energías no convexas (ver los trabajos citados por Rossi et al. [73, 74]). De esta manera, es posible explotar el abanico de propiedades destacables que se desprenden de las observaciones hechas en la sección anterior. El propósito de esta sección es complementar la discusión precedente, introduciendo un ejemplo simple de diseño de la microarquitectura de un metamaterial con inestabilidades.

La Figura 5.3(a) presenta una estructura que manifiesta inestabilidad, la cual consiste en una viga curva con desplazamientos restringidos en sus extremos y cargada transversalmente en el centro de la luz. En la figura se indican los parámetros que definen su geometría. Una mayor conceptualización sobre el rol de este tipo de mecanismos se presenta en la Sección 5.4.1. Al integrar esta curva a una estructura de soporte de mayor rigidez es posible lograr una celda unidad (ver Figura 5.3(b), donde el color negro indica la estructura que brinda soporte), y cuya respuesta puede caracterizarse a través de una energía de deformación no convexa (el escenario de energía de deformación no convexa es estudiado por profundidad por Rossi et al. [73], Apéndice E). No deben confundirse aquí la celda unidad discutida en este contexto con el RVE de la Sección 5.2. Para clarificar la diferencia se puntualizan los siguientes aspectos relevantes:

- La celda unidad del metamaterial, mostrada en la Figura 5.3(b), esta conformada por dos constituyentes, un material hiperelástico (dibujado en color) y el vacío. El material hiperelástico es un material *clásico*, en el sentido de que cumple con los requisitos estándar de objetividad y convexidad, típicamente una goma.

- El comportamiento con inestabilidad corresponde a la respuesta promedio de la celda unidad. En este sentido, puede interpretarse a una celda unidad como un punto material del RVE analizado en la Sección 5.2. En la misma línea, la deformación micro $\varepsilon_\mu$ en un punto de $\Omega_\mu$ discutida en la sección previa, se asocia a la deformación promedio de la celda unidad, la cual surge de un campo de deformación punto a punto complejo (y con desplazamientos finitos) dentro de la celda unitaria mostrada en la Figura 5.3(b).

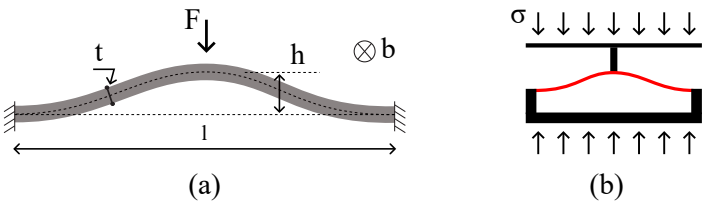


**Figura 5.3:** Metamaterial unidimensional. (a) Parámetros geométricos que definen la viga curva como mecanismo responsable de la inestabilidad. (b) Celda unidad que incorpora la viga curva, indicada en rojo, y un soporte de mayor rigidez, en negro.

A pesar de ser una estructura bidimensional, esta celda unidad exhibe transiciones de fase en una dirección, por lo que en este contexto se la considera como el punto de partida para un metamaterial unidimensional, comparable con el ejemplo de la Sección 5.2.

La Sección 2 del trabajo de Rossi et al. [74] (Apéndice F), presenta el análisis de las curvas de equilibrio estables (mínimos locales) en función de la concentración de fase $c$ y las implicancias de la transición entre curvas. El SVE elegido incluye un arreglo de $n = 20$ celdas unidad dispuestas en serie. Las conclusiones allí mencionadas coinciden con el análisis simple de la Sección 5.2: existen mínimos locales dependientes de $c$, la transición entre mínimos involucra una liberación de energía, no hay un orden preferencial para el arreglo interior de fases dentro del SVE.

## 5.3. Una línea discontinuada basada en optimización topológica

Sabiendo de la potencialidad del concepto de metamaterial como estrategia para lograr materiales con energías no convexas, se propuso inicialmente continuar con la línea de los Capítulos 3 y 4, y diseñar la microarquitectura de la celda unidad utilizando como herramienta central la optimización topológica. El objetivo que se planteó fue el de maximizar la energía posible de disipar por una cadena de celdas unidad.

A diferencia de lo realizado en los dos capítulos previos, no se cuenta con sensibilidades para el problema elástico no lineal por medio de la derivada topológica. Por esto se trabajó con la técnica de SIMP, revisada exhaustivamente por Bendsoe y Sigmund [29], actualizando las variables de diseño mediante el método de las asíntotas móviles de Svanberg [77]. Todas las implementaciones se realizaron en códigos propios.

En esta sección se presenta el trabajo realizado en esta dirección, incluyendo dificultades encontradas propias de este problema (no se discuten las dificultades típicas muy revisadas en la literatura como la formación de patrones en tablero de ajedrez o la eliminación de densidades intermedias), soluciones parciales a estas dificultades y un resultado de topología logrado. El trabajo que se muestra no fue plasmado en publicaciones, por lo que se elaboran ciertos aspectos con un grado de profundidad mayor que en el resto de la tesis.

### 5.3.1. Sobre la formulación del problema de optimización topológica

En los desarrollos de diseño topológico por optimización de los Capítulos 3 y 4, la homogeneización de la respuesta de una celda unidad constituyó un paso clave en la evaluación iterativa de función objetivo y sensibilidades (ver Sección 2.3.4). Siguiendo la discusión de la Sección 5.2, es claro que al existir respuestas inestables (ya sea material o geométrica), el no cumplimiento de la regla de Cauchy-Born resulta prohibitivo para el uso de estrategias de homogeneización convencionales de celdas unidad en compuestos periódicos.

Esto requiere de otro enfoque para establecer la conexión entre micro y macro escalas, el cual actualmente continúa siendo un tema de investigación.[3] Para no incurrir en errores conceptuales, se decidió como primera aproximación resolver el problema de diseño de la microarquitectura modelándola con las condiciones de borde de una estructura, sin realizar cálculos de homogeneización. Una representación de dominio de diseño y condiciones de borde típicos se muestra en la Figura 5.4. Esto concuerda con el enfoque de los trabajos de James y Waisman [78], Deng et al. [79], orientados a optimizar topológicamente metamateriales con inestabilidades.

Sin embargo, esta solución preliminar, respecto de las condiciones de borde a imponer, no genera una respuesta acerca de como determinar la capacidad de liberación de energía en la macroescala a partir

[3] Los estudios del doctorado cronológicamente posteriores a este intento con optimización topológica, permitieron un mejor entendimiento sobre esta conexión multiescala, el cual es expuesto el Capítulo 6. Sin embargo, una técnica de *homogeneización* numérica de celdas con inestabilidades geométricas no se encuentra aún disponible.

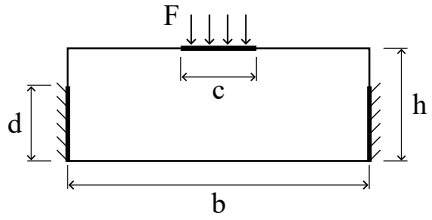


**Figura 5.4:** Dominio de diseño y condiciones de borde para el problema de optimización topológica no lineal.

de una única *celda*, la cual, en general, no presenta transiciones de fase en una respuesta homogénea (la curva de equilibrio es continua a desplazamiento controlado). Dicho de otra manera, no se cuenta con una forma de evaluar la función objetivo y las sensibilidades. Para sobrepasar este obstáculo se utilizaron resultados de Puglisi y Truskinovsky [80], Benichou y Givli [81], quienes sin conectar escalas de manera rigurosa, muestran que la disipación *para el caso de materiales con respuesta unidimensional*, en el límite de infinitas celdas dispuestas en serie, resulta del área encerrada por las dos curvas monótonas crecientes más próximas a la respuesta de una celda individual (ver Figura 5.5(a)).

Esto requiere de la evaluación numérica de una integral, por lo que involucra el monitoreo de un alto número de estados de equilibrio a lo largo del camino de deformación, lo cual incrementa el costo computacional asociado al cálculo de derivadas para obtener las sensibilidades. Siguiendo la propuesta de Deng et al. [79], se opta por un cálculo aproximado que se define únicamente a partir de caracterizar las cargas límite. De esta manera el problema de optimización topológica formulado es (ver Figura 5.5(b)):

$$\begin{aligned} \max\ D_{mech} \approx 0.5(\delta_{I^*} - \delta_I + \delta_{II} - \delta_{II^*})(F_I - F_{II}); \\ \text{tal que:} \qquad f_1 - f_1^* = 0\ , \end{aligned} \tag{5.9}$$

donde $F_I$ y $F_{II}$ hacen referencia a las cargas límite de la estructura, $\delta_I$ y $\delta_{II}$ son los desplazamientos correspondientes a estas cargas límite, $\delta_{I^*}$ y $\delta_{II^*}$ son los desplazamientos medidos en los puntos de la curva de equilibrio con igual carga a las cargas límite, y $f_1$ y $f_1^*$ son las fracciones de volumen real y objetivo. En la Figura 5.5(b) se indica la interpretación gráfica de este problema, que consiste en aproximar la disipación teórica máxima como el área de un paralelogramo, y el efecto de la función objetivo en los cuatro vértices del mismo.

### 5.3.2. Algoritmo de control, detección de puntos críticos, puntos de partida y sensibilidades

La decisión de incluir cargas límite en la función objetivo de la optimización topológica no es intrascendente. La evaluación de la propia función objetivo y de su sensibilidad respecto de las variables de diseño dependen en este caso del correcto cómputo y caracterización de las cargas límite. Para ello se implementa un algoritmo basado en la generación de un sistema extendido propuesto por Wriggers y Simo [82]. El mismo se basa en adicionar a las ecuaciones de equilibrio usuales, la condición de segunda derivada de la energía potencial nula que caracteriza a los puntos críticos:

$$\mathbf{K_t \Phi} = \mathbf{0}\ , \tag{5.10}$$

donde $\mathbf{K_t}$ es la matriz de rigidez tangente para una discretización por elementos finitos y $\mathbf{\Phi}$ es un vector de singularidad que caracteriza el tipo de punto crítico (límite o bifurcación).

Dentro del esquema iterativo de optimización, la resolución del sistema extendido se incorpora a un método de control del camino de equilibrio del tipo longitud de arco Crisfield [83]. De esta manera se cumple con dos propósitos: (i) se conoce la totalidad de la curva de equilibrio, necesario para conocer los puntos $I^*$ y $II^*$ (ver Figura 5.5(b)), (ii) se brinda al sistema extendido un punto inicial cercano al punto

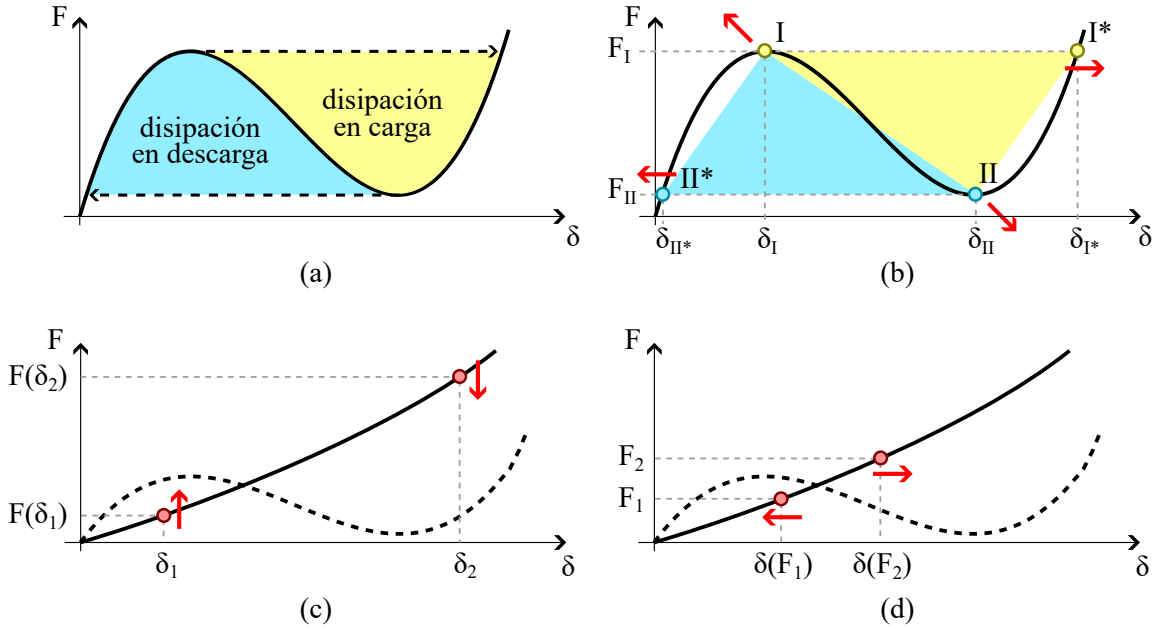


**Figura 5.5:** Formulación del problema de optimización topológica. (a) Representación gráfica de la capacidad máxima de disipación de una arreglo de elementos en serie a partir de la ley fuerza-desplazamiento de un único elemento. (b) Aproximación de la capacidad de disipación y representación gráfica de la formulación (5.9). (c) Representación gráfica de la formulación (5.11). (d) Representación gráfica de la formulación (5.12). En todos los casos los círculos indican los puntos de la curva de equilibrio donde se calculan función objetivo y sensibilidades, y las flechas rojas indican el efecto buscado con la optimización.

crítico buscado. Si bien en la respuesta esquemática de la Figura 5.5(b) la curva es lo suficientemente simple como para recorrerla con un control de desplazamiento, se remarca la importancia de la implementación de un método de control que tolere la formación de snap-backs en instancias intermedias del proceso de optimización.

En este punto el problema de optimización topológica no está aún bien colocado en general. Nótese que la formulación (5.9) asume a priori la existencia de las cargas críticas. Esto no se cumple para topología arbitrarias, y un caso típico es el del punto de partida, el cual suele elegirse como una distribución de material homogénea o aleatoria. Existen al menos tres alternativas para sobrepasar esta dificultad:

- Optimizar en dominios de diseño que propicien la inestabilidad independientemente de la topología. Ejemplos de esta estrategia fueron presentados por Deng et al. [79], Lindgaard y Dahl [84]. La misma es altamente restrictiva si el propósito es la obtención microarquitecturas, ya que el dominio de diseño no es periódico.

- Elegir como punto de partida una topología cuya respuesta incorpore la inestabilidad. Este enfoque fue usado por Deng et al. [79], y cuenta con la desventaja de generar un fuerte condicionamiento de la solución final con respecto a la topología del punto de partida.

- Formular un problema de optimización topológica preliminar que asegure la existencia de puntos críticos sin recurrir a las estrategias anteriores. Esta alternativa también fue explorada por Deng et al. [79], y fue el camino seguido para los trabajos de esta tesis. Se exponen a continuación las principales características.

Dada una topología cuya curva de equilibrio es arbitraria, existen al menos dos formulaciones del problema de optimización correctamente colocados que posibilitan la formación de inestabilidades del

tipo snap-through:

$$\begin{aligned} &\max\ F(\delta_1) - F(\delta_2); \\ &\quad \text{tal que:} \qquad f_1 - f_1^* = 0\ , \end{aligned} \tag{5.11}$$

donde $F(\delta_i)$ es la fuerza reactiva correspondiente al desplazamiento de control $\delta_i$. Además, $\delta_1$ y $\delta_2$ aproximan los desplazamientos de las cargas críticas. Variantes de esta formulación fueron usadas por James y Waisman [78], Deng et al. [79], Chen et al. [85]. Alternativamente, se pueden invertir la dependencia entre desplazamientos y fuerzas en la función objetivo obteniendo:

$$\begin{aligned} &\min\ \delta(F_1) - \delta(F_2); \\ &\quad \text{tal que:} \qquad f_1 - f_1^* = 0\ . \end{aligned} \tag{5.12}$$

Una explicación gráfica de estos enfoques de muestra en la Figura 5.5(c) y (d) respectivamente. Ambas formulaciones fueron probadas para generar estructuras con snap-through. En particular, el esquema (5.11) resulta mas efectivo en la optimización de la topología. Se comenta, sin embargo, un detalle de implementación. El valor de desplazamiento $\delta_2$, asociado a la carga límite inferior cuando la estructura optimizada manifiesta snap-through, suele ser inadmisiblemente alto para las topologías iniciales de rigidez medianamente homogénea en todo el dominio, generando efectos del tipo indentación. Este efecto negativo es mas notorio en dominios de diseño con mayores relaciones alto/ancho (h/b en Figura 5.4). Para corregir esto, los valores $\delta_1$ y $\delta_2$ no se consideran como magnitudes fijas desde el inicio de la optimización, sino que se adaptan progresivamente con el avance de las iteraciones. Adicionalmente, la función objetivo puede requerir de una ponderación de los sumandos para mejorar el comportamiento del optimizador.

Finalmente, la implementación de sensibilidades de desplazamientos a carga prestablecida, fuerzas a desplazamiento prestablecido y de cargas límite, necesarias para resolver los distintos problemas de optimización, se realizó siguiendo los trabajos de James y Waisman [78], Deng et al. [79], Lindgaard y Dahl [84], Chen et al. [85], Kemmler et al. [86].

### 5.3.3. El problema de la distorsión de los elementos de fase blanda

La optimización topológica bajo grandes deformaciones presenta problemas de inestabilidad numérica debido a la distorsión excesiva de los elementos finitos que constituyen la parte del dominio de fase blanda. La solución implementada siguió la propuesta de Wang et al. [87], la cual consiste en una interpolación de la energía del material, la cual se escribe como:

$$\phi(\mathbf{u}, \gamma) = \phi_{NL}(\gamma\mathbf{u}) - \phi_L(\gamma\mathbf{u}) + \phi_L(\mathbf{u})\ , \tag{5.13}$$

donde $\phi$, $\phi_{NL}$ y $\phi_L$ son las densidades de energía de deformación interpolada, de material no lineal y de material lineal respectivamente. Como modelo constitutivo no lineal se utilizó el correspondiente a un material NeoHookeano, la energía de este modelo está dada por la ecuación (2.14). Estas energías de deformación varían elemento a elemento en función de la rigidez asignada al mismo, como es típico en optimización topológica. Además, $\mathbf{u}$ es el campo de desplazamientos, y $\gamma$ es un factor de interpolación, y puede interpretarse como un campo escalar constante en cada elemento finito. El factor de interpolación varía entre $\gamma = 1$ para la fase rígida y $\gamma = 0$ para la fase blanda.

**Observación.** $\phi$ identifica la función de energía de deformación punto a punto de la microarquitectura del metamaterial, el cual es elástico, y cumple con los requisitos de policonvexidad típicos para las formulaciones de elasticidad no lineal bien planteadas. La energía de deformación no convexa $\psi$ que se pretende lograr, surge como el comportamiento homogeneizado de una *celda unidad* de este metamaterial.

La estrategia (5.13) implica resolver la parte del dominio con fase rígida con una energía no lineal $\phi_{NL}$ y la parte del dominio con fase blanda con una energía lineal $\phi_L$, asignando a regiones de rigidez intermedia una energía interpolada que "oculte" el malcondicionamiento de la matriz en caso de una distorsión excesiva. Es sencillo demostrar que el tensor gradiente de deformación $\mathbf{F}$ para el mapa $\gamma\mathbf{u}$ puede calcularse como:

$$\mathbf{F}(\gamma\mathbf{u}) = \gamma\tilde{\mathbf{F}}(\mathbf{u}) + (1-\gamma)\mathbf{I}\,, \tag{5.14}$$

donde $\tilde{\mathbf{F}}$ es el tensor gradiente de deformación calculado para el mapa $\mathbf{u}$ sin interpolar. Para el cálculo del modelo no lineal se utiliza el tensor $\mathbf{F}(\gamma\mathbf{u})$. La expresión (5.14) muestra que si la fase constitutiva es (parcialmente) blanda y los desplazamientos y distorsiones son altos, $\tilde{\mathbf{F}}(\mathbf{u})$ es propenso a presentar un determinante negativo, mientras que $\mathbf{F}(\gamma\mathbf{u})$ no, ya que $\gamma \to 0 \Rightarrow \mathbf{F} \to \mathbf{I}$.

Finalmente, el mapa $\gamma$ se determina a partir de una función de proyección Heaviside suave vinculada al campo de rigidez del dominio de diseño. Mayores detalles son presentados por Wang et al. [87].

### 5.3.4. Otras dificultades encontradas

Uno de los principales desafíos encontrados fue el de evitar el contacto o superposición de elementos de fase rígida separados por elementos de fase blanda, fenómeno que influye significativamente en el realismo de la curva de equilibrio obtenida. Para evitar esto James y Waisman [78] aumentan la rigidez de la fase blanda, con la desventaja de aumentar simultáneamente de forma artificial la rigidez global. Al mismo tiempo, James y Waisman [78] optimizan estructuras que se inestabilizan al ser traccionadas en vez de comprimidas, lo cual disminuye las chances de las zonas de material rígido de hacer contacto, aunque quita generalidad al método.

Otro punto sensible son las condiciones de borde (CB) impuestas al dominio de diseño. Si bien se descartan CB periódicas por los motivos antes mencionados referidos a la validez de la hipótesis de Cauchy-Born, las CB impuestas debieran tener sentido en un compuesto de microarquitectura periódica. En este sentido, la Figura 21 de James y Waisman [78] muestra una topología optimizada en ambas configuraciones estables, la cual revela que al imponer CB de desplazamientos puntuales la microarquitectura presenta *fisuras*, no aparentes en la configuración no deformada. Por otra parte, las Figuras 17 a 23 de Deng et al. [79] evidencian que los autores asumen simetría de la topología modelando 1/4 de celda, sin imponer apropiadamente las CB. Esto genera (aunque este trabajo no lo muestre en concreto) un solapamiento entre las mitades de la celda al ser comprimida.

En línea con esto, la imposición de CB de simetría puede ser conflictiva. Como es explicado por Lindgaard y Dahl [84], una estructura simétrica no asegura una configuración deformada simétrica, por lo que imponer este tipo de CB puede esconder modos de deformación mas flexibles (bifurcaciones).

Se observa también una fuerte sensibilidad del optimizador a pandeos locales en iteraciones intermedias. Al generarse una topología con ciertas zonas de baja rigidez debido a elementos finos (similar a columnas esbeltas), si el proceso de carga involucra un pandeo local, el cálculo de sensibilidades para la próxima iteración se afecta de manera importante, al punto de que en general no es posible recuperar una topología con cierta lógica asociada a la función objetivo.

Finalmente, de acuerdo a los comentarios realizados en la Sección 5.3.2, es evidente que hay diferentes aspectos difíciles de automatizar. Esto se opone a la lógica de la optimización topológica donde se espera *aprender* como resultado de un proceso libre de intervención del usuario. Algunas de estas y otras dificultades fueron mencionadas en el trabajo de Bruns y Sigmund [88], lo cual confirma lo desafiante de abordar este tipo de problemas mediante optimización topológica.

### 5.3.5. Resultados de este enfoque

A pesar del tiempo invertido y las dificultades parciales superadas, algunos de los obstáculos antes mencionados prueban ser insalvables, para constituir una metodología robusta de optimización topológi-

ca no lineal. Además, en los casos en que efectivamente se logran soluciones, las mismas no difieren estructuralmente de un elemento tipo barra inclinado respecto de la dirección de la carga (misma lógica que la viga curva de la Figura 5.3).

A modo de ejemplo, se muestran a continuación los resultados correspondientes a una de las topologías 2D logradas para el caso de una estructura bi-empotrada en toda su altura, cargada superiormente en el centro de su longitud. El dominio de diseño, representado en la Figura 5.6(a), es un rectángulo de $40mm$ x $10mm$, que constituye la mitad de la estructura. El mismo fue discretizado en una malla de 120 x 30 elementos finitos. El espesor es $5mm$. Condiciones de borde de simetría se aplican en el borde derecho. La carga se aplica en los $10mm$ de la derecha en el borde superior. Los parámetros materiales de la fase rígida son $E_1 = 48MPa$ y $\nu_1 = 0.40$, con una fracción de volumen impuesta $f_1^* = 0.30$. Estos valores son elegidos para comparación de los resultados con Chen et al. [85]. La optimización se hace en dos etapas. En primer lugar, partiendo de una distribución aleatoria de densidades se utilizó el esquema (5.11) para generar una estructura con una respuesta fuerza-desplazamiento no monótona, eligiendo como puntos de control $\delta_1 = 3mm$ y $\delta_2 = 11mm$. Una vez convergida esta primera instancia, se cambia el problema de optimización de acuerdo a la formulación (5.9), aunque la mejoría en el desempeño de la topología debido a esta segunda etapa es escasa. La respuesta fuerza-desplazamiento y topología finales se muestran en las Figuras 5.6(b) y (c) respectivamente. Nótese la formación de estructuras de mayor rigidez en el centro y los extremos, que aparecen para generar una mayor inclinación de la barra diagonal, responsable de la inestabilidad geométrica.

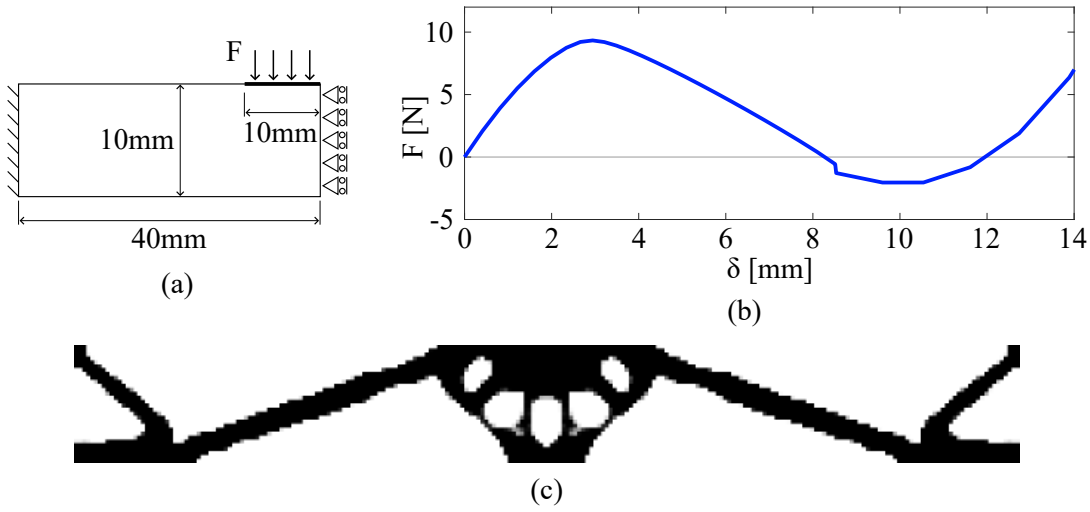


**Figura 5.6:** Optimización topológica 2D de estructuras con inestabilidades. (a) Dominio de diseño correspondiente a media estructura. (b) Respuesta fuerza-desplazamiento obtenida. (c) Resultado de la topología optimizada utilizando en etapas consecutivas los esquemas (5.11) y (5.9).

El objetivo de esta sección es mostrar y evidenciar las diversas dificultades encontradas para resolver adecuadamente el problema de optimización topológica de estructuras con inestabilidades del tipo snap-through, algunas de las cuales no pudieron ser solucionadas convincentemente. Esto no quita, sin embargo, que las técnicas de optimización topológica brindan una opción válida para ser nuevamente exploraradas en el futuro.

## 5.4. Giro hacia un diseño sin optimizar topológicamente

A pesar del tiempo dedicado a resolver el alto número de dificultades propias del problema de optimizar topológicamente estructuras con inestabilidades, la tarea de conformar un algoritmo de optimización

robusto se volvió inabordable en los plazos dispuestos para completar los estudios de doctorado, principalmente debido a la condición aún prematura del estado del arte. Debido a esto, se decidió postergar temporalmente esta línea, y enfocar el trabajo hacia un diseño empírico de las microarquitecturas.

En esta sección se explica como una revisión exhaustiva de los metamateriales existentes, junto con una serie de trabajos enfocados en el análisis de cadenas de elementos biestables, confluyeron en un modelo reducido basado en la topología mas comunmente utilizada en la literatura referida a los metamateriales con inestabilidades.

### 5.4.1. Generalidades de la microarquitectura: el histerón y el soporte

Una revisión profunda de los diseños de metamateriales que explotan fenómenos de inestabilidad en escalas de longitud menor a la escala estructural propuestos en la literatura muestra que, de modo general, la celda unidad de un material con cambio de fase elástica se construye a partir de elementos de microescala conformados por dos partes: el histerón y el soporte. El término histerón, tomado de Ding y van Hecke [89], hace referencia al mecanismo o dispositivo de la microescala responsable de la inestabilidad. Dicho de otra manera, el histerón es una estructura capaz de generar histéresis en ciclos de carga. Notablemente, un histerón es en sí mismo un elemento estructural convencional, y su condición de generador de inestabilidad depende de las condiciones de borde. Las condiciones de borde, que incluyen siempre algún tipo de restricción lateral al movimiento, son impuestas por una estructura de mayor rigidez que el histerón. Algunos ejemplos de la literatura se discuten a continuación. La Figura 5.7(a) muestra la propuesta de Tan et al. [90], la cual consiste en una cáscara de forma de tronco-cónica como histerón, y un anillo que impide la expansión como soporte. Liu et al. [91] presentan el elemento de la 5.7(b), donde el histerón es una viga o lámina que pandea ante un movimiento cizallante de su soporte, el cual es un marco. En la Figura 5.7(c) se muestra la propuesta de Jeong et al. [92], donde (similar al caso anterior) el histerón es el conjunto de cuatro vigas esbeltas , y el soporte esta conformado por un anillo exterior y una cruz interior, y la inestabilidad aparece ante una rotación relativa entre las partes. Por último, en la Figura 5.7(d) se muestra la estructura de Rafsanjani y Pasini [93], donde el histerón es el triángulo interior, que rota ante una separación de las tres partes exteriores que conforman el soporte.

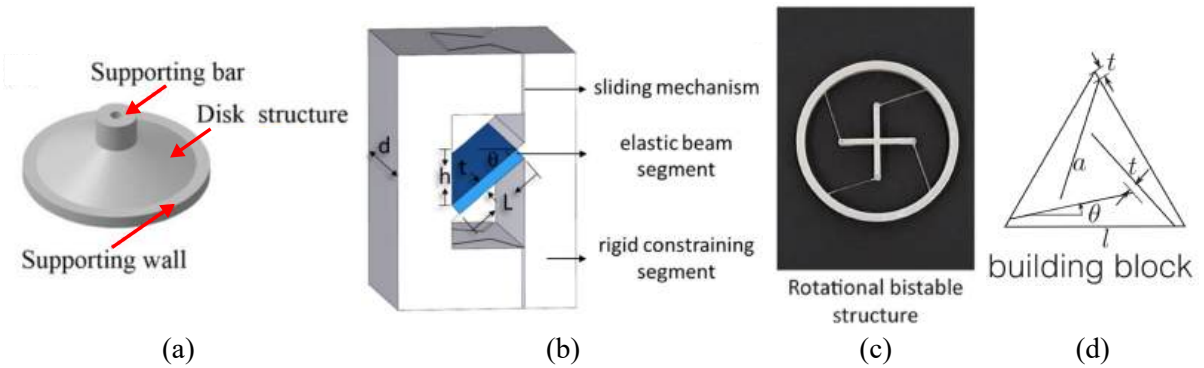


**Figura 5.7:** Ejemplos de elementos histerón + soporte propuestos en la literatura para conformar materiales con cambios de fase. (a) Tan et al. [90]. (b) Liu et al. [91]. (c) Jeong et al. [92]. (d) Rafsanjani y Pasini [93].

La característica fundamental de estos mecanismos para lograr el comportamiento deseado consiste en que, para un dado sentido de carga exterior, exista parcialmente una inversión en el sentido de acumulación de la energía elástica. Es decir, el sistema debe, manteniendo el sentido de la carga exterior, acumular-liberar-acumular energía. Siendo que el soporte es el elemento de mayor rigidez, es importante destacar que esta acummuanción de energía ocurre precisamente en el histerón.

**El histerón por excelencia**

En los últimos años, se han publicado un gran número de trabajos destinados al estudio de metamateriales con este tipo de cambios de fase, y a las propiedades efectivas interesantes que manifiestan, adicionalmente a la liberación de energía. Sorprendentemente, a pesar del creciente interés, una abrumadora mayoría de estas publicaciones utilizan diseños basados en variantes de la viga curva presentada en la Figura 5.3. Varios trabajos de este tipo pueden encontrarse en las referencias de Rossi et al. [73] (Apéndice E). Esto remarca la importancia de entender integralmente el comportamiento de esta estructura, para poder explotar su inclusión como histerón en el diseño de metamateriales de alto rendimiento. En este sentido, luego de una discusión sobre la estrategia de modelado de metamateriales con cambios de fase en la Sección 5.4.2, se retoma en la Sección 5.4.3 el análisis sobre esta estructura tan presente en la literatura.

### 5.4.2. El trabajo de Puglisi y Truskinovsky como punto de partida

Una vez definida una celda unidad a partir de los lineamientos generales mencionados en la Sección 5.4.1, es posible plantear, a través de un arreglo en serie de la misma, un estudio numérico o experimental que constituya una *aproximación discreta* del problema (5.2) de equilibrio macroescala de un material con inestabilidades. Existen diversas publicaciones que han abordado este trabajo a partir de variantes de la viga curva de forma sinuosidal como histerón. Entre ellos se puede mencionar los artículos de Restrepo et al. [14], Frenzel et al. [15], Tan et al. [90], Shan et al. [94], Rafsanjani et al. [95], Chen et al. [96].

Notablemente, el mismo tipo de análisis fue realizado de manera integral en una serie de trabajos de Puglisi y Truskinovsky [80, 97, 98, 99] a partir de un modelo mucho mas simple, sin especificar un diseño geométrico concreto. Estos autores lograron un conocimiento profundo de la física detrás de este tipo de arreglos estudiando una cadena unidimensional con un número finito de resortes en serie, con una ley constitutiva elástica biestable sencilla. La función de energía de cada uno de estos resortes contiene dos pozos convexos separados por una región espinodal. Dicho de otra manera, estudiaron el fenómeno a partir de elementos simples cuya inestabilidad se origina en el modelo constitutivo (al escoger un potencial elástico no convexo), y no debido a los cambios de geometría inducidos por las deformaciones de los elementos estructurales. Más aún, el planteo realizado está enmarcado en una cinemática de desplazamientos infinitesimales.

Partiendo de este modelo simplificado, Puglisi y Truskinovsky identificaron las siguientes características inherentes a estos sistemas, alguna de las cuales fueron discutidas en la Sección 5.2:

- En general, la cadena de elementos inestables desarrolla un número alto de soluciones no triviales con patrones de deformación no homogéneas, por lo tanto, no es válida la hipótesis de Cauchy-Born. Estas configuraciones corresponden a curvas de equilibrio metaestables (mínimos locales) que provienen de puntos de bifurcación.

- Solo existe liberación de energía cuando un resorte de la cadena cambia de fase.

- El sistema multiestable cuenta con la capacidad de recuperar deformaciones considerables a partir de histéresis, con liberación de energía controlada durante el proceso.

- Existen barreras de energía separando configuraciones metaestables compatibles con una misma deformación macro.

- La respuesta del sistema, en términos de tensión de equilibrio o de energía, es indiferente al arreglo interno de las fases, dependiendo únicamente de la cantidad de resortes en cada una (concentración de fases).

- Las curvas de equilibrio estable son continuas de a tramos. Esto surge de requerimientos de estabilidad del sistema, que impiden que haya resortes en la zona espinodal (al menos para un número suficientemente alto de resortes).

- Existe una correlación inversa entre la disipación de energía y la barrera de energía entre mínimos locales.

- Durante los eventos de transición de fase, resulta mas conveniente, debido a una disminución instantánea mayor de la energía potencial, una transformación secuencial de los elementos que una transformación simultánea de todos ellos. Por lo cual tiende a generarse (de manera aproximada) una *evolución suave de la concentración de fase*.

Además, los autores reconocen como principal desafío encontrar una descripción rigurosa del comportamiento homogeneizado de este sistema. Como aproximación evalúan su comportamiento para un número de resortes tendiendo a infinito y enfatizan sobre los siguientes resultados y conjeturas:

- Debido a la existencia de funciones de energía de deformación no convexas, la conexión entre escalas micro y macro no es trivial. Resulta claro que este límite no corresponde a la homogeneización tradicional de un elemento de la cadena en el problema discreto.

- A medida que se incrementa el número de resortes, el potencial de energía converge debilmente al soporte convexo de la función de un resorte individual, aunque permanecen las oscilaciones rápidas en el campo de deformaciones.

- Para concentración de fases constante, una curva de equilibrio estable está descripta por una función de energía interna convexa.

- La zona espinodal del modelo constitutivo influye en las barreras de energía y las características de la histéresis, la cual se comporta de manera independiente de la tasa de carga (rate-independent), similar a las aleaciones con memoria de forma.

- La transición entre mínimos locales requiere de una estrategia de evolución del estado del sistema. Dicha estrategia está vinculada a las barreras de energía, o de alternativamente, a las fuerzas configuracionales que propician la transición de fase. La tensión de Maxwell es el punto de máxima barrera y mínima fuerza configuracional (en valor absoluto). Ambas magnitudes están relacionadas con el nivel de tensiones.

Estos aspectos son fundamentales para desarrollar un modelo multiescala y están contemplados en el marco propuesto para el modelo macroescala que se presenta en el Capítulo 6.

### 5.4.3. Modelo subrogado del histerón

La simplicidad del modelo de Puglisi y Truskinovsky permite pensar que la física inherente al problema no es necesariamente la consecuencia de una descripción precisa de la inestabilidad geométrica debido a topologías complejas, sino que requiere únicamente de un potencial no convexo subyacente. Partiendo de esta idea, se propone extender este tipo de análisis a metamateriales bi-dimensionales. Los mismos son concebidos como entramados de histerones ubicados en distintas orientaciones, y donde estos histerones corresponden a elementos de geometría simple, con leyes constitutivas basadas en energías no convexas.

Para esto, debe definirse la forma de interacción entre estos elementos. En este sentido, el enfoque planteado es que el modelo constitutivo refleje lo más fielmente posible el comportamiento de microarquitecturas reales, en particular, celdas constituidas a partir de la viga curva mencionada en la Sección

5.4.1 como histerón más utilizado. Tomando como referencia el trabajo de Zhang et al. [100], el cual es una de las pocas referencias en las cuales se estudian diseños bidimensionales de comportamiento no trivial, se considera necesario incluir modos de deformación no simétricos como penalizadores del rendimiento en disipación de la estructura.

La propuesta se basa en utilizar elementos finitos unidimensionales, con cinemática lineal, capaces de soportar deformaciones axiales, transversales y rotaciones, y cuya respuesta constitutiva esté asociada a la respuesta geométricamente no lineal de la viga con forma sinusoidal. Con esta estrategia, no sólo se captura el comportamiento más fundamental del metamaterial sino que también se logra una reducción considerable de la carga computacional al evitar una descripción detallada de la deformación geométrica no lineal del histerón.

La Figura 5.8(a) representa la asociación general entre la estructura real y el elemento finito subrogado o reducido, donde $f$, $m$, y $t$ son las acciones exteriores actuantes en el histerón, y $n^{SM}$, $m^{SM}$, y $q^{SM}$ son las resultantes axiales, de momento, y transversales actuantes en el elemento finito. Tanto en la estructura real como en el elemento finito se definen las variables conjugadas de trabajo. Se tiene que $d_a$, $\theta$, y $d_t$ son los desplazamientos generalizados conjugados a $f$, $m$, y $t$ en la viga curva, y $\varepsilon$, $\kappa$, y $\gamma$ son las deformaciones (strains) generalizadas axial, de curvatura, y transversal en el elemento finito subrogado.

Por otra parte, la Figura 5.8(b) presenta los grados de libertad que describen la cinemática del elemento finito tipo marco (con funciones de forma de elementos tipo viga y tipo barra). Considerando que las deformaciones generalizadas son constantes en el elemento (ya que el mismo representa un único histerón), es posible conectar la cinemática de ambos casos a través de las relaciones: $d_a = \varepsilon L_e = v^{(2)} - v^{(1)}$, $\theta = \kappa L_e = \alpha^{(2)} - \alpha^{(1)}$, y $d_t = \gamma L_e = w^{(2)} - w^{(1)}$.

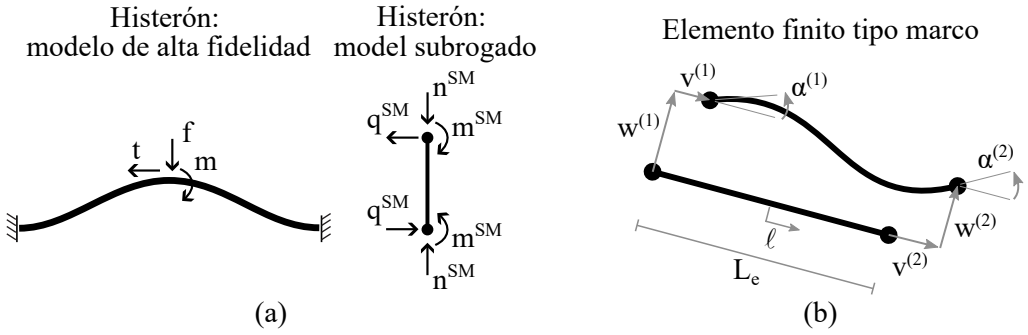


**Figura 5.8:** (a) Modelo reducido del histerón. (b) Elemento finito tipo marco, dos nodos, y seis grados de libertad.

El enlace entre el histerón y el elemento finito se obtiene asumiendo un principio variacional de equivalencia energética, análogo al principio de Hill-Mandel (2.28) (ver Sección 4 de Rossi et al. [73]), que implica que los trabajos virtuales en ambos modelos son idénticos:

$$f\delta d_a + m\delta\theta + t\delta d_t = \int_{L_e} \left[n^{SM}\delta\varepsilon + m^{SM}\delta\kappa + q^{SM}\delta\gamma\right] d\ell \tag{5.15}$$

Nótese que en la ecuación (5.15) se asumen conocidas las relaciones $f(d_a, \theta, d_t)$, $m(d_a, \theta, d_t)$, y $t(d_a, \theta, d_t)$, entre las fuerzas actuantes en el histerón y sus desplazamientos conjugados. El objetivo es determinar como caracterizar las resultantes internas al elemento finito reducido.

Incluyendo la conexión de la cinemática en ambos modelos, el principio variacional (5.15) puede reescribirse como:

$$f\delta d_a + m\delta\theta + t\delta d_t = \frac{1}{L_e}\int_{L_e} \left[n^{SM}\delta d_a + m^{SM}\delta\theta + q^{SM}\delta d_t\right] d\ell \qquad ; \quad \forall\, \delta d_a\,,\, \delta\theta\,,\, \delta d_t \tag{5.16}$$

donde la arbitrariedad de las variaciones $\delta d_a$, $\delta\theta$, y $\delta d_t$ determina que las fuerzas resultantes del elemento

subrogado sean las mismas fuerzas reactivas del histerón. Notablemente, a diferencia de un elemento estándar, esto no sólo genera leyes constitutivas no lineales, sino que también implica, dependiendo de la caracterización de las acciones en el histerón, un acople entre las fuerzas generalizadas.

Planteado de esta forma, el principio (5.16) establece que las ecuaciones constitutivas del elemento finito reducido dependen exclusivamente en las características geométricas y de material del histerón. Esto es especialmente conveniente porque implica que las caracterísitcas geométricas elegidas para el elemento finito (como su longitud, área transversal, o inercia a la flexión) no influyen en los resultados. El único aspecto geométrico a respetar son las orientaciones relativas entre histerones.

**Primera versión: esfuerzos desacoplados**

Los resultados de una versión inicial de este modelo fueron publicados por Rossi et al. [72] (Apéndice D). En dicho trabajo, como primera prueba para confirmar la validez de la propuesta, se asume que las tres acciones exteriores son independientes entre ellas, y solo dependen individualmente de sus desplazamientos conjugados. Es decir, se tienen leyes de la forma: $f(d_a)$, $m(\theta)$, y $t(d_t)$. Cada una de estas leyes se caracteriza mecánicamente partiendo de la configuración no deformada del histerón, por lo que se obtiene una respuesta axial que refleja un comportamiento no monótono, mientras que las fuerzas de momento y corte un comportamiento monónoto no lineal. Para considerar estas tres leyes se utilizan funciones de forma compatibles con la teoría de viga de Timoshenko.

Este enfoque es equivalente a construir la energía del material a partir de la suma de tres energías, una de ellas no convexa correspondiente al efecto axial. Un enfoque similar fue seguido por Khajehtourian y Kochmann [101] para caracterizar el salto de escala. Esto no se está argumentando en esta tesis y la concepción del salto de escala se plantea en el Capítulo 6.

Esta versión del modelo presenta una capacidad predictiva aceptable, capturando correctamente fenómenos como la histéresis, patrones de formación de microestructura, y transiciones de fase secuenciales. Sin embargo, a pesar de que se obtiene el comportamiento deseado de disminuir el rendimiento disipativo del material al intevenir los efectos de momento y corte, se observa que la caracterización desacoplada de las acciones externas genera una rigidez exagerada del modelo y cargas límite excesivas. Mayores detalles pueden encontrarse en el trabajo de Rossi et al. [72].

**Segunda versión: modelo cinemático preciso del histerón**

Para solucionar las desventajas mencionadas es necesario conocer la respuesta acoplada entre las acciones exteriores. Tomando como base el trabajo de Qiu et al. [102], se construye una descripción cinemática precisa del histerón a partir de una base de funciones conocidas que expanden las posibles configuraciones de equilibrio de la viga. Esto permite acoplar las acciones de la fuerza transversal y el momento, es decir se logran leyes constitutivas del tipo $f(d_a, \theta)$, $m(d_a, \theta)$. Se omite en este caso la acción $t$, asumiendo que sus efectos no son considerables dentro del comportamiento típico de estos metamateriales. Siendo que el desarrollo de esta descripción cinemática constituye un aporte en si mismo, se posterga la discusión correspondiente para la Sección 5.4.4. En este caso, debido a las relaciones constitutivas con las que se cuenta, se opta por utilizar funciones de forma compatibles con la teoría de Euler-Bernoulli para el elemento finito subrogado.

Las modificaciones introducidas al modelo prueban ser satisfactorias. Se incrementa notablemente la capacidad del mismo para replicar respuestas no lineales complejas de un modelo de alta fidelidad. Asimismo, permite estudiar el escenario no convexo de energía y obtener conclusiones valiosas acerca de los requisitos del camino de carga para que el histerón tenga capacidad disipativa. Los detalles de desarrollo, implementación y conclusiones de esta segunda versión fueron publicados por Rossi et al. [73] (ver Apéndice E).

### 5.4.4. El modelo cinemático generalizado de la viga curva

Este modelo fue explicado en profundidad por Rossi et al. [73] (ver Apéndice E). El propósito de esta sección es revisar las principales hipótesis y pasos para su construcción, así como plantear algunas de las conclusiones más importantes que de él se desprenden. El modelo consiste en una descripción cinemática a partir de una base de funciones $\{w_j(x)\}$ que expanden las posibles configuraciones de la viga. Esta base se constituye a partir de los modos de pandeo de una viga originalmente recta, cuyos extremos se encuentran empotrados, y que es axialmente comprimida:

$$\{w_j\} = \begin{cases} \text{para } j = 1,3,5,... \begin{cases} w_j(x) = h[1-\cos(N_j \frac{x}{l})] \\ N_j = (j+1)\pi \end{cases} \\ \text{para } \ j = 2,4,6,... \begin{cases} w_j(x) = h[1 - 2\frac{x}{l} - \cos(N_j \frac{x}{l}) + \frac{2}{N_j}\sin(N_j \frac{x}{l})] \\ N_j = 2.861\pi, 4.918\pi, 6.942\pi, ... \end{cases} \end{cases} \tag{5.17}$$

donde $N_j$ son las raíces de la ecuación: $\sin(N_j/2)[\tan(N_j/2) - (N_j/2)] = 0$. De esta manera, una configuración arbitraria de la viga se obtiene como:

$$w(x) = \sum_{j=1}^{\infty} A_j w_j(x) \tag{5.18}$$

donde $A_j$ son los coeficientes de ponderación de cada modo de pandeo. Partiendo de esto, se plantea una serie de normalizaciones para el tratamiento adimensional de las ecuaciones. Estas incluyen: coordendas $x \to X$, configuración $w \to W$, desplazamientos en el centro $d \to \Delta$, rotaciones en el centro $\theta \to \Theta$, longitud de la viga $s \to S$, fuerza transversal $f \to F$, momento $m \to M$, fuerza axial $p \to N^2$, energía de flexión $u_b \to U_b$, energía de compresión $u_s \to U_s$, y energía potencial de las cargas exteriores $u_e \to U_e$ (la nomenclatura es apropiadamente explicada por Rossi et al. [73]). Esto lleva a las siguientes expresiones en términos de los coeficientes $A_j$:

$$\Delta = 1 - 2 \sum_{j=1,5,9,...} A_j \ , \tag{5.19}$$

$$\Theta = - \sum_{j=2,4,6,...} \xi_j A_j \ , \tag{5.20}$$

$$S = R^2 + \sum_{j=1}^{\infty} \frac{A_j^2 N_j^2}{4} \ , \tag{5.21}$$

$$\frac{N^2}{12Q^2}\left(1 + \frac{N_1^2}{16R^2}\right) = \frac{N_1^2}{16} - \sum_{j=1}^{\infty} \frac{A_j^2 N_j^2}{4} \ , \tag{5.22}$$

$$U_b = \frac{\left(\frac{1}{2} - A_1\right)^2 N_1^4}{4} + \sum_{j=2}^{\infty} \frac{A_j^2 N_j^4}{4} \ , \tag{5.23}$$

$$U_s = \frac{6Q^2}{\left(1 + \frac{N_1^2}{16R^2}\right)} \left[\frac{N_1^2}{16} - \sum_{j=1}^{\infty} \frac{A_j^2 N_j^2}{4}\right]^2 \ , \tag{5.24}$$

$$U_e = -F\Delta - M\Theta \ . \tag{5.25}$$

Nótese que la ecuación (5.19) vincula los desplazamientos con los modos impares (modos simétricos)

con coordenada al centro no nula, mientras que la ecuación (5.20) relaciona las rotaciones con los modos pares (modos antisimétricos). Las expresiones (5.22) y (5.24) son lo más generales posibles, ya que incluyen, además del parámetro adimensional $Q = h/t$, un segundo parámetro adimensional $R = l/h$, el cual fue asumido lo suficientemente alto por Rossi et al. [73]. Esto implica que en la ecuación (5.20), $\xi_j = R\frac{dw_j}{dx}(\frac{l}{2})$. Resulta entonces que la energía potencial total normalizada es:

$$\Pi = U_b + U_s + U_e \,. \tag{5.26}$$

Siguiendo argumentos clásicos de minimización de $\Pi$, es posible llegar a ecuaciones de los descriptores cinemáticos $A_j$ que aseguran el equilibrio. Se observa que la naturaleza de la solución es fuertemente dependiente de $Q$. En este sentido, existen dos valores límtes especialmente importantes. Estos límites están relacionados a las magnitudes de la variable $N$ que permiten alcanzar. Para la presente discusión, se denomina $Q_2$ al límite tal que si $Q > Q_2$ se pueden lograr soluciones con $N > N_2$. Análogamente, $Q_3$ es el límite tal que si $Q > Q_3$ se pueden lograr soluciones con $N > N_3$. Donde $N$ es la fuerza que comprime axialmente la viga curva, y $N_2$ y $N_3$ son valores críticos que habilitan a bifurcaciones. Este comportamiento ya fue identificado en el trabajo de Qiu et al. [102], indicando que $Q_2 = 1.67$ y $Q_3 = 2.31$. Estos valores, sin embargo, dependen del número de modos activos en el análisis (el trabajo mencionado restringe la descripción al modo 1, admitiendo bifurcaciones de modo 2 y 3).

Para demostrar la importancia de estos límites se presentan en la Figura 5.9 los resultados del modelo descrito considerando 10 modos en la base, para tres casos: $Q = 1.5 < Q_2$, $Q_2 < Q = 2 < Q_3$, y $Q = 3 > Q_3$. La figura incluye las curvas de equilibrio y algunas configuraciones puntuales para el tercer caso, para dos caminos de carga. El panel (a) muestra un camino en el cual únicamente varía $\Delta$ y se mantiene fijo $\Theta = 0$ (camino de configuraciones simétricas), mientras que el panel (b) muestra un camino en el cual se modifica $\Theta$ y se mantiene fijo $\Delta = 1$. En ambos casos se muestran las respuestas de $F$ y $M$ a lo largo de estos caminos. Estos resultados no fueron publicados, y complementan los resultados presentados por Rossi et al. [73] (Apéndice E), mostrando la complejidad de las configuraciones posibles de lograr por una estructura tan simple (y utilizada) como la viga curva sinusoidal.

En análisis de estos resultados permite notar que $Q_2$ es el límite para tener una zona de rigidez negativa (snap-through) en la relación $M-\Theta$. Es decir, para vigas con $Q < Q_2$ no es posible que se desarrollen bifurcaciones de modo asimétrico. Asimismo, $Q_3$ es el límite que habilita bifurcaciones activando el modo 3 (cuyos caminos de equilibrio se indican en líneas negras a trazos).[4] Ambos comportamientos fueron señalados por Qiu et al. [102], en el primer caso restringiendo a una bifurcación en modo 2 que aquí es generalizada al incluir la rotación como descriptor del sistema. Adicionalmente, el enfoque seguido en esta tesis, permine observar que $Q_3$ también es un generador de snap-back en el camino principal de la respuesta $M - \Theta$, generando caminos de equilibrio de alta complejidad, acompañados de configuraciones deformadas que incluyen gran cantidad de modos antisimétricos. Este comportamiento con snap-back es, sin embargo, evitado ya que implica sobrepasar criterios de bifuración en modo 3, como indica la relación $F - \Theta$ del panel (b).

Notablemente, la existencia de snap-through para un camino con $\Delta = 1$, permite pensar que el mecanismo basado en la viga curva copiando modos de pandeo, puede utilizarse en histerones activados de distinta manera. Por ejemplo, en lugar de utilizar una configuracion inicial en modo 1, donde la inestabilidad principal es debido a una fuerza transversal, puede concebirse un histerón con configuración inicial en modo 2 y cuya acción desestabilizante sea un momento.

El análisis completo de este modelo y las implicancias de utilizar esta estructura como histerón en un metamaterial se presentan en las Secciones 3 y 4 de Rossi et al. [73].

[4] Se hace notar que existe un valor $Q_1$ que habilita a $N > N_1$. Valores de $Q < Q_1$ no son aquí considerados ya que prohiben la posibilidad de snap-through en la relación $F - \Delta$, eliminando el interés por este mecanismo

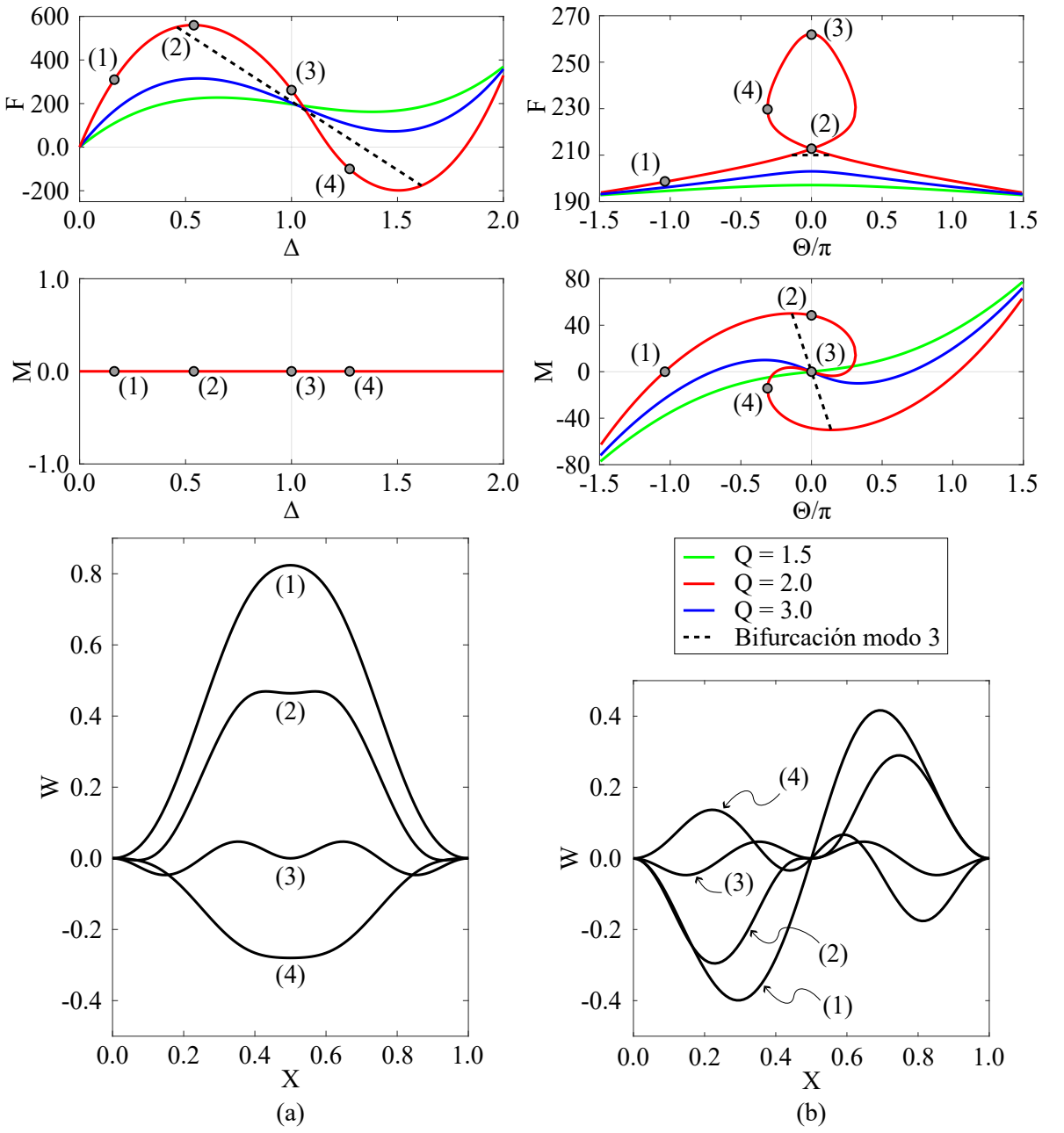


**Figura 5.9:** Resultados del modelo cinemático de la viga curva por descomposición en modos de pandeo. (a) Equilibrio correspondiente a un camino con $\Theta = 0$. (b) Equilibrio correspondiente a un camino con $\Delta = 1$. Parte superior: respuesta de la fuerza transversal $F$. Parte central: respuesta del momento $M$. Parte inferior: configuraciones deformadas para distintos instantes.

## 5.5. Estudio de metamateriales del tipo redes de histerones

La potencialidad de la metodología propuesta radica en poder estudiar, a bajo costo computacional, el comportamiento de metamateriales con transiciones de fase a través de la simulación de elementos de volumen de muestreo (SVE) incluyendo gran cantidad de histerones. Si bien ambas versiones fueron probadas para el modelado de este tipo de metamateriales, sólo se discuten ahora los correspondientes a la segunda versión, ya que es cualitativamente superior. Los resultados correspondientes a la primera versión pueden encontrarse en el trabajo de Rossi et al. [72] (Apéndice D).

El resultado logrado hasta el momento, presentado por Rossi et al. [74] (Apéndice F), es la apro-

ximación del comportamiento efectivo o límite cuasiestático *direccional*, para ciertas inclinaciones de carga, en distintas topologías de metamateriales. Para proponer estas topologías, concebidas como redes de histerones, se utilizan los conceptos de simetrías de cristales expuestos en la Sección 2.4, y se logra una topología para cada grupo de plano del sistema de cristal cuadrado. De esta forma se logran generar diseños más generales que los correspondientes a histerones colineales con los ejes coordenados, tan abundantes en la literatura. En la Figura 5.10 se presentan las tres topologías estudiadas por Rossi et al. [74] (Apéndice F), clasificadas según su grupo de plano e indicando los elementos de simetría existentes siguiendo la simbología de la Sección 2.4. En los tres casos se muestra una cantidad semejante de histerones para una mejor comparación, aunque para la topología con simetría $p4mm$ la celda primitiva incluye sólo cuatro histerones. Colores iguales de los elementos de simetría indican puntos o planos equivalentes.

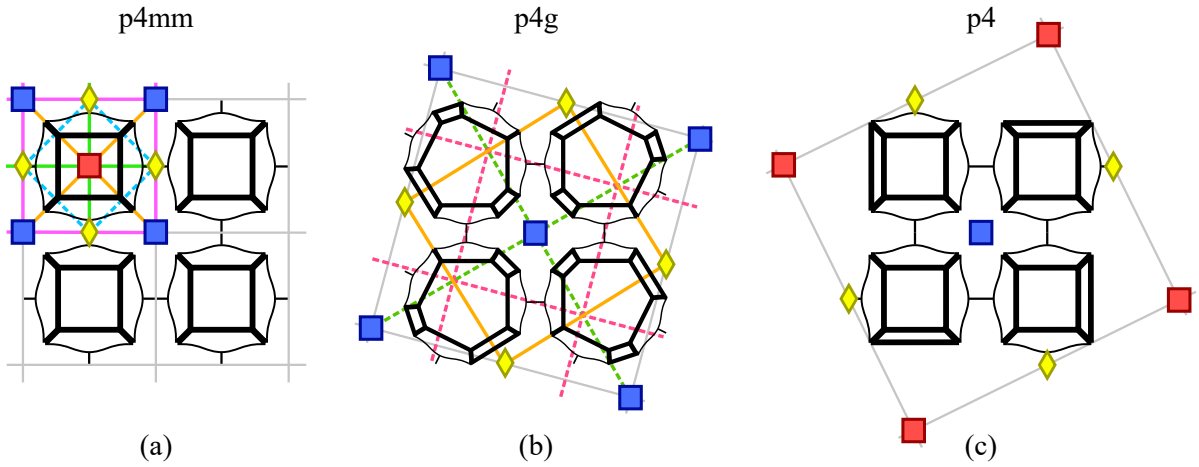


**Figura 5.10:** Topologías diseñadas y analizadas, clasificadas según su grupo de plano: (a) $p4mm$, (b) $p4g$, (c) $p4$.

Para este estudio, se decide caracterizar los histerones con un valor $Q < Q_3$, para evitar aumentar la dificultad de la descripción debido a la aparición de bifurcaciones y caminos de equilibrio complejos. Esto no afecta a la físca fundamental detrás de los metamateriales ya que ambas acciones, cargas transversales y momentos, presentan inestabilidades.

La caracterización del comportamiento límite expuesta en dicho trabajo incluye: i) la respuesta fuerza-despalzamiento en términos de la concentración de fase global, ii) la formación de microestructura y la evolución de los patrones de fase, iii) la disipación de energía, y iv) la influencia de la dirección de la carga en estos aspectos. Estos resultados se encuentran en la Sección 4 de Rossi et al. [74] (Apéndice F).

## 5.6. Conclusiones

En este capítulo se expone el trabajo realizado en cuanto al diseño de metamateriales mecánicos actuando en régimen elástico no lineal, especialmente orientados a la obtención de materiales con cambios de fase. Se presentan las dificultades (y algunas soluciones) relativas a abordar este problema por medio de optimización topológica, enfoque que se discontinuó. Al pasar a un diseño empírico, basado en un histerón muy utilizado en la literatura, se logran aportes en cuanto a una descripción detallada de su comportamiento. Esta descripción se utiliza finalmente como respuesta constitutiva de un modelo de elementos finitos reducido, apropiado para el análisis de redes de histerones. Como línea de investigación futura se menciona la posibilidad de extender la descripción cinemática de la viga curva, a configuraciones iniciales distintas, que incluyan posiblemente tanto modos simétricos como antisimétricos.

# Capítulo 6

# Multiescala de metamateriales con inestabilidades elásticas

## 6.1. Introducción

El objetivo de este capítulo es presentar el enfoque que se sigue en esta tesis para estudiar la respuesta multiescala de metamateriales con transiciones de fase elásticas en la microescala. En este sentido, se espera aportar a una discusión fundamental sobre el comportamiento mecánico de este tipo de materiales. Se presenta una recolección de ideas que aportan al entendimiento logrado, fruto de un extenso debate durante el doctorado sobre las implicancias en la homogeneización del no cumplimiento de un requerimiento tan elemental como garantizar un grado de convexidad de la energía. Los aportes de este capítulo son plasmados en el último artículo que constituye esta tesis Rossi et al. [74], el cual es replicado en el Apéndice F.

El resto del capítulo esta ordenado de la siguiente manera. En la Sección 6.2 se revisan nociones mínimas del concepto de relajación de potenciales no convexos, y se discute el vínculo de estas herramientas matemáticas con el problema de homogeneización de metamateriales con inestabilidades elásticas en la microescala. En la Sección 6.3 se presenta la idea de incluir estos fundamentos dentro de un modelo generalizado estándar descriptivo de la macroescala de este tipo de metamateriales, siendo este uno de los aportes de esta tesis. Finalmente, en la Sección 6.4, se presentan los primeros avances logrados en la línea de diseñar la microarquitectura de metamateriales funcionalmente tridimensionales, y su estudio multiescala. El desarrollo presentado en esta última sección constituye un trabajo en desarrollo que aún no ha sido publicado.

## 6.2. Teoría de relajación como modelo multiescala

Para iniciar la discusión, se retoma la descripción de materiales con transiciones de fase de la Sección 5.2, llevándola a un contexto general tridimensional. Extendiendo la condición de equilibrio (5.2) a mayores dimensiones, la minimización de energía en la **microescala** resulta:

$$\min_{\tilde{\boldsymbol{u}}_{\boldsymbol{\mu}}} \int_{\Omega_\mu} \psi\left(\boldsymbol{\varepsilon} + \nabla^s \tilde{\boldsymbol{u}}_{\boldsymbol{\mu}}\right) d\Omega_\mu \qquad , \qquad \text{con } \tilde{\boldsymbol{u}}_{\boldsymbol{\mu}} \in \tilde{\boldsymbol{\mathcal{U}}}_\mu \ , \tag{6.1}$$

donde se asume que la energía elástica de la microescala $\psi(\boldsymbol{\varepsilon}_{\boldsymbol{\mu}})$ es no convexa, caracterizando un material con múltiples fases. A pesar de que el material es homogéneo ($\psi$ no depende explícitamente del punto material dentro de $\Omega_\mu$), la no convexidad de la función de energía elástica da lugar a campos de deformaciones que difieren del estádo homogéneo $\boldsymbol{\varepsilon}$ en el RVE. Mas aún, las fluctuaciones $\nabla^s \tilde{\boldsymbol{u}}_{\boldsymbol{\mu}}$ del campo de deformaciones no tienen longitudes características definidas. Es este fenómeno precisamente

el responsable de que en ciertos casos no exista un mínimo global al problema (6.1) o la falta de unicidad en mínimos locales (ejemplificada en la Sección 5.2). A pesar de estas características, se ha demostrado en la literatura que es posible describir la respuesta macroescala del material a partir de valores medios, analizando una secuencia de patrones de deformación (microestructura) minimizantes de la energía elástica total.

Siguiendo los trabajos de Pipkin [103], Kohn [104], el enfoque de esta tesis es argumentar que existe una función de energía aparente o efectiva $\hat{\psi}(\boldsymbol{\varepsilon})$ que caracteriza la macroescala. Esta energía es tal que, al plantear el problema de equilibrio en la **macroescala**, el mínimo siempre existe y se obtiene a partir de la deformación homogénea:

$$\hat{\psi}(\boldsymbol{\varepsilon})\,|\Omega_\mu| = \min_{\tilde{\boldsymbol{u}}_{\boldsymbol{\mu}}} \int_{\Omega_\mu} \hat{\psi}\left(\boldsymbol{\varepsilon} + \nabla^s \tilde{\boldsymbol{u}}_{\boldsymbol{\mu}}\right) d\Omega_\mu \qquad , \qquad \text{con } \tilde{\boldsymbol{u}}_{\boldsymbol{\mu}} \in \tilde{\boldsymbol{\mathcal{U}}}_\mu \,, \tag{6.2}$$

Más importante aún, los mínimos al problema (6.2) corresponden a los límites débiles de las secuencias minimizantes (es decir, el ínfimo) para el problema (6.1). Para ello, la energía macroescala $\hat{\psi}$ se define como la relajación $\psi^{qc}$ de la energía microescala $\psi$:

$$\hat{\psi}(\boldsymbol{\varepsilon}) = \psi^{qc}(\boldsymbol{\varepsilon}) = \inf_{\tilde{\boldsymbol{u}}_{\boldsymbol{\mu}}} \frac{1}{|\Omega_\mu|} \int_{\Omega_\mu} \psi\left(\boldsymbol{\varepsilon} + \nabla^s \tilde{\boldsymbol{u}}_{\boldsymbol{\mu}}\right) d\Omega_\mu \qquad , \qquad \text{con } \tilde{\boldsymbol{u}}_{\boldsymbol{\mu}} \in \tilde{\boldsymbol{\mathcal{U}}}_\mu \,. \tag{6.3}$$

La energía $\psi^{qc}$ es precisamente el soporte cuasiconvexo (quasiconvex envelope) de la energía de microescala $\psi$. Notar que las expresiones (6.2) y (6.3) coinciden con la definición de Morrey [41] de cuasiconvexidad (2.12) dada en la Sección 2.2.2.

El concepto de relajación es más amplio que el de homogeneización convencional presentado en la Sección 2.3, ya que incluye, además de resolver el equilibrio, la búsqueda de patrones de microestructura óptimos, implícitos en la resolución del campo $\tilde{\boldsymbol{u}}_{\boldsymbol{\mu}}$ en el problema (6.3), debido a la posible aparación de inestabilidades. Asumiendo ahora, por simplicidad, un material de dos fases, donde $\psi$ tiene únicamente dos zonas convexas de energía $\psi_I$ y $\psi_{II}$ (ver ejemplo 1D de la Figura 5.1), la cuasiconvexificación (6.3) puede reescribirse como:[1]

$$\psi^{qc}(\boldsymbol{\varepsilon}) = \inf_{\chi} \inf_{\tilde{\boldsymbol{u}}_{\boldsymbol{\mu}}} \frac{1}{|\Omega_\mu|} \int_{\Omega_\mu} \left[(1-\chi)\,\psi_I\left(\boldsymbol{\varepsilon} + \nabla^s \tilde{\boldsymbol{u}}_{\boldsymbol{\mu}}\right) + \chi\,\psi_{II}\left(\boldsymbol{\varepsilon} + \nabla^s \tilde{\boldsymbol{u}}_{\boldsymbol{\mu}}\right)\right] d\Omega_\mu \quad , \quad \text{con } \tilde{\boldsymbol{u}}_{\boldsymbol{\mu}} \in \tilde{\boldsymbol{\mathcal{U}}}_\mu \,. \tag{6.4}$$

donde $\chi$ es una función característica periódica definida en el RVE, siendo $\chi = 0$ donde $\psi = \psi_I$ y $\chi = 1$ donde $\psi = \psi_{II}$. La función $\chi$ denota la naturaleza altamente oscilatoria de las deformaciones en la microescala. Determinar $\psi^{qc}(\boldsymbol{\varepsilon})$ implica encontrar el acomodamiento de las fases dentro del RVE de manera de minimizar la energía elástica del mismo, es decir, se deben encontrar las microestructuras óptimas. Kohn [104] señala que estas microestructuras no son únicas. Nótese además, que para un campo $\chi$ dado, la minimización en $\tilde{\boldsymbol{u}}_{\boldsymbol{\mu}}$ recupera la idea de energía homogeneizada para un compuesto periódico compuesto de dos fases, definidas respectivamente por funciones de energías convexas $\psi_I$ y $\psi_{II}$. Es posible entonces determinar la fracción de volumen o concentración de fase II, identificada con el símbolo $c$, como:

$$c = \frac{1}{|\Omega_\mu|} \int_{\Omega_\mu} \chi \, d\Omega_\mu \quad . \tag{6.5}$$

Para las microestructuras consideradas en esta tesis, la concentración de fase $c$ es suficiente para caracterizar la respuesta de una familia de soluciones, independientemente de la distribución $\chi$ específica. Esta idea fue discutida en la Sección 5.2 en un contexto menos formal.

[1] Esta definición puede extenderse a mayor cantidad de fases, aunque esto excede los objetivos de esta tesis.

### 6.2.1. Microestructura y compatibilidad entre estados preferenciales

El campo de deformaciones óptimo, que conforma el patrón de microestructura fina en la microescala, cumple con la condición de compatibilidad de Hadamard.[2] Esta condición establece que en la interfase:

$$[[\boldsymbol{\varepsilon}_{\boldsymbol{\mu}}]] = [[\nabla^s \tilde{\boldsymbol{u}}_{\boldsymbol{\mu}}]] = \tilde{\boldsymbol{u}}_{\boldsymbol{\mu}} \otimes_s \boldsymbol{n} \ . \tag{6.6}$$

donde $\boldsymbol{n}$ es el vector unitario normal a la interfase. Esto asegura para la energía aparente o efectiva de macroescala cumpla, al menos, la convexidad de rango 1 (2.16) y, por lo tanto, la condición de Legendre-Hadamard (2.4) mencionadas en la Sección 2.2. El patrón de microestructura depende de la función de energía microescala $\psi$ y de los estados de deformación preferenciales. Entendiéndose estado preferencial $\mathbf{d}_i$ como el estado de deformación (strain) micro de tensión nula (mínimo de energía $\psi$) correspondiente a la fase $i$.

Por ejemplo, para una energía $\psi$ definida por dos pozos de forma cuadrática con el mismo tensor constitutivo elástico, Pipkin [103], Kohn [104] demuestran que la microestructura laminada es óptima, aunque en general no es única. La formación de láminas fue reportada en la Sección 4 del trabajo de Rossi et al. [74] (Apéndice F) para metamateriales conformados como redes de histerones y es también discutida en un resultado preliminar de un metamaterial 3D presentado en la Sección 6.4.

Adicionalmente, la forma de la energía relajada $\psi^{qc}$ depende cualitativamente de la diferencia $\mathbf{d}_I - \mathbf{d}_{II}$ entre estados preferenciales. Por un lado, si estos estados son compatibles en el sentido de Hadamard, es decir $\mathbf{d}_I - \mathbf{d}_{II} = \boldsymbol{a} \otimes_s \boldsymbol{b}$, $\psi^{qc}$ es convexo. Esto sucede trivialmente en el caso 1D y es discutido en la Sección 3 del trabajo de Rossi et al. [74]. Por el contrario, cuando los estados preferenciales no son compatibles, $\psi^{qc}$ es no convexo, debido a que la mezcla de fases almacena una energía por la falta de coherencia o compatibilidad entre estados preferenciales. Mayores detalles pueden encontrarse en el trabajo de Rossi et al. [74], donde esta energía es denominada $W_m$. Esta forma de la energía aparente es especialmente importante en el análisis de los resultados que se presentan en la Sección 6.4.

### 6.2.2. Criterio para la transición de fase

Como ya fue mencionado, resolver el problema (6.4) implica encontrar, para una deformación macro $\boldsymbol{\varepsilon}$ dada, un arreglo de fases o microestructura $\chi$ (en algún sentido) minimizante. Cabe pregunar entonces cual es la *estrategia de evolución* de $\chi$ cuando ocurre un cambio de $\boldsymbol{\varepsilon}$. La mayoría de los trabajos en relajación, como los de Pipkin [103], Kohn [104], asumen que el material macroescala es capaz de minimizar globalmente la energía, lo que en los trabajos de Puglisi y Truskinovsky [80], Abeyaratne y Knowles [105] se denomina como transitar el camino de Maxwell. Este tipo de selección de $\chi$, entre otras cosas, implica que el material macroescala no disipa energía. De esta manera, la concentración de fase $c$, definida por la expresión (6.5), no es una variable independiente, ya que depende de $\boldsymbol{\varepsilon}$.

Por el contrario, el comportamiento observable en los metamateriales estudiados en Capítulo 5 (y las publicaciones asociadas) manifiesta histéresis, debido a la formación consecutiva de, y transición entre, mínimos locales. En particular, estos mínimos locales son dependientes de la concentración de fase $c$. La experiencia indica que estos metamateriales no tienen la capacidad de superar barreras de energía, por lo cual el camino recorrido corresponde a lo que estos autores denominan camino de máxima histéresis. Para recuperar este tipo de comportamiento, la estrategia de evolución de $c$ propuesta en esta tesis, surge de argumentar la existencia de un potencial disipativo en la macroescala. Este potencial define una condición crítica para una fuerza configuracional existente en la microescala. Para caracterizar el potencial disipativo, se utilizaron nociones de multiescala convencional. En particular, análogamente al principio de Hill-Mandel (2.28), se postula que la disipación en la macroescala surge de homogeneizar la liberación de energía (debido a transiciones de fase) en la microescala.

[2] El cumplimiento de la condición de Hadamard por parte del campo de deformaciones evita que surja una energía de interfase.

### 6.2.3. Relajación aplicada a metamateriales

El marco teórico de relajación discutido hasta el momento asume en la microescala un material homogéneo definido por una función de energía elástica no convexa, es decir, sin la existencia de una microarquitectura. Sin embargo, estos conceptos siguen siendo válidos dentro de la lógica de los metamateriales.

En la descripción del metamaterial a más "baja escala" se tiene una microarquitectura periódica conformada por materiales constitutivamente no lineales, que sufren deformaciones y desplazamientos finitos, pero cuyos modelos constitutivos que cumplen individualemente con los requisitos de cuasiconvexidad y elipticidad para ser definidos estables. La inestabilidad, en este caso, surge de un proceso geométrico de la deformación del compuesto.

El modelo subrogado presentado en la Sección 5.4.3 constituye una "escala intermedia" donde se preserva cierta información de la microarquitectura (direcciones relativas y conectividades entre histerones), pero traduciendo la inestabilidad geométrica de la microarquitectura de alta fidelidad en una inestabilidad material descrita con teoría de desplazamientos infinitesimales. En este escenario, mucho del comportamiendo discutido previamente es extrapolable al contexto de multiescala de metamateriales, donde resulta de particular importancia la energía aparente de macroescala $\hat{\psi}$. Análogamente a la expresión (6.3), es posible plantear la cuasiconvexificación en este caso como:

$$\hat{\psi}(\boldsymbol{\varepsilon}) = \psi^{qc}(\boldsymbol{\varepsilon}) = \inf_{\tilde{\boldsymbol{u}}_{\boldsymbol{\mu}}} \frac{1}{|\Omega_\mu|} \int_{\Omega_\mu} \phi\left(\boldsymbol{y}, \boldsymbol{\varepsilon} + \nabla^s \tilde{\boldsymbol{u}}_{\boldsymbol{\mu}}\right) \, d\Omega_\mu \qquad , \qquad \text{con } \tilde{\boldsymbol{u}}_{\boldsymbol{\mu}} \in \tilde{\boldsymbol{\mathcal{U}}}_\mu \, , \tag{6.7}$$

donde $\phi$ es la energía que depende de la coordenada microescala $\boldsymbol{y}$ dentro del RVE de acuerdo a la microarquitectura. Para determinar la energía $\hat{\psi}(\boldsymbol{\varepsilon})$, no es suficiente con homogeneizar una única celda unidad, ya que la formación de microestructura óptima involucrando múltiples celdas implica, en general, estados de menor energía. Estas soluciones de longitud de onda superior a la celda unidad son periódicas en dominios que incluyen varias celdas, lo cual genera una indeterminación en el tamaño del RVE $\Omega_\mu$ (esta idea fue presentada en la Sección 5.2.1 como "dependencia de malla").

Siguiendo el trabajo de revisión de Castañeda [106], este problema puede abordarse desde dos puntos de vista. Ambas estrategias han sido consideradas, al menos en forma aproximada, en esta tesis. Se establece la notación de $\Omega_\mu^{uc}$ al dominio correspondiente a una celda unidad. El primer enfoque consiste en redefinir la expresión (6.7) como:

$$\psi^{qc}(\boldsymbol{\varepsilon}) = \inf_{\boldsymbol{k}} \inf_{\tilde{\boldsymbol{u}}_{\boldsymbol{\mu}}} \frac{1}{|\boldsymbol{k}\, \Omega_\mu^{uc}|} \int_{\boldsymbol{k}\, \Omega_\mu^{uc}} \phi\left(\boldsymbol{y}, \boldsymbol{\varepsilon} + \nabla^s \tilde{\boldsymbol{u}}_{\boldsymbol{\mu}}\right) \, d\Omega_\mu \qquad , \qquad \text{con } \tilde{\boldsymbol{u}}_{\boldsymbol{\mu}} \in \tilde{\boldsymbol{\mathcal{U}}}_\mu \, , \tag{6.8}$$

donde el término $\boldsymbol{k}\, \Omega_\mu^{uc}$ indica conjuntos de celdas unidad en arreglos dados por el vector $\boldsymbol{k}$. La relajación (6.8) implica entonces la evaluación sucesiva de dominios que incluyen un mayor número de celdas unidad. Puede asimilarse al proceso de evaluar las secuencias minimizantes mencionadas en la Sección 6.2. Este enfoque es de fácil implementación numérica aunque poco práctico y de gran costo computacional. Los estudios presentados en la Sección 5.5 aproximan esta metodología, aprovechando de la eficiencia computacional ganada a partir del modelo subrogado desarrollado.

El segundo enfoque consiste en homogeneizar la energía $\psi^0$ de una única celda unidad, es decir:

$$\psi^0(\boldsymbol{\varepsilon}) = \inf_{\tilde{\boldsymbol{u}}_{\boldsymbol{\mu}}} \frac{1}{|\Omega_\mu^{uc}|} \int_{\Omega_\mu^{uc}} \phi\left(\boldsymbol{y}, \boldsymbol{\varepsilon} + \nabla^s \tilde{\boldsymbol{u}}_{\boldsymbol{\mu}}\right) \, d\Omega_\mu \qquad , \qquad \text{con } \tilde{\boldsymbol{u}}_{\boldsymbol{\mu}} \in \tilde{\boldsymbol{\mathcal{U}}}_\mu \, , \tag{6.9}$$

para luego determinar su soporte cuasiconvexo. Esta estrategia se asemeja más al enfoque teórico discutido en las secciones previas, considerando la energía de microescala $\psi = \psi^0$. De momento, este enfoque sólo ha podido utilizarse en microarquitecturas relativamente simples, como laminados y algunos compuestos matriz-fibra (para más detalles ver el trabajo de Castañeda [106]). Generalizar una técnica con

esta filosofía permitiría recuperar el muy conveniente aspecto planteado en la Sección 2.3 de realizar el salto de escala a partir del análisis de una única celda. Esto, sin embargo, continúa siendo al día de hoy un problema de estudio. El mayor aporte conceptual de esta tesis referido a la multiescala de estos materiales, se basa en este segundo enfoque, aproximando la energía $\psi^0$ de la celda real a una energía simplificada que cumple con las hipótesis establecidas por Pipkin [103], Kohn [104] (ver la Sección 3.2 de Rossi et al. [74]).

### 6.2.4. Sobre el enfoque multiescala utilizado

De manera general, y salvo casos simples como elasticidad lineal, al resolver numericamente un problema multiescala con microarquitectura compleja como los aquí abordados, no se tiene como objetivo lograr un modelo material descriptivo de la macroescala. Un ejemplo claro de esto se da en elastoplasticidad. Dada una cierta topología y un modelo elastoplástico de la microescala, el proceso de resolver ambas escalas en simultáneo (a través del traspaso de los descriptores cinemáticos) no concluye con un modelo específico de elastoplasticidad en la macroescala.

Con el propósito de validar la propuesta planteada, el enfoque en esta tesis para realizar el análisis multiescala de materiales con inestabilidades es esencialmente distinto. Caracterizando la respuesta de una celda unidad a partir de ciertas simplificaciones, se obtiene un modelo constitutivo macroescala, del cual se conocen los potenciales que lo definen. Esto simplifica la evaluación de las variables macro (como el estado tensiones, y las energías acumulada y disipada) y facilita un entendimiento mas fundamental del proceso de transición de fase con liberación de energía, logrando desacoplar la resolución de cada escala y evitando tener que recurrir a modelos del tipo $FE^2$ que aún continúan siendo caracterizados por una complejidad computacional muy alta.

## 6.3. Modelo estándar generalizado aplicado a metamateriales

Una vez conocidos los potenciales de energía libre (relajación de la energía microescala) y disipativo (homogeneización de la liberación de energía), es posible encuadrar la respuesta macroescala de los metamateriales con cambios de fase dentro del formalismo de los modelos estándar generalizados, descripto en la Sección 2.6. En particular, el potencial de energía elástica permite determinar las "fuerzas" conjugadas asociadas a las variables de estado, mientras que la relación de Biot determina la evolución de la variable interna a partir del potencial disipativo. Los detalles y resultados de validación de utilizar este procedimiento fueron expuestos por Rossi et al. [74] (Apéndice F) y no son repetidos en este texto. Para facilitar el entendimiento de la propuesta, se presenta a modo de ejemplo 1D, la formulación del modelo estándar de la energía (5.1). El propósito de este ejemplo es demostrar el comportamiento general de la propuesta, sin referir específicamente a una topología microescala (lo cual sí se hace en el trabajo citado).

### 6.3.1. Ejemplo del material estandar 1D

Por comodidad se vuelve a escribir la función de energía (5.1):

$$\psi(\varepsilon_\mu) = \left({\varepsilon_\mu}^2 - 1\right)^2 \ . \tag{6.10}$$

Para lograr la relajación de (6.10), se siguieron los desarrollos presentados por Pipkin [103]. Siendo $c$ la concentración del material en fase II, las deformaciones en cada fase de la microescala están dadas por:

$$\varepsilon_\mu = \varepsilon + \tilde{\varepsilon}_\mu = \begin{cases} \varepsilon - c\tilde{d} & \text{en fase I} \\ \varepsilon + (1-c)\tilde{d} & \text{en fase II} \end{cases} \ , \tag{6.11}$$

donde $\tilde{d}$ es la versión unidimensional del tensor de rango 1 indicado en la ecuación de compatibilidad (6.6). De esta manera, la energía cuasiconvexificada a $c$ dado resulta (ver ecuación (6.4) con restricción en el valor (6.5)):

$$\hat{\psi}(\boldsymbol{\varepsilon}, c) = \inf_{\tilde{d}} \left[ (1-c)\, \psi_I(\varepsilon_\mu) + c\, \psi_{II}(\varepsilon_\mu) \right] \ , \tag{6.12}$$

donde $\psi_I$ y $\psi_{II}$ corresponden a reemplazar las deformaciones (6.11) en la energía microescala (6.10). Reordenando algunos términos por conveniencia, la relajación de la energía se puede escribir como:

$$\hat{\psi}(\boldsymbol{\varepsilon}, c) = \inf_{\tilde{d}} \left[ \left( \boldsymbol{\varepsilon}^2 + c(1-c)\tilde{d}^{\,2} - 1 \right)^2 + c(1-c) \left( \tilde{d}^{\,2} + 2\tilde{d}(\boldsymbol{\varepsilon} - c\tilde{d}) \right)^2 \right] \ . \tag{6.13}$$

La minimización en $\tilde{d}$ implica encontrar las deformaciones micro que verifican la condición de equilibrio. El valor $\tilde{d}$ minimizante surge de resolver la ecuación cuadrática:

$$\tilde{d}^{\,2} \left[ 3c^2 - 3c + 1 \right] + \tilde{d} \left[ 3\boldsymbol{\varepsilon}(1-2c) \right] + \left[ 3\boldsymbol{\varepsilon}^2 - 1 \right] = 0 \ , \tag{6.14}$$

donde se utiliza la mayor de las raíces (la menor corresponde a invertir el sentido de $c$).[3] El dominio admisible de valores $(\boldsymbol{\varepsilon}, c)$ se obtiene de analizar la estabilidad de la función $\hat{\psi}$, esto elimina configuraciones que implican mezclas con parte del material en la zona espinodal.

Una vez calculado el potencial relajado, es posible obtener las tensiones macro $\sigma$ y las fuerzas $g$ conjugadas a la variable interna $c$ de acuerdo al modelo estándar (ver Sección 2.6). No se explicitan las expresiones debido a la complejidad de la mismas, las cuales no aportan mayor claridad al presente ejemplo. Expresiones simples, con una interpretación clara, de estas fuerzas para otra función de energía son presentadas en la Sección 3 del trabajo de Rossi et al. [74] (Apéndice F). Por otra parte, de manera simple, el potencial disipativo consiste en imponer que el material realiza una transición de fase en la microescala una vez alcanzado un valor límite de $g$.

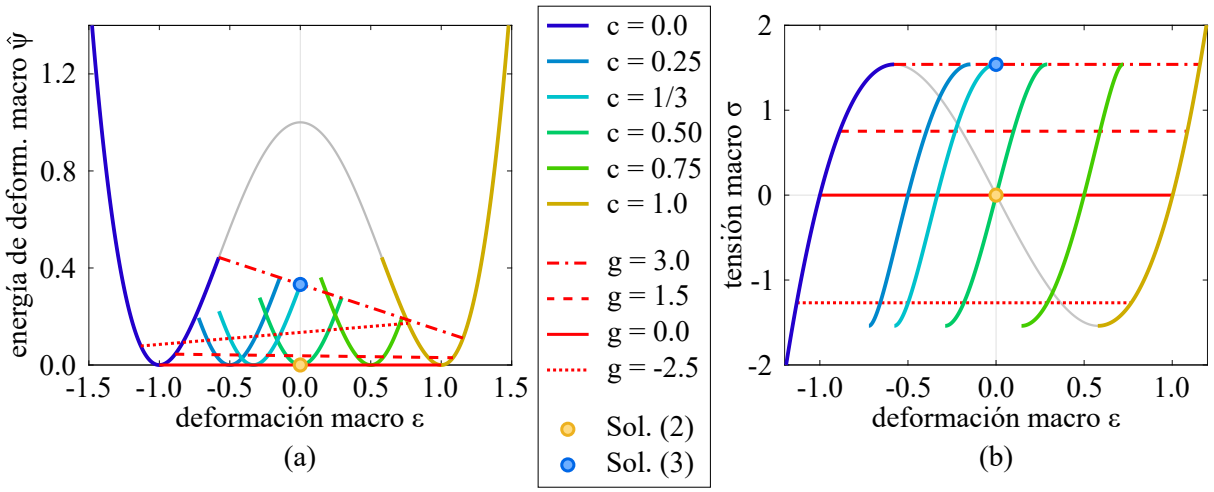


**Figura 6.1:** Modelo estándar aplicado a material con dos fases en la microescala. (a) Relación energía - deformación. (b) Relación tensión - deformación. Líneas grises: respuesta homogénea microescala. Líneas llenas en colores: ramas de equilibrio a concentración de fases $c$ constante obtenidas de la relajación de la energía no convexa microescala. Líneas rojas a trazos: curvas de fuerza configuracional $g$ constante relacionadas al estado para transicionar de fase. Círculos: estados macro comparables con las soluciones presentadas en la Figura 5.1.

En la Figura 6.1 se muestra el resultado de la convexificación de la energía (6.10). La Figura 6.1(a) muestra la relación energía de deformación vs. deformación, mientras que la Figura 6.1(b) presenta

[3] Nótese que, a diferencia del trabajo de Pipkin [103], al no tener los pozos de energía la misma variación ante un dado incremento en las deformaciones, el tensor de rango 1 $\tilde{d}$ es dependiente de $(\boldsymbol{\varepsilon}, c)$.

la relación tensión vs. deformación. En ambos casos, se muestran (algunas de las infinitas) ramas de equilibrio estables para distintos valores de concentración de fase $c$ en una escala de colores que varía de azul a amarillo. Se observa que las curvas para $c = 0$ y $c = 1$ coinciden con la respuesta homogénea microescala (en gris) hasta que la misma pierde convexidad. Si bien aquí solo se muestran algunas de las ramas de equilibrio para señalar el comportamiento general, cabe remarcar que este tipo de curvas también fueron reportadas por Puglisi y Truskinovsky [80] para el caso discreto.

Además, líneas rojas con distintos tipos de trazo muestran isocurvas de la fuerza $g$ constante. En la Figura 6.1(a), estas curvas unen puntos de ramas de distinto $c$ con igual pendiente. Si el valor $g$ de alguna de estas curvas fuese el valor límite, la curva representaría los estados en los cuales el material macroescala aumenta o disminuye $c$. Alternativamente, esto puede interpretarse considerando la relación evidente entre $g$ y la tensión macro $\sigma$. Un valor $g$ límite implica que el material transiciona una vez alcanzado un cierto valor de tensión. El valor límite de $g$ depende de la capacidad del material para superar barreras de energía locales. Por ejemplo, $g = 3.0$ corresponde a un material que no puede superar barreras de energía, y correponde al camino de máxima histéresis y, por lo tanto, máxima disipación. Por el contrario, $g = 0.0$ corresponde a un material que minimiza globalmente la energía, y sigue el camino de Maxwell. Este tipo de comportamiento es general mas allá del ejemplo 1D que se analiza. En particular para este caso, debido a la compatibilidad entre mínimos de energía, de seguirse este último camino se obtiene la convexificación del potencial $\psi$.

Finalmente, se indica que a partir de la expresión de la energía relajada y las tensiones que de ella se derivan, al reemplazar los pares $(\varepsilon, c)$ de acuerdo a las soluciones 2 y 3 presentados en la Sección 5.2, se replican los valores allí reportados. La principal diferencia a destacar es que, en este caso, estos resultados surgen de un modelo del continuo.

### 6.3.2. Relación con el trabajo de Abeyaratne y Knowles

Por completitud, se discuten brevemente las similitudes y diferencias del modelo macroescala propuesto en esta tesis con la línea de trabajo desarrollada por Abeyaratne y Knowles, resumida en su libro [105], quienes estudiaron exhaustivamente el problema de materiales con potenciales de dos pozos, y cuyo trabajo sirvió como fuente continua de consulta para esta tesis.

La principal diferencia conceptual reside en la interpretación del salto de escala. Abeyaratne y Knowles [105] proponen que la energía no convexa de dos pozos es la respuesta de un punto material perteneciente a un cuerpo macroescala. Esto hace que a nivel de la macroescala se observe la mezcla de fases y, asumiendo un ordenamiento que experimentalmente no se observa, fenómenos como la propagación de una superficie de interfase, la cual separa regiones del cuerpo macro en cada una de estas fases. Por el contrario, la propuesta de esta tesis es que estos comportamientos corresponden a la microescala, y que el modelo constitutivo de un punto material macroescala ya los incluye. De manera simplificada, el cuerpo macroescala de Abeyaratne y Knowles puede asociarse a lo que en esta tesis se entiende como RVE.

Mas allá de esta (importante) diferencia conceptual, estos autores lograron describir gran parte del comportamiento de este tipo de materiales, e identificaron la dificultad para describirlos mediante las ecuaciones de gobierno clásicas. Postularon la existencia de una fuerza configuracional (driving force) actuante en la interfase, que disipa energía ante un avance de la misma. Esto es análogo a la disipación en la microescala del modelo estándar producida por la fuerza $g$ ante un cambio en la concentración $c$. Además, determinaron que la magnitud de dicha fuerza está relacionada con el balance energético al cambiar de fase, y que en el caso cuasi-estático la magnitud de la fuerza configuracional coincide con el salto en la energía de Gibbs entre ambas fases. Adicionalmente, demostraron que sólo puede existir mezclas de fases con el material en alguna de las zonas de energía convexa. Esto es completamente análogo a la propuesta de esta tesis. Finalmente, notaron de la necesidad de incluir a las ecuaciones de gobierno un criterio de nucleación de la interfase y una relación cinética que gobierne la evolución de la

misma. En el modelo estándard propuesto, estos aspectos se desprenden naturalmente de las ecuaciones constitutivas que se derivan de la existencia de un potencial disipativo.

## 6.4. Metamaterial 3D con transiciones de fase volumétricas

Se concluyen los aportes de esta tesis con la presentación de resultados y discusiones preliminares de un trabajo actualmente en desarrollo. El objetivo es el diseño de la microarquitectura y el análisis multiescala de metamateriales 3D con inestabilidades basadas en mecanismos de deformación novedosos. En particular, se han realizado avances en la obtención de un metamaterial cuyos estados de deformación preferenciales difieren en un tensor esférico. El material que se presenta a continuación no ha sido aún publicado.

### 6.4.1. Propuesta de nuevo histerón

Se busca lograr un metamaterial funcionalemente 3D, es decir, con la posibilidad de transformar fase para estados de carga generales en el espacio, y, adicionalmente, cuya celda unidad tenga únicamente dos estados preferenciales. Esto resulta conveniente, en una segunda etapa, para contrastar la respuesta del SVE con modelos constitutivos relajados analíticos. Nótese que celdas unidad conformadas como arreglos del histerón mostrado en la Figura 5.3 dispuesto en distintas direcciones, por ejemplo la propuesta por Ren et al. [107], presentan mas de dos pozos de energía (en principio, tantos como histerones), por lo cual no son válidas dentro de la concepción propuesta.

El diseño original del histerón que aquí se presenta se inspira en la propuesta 2D de Rafsanjani y Pasini [93]. La Figura 6.2(a) muestra una versión simplificada de una de las microarquitecturas mostradas en dicho trabajo, adaptada para ser la cara de un histerón tridimensional cúbico. La idea consiste en tres elementos articulados entre sí que permiten rotaciones relativas, y que presentan biestabilidad si la condición de borde es una expansión volumétrica. En la versión que aquí se presenta, esta geometría 2D se define a partir de un único parámetro $a$, que corresponde al lado del cuadrado central. Utilizando los conceptos de simetrías de cristales presentados en la Sección 2.4, es posible generar una versión tridimensional a partir de de la aplicación de operaciones de simetría. En la Figura 6.2(b) se presenta el histerón tridimensional propuesto, junto con los elementos de simetría que incluye (comparación con la Figura 2.8 evidencia que estos elementos corresponden al grupo de punto 23).

Para mostrar el comportamiento del histerón se caracteriza al material base a partir de un modelo Neo-Hookeano, con módulo de elasticidad $E_1 = 2.1GPa$ y coeficiente de Poisson $\nu_1 = 0.3$, y se define la geometría con $a = 0.42$, lo cual corresponde a una fracción de volumen $f_1 = 0.65$. Las Figuras 6.2(c) y (d) muestran la respuesta de la energía acumulada $\psi$ y de la tensión hidrostática en función del Jacobiando de la deformación, para una expansión volumétrica progresiva. Los resultados muestran una etapa inicial de acumulación de energía, seguida por una liberación paulatina de la misma hasta alcanzar un segundo estado estable. Se hace notar que la existencia de articulaciones ideales entre las distitnas partes genera que el segundo estado estable sea libre de energía. Esto permite una versatilidad en el metamaterial para la elección en su configuración inicial al momento del uso. Es decir, puede disponerse de un material con inestabilidad antes una expansión volumétrica si se elige la configuración inicial como el primer estado estable, o de una inestabilidad ante una compresión volumétrica si se elige el segundo esta estable. Se muestran en la Figura 6.2(e) tres configuraciones del proceso de carga, que permiten visualizar el mecanismo por el cual el histerón genera la inestabilidad.

Si bien la microarquitectura en general cumple con la función esperada, aún restan varios estudios por realizar en cuanto a su diseño. La topología inicial es un aspecto clave para evitar contacto entre las partes para estados de deformación muy distorsionados (lo cual complejiza su modelación y no aporta al comportamiento fundamental), para esto se debe generalizar el diseño aumentando la cantidad de parámetros que lo definen. Estos parámetros también deben tener en cuenta restricciones de manufacturabilidad.

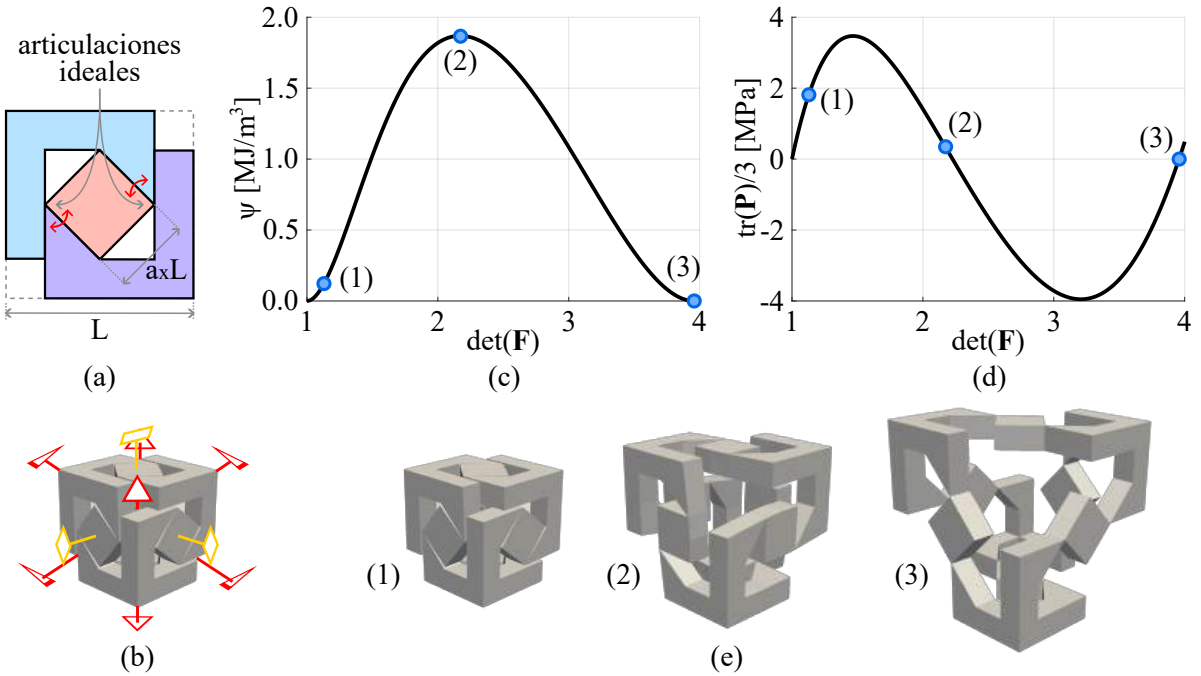


**Figura 6.2:** Histerón con cambio de fase volumétrico. (a) Diseño geométrico de la cara del histerón, a partir del parámetro $a$. (b) Elementos de simetría para conformar el diseño tridimensional. (c) Relación energía de deformación vs. variación volumétrica, y (d) Relación tensión hidrostática vs. variación volumétrica, para un material constitutivo definido por $E_1 = 2.1GPa$, $\nu_1 = 0.3$, y parámetro $a = 0.42$. (e) Instancias de deformación.

### 6.4.2. Resultados preliminares y discusión

Finalmente, se presentan los resultados correspondientes a una primera aproximación al salto de escala mediante el enfoque de aumentar el número de celdas en el SVE. Para ello, se menciona en primer lugar, que el histerón presentado no cumple con las condiciones de periodicidad geométrica para ser considerado como celda unidad. Para lograr una celda unidad periódica, se dispusieron 8 histerones, relacionados por planos de reflexión. El SVE analizado se compone de 4 de estas celdas por lado. Esta composición por niveles se esquematiza en la Figura 6.3(a). El SVE es sometido al mismo esquema de cargas que el histerón, correspondiente a una expansión volumétrica. Esto genera que el estado de deformación macro conecte los dos estados preferenciales, a pesar de que los mismos son cinemáticamente incompatibles a nivel de microescala (ver Sección 6.2.1).

En las Figuras 6.3(b) y (c) se compara la respuesta del SVE (en líneas negras) con la respuesta homogénea no convexa del histerón (en líneas grises a trazos). Se observan eventos de reacomodamiento interno de las fases bien marcados, coincidentes con caídas en el valor de las tensiones y la energía acumulada. Si bien no se ha realizado aún una búsqueda exhaustiva de todas las ramas de equilibrio (ver este procedimiento en la Sección 2 de Rossi et al. [74] -Apéndice F-), resulta notable que la energía no tiende a una forma convexa, sino mas bien a una zona cóncava de menor energía que la respuesta homogénea. Este comportamiento se debe a la existencia de una energía remanente por la falta de coherencia entre estados preferenciales, y está en gran acuerdo con las estimaciones de Pipkin [103], Kohn [104].

En la Figura 6.3(d) se muestran dos configuraciones logradas durante el proceso de carga que demuestran la formación de microestructura (sombreada en rojo en una de las caras, ver continuidad más claramente en la cara superior), responsable de la obtención de estados de menor energía. Se observa que la formación de esta microestructura conlleva el "desenrollamiento" de algunos histerones ubicados sobre planos perpendiculares a las diagonales principales del SVE. Esto revela que, a pesar del histerón no ser periódico, se comporta como celda unidad en el sentido de que es capaz de transicionar de fase

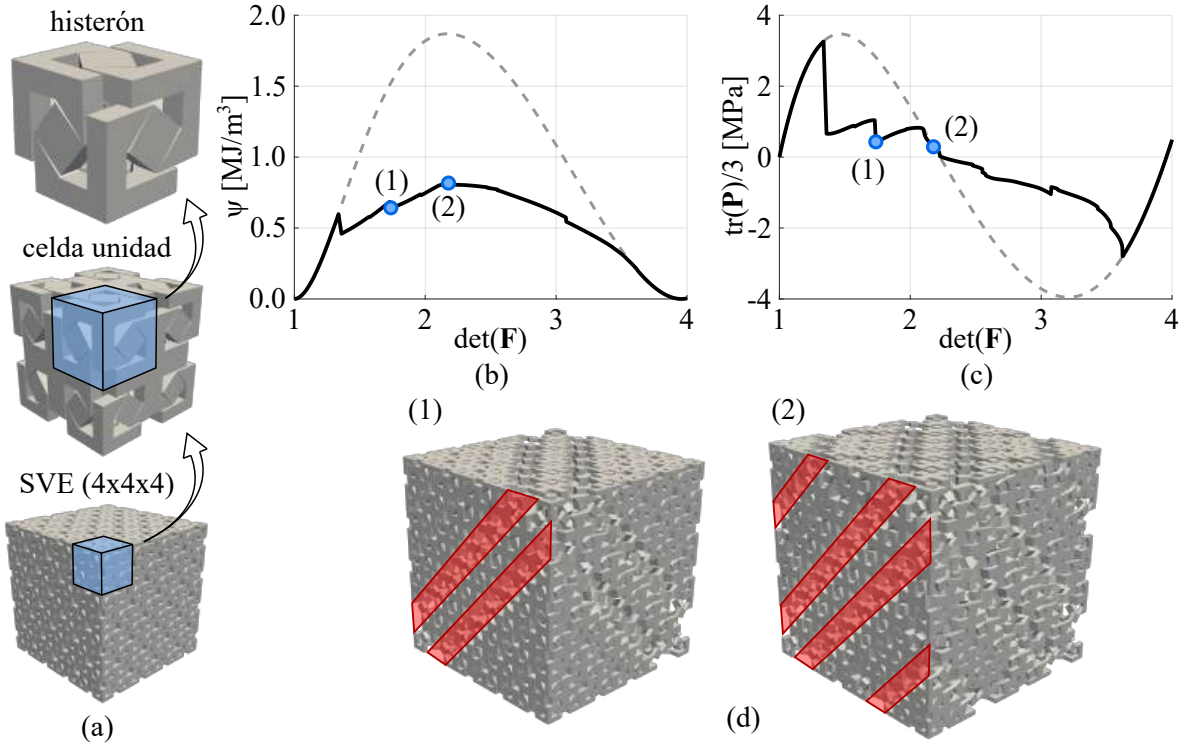


**Figura 6.3:** Respuesta de un SVE compuesto por 4x4x4 celdas unidad. (a) Transición en el ensamblaje desde el histerón hasta el SVE. (b) Relación energía vs. variación volumétrica, y (c) Relación tensión hidrostática vs. variación volumétrica, para un histerón de acuerdo a los módulos materiales y parámetro $a$ elegidos en la Figura 6.2. (d) Formación de patrones de microestructura en forma de láminas.

de manera independiente al histerón contiguo. Mas resultados y un análisis de mayor profundidad serán proximamente incluidos en una nueva publicación.

## 6.5. Conclusiones

En este capítulo se presentan las ideas fundamentales en la concepción de esta tesis respecto al análisis multiescala de metamateriales con transiciones de fase elásticas. Estas nociones fueron volcadas en la última publicación que conforma este texto (Apéndice F), donde se las aplicó al análisis de un metamaterial 1D. Además se presentaron resultados preliminares en el diseño de una microarquitectura novedosa cuya transición de fase está asociada a una deformación volumétrica. Estos resultados muestran un gran acuerdo cualitativo en relación a resulados teóricos establecidos en la literatura.

Como trabajo futuro que no fue posible abordar en esta tesis se puede mencionar:

- Desarrollar un procedimiento numérico orientado al segundo enfoque de relajación tratado en la Sección 6.2.3. Es decir, encontrar el soporte cuasiconvexo de la energía $\psi^0(\boldsymbol{\varepsilon})$ calculada en la expresión (6.9), a partir de la imposición de las ecuaciones de compatibilidad (6.6) analizando sólo una celda unidad. Este procedimiento recuperaría la muy conveniente característica de realizar el estudio multiescala a partir de la mínima información geométrica posible.

- Investigar métodos de relajación de potenciales con más de dos pozos. Esto permitiría formular modelos macroescala de los metamateriales concebidos como redes de histerones discutidos en la Sección 5.5, los cuales presentan más de dos estados preferenciales.

- Profundizar en el estudio de los metamateriales 3D con transiciones de fase. Esto incluye, entre otras cosas, analizar el proceso de formación de microestructura, caracterizar un modelo estándar generalizado (posiblemente en primera instancia a partir de las hipótesis de Kohn [104]), y generalizar la topología a partir de mayor cantidad de parámetros.
- Evaluar la respuesta de cuerpos macroescala, cuya respuesta constitutiva punto a punto esté dada por el modelo estándar generalizado aplicado a materiales con transiciones de fase en la multiescala. Esto acercaría los desarrollos realizados a una situación de uso real.

# Parte IV

# Conclusiones

# Capítulo 7

# Conclusiones

En este capítulo, se resumen las principales contribuciones logradas durante el desarrollo de esta tesis, y se enumeran las publicaciones en revistas indexadas y trabajos en congresos conseguidos. Distintas pautas para trabajos futuros para mejorar o extender los desarrollos conseguidos fueron presentados oportunamente al final de los cuatro capítulos de aportes (Capítulos 3 a 6).

## 7.1. Contribuciones

En esta tesis se desarrollan diversas herramientas y estrategias numéricas que asisten al diseño topológico computacional de metamateriales mecánicos. Todas estas herramientas han sido implementadas en código propio. Dada la naturaleza del comportamiento de los metamateriales en distintas longitudes de escala, las metodologías propuestas se enmarcan en el contexto del análisis multiescala. Para demostrar la validez de estas técnicas se eligen problemas de máxima exigencia para el desempeño en la macroescala o escala de uso del material, lo que se entiende como comportamiento extremo. De manera resumida y de acuerdo con los objetivos particulares planteados en la Sección 1.2.2, se pueden mencionar las siguientes contribuciones.

#### Contribuciones al diseño de metamateriales mediante optimización topológica

Se incorporan principios fundamentales de la física de cristales al diseño de metamateriales por homogeneización inversa. La base de la propuesta es adicionar al algoritmo de optimización topológica el principio de Neumann, que vincula la simetría de la microarquitectura con la simetría de la respuesta efectiva. En este sentido, dada una cierta simetría de la topología en la microescala (a través de un grupo de punto), este principio garantiza una simetría de la respuesta macroescala. Por lo tanto, esto permite asegurar o aproximar la simetría de una respuesta objetivo restringiendo el espacio de búsqueda a topologías con una simetría prestablecida.

Notablemente, la asociación de metamateriales con cristales clarifica varios aspectos del problema de diseño inverso. En primer lugar, se conocen todas las alternativas de grupos de plano o de espacio disponibles a imponer como restricciones a la topología y las simetrías en la respuesta efectiva que cada uno de estos grupos implica, por lo que el problema se vuelve mas sistemático. Además, la elección de un grupo de plano o de espacio trae emparentada una forma de celda unidad, la cual constituye para este problema tanto el RVE del material como el dominio de diseño del problema de optimización topológica. Este dominio es en general asumido cuadrado en la literatura, lo cual limita implícitamente (e incorrectamente) el espacio de búsqueda. Por otra parte, las propiedades racionales de las redes en cristales permiten una correlación entre soluciones 2D y 3D de propiedades efectivas dadas. Por último, desde el punto de vista algorítmico, la imposición de simetrías mejora la robustez y estabilidad del

optimizador, y propicia la obtención de resultados repetitivos que posibilitan la interpretación de mínimos locales.

En esta tesis, esta estrategia se combinó con métodos de optimización basados en una descripción de la topología por una función level-set y el cálculo de sensibilidades a través de la derivada topológica, logrando una estrategia de homogeneización inversa exitosa. Sin embargo, la idea es general, y puede adaptarse a otras técnicas.

Finalmente, un aspecto central de la metodología propuesta es la generalidad para su aplicación en otros problemas, como el diseño de metamateriales con propiedades efectivas térmicas, fotónicas o acústicas. Esto se debe a su sustentación en un principio fundamental, más general que el uso que se le ha dado en esta tesis.

**Contribuciones al problema de G-clausura de compuestos bifásicos isotrópicos de una escala**

Para demostrar el potencial y la eficiacia de la metodología de optimización topológica asistida por simetrías de cristales, la misma se utiliza para el estudio del problema de G-clausura de compuestos bifásicos isotrópicos en el régimen lineal en dos y tres dimensiones. Es decir, se buscan microarquitecturas de una escala que aproximen lo más posible los límites de propiedades efectivas elásticas alcanzables. En 2D el estudio incluye los 5 grupos de plano que aseguran isotropía, mientras que en 3D se consideran 4 de los 36 grupos de espacio que aseguran cubicidad para ejemplificar la operatoria propuesta.

Al considerarse compuestos exclusivamente periódicos, el orden aportado a las topologías por la imposición de simetrías tiene un rol preponderante. Se demuestra que las propiedades alcanzables y la simpleza de las microarquitecturas logradas mediante esta estrategia dependen fuertemente de las simetrías impuestas, denotando que la simetría adecuada para realizar un material extremo depende de la propiedad específica buscada, o de manera equivalente, la región de los límites de propiedades analíticas realizables que se plantea como objetivo del problema de optimización.

Se lograron obtener microarquitecturas cuyas respuestas efectivas cubren todos los comportamientos isotrópicos posibles, incluyendo alta rigidez, bajo módulo de corte y auxeticidad. Tanto en 2D como en 3D, metamateriales de alto módulo de compresibilidad se benefician de grupos de alta simetría. En el caso 3D, las microarquitecturas encontradas para esta propiedad tienen la forma de paredes delgadas de la fase mas rígida que encierran “burbujas” de la fase blanda desconectadas entre ellas. Por otra parte, materiales con modos flexibles, ya sea bajo módulo de corte o coeficiente de Poisson negativo, consiguen estos modos flexibles a partir de encuentros finos similares a articulaciones entre sus partes. Una distinción, sin embargo, entre estas respuestas con modos flexibles reside en que módulos de corte bajos son compatibles con altas simetrías pero coeficientes de Poisson negativos son beneficiados por bajas simetrías. En este último punto se observa que la imposición de ejes de rotación favorece la auxeticidad a partir de la generación de chiralidad. Además, para el caso 3D, se observa también una influencia del dominio de diseño (celda unidad) en la aproximación a las características extremas. Este análisis no tiene un paralelismo en 2D ya que todos los grupos de plano estudiados corresponden a la red (y por lo tanto celda) hexagonal.

**Contribuciones al modelado de metamateriales con inestabilidades basados en histerones**

Se presenta una estrategia de modelado para metamateriales con transiciones de fase en la microescala generadas por inestabilidades elásticas. Esta estrategia consiste en la reducción del costo computacional en la simulación de un histerón a partir de un modelo reducido o subrogado.

El histerón estudiado es una viga curva sinusoidal, que presenta inestabilidades del tipo snap-thourgh (y por lo tanto realiza histeresis) en ciclos de carga y descarga. La técnica de reducción se basa en una representación de la configuración de la viga a partir de una base de funciones constituida por los modos de pandeo de la misma viga si fuese inicialmente recta. A partir de esto, se formula un modelo semi-analítico que permite incorporar mecanismos de deformación asimétricos que perjudican el desempeño

del material para disipar energía, logrando una representación fehaciente del comportamiento del histerón. Este modelo se incorpora como relación constitutiva a un elemento finito con cinemática lineal, permitiendo la conformación de redes de histerones con arreglos geométricos arbitrarios.

El ahorro en costo computacional debido a la eficiencia de la metodología permite la simulación de distintos diseños topológicos cuyo SVE incluye un número alto de histerones. La metodología propuesta permite el análisis de características importantes para el comportamiento límite de los metamateriales como la relación fuerza-desplazamiento, relación energía de deformación-desplazamiento, formación de microestructura y evolución de patrones, disipación de energía extrínseca en ciclos de carga y descarga, y la dependencia de todas estas características con la dirección de la carga. Se proponen distintos arreglos de metamateriales del tipo redes de histerones, todos capaces de disipar energía extrínsecamente, siendo, por lo tanto, aptos como disipadores de energía reutilizables.

Se menciona finalmente que la estrategia basada en un modelo subrogado es transparente al mecanismo responsable de la histéresis, siempre que se puedan encontrar una relación entre las fuerzas y desplazamientos generalizadas en el mismo.

**Contribuciones al análisis multiescala de metamateriales con energías de deformación no convexas en la microescala**

Se presenta un marco conceptual para el análisis multiescala de metamateriales con transiciones de fase en la microescala debido a una energía de deformación no convexa. La propuesta concibe el material en la macroescala a partir de un modelo estándar generalizado, definido por dos potenciales: una función de energía libre y un potencial disipativo, donde ambos se obtienen de técnicas de homogeneización o promediado volumétrico de la microescala. El aspecto distintivo surge de que la energía libre se obtiene de la relajación o cuasiconvexificación de la energía de deformación de microescala, mientras que el potencial disipativo es la homogeneización de la liberación de energía extrínseca por parte de un material elástico.

Para la validación de la propuesta, y ante la falta de disponibilidad de métodos de relajación generales en la literatura, se realizan ciertas hipótesis simplificativas que permiten asumir ecuaciones cerradas de energías relajadas. La respuesta del modelo macro se compara con la simulación de la microescala de un metamaterial 1D, logrando un grado de acuerdo cualitativo y cuantitativo muy bueno.

**Contribuciones a la realización de estructuras parametrizadas**

Los aportes relativos a la obtención de microarquitecturas de comportamiento efectivo extremo y definidas por unos pocos parámetros se separan en dos partes, dependiendo al mismo tiempo del problema de estudio y del método de "inspiración" para llegar al diseño final.

En primer lugar se tienen las topologías correspondientes al problema de respuesta elástica lineal extrema. En este caso, las microarquitecturas propuestas se consiguen a partir de la interpretación de los resultados del problema de homogeneización inversa. La imposición de simetrías en la etapa de optimización topológica sirve como un fuerte indicador de mínimos locales recurrentes, que permiten identificar características topológicas clave para lograr el comportamiento deseado. Una de estas características es la inclusión de materiales laminados ortotrópicos en ciertas zonas como una segunda escala. Se presentan cuatro diseños bidimensionales (dos en el cuerpo de esta tesis y dos en una de las publicaciones), concebidos para aproximar un abanico de propiedades efectivas a partir de la modificación de los valores de los parámetros. Todos los diseños respetan el grupo de plano al cual pertenecen para toda combinación de parámetros, lo cual garantiza la simetría de la respuesta. Para los dos materiales de mejor desempeño, se realiza una optimización multi-objetivo que permite encontrar el conjunto de parámetros óptimos si se plantea como objetivo lograr comportamiento extremo.

En segundo lugar se propone una topología correspondiente al problema de funciones de energías de deformación no convexas en materiales elásticos. El objetivo es generar un material cuya energía de

microescala cuente únicamente con dos pozos, y que los mismos estén separados por una deformación esférica. Al no contar con un algortimo de optimización topológica robusto, la microarquitectura surge de la interpretación de los distintos mecanismos inestables existentes en la literatura. Se utilizan las simetrías de cristales como factor de orden en la topología generada. El material se encuentra aún en proceso de estudio, aunque resultados preliminares indican que logra satisfactoriamente inestabilidades ante expansiones volumétricas.

## 7.2. Publicaciones científicas

### 7.2.1. Publicaciones en revistas

- **Rossi, N.**, Romero, I., and Huespe, A. E (2024). "On the limit behavior of lattice-type metamaterials with bi-stable mechanisms". *International Journal of Mechanical Sciences*, 276, 109375.
- **Rossi, N.**, Méndez, C. G., and Huespe, A. E. (2023). "Surrogate model for a mechanical metamaterial undergoing microstructure instabilities and phase transformations". *International Journal of Mechanical Sciences*, 243, 107913.
- **Rossi, N.**, Podestá, J. M., Bre, F., Méndez, C. G., and Huespe, A. E. (2021). "A microarchitecture design methodology to achieve extreme isotropic elastic properties of composites based on crystal symmetries". *Structural and Multidisciplinary Optimization*, 63(5), 2459-2472.
- **Rossi, N.**, Yera, R., Méndez, C. G., Toro, S., and Huespe, A. E. (2020). "Numerical technique for the 3D microarchitecture design of elastic composites inspired by crystal symmetries". *Computer Methods in Applied Mechanics and Engineering*, 359, 112760.
- Yera, R., **Rossi, N.**, Méndez, C. G., and Huespe, A. E. (2020). "Topology design of 2D and 3D elastic material microarchitectures with crystal symmetries displaying isotropic properties close to their theoretical limits". *Applied Materials Today*, 18, 100456.

### 7.2.2. Publicaciones y presentaciones en congresos

- **Rossi, N.**, and Huespe, A.E. (2023). "Study of the limit behavior of mechanical metamaterials with elastic phase transitions". *MECOM 2023 - XXXIX Congreso Argentino de Mecánica Computacional - I Congreso Argentino Uruguayo de Mecánica Computacional.* Sesión: Modelado multiescala de la mecánica y la física de materiales complejos. Concordia, Argentina - Salto, Uruguay.
- Podestá, J. M., **Rossi, N.**, and Huespe, A.E. (2023). "Design of elastic metamaterials with volumetric phase transitions". *MECOM 2023 - XXXIX Congreso Argentino de Mecánica Computacional - I Congreso Argentino Uruguayo de Mecánica Computacional.* Sesión: Modelado multiescala de la mecánica y la física de materiales complejos. Concordia, Argentina - Salto, Uruguay.
- **Rossi, N.**, Mendez, C., and Huespe, A.E. (2022). "Análisis de Metamateriales Mecánicos con Transiciones de Fase Mediante un Modelo Simplificado". *MECOM 2022 - XXXVIII Congreso Argentino de Mecánica Computacional.* Sesión: Modelado multiescala de la mecánica y la física de materiales complejos. Bahía Blanca, Argentina.
- **Rossi, N.**, Mendez, C., and Huespe, A.E. (2022). "A new efficient methodology for the analysis of mechanical metamaterials with elastic instabilities". *En: WCCM-APCOM2022.* https://www.scipedia.com/public/Rossi_et_al_2022b. Yokohama, Japón.
- **Rossi, N.**, and Huespe, A.E. (2021). "Topology Optimization of Metamaterials which Dissipate Energy Elastically". *MECOM 2021 - XXXVII Congreso Argentino de Mecánica Computacional.*

Sesión: Modelado multiescala de la mecánica y la física de materiales complejos. Resistencia, Argentina.

- Yera, R., **Rossi, N.**, Forzani, L., Méndez, C. G., and Huespe, A.E. (2020). "Topological design of metamaterials with crystal symmetries for acoustic and mechanical applications". *14th World Congress on Computational Mechanics (WCCM) - ECCOMAS Congress 2020* Sesión: Multiscale and Multiphysics Systems. Mini-simposio: Computational multi-Scale modeling and design of new engineering materials. Paris, Francia.

- **Rossi Cabral, N. O.**, Yera Moreno, R., Méndez, C. G., and Huespe, A.E. (2019). "Use of crystallographic symmetries for topology design of extreme isotropic elastic metamaterials". *ENIEF 2019 - XXIV Congreso sobre Métodos Numéricos y sus Aplicaciones.* Sesión: Modelado multiescala de materiales. Santa Fe, Argentina.

- Podestá, J. M., **Rossi Cabral, N. O.**, Méndez, C. G., and Huespe, A.E. (2019). "Parametrization of 2D microstructures inspired by topology optimization to attain theoretical limits of elastic properties". *ENIEF 2019 - XXIV Congreso sobre Métodos Numéricos y sus Aplicaciones.* Sesión: Modelado multiescala de materiales. Santa Fe, Argentina.

- Yera, R., **Rossi Cabral, N.**, Toro, S., and Huespe, A.E. (2018). "Análisis de Eficiencia de Técnicas Tipo FEM y FFT para Homogeneización de Materiales". *MECOM 2018 - XII Congreso Argentino de Mecánica Computacional.* Sesión: Modelado multiescala de materiales. Tucumán, Argentina.

# Parte V

# Apéndices

# Apéndices

En el presente apartado se replican las publicaciones producto del trabajo desarrollado para esta Tesis. Los artículos se listan a continuación:

- Apéndice A: Yera, R., **Rossi, N.**, Méndez, C. G., and Huespe, A. E. (2020). "Topology design of 2D and 3D elastic material microarchitectures with crystal symmetries displaying isotropic properties close to their theoretical limits". *Applied Materials Today*, 18, 100456.
- Apéndice B: **Rossi, N.**, Yera, R., Méndez, C. G., Toro, S., and Huespe, A. E. (2020). "Numerical technique for the 3D microarchitecture design of elastic composites inspired by crystal symmetries". *Computer Methods in Applied Mechanics and Engineering*, 359, 112760.
- Apéndice C: **Rossi, N.**, Podestá, J. M., Bre, F., Méndez, C. G., and Huespe, A. E. (2021). "A micro-architecture design methodology to achieve extreme isotropic elastic properties of composites based on crystal symmetries". *Structural and Multidisciplinary Optimization*, 63(5), 2459-2472.
- Apéndice D: **Rossi, N.**, Mendez, C., and Huespe, A.E. (2022). "A new efficient methodology for the analysis of mechanical metamaterials with elastic instabilities". *En: WCCM-APCOM2022*. https://www.scipedia.com/public/Rossi_et_al_2022b. Yokohama, Japón.
- Apéndice E: **Rossi, N.**, Méndez, C. G., and Huespe, A. E. (2023). "Surrogate model for a mechanical metamaterial undergoing microstructure instabilities and phase transformations". *International Journal of Mechanical Sciences*, 243, 107913.
- Apéndice F: **Rossi, N.**, Romero, I., and Huespe, A. E (2024). "On the limit behavior of lattice-type metamaterials with bi-stable mechanisms". *International Journal of Mechanical Sciences*, 276, 109375.

El tesista declara haber participado activamente en el desarrollo de los nuevos conceptos aportados y llevado a cabo los experimentos numéricos necesarios para alcanzar los resultados que se exponen. Estas tareas fueron supervisadas por el Dr. Alfredo E. Huespe y el Dr. Pablo J. Sánchez, y realizadas en conjunto con los co-autores de cada artículo. Los abajo firmantes avalan esta declaración.

Dr. Alfredo E. Huespe
Director de Tesis

Dr. Pablo J. Sánchez
Codirector de Tesis

# Apéndice A

# Topology design of 2D and 3D elastic material microarchitectures with crystal symmetries displaying isotropic properties close to their theoretical limits

Yera, R., Rossi, N., Méndez, C. G., and Huespe, A. E. (2020). "Topology design of 2D and 3D elastic material microarchitectures with crystal symmetries displaying isotropic properties close to their theoretical limits". *Applied Materials Today*, 18, 100456.

# Topology design of 2D and 3D elastic material microarchitectures with crystal symmetries displaying isotropic properties close to their theoretical limits

**R. Yera[1], N. Rossi[1], C.G. Méndez[1], A.E. Huespe[1,2]1**

[1]CIMEC-UNL-CONICET, Predio Conicet "Dr Alberto Cassano", CP 3000 Santa Fe, Argentina
[2]E.T.S d'Enginyers de Camins, Canals i Ports, Technical University of Catalonia (Barcelona Tech) Campus Nord UPC, Mòdul C-1, c/ Jordi Girona 1-3, 08034, Barcelona, Spain

**Keywords:**Three and two-dimensional (3D and 2D) microarchitecture designs; extreme isotropic elastic properties; crystal symmetries; topology optimization; inverse homogenization technique.

**Abstract.** This paper evaluates the effect that different imposed crystal symmetries have on the topology design of two-phase isotropic elastic composites ruled by the target of attaining extreme theoretical properties. Extreme properties are defined by the Cherkaev-Gibiansky bounds, for 2D cases, or the Hashin-Shtrikman bounds, for 3D cases.

The topology design methodology used in this study is an inverse homogenization technique which is mathematically formulated as a topology optimization problem. The crystal symmetry is imposed on the material configuration within a predefined design domain, which is taken as the primitive cell of the underlying Bravais lattice of the crystal system studied in each case.

The influence of imposing crystal symmetries to the microstructure topologies is evaluated by testing five plane groups of the hexagonal crystal system for 2D problems and four space groups of the cubic crystal systems for 3D problems.

A discussion about the adequacy of the tested plane or space groups to attain elastic properties close to the theoretical bounds are presented. The extracted conclusions could be meaningful for more general classes of topology design problems in the thermal, phononic or photonic fields.

## A.1. Introduction

The notable increase in the use of additive manufacturing techniques for processing complex material microstructures opens the possibility of realizing materials designed for given targets ([3]). In line with this problem, we present a topology design methodology for two and three-dimensional (2D and 3D) two-phase periodic microarchitectures ruled by the objective of attaining extreme isotropic elastic properties[2]. The crucial point in this contribution is the imposition of crystal symmetries to the designed topologies, which has to be considered as a guiding principle in the context of the adopted methodology.

The design methodology that we follow is based on a well-established mathematical tool, an inverse homogenization technique formulated as a topology optimization problem, supplemented with the necessary geometrical constraints to get the required symmetries copying that of a predefined crystal. Then, using this approach, we study the effects induced by the imposition of different space groups onto the accomplishment of the problem targets.

The study of crystal symmetries and the related mathematical method, i.e., the group theory, is one of the most fundamental topics in crystallography, particularly in crystal physics. Thus, the general concepts associated with the crystal symmetry properties, the notions of point, plane and space groups, as well as

[1]Corresponding author. E-mail address: ahuespe@cimec.unl.edu.ar (A.E. Huespe).

[2]The concept of extreme material has been coined by Milton y Cherkaev [70]. They give this name to materials which elasticity tensors have some eigenvalues very large and the remaining ones are very small. Here, following to Sigmund [67], we use this concept in a slightly broader sense, including all those isotropic composites whose effective properties attain extreme bulk and shear modulus.

the symmetry classification which are necessary to develop this work, are taken from the International Tables for Crystallography, see [108]. Additional references are the books by Vainshtein [55] and Sólyom [109].

The space groups of 3D periodic arrangements of crystals characterize their symmetry properties. Symmetry elements of these space groups are constituted by rotation axes, mirror-reflection planes, inversion-rotation axes, glide-reflection planes, and screw axes. The point groups are the nexus, via the Neuman's theorem, between the symmetry of the microstructure topology, defined by the crystal space group, and the symmetry of the macroscopic effective physical properties, see Nye [54]. This concept is the cornerstone of the present approach.

Inverse homogenization techniques for topology designs are well-established in the literature. In this sense, the work pioneered by Sigmund [62], the numerous posterior contributions of this author and coworkers, as well as the huge number of papers addressed to this topic (see for example Torquato [110] and Osanov y Guest [111]), are a clear indication of the power of this technique to obtain new microarchitecture topologies which are hard to be imagined if using ad-hoc design methodologies, see, in particular, the brief discussion by Milton [112]. Inverse homogenization techniques can be formulated as a mathematical topology optimization problem posed in a spatial domain $\Omega_\mu$. Their solutions provide the optimal topologies, or spatial material layouts, satisfying the proposed targets. An overview of these techniques for different problems can be found in the book by Bendsoe y Sigmund [29].

We closely follow the works of Sigmund [67] and Andreassen y Lazarov [113], where, 3D (2D) microarchitecture design problems aiming at obtaining extreme composites using inverse homogenization techniques have been reported. Here, we solve the topology optimization algorithm with the necessary geometrical constraints to impose a space (plane) group to the obtained material layout. The space (plane) group is defined apriori according to the symmetry of the target effective elastic response.

The implementation of this approach has required the development of a particular numerical treatment for handling the high computational cost demanded by 3D microstructure designs. Nevertheless, we leave for a forthcoming paper a detailed description of the numerical aspects of the methodology. It is notably to remark here that the topology optimization algorithm is solved with a spatial filter to avoid the occurrence of thin microstructures. Therefore, the attained topologies have only one length scale. The authors have previously reported some studies performed with this methodology for 2D problems in Podestá et al. [114] and Podestá et al. [65] and 3D problems in Méndez et al. [115].

In this paper, initially and after a summary of the concepts on which this work is based on, we evaluate in Section A.3 several plane groups to design 2D microarchitectures aiming at obtaining extreme elastic properties. The material isotropy is guaranteed by taking plane groups of the hexagonal crystal system. Subsequently, in Section A.4, we perform a similar analysis for 3D problems. In these cases, the isotropic elastic response cannot be guaranteed by any space group[3]. Thus, we test four space groups with the highest and the lowest symmetries of the cubic crystal system, adding one isotropy constraint to the topology optimization problem. The 2D and 3D material configurations obtained with different plane and space groups are compared and discussed. Finally, the conclusions are presented.

Some representative 3D microstructures designed with this methodology are available as supplementary material in the dataset Yera et al. [116]. These microarchitectures are stored in .stl format and are ready for 3D printing.

[3]It is worth to remark that, when topologies with multiple length scales are allowed, the crystal symmetry does not matter for attaining isotropic effective responses, such as happens in randomly textured polycrystals with isotropic macroscopic response. However, the important point here is that topologies implying multiple length scales are not so practical and their consideration enlarges the design space which makes the optimization more difficult.

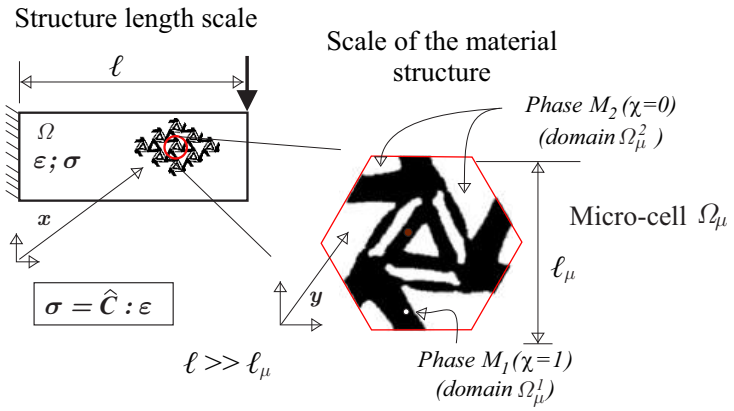


**Figura A.1:** Topology optimization problem. Cell $\Omega_\mu$ of the microstructured composite with phases $M_1$ and $M_2$ and the characteristic function $\chi$. At the macrostructural scale, the effective elastic properties of the composite are represented by the homogenized constitutive elasticity tensor $\hat{\mathbf{C}}$.

## A.2. Inverse material design problem

We design microstructures of periodic composites constituted by two isotropic phases, $M_1$ and $M_2$, and a given volume fraction $f_1$ of $M_1$. Two well-separated scales of lengths are assumed, see Figure A.1; the structure length scale, $\ell$, and the microstructural length scale $\ell_\mu$ in where the geometrical configuration of the phase distribution is defined. Thus, it is satisfied that $\ell \gg \ell_\mu$. The effective material properties are evaluated at the structural scale.

The composite has to display the closest effective isotropic elastic properties to its theoretically estimated bounds. In particular, for the here studied cases in 2D problems, these bound have been reported by Cherkaev y Gibiansky [51], and for 3D problems, they have been reported by Hashin y Shtrikman [22]. The elastic properties of the component phases are chosen to allow for effective properties with negative Poisson's ratios. Thus, the design of isotropic auxetic materials is an additional challenge addressed for some extreme target conditions.

In this Section, and after defining the theoretical bounds reported in the literature, we describe the optimization problems that are formulated to attain the closest properties to these bounds.

### A.2.1. Analytical bounds of two-phase composites with effective isotropic elasticity

The bounds described in this Section for the effective bulk and shear moduli, $\hat{\kappa}$ and $\hat{G}$, respectively[4], of isotropic two-phase composites, are valid for well-ordered composites, i.e. $\kappa_2 < \kappa_1$ and $G_2 < G_1$, where $\kappa_1$ and $G_1$ are the bulk and shear moduli of the stiff phase, $M_1$, and $\kappa_2$ and $G_2$ are the bulk and shear moduli of the soft phase, $M_2$. These bounds are next defined in the space $(\hat{K}, \hat{G})$ for 2D problems[5] and $(\hat{\kappa}, \hat{G})$ for 3D problems.

**Plane strain problems.** According to the analysis of Cherkaev et al., the effective moduli of an isotropic composite constituted by the phase $M_1$, with bulk modulus[6] $K_1 = 5/7$, shear modulus $G_1 = 5/13$ and volume fraction $f_1 = 0.5$, and the phase $M_2$, with bulk modulus $K_2 = K_1/200$ and shear modulus $G_2 = G_1/200$; can be bounded in the space $(\hat{K}, \hat{G})$ with an upper coupled bound defined by the curve:

[4]The symbol $\hat{(\cdot)}$ denotes an effective value of the elastic property.

[5]The plane strain modulus $K$ is given by $K = \kappa + G/3$, where $\kappa$ and $G$ are the conventional bulk and shear moduli of the three-dimensional theory. The elastic constant in the plane strain $\nu_p = \nu/(1-\nu)$, where $\nu$ is the conventional 3D Poisson's ratio and $-1 \leq \nu_p \leq 1$, is here taken as the plane strain Poisson's ratio. The parameter $K$ is known as the Kolosov constant. For additional details about the connection between the 2D and 3D elastic constants we reference the work by Thorpe y Jasiuk [117].

[6]Stifnesses and lengths are defined in arbitrary units.

$$\hat{G}^u(\hat{K}) = \frac{\omega^u(f_1G_1 + f_2G_2) + G_1G_2}{G_2f_1 + G_1f_2 + \omega^u} \quad ; \quad \omega^u = -G_1 + \frac{\alpha^u y_K}{\beta^u y_K - \gamma^u}; \tag{A.1}$$

and a lower coupled bound, defined by the curve:

$$\hat{G}^l(\hat{K}) = \frac{\omega^l(f_1G_1 + f_2G_2) + G_1G_2}{f_1G_2 + f_2G_1 + \omega^l} \quad ; \quad \omega^l = -G_1 + \frac{\alpha^l(\frac{1}{y_K} + \frac{1}{K_1})}{\beta^l(\frac{1}{y_K} + \frac{1}{K_1}) - \gamma^l}; \tag{A.2}$$

where

$$y_K = -K_1K_2 \frac{\hat{K} - \frac{1}{(\frac{f_1}{K_1} + \frac{f_2}{K_2})}}{\hat{K} - (f_1K_1 + f_2K_2)} \left(\frac{f_1}{K_1} + \frac{f_2}{K_2}\right); \tag{A.3}$$

The coefficient in (A.1)–(A.2) are: $\alpha^l = 0.4107$, $\beta^l = 1.0653$, $\gamma^l = 0.0110$, $\alpha^u = -0.1256$, $\beta^u = -0.2200$ and $\gamma^u = 2.0 \times 10^{-4}$.

The curves $(\hat{K}, \hat{G}^u)$ and $(\hat{K}, \hat{G}^l)$ are plotted in Figure A.2-a and, in the following, are denoted CG-bounds.

**Three-dimensional problems.** The best known bounds at the present time for 3D composites, when one phase is void, are the Hashin-Shtrikman bounds (denoted HS-bounds in the following) which are given by the expressions:

$$\hat{\kappa}^u = \kappa_1 + \frac{1 - f_1}{\frac{1}{\kappa_2 - \kappa_1} + 3\frac{f_1}{3\kappa_1 + 4G_1}} \quad ; \quad \hat{\kappa}^l = \kappa_2 + \frac{f_1}{\frac{1}{\kappa_1 - \kappa_2} + 3\frac{1-f_1}{3\kappa_2 + 4G_2}} \; ; \tag{A.4}$$

$$\hat{G}^u = G_1 + \frac{1 - f_1}{\frac{1}{G_2 - G_1} + \frac{6(\kappa_1 + 2G_1)f_1}{5G_1(3\kappa_1 + 4G_1)}} \quad ; \quad \hat{G}^l = G_2 + \frac{f_1}{\frac{1}{G_1 - G_2} + \frac{6(\kappa_2 + 2G_2)(1-f_1)}{5G_2(3\kappa_2 + 4G_2)}} \; .$$

By following to Andreassen y Lazarov [113], we adopt $\kappa_1 = 1.667$, $G_1 = 0.3571$, $\kappa_2 = \gamma\kappa_1$, $G_2 = \gamma G_1$, with the contrast factor $\gamma = 10^{-4}$, and the volume fraction $f_1 = 0.338$. For these composites, the HS-bounds are: $\hat{\kappa}^u = 0.170$; $\hat{\kappa}^l = 2.8 \times 10^{-4}$; $\hat{G}^u = 0.789$; $\hat{G}^l = 7.3 \times 10^{-5}$ and are plotted in Figure A.2-b, in the space $(\hat{\kappa}, \hat{G})$.

**Remark:** in two-dimensions the Cherkaev-Gibiansky bounds degenerate to the Hashin-Shtrikman bounds in the limit in which one phase is void. This is similar to the way the Berryman-Milton-Phan-Thien bounds degenerate in three dimensions to the Hashin-Shtrikman bounds, see Berryman y Milton [52] and references cited therein.

### A.2.2. Topology optimization problem

Let us consider a basic micro-cell, identified by $\Omega_\mu$, of the two-phase composite. The phases $M_1$ and $M_2$ occupy the domains $\Omega_\mu^1$ and $\Omega_\mu^2$, respectively, see Figure A.1.

In $\Omega_\mu$, we define a characteristic function $\chi(\boldsymbol{y})$ identifying the positions where the phase $M_1$ is placed. It is defined by:

$$\chi(\boldsymbol{y}) = \begin{cases} 0 & \forall \boldsymbol{y} \in \Omega_\mu^2 \\ 1 & \forall \boldsymbol{y} \in \Omega_\mu^1 \end{cases} \; . \tag{A.5}$$

The homogenized elasticity tensor of the composite, $\hat{\mathbf{C}}$, depends on the geometrical configuration of the phases $M_1$ and $M_2$ in $\Omega_\mu$. We make explicit this dependence by introducing the notation $\hat{\mathbf{C}}(\chi)$. If the effective properties of the composite are isotropic, then, $\hat{\mathbf{C}}$ can be determined accordingly with the effective bulk and shear moduli, denoted $\hat{\kappa}(\chi)$ and $\hat{G}(\chi)$, respectively.

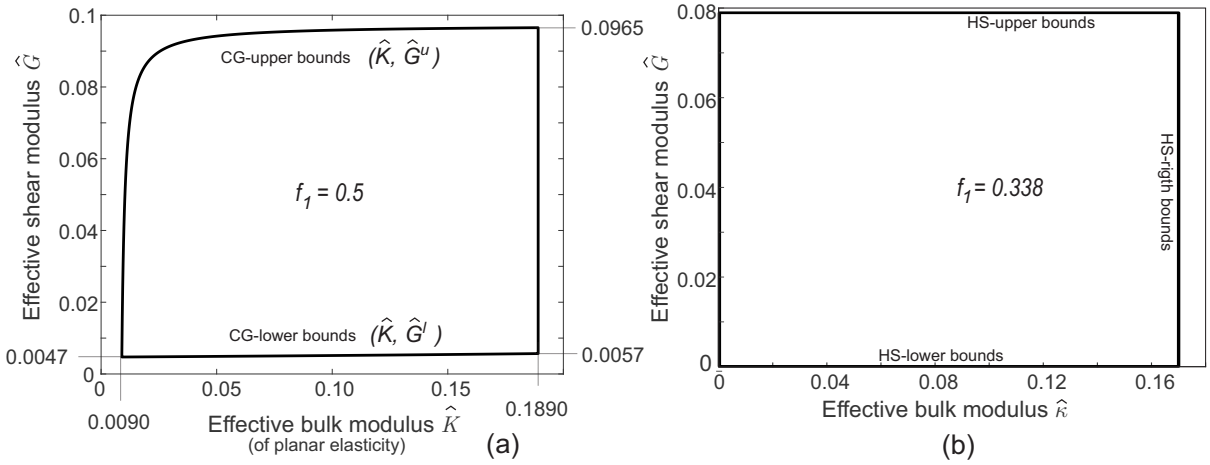


**Figura A.2:** Analytic bounds of effective properties for two-phase isotropic composites. a) Plane elasticity. Bounds according to Cherkaev y Gibiansky [51] (CG-bounds). Properties of phases $M_1$ and $M_2$ are $K_1 = 5/7$; $K_2 = K_1/200$; $G_1 = 5/13$; $G_2 = G_1/200$. Volume fraction of phase $M_1$ is $f_1 = 0.5$. b) 3D elasticity bounds according to Hashin y Shtrikman [22] (HS-bounds). Properties of phases $M_1$ and $M_2$ are $\kappa_1 = 1.667$, $G_1 = 0.3571$, $\kappa_2 = \gamma\kappa_1$, $G_2 = \gamma G_1$, contrast factor $\gamma = 10^{-4}$, volume fraction $f_1 = 0.338$.

### Three-dimensional topology optimization problems

The optimal design of microarchitecture topologies whose target effective properties are the points on the lower Hashin-Shtrikman bounds are obtained by solving a set of $n$ discrete topology optimization problems formulated as follows:

$$\begin{aligned} &\min_{\chi} \ \hat{G}(\chi); \\ &\text{such that:} \quad \hat{\kappa}(\chi) - \kappa_j^* = 0 \\ &\qquad\qquad \hat{\mathbf{C}}(\chi) \text{ is isotropic} \\ &\qquad\qquad f_1(\chi) - f_1^* = 0 \end{aligned} \tag{A.6}$$

where $\kappa_j^*$ (with $1 \leq j \leq n$) is the $j-$th target bulk modulus of the composite defined whitin the interval $\hat{\kappa}^l \leq \kappa_j^* \leq \hat{\kappa}^u$ and $f_1^*$ is the target volume fraction of phase $M_1$. The problem (A.6) expresses that the minimum of the effective shear modulus, $\hat{G}$, is searched by varying the characteristic function $\chi$ within $\Omega_\mu$.

Similarly, the Hashin-Strikman upper bound is approached by solving the maximum $\hat{G}(\chi)$, with identical constraints of problem (A.6).

Alternatively, the topologies approaching the left Hashin-Strikman bound are sought by solving the problems:

$$\begin{aligned} &\min_{\chi} \ \hat{\kappa}(\chi); \\ &\text{such that:} \quad \hat{G}(\chi) - G_j^* = 0 \\ &\qquad\qquad \hat{\mathbf{C}}(\chi) \text{ is isotropic} \\ &\qquad\qquad f_1(\chi) - f_1^* = 0 \end{aligned} \tag{A.7}$$

where now, the target effective shear modulus $G_j^*$ of the $j-$th optimization problem is chosen from the the interval $\hat{G}^l \leq G_j^* \leq \hat{G}^u$. The extreme composites on the right H-S bound are approached by changing

the minimum problem in (A.7) by one of maximizing the effective bulk modulus.

In the case that the effective elastic properties have cubic symmetry, situation that is guaranteed by taking a material configuration having a space group consistent with the cubic crystal system, the coefficients $\hat{C}_{ij}$, with $i,j = 1,...,6$, of the elasticity matrix[7] $\hat{\mathbf{C}}$ satisfy the general identities displayed in Table A.2, resulting: $\hat{C}_{11} = \hat{C}_{22} = \hat{C}_{33}$ ; $\hat{C}_{12} = \hat{C}_{13} = \hat{C}_{23}$ ; $\hat{C}_{44} = \hat{C}_{55} = \hat{C}_{66}$. The remaining coefficients of the elasticity matrix are zero. Any tensor $\hat{\mathbf{C}}$ with cubic symmetry is isotropic if additionally its coefficients satisfies:

$$\hat{C}_{11} - \hat{C}_{12} - \hat{C}_{44} = 0\,, \tag{A.8}$$

resulting:

$$\hat{G}^{iso} = \frac{\hat{C}_{44}}{2}\,, \tag{A.9}$$

$$\hat{\kappa}^{iso} = \frac{1}{3}(\hat{C}_{11} + 2\hat{C}_{12})\,, \tag{A.10}$$

where $\hat{\kappa}^{iso}$ and $\hat{G}^{iso}$ are the bulk and shear moduli of the effective elastic isotropic response. In the problems (A.6) and (A.7), the elastic isotropy is imposed by the equation (A.8).

Based on these identities we reformulate the problem (A.6) in terms of the components of $\hat{\mathbf{C}}$ as follows:

$$\begin{aligned} &\min_{\chi}\ \hat{C}_{44}, \\ &\text{such that:} \quad \hat{C}_{11} + 2\hat{C}_{12} - 3\kappa_j^* = 0\,, \\ &\qquad\qquad\ \ \hat{C}_{11} - \hat{C}_{12} - \hat{C}_{44} = 0\,, \\ &\qquad\qquad\ \ f_1(\chi) - f_1^* = 0\,, \end{aligned} \tag{A.11}$$

and problem (A.7) as follows:

$$\begin{aligned} &\min_{\chi}(\hat{C}_{12} + \frac{1}{3}\hat{C}_{44}), \\ &\text{such that:} \quad (\hat{C}_{11} - \hat{C}_{12} + \frac{3}{2}\hat{C}_{44}) - 5G_j^* = 0\,, \\ &\qquad\qquad\ \ \hat{C}_{11} - \hat{C}_{12} - \hat{C}_{44} = 0\,, \\ &\qquad\qquad\ \ f_1(\chi) - f_1^* = 0\,. \end{aligned} \tag{A.12}$$

The objective function in problem (A.12) results from replacing the isotropy constraint (A.8) in equation (A.10).

**Two-dimensional (plane strain) topology optimization problems**

The optimal design of 2D microstructures whose target is to attain an extreme isotropic material is also performed using a topology optimization algorithm with a slightly different formulation to those stated in (A.6) or (A.7). In this case, those problems are formulated without specifically imposing the isotropic elasticity constraint, because this property is guaranteed by enforcing topologies with hexagonal symmetry.

[7] We use Kelvin's notation.

**Tabla A.1:** Hexagonal (2D) Crystal system. Compatible point and plane groups. The elasticity matrix is isotropic and is represented in column 1, with the coefficient $C_{11}$ and $C_{12}$ characterizing the elastic properties.

| Elasticity Matrix | Crystal system | Point group | Plane group | Compatible Bravais lattice | Wigner-Seitz and primitive unit cell |
|---|---|---|---|---|---|
| $\begin{bmatrix} C_{11} & C_{12} & 0 \\ C_{12} & C_{11} & 0 \\ 0 & 0 & C_{11}-C_{12} \end{bmatrix}$ | hexagonal | 3 | p3 | hexagonal | 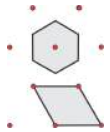 |
| | | 3m | p3m1 | | |
| | | | p31m | | |
| | | 6 | p6 | | |
| | | 6mm | p6mm | | |

### Topology optimization algorithm

The algorithm used for solving the problems (A.11)–(A.12) is based on a level-set method jointly with topological derivative evaluating the sensitivity of response with changes of the characteristic function $\chi$ defined in (A.5). The numerical technique follows the original proposal of Amstutz y Andrä [58] and Amstutz et al. [59]. The topological derivative has been studied by Novotny y Sokołowski [57]. Additional details of this algorithm for solving 3D problems can be found in Méndez et al. [115].

In all cases, the configurations for the algorithm onset are random distributions of the stiff phase in $\Omega_\mu$.

## A.2.3. Use of specific plane group and space group symmetries

We focus only on particular cases of space group symmetries for designing composites with isotropic effective elastic responses.

### Hexagonal crystal system for 2D isotropic material design

The isotropy of 2D elastic properties is guaranteed if the periodic material configuration is compatible with the *hexagonal crystal system* whose main properties are summarized in Table A.1. Thus, the plane groups $p3$, $p3m1$, $p31m$, $p6$, and $p6mm$[8] guarantee the obtention of isotropic effective elastic properties, and therefore, they are the ones tested in this work.

The symmetry elements of these plane groups are depicted in Figure A.3. The underlying Bravais lattice compatible with these plane groups is hexagonal.

### Cubic crystal system for 3D isotropic material design

There are 230 space groups characterizing periodic microstructures in 3D. None of them guarantee an isotropic effective elastic response. Under this circumstance, we study the cubic space groups, which have the highest possible crystal symmetries in 3D. We only focus on the *cubic crystal system* whose Bravais lattices are sc (primitive simple cubic) or bcc (body-centered cubic). A further analysis would include the fcc lattice.

[8] We use the Herrman-Maugin notation to identify point, plane and space groups, see International Tables of Crystallography [108].

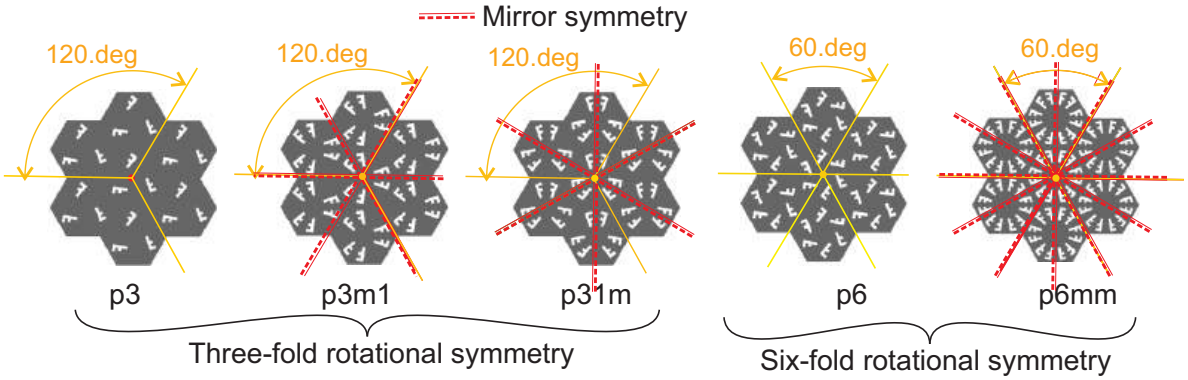


**Figura A.3:** Symmetry elements of plane groups $p3$, $p3m1$, $p31m$, $p6$, $p6mm$. Note that the mirror planes of the $p3m1$ plane group intersect the Voronoi cell differently to that of the $p31m$ plane group.

**Tabla A.2:** Cubic System. Compatible point and space groups. Two Bravais lattices compatible with the cubic systems are sc and bcc. Conventional (or Centered) and Wigner-Seitz cells of the two Bravais lattices. The elasticity matrix in the natural bais is represented in column 1. The symbol "$*-*$" linking two coefficients means that they are equal. Thus, only three coefficients define the elasticity matrix in natural basis. The evaluated point and space groups are denoted in bold.

| Elasticity Tensor | Crystal System | Point Groups | Space Groups | |
|---|---|---|---|---|
| 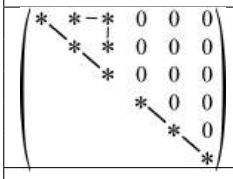 | Cubic | **23** | **P23**, P$2_13$ | **I23,** I$2_13$ |
| | | m$\bar{3}$ | Pm$\bar{3}$, Pn$\bar{3}$, Pa$\bar{3}$ | Im$\bar{3}$, Ia$\bar{3}$ |
| | | 432 | P432, P$4_232$, P$4_332$, P$4_132$ | I432, I$4_132$ |
| | | $\bar{4}$3m | P$\bar{4}$3m, P$\bar{4}$3n | I$\bar{4}$3m, I$\bar{4}$3d |
| | | **m$\bar{3}$m** | **Pm$\bar{3}$m**, Pn$\bar{3}$n, Pm$\bar{3}$n, Pn$\bar{3}$m | **Im$\bar{3}$m**, Ia$\bar{3}$d |
| Compatible Bravais lattice (Conventional cells) | | | 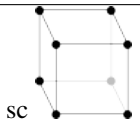 sc | 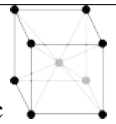 bcc |
| Wigner-Seitz cell | | | 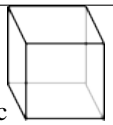 sc | 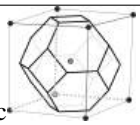 bcc |

Additional details about the *cubic crystal system* are presented in Table A.2. Column 4 of this Table displays all the space groups that are compatible with the sc and bcc lattices. Point and space groups being compatible are described in identical lines of columns 3 and 4. It can be guaranteed that the effective elasticity properties of any composite whose material layout has a symmetry compatible with a point group listed in column 3 satisfy cubic symmetry, and therefore, the corresponding elastic matrix coefficients, expressed in natural basis, should satisfy the identities shown in column 1. In the last two rows of Table A.2, we show the Conventional and Wigner-Seitz (Voronoi) cells of both lattices which are here studied[9]. Primitive cells of this lattice are shown in Figure A.4. The primitive and the conventional unit cells are identical for the sc lattice and different for the bcc lattice.

We only analyze the design of topologies with space groups $P23$, $I23$, $Pm\bar{3}m$ and $Im\bar{3}m$. Some of the symmetry elements of these space groups are shown in Figure A.5.

The space groups $P23$ and $I23$ have fewer symmetry elements than the $Pm\bar{3}m$ and $Im\bar{3}m$ cases. The first ones can be considered as the space groups with the lowest symmetries and the second ones with the highest of the *cubic crystal system*. Also, the space groups $P23$ and $Pm3m$ are compatible with

[9]In this work, three types of unit cells are mentioned and used: *i)* Wigner-Seitz (or Voronoi) unit cells; *ii)* primitive unit cells defined by the primitive vectors of the lattice and *iii)* the conventional cells whose faces are planes parallel to the coordinate planes. Voronoi and primitive cells have minimum volume, while conventional cells, in general, do not have minimum volume

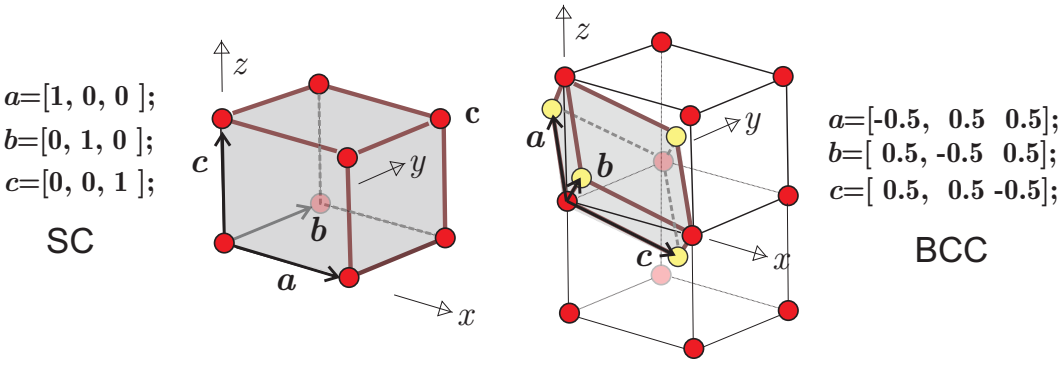


**Figura A.4:** Primitive cells of cubic Bravais lattices of sc and bcc lattices are defined by the primitive vectors $\boldsymbol{a}, \boldsymbol{b}, \boldsymbol{c}$. The volumes of the primitive unit cells are $V_{sc} = 1$, $V_{bcc} = 0.5$. Conventional cells are defined in both cases by the vectors $(1, 0, 0)$, $(0, 1, 0)$ and $(0, 0, 1)$.

an sc Bravais lattice, while the $I23$ and $Im\bar{3}m$ are compatible with a bcc Bravais lattice. Note further that the space group $I23$ has two-fold screw axes which provide higher symmetry properties than that of the space group $P23$. As will be observed in the following, this higher symmetry of the $I23$ space group affects the capacity for obtaining some minimal/maximal properties close to the extreme materials.

The objective here is to make a comparative analysis of the topologies obtained using both extreme cases of symmetries, with point groups 23 and $m\bar{3}m$, and two different Bravais lattices, sc and bcc.

### A.2.4. Technique for solving the inverse design problem

Significant issues for solving the topology optimization algorithm summarized in sub-Section A.2.2 are next remarked.

*i)* **Selection of the design domain $\Omega_\mu$:** following to Podestá et al. [65], $\Omega_\mu$ is taken as the primitive cell of a Bravais lattice having a point group symmetry compatible with the target elastic properties. This lattice is identified as the underlying Bravais lattice of the composite. For 2D problems, the hexagonal Bravais lattice is taken, and the corresponding primitive cell is the parallelogram depicted in Figure A.6. In 3D problems, the domain $\Omega_\mu$ coincides with the primitive cell of the underlying Bravais lattice[10]. The primitive cells of SP and bcc lattices are shown in Figure A.4.

*ii)* **Computational homogenization:** the effective properties of the composite are evaluated using a base cell coinciding with $\Omega_\mu$. Periodic conditions of the material layout, by repeating the pattern defined by this base cell, are coincident with the primitive directions of the underlying Bravais lattice. Thus, periodic boundary conditions of the displacement fluctuations compatible with this criterion are imposed on the base cell.

In 3D problems, the homogenization of the effective properties is computed with an FFT (Fast Fourier Transform) technique[11].

*iii)* **Implementation of the space group symmetry:** the symmetry of the microarchitecture topology agreeing with a pre-established space group is imposed in two steps. The first step consists of

[10] Selecting the primitive unit cell of the Bravais lattice instead of the conventional cell means that the design domain would represent the minimum possible volume of the composite which tesselation reproduce the periodic microstructure. Then, for identical microstructures, the minimum volume of $\Omega_\mu$, instead of using a conventional cell, implies to search for a simpler material configuration.

[11] The FFT technique for homogenization implemented in this work has been taken from Eyre y Milton [119]. In 2D, this step of the inverse homogenization problem is computed with a Finite Element technique. Additional details of the numerical aspects of this technique are addressed in Rossi et al. [61].

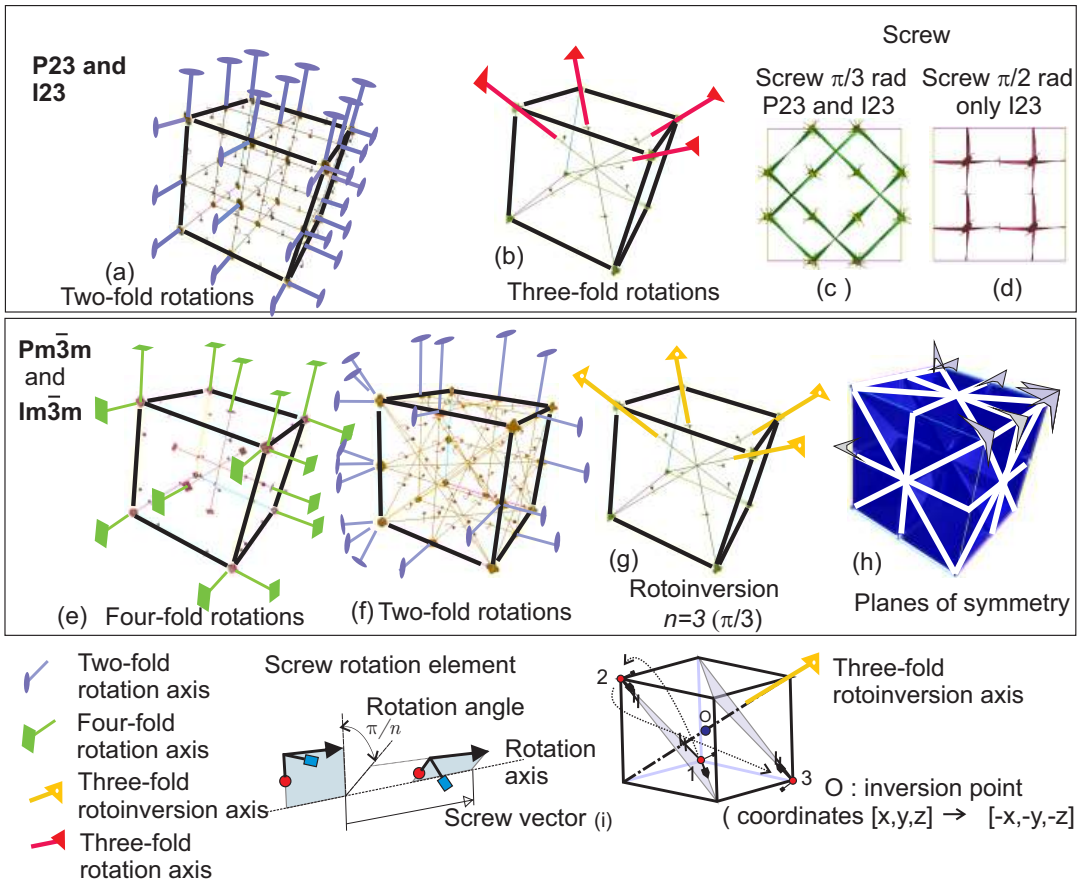


**Figura A.5:** (a) to (h) Symmetry elements in conventional sc and bcc cells, of the space groups $P23$, $I23$, $Pm\bar{3}m$ and $Im\bar{3}m3$. Glide and screw elements of space groups $Pm\bar{3}m$ and $Im\bar{3}m3$ are not shown. c) and d) orthogarphic view of screw elements of space groups $P23$ and $I23$. i) representation of the screw rotation and rotoinversion symmetry elements. The symmetry elements of space groups can be interactively visualized with the software *"Space Group Visualizer"* described in [118].

defining a set of points in the primitive cell, known as the asymmetric unit domain[12], and then to find their image points. The asymmetric domain is the reduced volume of the primitive cell which can be replicated by applying the symmetry operations of the space group to obtain the full primitive cell configuration. Therefore, the asymmetric unit contains the complete information necessary for the description of the crystal structure. In Figure A.6, we depict the plane group consistent with the *hexagonal crystal system* and the asymmetric unit domains in red. In different colors are depicted the image points. The asymmetric unit domains, as well as the image points of the conventional cells for all plane and space groups, are defined in the International Tables for Crystallography ([108]).

## A.3. Design of 2-D isotropic materials

The attainment of a 2D microstructure with isotropic effective elastic response is strictly guaranteed[13] by imposing the following plane groups $p3$, $p3m1$, $p31m$, $p6$ and $p6mm$ which are ordered from the lowest to the highest symmetries. We take a primitive unit cell of the hexagonal Bravais lattice to solve the topology optimization algorithm.

[12] See point 2.1.3.8 in[108]

[13] The effective elasticity tensor of all the 2D microarchitectures displayed in this Section are exactly isotropic until the machine precision.

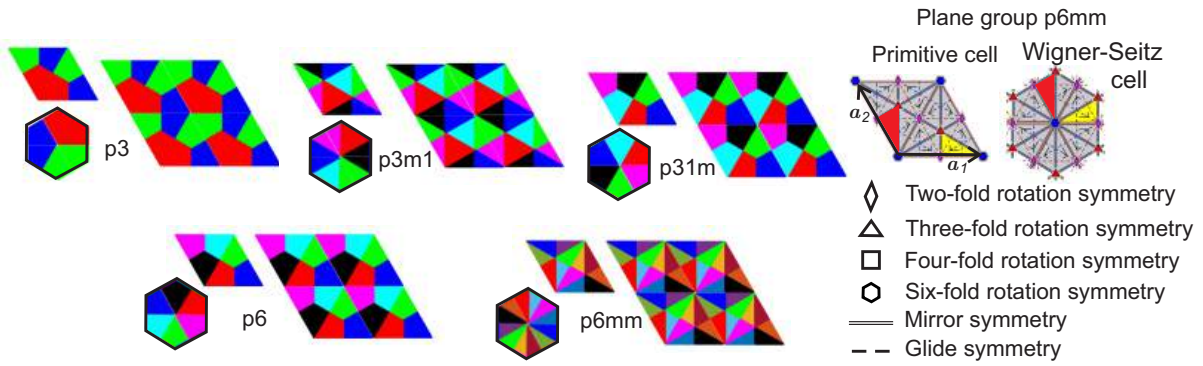


**Figura A.6:** Five plane groups of the *hexagonal crystal system*. Asymmetric units in red and their image points. The asymmetric unit domain is easily distinguished in the Wigner-Seitz cell but hardly recognized in primitive cells. Symbols used for identifying the symmetry elements in plane groups.

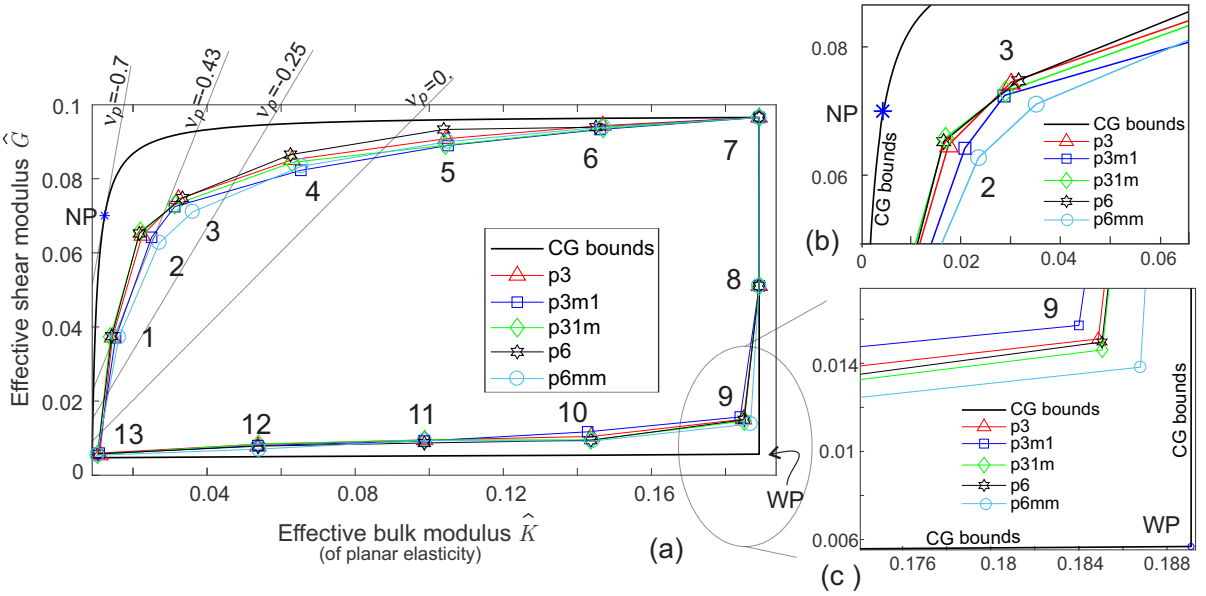


**Figura A.7:** Two-dimensional design of extreme isotropic microstructures: a) Cherkaev y Gibiansky [51] bounds (CG-bounds)) and best solutions obtained with plane groups $p3$, $p3m1$, $p31m$, $p6$ and $p6mm$; b) zoom of the region near to the most negative Poisson's ratio (Point NP) of the CG-bounds: c) zoom of the region near to the Walpole Point (Point WP).

The designs of materials whose properties are close to the bounds, for two-phase composites defined in Section A.2.1, are studied for 13 different target conditions identified by the corresponding points in the space ($\hat{K}$,$\hat{G}$) depicted in Figure A.7-a. The bounds reported by Cherkaev et al. are displayed again in the Figure, as well as some isolines of negative Poisson's ratios. The Point NP marks the elastic properties with the most negative Poisson's ratio estimated with the CG-bounds.

### A.3.1. Discussion of results

After evaluating these solutions, the following discussion can be addressed.

**1)** The enforcement of a plane group with the highest symmetry ($p6mm$) is the most adequate to attain microarchitectures with elastic properties close to the region with low shear and high bulk moduli, i.e., near the Walpole Point (Point WP in Figure A.7-a and c);

**2)** The enforcement of a plane groups with a hexagonal Bravais lattice and only few symmetry elements guaranteeing isotropy ($p3$, $p31m$ and $p6$) are useful to attain elastic properties close to the

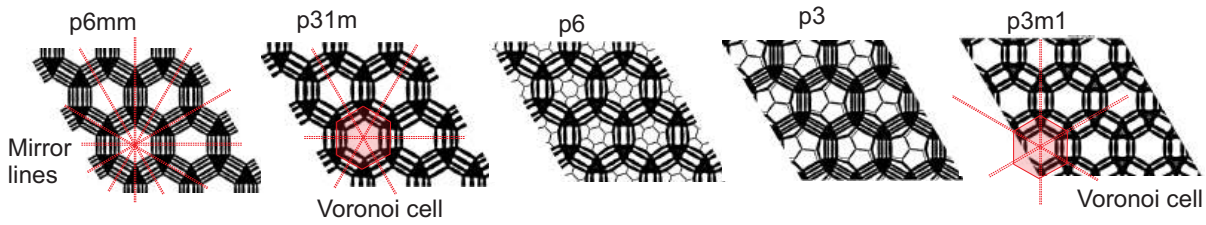


**Figura A.8:** Two-dimensional design of extreme isotropic microstructures: Walpole Point WP in Figure A.7-a and c. Topologies obtained with plane groups $p6mm$, $p31m$, $p6$, $p3$, $p3m1$. Mirror lines and Voronoi cells.

bounds in the region with high shear and low bulk moduli, near the points with negative Poissonś ratios denoted NP in Figure A.7-a and b;

**3)** There are no substantial differences by using plane groups with high or low symmetries for capturing extreme materials close to the other two vertices defined by the CG-bounds.

**Problem target: Walpole Point (Problem 9 in Figure A.7-a)**

The material layouts obtained with different plane groups for the WP point (of Figure A.7-a and c) are depicted in Figure A.8. These solutions confirm the conclusions reported by Sigmund [67]. The most extreme properties are attained with the symmetry $p6mm$ and the topology agrees with that reported by Sigmund in the same paper. Notably in this case, the microstructure is constituted by laminated bars and rigid joints. Sigmund has proven that parameterizing this topology and performing an optimization of the geometry configuration through these parameters, the material almost reaches the Walpole Point. It is evident that the additional symmetry lines of the $p6mm$ plane group guide the algorithm to attain a more adequate limit condition.

The same Figure A.8 shows that when a lower symmetry is imposed, for example $p3$, the algorithm searches for a solution tending to capture similar symmetry elements to those shown by the $p6mm$ plane group.

It is remarked that the Walpole point is asymptotically attained when one phase is void, both in two and three dimensions, such as mentioned in the introduction of the paper by Milton y Camar-Eddine [120].

**Problem target: minimum Poisson's ratio (Problem 2 in Figure A.7-a)**

The resulting topologies for the problem identified with number 2 in Figure A.7-a, whose target is to attain the bound for the composite with the most negative Poisson's ratio (Point NP in the CG-bounds), are shown in Figure A.9. In general, these topologies agree with the ones reported in the paper by Podestá et al. [65]. We note in Figure A.7-a and b that the effective response is rather sensitive to the imposed plane group. The microarchitectures giving a good tendency are either chiral (obtained with the plane groups $p6$ and $p3$ without mirror symmetry lines) as well as not chiral (obtained with the plane group $p31m$ with one system of mirror symmetry line). Again, we note that $p31m$, $p6$ and $p3$ plane groups try to attain microstructures constituted by laminate bars. Note the similarity of the configuration attained with $p6$ symmetry and the parameterized microstructure studied in Ostanin et al. [121].

The solutions with the plane groups $p3m1$ and $p6mm$ are clearly inefficient if compared with the $p6$ and $p3$ solutions. This response can be explained by the mirror lines of the plane group $p6mm$ yielding an inadequate topology for emulating the deformation mechanisms typical of auxetic materials. The inefficiency of the solutions for both plane groups $p3m1$ and $p6mm$ are additionally confirmed by observing the intricate resolved microarchitectures displayed in Figure A.9.

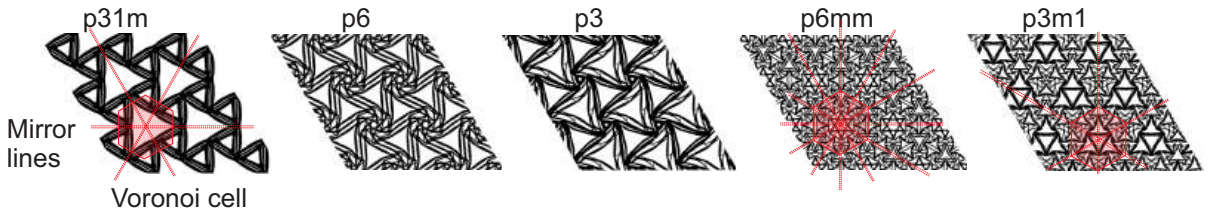


**Figura A.9:** Two-dimensional design of isotropic microstructures: most negative Poisson's ratio (Point NP in Figure A.7-a and b). Topologies obtained with plane groups $p31m$, $p6$, $p3$, $p6mm$, and $p3m1$. Mirror lines and Voronoi cells.

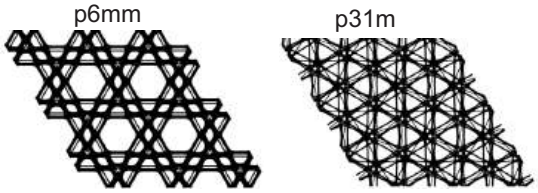


**Figura A.10:** Two-dimensional design of extreme isotropic microstructures: maximum shear and bulk moduli (Problem 7 in Figure A.7-a). Topologies obtained with plane groups $p6mm$ and $p3m1$.

The above discussed conclusions are valid for designing extreme composites whose target properties lay on a larger part of the left and upper CG-bounds, for example, for the problems denoted with the numbers 1 to 5 in Figure A.7-a.

#### Problem target: maximum shear and bulk moduli (Problem 7 in Figure A.7-a)

Similar microstructures are obtained with the five plane groups when searching for the stiffer microstructure at the upper right vertex of the CG-bounds, maximum shear and bulk moduli.

Figure A.10 depicts the solutions attained with the plane groups $p6mm$ and $p31m$. They are similar microstructures to those reported by Sigmund [67].

#### Smooth transition of topologies along the CG-bounds

Figure A.11 displays a sequence of the microarchitectures attained in problems 1 to 4 (with plane group $p31m$), as well as, 8 to 11 (with plane group $p6mm$). There can be seen a smooth and continuous transition of topologies for the problems along the CG-boundary. These results open the possibility to define families of microarchitectures, via parametrization of their geometrical configuration, which could be used as a tool, by appealing to parameter optimization, for attaining topologies with properties even closer to the limits.

## A.4. Design of 3-D isotropic materials

Four different space groups $P23$, $Pm\bar{3}m$ (with sc Bravais lattices) and $I23$, $Im\bar{3}m$ (with bcc Bravais lattices) are adopted for designing the 3D topologies. All the solutions have been got with a Fast Fourier Transform procedure to compute the homogenized elastic properties. The cells have $100 \times 100 \times 100$ voxels in all cases.

Figure A.12 plots the results in the space $(\hat{\kappa}, \hat{G})$. The HS-upper and lower bounds and some isolines of properties with negative Poisson's ratios are depicted, as well as 13 sets of solutions obtained with the four mentioned space groups. Each set of solutions are denoted with the numbers 1 to 13. Several instances have been run for every set of Problems 1 to 13 and for every space group. The solutions depicted in Figure A.12 correspond to the best obtained case of all the runs for each space group.

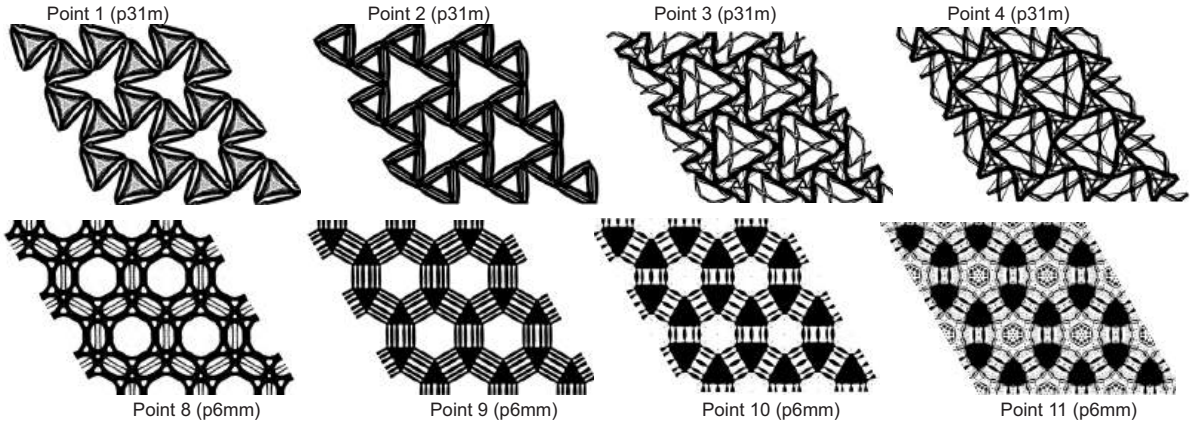


**Figura A.11:** Transitions of topologies (Points 1 to 4 with $p31m$ plane group (above) and 8 to 11 with $p6mm$ plane group (below)). The problem numbers are identified in Figure A.7-a.

**Tabla A.3:** Zener ratio $\xi$ quantifying the anisotropy of 3-D microarchitecture design solutions with space groups $P23$, $I23$, $Pm\bar{3}m$ and $Im\bar{3}m$. The number of the problem in column 1 coincides with the problem number identified in Figure A.12.

| Problem | $P23$ | $I23$ | $Pm\bar{3}m$ | $Im\bar{3}m$ |
|---|---|---|---|---|
| 1 | 1.009 | 1.012 | 0.943 | 0.995 |
| 2 | 0.978 | 1.014 | 1.047 | 1.005 |
| 7 | 1.035 | 1.010 | 1.004 | 0.987 |
| 12 | 1.455 | 1.539 | 1.140 | 0.995 |

**Isotropy analysis**

With the coefficients of the homogenized elasticity tensor $\hat{C}$, we compute the Zener ratios[14] of some representative microarchitectures as follows:

$$\xi = \frac{\hat{C}_{44}}{\hat{C}_{11} - \hat{C}_{12}} \tag{A.13}$$

A value 1 for this ratio indicates that $\hat{C}$ is isotropic[15]. Contrarily, a large value of $\xi$ indicates that $\hat{C}$ is far from being isotropic. Some Zener ratios are reported in Table A.3. In general, they are close to 1, meaning that the effective response almost satisfies the isotropy constraint imposed on the topology optimization algorithm.

### A.4.1. Discussion of results

After evaluating the results plotted in Figure A.12 and Table A.3, the following conclusions can be drawn:

*1)* In the region of the space $(\hat{\kappa}, \hat{G})$ corresponding to small $\hat{\kappa}$ and large $\hat{G}$, i.e., negative or small Poisson's ratios, the point group (either 23 or $m\bar{3}m$) have a higher influence than the Bravais lattice (sc or bcc) to achieve properties close to the bounds. The closest solutions are attained with the point group 23, which has fewer symmetry elements than the $m\bar{3}m$ point group.

[14]The Zener ratio quantifies the anisotropy of the effective material properties having cubic symmetry.

[15]For the subsequent analysis, the elasticity tensors whose Zener ratios are different from 1 are projected to the space of isotropic tensors using the technique reported by Meille y Garboczi [122].

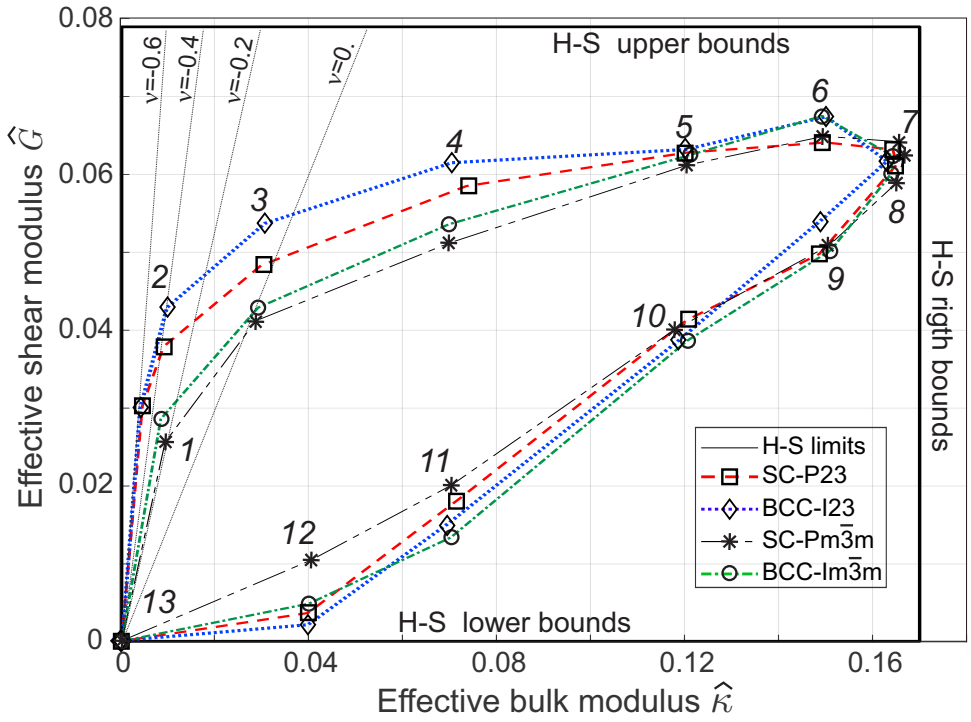


**Figura A.12:** Three-Dimensional design of composites whose properties are close to the theoretical bounds. Hashin-Shtrikman bounds in the space $(\hat{\kappa}, \hat{G})$. Solutions for 13 different sets of problems using four space groups $P23$, $Pm\bar{3}m$ (with sc Bravais lattice) and $I23$, $Im\bar{3}m$ (with bcc Bravais lattice). Isolines of properties with negative Posson's ratios are shown.

*2)* In the region of the space $(\hat{\kappa}, \hat{G})$ corresponding to high bulk and shear moduli, problems 6 and 7, the solutions are similar for identical lattices, independently of the point group. The reason for this response is that topologies with the highest symmetries display properties closer to the limit values in this specific region of the space $(\hat{\kappa}, \hat{G})$. Thus, when a space group with lower symmetry is imposed in the algorithm, it seeks for solutions with higher symmetry than the enforced one.

According to this conclusion, which is similar to that presented at the end of sub-Section A.3.1, there would be a tendency to think that, in all cases, the imposition of the lowest symmetries is preferable to the highest ones and leaving to the algorithm, the search for higher symmetries, if it were the case. However, this conclusion is not correct in general. We have discussed in sub-Section A.3.1 that the enforcement of appropriate symmetries has been beneficial for obtaining a marginally closer solution to the theoretical limits, as well as, to achieve notably more stable, robust and repetitive responses of the topology optimization algorithm.

*3)* The following tendency has been observed in general for attaining the points on the HS-upper and right bounds. The bcc lattice provides solutions with larger values of $\hat{G}$, while the sc lattice provides solutions with slightly larger values of $\hat{\kappa}$.

*4)* In the HS-lower bound region, problem 12, where the HS-bound estimates the occurrence of penta-mode materials, the solutions with space groups $P23$, $I23$ and $Im\bar{3}m$ give lower shear stiffnesses. However, according to the results in Table A.3, the $P23$ and $I23$ solutions cannot be considered as isotropic. Alternatively, the $Im\bar{3}m$ solution attains a low shear modulus with a closely isotropic response.

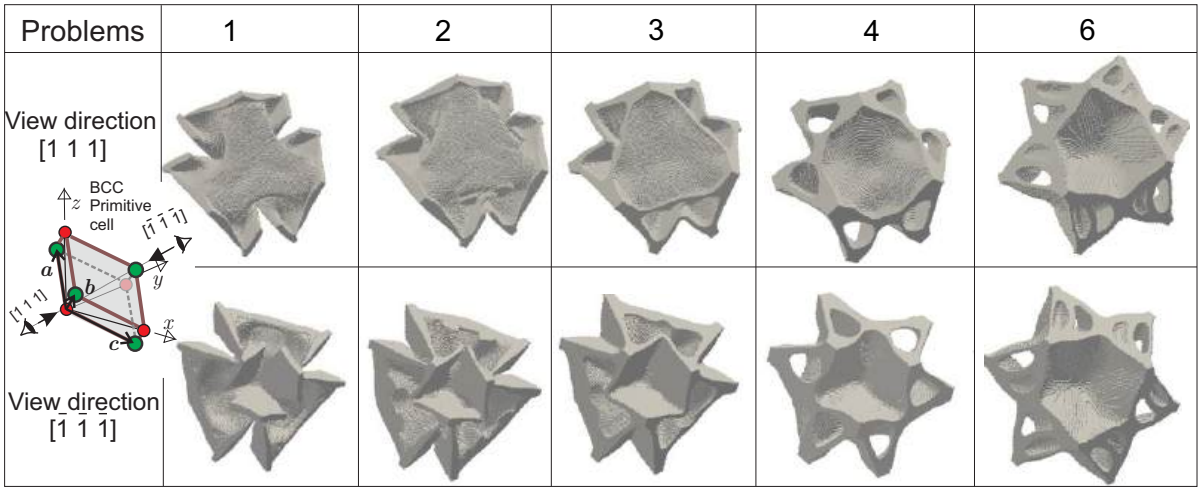


**Figura A.13:** Microarchitecture transitions with maximal shear stiffness and target points along the HS-upper bound. Space group $I23$. Problems 1, 2, 3 , 4 and 6 are in correspondence with those in Figure A.12. Topologies of the bcc primitive cell observed from two points of view: [1 1 1] and [$\bar{1}\,\bar{1}\,\bar{1}$].

### Microarchitecture transition along the upper bound

An almost continuous transition of topologies with the imposed space group $I23$ is attained when designing microstructures with maximum shear modulus close to the HS-upper bound. These microarchitectures are depicted in Figure A.13 and correspond to solutions of Problems 1, 2, 3, 4, and 6 of Figure A.12. The attained microarchitectures are displayed from two opposite points of view, according to the directions [1 1 1] and [$\bar{1}\,\bar{1}\,\bar{1}$], respectively[16].

Due to the characteristic symmetries of space group $Im\bar{3}m$, the topologies with this space group display an identical appearance when viewed from both directions $[1\,1\,1]$ and $[\bar{1}\,\bar{1}\,\bar{1}]$ because in this point group $m\bar{3}m$, both directions belongs to the same family $\langle 111\rangle$. Such property is not satisfied, in general, by topologies with $I23$ space group, property which is confirmed in Figure A.13. However, the similar appearance observed from both points of view is noted in the solution of Problem 6, Figure A.13.

The above observation confirms once again the previously discussed concept about that the imposition of a low symmetry condition, such as the $I23$, does not inhibit the attainment of topologies with higher symmetries, copying that of the space group $Im\bar{3}m$. This observation is additionally supported by the fact that solutions obtained with space groups $I23$ and $Im\bar{3}m$ have almost the same elastic properties stated in Figure A.12,

### Microarchitecture of auxetic materials

Several designed 3D microarchitectures with auxetic properties show topologies characterized by similar deformation mechanisms to those reported in the literature for 2D problems. A typical case is a microstructure designed to have minimum Poisson's ratio (Problem 1 in Figure A.12) using the spatial group $I23$. Two different solutions are depicted in Figure A.14 called Instances 1 and 2. It can be noted that the conventional cell of *Instance 1*, Figure A.14-c, consists of eight blocks, similar to rigid cubes, connected at their edges with joints. These rigid cubes are allowed to have a relative rotation between them. Thus, the deformation mechanism to get the required auxetic behavior is similar to the 2D microstructure reported in the literature and called *rotating polygonal models*, see Ren et al. [123] and Attard

[16]We use Miller indices to identify crystallographic directions and planes. A family of planes is denoted between braces "{...}" and collect all the planes which are related through the symmetry operations of the point group. Therefore, two families of planes with identical Miller indices but different point groups may indicate different sets of planes. The same observation is done for the family of directions denoted between angle brackets "⟨...⟩".

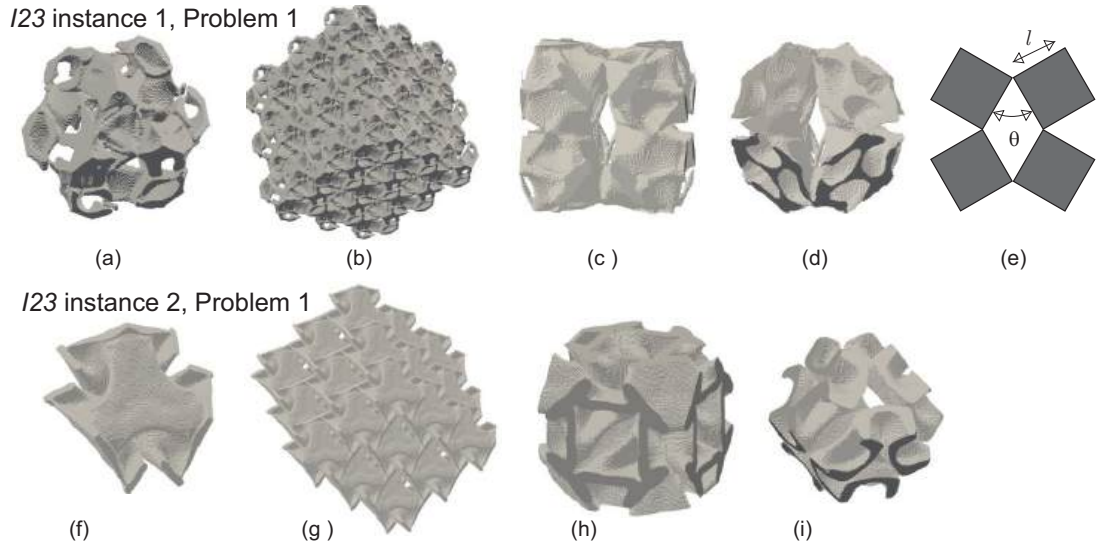


**Figura A.14:** Two instances of composites with minimum Poisson's ratio attained with Problem 1 in Figure A.12, space group $I23$. **Instance 1**: a) primitive cell; b) assembled microstructure; c) conventional cell; d) Voronoi cell; e) 2D rotating polygonal models described in Ren et al. [123]. **Instance 2**: f) primitive cell; g) assembled microstructure; h) conventional cell; i) Voronoi cell.

y Grima [124]. For comparison, the rotating polygonal microstructure is reproduced in Figure A.14-e. Some other three-dimensional microarchitectures having a Poisson's ratio approaching $-1$ are reported in Milton [125].

One additional attained microstructure with similar elastic properties is denoted *Instance 2*. It is displayed in Figure A.14 f-i. The Voronoi cell of this microstructure shows four identical independent substructures which stay interconnected after the cell assembling. At the best of our knowledge, this microstructure has not been previously reported in the literature.

**Configurations resulting from the auxetic 3D microstructures projected onto cutting planes**

An additional aspect which shed some light on the understanding of the attained 3D microstructures comes from the analysis of the resulting projected topologies by cutting the designed microarchitectures with specific families of planes. Of particular interest are those projected topologies onto planes containing symmetry elements.

We analyze the projected configuration onto planes orthogonal to three families of directions: $\langle 1\,0\,0\rangle$, $\langle 1\,1\,0\rangle$ and $\langle 1\,1\,1\rangle$.

This analysis is restricted to the solutions of problems 1 and 2 of Figure A.12 displaying the most negative Poissson's ratios.

**a) Cutting planes orthogonal to** $\langle 1\,0\,0\rangle$

**a.1) Space groups** $P23$ **and** $I23$

The projected configurations onto generic planes orthogonal to $\langle 1\,0\,0\rangle$ of topologies with point groups 23 display a plane group $p2$ with a square lattice. However, there are some specific positions of these cutting planes in where the projected topology may displays additional symmetry elements.

Particularly, when the position of the cutting plane is at the middle distance between two consecutive planes of the family $\{2\,0\,0\}$, the space group $I23$ projects as a plane group $p2gg$. This result is a consequence of the additional two-fold screw axes existing in the $I23$ space group exhibited in Figure A.5-d. Therefore, the space group $P23$ does not possess this symmetry. Figure A.15, case A, display the projected configuration of both space groups onto this particular plane. Although both configurations display analogous patterns, as a consequence of the additional glide reflection elements in the space group

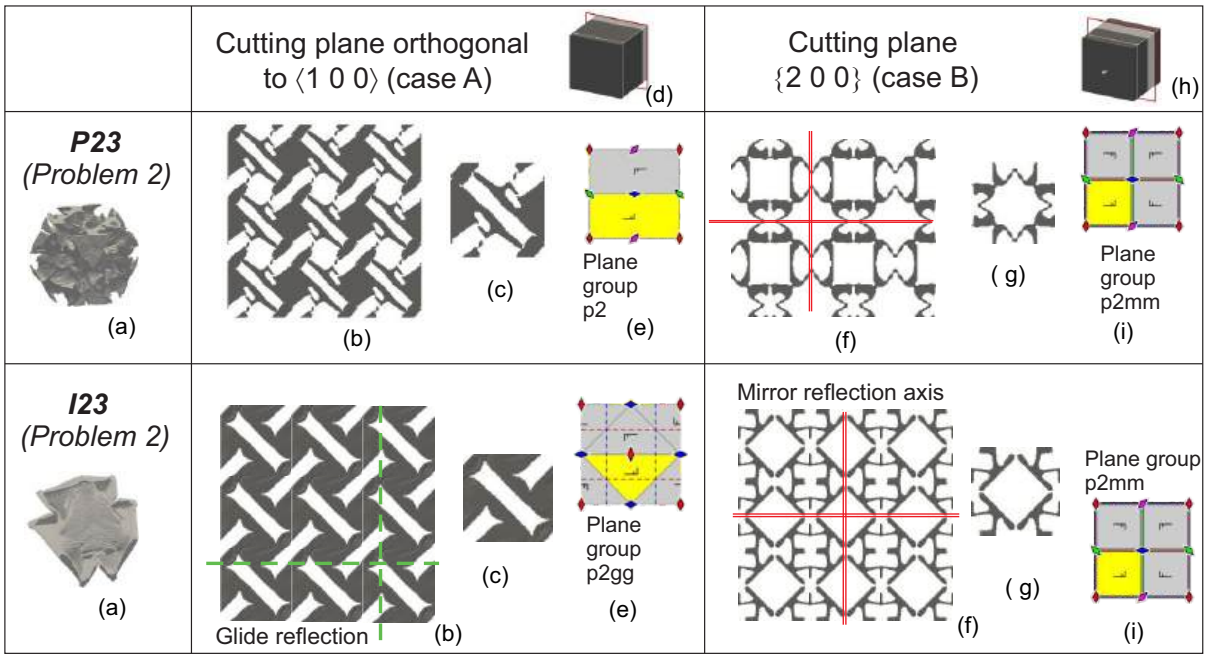


**Figura A.15:** Projected microstructures attained of problem 2 in Figure A.12. Space groups $P23$ and $I23$. Two projected configurations according to two different cut plane positions (cases A and B). a) primitive cells; b) and f) projected topologies of the assembled composites; c) and g) projected topologies of the conventional unit cells; d) positions in the conventional cell of the cutting planes; e) and i) plane groups and symmetry elements. The symbols representing the plane group symmetry elements are described in Figure A.6.

$I23$, this microstructure presents a better resolution and, according to Figure A.12, shows closer elastic properties to the bounds.

It is interesting to compare the similitude between the configuration displayed in Figure A.15-b of space group $I23$, and the layout reported as antitetrachiral by Alderson et al. [126]. We observe that the here obtained projected topology is an anti-tetrachiral configuration. Notably, the anti-tetrachiral configuration is a $p4gm$ plane group. Such as mentioned by Alderson et al. [126], in 2D cases, the anti-tetrachiral configuration, if compared with alternative chiral configurations, is the most performer one for attaining Poisson's ratios close to -1, see Chen et al. [127].

Additionally, the topologies projected onto planes belonging to the family $\{2\,0\,0\}$, which contains two-fold rotation axes, have mirror lines resulting with a plane group $p2mm$, such as shown in Figure A.15-f. This plane group penalizes the realization of auxetic materials. However, apparently, the arising of this detrimental configuration in a small number of planes is not sufficient to generate an inadequate response of the full microarchitecture.

Next, based on the results obtained in Problems 1 and 2 of Figure A.12 with the spaces groups $P23$ and $I23$, we re-examine an issue already discussed above. We note that the imposition of a space group, $P23$, with a less number of symmetry elements on the topology optimization algorithm, leaving it to attain the adequate configuration symmetry, does not work correctly in Problem 2. In this case, the solution with the $I23$ space group is notably better than the solution obtained with the $P23$ space group. However, this conjecture does work when analyzing the results of Problem 1. Examining the projected configuration of the $P23$ solution of Problem 1, depicted in Figure A.16, we note that it tends to capture a higher symmetry, with mirror symmetry lines, and which additionally is similar to the topologies $I23$ displayed in Figures A.15-b.

At this point, it is necessary to distinguish between the point groups $p2mg$ and $p2mm$ and their capacity to achieve auxetics 2D composites. The glide symmetry element of the $p2mg$ plane group is not necessarily so prejudicial as the mirror symmetry element is in the $p2mm$ case. There are several

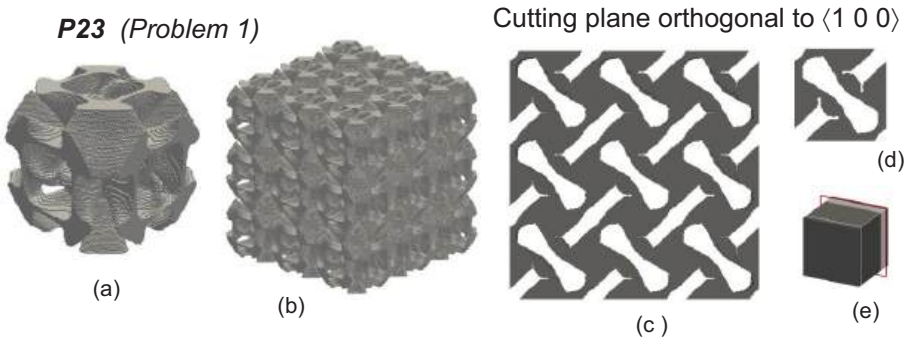


**Figura A.16:** Microstructure attained with Problem 1 in Figure A.12. Space group $P23$. a) primitive cell; b) assembled microstructure; c) projected topology of the assembled composite onto the plane orthogonal to $\langle 1\,0\,0\rangle$ situated between two consecutive planes of the family $\{2\,0\,0\}$; d) projected topology of the primitive unit cell onto the same plane; e) Position of the cutting plane relative to the primitive cell.

topologies in 2D having plane group $p2mg$ with isotropic elastic properties and negative Poisson's ratio, see the discussion in Section 5.1.5 of the paper by Podestá et al. [65].

**a.2) Space groups $Pm\bar{3}m$ and $Im\bar{3}m$**

The $Pm\bar{3}m$ and $Im\bar{3}m$ space groups project onto a plane group $p4mm$ when the cutting plane is a generic plane orthogonal to $\langle 1\,0\,0\rangle$. Figure A.17-f shows the symmetry elements of this plane group, and Figures A.17-c and d display the material configurations of the designed microstructures of Problem 1 in Figure A.12 projected onto this plane. Observe the complex topology shown by both microstructures.

According to the conclusions achieved for 2D topologies, the plane group $p4mm$ involves a large number of mirror symmetry elements, which is very detrimental to obtain large negative Poisson's ratios. The same conclusion can be generalized to be applied to the results obtained in 3D designs with both spaces groups $Pm\bar{3}m$ and $Im\bar{3}m$. The bad performances displayed in Figure A.12, Problems 1 and 2 , by the elastic properties of these space groups, can then be associated with this feature.

**b) Cutting planes orthogonal to $\langle 1\,1\,0\rangle$**

**b.1) Space groups $P23$ and $I23$**

The projected lattice onto the cutting planes orthogonal to $\langle 1\,1\,0\rangle$ generate a Rectangular Primitive lattice for the three-dimensional sc lattice and a Rectangular Centered one for the bcc lattice. In both cases, the aspect ratios of the conventional plane cells are $\sqrt{2}$.

The projections of the spaces groups $P23$ and $I23$ onto generic planes orthogonal to $\langle 1\,1\,0\rangle$ do not generate any symmetry element. Therefore, the plane group is $p1$. However, in the particular case of the plane family $\{2\,2\,0\}$, which contains the two-fold rotation axes, the plane group projected by the space groups $P23$ and $I23$ change to $pm$ and $cm$, respectively. Thus, the topologies obtained with $P23$ and $I23$ for the Problem 2 projected onto that specific plane family are shown in Figure A.18. Also, Figure A.18-c identifies the symmetry lines of the projected configurations. Note that the plane group $pm$ has two parallel symmetry mirror lines, while the $cm$ has only one mirror line and one glide reflection line, such as exhibited in Figure A.18-e. A consequence of these attributes is that the space group $P23$ displays a projected topology with two different types of triangles, while the $I23$ displays only one type of triangle. It is interesting to compare the resemblance between these topologies with the 2D configuration depicted in Figure A.9, $p31m$ plane group, which is one of the best plane groups to attain negative Poisson's ratio.

**b.2) Plane groups $Pm\bar{3}m$ and $Im\bar{3}m$**

The space group $Pm\bar{3}m$ projects onto the generic planes orthogonal to $\langle 1\,1\,0\rangle$ as a plane group $p2mm$ and the $Im\bar{3}m$ as a plane group $c2mm$. Again, and such as observed for 2D problems, for both

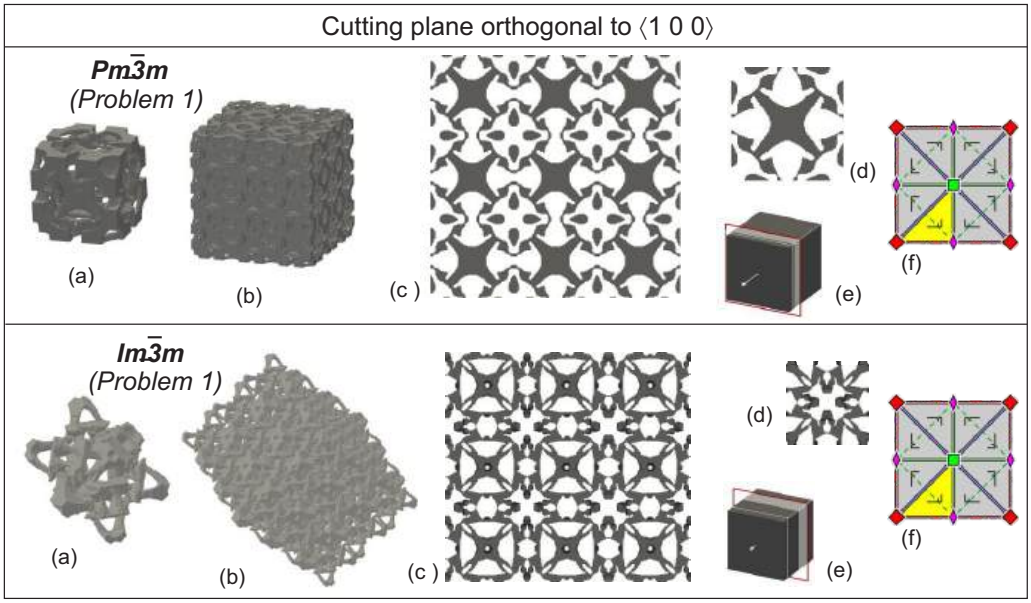


**Figura A.17:** Microstructure attained with Problem 1 in Figure A.12. Space groups $Pm\bar{3}m$ and $Im\bar{3}m$. a) primitive cells; b) assembled microstructures; c) projected topologies of the assembled composites onto a generic plane orthogonal to $\langle 1\,0\,0\rangle$; d) projected topologies of the conventional unit cells onto the same plane; e) Positions of the cutting planes relative to the conventional cells; f) symmetry elements of $Pm\bar{3}m$ and $Im\bar{3}m$ configurations projected onto the generic plane. The symbols representing the plane group symmetry elements are described in Figure A.6.

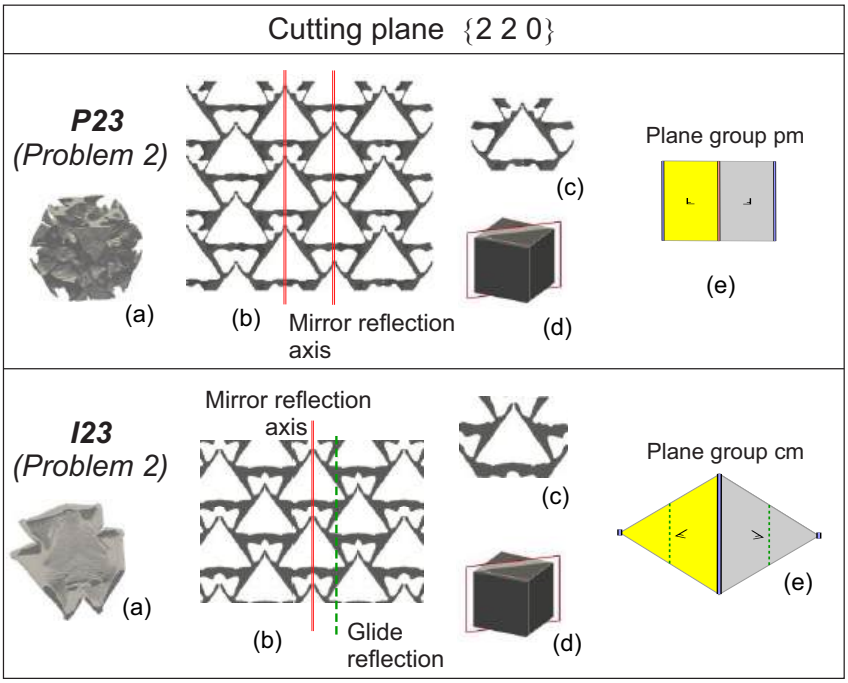


**Figura A.18:** Projected microstructures attained with Problem 2 in Figure A.12. Space groups $P23$ and $I23$. Cutting plane $\{2\,2\,0\}$. a) primitive cells; b) projected topologies of the assembled composites; c) projected topologies of the conventional unit cells; d) Positions of the cutting planes relative to the conventional cells; e) plane groups and symmetry elements. The symbols representing the plane group symmetry elements are described in Figure A.6.

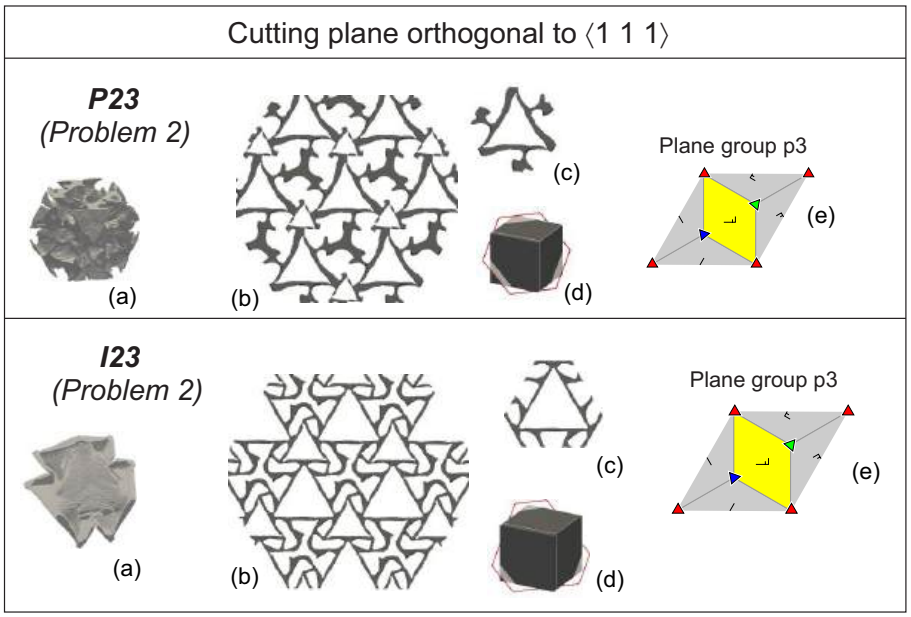


**Figura A.19:** Projected microstructures attained with Problem 2 in Figure A.19. Space groups $P23$ and $I23$. Column 1: Cutting planes orthogonal to $\langle 1\,1\,1\rangle$. a) primitive cells; b) projected topologies of the assemble composites; c) projected topologies of the conventional unit cells; d) Positions of the cutting planes relative to the conventional cells; e) plane groups and symmetry elements. The symbols representing the plane group symmetry elements are described in Figure A.6.

space groups, the enforced symmetry onto these planes are not convenient for attaining negative Poisson's ratios.

**c) Cutting planes orthogonal to** $\langle 1\,1\,1\rangle$

**c.1) Plane groups** $P23$ **and** $I23$

The projected configurations onto generic planes orthogonal to $\langle 1\,1\,1\rangle$ of the space groups $P23$ and $I23$ display a configuration with a hexagonal Bravais lattice and plane group $p3$. The symmetry elements of the plane group $p3$ are shown in Figure A.19-e. The topologies of the obtained microarchitectures with these space groups ($P23$ and $I23$) are displayed in Figure A.19-b. These topologies have a tendency to attain a higher symmetry than the $p3$ enforced by the space groups.

The topologies attained in Problem 1 of Figure A.12 projected onto planes orthogonal to $\{1\,1\,1\}$ almost copy, even with more confidence than in projections onto generic planes $\langle 1\,1\,1\rangle$, a plane group $p3m1$. They are shown in Figure A.20-c and d.It is notable that the algorithm searches for configurations with higher symmetries than the imposed ones also on planes orthogonal to $\langle 1\,0\,0\rangle$ and $\langle 1\,1\,0\rangle$.

Analyzing the attained symmetries in these cases, we observe that they are compatible with space group configurations $P\bar{4}3m$ and $I\bar{4}3m$ projected onto the same family of planes. This conclusion may be a symptom that these space groups are better than the imposed ones for reaching the problem target.

**c.2) Plane groups** $Pm\bar{3}m$ **and** $Im\bar{3}m$

Figure A.21 shows the topologies attained with $Pm\bar{3}m$ space group and projected onto cutting planes orthogonal to $\langle 1\,1\,1\rangle$. In this generic plane, the projected topology has $p3m1$ plane group. Particularly, if the cutting plane belongs to the family $\{2\,2\,2\}$, which contains the inversion center of the point group element $\bar{3}$, the plane group is a $p6mm$. Identical symmetry properties are valid for topologies with $Im\bar{3}m$ space groups, except that the family of planes containing the inversion centers is the $\{4\,4\,4\}$.

Again in this case, the results obtained with the space group $Pm\bar{3}m$ and $Im\bar{3}m$ confirm the comment mentioned in sub-Section A.3.1 about that the plane group $p6mm$ penalizes severely the capturing of

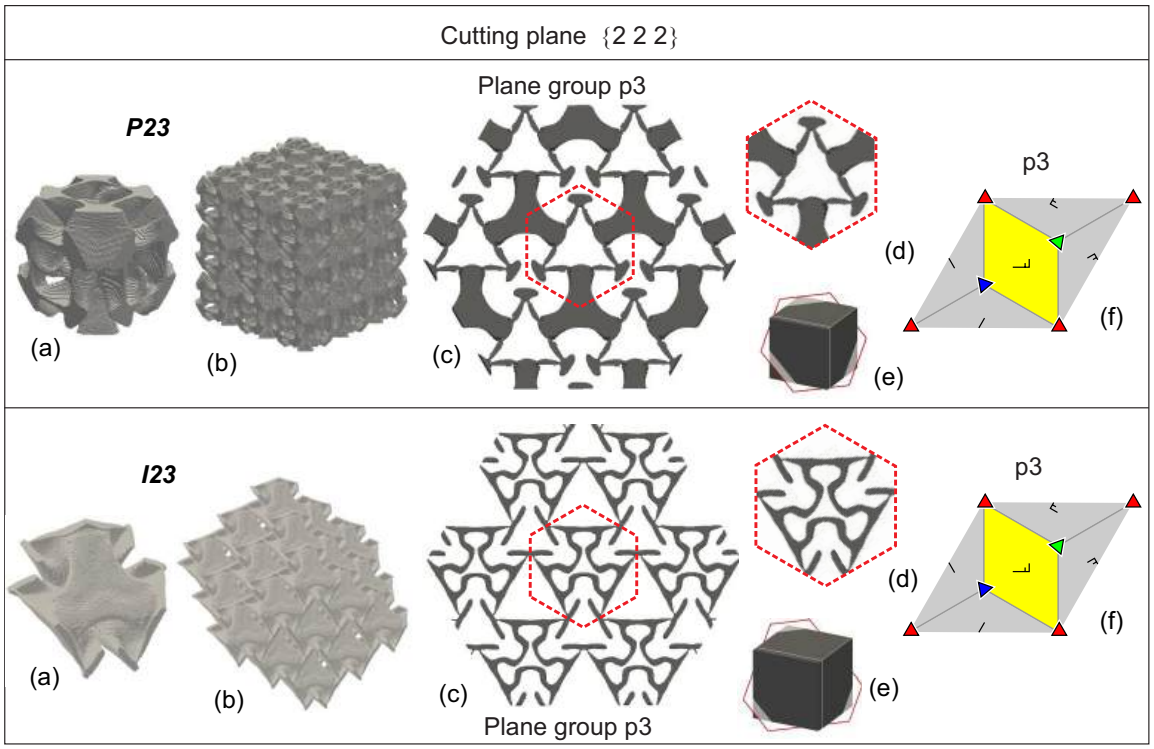


**Figura A.20:** Microstructure attained with Problem 1 in Figure A.12. Space groups $P23$ and $I23$. a) primitive cells; b) assembled microstructure; c) projected topologies of the assembled composite onto the family of planes $\{2\,2\,2\}$; d) Voronoi unit cell of the projected topologies; e) Positions of the cutting planes relative to the conventional cells; f) Projected symmetry elements onto a generic plane orthogonal to $\langle 1\,1\,1\rangle$ of space groups $P23$ and $I23$. The symbols representing the plane group symmetry elements are described in Figure A.6.

auxetic materials.

### Microarchitectures for pentamode materials

The lower estimation of the HS-bounds corresponds to isotropic materials with close to zero shear modulus. Therefore, according to the denomination of Milton y Cherkaev [70], they are pentamode materials[17].

By solving the isotropic problem of minimum shear modulus for the bulk modulus $\hat{\kappa} = 0.04$ (Problem 12 in Figure A.12), we obtain a similar microstructure to that reported in the literature for this family of metamaterials, see Milton y Cherkaev [70], Kadic et al. [7] and Kadic et al. [128]. As can be observed in Figure A.22, the microstructures obtained using the present methodology with space groups $P23$ and $Im\bar{3}m$ are constituted by two independent sub-microarchitectures in the cubic cell, respectively. Each sub-microstructure is approximately similar to the ones reported by Kadic et al. [7] in Figure 1-b and are, typically, constituted by rigid elements connected through flexible joints.

The homogenized elasticity tensors of the microstructure obtained with the $P23$ space group has the following six eigenvalues: $0.1196$; $0.0098$; $0.0098$; $0.0084$ ; $0.0084$ ; $0.0084$, and the ratio between the maximum and minimum is approximately 14.

The homogenized elasticity tensors of the microstructure obtained with the $Im\bar{3}m$ space group has

[17] A Pentamode material is a class of extremal material having five easy (compliant) modes of deformation in a three-dimensional space, and having only one non-easy (stiff) mode of deformation. The elasticity tensor of this material has one non-null eigenvalue and five null eigenvalues (hence the name of pentamode given to this class of materials). In 1995, Milton y Cherkaev [70] have coined the name of pentamode materials in the context of linear elasticity. In the same year, Sigmund [66] has independently introduced it in the context of inverse homogenization problems.

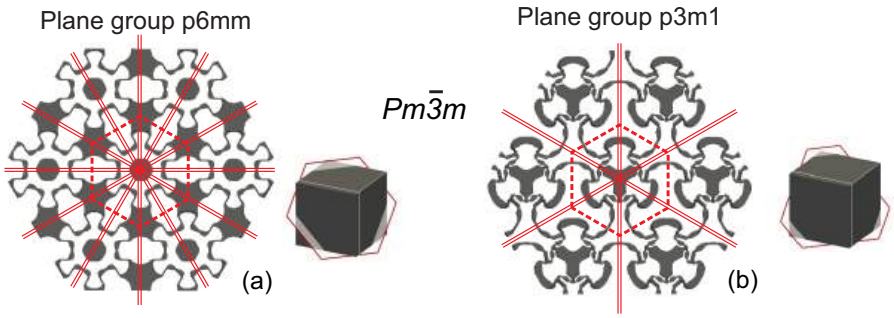


**Figura A.21:** Projected topologies onto planes orthogonal to $\langle 1\,1\,1\rangle$ of the microarchitectures at Problem 1 in Figure A.12, space group $Pm\bar{3}m$. a) cutting plane belongs to the family $\{2\,2\,2\}$; b) generic cutting plane orthogonal to $\langle 1\,1\,1\rangle$.

the following six eigenvalues: 0.1204, 0.0098 ; 0.0098 ; 0.0098; 0.0098; 0.0098. The ratio between the maximum and minimum is approximately 12.

The $I23$ solution, which gives the lowest shear modulus, display eight sub-microstructures, and a second instance of the $P23$ solution, not shown here, displays four sub-microstructures. Thus, according to the present results, we perceive that an increase in the number of sub-microstructures entails a decrease of the shear modulus.

## A.5. Conclusions

In this paper, we have analyzed the role that the symmetries of crystals play in the topology design of isotropic elastic materials when the design target is to attain properties close to the theoretical bounds, and the optimum design methodology is based on an inverse homogenization technique. The summary of the attained results are depicted in Figures A.7 and A.12. They are a demonstration that the maximal/minimal achievable properties strongly depend on the crystal symmetries imposed on the mathematical technique. And most important, the adequate crystal symmetries to reach these maximal/minimal properties change with the limit target point, or sector, on the CG and HS-bounds in the plane $(\hat{\kappa}, \hat{G})$. In both cases, 2D and 3D, we have found that the bounds on the right part of the plane, with maximum $\hat{\kappa}$, can be approximated with the higher crystal symmetries. Contrarily, to approach the left bound, it is better to explore other types of symmetries.

In 2D problems, the isotropy of the composite is guaranteed by adopting plane group symmetries consistent with the *hexagonal crystal system*. However, not all these plane groups have identical effects. For example, to attain auxetic composites, it is convenient to explore the $p3$, $p31m$ and $p6$ plane groups, while the $p6mm$ and $p3m1$ are unsuitable in these cases. Notably, the plane groups $p6$ and $p3$ allow for the development of chiral configurations. Conclusions are different if the extreme target properties are the maximal bulk and minimal shear moduli (the Walpole Point). In this case, the plane group $p6mm$ is the most effective one. For this particular problem, we have also shown that the imposition of a plane group with low symmetry, such as $p3$, does not provide as good solutions as those attained by imposing the $p6mm$ plane group. This result proves that a procedure which takes a plane group with low symmetry ($p3$) and leaving the algorithm for searching the higher symmetry ($p6mm$) does not work, in general, with the best performance.

In 3D problems, we have only analyzed symmetries of the *cubic crystal system*. In this case, the dependence on the space group for attaining maximal/minimal properties is still more pronounced than in 2D cases. The space groups $I23$ and $P23$ are notably more suitable to attain maximal properties in the region close to the HS-left-upper bound, coincident with the response of auxetic materials. A similar conclusion about the proper selection of the cell defining the optimization domain $\Omega_\mu$ can be drawn. The bcc primitive cell has turned out to be notably more advantageous than the simple cubic (sc) cell to get

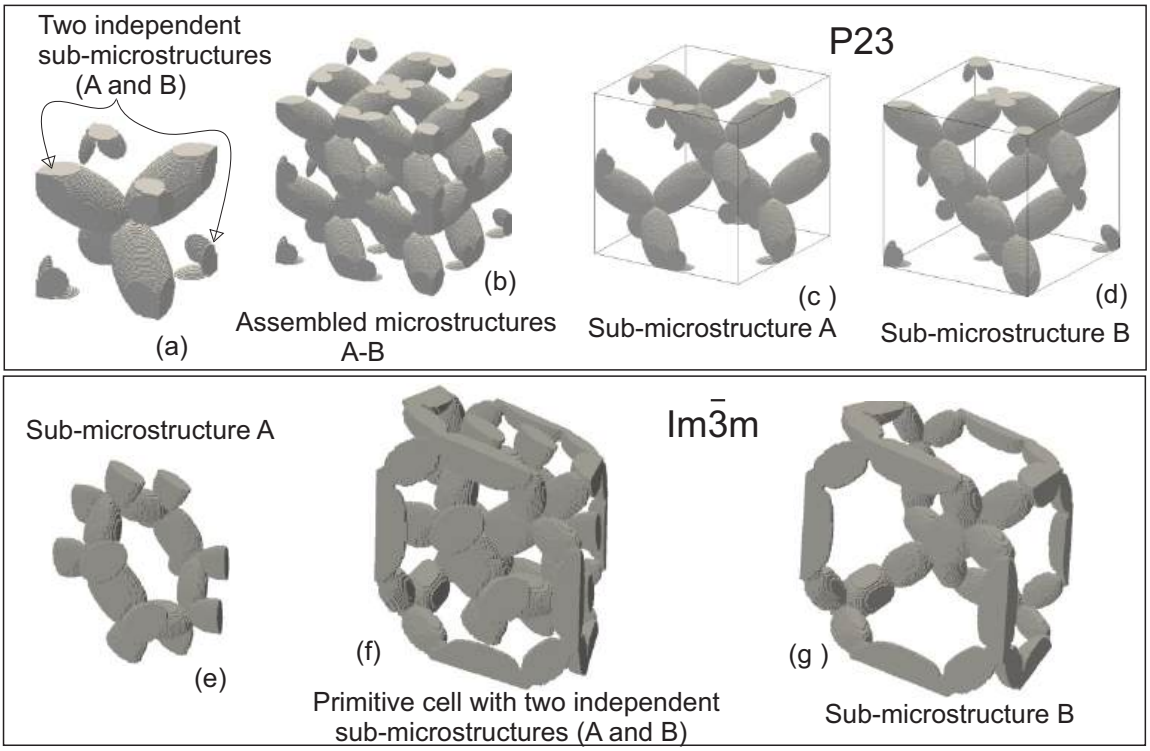


**Figura A.22:** Topologies attained with Problem 12 in Figure A.12 by enforcing a space group $P23$ (a to d) and $Im\hat{3}m$ (e to g). a) and f) are the primitive unit cells; b) assembled microstructures; c, d e and g) sub-microstructures.

maximal properties in some sectors of the plane $(\hat{\kappa}, \hat{G})$, along the HS-upper bound.

Even when we have not specifically analyzed the numerical response of the topology optimization algorithm, we envisage that the additional crystal symmetry constraints notably increase the robustness and stability of the algorithm, by limiting the search space of the geometrical variables defining the topology.

Finally, we remark that the use of crystal symmetries for topology design can be easily extended to other more general thermal, photonic, acoustic microarchitecture design problems, anticipating similar potential benefits to those here explored.

## Acknowledgments

The authors acknowledge the financial support from CONICET and ANPCyT (grants PICT 2014-3372 and 2016-2673).

# Apéndice B

# Numerical technique for the 3D microarchitecture design of elastic composites inspired by crystal symmetries

Rossi, N., Yera, R., Méndez, C. G., Toro, S., and Huespe, A. E. (2020). "Numerical technique for the 3D microarchitecture design of elastic composites inspired by crystal symmetries". *Computer Methods in Applied Mechanics and Engineering*, 359, 112760.

# Numerical technique for the 3D microarchitecture design of elastic composites inspired by crystal symmetries

**N. Rossi[1], R. Yera[1], C.G. Méndez[1], S.Toro[1], A.E. Huespe[1,2][1]**

[1]CIMEC-UNL-CONICET, Predio Conicet "Dr Alberto Cassano", CP 3000 Santa Fe, Argentina
[2]E.T.S d'Enginyers de Camins, Canals i Ports, Technical University of Catalonia (Barcelona Tech) Campus Nord UPC, Mòdul C-1, c/ Jordi Girona 1-3, 08034, Barcelona, Spain

**Keywords:**3D microarchitecture synthesis; topology optimization algorithm; topology design inspired by crystal symmetries; 3D elastic metamaterials; auxetic materials; pentamode composites; stiffest composite.

**Abstract.** A numerical methodology developed for the microarchitecture design of 3D elastic two-phase periodic composites with effective isotropic properties close to the theoretical bounds is here presented and analyzed. This methodology is formulated as a topology optimization problem and is implemented using a level-set approach jointly with topological derivative.

The most salient characteristic of this methodology is the imposition of preestablished crystal symmetries to the designed topologies; we integrate a topological optimization formulation with crystal symmetries to design mechanical metamaterials.

The computational homogenization of the composite elastic properties is determined using a Fast Fourier Transform (FFT) technique. Due to the design domains are the primitive cells of Bravais lattices compatible with the space group imposed to the material layout, we have adapted the FFT technique to compute the effective properties in 3D parallelepiped domains.

In this work, to find the topologies satisfying the proposed targets, we test four space groups of the cubic crystal system. Thus, the achievement of composites with effective elasticity tensor having cubic symmetry is guaranteed, and the isotropic response is then enforced by adding only one scalar constraint to the topology optimization problem.

To assess the methodology, the following microarchitectures are designed and reported: two auxetic composites, three pentamode materials, and one maximum stiffness composite. With only one exception, all the remaining topologies display effective elastic properties with Zener coefficients approximating to 1.

## B.1. Introduction

The microarchitecture synthesis of composites with unusual properties that could be manufactured using a rapid prototyping technique has recently risen an enormous interest in the community, see Kadic et al. [3] and references cited therein. This interest is mainly due to the notorious advances observed in this type of material processing technique that opens the possibility of manufacturing complex microstructures.

Closely related to this topic, the authors of this paper, see Yera et al. [60], have developed a topology design technique for the microarchitecture synthesis of composites where the resulting material configurations at the microscale copy the symmetry of crystals. The design goal is to attain two-phase, stiff and void, composites with periodic microstructures and isotropic effective elastic properties close to the theoretical bounds. The crucial point of this approach is the imposition of crystal symmetries to the designed microarchitectures. This criterion could be adopted as a guiding principle in the design of new microarchitectures. A discussion about the effect that different space groups have on the realization of

[1]Corresponding author. E-mail address: ahuespe@cimec.unl.edu.ar (A.E. Huespe).

composites with properties close to the bounds have also been addressed in the contribution of Yera et al. In this work, we study the numerical aspects related to this design methodology.

The above-mentioned topology design technique is formulated as an inverse homogenization problem which closely follows the original methodology reported by Sigmund [62], Sigmund [67] and clearly explained in the book by Bendsoe y Sigmund [29]. In particular, the topology optimization algorithm that we have implemented is based on a level-set-technique with a topological derivative that has been originally reported by Amstutz y Andrä [58] and Amstutz et al. [59]. It is also worth to mention that an analogous methodology, having some elements in common with the here presented procedure, is the level-set technique reported by Allaire and co-authors, see Allaire et al. [129]. Alternative level-set-techniques for topology optimization problems can be found in the review paper by Van Dijk et al. [31].

In the present approach, the crystal symmetries are imposed to the attained topologies via a geometrical constraint on the materials configurations that are tested during the topology optimization procedure. Due to the characteristic properties of crystal symmetries, the imposition of these constraints into the topology optimization problem introduces several distinguishing features which can be summarized as follows: i) a correct selection of the space group symmetry will automatically provide the required symmetry of the target effective physical property. ii) the geometrical symmetry constraining the admissible topologies restricts the design space, or material distribution space, determining a robust performance of the topology optimization algorithm. Furthermore, we show that by imposing suitable crystal symmetries, then, a wide range of topologies can be obtained, including the well-known pentamode diamond-like microarchitecture reported by Milton y Cherkaev [70]. This solution is analyzed in sub-Section B.4.2.

Intrinsically associated to this design approach is the evaluation of the effective properties of the tested composite through a computational homogenization technique. This step is by far the most demanding computational burden of the optimization algorithm, and we adopt a Fast Fourier Transform (FFT) technique to perform it. In the case of imposing crystal symmetries, the computational homogenization may be conveniently performed in spatial domains with non-conventional shapes, such as suggested by Méndez et al. [115] and Podestá et al. [65]. Due to the FFT technique is not well suited for solving homogenization problems in design domains with complex shapes, we have adapted it to parallelepiped domains, which is sufficient for our purposes. A validation test that we present in this paper shows the performance of the FFT technique to compute the 3D elasticity tensor homogenization of the tested composites.

The authors have analyzed in Yera et al. [60] the use of several space groups of the cubic system to attain two-phase microstructures, one of them is void. In those cases, similar to the present work, the target has been the design of isotropic elastic composites whose effective properties are close to the theoretical bounds of Hashin-Shtrikmann. Here, we specifically present a restricted set of solutions that corresponds to three kind of composites, one auxetic, one maximum stiffness and three pentamodes, using cells with $256 \times 256 \times 256$ voxels. Therefore, these solutions display well-refined details.

A brief description of the paper is the following. First, in Section B.2, we summarize the topology design approach followed in this work. We emphasize the description of the FFT technique applied to problems with non-orthogonal domains. Then, this technique is validated, and its performance is assessed and compared with the finite element method.

In Section B.3, we particularize the topology design approach for solving microarchitecture design problems of isotropic composites whose effective properties are close to the theoretical bounds. In sub-Section B.3.4, we address some important issues concerning the implementation of the level-set algorithm and the imposition of crystal symmetries to the tested solutions.

Section B.4 presents the numerical assessments of the algorithm. The microarchitectures of some representative composites are designed using six space groups of the cubic crystal system to attain the isotropic response. The conclusions are presented in Section B.5. Finally, some specific aspects of the

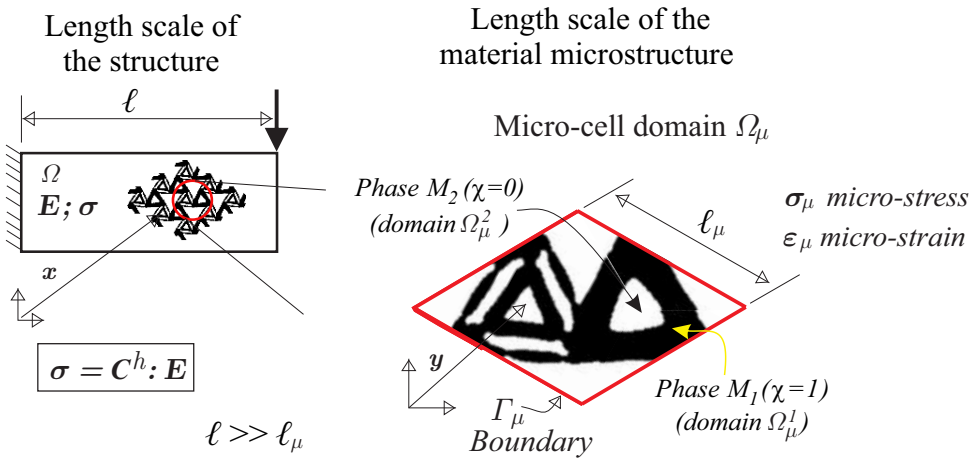


**Figura B.1:** Multiscale structural problem. Cell $\Omega_\mu$ of the composite periodic microstructure with phases $M_1$ and $M_2$. Characteristic function $\chi$. At the macrostructure scale, points are identified with $\mathbf{x}$ and the effective elastic properties of the composite are characterized by the homogenized constitutive elasticity tensor $\mathbf{C}^h$. At the microscale, points are identified with $\boldsymbol{y}$ and elasticity tensors with $\mathbf{C}$.

topological derivative of 3D homogenization problems, which is a crucial issue of the present approach, are briefly described in Appendix I. The general algorithm is presented in Appendix II.

## B.2. Topology design approach

Let us consider the structure sketched in Figure B.1 which displays a dominating size $\ell$ and is built with a material composed of two phases $M_1$, $M_2$. This composite has a periodic microstructure with a characteristic length, $\ell_\mu$. A very fundamental supposition in this work is that $\ell_\mu \ll \ell$. It is noteworthy to remark that all periodic microstructures have underlying Bravais lattices, whose features are widely exploited in this work. According to this observation, $\ell_\mu$ can be associated with the size of the primitive vectors of the lattice.

At the structural length scale, the effective elastic properties of the composite can be described through the homogenized elasticity tensor $\mathbf{C}^h$, which relates the macro-strains $\boldsymbol{E}$ with the macro-stresses $\boldsymbol{\sigma}$. A representative cell $\Omega_\mu$ of the microstructure is used to compute $\mathbf{C}^h$. For those composites displaying effective isotropic elastic responses, $\mathbf{C}^h$ is fully characterized by the effective bulk modulus $\kappa^h$ and the effective shear modulus $G^h$.

Let us suppose additionally that the material configuration at the microscale can be described with a characteristic function $\chi(\boldsymbol{y})$ defined on $\Omega_\mu$, which is 1 in the points $\boldsymbol{y}$ where phase $M_1$ exists and is 0 where phase $M_2$ exists. Thus, the expressions $\mathbf{C}^h(\chi)$, $\kappa^h(\chi)$ and $G^h(\chi)$ manifest that the homogenized elastic properties depend on the spatial distribution of phases in $\Omega_\mu$.

Under these conditions, a possible topology optimization problem consists of determining the function $\chi$ satisfying the minimum of a given target function, $f(\mathbf{C}^h)$ subjected to specified constraints.

A suitable topology optimization problem for the objective pursued in this work is defined in Section B.3. But before addressing this topic, we present with some detail, in the next two sub-Sections, two important aspects of the methodology. They are a procedure to select suitable spatial optimization domains, according to the target problem; as well as, an efficient technique for computing the homogenized elasticity tensor $(\mathbf{C}^h)$ in such optimization domains. More conventional issues about the formulation and evaluation of the elasticity tensor homogenization are presented in Appendix I.

### B.2.1. Selection of the design domain $\Omega_\mu$: Bravais lattices and unit cells

The most salient feature of the present design methodology consists of imposing a predefined crystal symmetry to the designed microarchitecture with the condition that this symmetry is compatible with the target effective elastic symmetry of the problem. For a composite with periodic microstructure, the nexus between the symmetry of its microarchitecture material configuration and the symmetry displayed by its effective physical property is given by the Neumann's principle, broadly applied in crystallography, see Nye [54].

Following this principle, Yera et al. [60] suggest the adoption of a crystal symmetry assuring the fulfillment of the target effective elastic symmetry. Recalling that the target problem in this work aims at attaining the isotropic symmetry, then, in 2D topologies, the hexagonal crystal system guarantees the attainment of this property. Contrarily, there is not any crystal system in 3D problems guaranteeing such symmetry. According to this observation, we will be only testing space groups compatible with the Cubic crystal system because it displays the higher symmetry for 3D topologies.

The geometrical symmetry characterizing a periodic microstructure can be additionally categorized with a specific crystal space group and point group[2]. Every Bravais lattice has a point group symmetry. Therefore, there is a compatibility relationship between the symmetry of the pursued effective property and a given Bravais lattice through the associated point group. This connection has been studied in greater details by the authors in previous works, see [114], [65] and [115].

Using these ideas, we propose a procedure which can be explained with the information described in Table B.1. In this Table, we show the compatibility relationships between the space groups, the point groups and the Bravais lattices for the Cubic crystal system.

Let us consider, for example, a target effective property with cubic symmetry. Then, five point groups and 36 space groups are compatible with this symmetry, such as shown in the third and fourth columns of the Table. One of these space groups is chosen with a given criterion, for example, the $I23$. Automatically, the bcc Bravais lattice is associated with it, such as shown in the last column of the table. Finally, for solving this problem with the imposed symmetry $I23$, the primitive cell of the bcc Bravais lattice should be tentatively defined as the topology optimization domain $\Omega_\mu$. Following the same idea, if the space group $P23$ were chosen, the simple cubic Bravais lattice is compatible and the corresponding simple cubic primitive cell should be adopted.

### B.2.2. Computational homogenization using a FFT technique in parallelepipedic domains

The FFT-based homogenization techniques have been introduced by Moulinec y Suquet [130] for computing the tensor $\mathbf{C}^h$ of composites with rather arbitrary microstructures. Afterward, these techniques have been improved by several authors, and particularly, Eyre y Milton [119] have introduced a specific algorithm exhibiting better convergence properties for the homogenization of composites with a large stiffness contrast between the two constituent phases. In our implementation, we follow this last approach.

Due to these techniques are now well-established, they are not shown here. Thus, the interested reader is addressed to the reference works for further details of implementations. The only issue which deserves specific attention in this work is the computation of the FFT operations in non-orthogonal domains. The effective elastic properties of the designed composites are computed with micro-cells coinciding with the spatial domains where the topology optimization problems are solved. As explained above, in general,

[2]Further details about the classification and properties of space and point groups can be found in [108] and Vainshtein [55]. The readers could also visit the web-page [118] for visualizing the symmetry elements of different space groups.

**Tabla B.1:** Cubic System. Compatible point and space groups. Bravais lattices compatible with the cubic systems are: Simple Cubic (SC), Face Centered Cubic (fcc) and Body Centered Cubic (bcc). Primitive cells of the three Bravais lattices with volumes $|\Omega_\mu^{SC}| = 1.$, $|\Omega_\mu^{fcc}| = 0.25$ and $|\Omega_\mu^{bcc}| = 0.5$. The elasticity matrix with cubic symmetry in the natural basis is represented in column 1. The symbol "$*-*$" linking two coefficients means that they are equal. Only three coefficients define the elasticity matrix in natural basis. Point and spatial groups denoted in bold text are tested in this work. The number of symmetry elements in space and point groups increases toward the descending direction of rows.

| Elasticity Tensor | Crystal System | Point Groups | Space Groups | | |
|---|---|---|---|---|---|
| $\begin{pmatrix} * & *-* & 0 & 0 & 0 \\ & * & * & 0 & 0 & 0 \\ & & * & 0 & 0 & 0 \\ & & & * & 0 & 0 \\ & & & & * & 0 \\ & & & & & * \end{pmatrix}$ | Cubic | **23** | **P23**, $P2_13$ | F23 | **I23**, $I2_13$ |
| | | $m\bar{3}$ | $Pm\bar{3}$, $Pn\bar{3}$, $Pa\bar{3}$ | $Fm\bar{3}$, $Fd\bar{3}$ | $I\bar{3}$, $Ia\bar{3}$ |
| | | 432 | P432, $P4_232$, $P4_332$, $P4_132$ | F432, $F4_132$ | I432, $I4_132$ |
| | | **$\bar{4}3m$** | $P\bar{4}3m$, $P\bar{4}3n$ | **$F\bar{4}3m$**, $F\bar{4}3c$ | **$I\bar{4}3m$**, $I\bar{4}3d$ |
| | | **$m\bar{3}m$** | **$Pm\bar{3}m$**, Pn3n, Pm3n, Pn3m | Fm3m, Fm3c, Fd3m, Fd3c | **$Im\bar{3}m$**, Ia3d |
| Compatible Bravais lattice | | | 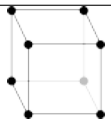 simple cubic (SC) |  fcc |  bcc |
| Primitive unit cells<br>Primitive vectors are $\boldsymbol{g}_\alpha$, $\boldsymbol{g}_\beta$ and $\boldsymbol{g}_\gamma$ | | | 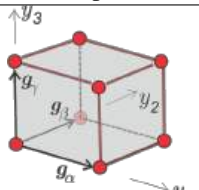 $\boldsymbol{g}_\alpha$=[1, 0, 0 ];<br>$\boldsymbol{g}_\beta$=[0, 1, 0 ];<br>$\boldsymbol{g}_\gamma$=[0, 0, 1 ]; | 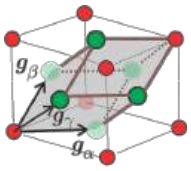 $\boldsymbol{g}_\alpha$=[0.5, 0.5 0. ];<br>$\boldsymbol{g}_\beta$=[0. , 0.5 0.5];<br>$\boldsymbol{g}_\gamma$=[0.5, 0. 0.5]; | 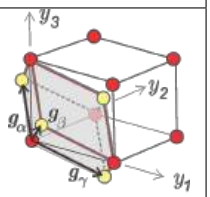 $\boldsymbol{g}_\alpha$=[-0.5, 0.5 0.5];<br>$\boldsymbol{g}_\beta$=[ 0.5, -0.5 0.5];<br>$\boldsymbol{g}_\gamma$=[ 0.5, 0.5 -0.5]; |

these domains are constituted by parallelepipeds defined by the primitive vectors of Bravais lattices, and therefore, they are not rectangular prisms.

### FFT in non-orthogonal coordinates

For simplicity, we describe the computation of the FFT in non-orthogonal coordinates using a two-dimensional geometry. Its generalization to 3D problems is direct.

Let us consider a periodic material whose underlying Bravais lattice has non-orthogonal primitive vectors, $\boldsymbol{g}_\alpha$ and $\boldsymbol{g}_\beta$, such as sketched in Figure B.2. We introduce the basis $\{\boldsymbol{g}_\alpha, \boldsymbol{g}_\beta\}$ to define a non-orthogonal coordinate system with an homogeneous metric tensor. A position vector $\boldsymbol{y}$ in this basis is expressed according to $\boldsymbol{y} = \theta^\alpha \boldsymbol{g}_\alpha + \theta^\beta \boldsymbol{g}_\beta$ ($\alpha$ and $\beta$ identify different basis vectors, and therefore, the summation convention of repeated index is not applied), where $\{\theta^\alpha, \theta^\beta\}$ are the corresponding pair of coordinates, i.e., the contravariant components of $\boldsymbol{y}$.

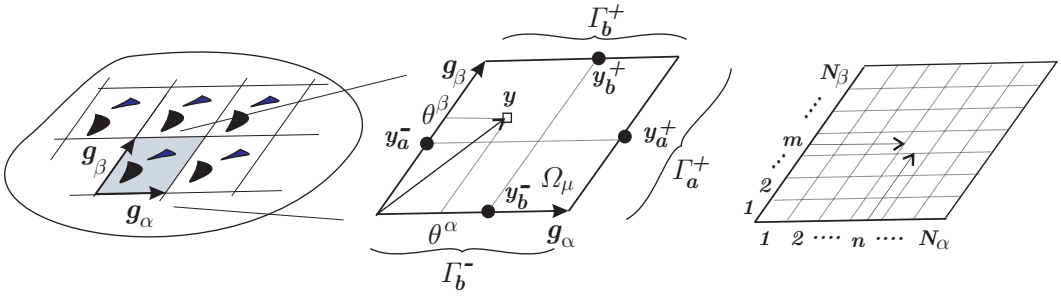


**Figura B.2:** Periodic microcell along non-orhogonal directions $\boldsymbol{g}_\alpha$ and $\boldsymbol{g}_\beta$. Identification of the $nm$-th pixel.

Let us also consider a periodic mechanical problem such that the fluctuation of the micro-displacements $\tilde{\boldsymbol{u}}$ and micro-tractions $\boldsymbol{t}$ are periodic and antiperiodic, respectively, along the directions $\boldsymbol{g}_\alpha$ and $\boldsymbol{g}_\beta$. Therefore, by defining the unit cell domain $\Omega_\mu$, the following identities are satisfied on its boundary:

$$\begin{aligned} \tilde{\boldsymbol{u}}(\boldsymbol{y}_a^+) = \tilde{\boldsymbol{u}}(\boldsymbol{y}_a^-)\ ;\ \boldsymbol{t}(\boldsymbol{y}_a^+) = -\boldsymbol{t}(\boldsymbol{y}_a^-) \quad \forall \boldsymbol{y}_a^+ \in \Gamma_a^+ \text{ and } \boldsymbol{y}_a^+ = \boldsymbol{y}_a^- + \boldsymbol{g}_\alpha \\ \tilde{\boldsymbol{u}}(\boldsymbol{y}_b^+) = \tilde{\boldsymbol{u}}(\boldsymbol{y}_b{}^-)\ ;\ \boldsymbol{t}(\boldsymbol{y}_b^+) = -\boldsymbol{t}(\boldsymbol{y}_b^-) \quad \forall \boldsymbol{y}_b{}^+ \in \Gamma_b^+ \text{ and } \boldsymbol{y}_b^+ = \boldsymbol{y}_b^- + \boldsymbol{g}_\beta \end{aligned} \tag{B.1}$$

Furthermore, we can express every component of the displacements, the strains and the stresses as fields in terms of the contravariant coordinates. Let one of these periodic function, for example a strain component, be denoted $f(\theta^\alpha, \theta^\beta)$. Then, $f$ satisfies $f(\theta^\alpha + \Delta\theta^\alpha, \theta^\beta) = f(\theta^\alpha, \theta^\beta)$ and $f(\theta^\alpha, \theta^\beta + \Delta\theta^\beta) = f(\theta^\alpha, \theta^\beta)$ with $\Delta\theta^\alpha = 1$ and $\Delta\theta^\beta = 1$. These fields can be transformed to the frequency domain using the Fourier Transform along the directions $\boldsymbol{g}_\alpha$ and $\boldsymbol{g}_\beta$:

$$\hat{f}(\zeta_\alpha, \zeta_\beta) = \int_0^1 \int_0^1 f(\theta^\alpha, \theta^\beta) e^{-i(\zeta_\alpha \theta^\alpha + \zeta_\beta \theta^\beta)} d\theta^\alpha d\theta^\beta\ ; \tag{B.2}$$

where the two frequencies $(\zeta_\alpha, \zeta_\beta)$ can be interpreted as the covariant components of the frequency vector $\boldsymbol{\xi} = \zeta_\alpha \boldsymbol{G}^\alpha + \zeta_\beta \boldsymbol{G}^\beta$, being $\{\boldsymbol{G}^\alpha, \boldsymbol{G}^\beta\}$ the reciprocal basis of $\{\boldsymbol{g}_\alpha, \boldsymbol{g}_\beta\}$ satisfying $\boldsymbol{G}^i \cdot \boldsymbol{g}_j = \delta_{ij}$ with $\delta_{ij}$ the Kronecker delta function.

By taking into account these preliminary concepts, the homogenized properties of periodic composites characterized by unit cells defined by non-orthogonal primitive vectors can be computed with the FFT algorithm. A brief summary of this algorithm implementation is next described:

*1* First, the unit cell is partitioned in $(N_\alpha \times N_\beta)$ pixels[3]; $N_\alpha$ in the direction $\boldsymbol{g}_\alpha$ and $N_\beta$ in the direction $\boldsymbol{g}_\beta$, such as shown in Figure B.2. The following set of discrete frequencies are defined:

$$\begin{aligned} \boldsymbol{\zeta}_\alpha = [\zeta_\alpha^{(1)}, \zeta_\alpha^{(2)}, ..., \zeta_\alpha^{(n)}, ..., \zeta_\alpha^{(N_\alpha)}] = \left[-\frac{N_\alpha}{2} + 1, -\frac{N_\alpha}{2} + 2, ..., \frac{N_\alpha}{2}\right] \quad ; \\ \boldsymbol{\zeta}_\beta = [\zeta_\beta^{(1)}, \zeta_\beta^{(2)}, ..., \zeta_\beta^{(m)}, ..., \zeta_\beta^{(N_\beta)}] = \left[-\frac{N_\beta}{2} + 1, -\frac{N_\beta}{2} + 2, ..., \frac{N_\beta}{2}\right] \quad ; \\ \text{for } N_\alpha \text{ and } N_\beta \text{ even,} \end{aligned}$$

(if $N_\alpha$ or $N_\beta$ are odd, the formula in Moulinec et al. can be used). From them, we define the $(N_\alpha \times N_\beta)$ vectors of discrete frequencies transformed to the Cartesian coordinates:

$$[\boldsymbol{\xi}^{(n,m)}] = \zeta_\alpha^{(n)} \boldsymbol{G}^\alpha + \zeta_\beta^{(m)} \boldsymbol{G}^\beta\ . \tag{B.3}$$

*2* The Green operator in the frequency space, $\boldsymbol{\Gamma}^0$, is evaluated for every vector $\boldsymbol{\xi}^{(n,m)}$ as follows:

$$\boldsymbol{\Gamma}^0(\boldsymbol{\xi}^{(n,m)}) = \boldsymbol{\xi}^{(n,m)} \left(\boldsymbol{\xi}^{(n,m)} \cdot \mathbf{C}^0 \cdot \boldsymbol{\xi}^{(n,m)}\right)^{-1} \boldsymbol{\xi}^{(n,m)}\ . \tag{B.4}$$

with $\mathbf{C}^0$ being a reference elasticity tensor. Note that equation (B.4), expressed in intrinsic notation, could be computed using Cartesian components, in particular $\mathbf{C}^0$ is the conventional matrix of the elastic Hooke law in Cartesian components.

*3* Proceed in a standard way with the algorithm defined in Eyre et al.

Note that the stress and strain fields in both, space and frequency, domains that arise in the algorithm (10) of the reference work have the components described in Cartesian basis.

[3]The generalization to three-dimensional microcell homogenization is direct by considering $N_\alpha \times N_\beta \times N_\gamma$ voxels.

In the following, we use indices with Arabic numerals for denoting the components of tensors in Cartesian coordinates. Additionally, we use Kelvin notation for second and fourth order tensors. The stress tensor components $\{\sigma_{y_1y_1}, \sigma_{y_2y_2}, \sigma_{y_3y_3}, \sigma_{y_1y_2}, \sigma_{y_1y_3}, \sigma_{y_2y_3}\}$ are represented with Arabic numeral indices as follows: $\{\sigma_1, \sigma_2, \sigma_3, \sigma_4, \sigma_5, \sigma_6\}$, respectively. The stress vector in Kelvin notation results $(\sigma_1, \sigma_2, \sigma_3, \sqrt{2}\sigma_4, \sqrt{2}\sigma_5, \sqrt{2}\sigma_6)$. An identical criterion is used for strains. In consequence, the corresponding elasticity matrix are denoted with two Arabic indices: $C_{ij}$, with $i, j = 1, ..., 6$.

**Validation tests**

Next, we validate the FFT technique. The effective elasticity tensor of a composite constituted of a stiff phase with an array of spherical voids geometrically placed in the positions occupying the atoms of a face-centered cubic (fcc) Bravais lattice is computed. Then, we analyze the computational cost (time) vs. accuracy that demands to solve this problem with the FFT, using different densities of grids. We also compare these results with those obtained with the Finite Element Method (FEM).

Due to the symmetry of this microarchitecture, the effective elasticity tensor displays cubic symmetry. The Young modulus of the stiff phase, $M_1$, is $E_1 = 1$ and the Poisson's ratio is $\nu_1 = 0.4$. The spherical voids have a radius of 0.15, wherewith the volume fraction of the composite stiff phase is $f_1 = 0.9435$. The analytic reference solution of the effective elastic moduli, reported by Cohen [131], is given by: $(C^h_{ref})_{11} = (C^h_{ref})_{22} = (C^h_{ref})_{33} = 1.7415$, $(C^h_{ref})_{12} = (C^h_{ref})_{23} = (C^h_{ref})_{13} = 1.0982$ and $(C^h_{ref})_{44} = (C^h_{ref})_{55} = (C^h_{ref})_{66} = 0.6456$. This solution is calculated considering that the second phase is void.

In the numerical model, the void phase, $M_2$, is assumed to be a soft elastic material whose Young modulus is $E_2 = \gamma E_1$ with the contrast factor $\gamma = 10^{-4}$. We also show here that this factor is small enough to simulate the void. The Poisson's ratio is taken as $\nu_2 = \nu_1$.

The computational homogenization is evaluated on a primitive micro-cell $\Omega^p_\mu$ of the fcc lattice, such as displayed in Figure B.3-c. Conventional and primitive cells are shown in Figure B.3-a and c. Superscript $p$ and $c$ indicates primitive and conventional unit cells, respectively. The conventional unit cell size is $1 \times 1 \times 1$. Note that the primitive cell has a volume $|\Omega^p_\mu| = 0.25$ compared with the volume of the conventional unit cell whose volume is $|\Omega^c_\mu| = 1$. Therefore, to attain similar accuracies, the micro-cell $\Omega^c_\mu$ requires 4 times more voxels than the micro-cell $\Omega^p_\mu$. This feature of the primitive cell is remarkably most important for the design of microarchitectures. In fact, for the same composite, the primitive cell displays simpler topologies respect to those described by the conventional unit cell.

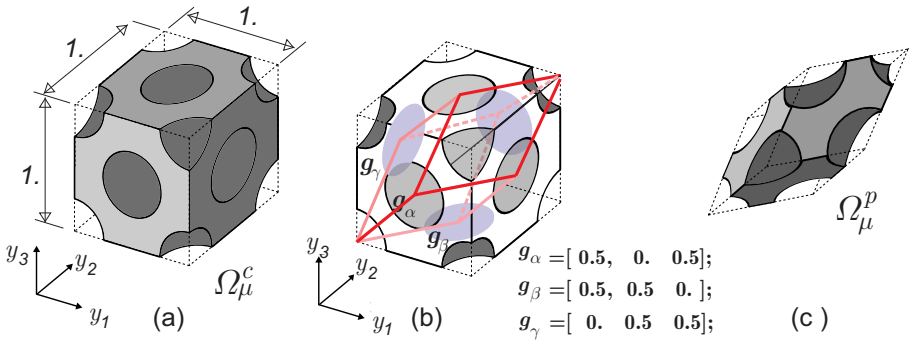


**Figura B.3:** Validation tests. Composite microstructure. (a) Conventional unit cell $\Omega^c_\mu$; (b-c) primitive unit cell $\Omega^p_\mu$. The primitive vectors $\boldsymbol{g}_\alpha$, $\boldsymbol{g}_\beta$ and $\boldsymbol{g}_\gamma$ also define the periodicity directions.

Results are plotted in Figure B.4. The curves show the computation time needed for solving every problem vs. the solution error using the primitive cell $\Omega^p_\mu$. The errors are computed as the normalized Frobenius norm of the difference between the computed elasticity tensor $\mathbf{C}^h$ and the reference one $\mathbf{C}^h_{ref}$. The numbers in the Figure indicate the grid densities and represent the number of voxels in each di-

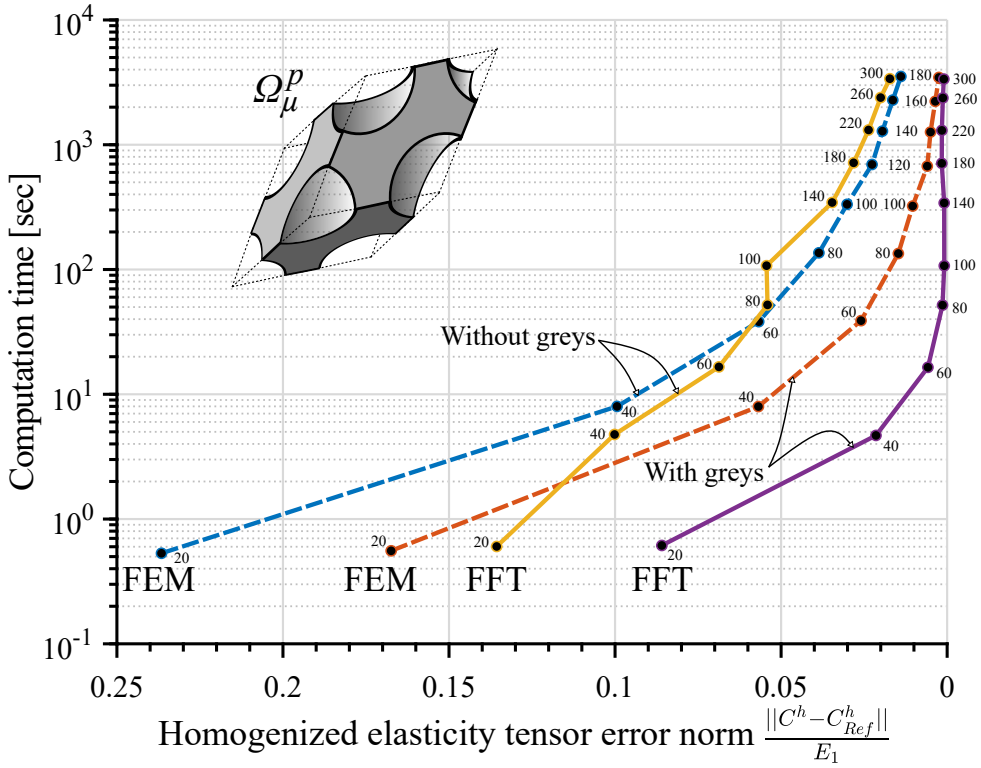


**Figura B.4:** Computation time vs. normalized errors to evaluate the homogenized elasticity tensors (Frobenius norm). Solutions obtained with a primitive cell ($\Omega^p_\mu$). Numbers indicate the grid density size of each solution. Comparison of FEM vs. FFT solutions.

mension. For example, the number 300 indicates that the solution is obtained with a discretization of $300 \times 300 \times 300$ voxels. The finite element mesh is built by taking the same spatial distribution of voxels and dividing each one of them into six linear tetrahedra. Solutions denoted "*without greys*" are obtained with voxels (FFT) or finite elements (FEM) having the properties of only one of the two phases. On the other hand, solutions denoted "with greys" apply the below formulas (B.20) and (B.21) to define the material properties of voxels and tetrahedra. In the case of the FFT solutions, the eight vertices of each voxel are used for this determination, but for the FEM solutions, the four nodes of every tetrahedron are used to define the property of the finite element.

As expected, the FEM and FFT methodologies tend to the correct solution by increasing the grid density. However, it is notable the effect induced by the inclusion of the grey material in both methodologies. This effect is still more remarkably in the FFT technique, there are striking differences in favor of this technique. To attain similar error levels in the computation of the effective elasticity tensor, the cost of FEM solutions is more than one order higher than that using the FFT technique. A different conclusion would be attained if grey elements were removed from the model.

The FEM uses a linear equation system iterative solver (conjugate gradient method) with incomplete Cholesky preconditioning (IChol). The error tolerances for both methodologies (FEM with iterative solver and FFT) have been fixed to $10^{-6}$, and their implementations have been optimized to run in MATLAB using an Intel i9-9900K Processor with 64GB of memory ram and Intel Turbo Boost activated.

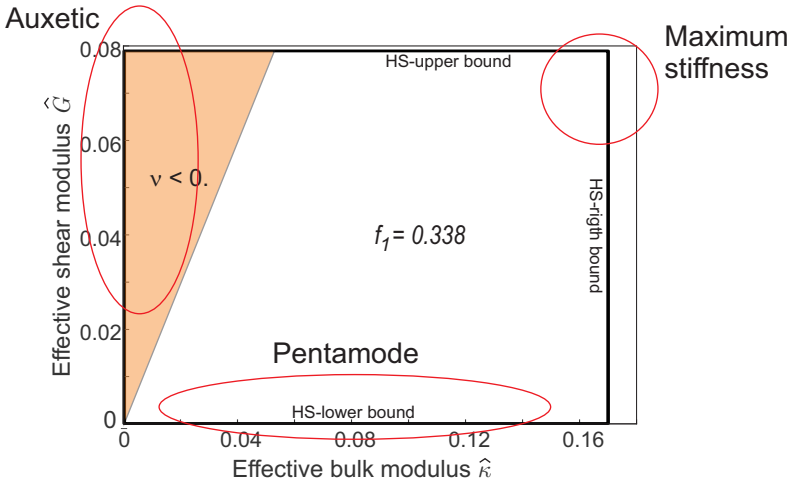


**Figura B.5:** Theoretical bounds of effective properties for two-phase isotropic 3D composites according to Hashin y Shtrikman [22] (HS-bounds). Properties of phases $M_1$ and $M_2$ are $\kappa_1 = 1.667$, $G_1 = 0.3571$, $\kappa_2 = \gamma\kappa_1$, $G_2 = \gamma G_1$, contrast factor $\gamma = 10^{-4}$, volume fraction $f_1 = 0.338$.

## B.3. Microarchitecture design of isotropic elastic composites

### B.3.1. Bounds of the effective elastic property of two-phase well-ordered composites

Let us consider the full set of periodic composites with isotropic effective elastic properties and two isotropic elastic phases $M_1$ and $M_2$ whose bulk moduli are $\kappa_1$, $\kappa_2$, with $\kappa_2 < \kappa_1$, and shear moduli $G_1$, $G_2$, with $G_2 < G_1$, respectively, and a volume fraction of $M_1$ equal to $f_1$. Then, the effective properties of these composites, typically the bulk and shear effective moduli, $\hat{\kappa}$ and $\hat{G}$, are bounded: $\hat{\kappa}^l \leq \hat{\kappa} \leq \hat{\kappa}^u$, $\hat{G}^l \leq \hat{G} \leq \hat{G}^u$, where $\hat{\kappa}^u$ and $\hat{\kappa}^l$ are the upper and lower bounds of the effective bulk modulus, and, $\hat{G}^u$ and $\hat{G}^l$ are the upper and lower bounds of the effective shear modulus. These bounds have been theoretically estimated with the expressions derived by[4] Hashin y Shtrikman [22] as follows:

$$\hat{\kappa}^u = \kappa_1 + \frac{1-f_1}{\frac{1}{\kappa_2-\kappa_1} + 3\frac{f_1}{3\kappa_1+4G_1}} \quad ; \quad \hat{\kappa}^l = \kappa_2 + \frac{f_1}{\frac{1}{\kappa_1-\kappa_2} + 3\frac{1-f_1}{3\kappa_2+4G_2}} \; ; \tag{B.5}$$

$$\hat{G}^u = G_1 + \frac{1-f_1}{\frac{1}{G_2-G_1} + \frac{6(\kappa_1+2G_1)f_1}{5G_1(3\kappa_1+4G_1)}} \quad ; \quad \hat{G}^l = G_2 + \frac{f_1}{\frac{1}{G_1-G_2} + \frac{6(\kappa_2+2G_2)(1-f_1)}{5G_2(3\kappa_2+4G_2)}} \; .$$

For composites constituted of two phases characterized by $\kappa_1 = 1.667$, $G_1 = 0.3571$, $\kappa_2 = \gamma\kappa_1$, $G_2 = \gamma G_1$, with the contrast factor $\gamma = 10^{-4}$, and a volume fraction $f_1 = 0.338$, these bounds are: $\hat{\kappa}^u = 0.170$; $\hat{\kappa}^l = 2.8 \times 10^{-4}$; $\hat{G}^u = 0.789$; $\hat{G}^l = 7.3 \times 10^{-5}$ and they are plotted in Figure B.5 and are denoted the HS-bounds.

### B.3.2. Topology optimization problems

The goal is to design the family of two-phase composites with a predefined volume fraction, whose effective properties are isotropic and furthermore, they are the closest one to the four HS-bounds. The mathematical formulations chosen for solving this problem are the following.

Given the micro-cell $\Omega_\mu$, we define the characteristic function $\chi(\boldsymbol{y})$ identifying the positions where

[4]Tighter bounds were reported by Berryman y Milton [52]. However, the bounds coincide with the Hashin-Shtrikmann ones when one of the phases is void.

the phase $M_1$ is placed. It is defined by:

$$\chi(\boldsymbol{y}) = \begin{cases} 0 & \forall \boldsymbol{y} \in \Omega_\mu^2 \\ 1 & \forall \boldsymbol{y} \in \Omega_\mu^1 \end{cases} . \tag{B.6}$$

Then,

*i)* To approach the inferior HS-bound, the problem is written as:

$$\begin{aligned} &\min_{\chi} \; G^h(\chi); \\ &\text{such that:} \quad \kappa^h(\chi) - \kappa^{tg} = 0 \\ &\qquad\qquad \mathbf{C}^h(\chi) \text{ is isotropic} \\ &\qquad\qquad {f_1}^h(\chi) - {f_1}^{tg} = 0 \end{aligned} \tag{B.7}$$

where $\kappa^{tg}$ is the target bulk modulus of the composite defined within the interval $\hat{\kappa}^l \leq \kappa^{tg} \leq \hat{\kappa}^u$, ${f_1}^h(\chi) = \int_{\Omega_\mu} \chi \, d\Omega$ is the volume fraction of phase $M_1$ and ${f_1}^{tg}$ is the target volume fraction. The solutions approaching the HS-lower bound can be obtained by solving a series of problems (B.7), with $\kappa^{tg}$ sweeping the range of the interval $[\hat{\kappa}^l, \hat{\kappa}^u]$.

*ii)* An alternative problem is formulated to approach the left Hashin-Strikman bound, as follows:

$$\begin{aligned} &\min_{\chi} \kappa^h(\chi); \\ &\text{such that:} \quad G^h(\chi) - G^{tg} = 0 \\ &\qquad\qquad \mathbf{C}^h(\chi) \text{ is isotropic} \\ &\qquad\qquad {f_1}^h(\chi) - {f_1}^{tg} = 0 \end{aligned} \tag{B.8}$$

where now, the target effective shear modulus $G^{tg}$ is chosen from the interval $\hat{G}^l \leq G^{tg} \leq \hat{G}^u$. Similarly as described above, the solutions approaching the HS-left bound can be obtained by solving a series of problems with $G^{tg}$ sweeping the range of the interval $[\hat{G}^l, \hat{G}^u]$.

*iii)* In a similar way, the Hashin-Strikman superior and right bounds are approached by changing the minimization problems in (B.7) and (B.8) respectively, by one of maximization.

### B.3.3. Rephrasing the topology optimization problems for microstructures with cubic crystal symmetries

Microstructures possessing a cubic crystal system have effective elastic responses with cubic symmetry. Thus, such as shown in Table B.1, the coefficients of their elasticity matrices satisfy the following identities: $C_{11}^h = C_{22}^h = C_{33}^h$ ; $C_{12}^h = C_{13}^h = C_{23}^h$ ; $C_{44}^h = C_{55}^h = C_{66}^h$. The remaining coefficients are strictly equal to zero.

According to this observation, as long as it can be guaranteed in advance that the microstructure will have a cubic system, the topology optimization problems (B.7)–(B.8) can be rephrased in terms of the elasticity matrix coefficients as follows:

$$\begin{aligned} &\min_{\psi \in C^0} \; C_{44}^h; \\ &\text{such that:} \quad h_1 = C_{11}^h + 2C_{12}^h - 3\kappa^{tg} = 0 \\ &\qquad\qquad h_2 = C_{11}^h - C_{12}^h - C_{44}^h = 0 \\ &\qquad\qquad h_3 = {f_1}^h(\chi) - {f_1}^{tg} = 0 \end{aligned} \tag{B.9}$$

$$\min_{\psi\in C^0}(C^h_{12}+\frac{1}{3}C^h_{44}); \tag{B.10}$$

$$\begin{aligned}\text{such that:}\quad & h_1 = C^h_{11}-C^h_{12}+\frac{3}{2}C^h_{44}-5G^{tg}=0\\ & h_2 = C^h_{11}-C^h_{12}-C^h_{44}=0\\ & h_3 = f^h_1(\chi)-{f_1}^{tg}=0\end{aligned}$$

Note that the coefficients of any isotropic elasticity tensor satisfy the following conditions: *a)* $C^h_{44}=2G$, *b)* $C^h_{12}+\frac{1}{3}C^h_{44}=\kappa$ , *c)* $C_{11}+2C_{12}=3\kappa$, and *d)* $C_{11}-C_{12}+3C_{44}/2=5G$; being $\kappa$ and $G$ the bulk and shear moduli of the material. Thus, after assuming that $\kappa$ is the target bulk modulus of the problem (B.7), the objective function of this problem is replaced by the identity *a)*. The first constraint can be replaced by *c)*, which results the constraint $h_1$ in the rephrased formulation (B.9), while $h_2$ of the rephrased formulation ensures the isotropic response. An identical consideration can be applied to reformulate the problem (B.8). In this case, by assuming that $G$ is the target shear modulus, the objective function of (B.8) is replaced by *b)*, the first constraint is replaced by *d)*, which results the constraints $h_1$ in the rephrased formulation (B.10) and constraint $h_2$ ensures the isotropic response.

### B.3.4. Level-Set topology optimization algorithm

The topology optimization algorithm for solving the problems (B.9)–(B.10) uses the level-set method, combined with topological derivatives. The topological derivative provides the sensitivity of the target properties with changes of the characteristic function $\chi$. The numerical technique based on these ingredients, and which is used in this paper, follows the original ideas of the algorithm presented by Amstutz y Andrä [58] and Amstutz et al. [59]. The topological derivative concept is well described in the book by Novotny y Sokołowski [57]. Alternative formulations of topology optimizations problems using topological derivative and level-set functions have also been reported in the works of Allaire and co-authors, see Allaire et al. [129] and references cited therein.

Let us introduce a smooth level-set function $\psi$ defined in the microcell $\Omega_\mu$, $\psi\in C^0(\Omega_\mu)$, satisfying

$$\psi(\boldsymbol{y})=\begin{cases}>0 & \forall \boldsymbol{y}\in\Omega^2_\mu\\ <0 & \forall \boldsymbol{y}\in\Omega^1_\mu\\ =0 & \forall \boldsymbol{y}\in\partial\Omega^1_\mu\end{cases}, \tag{B.11}$$

then, the characteristic functions $\chi(\boldsymbol{y})$ in $\Omega_\mu$, given by expression (B.6), can be redefined as follows:

$$\chi_\psi=\begin{cases}1 & \forall\psi\le 0\\ 0 & \forall\psi>0\end{cases}. \tag{B.12}$$

and problems (B.9)–(B.10) can be written in terms of $\chi_\psi$:

$$\min_{\psi\in C^0}\ C^h_{44}(\chi_\psi); \tag{B.13}$$

$$\begin{aligned}\text{such that:}\quad & h_1 = C^h_{11}(\chi_\psi)+2C^h_{12}(\chi_\psi)-3\kappa^{tg}=0\\ & h_2 = C^h_{11}(\chi_\psi)-C^h_{12}(\chi_\psi)-C^h_{44}(\chi_\psi)=0\\ & h_3 = f^h_1(\chi_\psi)-{f_1}^{tg}=0\end{aligned}$$

$$\min_{\psi \in C^0} (C^h_{12}(\chi_\psi) + \frac{1}{3} C^h_{44}(\chi_\psi)); \tag{B.14}$$

$$\begin{aligned} \text{such that:} \quad & h_1 = C^h_{11}(\chi_\psi) - C^h_{12}(\chi_\psi) + \frac{3}{2} C^h_{44}(\chi_\psi) - 5G^{tg} = 0 \\ & h_2 = C^h_{11}(\chi_\psi) - C^h_{12}(\chi_\psi) - C^h_{44}(\chi_\psi) = 0 \\ & h_3 = f^h_1(\chi_\psi) - {f_1}^{tg} = 0 \end{aligned}$$

By making use of an augmented Lagrangian technique, see Lopes et al. [132], problem (B.13) (similarly for (B.14)) is reformulated as follows:

$$\max_{\lambda} \min_{\psi} \mathcal{T}(\chi_\psi, \lambda), \tag{B.15}$$

with:

$$\mathcal{T}(\chi_\psi, \lambda) = C^h_{44} + \lambda_1 h_1 + \lambda_2 h_2 + \lambda_3 h_3 + \frac{\alpha}{2} \left( h_1^2 + h_2^2 + h_3^2 \right) \tag{B.16}$$

where the $\lambda_i$, with $i = 1, 2, 3$, are the Lagrange multipliers and $\alpha$ is the penalty parameter of the augmented term.

The solution of problem (B.15) is found by using a descent direction algorithm. Neither the Lagrangian (B.16) nor the fields involved in this expression are differentiable for changes of topologies. However, the sensitivities of the field and the Lagrangian can be obtained by applying the topological derivative concept which formally follows the rules of the differential calculus, typically, the chain rule, such as suggested by Amstutz y Andrä [58].

Following the above-mentioned reference works on this topic, the topological derivative of $\mathcal{T}$ at point $\boldsymbol{y}$, denoted $D_T\mathcal{T}(\boldsymbol{y})$, provides the sensitivity of the functional $\mathcal{T}$ with changes of $\chi$ at the same point. Let us consider the perturbed characteristic function, $\chi_\epsilon$, of the characteristic function $\chi$, that is defined after an interchange of phases within a ball of radius $\epsilon$ and centered at the point $\boldsymbol{y}$. Then the topological derivative satisfies:

$$\mathcal{T}(\chi_\epsilon, \lambda) = \mathcal{T}(\chi, \lambda) + f(\epsilon) D_T\mathcal{T}(\boldsymbol{y}, \lambda) + \mathcal{O}(\epsilon^3) \tag{B.17}$$

where $f(\epsilon)$ is a term proportional to the perturbed ball volume, and therefore, to $\epsilon^3$ in 3D problems. Equation (B.17) allows to identify $D_T\mathcal{T}(\boldsymbol{y}, \lambda)$ as the element indicating, at every point of the domain, if a phase change would induce, or not, a decrease of the functional $\mathcal{T}$. This criteria naturally provides a descent direction for modifying the level-set function during an iterative process. This point is further developed in sub-Section B.3.4.

The expression for the topological derivative of $\mathcal{T}$ can be written in terms of the topological derivative of the components of the homogenized elasticity tensor $C^h_{ij}$, denoted $D_T C^h_{ij}$, by simply applying the conventional chain rule to (B.16), as follows:

$$D_T\mathcal{T}(\boldsymbol{y}, \lambda) = D_T C^h_{44}(\boldsymbol{y}) + \sum_{i=1}^{3} \lambda_i \, D_T h_i(\boldsymbol{y}) + \alpha \sum_{i=1}^{3} \left( h_i \, D_T h_i(\boldsymbol{y}) \right) \ , \tag{B.18}$$

and the expressions of the derivatives of the constrains $D_T h_i$ are:

$$\begin{aligned} D_T h_1 &= D_T C^h_{11} + 2 D_T C^h_{12} \\ D_T h_2 &= D_T C^h_{11} - D_T C^h_{12} - D_T C^h_{44} \\ D_T h_3 &= 1 \end{aligned} \tag{B.19}$$

Furthermore, the topological derivative terms, $D_T C^h_{ij}$, can be computed with the expression (B.35) described in Appendix I.

Analogous treatment is performed on equation (B.14), but it is not shown here.

**Algorithm implementation**

Next, we describe the implementation of the level-set methodology in the context of an FFT technique for computational homogenization. This implementation can be compared with alternative approaches of level-set-methodologies reported in the revision paper by Van Dijk et al. [31].

The iterative algorithm for solving the topology optimization problems (B.13) and (B.14) are described in Appendix II. In particular, two alternative schemes are defined for computing the iterative step length.

*i)* **Parametrization of the level-set-function (LSF)**

The FFT technique makes use of a discretization of the unit cell defined through a uniform grid of $(N_\alpha+1)\times(N_\beta+1)\times(N_\gamma+1)$ points, such as schematized in Figure B.6. These points divide the volume in $N_\alpha \times N_\beta \times N_\gamma$ voxels; being $N_\alpha$, $N_\beta$ and $N_\gamma$ the number of voxels along the coordinate directions $\boldsymbol{g}_\alpha$, $\boldsymbol{g}_\beta$ and $\boldsymbol{g}_\gamma$, respectively. The vertices of these voxels are the grid points.

The level-set-function $\psi(\boldsymbol{y})$ is defined in the grid points and is identified by $\hat{\psi}_p = \psi(\boldsymbol{y}_p)$, where $\boldsymbol{y}_p$ is the spatial position of the $p-$th grid point. The set $\{\hat{\psi}_p\}$, for: $p = 1, ..., (N_\alpha+1)(N_\beta+1)(N_\gamma+1)$ are the level-set-function parameters.

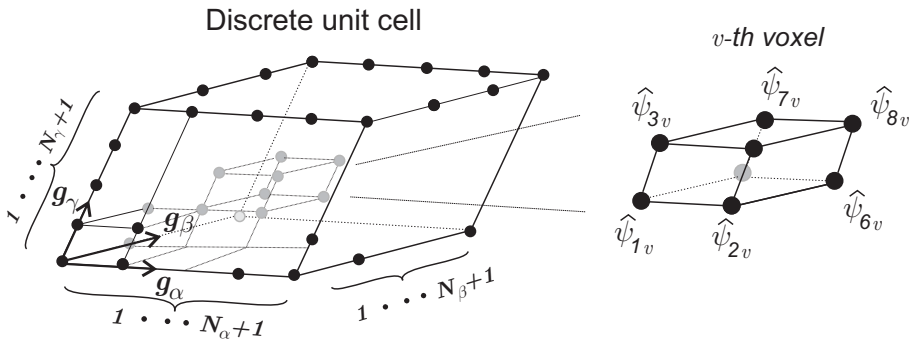


**Figura B.6:** Discrete unit cell. Parameters of the level-set-function associated with the $v-$th voxel.

*ii)* **Geometry mapping from the LSF parametrization**

The elastic property of the $v-$th voxel represented in Figure B.6, is characterized with the elasticity tensor $\hat{\mathbf{C}}^v$ that is computed with the convex combination of the elasticity tensors $\mathbf{C}_{M_1}$ and $\mathbf{C}_{M_2}$, of phases $M_1$ and $M_2$ respectively, as follows:

$$\hat{\mathbf{C}}^v = \hat{\omega}^v \mathbf{C}_{M_1} + (1-\hat{\omega}^v)\mathbf{C}_{M_2} \tag{B.20}$$

where the coefficient $\hat{\omega}^v$, of the $v-$th voxel, is evaluated with the eight level-set function parameters, $\hat{\psi}_{p_v}$ for: $p_v = 1, ..., 8$, that correspond to the $v-$th voxel vertices, as follows

$$\hat{\omega}^v = \frac{\sum_{p_v=1}^{8} |\hat{\psi}^-_{p_v}|}{\sum_{p_v=1}^{8} |\hat{\psi}_{p_v}|} \quad ; \quad \hat{\psi}^-_{p_v} = \begin{cases} \hat{\psi}_{p_v} & \text{if: } \hat{\psi}_{p_v} < 0; \\ 0 & \text{otherwise} \end{cases} \tag{B.21}$$

with $\hat{\omega}^v \in [0,1]$. The numerator of this expression is the addition of the absolute values of the level-set function parameters with negative values.

The term $\hat{\omega}^v$ plays the role of a smoothed characteristic function, similar to $\chi$ defined in equation (B.6). According to equations (B.20) and (B.21), if the eight level-set-function parameters of a voxel are negative (positive), the elasticity tensor coincides with the elasticity tensor of phase

$M_1$ ($M_2$). Alternatively, if the level-set function parameters are positive and negative, the material elastic stiffness can be interpreted as a mixture with proportional stiffness to $\hat{\omega}^v$. The salient feature of equation (B.21) is that a smooth transition from $\mathbf{C}_{M_1}$ to $\mathbf{C}_{M_2}$ is induced by a continuous movement of the interface, i.e., the zero iso-surface level-set function, across the voxel.

*iii)* **Updating the LSF parameters**

Once the topological derivative of $\mathcal{T}$ is known, the level-set-function is updated, at iteration $k+1$, as follows:

$$\psi^{k+1} = \psi^k + \tau g, \tag{B.22}$$

where $g(\boldsymbol{y})$ is defined by:

$$g(\boldsymbol{y}) = \begin{cases} -(D_T\mathcal{T}) & if : \psi < 0 \\ +(D_T\mathcal{T}) & if : \psi > 0 \end{cases} , \tag{B.23}$$

and can be interpreted as a descent direction of $\mathcal{T}$, and $\tau$ is a step length. Additional discussions for determining the value of the $\tau$ are presented in Appendix II.

For the problem (B.13), the topological derivative of $\mathcal{T}$ is initially computed in the $N_\alpha \times N_\beta \times N_\gamma$ voxels according to equations (B.18), (B.19) and (B.35). Then, they are mapped to the grid points by averaging the values of the neighboring voxels. The resulting nodal derivative at the generic grid point $p$ is denoted $\hat{g}_p$. Finally, the level-set function parameters in the grid points are updated with equation (B.22).

The iterative updating of the Lagrange multipliers $\lambda_i$ of the Lagrangian function $\mathcal{T}$ are further discussed in the Appendix II.

*iv)* **Regularization and filtering of the LSF parameters**

The level-set function parameters are filtered through a discrete convolution product

$$\psi^f(\boldsymbol{y}_p) = (\psi * K)(\boldsymbol{y}_p) \; ; \tag{B.24}$$

where $\psi^f$ are the level-set function parameters after the filtering and the discrete convolution product is defined as

$$\psi^f(\boldsymbol{y}_p) = (\psi * K)(\boldsymbol{y}_p) = \sum_{k=1}^{(N_\alpha+1)\times(N_\beta+1)\times(N_\gamma+1)} \hat{\psi}_k K(\boldsymbol{y}_k - \boldsymbol{y}_p) \; ; \tag{B.25}$$

and the Kernel $K$ is

$$K(\mathbf{x}) = \begin{cases} \beta - \frac{\|\mathbf{x}\|}{\ell_f} & if : \|\mathbf{x}\| < \ell_f \\ 0 & if : \|\mathbf{x}\| > \ell_f \end{cases} \; ; \tag{B.26}$$

with the coefficient $\beta$ being taken such that $\sum_k K(\boldsymbol{y}_k - \boldsymbol{y}_p) = 1$, for all $p$. The filter radius $\ell_f$ determines the minimum allowed length scale of the designed topology. The topological derivative is also filtered with a similar expression.

*v)* **Convergence criterion**

Convergence is achieved when the following two criteria are accomplished:

*a)* Following to Amstutz [133], a local optimality criterion of problem (B.15) is given by the condition

$$D_T\mathcal{T} > 0 \quad ; \quad \forall \boldsymbol{y} \in \Omega_\mu$$

which can be implemented by verifying the inequality

$$\frac{\hat{\boldsymbol{g}} \cdot \hat{\boldsymbol{\psi}}}{\|\hat{\boldsymbol{g}}\|\|\hat{\boldsymbol{\psi}}\|} > (1 - tol_{\psi}) \; ; \tag{B.27}$$

where the vectors $\hat{\boldsymbol{g}}$ and $\hat{\boldsymbol{\psi}}$ collect the values of $\hat{g}$ and $\hat{\psi}$, respectively, of the grid points ($\hat{\boldsymbol{g}} = \{\hat{g}_p\}$ and $\hat{\boldsymbol{\psi}} = \{\hat{\psi}_p\}$, with $p = 1, ..., (N_\alpha + 1) \times (N_\beta + 1) \times (N_\gamma + 1)$).

*b)* All constraints must be satisfied with given prescribed tolerances:

$$|h_i| < tol_{h_i} \quad ; \quad \text{with } i = 1, 2, 3 \tag{B.28}$$

*vi)* **Nested grid refinements**

The optimization problems are solved using a grid refinement scheme. Initially, they are solved with a rather coarse grid of points. Once their solutions attain the convergence criteria in this coarse grid, the solutions are projected onto a finer grid, and the iterative scheme is restarted.

Each refinement step consists of exactly doubling the number of voxels per cell side, and therefore, from one step to the next, the number of voxels increases with a factor 8. Using this approach, the level-set function parameters of the coarser grid are projected onto the finer one. The projection procedure is the following: i) For coincident points of both grids, the parameters are identically copied. ii) For those points of the finer grid not coinciding with the points of the coarser grid, the parameters are the average values of the parameters defined in the closest points of the coarser grid, such as it is sketched for a 2D problem in Figure B.7.

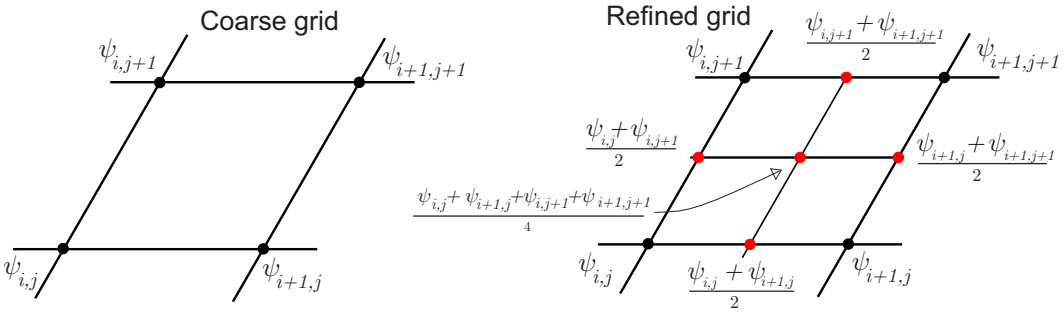


**Figura B.7:** Nested grid refinement procedure. Mapping of the level-set function parameters, from the coarser grid onto the finer one.

### B.3.5. Strategy for imposing the space group symmetry

The topology computed at each iteration of the optimization algorithm is forced to exhibit the crystal symmetry defined by a preestablished space group. To get this objective, we adopt the following strategy.

*a)* First, the set of points belonging to the asymmetric unit[5] of the design domain is identified.

*b)* The image points, related to the asymmetric unit points through the symmetry operations of the space group, are next identified. Both set of points depend on the crystal space group.

*c)* In each iteration of the optimization algorithm, the average values of the level-set function parameters and topological derivatives of the asymmetric unit point and its image points are computed. These average values are assigned to all of them.

[5]The asymmetric unit and the corresponding image points are defined for all the space groups in the International Tables of Crystallography ([108]).

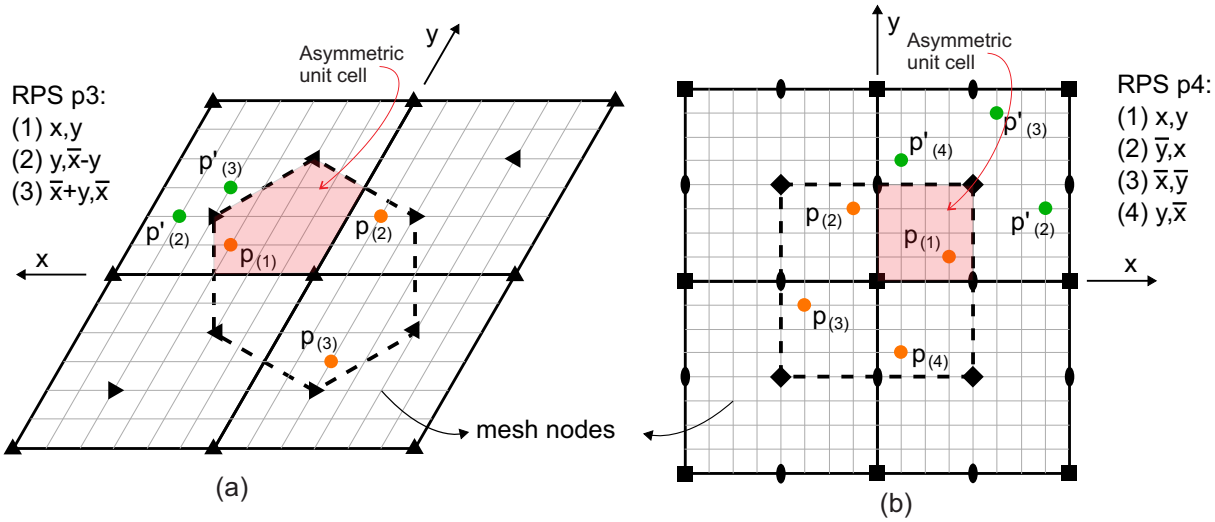


**Figura B.8:** Procedure to impose the 2D crystal symmetry. Plane groups (a) $p3$ and (b) $p4$. Primitive cells are depicted with solid lines and Wigner-Seitz (Voronoi) cells with dotted lines. Orange dots are image points which are located using the RPS information for every point in the asymmetric unit cell. Green dots are the result of the symmetry translations of orange points that lay outside the parallelepiped cell.

For regular grids of points, such as those used in the FFT scheme, the identification of the image points associated with every point in the asymmetric unit is achieved by using the regular point system (RPS)[6], see Vainshtein [55]. Examples of RPS and the mechanism of locating the image points in the grid are shown in Figure B.8 for two 2D cases. Information about the adopted origin of the coordinate system and the RPS for plane and space groups are specified in the International Tables for Crystallography [108]. In the case of the plane group $p3$, the coordinates taken as examples of generic coordinates are $x = 3/6$ and $y = 1/6$, while for the plane group $p4$, these coordinates are $x = 3/8$ and $y = 1/8$. [7]

## B.4. Numerical assessments

Microarchitecture design problems to attain composites with isotropic elastic properties close to the theoretical estimated bounds are next solved. Main results of this task have been presented by the authors elsewhere, see Yera et al. [60], where the influence of imposing crystal symmetries to attain the desired objective has been evaluated by testing four space groups of the cubic crystal systems for 3D problems. Additional results of similar problems have been reported by Andreassen y Lazarov [113].

The numerical performance of the topology optimization algorithms is analyzed in three specific design cases. They aim at attaining microstructures whose effective properties display: a) one of the most negative Poisson's ratios (auxetic composite); b) the stiffest response and c) pentamodal features. The effective elastic properties of these composites in the space $(\hat{\kappa}, \hat{G})$ occupy the locations displayed in Figure B.5. The composites with negative Poisson's ratios have their properties on the left region of the HS-bound. They are composites demanding high shear modulus and small bulk modulus. The stiffest composite is positioned at the upper right bound in the $(\hat{\kappa}, \hat{G})$ space, demanding high $\hat{\kappa}$ and $\hat{G}$ moduli, and pentamode composites are characterized by small shear modulus and are positioned at the lower HS-bound in the same space. Three instances of pentamode composites are solved.

The attained optimal solutions depend on the crystal symmetry adopted for solving the topology

[6] An RPS is the set of points that are associated with one generic point, occupying an arbitrary spatial position, through the symmetry group operations. The coordinates of these points are expressed as a function of the generic point coordinates.

[7] To be consistent with the notation used in the International Tables of Crystallography ([108]), the coordinates in Figure B.8 are denoted $(x, y)$ instead of the usual notation for the contravariant coordinates that we have adopted in this work.

optimization problem. Yera et al. have shown that closer solutions to the theoretical bounds can be found by choosing suitable crystal space groups for each case. For example, the space groups $I23$ and $P23$ are appropriate to attain maximal properties in the region close to the HS-left bound, coincident with the response of auxetic materials. Furthermore, the proper selection of the optimization domain, $\Omega_\mu$, has also a notable influence. In the same paper, Yera et al. also show that topologies with bcc primitive cell provide topologies with closer properties to the HS upper bound than those provided by a simple cubic cell.

### B.4.1. Specific technique for solving the present numerical assessments

The topology optimization algorithm described in Appendix II, with scheme 2, has been used for solving the auxetic composite. The remaining microarchitectures reported in this Section have been obtained with the same algorithm but using scheme 1.

The optimization process starts by taking a grid with $32 \times 32 \times 32$ voxels. It is followed by posterior refinements till reaching grids of $256 \times 256 \times 256$ voxels[8]. The initial topology configurations in all cases are a random distribution satisfying the target volume fraction of the stiff phase.

The solutions of the problems reported in this work are obtained with the filter radius fixed to zero. However, as it can be observed in the attained topologies of Figures B.10 to B.14, they do not display a finer sub-scale. This outcome may be due to the adopted grid refinement strategy. The coarse grid taken for starting the optimization process precludes the generation of a fine topology structure. We have observed that in the posterior grid refinement steps, the algorithm does not longer introduce a sub-scale.

### B.4.2. 3D topology design problems

The designed composites have the same elastic properties, for both phases, defined in the previous sub-Section B.3.1. Therefore, the Figure B.9 copies the HS-bounds in the space $(\hat{\kappa}, \hat{G})$ depicted in Figure B.5. In the same Figure B.9, we also show four solutions A; B, C, and D that have been obtained with the present methodology. They are discussed in sub-Sections B.4.2, B.4.2, B.4.2:case-a and B.4.2:case-b, respectively. Following the suggestions raised by Yera et al., different space groups have been imposed on the topology optimization problems to get these solutions. The results reported by these authors using grids of 100 voxels are also shown in the Figure.

Finally, the last example in sub-Section B.4.2:case-c, describes a particular solution of a pentamode composite with a smaller volume fraction $f_1 = 0.1$.

#### Auxetic materials

The synthesis of auxetics materials has recently raised an enormous interest in the community due to the unusual properties that they display, such as increased resistance to indentation, synclasticity, improvement of fracture toughness, etc. (Saxena et al. [134] and Cabras y Brun [135]). For example, Podestá et al. [114] have shown that optimal design of elastic structures demands the use of auxetics materials.

In this test, the objective is to attain an isotropic composite with minimum Poisson's ratio for a relatively high target shear modulus. The problem formulation (B.14) is used in this case with a target shear modulus[9] $G^{tg} = 0.03$.

The designed microarchitecture has been solved with an imposed space group $I23$ of the cubic crystal system. Figure B.10 displays the resulting topology, and their effective elastic properties are plotted in Figure B.9, point A. The components of the attained homogenized elasticity tensor are: $C^h_{11} = C^h_{22} =$

[8] The sequence of grid refinements consists of taking $32, 64, 128$ and $256$ voxels per spatial dimension.

[9] It is worth to mention that solutions reported by Yera et al. [60] and Andreassen y Lazarov [113] show that it is possible to attain more negative Poisson's ratios using smaller target values of the shear modulus $G^{tg}$.

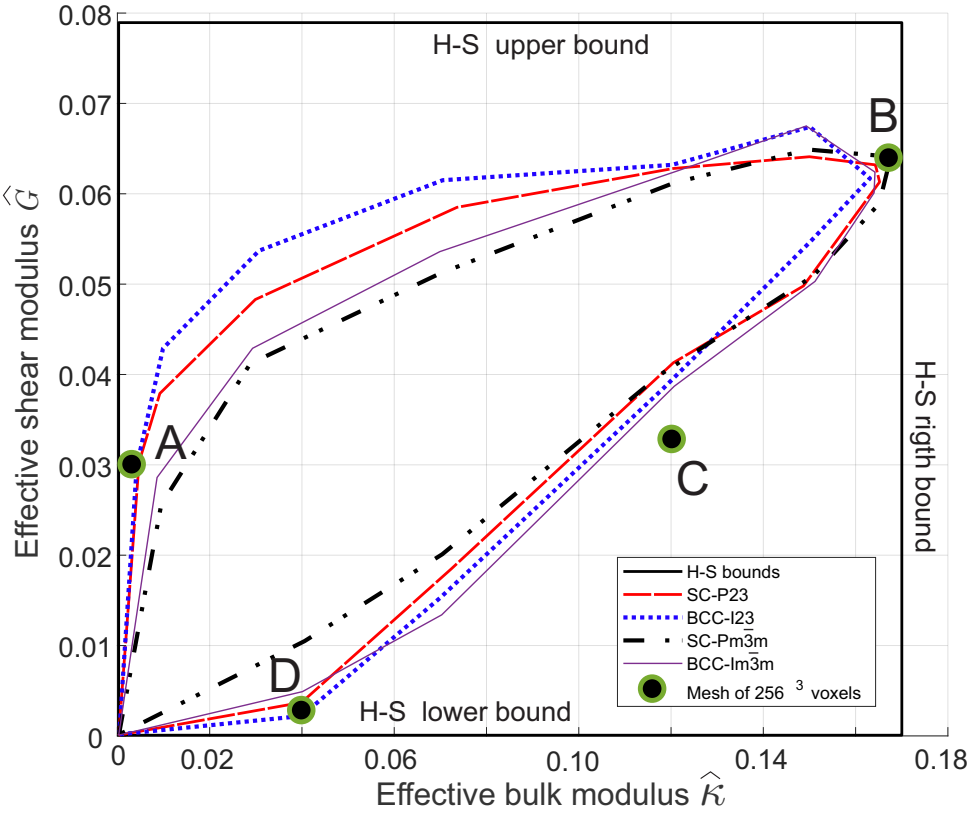


**Figura B.9:** The points A, B, C and D in the plane $(\hat{\kappa}, \hat{G})$ have been obtained with the present methodology and grids of $256 \times 256 \times 256$ voxels. The curves have been taken from Yera et al. [60] with the space groups and unit cells of the cubic crystal system: P23 with a primitive cubic cell (SC-P23), I23 with a bcc primitive cell (BCC-I23), $Pm\bar{3}m$ with primitive cubic cell (SC-$Pm\bar{3}m$) and $Im\bar{3}m$ with bcc primitive cell (BCC-$Im\bar{3}m$). HS-bounds of effective properties for two-phase isotropic 3D composites according to Hashin y Shtrikman [22] (HS-bounds).

$C^h_{33} = 0.041500$, $C^h_{12} = C^h_{23} = C^h_{13} = -0.018739$ and $C^h_{44} = C^h_{55} = C^h_{66} = 0.060176$. Thus, the attained Poisson's ratio is $-0.82$ and the volume fraction is $f_1 = 0.3383$.

We use the Zener ratio to quantify the anisotropy of the effective material properties having cubic symmetry. The Zener ratio is computed with the formula: $\xi = C^h_{44}/(C^h_{11} - C^h_{12})$. A value 1 for this ratio indicates that $\mathbf{C}^h$ is isotropic.

The present solution has a Zener ratio of value $\xi = 0.9989$, very close to 1, and therefore, it satisfies almost exact isotropic response. It is important to remark that several auxetic composites reported in the literature are strongly anisotropic.

### Deformation mechanism of the designed auxetic material

Additional insight respect to the deformation mechanism characterizing the microarchitecture of Figure B.10 can be conceived by analyzing an alternative, but equivalent, solution. First, notice that the topology depicted in Figure B.10, obtained with the space group $I23$, tends to show a higher symmetry than the enforced one. According to this observation, we achieve a simpler microstructure, though slightly less efficient, by imposing the space group $I\bar{4}3m$. The so-attained microstructure is described in Figure B.11 and its effective Poisson's ratio is -0.74. The homogenized elasticity tensor components of the microarchitecture is: $C^h_{11} = C^h_{22} = C^h_{33} = 0.042101$, $C^h_{12} = C^h_{23} = C^h_{13} = -0.017933$ and $C^h_{44} = C^h_{55} = C^h_{66} = 0.0600$. The Zener ratio is $\xi = 0.9994$. Notice that the main difference between the solutions of Figures B.10 and B.11 lies on the thin sub-structures that are commonly attained when extreme materials are designed.

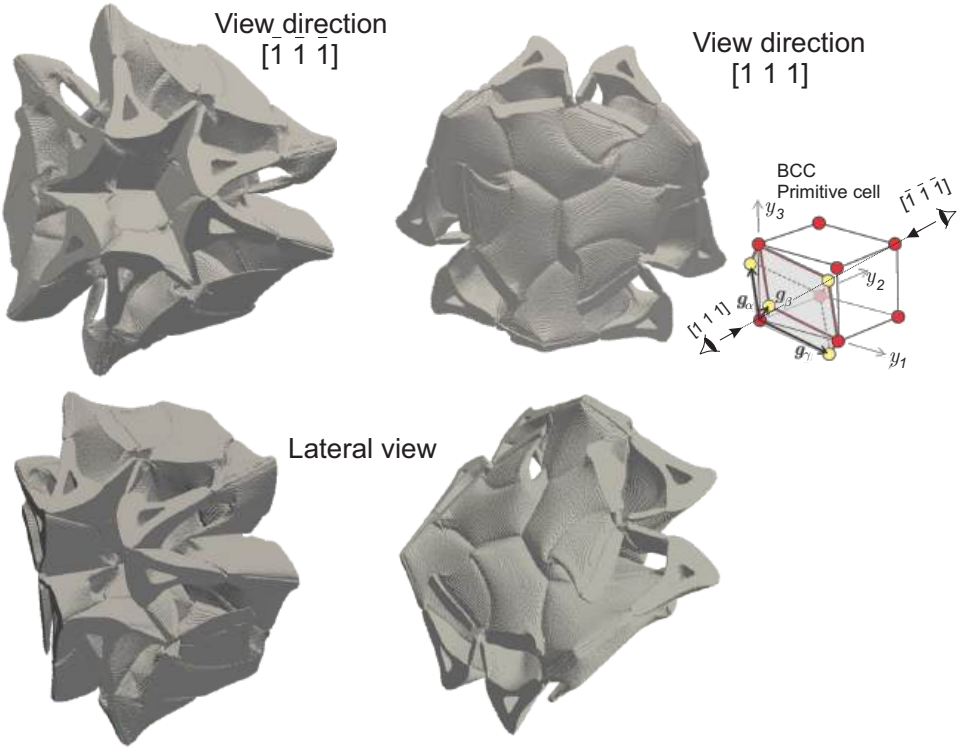


**Figura B.10:** Primitive cell of the composite with elastic properties corresponding to Point A in Fig B.9. Imposed space group $I23$. Primitive cell observed from two opposite viewpoints: $[\bar{1}\bar{1}\bar{1}]$ and $[111]$ . The Poisson's ratio of this microstructure is $-0.82$, the effective shear modulus $\hat{G} = 0.0301$ and the effective bulk modulus $\hat{\kappa} = 0.0013405$.

The deformation mechanism of the simpler microstructure in Figure B.11 is next explained. Figures B.11 (a) and (b) show the primitive and conventional cells. Figures B.11 (d) and (e) present the details of the interior region of the conventional cell and the external faces of the conventional cell, respectively. Also, they sketch the deformation mechanism when the microstructure is subjected to a macroscopic strain.

Three cell configurations are presented in Figures B.11 (d) and (e). The central pictures display the original configurations of the cell. The pictures on the right side display the deformed cell when it is stretched in the direction $[1\,0\,0]$. The pictures on the left side display the deformed cell when it is compressed in the same direction. Notice the original and deformed positions of the points 1, 2 and 3 in the three configurations of Figure B.11 (d). It can be seen the microstructure unfolding mechanism that is activated when it is stretched; the points are moving away and the dihedral angle $\alpha$ increases. Alternatively, in the reverse direction, in a compressive regime, the microstructure folding mechanism is activated; the points are approaching and the dihedral angle $\alpha$ decreases. The points 1, 2 in the three configurations of the Figure B.11 (e) display a similar folding/unfolding mechanism.

We point out that the deformation mechanism of the microstructure could be envisaged through the simpler deformation mechanism displayed by the origami in Figure (c). Both structures deform following a similar pattern.

### Maximum stiffness materials

With the present approach, we have noted that the topology optimization algorithm finds solutions close to the HS-right bound more easily than solutions close to the HS-upper bound. According to this observation, in this problem, we find the topology by solving a maximization problem with the formulation (B.13). The target bulk modulus is $\kappa^{tg} = 0.167$ close to the upper bulk modulus, $\kappa^{u} = 0.1704$,

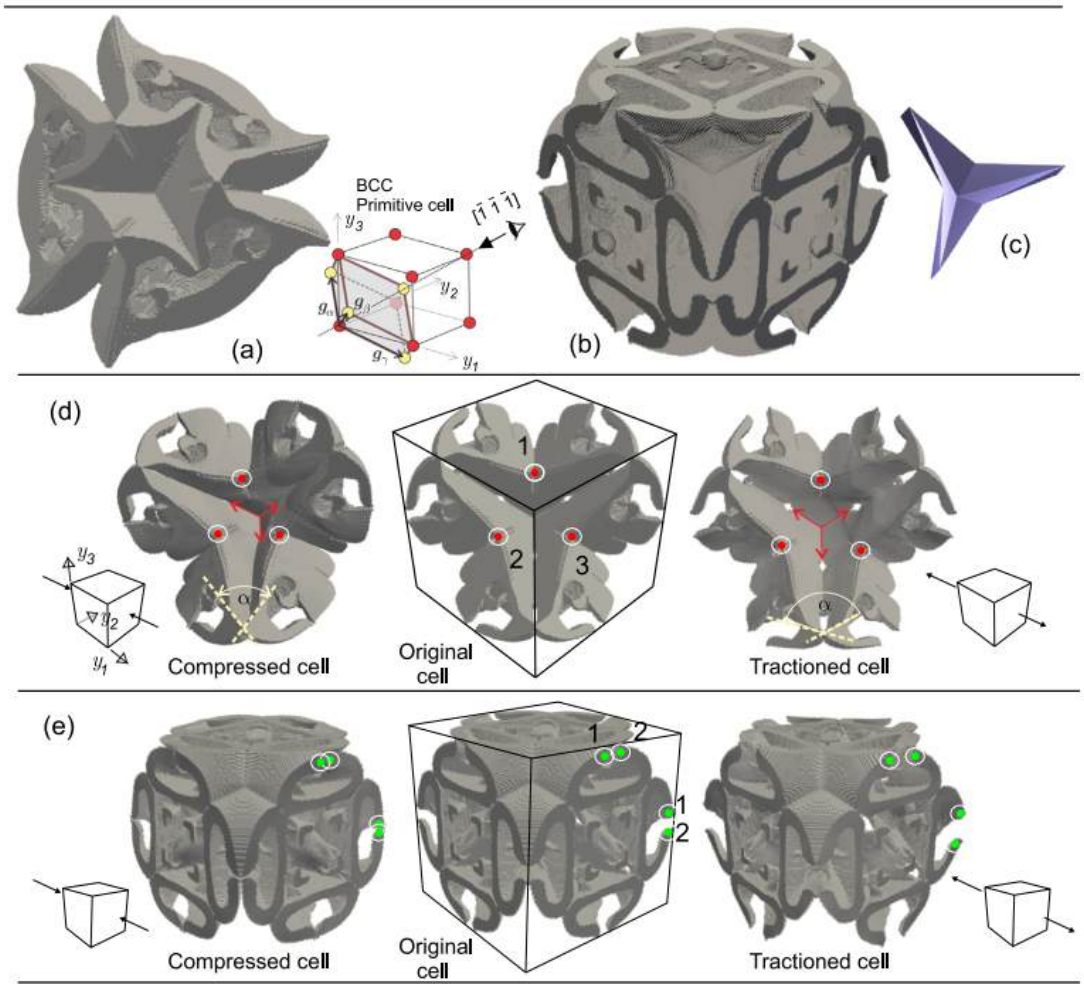


**Figura B.11:** Auxetic composite with space group $I\bar{4}3m$ and Poisson's ratio $-0.74$. (a) Primitive cell observed from viewpoint $[\bar{1}\,\bar{1}\,\bar{1}]$. (b) Conventional cell. (c) Origami displaying a similar deformation mechanism to the auxetic composite. (d) Half of the conventional cell constituted by the contribution of four primitive cells. Internal region views. (e) External views of the conventional cell.

estimated by the HS-bounds. The enforced space group is $Pm\bar{3}m$. The design domain is the primitive cell of the simple cubic Bravais lattice.

Figure B.12 displays the attained topology. It is constituted of a void volume covered with a layered structure in three orthogonal directions that contributes to increasing the shear stiffness. This topology can be compared with the microstructure of Figure B.14 obtained for high bulk modulus and low shear stiffness.

The homogenized elasticity tensor components of the microarchitecture displayed in Figure B.12 is: $C^h_{11} = C^h_{22} = C^h_{33} = 0.252523$, $C^h_{12} = C^h_{23} = C^h_{13} = 0.124672$ and $C^h_{44} = C^h_{55} = C^h_{66} = 0.127826$, with effective bulk and shear moduli plotted in Figure B.9, point B. The Zener ratio is $\xi = 0.9998$.

### Pentamode materials

The name of pentamode materials has been coined by Milton y Cherkaev [70][10] to designate the class of composites displaying a stiff response for one characteristic strain mode while displaying easy

[10] At the same time, Sigmund [66] has independently introduced this kind of composites in the context of inverse homogenization problems.

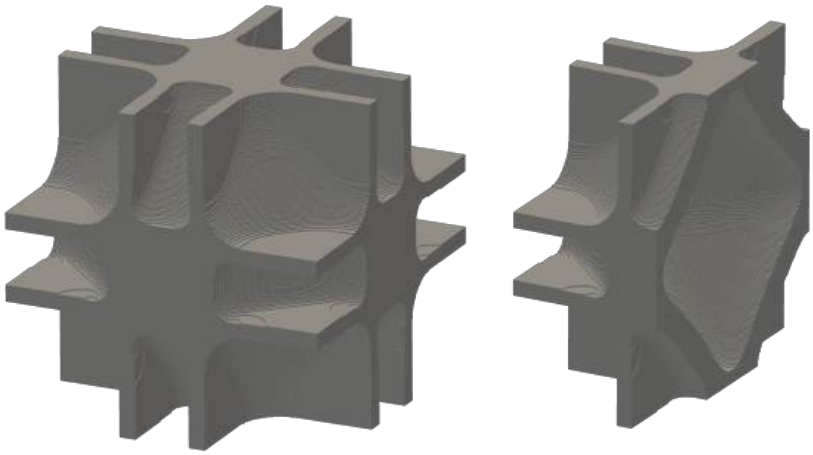

**Figura B.12:** Topology of the maximum stiffness composite, point B in Figure B.9, designed with a $Pm\bar{3}m$ space group. (a) Primitive cell. (b) Trimmed microcell showing the interior void.

modes of deformations for the remaining five characteristic strain modes. We consider that the characteristic strain modes are assumed to be the six eigenvectors of the elasticity tensor. Thus, for a typical isotropic material, the stiff deformation mode can be associated with the eigenvalue coinciding with the bulk modulus, while the compliant response is associated with the shear modulus. It means that a pentamode material displays an almost null shear modulus jointly with a non-null bulk modulus. Pentamode materials have an interest because any achievable effective elastic material can be generated using an assemblage of pentamode materials, such as mentioned in the paper by Milton y Cherkaev [70]. In this reference work, the authors also propose a natural candidate for the pentamode materials, being a diamond-type structure in which four linkages meet at a point.

**Case a: microstructure of a pentamode composite attained with $P23$ space group (point D in Figure B.9)**

We solve the problem (B.13) with $\kappa^{tg} = 0.04$ and the imposed space group $P23$. The solved microstructure is displayed in Figure B.13, and it has effective properties which correspond to the point D in Figure B.9. The components of its homogenized elasticity tensor are: $C^h_{11} = C^h_{22} = C^h_{33} = 0.04363$, $C^h_{12} = C^h_{13} = C^h_{23} = 0.03817$ and $C^h_{44} = C^h_{55} = C^h_{66} = 0.00630$. Thus, the Zener coefficient is $\xi = 1.1538$, with a ratio: $\kappa^h/G^h \approx 13$. The six eigenvalues of the elasticity tensor are $0.1997$, $0.0630$, $0.0630$, $0.0630$, $0.0547$ and $0.00547$, respectively, Then, the ratios between the maximum $\lambda_{max}$, the medium $\lambda_{med}$ or the minimum $\lambda_{min}$ eigenvalues are: $\lambda_{max}/\lambda_{med} = 19$ and $\lambda_{max}\lambda_{min} = 22$,

The topology is constituted of four interconnected helix-like sub-structures. Each sub-structure is formed by three linked bulky elements. Details of the links are displayed in Figure B.13-b. Unlike the Milton microstructure that is analyzed in the following case-c, in this topology, the linkage of the three bulky elements is not reduced to a point. Additionally, as it can be observed in Figure B.13-a, the internal region of the cell displays the four helix-like sub-structures which are interconnected through a small microstructure constituted by four bars.

From this result, we can conclude that the deformation mechanisms generated by the four helix-like linked substructures are responsible for providing an almost isotropic effective elastic response of the composite, while their linkage would probably need the introduction of a sub-topology, with a smaller length scale to further decrease the effective shear modulus.

**Case b: Microstructure of a pentamode composite attained with the $Im\bar{3}m$ space group (point C**

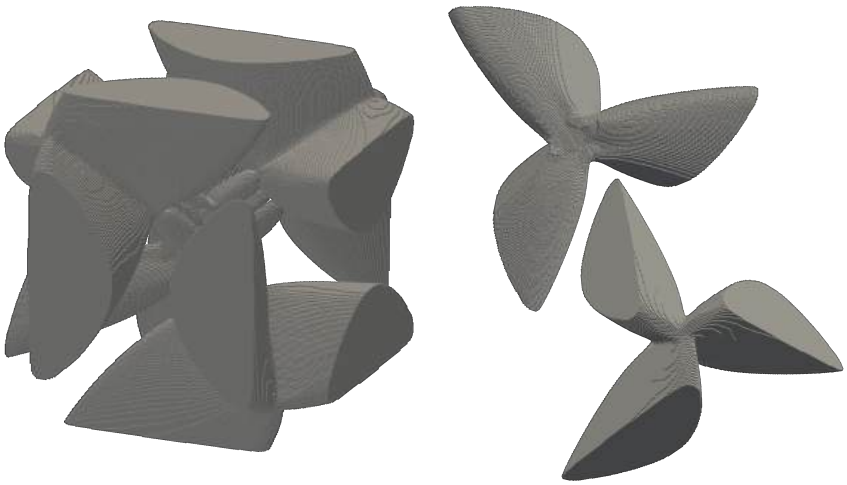

**Figura B.13:** Pentamode material attained with the space group $P23$. Effective properties corresponds to point D of Figure B.9. (a) Primitive cell; (b) detail of the joints of the substructures.

**in Figure B.9)**

Although the microstructure of Figure B.13 displays a high bulk to shear moduli ratio, it is attained by imposing a low target bulk modulus $\kappa^{tg} < \kappa^u/4$. With higher values of $\kappa^{tg}$, the ratio $\kappa^h/G^h$ of the attained composites decreases and their material properties tend to move away from the lower theoretical HS-bound.

A typical case is the topology shown in Figure B.14, which corresponds to Point C in Figure B.9, obtained with the formulation (B.13), with $\kappa^{tg} = 0.12$ and imposing a space group symmetry $Im\bar{3}m$. This result shows two well-recognized sub-structures which are linked through a bar-like system of elements. The components of the homogenized elasticity tensor of this microstructure are: $C^h_{11} = C^h_{22} = C^h_{33} = 0.16458$, $C^h_{12} = C^h_{13} = C^h_{23} = 0.09815$ and $C^h_{44} = C^h_{55} = C^h_{66} = 0.06500$. Thus, the Zener coefficient is $\xi = 0.9785$,

The attained shear modulus of this microstructure is far from the lower HS-bound. However it is interesting to note certain similitude with the topologies reported by Sigmund [67] for the equivalent problem, identified as the Walpole point problem in 2D. Both 2D and 3D structures have the maximum possible symmetry, i.e. $p6mm$ with a hexagonal lattice in the 2D case, and $Im\bar{3}m$ with a bcc lattice in the 3D case. Another remarkable aspect is that both topologies tend to include additional sub-structures displaying a smaller length scale. Compare Point 9 of Figure 7 in Sigmund's work and the details in Figure B.14-(b). In the 2D case, the lower length scale structure is a laminated material.

In the 3D case reported here, two independent saddle-shaped sub-structures conform, after cell assembly, a system of hollow "tubes" which are interconnected by parallel bars/cylinders in three directions, such as observed in the details depicted in Figure B.14. Remarkably, Milton y Camar-Eddine [120] have recently discussed similar kinds of microstructures in the context of isotropic pentamode material. The microstructures proposed by these authors have almost zero shear modulus and can be realized with a system of parallel cylinders, having characteristic sizes much lower than the microarchitecture size, which are inserted into structures having maximum bulk and shear moduli. These cylinders are placed in a sufficient number of orientations to ensure the isotropy of the composite. Additionally, in the discussion presented by Milton et al. [136], it has been pointed out that multiscale substructures are necessary to achieve simple topologies with properties close to the theoretical bounds. According to these comments and due to the design constraints that we adopt in this work, the bar system observed in Figure B.14 does not constitute a true lower scale length of the microstructure, and therefore, they could be the reason for preventing an additional decrement of the shear modulus.

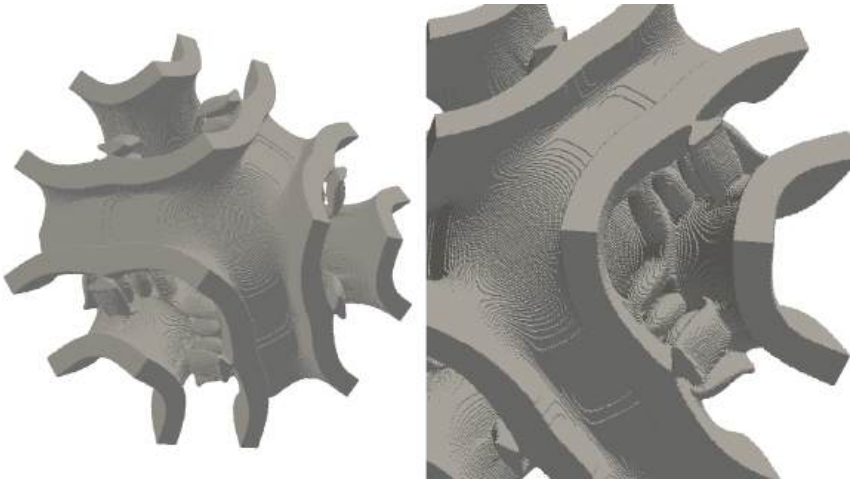

**Figura B.14:** Topology obtained with the $Im\bar{3}m$. Effective properties corresponds to Point C in Fig B.9. Primitive cell and details of links between the two sub-structures constituting the composite.

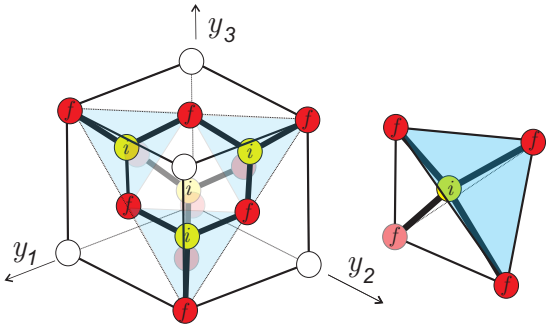


**Figura B.15:** Diamond's crystal structure. Atoms $f$ are on the unit cell faces and atoms $i$ are on the interior of the cell.

### Case c: microstructure of a pentamode composite attained with $F\bar{4}3m$ space group and smaller volume fraction

The diamond's cubic structure depicted in Figure B.15, with the internal atoms *i* equal to the face atoms $f$ of the conventional cell, has a crystal symmetry with the $Fd\bar{3}m$ space group and fcc Bravais lattice. When the atoms *i* are different to atoms *f*, the crystal symmetry is lowered to the space group $F\bar{4}3m$.

An interesting point demonstrating the potentiality of the present methodology lies in the fact that by imposing a space group $F\bar{4}3m$, with fcc Bravais lattice, we attain a microarchitecture similar to that proposed by Milton et al., displaying the higher symmetry $Fd\bar{3}m$ of the diamond-like structure. This solution is shown in Figure B.16 and has been obtained for a stiff volume fraction of $0.1$. This microstructure is slightly different from that reported by Kadic et al. [7]. In the present case, the optimal bars conforming the diamond-like microstructure are similar to ellipsoids, with the section of the bars not being exactly circular but similar to hexagons with rounded vertices, as can be noted in the Figure.

A detail of the geometry of the bar joints are shown in Figure B.16-(b).

The homogenized elasticity tensor is $C_{11} = 0.00994$, $C_{12} = 0.00936$ and $C_{44} = 0.00157$. The six eigenvalues of this tensor are: $0.02866$, $0.00157$, $0.00157$, $0.00157$, $0.00057$, and $0.00057$. Thus, the six eigenvalues of the elasticity tensor are $0.02866$, $0.00157$, $0.00157$, $0.00157$, $0.00057$, and $0.00057$, respectively. And the ratios between the maximum, $\lambda_{max}$, the medium, $\lambda_{med}$ or the minimum, $\lambda_{min}$, eigenvalues are: $\lambda_{max}/\lambda_{med} = 18$ and $\lambda_{max}/\lambda_{min} = 50$. The Zener coefficient is $\xi > 2$ resulting a composite whose properties are far from being isotropic. In this case, the specific tolerance of the

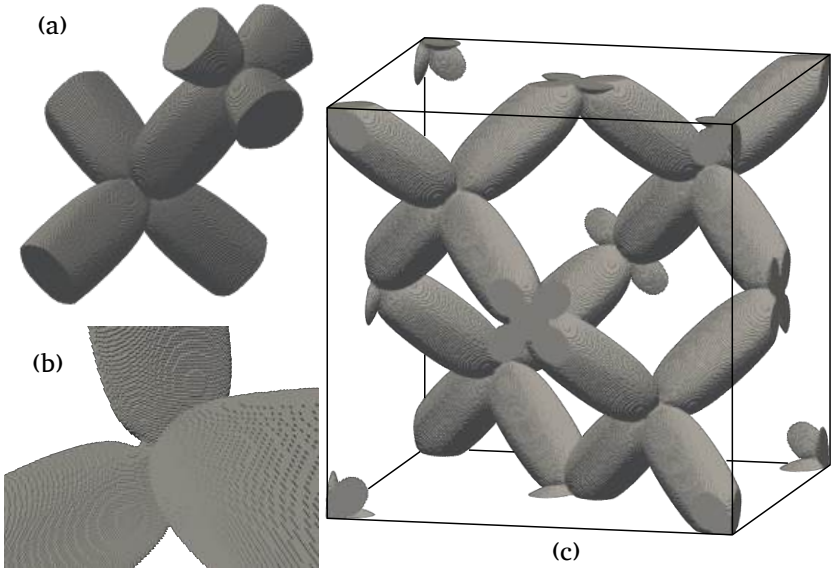


**Figura B.16:** Topology obtained with space group $F\bar{4}3m$. (a) Primitive parallelepiped cell; (b) Detail of the joints shape; (c) Conventional cell.

algorithm corresponding to the isotropy constraint has been handled to force the convergence conditions.

The ratio $\kappa^h/G^h = 16$ is low if compared with the results reported by Kadic et al. However, note that the solution of Kadic et al. corresponds to a volume fraction less than $0.05$.

### B.4.3. Computational burden for solving the topology optimization problems

Several additional tests have been performed to assess the computational burden demanded by the present methodology. The four topology optimization problems denoted A, B, C and D in Figure B.9 have been solved with:

*i)* two space groups: $P23$ and $I23$, and

*ii)* using the iterative schemes 1 and 2 described in Appendix II.

Ten instances of each problem have been tested. For each instance, the iterative process is initiated with a random distribution of the stiff phase and a grid of $32 \times 32 \times 32$ voxels. After convergence, a new iterative process is started with a grid of $64 \times 64 \times 64$ voxels. In this case, the initial material configuration is the projection of the coarse grid solution onto the fine grid.

The results, in terms of computational burden, are reported in Table B.2. This table compares the number of tests that have converged, the total number of iterations required to converge, the number of homogenization evaluations that have been performed and the attained best objective function value of each problem.

The Table rows denoted: *C/T* report the ratio between the number of converged tests divided by the total numbers of tested instances, which is 10 in all cases; *MNI* report the number of iterations needed to converge (the mean value of the converged instances); *MNH* report the number of times (average) that the homogenization elasticity tensor has been computed; and *BOf* report the attained optimum value of the objective function.

The Table columns $P23$ and $I23$ report the results of the five problems with topologies satisfying the crystal symmetries with either the $P23$ or $I23$ space groups; *Grid* $32^3$ and *Grid* $64^3$ identify the results obtained with either $32 \times 32 \times 32$ or $64 \times 64 \times 64$ voxels; and *Sch 1* and *Sch 2* identify the iterative scheme, described in Appendix II, adopted to solve the problem. The scheme using a predefined step

**Tabla B.2:** Computational burden for solving the topology design problems A, B, C and D of Figure B.9. First column identifies the problem.

| | | P23 | | | | I23 | | | |
|---|---|---|---|---|---|---|---|---|---|
| | | Grid $32^3$ | | Grid $64^3$ | | Grid $32^3$ | | Grid $64^3$ | |
| | | Sch 1 | Sch 2 | Sch 1 | Sch 2 | Sch 1 | Sch 2 | Sch 1 | Sch 2 |
| A | C/T | 6/10 | 10/10 | 5/6 | 10/10 | 10/10 | 10/10 | 10/10 | 10/10 |
| | MNI | 843 | 366 | 193 | 114 | 816 | 264 | 94 | 87 |
| | MNH | 845 | 1120 | 194 | 447 | 818 | 872 | 95 | 305 |
| | BOf | 5.94e-3 | 6.67e-3 | 3.67e-3 | 3.74e-3 | 4.98e-3 | 5.30e-3 | 3.18e-3 | 2.44e-3 |
| B | C/T | 9/10 | 10/10 | 9/9 | 10/10 | 5/10 | 9/10 | 4/8 | 8/9 |
| | MNI | 409 | 607 | 68 | 78 | 702 | 906 | 127 | 198 |
| | MNH | 411 | 2162 | 69 | 221 | 704 | 2752 | 128 | 457 |
| | BOf | 6.67e-2 | 6.58e-2 | 6.69e-2 | 6.79e-2 | 6.66e-2 | 6.39e-2 | 6.66e-2 | 6.54e-2 |
| C | C/T | 10/10 | 10/10 | 10/10 | 8/10 | 9/10 | 6/10 | 9/9 | 6/6 |
| | MNI | 973 | 629 | 166 | 118 | 875 | 309 | 88 | 58 |
| | MNH | 975 | 1522 | 167 | 385 | 877 | 915 | 89 | 167 |
| | BOf | 3.51e-2 | 3.72e-2 | 3.40e-2 | 3.50e-2 | 3.91e-2 | 3.97e-2 | 3.75e-2 | 3.83e-2 |
| D | C/T | 5/10 | 8/10 | 4/5 | 8/8 | 7/10 | 8/10 | 7/7 | 7/8 |
| | MNH | 859 | 736 | 23 | 36 | 929 | 630 | 228 | 107 |
| | MNH | 861 | 2060 | 24 | 116 | 931 | 1754 | 229 | 317 |
| | BOf | 3.62e-3 | 3.34e-3 | 2.92e-3 | 2.50e-3 | 5.58e-3 | 3.14e-3 | 3.99e-3 | 2.61e-3 |

length (parameter $\tau$ in equation (B.22)) is denoted with *Sch 1*. The line search scheme is denoted with *Sch 2*.

According to the data reported in Table B.2, we observe that the number of iteration required for convergence notably changes according to the problem. Additionally, we can estimate the robustness performance of the algorithm by analyzing the number of converged solutions respect to the total number of performed tests.

In most tested cases, scheme 2 demands more homogenization evaluations than scheme 1 to achieve the solution, resulting in a more costly procedure. However, scheme 2 does not need to guess the step length for generic cases, which yields a more reliable procedure.

## B.5. Conclusions

In this paper, we have shown that the microarchitecture design of elastic materials attained through the solution of topology optimization problems, combined with the imposition of pre-defined crystal symmetries, is a viable and robust methodology for designing 3D metamaterials with effective elastic properties close to the theoretical bounds.

To reach this objective, we have adopted two similar topology optimization problems that are formulated as inverse homogenization techniques. The implementation details of the algorithm for solving these formulations have also been presented. The algorithm is based on a level-set function technique with the sensitivities, for the iterative correction of the level-set function, evaluated through the topology derivative of the problem.

We have used an FFT technique reported in the literature to compute efficiently the homogenized elastic properties of 3D composites. The contrast factor for modeling the void phase has been taken small

enough to provide accurate solutions without substantially penalizing the computational cost required by the FFT technique. A good performance of the FFT technique has been attained after introducing grey voxels in the interfaces which simulate materials with intermediate properties of the constituent phases.

To confirm the computational efficiency of this homogenization technique, we have presented a detailed numerical assessment consisting of computing the homogenized elasticity tensor of a periodic microstructure with an fcc Bravais lattice. Results, in terms of computational time vs. accuracy, have been compared with solutions obtained using the FEM. Under these circumstances and including the grey material in the model, the FFT technique has a favorable performance if compared with the FEM.

The design technique, as well as the computation of the homogenized elastic properties of composites with arbitrary crystal symmetries and periodic topologies, requires the use of primitive cells of Bravais lattices that are associated with the pre-defined space group imposed to the topology. One of the most salient features of these cells is that they are not necessarily rectangular prisms. Therefore, the use of the FFT technique reported in the literature has to be adapted to these situations where the cell faces are non-orthogonal. This issue has specifically been addressed in this work.

To attain the microarchitectures with effective properties close to the theoretical bounds, we have imposed crystal symmetries with different space groups which have been adopted in concordance with the conclusions of a previous paper of the authors (Yera et al. [60]). The imposed space groups are compatible with the cubic crystal system. Therefore, the obtained topologies have effective elastic properties with cubic symmetry. Based on this evidence, the isotropy of these microstructures can be measured with the Zener coefficient who is reported for all cases discussed in the paper. Excluding the pentamode material of case c in sub-Section B.4.2, in all the remaining cases, the Zener coefficients are close to 1. Therefore, we conclude that the isotropic response is fulfilled in almost the complete set of designed topologies.

In sub-Section B.4.3, we have evaluated the computational burden required for solving several topology design cases. An important conclusion can be drawn from the data reported in Table B.2. It refers to the relatively high number of tests that have reached convergence. We conclude that the methodology with the crystal symmetry ingredients displays good and robust performances.

An interesting final remark about the integrated design strategy, here discussed, is its suitability for imposing different space group symmetries due to the regular grids used for solving the FFT scheme.

### Acknowledgments

The authors acknowledge the financial support from CONICET and ANPCyT (grants PIP 2013-2015 631 and PICT 2014-3372 and 2016-2673).

We thank Dr. Ricardo Lebensohn, from Los Alamos National Laboratory, for the discussion hold about some topics related to the FFT homogenization technique in parallelepiped domains addressed in this work.

## APPENDIX I: Homogenized elasticity tensor and its topological Derivative

Let us consider the problem sketched in Figure B.1. The macro-stress $\boldsymbol{\sigma}$ and macro-strain $\boldsymbol{E}$ are the volumetric average, in the micro-cell $\Omega_\mu$, of the corresponding micro-stress $\boldsymbol{\sigma}_\mu$ and micro-strain $\boldsymbol{\varepsilon}_\mu$ observed at the micro-scale: $\boldsymbol{\sigma} = \langle \boldsymbol{\sigma}_\mu \rangle$ and $\boldsymbol{E} = \langle \boldsymbol{\varepsilon}_\mu \rangle$. Also, $\boldsymbol{\varepsilon}_\mu(\boldsymbol{y})$ can be split into the average strain $\boldsymbol{E}$ plus a fluctuation term $\tilde{\boldsymbol{\varepsilon}}_\mu(\boldsymbol{y})$ with zero average value in $\Omega_\mu$:

$$\boldsymbol{\varepsilon}_\mu(\boldsymbol{y}) = \boldsymbol{E} + \tilde{\boldsymbol{\varepsilon}}_\mu(\boldsymbol{y}) \; . \tag{B.29}$$

The fluctuation micro-strain is the symmetric gradient of a fluctuation displacement field, $\tilde{\boldsymbol{u}}$ which is periodic on the boundary $\Gamma_\mu$ of $\Omega_\mu$. The displacement fluctuations $\tilde{\boldsymbol{u}}$ are periodic along the directions defined by the primitive vectors of the Bravais lattice.

Stresses and strains at the macro-scale are related through the homogenized elasticity tensor $\mathbf{C}^h$:

$$\boldsymbol{\sigma} = \mathbf{C}^h \boldsymbol{E} \,, \tag{B.30}$$

and stresses and strains at the micro-scale are related through the constitutive law:

$$\boldsymbol{\sigma}_\mu(\boldsymbol{y}) = \mathbf{C}(\boldsymbol{y})\boldsymbol{\varepsilon}_\mu(\boldsymbol{y}) \,. \tag{B.31}$$

where $\mathbf{C}(\boldsymbol{y})$ is the elasticity tensor of phase at the point $\boldsymbol{y}$. Additionally, $\boldsymbol{\sigma}_\mu$ is a self-equilibrated stress field: $\nabla \cdot \boldsymbol{\sigma}_\mu = \mathbf{0}$ in $\Omega_\mu$.

By following to Moulinec et al, the micro-scale field equations with the corresponding boundary conditions can be rewritten as an auxiliary problem and reduced to the Lippmann-Schwinger integral equation for $\tilde{\boldsymbol{\varepsilon}}_\mu(\tilde{\boldsymbol{u}})$, which, finally, can be iteratively solved in the frequency space, using a fixed-point algorithm.

**Homogenized elasticity tensor**

Let us define the canonical base of the macro-strain tensors $\mathcal{E} := \{\boldsymbol{E}^{I_1}, ..., \boldsymbol{E}^{I_6}\}$, where the indices $I_1, I_2, ..., I_6$ identify every one of the six strain bases $\boldsymbol{E}^{I_m}$. The six components of each strain base is written in the conventional way, $E_{ij}^{I_n}$, with $i, j = 1, 2, 3$. Then, the components of the canonical strain bases are defined by

$$\boldsymbol{E}_{ij}^{I_n} = \begin{cases} 1 & \text{if } (i,j) \in I_n \\ 0 & \text{if } (i,j) \notin I_n \end{cases} \tag{B.32}$$

where the following association between component indices, $i, j$, and strain base indices, $I_n$, is defined: $(1,1) \in I_1$; $(2,2) \in I_2$; $(3,3) \in I_3$; $\{(1,2),(2,1)\} \in I_4$; $\{(2,3),(3,2)\} \in I_5$; $\{(1,3),(3,1)\} \in I_6$.

The components of the homogenized elasticity matrix[11] is computed with the expression:

$$\mathbf{C}_{mn}^h = \boldsymbol{\sigma}(\boldsymbol{E}^{I_m}) : \boldsymbol{E}^{I_n} \qquad ; \qquad m, n = 1, 2, ..., 6 \; ; \tag{B.33}$$

where $\boldsymbol{\sigma}(\boldsymbol{E}^{I_m})$ is the homogenized macro-stress satisfying the multiscale equations, defined above, for the given macro-strain $\boldsymbol{E}^{I_m}$.

Thus, six problems $\boldsymbol{\sigma}(\boldsymbol{E}^{I_m})$, with $m = 1, ...6$, are solved. Associated to each one of them, the micro-strain $\varepsilon_\mu^{I_m}$ and the micro-stress $\boldsymbol{\sigma}_\mu^{I_m}$ are also computed in the micro-cell. According to equation (B.29), the micro-strain $\boldsymbol{\varepsilon}_\mu^{I_m}$ is split as follows:

$$\boldsymbol{\varepsilon}_\mu^{I_m}(\boldsymbol{y}) = \boldsymbol{E}^{I_m} + \tilde{\boldsymbol{\varepsilon}}_\mu^{I_m}(\boldsymbol{y}), \tag{B.34}$$

where $\tilde{\boldsymbol{\varepsilon}}_\mu^{I_m}$ is a fluctuation term with zero average value on the micro-cell.

**Topological derivative of the homogenized elasticity tensor**

The book by Novotny y Sokołowski [57] describes the topological derivative of the energy function associated with an elastic boundary value problem defined in a given spatial domain. Following this approach, Giusti [137] develops the topological derivative of the effective elasticity tensor obtained using a computational homogenization procedure for 2D problems. This term has subsequently been used by Amstutz et al. [59] for solving a topology optimization algorithm. Here, we only present a summary of these concepts and the expression used for the topology derivative in 3D problems, see Giusti [138] and Lopes et al. [132].

The topological derivative of the homogenized elasticity tensor represents the sensitivity of this tensor to infinitesimal spherical perturbation in the homogenization domain, such as sketched in Figure

[11] At this point, we are implicitly introducing the Kelvin notation for tensors.

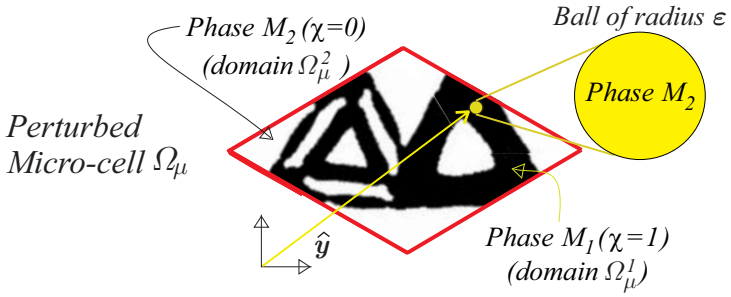


**Figura B.17:** Perturbed micro-cell domain.

B.17. Let us consider that, at the point $\hat{\boldsymbol{y}}$ of the microcell, it exists the base elastic material with the Lamè parameters $(\lambda;\mu)$ and Poisson's ratio $\nu$. This material is substituted by an infinitesimal spherical perturbation with another elastic material with parameters $(\lambda_0;\mu_0)$. Then, the topological derivative of the homogenized elasticity tensor can be computed with the expression:

$$D_T\mathbf{C}^h_{mn}\left(\chi(\hat{\boldsymbol{y}})\right) = \boldsymbol{\varepsilon}^{I_m}_\mu(\hat{\boldsymbol{y}}) : \mathbb{P} : \boldsymbol{\varepsilon}^{I_n}_\mu(\hat{\boldsymbol{y}}) \qquad ; \qquad m,n = 1,...,6 \tag{B.35}$$

where $\mathbb{P}$ is the polarization tensor[12].

$$\mathbb{P} = \alpha_1\left(\alpha_2(\mathbf{1}\otimes\mathbf{1}) + 2\mathbb{I}\right) \; ; \tag{B.36}$$

the symbols $\mathbf{1}$ and $\mathbb{I}$ represent the second and fourth order unit tensor, respectively, and the coefficient $\alpha_1$ and $\alpha_2$ are:

$$\begin{aligned}
\alpha_1 &= \left(\frac{15\mu\delta_\mu(\nu-1)}{15\mu(1-\nu)+2\delta_\mu(5\nu-4)}\right); \\
\alpha_2 &= \frac{\delta_\lambda\left[15\mu\lambda(1-\nu)+2\lambda\delta_\mu(5\nu-4)\right]-2\delta_\mu(\lambda\delta_\mu-5\mu\nu\delta_\lambda)}{5\delta_\mu\left[3\mu\lambda(1-\nu)-3\mu\nu\delta_\lambda-\lambda\delta_\mu(1-2\nu)\right]};
\end{aligned} \tag{B.37}$$

with $\delta_\lambda = \lambda - \lambda_0$; $\delta_\mu = \mu - \mu_0$.

The strains $\boldsymbol{\varepsilon}^{I_m}_\mu$ and $\boldsymbol{\varepsilon}^{I_n}_\mu$ in equation (B.35) are the solutions of the FFT technique to each one of the six problems $(m,n = 1,2,...,6)$ and are given by equation (B.34). Note from (B.35) that the topological derivative of $\mathbf{C}^h$ is defined in each point of the micro-cell ($\hat{\boldsymbol{y}} \in \Omega_\mu$).

# APPENDIX II: Iterative schemes for solving the optimization algorithms

We have implemented two alternative iterative schemes for solving the equations governing the optimization algorithm which are described in sub-Section B.3.4. In this Appendix, we describe both implementations.

Both implementations are inspired by the Augmented Lagrangian technique and adopt a fixed penalty parameter. The first scheme uses a pre-defined linearly decreasing step size, $\tau$. This parameter determine the size the level-set function update equation (B.22). The second scheme determines the step size, $\tau$, using a linear search technique. The step size of the first scheme and how it is decreased is defined through a previous adjust procedure.

Both schemes are summarized in the following Box.

[12] Additional description and properties of the polarization tensor for 3D problems can be found in [63], where it is called the Elastic Moment Tensor (EMT)

**General Algorithm**

**Initialization:** Level-set function $\psi^0$; Lagrange multipliers $\lambda_i^0$; penalty parameter $\alpha$; Amstutz criteria tolerance $tol_\psi$; constraints tolerances $tol_{h_i}$.

Iteration $k+1$:

1. Build the characteristic function $\chi(\psi^k)$ defined in equation (B.12).
2. Perform the homogenization.
3. Evaluate the augmented Lagrangian $\mathcal{T}(\psi^k, \lambda^k)$ defined in equation (B.16)
4. Compute the topological derivative $D_\psi \mathbf{C}^h_{mn}\left(\chi(\hat{\boldsymbol{y}})\right)$ using equation (B.35); apply the filter; impose the symmetries.
5. Compute the search direction of the augmented Lagrangian problem, $g^k$, with equation (B.23), and using $D_\psi \mathcal{T}(\psi^k, \lambda^k)$ from equation (B.18).
6. Determine the steep size parameter $\tau$.
   - **scheme 1:** *Linearly decreased with k.*
   - **scheme 2:** $\begin{cases} Choose\ a\ safewarded\ minimum\ step\ size\ \tau_{min}. \\ Perform\ a\ linear\ search:\ \tau \in [\tau_{min}, 1]. \end{cases}$
7. Update the level-set function $\psi^{k+1}$ with equation (B.22); apply the filter; impose the symmetries.
8. Update the Lagrange multipliers: $\lambda_i^{k+1} = \lambda_i^k + \alpha h_i$.
9. Convergence test using equations (B.27) and (B.28)

The line search procedure for determining the step size, scheme 2, is based on the Moré and Thuente [139] algorithm. We use the topological derivative in the sense of the usual derivative.

# Apéndice C

# A microarchitecture design methodology to achieve extreme isotropic elastic properties of composites based on crystal symmetries

Rossi, N., Podestá, J. M., Bre, F., Méndez, C. G., and Huespe, A. E. (2021). "A microarchitecture design methodology to achieve extreme isotropic elastic properties of composites based on crystal symmetries". *Structural and Multidisciplinary Optimization*, 63(5), 2459-2472.

# A Microarchitecture Design Methodology to Achieve Extreme Isotropic Elastic Properties of Composites Based on Crystal Symmetries

**Nestor Rossi[1], Juan M. Podestá[2], Facundo Bre[1], Carlos G. Méndez[1], Alfredo E. Huespe[1,3][1]**

[1]Centro de Investigación de Métodos Computacionales (CIMEC), UNL, CONICET. Predio "Dr. Alberto Cassano", Colectora Ruta Nacional 168 s/n, Santa Fe, 3000, Argentina
[2]Computational Mechanics Laboratory (LAMEC-IMIT). Northeast National University (UNNE) - National Scientific and Technical Research Council (CONICET). Resistencia, 3500, Argentina
[3]Universitat Politècnica de Catalunya (UPC) - BarcelonaTech. Barcelona, 08034, Spain

**Abstract.** The present contribution describes an optimization-based design technique of elastic isotropic periodic microarchitectures with crystal symmetries aiming at the realization of composites with extreme properties. To achieve this goal, three consecutive procedures are followed: i) a series of inverse homogenization problems with symmetry constraints, ii) a correlation analysis between symmetries and effective elastic properties of the attained microarchitectures, and, iii) the pattern resemblance recognition of these topologies and their redesign, by adopting microstructures with two length-scales, through optimized parametric geometries. This paper is devoted to assessing the third procedure because the first two procedures have been evaluated in previous works of the authors, and here they are only summarized.

By applying the methodology, two plane group symmetries are assessed to define two families of 2D periodic parameterized microarchitecture. Once the parameters have been optimized, the resulting composites achieve elastic isotropic properties close to the whole range of the theoretically estimated bounds. Particularly, an unprecedented microstructure attaining the theoretical maximum stiffness is reported. Starting from these parameterized topologies, simple, one-length scale and easily manufacturable geometries are defined. One of the so-designed microarchitectures has been manufactured and tested, displaying an effective Poisson's ratio of -0.90 simultaneously with a high shear modulus.

**Keywords:** extreme elastic properties, parameterized microstructure designs, topology optimization, multi-objective optimization, crystallographic symmetries, auxetic composite

## C.1. Introduction

The synthesis of composites with unusual effective properties constitutes an important goal in manufacturing new metamaterials with a wide range of applications. Concerning the ground-breaking technology of additive manufacturing, full use of optimization tools, typically those based on topology optimization, can be successfully exploited to design and develop geometrically complex, but realizable, microstructures with extreme effective properties [32, 140].

In this contribution, the attention is addressed to the optimal design of the microstructure of composites where the geometrical distribution of the constituent phases, rather than their physical or chemical compositions, determine unusual extreme elastic properties. In these cases, the microarchitecture configuration plays a central role in reaching such properties; and their design results in a significant issue to find out an optimal solution.

Concerning two-dimensional well-ordered biphasic composites with effective isotropic elastic properties, the theoretically estimated bounds for their mechanical properties have been reported by Cherkaev and Gibiansky [51], henceforth named the CG-bounds. By denoting $K$ and $G$ the effective bulk and shear moduli of the composite constituted by a stiff phase $M_1$ and a soft phase $M_2$, with volume fractions

[1]Corresponding author. E-mail address: ahuespe@cimec.unl.edu.ar (A.E. Huespe).

$f_1$ and $f_2$ (with $f_1 + f_2 = 1$), shear moduli $G_1$ and $G_2$, and bulk moduli $K_1$ and $K_2$, respectively; they are limited above by the upper bound $G^u(K)$ defined by:

$$G^u(K) = \frac{\omega^u(f_1G_1 + f_2G_2) + G_1G_2}{G_2f_1 + G_1f_2 + \omega^u} \quad ; \quad \omega^u = -G_1 + \frac{\alpha^u y_K}{\beta^u y_K - \gamma^u}; \tag{C.1}$$

and below by the lower bound $G^l(K)$ defined by:

$$G^l(K) = \frac{\omega^l(f_1G_1 + f_2G_2) + G_1G_2}{f_1G_2 + f_2G_1 + \omega^l} \quad ; \quad \omega^l = -G_1 + \frac{\alpha^l(\frac{1}{y_K} + \frac{1}{K_1})}{\beta^l(\frac{1}{y_K} + \frac{1}{K_1}) - \gamma^l}; \tag{C.2}$$

where

$$y_K = -K_1K_2\frac{K - \frac{1}{(\frac{f_1}{K_1} + \frac{f_2}{K_2})}}{K - (f_1K_1 + f_2K_2)}\left(\frac{f_1}{K_1} + \frac{f_2}{K_2}\right); \tag{C.3}$$

and the coefficients $\alpha$, $\beta$, $\gamma$ depend on $K_1$, $G_1$, $K_2$, and $G_2$.

It is usually assumed that material moduli of the phases are related by a stiffness ratio or contrast factor $r = K_1/K_2 = G_1/G_2$. Particularly, for a composite whose phases are characterized by the elastic parameters: $K_1 = 5/7$, $G_1 = 5/13$, $f_1 = 0.5$, and $r = 200$; the coefficients $\alpha$, $\beta$, $\gamma$ result: $\alpha^l = 0.4107$, $\beta^l = 1.0653$, $\gamma^l = 0.0110$, $\alpha^u = -0.1256$, $\beta^u = -0.2200$ and $\gamma^u = 2.0 \times 10^{-4}$. The upper and lower bounds for the effective bulk modulus coincide with the Hashin-Shtrikman bounds [141]:

$$K^u_{HS} = K_1 + \frac{f_2}{\frac{1}{K_2 - K_1} + \frac{f_1}{K_1 + G_1}} \quad ; \tag{C.4}$$

$$K^l_{HS} = K_2 + \frac{f_1}{\frac{1}{K_1 - K_2} + \frac{f_2}{K_2 + G_2}} \quad . \tag{C.5}$$

The CG-bounds are plotted in Figure C.1. Alternatively to the *K*-*G* space of effective properties, CG-bounds can be plotted in the *E*-$\nu$ space, with *E* being the effective Young modulus and $\nu$ the Poisson's ratio, as it is also depicted in Figure C.1. In this work, it is indistinctly made reference to both spaces according to what is more convenient to perform the desired analysis. Moreover, composites with effective properties lying on the analytical CG-bounds are herein called extreme materials.

Figure C.1 also indicates the regions of these bounds defining composites with extreme properties displaying interesting features that could be technically exploited. For example, the composites whose properties stay on the CG-bounds along the gray zone are auxetics (i.e., negative Poisson's ratios: $\nu < 0$). Also, the composite with the most negative Poisson's ratio, represented by point B, corresponds to the point on the CG-bounds which is tangent to the straight lines crossing the origin of coordinates, in the *K*-*G* space. The stiffest isotropic composite which could be attained with phases $M_1$ and $M_2$, and a given volume fraction $f_1$ corresponds to the upper-right vertex. Another specific class of composites is the isotropic bimode materials, which, according to [70], count with a high $K/G$ ratio. They are located on and near the lower bound, with minimum G[2]. Bimode materials have been proposed for acoustic cloaking applications in [8, 142–144]. Some of these remarkable features (auxetic composites region and minimum Poisson's ratio) are more clearly enlightened in the *E*-$\nu$ space.

For a long time, it has been of interest to know if extreme materials are realizable. Recent contribu-

[2]It is worth remarking that void is needed as the soft phase to achieve null eigenvalues of the constitutive tensor, achieving strict bimode materials.

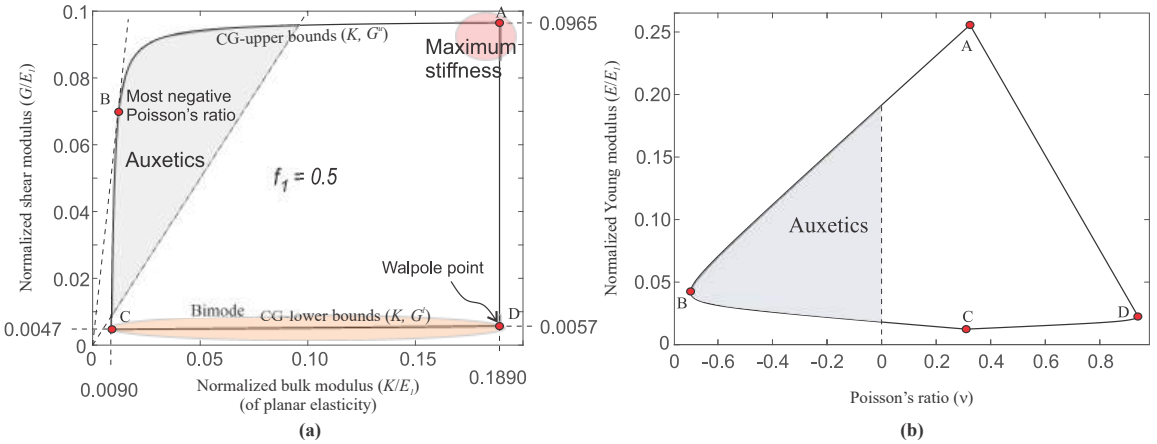


**Figura C.1:** Analytic bounds of effective properties for two-phase isotropic composites according to [51] (CG-bounds). Plane elasticity. a) Bounds in the space $(K, G)$ ; b) same bounds in the space $(E, \nu)$. Properties of phases $M_1$ and $M_2$ are $K_1 = 5/7$; $K_2 = K_1/r$; $G_1 = 5/13$; $G_2 = G_1/r$, $r$ =200 ($E_1$=1, $E_2 = E_1/r$, $\nu_1 = \nu_2$=0.3). Volume fraction of phase $M_1$ is $f_1 = 0.5$.

tions aiming at this objective for non-periodic microstructures are [145, 146] and references cited therein. The assemblage of coated spheres [22, 147], Vigdergauz structures [71], and the composite class reported by Sigmund [67] are materials attaining the theoretical maximum *K*. Additionally, maximum and minimum stiffness materials (upper-right and lower-left corners of the CG-bounds in the *K*-*G* space) can be achieved by sequential laminates [148, 149], specifically by rank-3 laminates [150]. Besides, the closest known solution to the Walpole point (lower-right corner in *K*-*G* space), is the hexagon structure reported by Sigmund [67]. A more detailed discussion on the effect that different microarchitecture topologies have to attain extreme materials can be found in [136]. Despite the previously mentioned families of microstructures, it has not yet been reported that the entire CG-bounds are attainable. Furthermore, excluding Vigdergauz structures, these microarchitectures achieving the theoretical CG-bounds correspond to topologies displaying more than one length-scale, which seems to benefit the possibility of attaining an extreme response but seriously limits the manufacturability and use of the composites in actual applications. Additionally, as recently reported by Milton [151], auxetic biphasic composites, with void as the soft phase and effective Poisson's ratio tending to -1, besides of having a vanishing bulk modulus, generally present a vanishing shear modulus.

The microarchitecture design methodology reported in this work pursues the attainment of simple two-length-scale parameterized periodic topologies, defined by only a few design parameters. These microstructures should be able to attain properties near to the whole theoretical bounds and should satisfy crystal symmetries. The adequate symmetries to be imposed on these topologies are assessed as an additional result from the same methodology. Additionally, it is shown that the designed auxetic microstructures retain high shear stiffness in the limiting case of the stiffness ratio between phases going to infinite.

To achieve this target, an optimization-based design methodology consisting of three consecutive procedures is proposed and is briefly described in Section C.2. The remaining part of the paper is organized as follows. Section C.3 describes a brief overview of inverse homogenization problems assuming crystal symmetries. In Section C.4, the geometrical patters regarding material distribution are analyzed and the novel parameterized microstructures are introduced. Section C.5 presents a multi-objective optimization study to validate the extreme properties attainable by the parameterizations. Results are presented and discussed in Section C.6. Section C.7 explores the influence that similar one-length-scale topologies have on the microarchitecture capability to achieve extreme effective properties. Additionally, in the same Section, the experimental results of a manufactured specimen is reported. Finally, Section C.8 establishes the main conclusions of this work.

## C.2. Microstructure design methodology

The main idea behind the present approach is to enforce predefined crystallographic symmetries throughout the optimal topology design process of composite microarchitectures to attain unusual effective elastic properties. Recently, several works have reported the use of symmetries in microstructure design [3, 152–158]. The periodic pattern assumed for the microarchitecture topology jointly with the prescribed symmetries generates microarchitectures that can be assimilated to crystals.

Inspired by this concept, the proposed design methodology is based on three successive procedures summarized in the following items:

*i)* the first step in the design procedure consists of solving several topology optimization problems with an appropriate mathematical formulation posed as an inverse homogenization problem [62]. The target properties of these optimization problems are defined according to the CG-bounds; a point on the CG-bounds defines the effective target properties of the optimization problem which is solved. The attained microarchitecture configurations are forced to have different crystal symmetries that have to be consistent with the symmetry of the target effective properties. This procedure is repeated for several points on the CG-bounds.

*ii)* The elastic properties of the designed microarchitectures are evaluated by correlating the attained closeness to the CG-bounds with the imposed symmetries, see [60, 61, 65, 115]. Conclusions on the most suitable crystal symmetries to approach the full range of the CG-bounds are assessed.

*iii)* The patterns of the topologies obtained with those crystal symmetries are identified and redefined through a geometrical parameterization, by adopting a two-scale material distribution, respecting the symmetries[3] that inspired them. Finally, with the proposed configurations, a multi-objective optimization problem is solved to attain the set of parameters defining the microarchitectures whose effective properties are the closest ones to those of extreme materials.

The above mentioned procedures in items *i)* and *ii)* have been studied and reported by the authors in previous works [60, 61, 65, 115] and are summarized in Section C.3 for the sake of completeness, while the topic mentioned in item *iii)* is developed in detail in Sections C.4 and C.5 and constitutes the main contribution of this paper.

## C.3. Inverse homogenization problems assuming crystal symmetries

A basic micro-cell $\Omega_\mu$ of a two-phase periodic composite is considered, such as is schematically shown in Figure C.2. The phases $M_1$ and $M_2$ occupy the domains $\Omega_\mu^1$ and $\Omega_\mu^2$, respectively. A characteristic function $\chi(\boldsymbol{y})$, in $\Omega_\mu$, identifies the positions where the phase $M_1$ is placed, such as indicated in the same Figure.

Following the procedure established in [60, 65], a micro-architecture inverse design problem is formulated as a topology optimization problem [30, 111, 159] to find a composite whose effective properties are a given target pair of values $K^t$ and $G^t$. A sequence of target values $K^t$ and $G^t$ on the CG-bounds are chosen, and the corresponding topology optimization problems are solved to find the microarchitectures providing the closer elastic properties to the CG-bounds. In [60, 61, 65, 115], the single length-scale microarchitectures are found using a topology optimization algorithm based on a smooth level-set function and with the sensitivities being computed through the topological derivative, see [58, 59, 160]. Discussion about topological derivatives can be found in [57, 161].

[3] It is commonly observed that solutions of the inverse homogenization problem, in step 1 of item i), may provide microarchitectures with higher symmetry to the imposed one. In these cases, the procedure in item iii) adopts this higher symmetry.

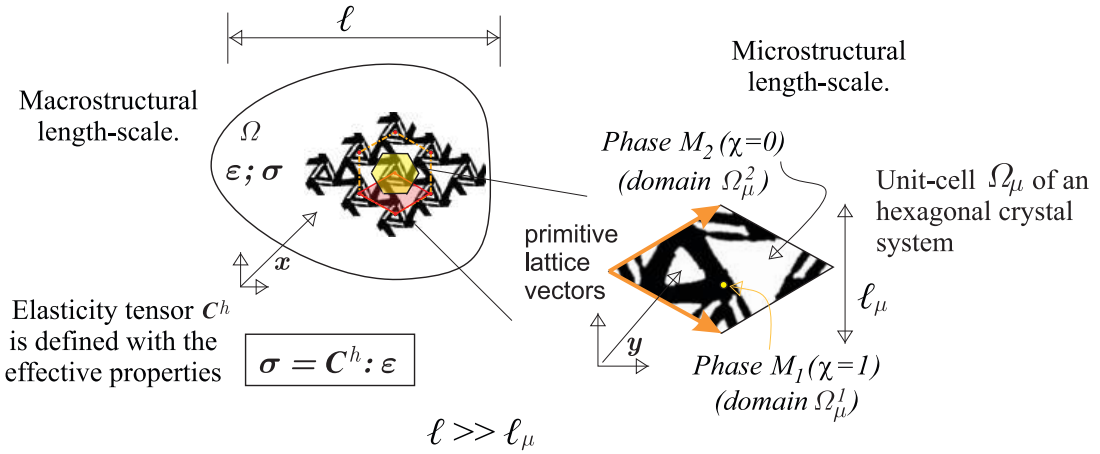


**Figura C.2:** Inverse homogenization problem to determine the characteristic function $\chi$ of a periodic composite whose microstructure has hexagonal crystal symmetry. The domain $\Omega_\mu$ adopted for the topology design problem is a unit cell of the underlying hexagonal Bravais lattice. The periodicity directions are defined by the primitive vectors of the lattice. The effective elasticity tensor $\mathbf{C}^h$ relating the macrostrain $\boldsymbol{\varepsilon}$ with the macrostress $\boldsymbol{\sigma}$ is evaluated with a computational homogenization technique using the same cell.

### C.3.1. Selection of the computational design domain

The selection of the shape of $\Omega_\mu$, i.e., the spatial domain where the inverse homogenization problem is solved, can be related to the symmetry of the target effective response. The procedure through which both features, the shape of $\Omega_\mu$ and the symmetry of the effective response, are related is summarized in Table C.1. In this Table, column two shows that any material configuration compatible with the hexagonal crystal system possesses an isotropic elasticity tensor, such as shown in column one. Columns three and four display the point groups and plane groups compatible with the hexagonal system. Furthermore, this crystal system is only compatible with a hexagonal Bravais lattice which has two unit cells shown in column six. The hexagonal domain is the Weigner-Seitz cell and the parallelogram is the primitive cell of the lattice. This primitive cell is taken here as the region where the topology optimization problem is solved. Additional details about this point are presented in [65].

The five plane groups defined in column four of Table C.1 are tested to attain the solutions of the optimization problem. These plane groups are imposed on the material distribution by enforcing the corresponding symmetry operations to the $\chi$ function, as it is explained in detail in [61]. Therefore, the isotropic effective response of the designed microstructure is automatically guaranteed without explicitly imposing any constraint to the topology optimization problem.

**Tabla C.1:** Hexagonal (2D) Crystal System. Compatible point and plane groups. The elasticity matrix is isotropic and is represented in column 1, with the coefficient $C_{11}$ and $C_{12}$ characterizing the elastic properties. The conventional Kelvin notation for fourth order tensors of plane elasticity is used.

| Elasticity Matrix | Crystal system | Point group | Plane group | Compatible Bravais lattice | Wigner-Seitz and primitive unit cell |
|---|---|---|---|---|---|
| $\begin{bmatrix} C_{11} & C_{12} & 0 \\ C_{12} & C_{11} & 0 \\ 0 & 0 & C_{11}-C_{12} \end{bmatrix}$ | hexagonal | 3 | *p3* | hexagonal | 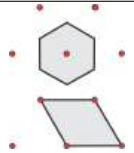 |
| | | 3m | *p3m1* | | |
| | | | *p31m* | | |
| | | 6 | *p6* | | |
| | | 6mm | *p6mm* | | |

### C.3.2. Computational homogenization

The effective properties of the composites are evaluated in the primitive cell of the so-designed periodic microstructure, which is coincident with the same domain taken for the topological optimization problem. This procedure defines the tensor $\mathbf{C}^h$ and is schematically shown in Figure C.2.

The computational homogenization follows a conventional technique that is well-described in the literature, see for example [48] and references cited therein. Periodic boundary conditions on the displacement fluctuation field, along the primitive vectors of the underlying Bravais lattice, are imposed.

### C.3.3. Solutions attained with the inverse homogenization problems

Results of topology optimization problems using the above-mentioned methodology to attain near extreme effective isotropic properties, which show different plane groups compatible with the hexagonal crystal system, have been reported in [60, 65]. These solutions are obtained by restricting the topology to have only one length-scale.

The analysis in these works leads to the following conclusions. Plane groups *p3*, *p31m* and *p6* are well-suited for the top-left region in the *K*-*G* space, while plane groups *p3m1* and *p6mm* are more convenient for the bottom-right sector, such as shown in Figure C.3. The same Figure shows some of the optimum microstructures, denoted T1,..., T7, whose effective elastic properties approximate the bounds, see Figures C.3a and b.

The microarchitectures in Figure C.3 display common patterns motivating the present work, as it is explained in the next Section.

A further discussion about the sensitivity of each plane group consistent with the hexagonal crystal system to attain extreme properties in different sectors of the CG-bounds appears in [60]. The reader is addressed to this reference work for additional details about this specific point related to the microarchitecture design problem.

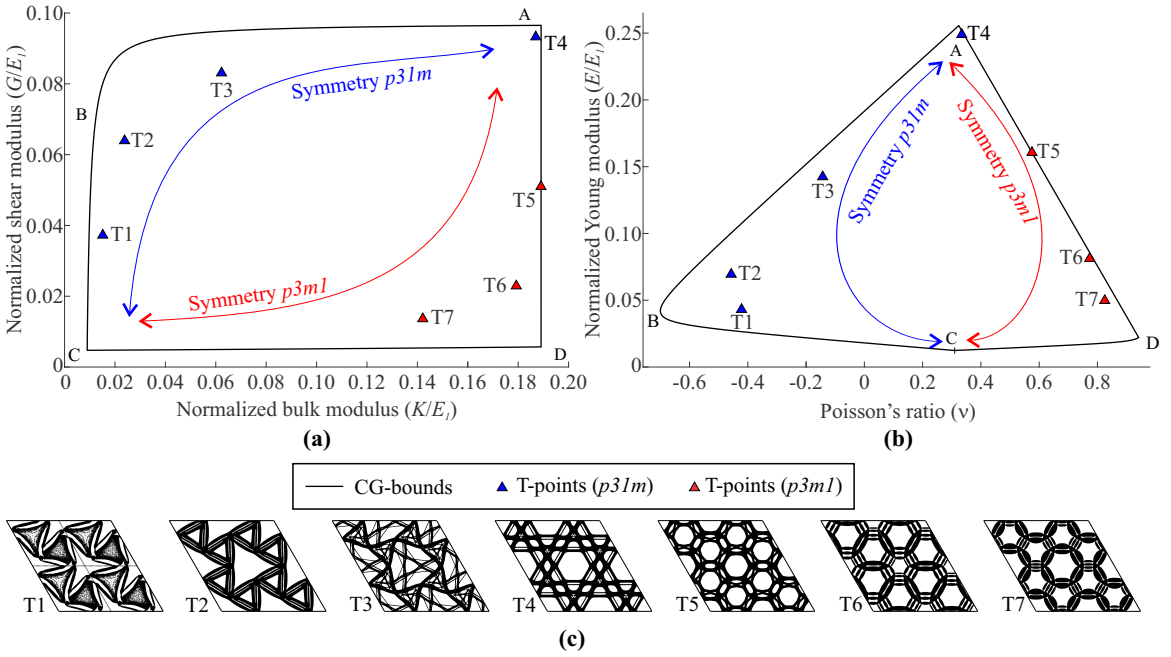


**Figura C.3:** CG-bounds of well-ordered biphasic composites with isotropic properties in the space of effective normalized properties: a) *K*-*G*, and b) *E*-$\nu$. Composites with stiff phase volume fraction: $f_1$=0.5. Elastic properties of the stiff phase: $E_1$=1, $\nu_1$=0.3. Stiffness ratio between phases: $r$=2×10$^2$. c) Microstructures obtained by topology optimization, a procedure formulated as a mathematical problem (inverse homogenization problem) (2×2 unit cells), instances T1 to T7 reported in [60].

## C.4. Geometrical pattern recognition of microstructures and their parameterization

In small sectors of the CG-bounds, a large number of solutions are obtained with the inverse homogenization problems. Based on these results, and noting that the enforcement of the symmetry constraints promotes the attainment of solutions displaying similar topologies for small changes of the targets, it is possible to recognize a geometrical material distribution that represents the composite microstructure for that given sector of the CG-bounds.

By employing this approach, it is possible to assess common geometrical patterns that suggest a road to reduce the original complex morphologies, provided by the topology optimization algorithm, to simpler ones. Specifically, simpler representative microarchitectures are adopted, based on the geometrical parameterization of the material configurations.

The assessment of some common geometrical patterns in the microstructures displayed in Figure C.3c can be summarized as follows:

- Figure C.4 replicates the microarchitectures T1,..., T4 with their corresponding unit cells. It can be observed that these microstructures have a material distribution notoriously resembling a pair of triangles with symmetry *p31m*, rotating relatively one to other as the target elastic properties move from the lower-left to the upper-right CG-bounds (see Figure C.3a). These triangles are highlighted in dashed red lines in the unit cells.

- The microarchitectures T5,..., T7 in Figure C.4 have a material distribution resembling a pair of irregular hexagons, highlighted in dashed red lines, with symmetry *p3m1*, whose shape continuously changes as the target elastic properties move from the upper-right to the lower-left CG-bounds.

- Additionally, a bar-like substructure recurrently appears in the sides of these polygons, a feature already noted by Sigmund [67] when trying to attain the Walpole point.

- The symmetry elements of both plane groups *p31m* and *p3m1* are shown in Figure C.4. Note that they have analogous symmetry elements: a three-fold rotational symmetry and three mirror planes. However, the mirror planes of the *p3m1* plane group intersect the Weigner-Seitz cell differently to that of the *p31m* plane group. This variant makes a big difference to obtain suitable results in different regions of the CG-bounds.

These observations motivate the development of two families of parameterized microstructures, with symmetries *p31m* and *p3m1*. As explained later, the symmetry of each family defines the region of the CG-bounds where the parameterized family is appropriate to approach the extreme properties.

The parameterized microstructures are defined by three constituents, see Figure C.5. Further to the soft and stiff phases, and inspired by the microstructures adopted in Sigmund's work [67], the bars in the sides of these polygons are replaced by laminated components. Each laminate is assumed as a sequence of layers of the same soft and stiff phases of the original biphasic composite. The width of each layer is much smaller than the unit cell size, introducing in the geometrical configuration a lower length scale respect to that of the cell size. A similar procedure has been reported recently by [121].

The geometrical parameters defining the material configurations of the two proposed microstructure families are described in Figure C.5. Black regions identify the stiff phase, white regions are the soft phase, and gray regions represent the laminated components. The laminate grayscale identifies the volume fractions of the laminate and the dashed red lines indicate the layer directions of the laminate.

In the configuration *p31m*, an angle $\alpha$ characterizes the rotation of two identical equilateral triangles. In the configuration *p3m1*, the dimensionless parameter $d$ defines two identical irregular hexagons.

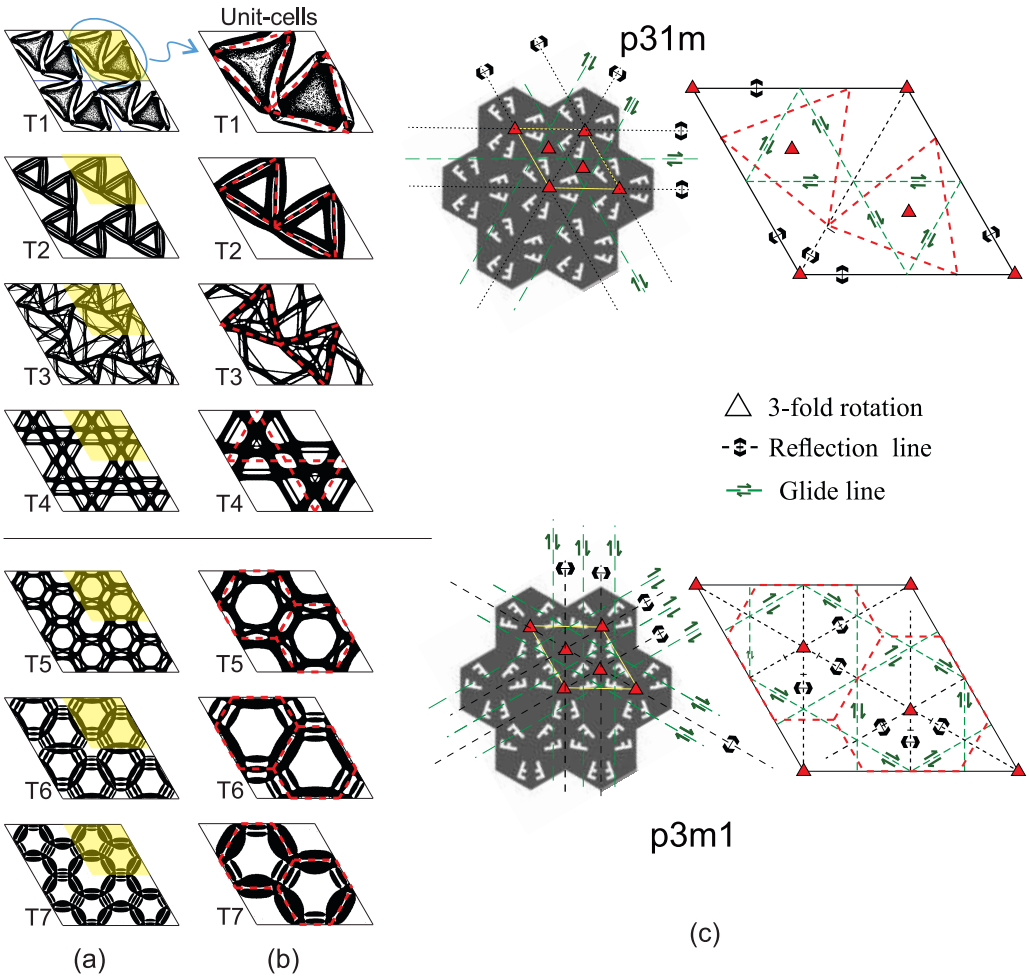


**Figura C.4:** Geometrical pattern recognition. a) Microarchitecture configurations T1 to T7. b) unit-cells ; c) symmetry elements of plane groups $p3m1$ and $p31m$. Dashed red lines indicate the underlying material distribution pattern.

The configuration *p31m* is defined by three parameters, $\alpha$, $\gamma$ and $t$, and the configuration *p3m1* is defined by five parameters, $d$, $\gamma_1$, $\gamma_2$, $\gamma_3$, and $t$. In both cases, the thickness $t$ of the laminate areas, common for all of them, comes as a result of the values of the other parameters, once the target volume fraction $f_1^t$ is imposed.

### C.4.1. Computational homogenization of the parameterized microarchitectures

A summary of the numerical implementation technique for assessing the effective properties of the parameterized microarchitectures is given next. These properties are assessed through computational homogenization, such as explained in Subsection C.3.2. However, in this case, to increase the numerical accuracy, all the computed unit-cells are modeled employing conformal meshes of finite elements that exactly capture the geometry of the interfaces. Thus, a procedure has been developed to adjust the finite element mesh to every particular tested combination of parameters.

At the length-scale corresponding the unit-cell observation, the laminate component is modeled as a homogeneous orthotropic elastic phase with an effective elasticity tensor with components:

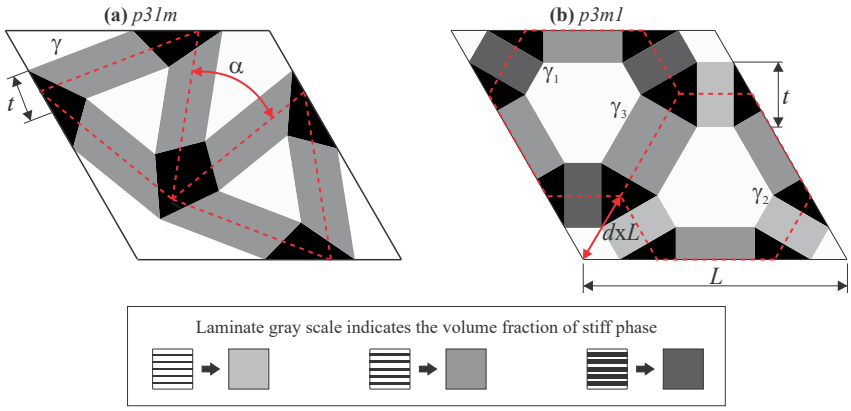


**Figura C.5:** Parameterizations of the unit-cell geometries. Configurations: a) *p31m* and b) *p3m1*. Black and white domains represent stiff and soft phases. Gray domains represent laminates constituted of a sequence of stiff and soft layers parallel to the red lines. The volume fractions of the laminate phases are determined by the parameters $\gamma$, $\gamma_1$, $\gamma_2$, and $\gamma_3$, respectively.

$$C_{11} = \frac{(K_1 + G_1)(K_2 + G_2)}{(1-\gamma)(K_1 + G_1) + \gamma(K_2 + G_2)}; \tag{C.6}$$

$$C_{12} = \frac{(K_1 - G_1)(K_2 + G_2) + 2(1-\gamma)(K_2 G_1 - K_1 G_2)}{(1-\gamma)(K_1 + G_1) + \gamma(K_2 + G_2)}; \tag{C.7}$$

$$C_{22} = C_{11} + \frac{4\gamma(1-\gamma)(K_1 - K_2)(G_1 - G_2)}{(1-\gamma)(K_1 + G_1) + \gamma(K_2 + G_2)}; \tag{C.8}$$

$$C_{33} = \frac{2G_1 G_2}{(1-\gamma)G_1 + \gamma G_2}; \tag{C.9}$$

where the vertical direction in this case (axis 2) is parallell to the laminate direction.

### C.4.2. Range of parameters, topological changes and special cases

The range of the parameters defining the microarchitecture geometries are limited by evident geometrical reasons and depends on the plane group characterizing the topology.

Regarding the *p31m* family of microstructures, the criteria to define the parameters bounds is the topological change that occur if some of the soft material regions collapse into a point. For instance, in the microarchitecture displayed in Figure C.5a, if the parameter $\alpha$ reaches a sufficiently small value, the soft material in the vertices of the the cell disappear. Similar effects happen if the stiff material volume fraction $f_1$ increases or the laminate volume fraction $\gamma$ decreases, which also affect the soft material triangles in the interior of the unit cell. Despite this, there are obvious values that cannot be surpassed: $0^o \leq \alpha \leq 120^o$, $0 \leq \gamma \leq 1$, and $0 \leq f_1 \leq 1$.

In the case of the *p3m1* family of microstructures analogous criteria is used, although laminated regions are allowed to disappear. By taking the microarchitecture displayed in Figure C.5b, the $d$ parameter reaches the lower bound when laminates regions with volume fractions $\gamma_1$ and $\gamma_2$ vanish. In this case, if $\gamma_3$=0.5, the Sigmund's triangle structure reported in [67] is obtained. On the contrary, if $d$ increases, the laminate region of $\gamma_3$ may vanishes. However, this is not a criterion to limit the upper value of $d$, which

may increase up to $d$=0.5, since in this situation, laminates with $\gamma_1$ and $\gamma_2$ get aligned[4]. Two characteristics of this parameterization are noted: i) *p6mm* symmetry is attained if $\gamma_1$=$\gamma_2$, and ii) for $\gamma_1$=$\gamma_2$=$\gamma_3$=0.5 and $d$=1/3, the above mentioned Sigmund's hexagon structure is recovered. The limits that cannot be surpassed in this parameterization are: $0 \leq d \leq 0.5$, $0 \leq \gamma_1 \leq 1$, $0 \leq \gamma_2 \leq 1$, $0 \leq \gamma_3 \leq 1$, and $0 \leq f_1 \leq 1$. In addition, note that both configurations coincide if, having every $\gamma$ the same value, the parameter $d$=0.5 and $\alpha$=120º.

## C.5. Optimized parametric microstructures

The optimal set of parameters defining the composites whose effective properties are closer to the CG-bounds, are assessed through a multi-objective optimization technique. The space of design variables $\mathbf{p}$, where $\mathbf{p} = \{\alpha, \gamma, t\}$ for the *p31m* parameterization and $\mathbf{p} = \{d, \gamma_1, \gamma_2, \gamma_3, t\}$ for the *p3m1* parameterization, is the admissible set of geometrical parameters $\mathcal{V}$ identifying the microstructure configuration, which is bounded by the criteria specified in the previous sub-Section C.4.2.

According to Figure C.6, the full CG-bounds could be approximated by solving four bi-objective optimization problems formulated as follows:

$$\begin{aligned} \min_{\mathbf{p}\in\mathcal{V}} \quad & [h_1(\mathbf{p}), h_2(\mathbf{p})] \\ \text{subject to:} \quad & f_1(\mathbf{p}) - f_1^t = 0, \end{aligned} \tag{C.10}$$

where $h_1(\mathbf{p})$ and $h_2(\mathbf{p})$ are the objective functions, while $f_1(\mathbf{p})$ and $f_1^t$ are the cell volume fraction and the target volume fraction respectively. The objective functions, $h_1$, $h_2$, for each problem are specified as follows:

- Problem 1: to attain the boundary A-B, $h1 = \nu$ and $h2 = -E$;
- Problem 2: to attain the boundary B-C, $h1 = \nu$ and $h2 = E$;
- Problem 3: to attain the boundary C-D, $h1 = -\nu$ and $h2 = E$;
- Problem 4: to attain the boundary A-D, $h1 = -\nu$ and $h2 = -E$;

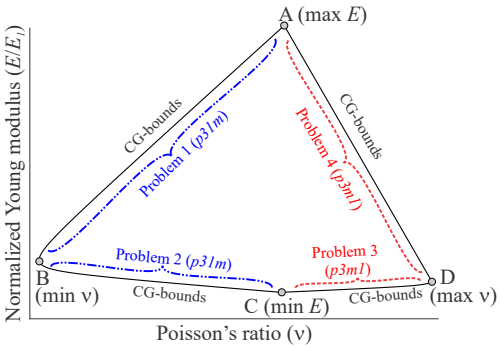


**Figura C.6:** Four bi-objective optimization problems formulated to attain the CG-bounds.

Configurations *p31m* are used to solve problems 1 and 2, then

$$f_1 = \frac{\gamma\, \Omega_{lam}(\alpha, t) + \Omega_1(\alpha, t)}{\Omega_\mu}. \tag{C.11}$$

[4]Note that orthogonality of the laminate axis and the stiff material on the interphase is lost when $d$ is increased once laminate with $\gamma_3$ vanishes.

Instead configurations *p3m1* are used to solve problems 3 and 4, where

$$f_1 = \frac{\gamma_1\,\Omega_{lam1}(d,t) + \gamma_2\,\Omega_{lam2}(d,t) + \gamma_3\,\Omega_{lam3}(d,t) + \Omega_1(d,t)}{\Omega_\mu}. \tag{C.12}$$

In both cases, $\Omega_{lam}$, $\Omega_{lam1}$, $\Omega_{lam2}$, and $\Omega_{lam3}$ are the total areas occupied by the laminate materials and $\Omega_\mu$ is the area of the unit cell. Full expressions of the volume fraction constraints (C.11) and (C.12) are described in the Appendix.

Solutions of problems 1 to 4 are given through the set of non-dominated optimal design variables, known as Pareto fronts. Given the contradictory nature of these multi-objective optimization problems, the set of parameters defining each Pareto front is found using the NSGA-II (non-dominated sorting genetic algorithm-II) [162].

## C.6. Results and discussion

The Pareto fronts resulting from problems 1 to 4 using the parametrized microstructures previously defined are plotted in Figures C.7a and b. For each of these problems, an average of approximately 275 non-dominated optimal solutions have been obtained. Thus, around 1100 points of attainable composites conform the complete front. Some microarchitectures of interest belonging to such extreme solutions (Pareto front) are depicted in Figure C.7c, denoted as instances P1,..., P7. Figures C.7a and b show their corresponding effective elastic properties which are compared with inverse homogenization problem solutions: T1,..., T7. The parameters of the optimal microstructures obtained for the instances P1,..., P7 are detailed in Figure C.7d.

Further insight into the obtained microstructures is discussed next. The results displayed by the P-points, compared with the T-points in Figures C.7a and b, exhibit a notable improvement for approaching the extreme properties of the parameterized microstructures. This is the result of including the smaller length scale incorporated by the laminate.

Regarding the configurations with symmetry *p31m*, effective Poisson's ratios close to the theoretical limits are achieved for the full range of admissible values of $E$ along the Pareto front close to the A-B boundary, such as shown in Figure C.7b. The angle $\alpha$ has a strong connection with the effective properties of the composite along this front; the greater the angle $\alpha$, the larger the effective Young modulus, while the parameter $\gamma$ takes an almost constant value, around $\gamma{\approx}0.5$. The P4 configuration, defined by the parameters $\alpha$=120$^o$ and $\gamma$=0.5, attains simultaneously the theoretical maximum $K$ and maximum $G$. This configuration constitutes an alternative solution to the Francfort and Murat's rank-3 laminate, although due to the geometrical constraint of the parameterized configuration explained in Section C.4.2, it is only correctly defined for $f_1{\leq}0.5$.

Although the mechanism inducing the auxetic response of the herein reported *p31m* architectures resembles the already known rotating triangles structures, or Kagome lattices, the use of laminated areas with variable volume fractions, instead of rigid triangles or bars connected by hinges, defines an alternative microarchitecture.

Solutions generated with the *p3m1* parametric configurations display a closer approach to the theoretical bounds in the regions denoted A-D and C-D. Configurations obtained with $\gamma_1$=$\gamma_2$=$\gamma_3$=0.5 attain the maximum $K$-bound (these composites belong to the class reported by Sigmund [67]). A further property of the present parameterization is that a change of the parameter $d$ induces a modification of the effective shear modulus $G$, allowing to move along the right CG-bound in the $K$-$G$ space. This effect is observed in the P5 and P6 configurations of Figure C.7.

Microstructures P1 and P7 reveal that in the transitions from points B to C, and D to C, respectively, a decrement of the laminate volume fraction is required. Thus, optimal parameterized configurations attaining the lower-left corner of the $K$-$G$ space tend to topologies with disconnected stiff areas.

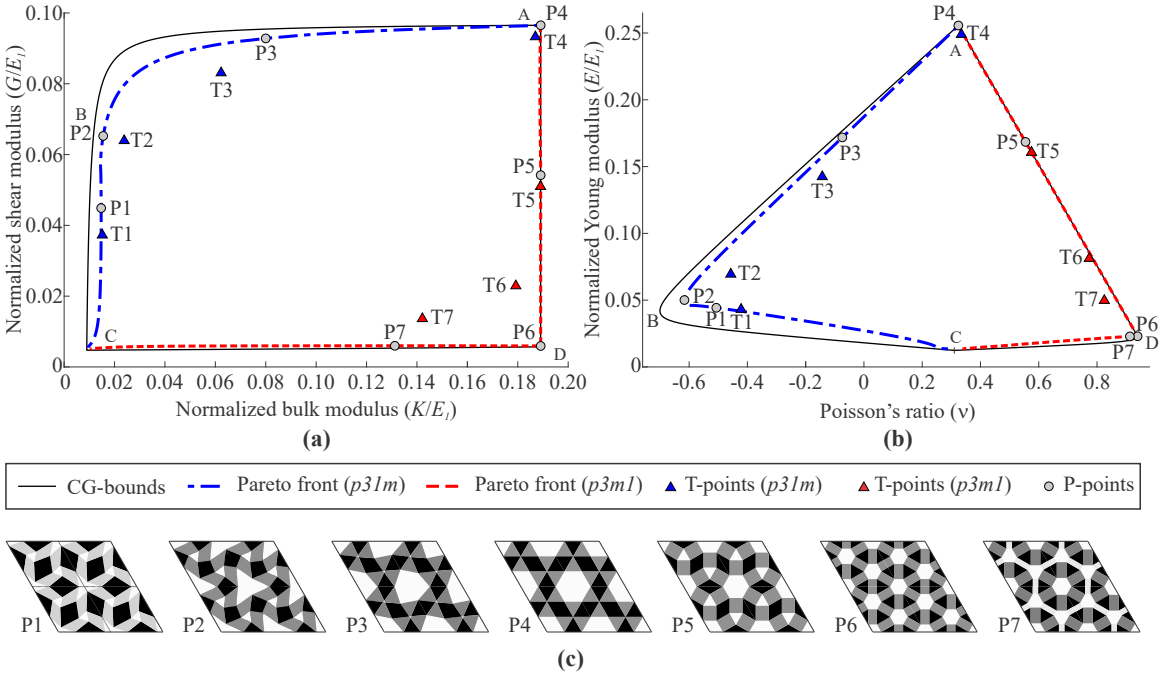


(d)

| Instance | | | P1 | P2 | P3 | P4 | P5 | P6 | P7 |
|---|---|---|---|---|---|---|---|---|---|
| *Configuration* | *p31m* | α [°] | 36.43 | 48.81 | 97.78 | 120 | - | - | - |
| | | γ [-] | 0.20 | 0.52 | 0.54 | 0.50 | - | - | - |
| | *p3m1* | *d* [-] | - | - | - | 0.50 | 5/12 | 1/3 | 0.36 |
| | | $\gamma_1$ [-] | - | - | - | 0.50 | 0.50 | 0.50 | 0.56 |
| | | $\gamma_2$ [-] | - | - | - | 0.50 | 0.50 | 0.50 | 0.56 |
| | | $\gamma_3$ [-] | - | - | - | - | - | 0.50 | 0.10 |

**Figura C.7:** Near optimal parameterized microstructures. CG-bounds of well-ordered biphasic composites with isotropic properties in the space of effective normalized properties: a) *K*-*G*, and b) *E*-$\nu$. Composites with stiff phase volume fraction: $f_1$=0.5. Elastic properties of the stiff phase: $E_1$=1, $\nu_1$=0.3. Stiffness ratio between phases: $r$=2×10$^2$. c) Family of parameterized microarchitectures with elastic properties close to the CG-bounds. Instances P1 to P7 (2×2 unit cells) d) Parameters defining the geometrical configurations of P1 to P7 microstructures.

The complete set of parameterized microstructures with properties lying on the Pareto fronts in Figures C.7a and b is presented in a supplementary .csv file and in a supplementary material video (see Data availability Section).

**Analysis of the results with stiffness ratio between phases going to infinite** The solutions of additional multi-objective optimization problems with increasing stiffness ratios, $r$, between both phases of the composites, reveal that the optimal parameterized microstructures have effective elastic parameters that are much closer to the CG-bounds if compared with the solution having a lower stiffness ratio $r$. Pareto fronts obtained for composites with $r$=2×10$^4$ and $f_1$=0.5 are shown in Figure C.8a and b with blue and red dashed lines. From these results, it can be seen that the CG-bounds are almost reached throughout their entire extension, except in the top-left corner in the *K*-*G* space. Also, a variety of structures with the minimum Poisson's ratio $\nu$=-1 and a wide range of $G$ values can almost be attained.

Next, attention is paid to the case of *p31m* parameterization to obtain the left and upper regions of the CG-bounds. Let examine the variation of the optimum parameter $\alpha$ with increasing stiffness ratio $r$ while the parameter $\gamma$ is hold fixed. These results are illustrated in Figure C.9, where three set of parameters $\alpha = 50^o$, $110^o$ and $120^o$ are assessed, and the stiffness ratio is increased from $r = 200$, 500 to $2 \times 10^{10}$.

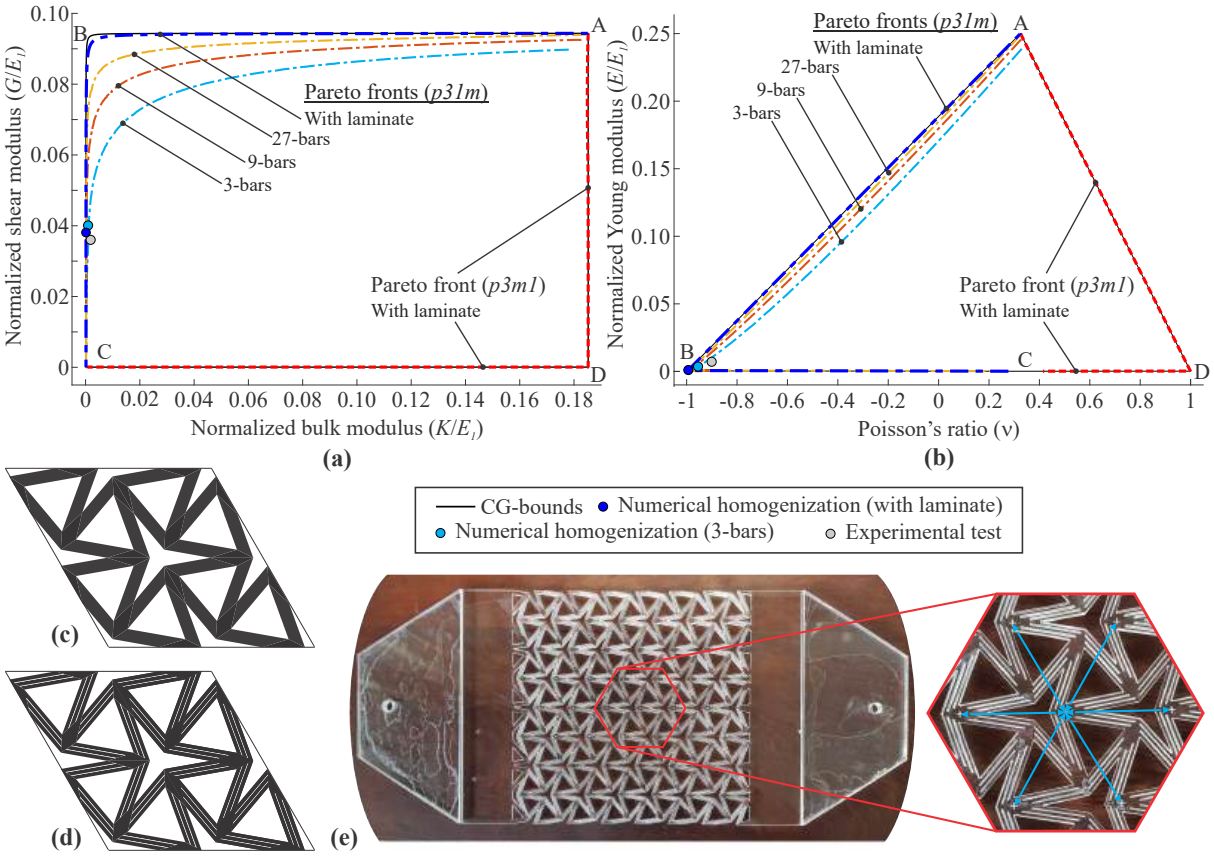


**Figura C.8:** Composites with stiff phase volume fraction: $f_1$=0.5. Elastic properties of the stiff phase: $E_1$=1, $\nu_1$=0.3. Stiffness ratio between phases: $r$=2×10$^4$. Spaces of normalized a) $K$-$G$ and b) $E$-$\nu$. Configurations with *p31m* symmetry, $\alpha$=20$^o$ and $\gamma$=0.9 (2×2 unit cells): c) with laminate material and d) with three bars; e) Manufactured auxetic composite. Details of the points taken for measuring the relative displacement vectors.

In the figure, instances a, b and c for every set of $\alpha$-parameter is indicated with an identical color to that identifying the respective $r$-parameter. The solution with $\alpha = 120^o$ reaches the theoretically stiffest composite, independently of $r$. The solution with $\alpha = 50^o$ achieves auxetic composites. However, for the specific cases of solutions with $\alpha = 110^o$, there is observed a transition from solutions with high $K$ and high $G$ moduli, for low $r$, to solutions with low $K$ and high $G$ moduli, for high $r$.

## C.7. Microstructures with a single length scale

Based on the previous discussion and with the objective to attain manufacturable microarchitectures, it is performed further numerical research related to the solutions obtained with the *p31m* geometrical configurations.

The laminate material is replaced by a small number of bars with finite thickness. The thickness of the bars are defined to maintain the volume fraction $\gamma$ of the removed laminate unchanged. The transition from the laminate material to a 3-bars configuration is depicted in Figures C.8c and d, respectively. With these bar configurations, new multi-objective optimizations are performed to obtain the corresponding Pareto fronts in the regions A-B and B-C of the CG-bounds. One Pareto front is obtained for each number of adopted bars. The results are depicted in Figures C.8a and b for configurations with 3, 9, and 27 bars.

The solutions move away from the CG-bounds when the bar number decreases, indicating that the bar bending stiffness plays a central role to achieve auxetic behavior and high $G$ values. It was observed that, along the A-C region of the CG-bounds, the increase in the number of bars, while holding the parameters

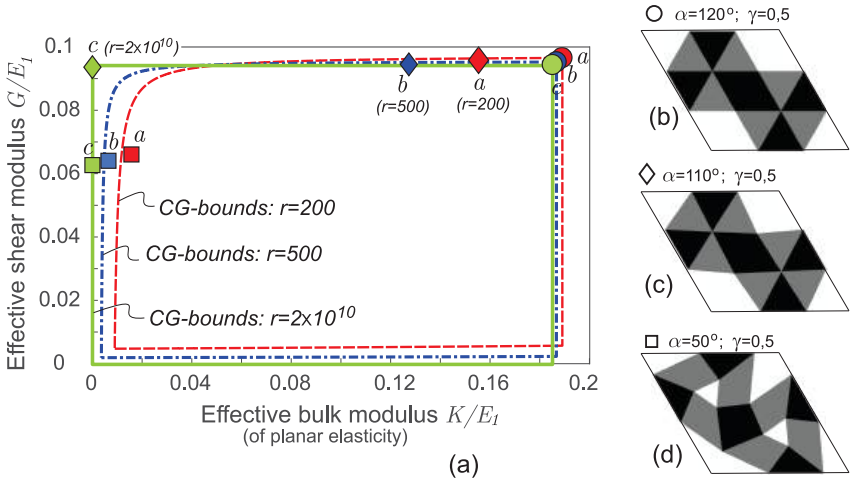


**Figura C.9:** Analysis of the influence of stiffness ratio between phases on the effective properties. Composites with stiff phase volume fraction $f_1$=0.5, and laminate volume fraction $\gamma$=0.5. Elastic properties of the stiff phase: $E_1$=1, $\nu_1$=0.3. a) CG-bounds in the space of normalized *K*-*G* for three stiffness ratios: $r = 200$ in red, $r = 500$ in blue and $r = 2 \times 10^{10}$ in green and effective properties for every stiffness ratio between phases of the displayed microstructures. Microarchitectures defined for: b) $\alpha = 120^o$, c) $\alpha = 110^o$, d) $\alpha = 50^o$.

fixed, decreases the effective bulk modulus, while the shear modulus is not substantially modified. Thus, the higher the bar number, the lower the bending bar stiffness, the lower the bulk modulus, and the closer to the extreme properties.

**Experimental test of an auxetic microstructure** A specimen is manufactured with the microstructure of Figure C.8d, with parameters $\alpha$=20$^o$ and $\gamma$=0.9, and is subjected to a tensile test to validate the previous numerical results.

The effective properties for this optimal microstructure, adopting a laminate component (Figure C.8c), result as shear modulus $G$=0.03799 and Poisson's ratio $\nu$=-0.99998. If the laminate material is replaced by three bars (Figure C.8d), the effective properties obtained are shear modulus $G$=0.04009 and Poisson's ratio $\nu$=-0.95481. These two points are shown in Figure C.8a and b as blue and light blue dots respectively. Thus, the relative errors obtained between the 3-bars approximation of the laminate and the optimal microstructure that correspond to a laminate phase are $\epsilon_G$=5,53 % and $\epsilon_\nu$=4,52 % for the shear modulus and the Poisson's ratio respectively.

A PMMA sheet of 3 mm thickness has been cut with a laser beam, furnishing the specimen depicted in Figure C.8e. The effective area of the metamaterial is 228 mm$\times$197 mm, counting with 48 unit cells. The Young modulus of the PMMA sheet, $E_{\text{PMMA}}$=1.8 GPa, is used to normalize the effective Young modulus of the manufactured composite.

Through numerical assessment, it is checked that the loaded specimen displays a reasonably periodic displacement field in its central part. This condition guarantees a reliable measurement of the effective properties in that region. Also, the numerical solution shows that the effective strains on the plane of the sheet are much larger than the transverse strains guaranteeing the plane strain condition assumed in this work.

The relative displacement vectors between equivalent points of the periodic microstructure, in the central region of the specimen, shown in the detail of Figure C.8e, are monitored with a Digital Image Correlation (DIC) technique. These displacements furnish an effective strain tensor which is finally used to assess the effective Young modulus and Poisson's ratio. The effective properties assessed in the specimen with this technique are plotted in Figures C.8a and b as a gray dot. The Poisson's ratio is -0.9007 and the normalized shear modulus is 0.0360. Then the relative errors obtained between the experimental results and the Pareto front result that correspond to a laminate phase are $\epsilon_G$=5,53 % and $\epsilon_\nu$=9,93 % for

the shear modulus and the Poisson's ratio respectively.

## C.8. Conclusions

A microarchitecture design methodology, based on crystal symmetries particularly addressed to attain extreme materials involving three sequential procedures, is presented. It involves a topology optimization stage, formulated as an inverse homogenization problem, the symmetry sensitivity analysis, and the pattern identification stage together with a parameterization of the microarchitecture geometrical configuration. Both the topology optimization and the symmetry sensitivity analysis to capture the CG-bounds have been adressed in previous works by the authors and their main aspects and conclusions has been summarized in this paper. The incorporation of crystal symmetries as an additional constraint allows obtaining simpler configurations with isotropic properties at the first design stage. This guiding rule also makes much easier the posterior topology pattern identification. Remarkably, for the analyzed target, only two crystallographic plane group symmetries are enough to approximate the entire CG-bounds. Geometrical parameterizations characterized by two length scales are proposed. This feature has a significant influence to attain extreme properties. The extreme effective material properties attainable by the parameterized microstructures (Pareto-fronts) are evaluated through multi-objective optimization providing a broad spectrum of possible microstructures with the closest properties to the CG-bounds. For composites of stiff and void phases, the optimum structures expand over almost the full theoretical bounds. As a notable structure, a new solution with simultaneous maximum bulk and shear moduli and only two well-differentiated length scales, is reported for volume fractions, at most, of 0.5, regardless of the contrast between constituent phases. Manufacturability is included in the study, in the sense that simpler geometrical configurations characterized by a single length scale are evaluated. An experimental test is performed on an auxetic composite with a high shear modulus. The test agrees with the numerical predictions. Finally, the potential of this methodology lies in the three prescribed sequential actions providing a practical guide for designing more challenging problems, such as 3D microarchitectures. In these cases, it is rather complex to achieve simple parameterized geometries without the support provided by topology optimization jointly with the imposition of symmetry constraints.

## Acknowledgements

The authors are grateful to Juan Marcos Banegas and Javier Andrés Acosta of CIESE-UTN FRSF for their help with the experimental study.

## APPENDIX: Equations used in the multi-objective optimization problems

In the mathematical formulation of the multi-objective problem (C.10), the volume fraction constraints are written as follows.

In the case of *p31m* microstructure, replacing (C.11) into (C.10):

$$\gamma\,\Omega_{lam}(\alpha,t)+\Omega_1(\alpha,t)-f_1^t\,\Omega_\mu=0, \tag{C.13}$$

where,

$$\begin{aligned}\Omega_{lam} = 6 \times (&\frac{\sqrt{3}/2}{sin(120^o - \alpha/2) + sin(\alpha/2)} \times L \times t \\ &- \frac{sin(\beta_1 + 60^o - \alpha/2)}{sin(\beta_1 + 90^o - \alpha/2)} \times t^2 - \frac{sin(\beta_2 - 60^o + \alpha/2)}{sin(\beta_2 - 30^o + \alpha/2)} \times t^2), \\ \Omega_1 = &\frac{3}{2} sin(30^o + \alpha/2) \times (\frac{1}{sin(\alpha/2)} + \frac{1}{cos(30^o - \alpha/2)}) \times t^2, \\ &\Omega_\mu = \frac{\sqrt{3}}{2} L^2.\end{aligned} \tag{C.14}$$

The angles $\beta_1$ and $\beta_2$ depend on $\alpha$, and are calculated from the following expressions:

$$\begin{aligned}tan(\beta_1) &= \frac{3 - 2 \times sin(30^o + \alpha)}{\sqrt{3} - 2 \times cos(30^o + \alpha)}, \\ tan(\beta_2) &= \frac{3 + 2 \times cos(\alpha)}{\sqrt{3} + 2 \times sin(\alpha)}.\end{aligned} \tag{C.15}$$

In the case of the *p3m1*, by replacing (C.12) into (C.10):

$$\gamma_1 \, \Omega_{lam1}(d,t) + \gamma_2 \, \Omega_{lam2}(d,t) + \gamma_3 \, \Omega_{lam3}(d,t) + \Omega_1(d,t) - f_1^t \, \Omega_\mu = 0, \tag{C.16}$$

where $\gamma_1$, $\gamma_2$, $\gamma_3$ and $f_1^t$ are parameters defined in Figure C.5 and

$$\begin{aligned}\Omega_{lam1} = \Omega_{lam2} &= 3 \times d \times L \times t - \sqrt{3} \times t^2, \\ \Omega_{lam3} &= 3 \times (L - 2 \times d \times L) \times t - \sqrt{3} \times t^2, \\ \Omega_1 &= \frac{3\sqrt{3}}{2} t^2, \\ \Omega_\mu &= \frac{\sqrt{3}}{2} L^2.\end{aligned} \tag{C.17}$$

The $d$ parameter may increase beyond the vanishing of the $\gamma_3$ laminate region (see for example microstructures P4 and P5 in Figure C.7). in this situation the relation between the parameters to respect a given volume fraction comes from:

$$\gamma_1 \, \Omega_{lam1}(d,t) + \gamma_2 \, \Omega_{lam2}(d,t) + \Omega_1(d,t) - f_1^t \, \Omega_\mu = 0, \tag{C.18}$$

where

$$\begin{aligned}\Omega_{lam1} = \Omega_{lam2} &= 3 \times (L - d \times L) \times t - 2 \times \sqrt{3} \times t^2, \\ \Omega_1 &= 2 \times \sqrt{3} \times t^2 - 6 \times \sqrt{3} \times (L/2 - d \times L)^2.\end{aligned} \tag{C.19}$$

## Declarations

**Funding:** CONICET and ANPCyT - Argentina (grants PICT 2016-2673).
**Conflict of Interest:** The authors declare that they have no conflict of interest.
**Availability of data and material:** A video showing the transition of the microstructures attained along the four Pareto fronts, and a .csv file describing the values of the parameters and properties of all the

microstructures lying on the Pareto fronts, can be found in the open-source online data repository hosted at Mendeley Data [163].
**Code availability:** the homemade code is written in Matlab and is freely available under request.

## Replication of results

The homemade codes, including the inverse homogenization of Section C.3, the geometrical description of the parameterized microstructures with conformal meshes of Section C.4 and the multi-objective optimization using a genetic algorithm of Section C.5, have been implemented in Matlab. Numerical data characterizing the presented results, for instance, material properties of the phases, and optimal parameters are displayed in the paper. The full set of numerical and experimental data, as well as the codes are freely available under request.

# Apéndice D

# A new efficient methodology for the analysis of mechanical metamaterials with elastic instabilities

Rossi, N., Mendez, C., and Huespe, A.E. (2022). "A new efficient methodology for the analysis of mechanical metamaterials with elastic instabilities". *In: WCCM-APCOM2022, 500.* https://www.scipedia.com/public/Rossi_et_al_2022b

# A NEW EFFICIENT METHODOLOGY FOR THE ANALYSIS OF MECHANICAL METAMATERIALS WITH ELASTIC INSTABILITIES

**NESTOR ROSSI*, CARLOS G. MÉNDEZ AND ALFREDO E. HUESPE**

Centro de Investigación de Métodos Computacionales (CIMEC), UNL, CONICET.
Predio "Dr. Alberto Cassano", Colectora Ruta Nacional 168 s/n, Santa Fe, 3000, Argentina.
https://cimec.conicet.gov.ar/
*e-mail: nrossicabral@gmail.com

**Keywords:** metamaterials, reusable energy manipulation, surrogate model of hysteretic elements, microarchitectures with elastic phase transitions.

**Abstract.** *This work addresses the analysis of mechanical metamaterials exhibiting, as a distinguishing feature, snap-through instabilities in the elastic regime. Among the various opportunities offered by this feature is the manipulation of the material deformation energy [17] that allows the conception of reusable energy-trapping or energy-dissipation devices [100]. As a task to reach this objective, we present a novel computational methodology for analysing microarchitectures displaying elastic snap-through instabilities. The strategy is based on the construction of a surrogate model that reduces the computational burden if compared with full high-fidelity models of non-linear volumetric finite elements or with non-linear beam elements. The surrogate model opens the possibility to analyse a large number of unit cells of periodic metamaterials with instabilities. In addition, it permits an efficient assessment of different geometrical configurations proving a suitable tool for its use in microarchitecture topology optimization processes. Noting that, in general, existing designs of this class of metamaterials only achieve energy manipulation in a specific predefined loading direction, in this work, and based on the proposed computational technique, we aim at the analysis of reusable multidirectional isotropic energy manipulation. This objective agrees with more realistic uses of metamaterials in which general boundary conditions, typically the loading directions, are not established a priori.*

## D.1. INTRODUCTION

Within the extensive field of metamaterials (composites whose microarchitecture is carefully designed to achieve outstanding effective properties), an abundant literature has been published in recent years aiming at exploring the possibility of incorporating elastic snap-through instabilities as functional mechanisms influencing the material deformation process.

In this context, instability refers to a negative incremental stiffness, which could be leveraged to explore interesting and promising prospects, including extreme damping [164], auxeticity with tunable Poisson's ratio [6], control of resonance frequencies through low effective stiffness [165], pattern formation used to control the functionalities and response of the material [166], vibration control [167] and micro-scale mass sensing [168].

The material with snap-through instability arises as a consequence of the non-convexity of its elastic strain energy. This loss of convexity may be the result of non-linear deformation mechanisms, possibly promoted by the geometric deformation phenomena, happening at a lower scale (micro-scale). In the framework of a phenomenological non-linear elasticity description, the loss of convexity (strictly loss of rank-one convexity) allows the material to display different stable states of deformation (characterized by positive stiffness) called phases, separated by spinodal regions of unstable states. A typical response of this kind of material with two stable phases and one spinodal region is sketched in Figure D.1, where the non-convex strain energy function and the corresponding stress-strain response is depicted. Considering that, for certain load levels, the total potential energy may have multiple local minima, then, heterogeneous states of strain, corresponding to different phases, may coexist with a homogeneous state of stress [105].

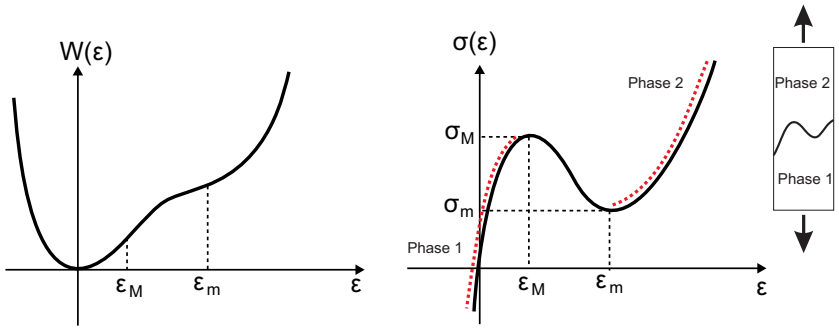


**Figura D.1:** Material with two stable phases and one spinodal region. Left plot: non-convex strain energy $W(\varepsilon)$; central plot: stress ($\sigma$)-strain ($\varepsilon$) response; right plot: coexisting phases due to a homogeneous state of stresses.

In the context of applications addressed in the present paper, the remarkable issue about this kind of materials is that, even considering that they are essentially hyperelastic, the phase transitions happening during a loading-unloading process involves an extrinsic mechanical energy dissipation which can be exploited to design adequate devices.

## D.2. MOTIVATION

Our interest in this work resides on the analysis of elastic metamaterials with a periodic microarchitecture, capable of producing repetitively energy dissipation induced by phase transitions that result from multistable elastic systems, typically, from systems displaying snap-through instabilities in more than one direction of loading. Of special importance is to fully understand the connection between the mechanics happening at the micro scale, where phase transition phenomena happens, and the scale where the apparent or effective properties of the material are of interest.

The use of conventional homogenization techniques to reach this objective, an approach that is typically used for analysing and designing mechanical metamaterials in linear elastic regime [60, 61, 69], must be examined carefully for problems displaying instabilities and phase transitions [169]. Note that constant stress states may cause heterogeneous strain states, with the possible coexistence of different phases [105]. On the other hand, the evaluation of the apparent response of the material by including a large number of unit cells also presents a major drawback. An increasing number of unit cells in the model does not only increase the number of (non-linear) equations of the system but also enlarges the number of alternative equilibrium paths and bifurcation points of possible solutions, features being typical of structures with instabilities.

As an alternative to these approaches, we describe in this work a surrogate model that substantially saves computational effort by appropriately capturing the essence of the unstable microarchitecture response through a few degrees of freedom. The underlying idea behind this model is to represent the micro-scale *hysteron* (mechanical component causing the snap-through instability, or phase transition, and hysteresis in a closed cycle of loading) through a single 1D finite element endowed with appropriate constitutive law. Although this procedure greatly simplifies the topological complexity of the material structure, it preserves the general characteristic behavior of the material as a whole.

Our approach closely follows an analytical procedure for functionally 1D structures which has been described in [80, 98, 99]. The authors of these works analyze chains of springs in series. The springs show regions with negative stiffness and are modeled with a simplified non-monotonic force-displacement law. Constructive details of the springs leading to such non-linear response at the lower scale are disregarded in this approach. Notably, however their simplicity, such a kind of models is able to capture the same phenomenology obtained with high-fidelity models taking into account the whole microstructure details. Some of these phenomena include: phase transformation and hysteretic material response with serrated

loading and unloading plateau [14], energy-absorbing and self-recovering [15], elastic energy trapping without dissipation [94], with a repeatable rate-independent behavior in every case.

The rest of the paper is organized as follows. In section D.3, we present the methodology, particularizing it for the case when the hysteron capable of phase transformation is a curved beam. In section D.4, we assess the model and compare our results with those obtained by high-fidelity finite element models. Finally, section D.5 summarizes the conclusions of the work.

## D.3. METHODOLOGY OF ANALYSIS: A FINITE ELEMENT REDUCED MODEL

Let us consider a periodic metamaterial whose unit cell is constituted by an assembly of hysterons (mechanical elements which may snap in one direction). The present methodology proposes to replace each of these snapping elements by one specially constructed 1D beam finite element.

**Beam model**

The beam model is formulated according to the kinematic description of the Timoshenko beam, using a small deformation-small displacement theory and a non-linear material. As usual, the kinematics is determined through two fields defined along the beam neutral axis, the vector $\mathbf{w}$ is the displacement of the beam neutral axis and $\theta$ is the rotation angle of the beam section that in the reference configuration is orthogonal to the neutral axis. The three generalized strains: axial $e(\mathbf{w}, \theta)$, curvature $\kappa(\mathbf{w}, \theta)$ and shear $\gamma(\mathbf{w}, \theta)$ are associated with the three generalized stress resultants: axial $N$, moment $M$, and shear $Q$ by appropriate constitutive relations.

The beam finite element implemented in this work has two nodes with three d.o.f. each. These d.o.f. are the nodal axial and transverse displacements $(\Delta_N, \Delta_Q)$ and the rotation of the original orthogonal section $(\theta)$. As usual, the full kinematics of the beam element as well as the generalized stress resultants are determined as functions of these six d.o.f.: axial force $N(\Delta_N, \Delta_Q, \theta)$, moment $M(\Delta_N, \Delta_Q, \theta)$, and shear force $Q(\Delta_N, \Delta_Q, \theta)$.

This type of beam element implemented with a suitable set of constitutive equations is used as a representation of the 1D reduced model of the hysteron element. The reduced model finite element is called *RM-BFE* (Reduced Model-Beam Finite Element) its constitutive equations are discussed below.

**Description of the hysteron element studied in this work**

In this work, we assume that the hysteron of the metamaterial is constituted by a bistable sinusoidal curved beam with restricted lateral displacements. Figure D.2(a) shows the hysteron studied in this work, and Figure D.2(c) depicts a possible microarchitecture unit cell after assemblage. This element displays a phase transition; the system may jump from one stable position to an alternative one when compressed in the vertical direction (snap-through driven condition). Following previous works, see [80, 98, 99], the phase transition effect is conferred to the axial response of the *RM-BFE* element, that is also schematized in Figure D.2(a). Thus, to model this effect, the axial stiffness of the *RM-BFE* element is characterized with a non-monotonic response. Instead, as will shown in the following, the bending and shear forces remain monotonic functions with convex energies.

*REMARK. The choice of the transversely loaded curved beam as the element inducing the phase transition (hysteron element) is due to the fact that it has been extensively studied (see [170, 171] and many of the previous references), which allows us to account for an extensive bibliography to compare our results. However, alternative snap elements have been proposed in the literature, such as the mechanism described in [92], where the jump between two stable positions is produced employing rotations, or the mechanism proposed in [91], where phase transitions result from a shear effect. We remark that the present methodology can be easily adapted to represent these alternative hysterons.*

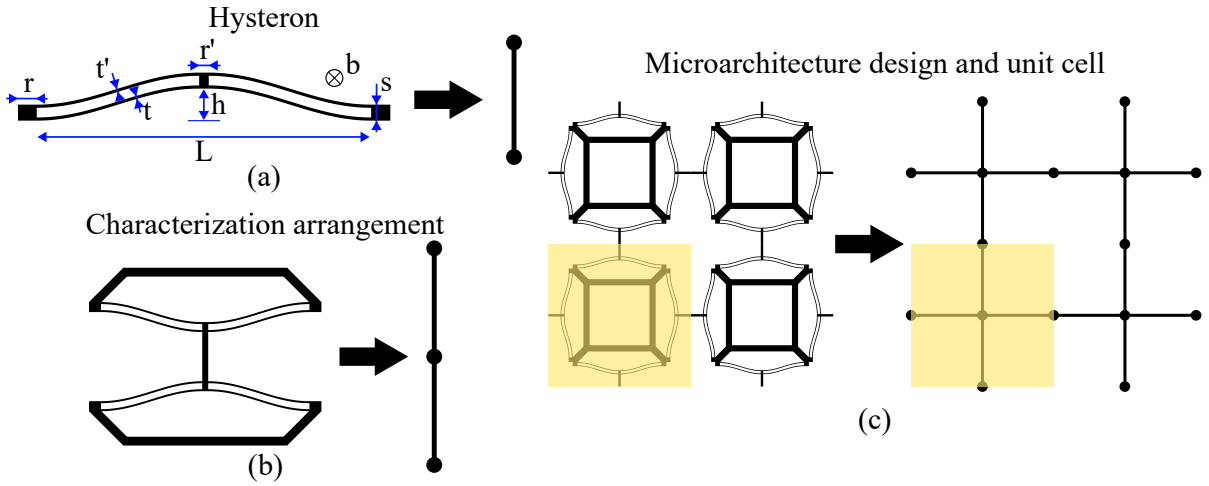


**Figura D.2:** Idealization of the hysteron element as a reduced 1D model. (a) Hysteron with the geometrical dimensions that define its response and a single RM-BFE. (b) Arrangement of two hysterons in series to perform the stiffness characterization of the RM-BFE. (c) Assemblage of four unit cells (yellow shadow) for a square microarchitecture design (proposed by [100, 107])

### D.3.1. RM-BFE constitutive characterization

The RM-BFE stiffness characterization in our model depends on the kinematical restriction of the curved beam that is subjected to snap-through conditions. In the case studied in the present work, we replicate the configurations reported by [100]. These authors show structures with extrinsic energy dissipation which are functionally 2D with two paired curved beams, one in front of the other, which operate in series. Thus, to obtain suitable results in our model, we characterize the RM-BFE stiffness following a similar configuration that is shown in Figure D.2(b), and we call characterization arrangement. The geometrical parameters defining the initial geometry of the curved beam device are specified in Table D.1.

**Tabla D.1:** Selected parameters for stiffness characterization [100]. Figure D.2 present the graphical description of parameters $L, h, t, t', s, r, r', b$. The Young modulus of the material of the beams is $E_{mat}$

| $L[mm]$ | $h[mm]$ | $t[mm]$ | $t'[mm]$ | $s[mm]$ | $r[mm]$ | $r'[mm]$ | $b[mm]$ | $E_{mat}[MPa]$ |
|---|---|---|---|---|---|---|---|---|
| 71 | 7 | 0.7 | 0.7 | 3.5 | 4.2 | 2.1 | 25 | 2267 |

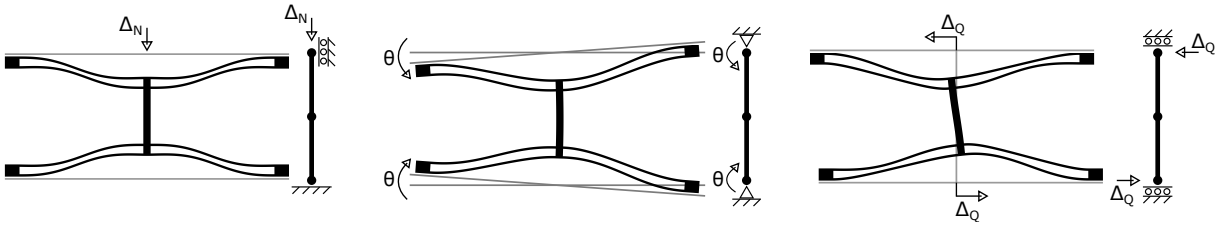


**Figura D.3:** Scheme of the mechanical tests performed on the characterization arrangement of two faced hysterons, to define the constitutive relations of the reduced model

To define the three RM-BFE constitutive relations determining the generalized stress resultants $N$, $M$, and $Q$, in terms of the generalized displacements, we assume that they are independent of each other and are only influenced by their respective generalized displacements as follows: $N(\Delta_N)$, $M(\theta)$,

$Q(\Delta_Q)$. These three functions are characterized through three separate mechanical test schematized in Figure D.3[1].

As a particular case, the expressions reported in [102] are used to characterize the axial stiffness of the RM-BFE element. These authors report the relationship $N(\Delta_N)$, where $N$ is the axial vertical force applied to the curved beam and $\Delta_N$ is the vertical displacement of the loading application point, see Figure D.3. The function $N(\Delta_N)$ is approximated by a cubic polynomial if the ratio $h/t < 2.31$ is satisfied, or alternatively, it is approximated by a trilinear law. For the parameters indicated in Table D.1, we obtain a ratio $h/t = 10$, which implies that the axial force law $N(\Delta_N)$ is trilinear, and it is defined by the position of the following three points (see Figure 4 and equations (43) and (44) in [102]): the first limit load $(d_I, N_I)$, the second limit load $(d_{II}, N_{II})$, and the second stable configuration with null load $(d_{III}, 0)$:

$$\begin{aligned} N_I &= -18.76\ 10^{-4} MN\ , \\ d_I &= -11.2\ 10^{-4} m\ , \\ N_{II} &= 9.38\ 10^{-4} MN\ , \\ d_{II} &= -134.4\ 10^{-4} m\ , \\ d_{III} &= -139.3\ 10^{-4} m\ . \end{aligned} \tag{D.1}$$

The moment-curvature law $M(\theta)$ and the shear force-shear displacement $Q(\Delta_Q)$ are instead characterized through results assessed from a high-fidelity finite element model of the curved beams. The outcome of these numerical results are fitted with cubic polynomials. These constitutive relationships are:

$$M = 8.81\ 10^{-5} MNm\ \theta + 71.24\ 10^{-5} MNm\ \theta^3\ , \tag{D.2}$$

$$Q = 1.624 MN/m\ \Delta_Q + 1.521\ 10^5 MN/m^3\ \Delta_Q^3\ . \tag{D.3}$$

Figure D.4 compares both full- high fidelity finite element results (curves in blue lines) and the reduced model results (curves in red lines) for the tests schematized in Figure D.3.

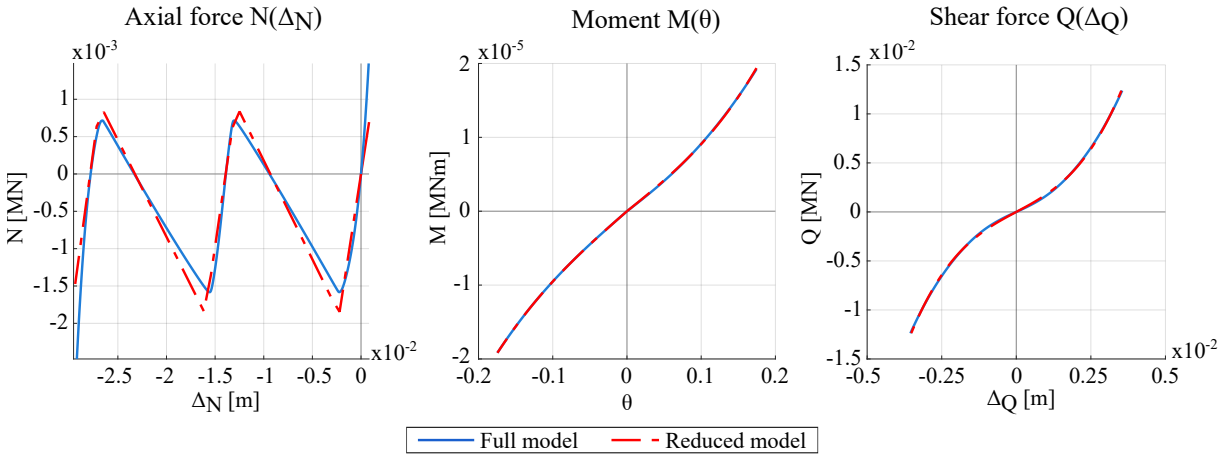


**Figura D.4:** Comparison of the generalized stress resultant curves obtained with a full-high fidelity model (curves in blue lines) and the reduced model endowed by constitutive relationships (D.1), (D.2) and (D.3) (curves in red lines)

[1]This characterization will be improved in a future work to include the coupling effects between the generalized forces in a generic loading path.

### D.3.2. Iterative scheme to solve the balance equations

A critical aspect of the numerical methodology used in this work to obtain the balance equation solutions in structures having a rather large number of hysterons is to choose a suitable iterative scheme. As usual, convergence of the iterative scheme strongly depends on the structural stiffness matrix, which, in the present type of (non-convex) problems is in general non-positive definite. This condition implies that a Newton-Raphson scheme is not an adequate procedure for solving the equation system. Alternatively, to override this problem, we choose a BFGS method together with a line search technique satisfying the Wolfe conditions. This guarantees that the (secant) stiffness matrix is at all times positive definite. For major details see [172].

## D.4. RESULTS

We replicate the results of two 2D microarchitectures reported in [100]. The numerical assessments of the simulated specimens are obtained with the RM-BFE model. The objective of the present assessment is to show the potentiality of the methodology.

The tests are performed on the S-type (S for square type) and T-type (T for triangular type) cellular materials. Both configurations are depicted in Figure D.5. The original unit cells designed and tested by [100] and the reduced model unit cells are shown in the same figure. This figure clarifies the association that we introduce between every hysteron, in the original structure, and the individual RM-BFE element. Also, the figure shows the colour code used to report the results. Beams in red indicates that the RM-BFE element remains in phase 1, the stable low deformation phase, while beams in blue indicates that the RM-BFE element has transitioned to phase 2, the stable phase of high deformation.

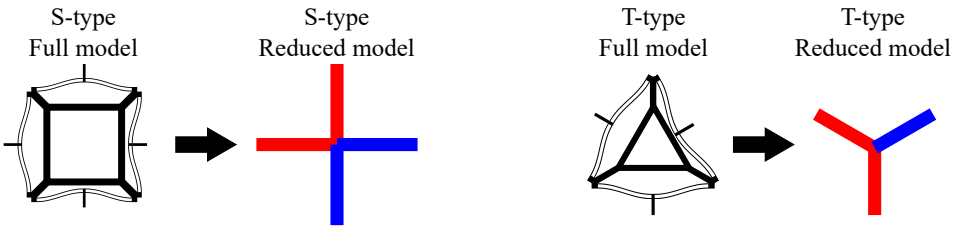


**Figura D.5:** Unit cells of Zhang et al. [100]. S-type (on the left) and T-type (on the right) cellular materials and the corresponding reduced model.

### D.4.1. Analysis of functionally multidirectional materials

Uniaxial, quasi-static, compressive load-unload tests are performed in the two types of structures. A random variability of 1 % is imposed in the $t$ geometrical parameter defining the geometry of the curved beam, see Figure D.2. This geometrical perturbation is introduced to avoid convergence problems in the numerical iterative algorithm. This magnitude of variation does not affect notoriously the results and also approximates manufacturability errors.

Following the nomenclature established in [100], in addition to the type of microstructure (S-type or T-type), an angle is given in curly brackets to fully characterize the test. This angle indicates the inclination between a system of local axes attached to the microstructure and the load direction. In all cases, the load is vertically imposed, and the microstructure is rotated accordingly with the indicated angle. Note that both types of microarchitectures have symmetry axes. Therefore, the loading rotation angle conform an equivalence class. Then, for conciseness, we sometimes only refer to one element of the class.

Figure D.6 displays the simulation results of the S-type configuration loaded in the direction {0°,90°}. Figure D.7 shows the results of the S-type at load direction {45°,135°}. Figure D.8 shows the results of the T-type configuration loaded along the direction {0°,60°,120°}, and Figure D.9 displays the results of the T-type at load direction {30°,90°,150°}. The plots in these figures display the load-displacement curves in closed cycles of loading, as well as three snapshots of the deformation pattern at sequential loading stages. Note in the force vs displacement plots, the hysteresis loop generated when subjected to a closed loading cycle. The area enclosed by the hysteresis loop represent the extrinsic energy dissipation of each system. Compare these results with Figures 3 to 7 of [100] (note that in our graphics compression loads have negative sign).

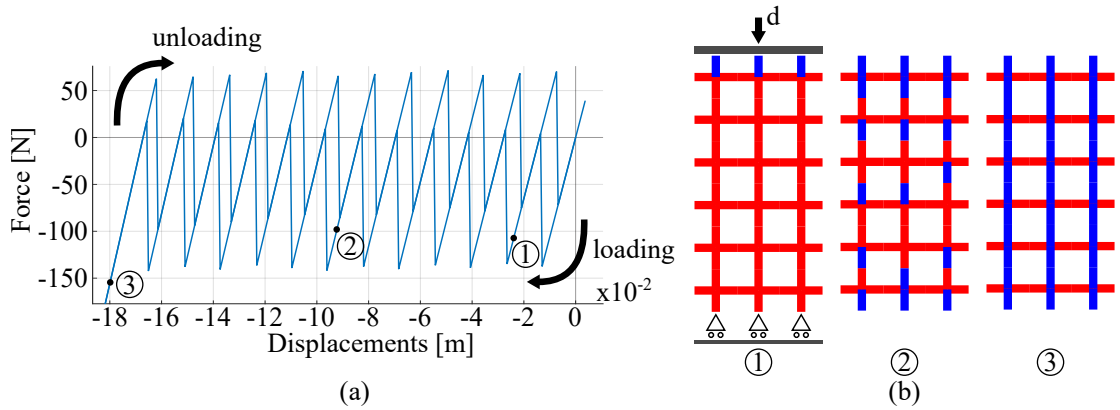


**Figura D.6:** S-type configuration. Load direction {0°,90°}. (a) total vertical force vs. displacement of the specimen top (closed loading cycle). (b) sequence of phase transitions at points 1, 2, and 3 accordingly with the position displayed in the left plot.

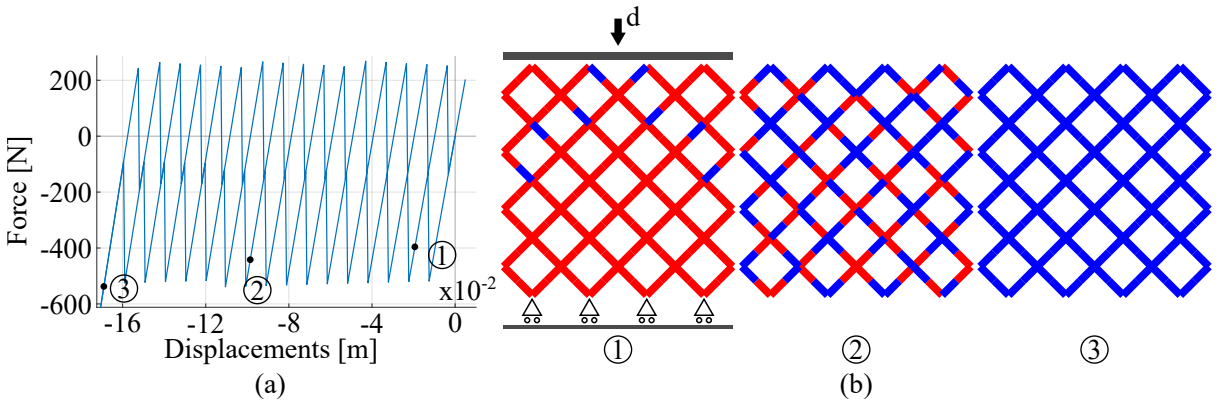


**Figura D.7:** S-type configuration. Load direction {45°,135°}. (a) total vertical force vs. displacement of the specimen top (closed loading cycle). (b) sequence of phase transitions at points 1, 2, and 3 accordingly with the position displayed in the left plot.

The results of the simulations obtained with the reduced model show good agreement with many important features reported in the experimental and results of [100]. The model captures every snapping event (limit loads when a row of the microstructure performs a phase transition), obtaining the correct deformation patterns in every case. Typically, in Figures D.6 and D.9 (S-type at {0°} and T-type at {90°} structures), we show that the RM-BFE elements orthogonal to the loading directions do not perform a phase transition. Also, Figure D.8 shows that vertical RM-BFE elements in the T-type {0°} perform the phase transition first, and subsequently, the inclined ones. Note also the phase transition pattern, like a "V", of the S-type {45°} structure in the first snapshot of Figure D.7.

Additionally, the model captures the typical serrated loading and unloading plateaus. For the T-type

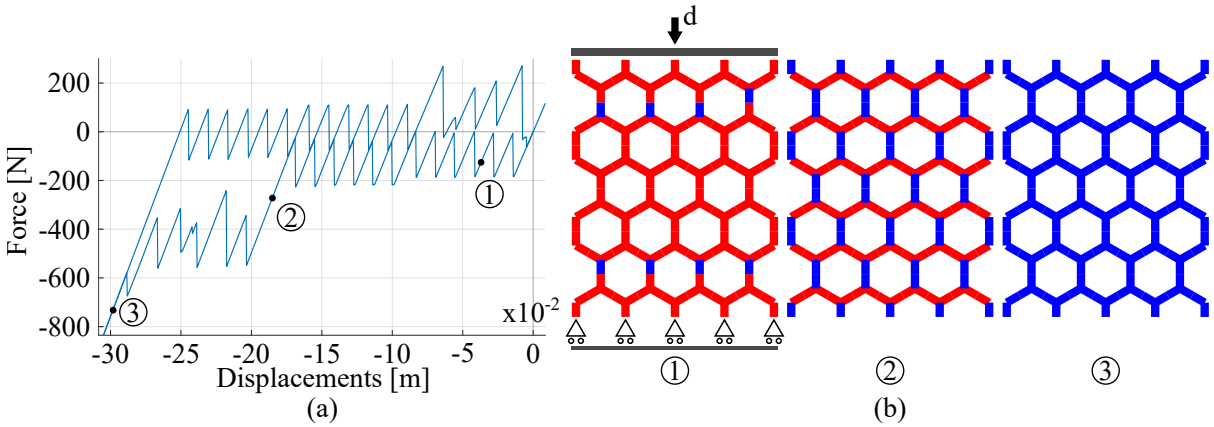


**Figura D.8:** T-type configuration. Load direction {0°,60°,120°}. (a) total vertical force vs. displacement of the specimen top (closed loading cycle). (b) sequence of phase transitions at points 1, 2, and 3 accordingly with the position displayed in the left plot.

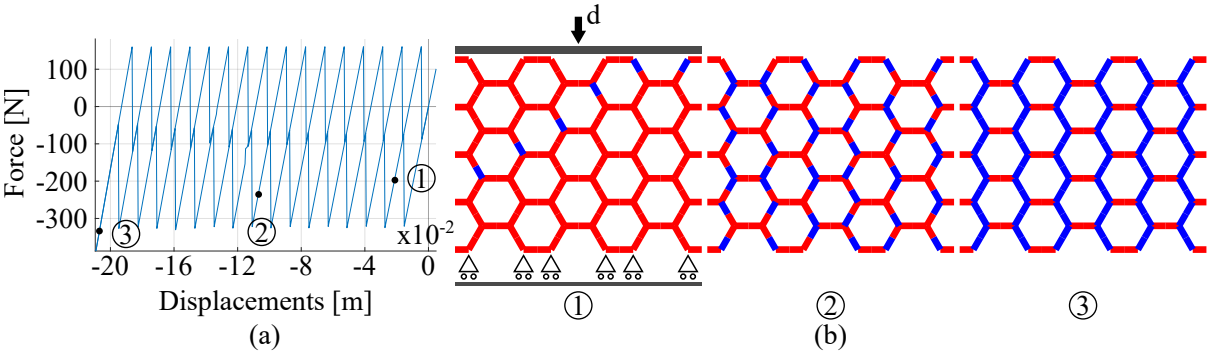


**Figura D.9:** T-type configuration. Load direction {30°,90°,150°}. (a) total vertical force vs. displacement of the specimen top (closed loading cycle). (b) sequence of phase transitions at points 1, 2, and 3 accordingly with the position displayed in the left plot.

{0°} structure, it also predicts two different levels of plateaus corresponding to the orientation of the hysteron elements subjected to phase transformation.

The reduced model quantitatively predicts correct displacement values, both for individual snapping events and at the maximum loading condition reached in the simulation, when the dissipation capacity is exhausted. However, limit load values are not sufficiently well predicted. This may be mainly due to the following two reasons:

*i)* First, Qiu's law [102], which is used to characterize the axial response of the RM-BFE element, assumes that curved-beams are perfectly fixed in the lateral direction. This type of constraint is difficult to manufacture and obtain in assembled microstructures, since the interior frames constraining the lateral displacements of the curved-beams are not infinitely stiff. The lateral restriction compliance, even being small, generates a decrease in the hysteron limit load which may explain part of the difference between the numerical and experimental limit loads in the S-type {0°} structure.

*ii)* The second reason may be associated with the performance of the model. The performance may be particularly affected when the RM-BFE elements are not aligned to the loading direction. Considering the RM-BFE constitutive law adopted for the bending and shearing effects, larger inclinations of the loading direction respect to the RM-BFE longitudinal axis induce a decreasing effect of the axial response, and the total energy of the system tends toward convexity. Thus, the capacity of the

system to dissipate energy decreases. It is worth mentioning that capturing the right limit loads in RM-BFE elements under inclined loads is a challenge, see for example [100].

### D.4.2. Isotropy of the energy dissipation

From the equilibrium paths displayed in the plots of Figures D.6–D.9, we estimate the averaged dissipated energy per RM-BFE element for both configurations (S and T-types) along the two possible axes of symmetry.

However, since the effectiveness of the structural energy dissipation depends on the number of hysterons in series, we initially perform a convergence analysis by increasing the number of rows (hysterons in series) in the specimen that perform a snapping event until the average dissipation is stabilized. The attained results for S-type loaded at $\{0°\}$ and $\{45°\}$ and for T-types of configurations loaded at $\{0°\}$ and $\{90°\}$ are plotted in Figure D.10(a), and the stabilized converged values of average dissipated energy per RM-BFE are displayed in the polar diagram of Figure D.10(b).

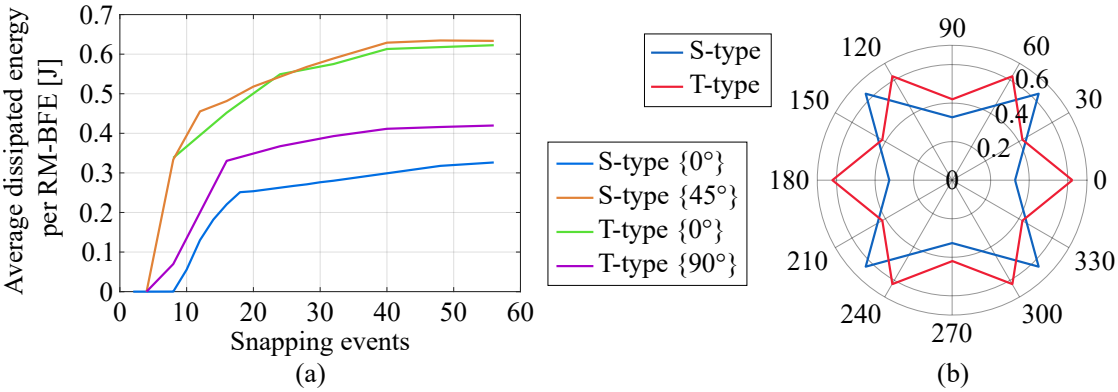


**Figura D.10:** Energy dissipation for different loading directions. (a) Convergence of the average dissipated energy per RM-BFE as a function of the amount of snapping events (or hysterons in series), for both S-type and T-type microstructures and in two loading directions. (b) Average dissipated energy as a function of the loading direction for both designs.

In relation with the tendency of the model to overestimate load values if elements are inclined, it is likely that the dissipated energy is also overestimated, particularly affecting S-type 45 and T-type 0, since their elements have greater inclinations.

### D.4.3. Computational efficiency

To show the potentiality of the reduced model regarding computational cost, we compare the required CPU times to perform the simulations of the test discussed in Figure D.4, and using either the High-Fidelity finite element model (HF) (blue curves in Figure D.4) or the Reduce Model (RM) (red curves in Figure D.4). Table D.2 shows the required CPU time, in seconds, to perform the full analysis of $N(\Delta_N)$, $M(\theta)$, and $Q(\Delta_Q)$ using both HF and RM models.

**Tabla D.2:** Elapsed times in seconds to perform the analyses of $N(\Delta_N)$, $M(\theta)$, and $Q(\Delta_Q)$ using either the High-Fidelity finite element model (HF) or the surrogate model (RM) (simulated tests correspond to those displayed in FigureD.4)

| $N(\Delta_N)$ HF | $N(\Delta_N)$ RM | $M(\theta)$ HF | $M(\theta)$ RM | $Q(\Delta_Q)$ HF | $Q(\Delta_Q)$ RM |
|---|---|---|---|---|---|
| 237.6 | 4.4 | 51.0 | 0.7 | 42.5 | 1.4 |

The drastic CPU saving time shown by the RM model, in comparison to that demanded by the HF model, is due to the drastic dimensionality reduction of the problem. The HF model uses $1.6 \times 10^5$ d.o.f. compared against only one finite element and six d.o.f. used by the RM approach. [2]

## D.5. CONCLUSIONS

We present an efficient tool for the analysis of metamaterials displaying snap-through instabilities and phase transformation. Although the challenges of modeling mechanical structural response with large number of instabilities (including bifurcation points, multiple solutions, etc.) are still present, the reduced model here reported provides a computational robustness increase when a rather large number of hysterons are simulated.

The hysteron that is chosen to assess the reduced model consists of a bistable curved/beam. However, we hold that the reported procedure to define the reduced model is transparent to the mechanism introducing the snap-through instability phenomenon. Therefore, the model could be quite straightforwardly generalized for hysterons generated by different mechanical devices.

Furthermore, this reduced model displays an acceptable qualitative predictive capacity regarding cyclic loading paths. This predictive capacity includes patterns of phase transformations, serrated plateaus in the load-displacement plots with hysteresis, and energy dissipation decrease when the hysteron is not aligned with the loading direction.

Quantitatively, the model correctly predicts displacement values, although overestimates load values. This drawback could be overridden by improving the constitutive description of the RM-BFE element. This is a work in development.

The saved computational cost makes this methodology especially suitable for its use in an optimization process where different configurations of hysterons could be tested. This aspect of the problem is also to be explored by the authors in the near future.

## ACKNOWLEDGMENT

Nestor Rossi gratefully acknowledges the support received by AUIP (Asociación Universitaria Iberoamericana de Postgrado) under the program of academic mobility between the institutions associated to the AUIP. This research has been supported with grants provided by CONICET, the National University of Litoral, and the fund from ANPCyT: PICT-2020-SERIEA-02793, Argentina.

[2] Additionally, note that the HF model is defined in terms of a full non-linear geometry and material theory, whereas the RM model is defined in terms of small deformation and small strain theory with a non-linear constitutive model.

# Apéndice E

# Surrogate model for a mechanical metamaterial undergoing microstructure instabilities and phase transformations

Rossi, N., Méndez, C. G., and Huespe, A. E. (2023). "Surrogate model for a mechanical metamaterial undergoing microstructure instabilities and phase transformations". *International Journal of Mechanical Sciences*, 243, 107913.

# Surrogate model for a mechanical metamaterial undergoing microstructure instabilities and phase transformations

**N. Rossi**[*†], **C.G. Mendez** [*‡], **A.E. Huespe**[*]

[*]Centro de Investigación de Métodos Computacionales (CIMEC), UNL, CONICET. Santa Fe, 3000, Argentina.
[†]Computational Mechanics Laboratory (LAMEC-IMIT-CONICET), Northeast National University (UNNE), Av. Las Heras 727, 3500 Resistencia, Chaco, Argentina.
[‡] Chemical Engineering Faculty, National University of Litoral (UNL), Argentina.

**Keywords:** Mechanical metamaterials; Microstructure instabilities; Extrinsic energy dissipation; Bistable curved beams; Buckling mode decomposition.

**Abstract.** This paper addresses the modeling of periodic metamaterials with microstructure instabilities. Such instabilities are produced by bistable elastic mechanisms, i.e., snap-through deformation mechanisms, inducing phase transformations. Metamaterials with these features can be used for energy dissipation in elastic regimes between other applications.

A new surrogate model of the bistable mechanism to replace High-Fidelity Finite Element simulations is developed in two sequential stages. In the first stage, a semi-analytical model of the bistable structural element is presented. Following an approach taken from the literature, the analysis of the bistable element is generalized to include load cases that had not been considered in the original study. These loading conditions naturally happen in functionally 2D and 3D metamaterials with complex microarchitectures. In a second stage, a frame element with linear kinematics and small deformations is described. The constitutive relations of the frame element, i.e., axial stress and moment in terms of axial strain and curvature, follow the same equations of the semi-analytical model derived in the first stage. A Variational Principle of Energetic Equivalence supplies the link between the semi-analytical model of the curved beam and the frame element. In this way, the response of this frame element, of only six degrees of freedom, reproduces the non-linear geometric behavior of the bistable element.

The surrogate model is particularly efficient for simulating a large number of unit cells of the metamaterial and with the capacity to reproduce its behaviour under general loading conditions. Thus, it is appropriate to assessing the metamaterial limit behavior, typically concerning phenomena such as energy dissipation and hysteresis under closed load cycles.

## E.1. Introduction

In the last two decades, there has been a growing interest in the development of new metamaterials taking advantage of micro-mechanical instabilities to achieve unusual apparent properties. For example, instabilities such as buckling, folding, or wrinkling, may lead to attain extreme damping [164], pattern formation and change in structure morphologies [12, 13, 19, 105, 173], auxetic behavior in 2D and 3D cases [6, 174], manipulation of elastic waves in different types of structures [16, 175–177], achiral to chiral pattern switching [178], morphing of composites from 2D plates to 3D shells [179], cyclic response due to material and geometrical non-linearities [180] and energy absorption [181]. An extensive revision of metamaterials exploiting mechanical instabilities with a wide range of applications and potentialities have been reported by Kochmann y Bertoldi [17].

Closer to the goal of the present work, there exist applications in metamaterials exploiting specifically elastic snap-through-type mechanisms. Unlike the above mentioned instabilities, this unstable behavior is intimately related to scenarios linked to mechanical systems displaying non-convex energies and bistability. In this paper, the term bistability indicates the existence of a potential energy landscape with a double well for a given load level. Double well means two possible equilibrium configurations of the

system, one of them is energetically preferred. Multiple solutions also imply that the system can switch between different stable phases through elastic processes. Snap-through instabilities may be utilized in elastic metamaterials and metadevices to induce hysteresis in closed cycles of load with large reversible deformations [182, 183], an effect that can be utilized to design reusable mechanical energy dissipation devices [184, 185], energy harvesting [94, 186, 187], as well as, vibration isolation [188–191], between other applications. Further contributions using snap-through instabilities refer to the study of propagating shock fronts across bodies [105, 169, 192, 193], the relation between rate, temperature and energy barriers [194], triggering of large deformation in response to combined acousto-mechanical actions [195], formation of domain walls [196], adaptability to multi and monostability [197], directional snapping in tensegrity structures [198], and rapid configuration changes [199].

Following a related approach, we focus on elastic metamaterials displaying phase transformations that emerge from snap-through mechanisms. The attribute of such phase transformations happening in elastic regime is one of the most notable features explored for manufacturing fully recoverable materials which dissipate energy. Commonly, these metamaterials are built using lattices of hysterons. A hysteron, terminology coined by [89], is the micro-device causing the unstable mechanism. A commonly employed hysteron is realized through a bistable curved beam subjected to transversal loads, as depicted in Figure E.1. The metamaterial unit cell may have several hysterons interacting between them, and may be designed to support loads either in one direction [14, 15, 171, 200, 201], in two directions [100, 107, 202], or in three non-coplanar directions resulting functionally 3D materials [90, 202, 203]. Hysterons utilizing alternative snap-through mechanisms have also been proposed in the literature. Typically, they are based on the snapping of shear forces [91], of rotations [92], or volumetric expansions [93, 204].

The mechanism through which elastic phase transformations produce extrinsic energy dissipation is outlined through a simple 1D problem. Let us consider the spring shown in Figure E.2. It represents a bistable element and has a non-convex strain energy, $U(d)$ with $d$ being the spring displacement. The strain energy is convex in two disjoint intervals separated by a spinodal region with concave energy. The two intervals with convex energy are denoted phase I and III, respectively, and the spinodal region is denoted phase II. Due to the non-convex character of $U$, the spring response is characterized by a non-monotonous $f$ versus $d$ relationship. With a prescribed force $f$, the system can undergo a phase transformation in a soft mode, the system switches from phase I ( point $R$) to phase III (point $T$) [1]. From thermodynamic (kinetic energy is assumed overdamped contributing to dissipation), the total mechanical dissipation of the system, $\mathcal{D}_{mech}$, produced during this process is:

$$\mathcal{D}_{mech} = \int_R^T (\mathcal{P}^{ext} - \dot{U})dt \tag{E.1}$$

where $\mathcal{P}^{ext} = f_{RT}\dot{d}$ is the external power during the phase transformation, under a fixed load $f_{RT}$, and $\dot{U}(d) = f(d)\dot{d}$ is the strain energy rate of the spring. Considering the total potential energy function $\Pi(f, d) = U(d) - fd$, the energy dissipation can be reinterpreted in terms of $\Pi$ as the difference between the total potential energies in the equilibrium states $R$ and $T$ (see Abeyaratne y Knowles [105]):

$$\mathcal{D}_{mech} = \Pi(f_{RT}, d_R) - \Pi(f_{RT}, d_T) \tag{E.2}$$

Then, $\mathcal{D}_{mech}$ can be graphically represented in different plots, for example, $U(d)$ in Figure E.2-a, $f(d)$ in Figure E.2-b, $\Pi(f_{RT}, d)$ in Figure E.2-c, or $\Pi(f)$ at equilibrium conditions in Figure E.2-d. The area $\mathcal{A}$ in Figure E.2-b is identified as the energy barrier in Figure E.2-d.

It is of particular interest to appraise the maximum amount of energy that a soft device[2] is capable of dissipating during a phase transformation. This dissipation is reached, when the switching between phases occurs at the limit load $f_{lim}$, i.e., when the energy barrier $\mathcal{A}$ vanishes. Alternatively, if this switch

[1] Phase transformations in a soft mode are of particular relevance for the limit behavior of the device.

[2] The terminology soft device and hard device is taken from [80].

happens at the Maxwell load $f_M$, then, $\mathcal{D}_{mech} = 0$.

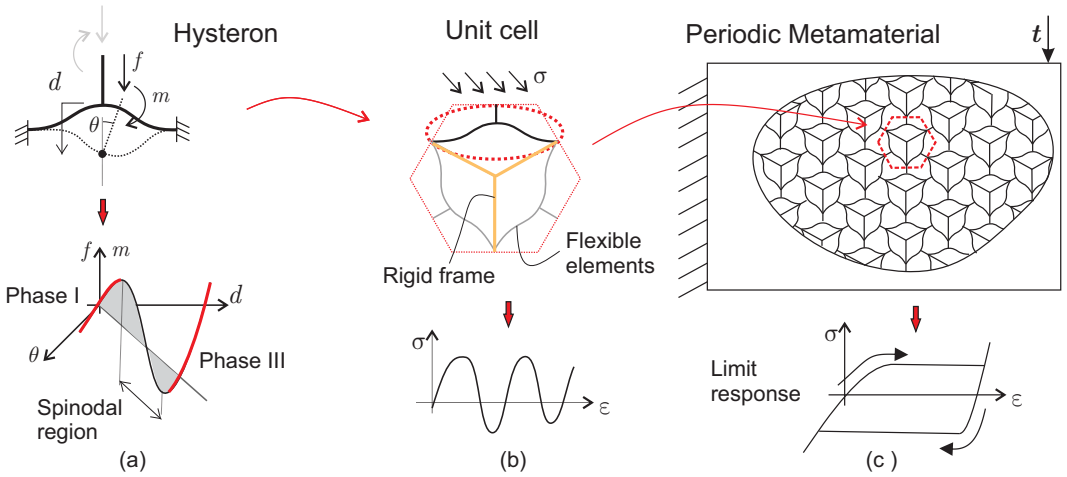


**Figura E.1:** Sketch of a structure built with a metamaterial undergoing phase transformations. a) Microscale device (hysteron) displaying a bistable deformation mechanism and its load-displacement response; b) assembling of hysterons forming a micro-cell and their combined stress-strain response; c) continuum model at the macroscale displaying hysteresis.

### Motivation and objective of this work

This paper aims at studying metamaterials undergoing mechanical snap-through instabilities at the microscale. Our interest points out mechanical periodic metamaterials having microarchitectures of hysteron lattices, such as sketched in Figure E.1, and with the focus on capturing apparent, or limit, material responses once a sufficiently large amount of unit cells is considered.

Understanding how these microscale unstable mechanisms yield, as a limit behavior, a macroscale continuum model (i.e., the transition from the response depicted in Figure E.1-a to that depicted in Figure E.1-c) results in a challenging problem and remains an open question. Thus, the micro to macro transition modeling of such mechanisms entails special attention. Although the use of continuous models has been proposed for evaluating these properties, [101, 205], the most widely adopted procedure is to obtain the limit behavior by simulating a sufficiently large arrangement of unit cells [14, 80, 81, 98, 100, 105, 206, 207]. However, taking a large material volume with a detailed modeling of the microarchitecture topology, is hard to accomplish. An increasing number of unit cells not only augment the number of (nonlinear) equations of the system but also enlarges the number of alternative equilibrium paths and bifurcation points of possible solutions, features that are typical of structures with instabilities.

Addressed to this issue, we describe a reduced model, or Surrogate Model (SM) of the micro-device inducing the phase transformation. The SM substantially saves computational effort by appropriately capturing the unstable microarchitecture response essence through a few degrees of freedom. The underlying idea behind this model is to represent the bistable micro-device through a single 1D finite element endowed with appropriate constitutive laws. Although this procedure simplifies the geometrical complexity of the material structure, it maintains the topology of the microarchitecture and preserves the general intricate characteristic behavior of the material as a whole. Furthermore, the surrogate model allows for simulating the metamaterial behavior under general loading conditions at an intermediate scale of length, including a large number of microcells, without specifically appealing to any average-based homogenization technique.

In summary, the paper aims to understand and describe, by means of a model with few degrees of freedom, the complex energy landscape associated with bistable microstructures and the influence that different macroscale load distributions have on the metamaterial dissipative and hysteretic response.

The paper is organized as follows. Section E.2 establishes the general modeling strategy of the bis-

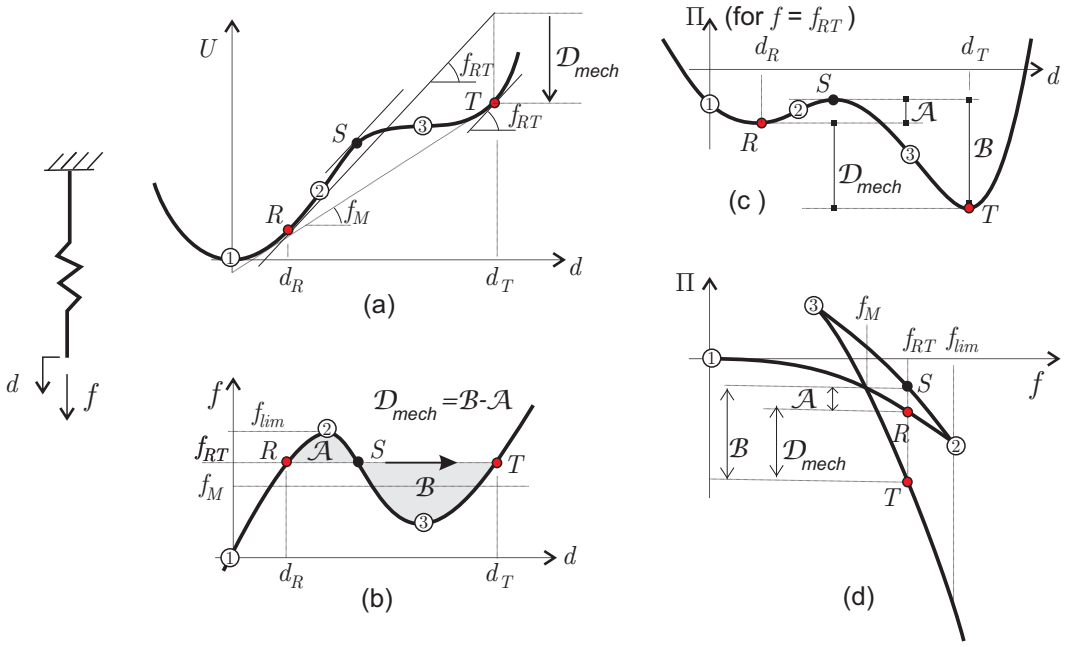


**Figura E.2:** Phase transformation ($R \rightarrow T$) of spring with non-convex strain energy. a) strain energy $U$ in terms of displacement $d$; b) non-monotonic load $f$ versus $d$; c) total potential energy function $\Pi(f_{RT}, d)$ with two-wells at displacements $d_R$ and $d_T$, respectively; d) total potential energy function $\Pi(f)$ at equilibrium conditions. $\mathcal{D}_{mech}$ is the mechanical dissipation during the phase transformation process, $\mathcal{A}$ represents the energy barrier, $f_M$ is the Maxwell load.

table microstructure that consists of a two-stage procedure. Sections E.3 and E.4 describe each of these stages, respectively. These two Sections include the main contributions of the paper. Section E.5 addresses the numerical assessments of the SM of the bistable micro-device and the discussion of the results. Section E.6 presents the conclusions of the work. Additional information regarding specific topics developed in Sections E.3 and E.4 are shown in two Appendices.

## E.2. Modeling strategy

We consider hysterons realized through double-clamped curved beams under transversal loads, such as depicted in Figure E.3. The undeformed configuration of the beam copies the first buckling mode of an axially compressed beam with clamped ends. This curved beam configuration is known to provide bistability conditions under transversal actuation forces, $f$, collinear with the beam transverse symmetry axis. The load $f$ induces a snap-through type deformation mechanism with an associated non-convex strain energy landscape. This device has been previously studied by Vangbo [208] and Qiu et al. [102]. Further studies of curved beams with a moving $f$ have been reported by Cazottes et al. [209] and Camescasse et al. [210]. Modeling of curved-beam with applications to several compliant devices, including bistable mechanisms, have been presented by Chen et al. [211].

**Remark:** In the context of metamaterials, hysterons are designed to maximize the energy dissipation and hysteretic effects in closed cycles of transversal loads. However, when transversal loads are combined with moments, a notable reduction of energy dissipation is observed. Moments activate the anti-symmetric deformation modes of the beam. To avoid this unwanted effect, Qiu et al. propose a double beam configuration restricting the development of anti-symmetric modes. However, this remedy is not a complete solution when relatively high non-collinear loads exist in the device, such as reported in Zhang et al. [100].

Considering this issue and that the present SM of the hysteron aims to simulate microarchitecture configurations supporting loads in several directions, i.e., functional 2D and 3D materials, we need to assess the effects of moments on the dissipation energy features.

The reduced model is built in two stages:

- In the first stage, a semi-analytical model of the curved beam is developed in Section E.3. At this point, we closely follow the work of Qiu et al. We generalize Qiu et al's model to contemplate the existence of a moment $m$ and a transversal force $f$. Such as mentioned above, the moment $m$ induces a notable effect on the capacity of the system to dissipate energy.
- In the second stage, we develop in Section E.4 a frame model, and the corresponding finite element approach, that incorporates the semi-analytical model as a constitutive relation. The link between the frame constitutive response and the semi-analytical model is supplied by a Variational Principle of Energetic Equivalence. The role of this Principle, connecting both approaches, is similar to the role played by the Hill-Mandel Variational Principle to bridge models at different length scales in material homogenization techniques.

The reduced model characterized by the frame element captures the relevant dissipative and hysteretic phenomenon of the hysteron assemblies.

## E.3. Semi-analytical (SA) model of the hysteron

We study the behavior of the structure depicted in Figure E.3. It is composed of an elastic curved beam with an initial unstressed configuration copying the first-buckling mode of an axially compressed straight beam with clamped ends. The beam is fixed at its ends, with restricted displacements and rotations. Besides, it is subjected to a double actuation composed of a transversal force $f$ and a moment $m$, both applied at the beam center.

The geometry of the beam is described by the parameters indicated in Figure E.3: span $l$, central height $h$, thickness $t$, depth $b$, and the ratio $Q = h/t$. Thus, the moment of inertia is $I = bt^3/12$. Besides the material is assumed to be linear, characterized by Young's modulus $E$. We follow the nomenclature utilized by Qiu et al. [102] to ease the reader's understanding of the generalization presented in this work.

As depicted in Figure E.3, two generalized displacements, deflection $d$ and rotation $\theta$, are considered at the center of the beam. They are work conjugate variables to the actions $f$ and $m$.

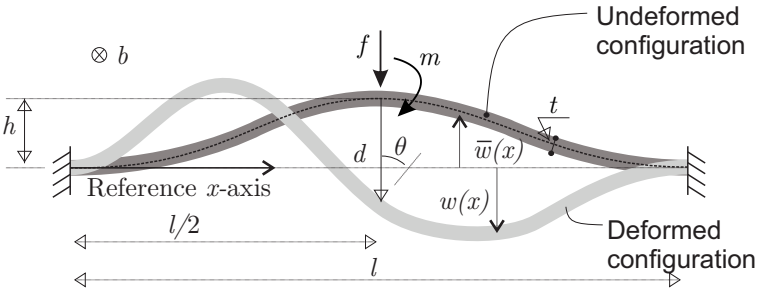


**Figura E.3:** Double-clamped bistable curved beam representing the hysteron. Geometrical parameters and notation.

### Kinematics of the curved beam and total potential energy

We adopt the kinematic description of an Euler-Bernoulli beam with the $x$-axis being the reference configuration of the neutral axis. Let us consider a basis of functions $\{w_j(x)\}$ to span the curves representing the deflections of the neutral axis at different loads. This basis is constituted by the buckling modes of an originally axially compressed straight clamped-clamped beam as follows:

$$\{w_j\} = \begin{cases} \text{for } j = 1,3,5,... \begin{cases} w_j(x) = h[1-\cos(N_j \frac{x}{l})] \\ N_j = (j+1)\pi \end{cases} \\ \text{for } \ j = 2,4,6,... \begin{cases} w_j(x) = h[1 - 2\frac{x}{l} - \cos(N_j \frac{x}{l}) + \frac{2}{N_j}\sin(N_j \frac{x}{l})] \\ N_j = 2.861\pi, 4.918\pi, 6.942\pi, ... \end{cases} \end{cases} \tag{E.3}$$

where $N_j$ are the roots of the equation: $\sin(N_j/2)[\tan(N_j/2) - (N_j/2)] = 0$. Even when the coefficients of $w_j(x)$ may be an arbitrary constant with the dimension of length, in the following, this coefficient is taken as $h$, which is the distance between the undeformed beam apex and the reference axis $x$, such as indicated in Figure E.3. Considering the inner product: $\langle w_j, w_k \rangle = (1/l)\int_l w_j w_k dx$, the set of functions $\{w_j\}$ are orthogonal, as well as their first and second derivatives.

The beam undeformed configuration, $\bar{w}(x) = w_1(x)/2$, represents the distance between the undeformed curved beam neutral axis and the reference $x$-axis, as shown in Figure E.3. Note that $w_1$ is the first bifurcation mode of an axially compressed straight beam.

Also, the current, or deformed, configuration of the beam is described as the distance $w(x)$ between the curved beam neutral axis and the reference $x$-axis. We express $w(x)$ as a linear combination of the basis $\{w_j\}$, as follows:

$$w(x) = \sum_{j=1}^{\infty} A_j w_j(x) \tag{E.4}$$

Where $A_j$ are the weighting coefficients of every buckling mode in the deformed configuration. These coefficients are the kinematical descriptors of the model. Then, the vertical displacement, $d$, results:

$$d = \bar{w}\left(\frac{l}{2}\right) - w\left(\frac{l}{2}\right) \tag{E.5}$$

with a positive displacement $d$ indicating that the beam apex moves downwards. The rotation of the beam axis results from the difference between the initial axis slope and the current axis slope In particular, the rotation of the axis at the beam center is:

$$\theta = -\frac{dw}{dx}\left(\frac{l}{2}\right) \tag{E.6}$$

For completeness we replicate the equations of Qiu et al. [102] regarding the total length of the beam neutral axis $s$, the axial load $p$, and the three energies participating in the equilibrium, i.e., the strain energies due to bending, $u_b$, compression, $u_s$, and the potential energy of the external loads $u_e$, resulting:

$$s = \int_0^l \sqrt{1 + \left(\frac{dw}{dx}\right)^2} dx \approx \int_0^l \left[1 + \frac{1}{2}\left(\frac{dw}{dx}\right)^2\right] dx \tag{E.7}$$

$$p = Ebt\frac{\Delta s}{s|_{\bar{w}}} \tag{E.8}$$

$$u_b = \frac{EI}{2}\int_0^l \left(\frac{d^2\bar{w}}{dx^2} - \frac{d^2w}{dx^2}\right)^2 dx \ ; \ u_s = \frac{Ebt}{2s|_{\bar{w}}}\Delta s^2 \approx \frac{Ebt}{2l}\Delta s^2 \ ; \ u_e = -(fd + m\theta) \tag{E.9}$$

The term $s|_{\bar{w}}$ in equation (E.8) refers to the neutral axis length in the undeformed configuration, and $\Delta s = s|_{\bar{w}} - s$ to its variation. In (E.9), we follow Qiu et al. by assuming that $s|_{\bar{w}}$ approximates the length of the beam span. This assumption performs well for ratios $l/h > 10$. Thus, $p$ results positive in compression.

The model accounts for the geometrical nonlinearity through equation (E.7). Thus, the compression energy, $u_s$, introduces the non-convexity of the potential energy and the snap-through instability.

We also define the following dimensionless variables:

$$X = \frac{x}{l} \quad ; \quad W(X) = \frac{w(Xl)}{h} \quad ; \quad \frac{dW}{dX}(X) = \frac{l}{h}\frac{dw}{dx}(Xl) \; ; \tag{E.10}$$

from where, the normalized displacements are:

$$\Delta = \frac{d}{h} \; ; \; \Theta = \frac{l}{h}\theta \; ; \; \Delta S = \Delta s \frac{l}{h^2} \; . \tag{E.11}$$

Dimensionless external actions $F$, $M$, and axial force $N^2$ are also defined as follows:

$$F = \frac{fl^3}{EIh} \; ; \; M = \frac{ml^2}{EIh} \; ; \; N^2 = \frac{pl^2}{EI} \tag{E.12}$$

Dimensionless strain energies due to bending, $U_b$, compression $U_s$, and potential energy of the external loads, $U_e$, are defined as follows:

$$U_b = \frac{u_b l^3}{EIh^2} \; ; \; U_s = \frac{u_s l^3}{EIh^2} \; ; \; U_e = \frac{u_e l^3}{EIh^2} \; . \tag{E.13}$$

According to the previous expressions, the equations (E.5-E.9) can be rewritten in terms of the coefficients $A_j$ and dimensionless form as follows:

$$\Delta = 1 - 2 \sum_{j=1,5,9,\ldots} A_j \tag{E.14}$$

$$\Theta = - \sum_{j=2,4,6,\ldots} \xi_j A_j \tag{E.15}$$

$$\Delta S = \frac{N_1^2}{16} - \sum_{j=1}^{\infty} \frac{A_j^2 N_j^2}{4} \tag{E.16}$$

$$\frac{N^2}{12Q^2} = \frac{N_1^2}{16} - \sum_{j=1}^{\infty} \frac{A_j^2 N_j^2}{4} \tag{E.17}$$

where, in (E.14), it has been used that $W_j(1/2) = 2$ for $j = 1, 5, 9, ...$, $W_j(1/2) = 0$ for $j = 3, 7, 11, ...$, and $W_j(1/2) = 0$ for $j = 2, 4, 6, ....$ In (E.15) $\xi_j = \frac{dW_j}{dX}(\frac{1}{2})$ and it has been used that $\xi_j = 0$ for $j = 1, 3, 5, ...$

Additionally, the normalized energies take the following expressions:

$$U_b = \frac{\left(\frac{1}{2} - A_1\right)^2 N_1^4}{4} + \sum_{j=2}^{\infty} \frac{A_j^2 N_j^4}{4} \tag{E.18}$$

$$U_s = 6Q^2 \left[ \frac{N_1^2}{16} - \sum_{j=1}^{\infty} \frac{A_j^2 N_j^2}{4} \right]^2 \tag{E.19}$$

$$U_e = -F\Delta - M\Theta \tag{E.20}$$

The strain energy of the structure results from the addition of the bending and compression energies:

$$U_i = U_b + U_s \tag{E.21}$$

The expression of the strain energy in terms of the normalized displacements is evidenced after replacing (E.14) and (E.15) in (E.21), although, in general, it is not possible to obtain the corresponding explicit expression.

The total potential energy is:

$$\Pi = U_b + U_s + U_e\,. \tag{E.22}$$

**Variational equilibirum equations**

Equilibrium conditions arise after imposing the minimization of the total potential energy, $\Pi$, in terms of the kinematical descriptors. If kinematical descriptors are unconstrained, the equilibrium condition is equivalent to finding the coefficients $A_j$ $(j = 1, 2, ...)$ satisfying:

$$\begin{aligned}\delta\Pi \;=\; & \delta U_b + \delta U_s + \delta U_e = \left(\frac{N_1^4 - N^2N_1^2}{2}A_1 - \frac{N_1^4}{4} + 2F\right)\delta A_1 + \\ & + \sum_{j=2,4,6,\ldots}\left(\frac{N_j^4 - N^2N_j^2}{2}A_j + \xi_j M\right)\delta A_j + \sum_{j=3,7,11,\ldots}\left(\frac{N_j^4 - N^2N_j^2}{2}A_j\right)\delta A_j + \\ & + \sum_{j=5,9,13,\ldots}\left(\frac{N_j^4 - N^2N_j^2}{2}A_j + 2F\right)\delta A_j = 0\,; \qquad \forall\,\delta A_j\end{aligned} \tag{E.23}$$

Thus, equation (E.23) results in the following coefficients:

$$A_1 = -\frac{N_1^2}{2(N^2 - N_1^2)} + \frac{4F}{N_1^2(N^2 - N_1^2)}, \qquad \text{for: } j = 1; \tag{E.24}$$

$$A_j = \frac{2\xi_j M}{N_j^2(N^2 - N_j^2)}, \qquad \text{for: } j = 2, 4, 6, ...; \tag{E.25}$$

$$A_j = \frac{4F}{N_j^2(N^2 - N_j^2)}, \qquad \text{for: } j = 5, 9, 13, ...; \tag{E.26}$$

and for $j = 3, 7, 11, ...$:

$$A_j \begin{cases} = 0 & \text{if } N^2 < N_j^2 \\ \text{can take any value} & \text{if } N^2 = N_j^2 \end{cases} \tag{E.27}$$

We remark that equations (E.15) and (E.25) indicate that whenever the actions involve rotations and its respective reactive moment, then, the $j$-th even modes may be active.

Expressions (E.14), (E.15), and (E.17) together with (E.24), (E.25), and (E.26) conform a set of three implicit functions with five variables:

$$\underline{\mathbf{g}}(\Delta, \Theta, F, M, N^2) = \underline{\mathbf{0}} \tag{E.28}$$

Depending on the actions applied on the curved beam, one may choose two of these variables as the independent ones, while the remaining three are determined from solving the implicit functions. Thus, when displacement and rotation are controlled, the variables $(\Delta, \Theta)$ are naturally the independent terms. But, when force and moments are applied, the $(F, M)$ terms are naturally the independent variables.

In the following, we study the more stable displacement control case (hard device). Then, the condition (E.28) can be rewritten as follows:

$$\begin{aligned} F &= F(\Delta,\Theta) \\ M &= M(\Delta,\Theta) \\ N^2 &= N^2(\Delta,\Theta) \end{aligned} \tag{E.29}$$

In general, (E.29) cannot be solved in closed analytical form. Therefore, a numerical procedure is proposed and explained in Appendix I. In addition, closed analytical solutions are possible if all the modes $A_j$, except the first three (with $j = 1, 2, 3$), are constrained to zero. This analysis is presented in Appendix II.

**Bifurcation condition**

A further inspection of equation (E.27) shows that a bifurcation condition of the system is attained when the bottom expression in (E.27) is satisfied. Then, the first bifurcation condition: $N^2 = N_b^2$ is reached through the lowest mode of the set: $b = 3, 7, 11, ....$ Note that contrarily to the general case, since $N^2$ is constant in a bifurcation path, the equation system (E.29) is decoupled resulting $F = F(\Delta)$ and $M = M(\Theta)$. Replacing (E.24) and (E.26) in (E.14), and (E.25) in (E.15), with $N^2 = N_b^2$: $b = 3, 7, 11, ...$:

$$F = \frac{N_b^2}{(N_b^2 - N_1^2)\sum_{j=1,5,9,...} \frac{8}{N_j^2(N_b^2-N_j^2)}} - \frac{1}{\sum_{j=1,5,9,...} \frac{8}{N_j^2(N_b^2-N_j^2)}}\Delta \tag{E.30}$$

$$M = -\frac{1}{\sum_{j=2,4,6,...} \frac{2\xi_j^2}{N_j^2(N_b^2-N_j^2)}}\Theta \tag{E.31}$$

The strain energy, considering the bifurcation path with the b-mode staying active, results:

$$U_i = U_b + U_s = \frac{\left(\frac{1}{2} - A_1\right)^2 N_1^4}{4} + \sum_{j=2}^{\infty} \frac{A_j^2 N_j^4}{4} + N_b^2 \left[\frac{N_1^2}{16} - \sum_{j=1}^{\infty} \frac{A_j^2 N_j^2}{4}\right] - \frac{N_b^4}{24Q^2} \tag{E.32}$$

The last constant term in (E.32) arises after considering that both expressions, (E.21) and (E.32), are equal in the change of regime, i.e., when the bifurcation condition ($N^2 = N_b^2$) is satisfied.

**Remark:** Equations (E.6), (E.11), (E.15), and (E.25) generalize the model of [102] by admitting loads consisting of moments or prescribed rotations. This extended model is one of the contributions of this paper.

### E.3.1. Validation of the semi-analytical model

The accuracy of the semi-analytical model characterizing the behavior of a curved beam depends on the number of modes taking place in the expansion (E.4). In the following, the accuracy of the semi-analytical model is assessed with 30 modes.

We compare the solutions of the responses $F$ versus $\Delta$ and $M$ versus $\Theta$ of several hysterons against those obtained with a high-fidelity finite element model. The hysterons are curved beams clamped at both ends, as shown in Figure E.3. The beams are loaded under a combined monotonous increase of displacement $\Delta$ and rotation $\Theta$ until reaching the normalized values: $\Delta = 2$ and $\Theta = 0.5\pi$. Three geometries with parameters $Q = 2$, $Q = 3$, and $Q = 10$ are studied. In these three cases, we adopt a ratio $L/h = 30$. The high-fidelity finite element models follow a large deformation theory with a Kirchhoff-Saint Venant material model[3]. The beams are modeled as a 2D domain using bilinear quadrilateral elements. Structu-

[3] Analysis performed using a Neo-Hookean constitutive model confirms that the hypothesis of constant moduli is valid for

red meshes are used for the 2D domains with $n_x$ elements along $L$ and $n_y$ elements in the beam thickness $t$. Both numbers of elements, $n_x$ and $n_y$, are chosen to define elements with aspect ratios close to 1. Table E.1 gives details of the meshes used in each case. The meshes are fine enough to guarantee accurate solutions.

| | $n_x$ | $n_y$ | Number of FE | Number of nodes |
|---|---|---|---|---|
| $Q = 2$ | 1400 | 22 | 30800 | 32223 |
| $Q = 3$ | 1700 | 18 | 30600 | 32319 |
| $Q = 10$ | 3000 | 10 | 30000 | 33011 |

**Tabla E.1:** High-fidelity finite element models. Parameters of meshes.

Figure E.4 depicts the curves $F$ versus $\Delta$ and $M$ versus $\Theta$ corresponding to both, semi-analytical and high fidelity finite element, models. Even considering the highly non-linear responses of these systems, the results of both models agree very closely. Figure E.4-c displays three deformed configurations of the curved beams with $Q = 10$ at instants (1), (2), and (3). As can be observed, these configurations are the superposition of several buckling modes, including symmetrical and non-symmetrical buckling modes.

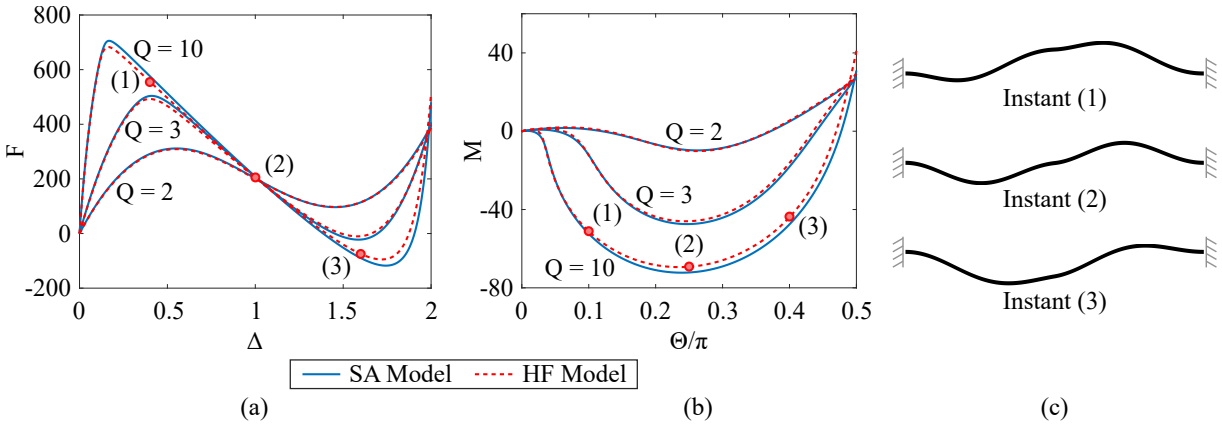


**Figura E.4:** Comparison of results between a high-fidelity (HF) finite element model and the semi-analytical (SA) model with 30 modes for different Q values. The beams are loaded under a combined monotonous increase of displacement $\Delta$ and rotation $\Theta$ until reaching the normalized values: $\Delta = 2$ and $\Theta = 0.5\pi$. a) $F$ vs. $\Delta$; b) $M$ vs. $\Theta$; c) deformed configurations of the curved beam with a displacement scale factor equal to 1, $Q = 10$, at three load instants: (1), (2), and (3) identified in plots a) and b).

## E.4. Surrogate model (SM) of the hysteron

With the objective of building a reduced order model of the hysteron, we develop a frame model with linear kinematics and a reduced number of degrees of freedom capable of carrying axial and transverse loads and moments, see Figure E.5. Such a SM of the curved beam captures the complex and highly non-linear geometrical response analyzed in the previous Section.

The frame model is developed by assuming small deformations, linear kinematics and is equipped with non-linear constitutive responses in both, axial and bending, effects. These constitutive relations are determined according to the laws defined by (E.29). The SM is completed by imposing a Variational Principle of Energetic Equivalence between both models, the frame and the curved beam SA model, with prescribed load and moment.

this test.

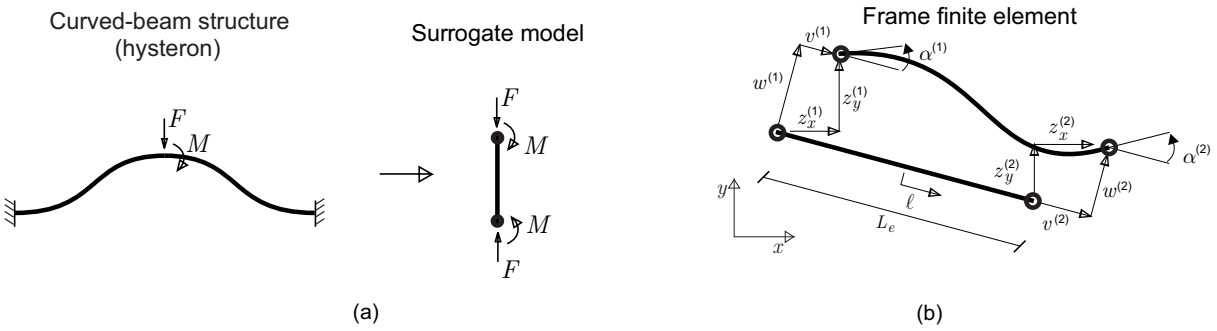


**Figura E.5:** (a) Frame model of the hysteron. (b) Frame finite element, two nodes, and six degrees of freedom.

The bending effect of the frame follows the assumption of an Euler-Bernoulli beam model, neglecting shear strains, with small deformation and displacement theory and a non-linear material. Also, the axial effect follows the assumption of a small deformation-small displacement bar theory endowed with a non-linear constitutive law.

The kinematics, illustrated in Figure E.5-b, is determined through the displacement vector of the beam neutral axis, $\boldsymbol{z}(\ell)$, where $\ell$ is the arc-length coordinate along the neutral axis. This vector field is decomposed in the axial displacements $v$ and the transverse deflections $w$. The rotations, $\alpha$, of the cross sections orthogonal to the neutral axis result from $\alpha = dw/d\ell$. The frame constitutive relations associate the two generalized strains: axial $e(\boldsymbol{z}) = dv/d\ell$, and curvature $\kappa(\boldsymbol{z}) = d^2w/d\ell^2$ with the two generalized forces or stress resultants: axial $n^{SM}$ and moment $m^{SM}$. Thus, the internal mechanical power of the SM, $\dot{\pi}^{SM}$, results:

$$\dot{\pi}^{SM} = \int_{L_e} [n^{SM}\dot{e} + m^{SM}\dot{\kappa}]\, d\ell \,. \tag{E.33}$$

Appropriate constitutive relations of the form $n^{SM}(e,\kappa)$ and $m^{SM}(e,\kappa)$ are next discussed.

**Variational Principle of Energetic Equivalence**

An additional assumption of the model is the existence of a Variational Principle of Energetic Equivalence (VPEE) between the SM and the SA model. This assumption determines the transition equations from the geometrically non-linear SA model of the hysteron to the frame model with small displacements and small strains and non-linear constitutive laws.

The assumed VPEE is stated as the equality between the variational internal (strain) energy of the semi-analytical model and the surrogate one, and is mathematically expressed as follows:

$$\delta(u_b + u_s) = \delta\pi^{SM} \tag{E.34}$$

where $(u_b + u_s)$ is the internal energy defined in equation (E.9) and $\pi^{SM}$ the internal energy in (E.33). Equation (E.34) is valid for any admissible kinematical variation expressed in terms of the kinematical descriptors.

After considering the equilibrium condition in the semi-analytical model, i.e., $\delta(u_b + u_s) = -\delta u_e$, for any kinematically admissible variation, equation (E.34) can be rewritten as follows:

$$f\delta d + m\delta\theta = \int_{L_e} [n^{SM}\delta e + m^{SM}\delta\kappa]\, d\ell \tag{E.35}$$

## E.4.1. Frame finite element

The frame finite element implemented in this work has two nodes with three degrees of freedom each, two displacements and one rotation. The element couples a linear axial displacement $v_h$ with a $C^1$

interpolation (using cubic Hermite polynomials) of displacements $w_h$ with continuity of displacements and their first derivatives between elements.

The element generalized displacements, $\underline{D}^n$ can be expressed as follows

$$\underline{\mathbf{D}}^n = \left[ z_x^{(1)} \;\; z_y^{(1)} \;\; \alpha^{(1)} \;\; z_x^{(2)} \;\; z_y^{(2)} \;\; \alpha^{(2)} \right]^T \tag{E.36}$$

where superscripts indicate values defined at the nodes 1 and 2, respectively. The generalized strains $e$ and $\kappa$ can be expressed as:

$$\begin{aligned} e &= \underline{\mathbf{B}}_e \underline{\mathbf{D}}^n \\ \kappa &= \underline{\mathbf{B}}_\kappa \underline{\mathbf{D}}^n \end{aligned} \tag{E.37}$$

Where the matrix $\underline{\mathbf{B}}_e$ gathers the derivatives of the shape functions of the truss finite element, and the matrix $\underline{\mathbf{B}}_\kappa$ gathers the derivatives of the shape functions of the finite element (further details about the matrices $\underline{\mathbf{B}}$ using the present interpolation functions can be consulted in [212]). The internal force vector, $\underline{\mathbf{F}}_i$, and the tangent stiffness matrix, $\underline{\underline{\mathbf{K}}}_t$, result:

$$\underline{\mathbf{F}}_i = \int_{L_e} \left[ \underline{\mathbf{B}}_e^T n^{SM} + \underline{\mathbf{B}}_\kappa^T m^{SM} \right] dL \; , \tag{E.38}$$

and

$$\underline{\underline{\mathbf{K}}}_t = \int_{L_e} \left[ \underline{\mathbf{B}}_e^T \frac{\partial n^{SM}}{\partial e} \underline{\mathbf{B}}_e + \underline{\mathbf{B}}_e^T \frac{\partial n^{SM}}{\partial \kappa} \underline{\mathbf{B}}_\kappa + \underline{\mathbf{B}}_\kappa^T \frac{\partial m^{SM}}{\partial e} \underline{\mathbf{B}}_e + \underline{\mathbf{B}}_\kappa^T \frac{\partial m^{SM}}{\partial \kappa} \underline{\mathbf{B}}_\kappa \right] dL \; , \tag{E.39}$$

respectively.

The generalized forces are derived from an elastic potential, therefore, the cross derivatives are equal and the stiffness matrix is symmetric.

**Constant curvature constraint**

The exact numerical integration of the C1 beam element requires a Gaussian quadrature rule with at least two integration points. It means that the beam curvature has to be evaluated in both quadrature points. Considering that the moment-curvature law may be subjected to softening, the evaluation in two independent quadrature points may induce spurious instabilities and loss of uniqueness. To avoid this issue, we force the beam curvature to be constant, i.e., the curvature in both integration points is constrained to be equal. Note that, by construction, the axial strain is constant.

The constant curvature constraint is written in terms of the local (aligned) degrees of freedom as:

$$\frac{w^{(2)} - w^{(1)}}{L_e} = \frac{\alpha^{(1)} + \alpha^{(2)}}{2} \; , \tag{E.40}$$

and is incorporated to the force balance equation through a Lagrange multiplier technique.

This constraint causes that, for certain assembly of frame finite elements and boundary conditions, the system may exhibit locking. In our case, this is not an issue because microstructures are always constructed by using pairs of elements in series, which avoids locking, independently of the boundary conditions.

**Kinematic connection with the SA model. Constitutive relations of the SM**

From (E.37) and considering a constant curvature, the axial strain and curvature of the frame element result:

$$e = \frac{v^{(2)} - v^{(1)}}{L_e} \qquad , \qquad \kappa = \frac{\alpha^{(2)} - \alpha^{(1)}}{L_e} \tag{E.41}$$

Then, the kinematics of the SM is connected with the kinematics of the SA model through the following

equations:

$$d = h\Delta = eL_e = v^{(2)} - v^{(1)} \qquad , \qquad \theta = \frac{h\Theta}{l} = \kappa L_e = \alpha^{(2)} - \alpha^{(1)} \tag{E.42}$$

Then, using expressions (E.42) and the fact that $e$ and $\kappa$ are uniforms in the frame element, we rewrite the VPEE (E.35) as follows.

$$f\delta d + m\delta\theta = \frac{1}{L_e}\int_{L_e} \left[n^{SM}\delta d + m^{SM}\delta\theta\right] d\ell \qquad ; \quad \forall\, \delta d\,,\, \delta\theta \tag{E.43}$$

Arbitrary variations of $\delta d$ and $\delta\theta$ determine the generalized forces of the SM in terms of $f$ and $m$. Using the normalized expression of these actions and taking into account that $n^{SM}$ and $m^{SM}$ are uniforms along the element and that, according to (E.42), $\Delta$ and $\Theta$ can be expressed in terms of $e$ and $\kappa$, we finally obtain:

$$n^{SM} = \frac{EIh}{l^3}F(\Delta(e), \Theta(\kappa)) \qquad ; \qquad m^{SM} = \frac{EIh}{l^2}M(\Delta(e), \Theta(\kappa)) \tag{E.44}$$

which result in the constitutive responses of the frame element. Further, the strain energy of the frame element is given by:

$$\pi^{SM} = \frac{EIh^2}{l^3}U_i^M(\Delta(e), \Theta(\kappa)) \tag{E.45}$$

**Remark:** From the above constitutive equations, it is noted that the so-characterized frame element response depends on the geometrical characteristics of the hysteron, but it does not depend on its proper geometry, i.e., $L_e$, area, and moment of inertia. Therefore, the only geometrical feature to be preserved in the SM is the hysteron assembling direction, i.e., the frame finite element axis has to be parallel to the transverse symmetry axis of the curved beam.

**Remark:** independently of the particular device inducing the phase transformation mechanism, the development of a surrogate model mimicking such a snapping device lies on two general guidelines connected with Stage 2 of the present work: 1) the hypothesis about that: *"it is enough to adapt a continuum model with a few degrees of freedom, linear kinematics, and non-linear constitutive laws to assess the highly complex non-linear geometrical effect of the snapping device"*, and 2) the Variational Principle postulating that *"the variational integral strain energy of the device is equal to that of the continuum element"*. This principle demands a link between some governing kinematical variables of the device with those of the continuum model. The specific point which should be adjusted to every snapping mechanism refers to the adequate definition of the non-linear constitutive law assigned to the surrogate element (i.e., the frame element in the present work).

## E.5. Numerical assessments

In Sub-Section E.5.1, using the SA model, we focus on the study of several performances and characteristics of bistable curved beams undergoing combined displacement and rotation loads. These combined load conditions are commonly observed in microstructures of functionally 2D and 3D metamaterials. The objective is to assess the capacity of parameterized hysterons to dissipate energy under different types of loads. Hence, we study the landscapes of the normalized transverse force, moment, axial force, and internal energy in terms of the loading parameters. The SA model determining these responses utilizes 30 modes.

In Sub-Section E.5.2, we assess the predictive capacity and performances of the SM. We study the response of two hysterons in series, which is a typical subsystem useful for designing microarchitectures with energy dissipation, see Zhang et al. [100]. We show the markedly non-linear behavior displayed by this hysteron subsystem and the capability of the SM to reproduce this feature.

Finally, in Sub-Section E.5.3, we evaluate the hysteresis of a metamaterial sample undergoing a closed cycle of loads. The obtained SM outcome is compared with solutions and experiments reported in the literature. We assess the pattern formation as a consequence of phase transformations.

### E.5.1. Analysis of the curved beam capacity for dissipating energy

Adopting some representative curved beams, we assess four normalized magnitudes, $F$, $M$, $N^2$, and $U_i$, in terms of the normalized displacements and rotations $\Delta$ and $\Theta$ of the load application point. These results are obtained with the SA model.

Then, several paths of deformations in the space $(\Delta, \Theta)$ are studied to motivate the influence of the loading conditions on the curved beam features. Special attention is paid to the capacity of this structure for dissipating energy. This feature is assessed in terms of the strain energy landscape, $U_i$. According with this criterion, we distinguish two types of responses resulting from curved beams with either low or high values of Q. Low values of Q inhibit the arising of bifurcations in the system. The paper [102] reports a critic value $Q^{crit} = 2.31$, below this value, the curved beams do not display bifurcations. Contrarily, systems with higher values of $Q^{crit}$ can bifurcate and shown a second stable solution for zero loads.

Results obtained with low Q-values, $Q = 2 < Q^{crit}$, are shown in Figure E.6-a to d. Four isolevel plots of $F$, $M$, $N^2$, and $U_i$, in terms of $\Delta$ and $\Theta$ are presented. Red and blue colors indicate the higher and the lower values, respectively.

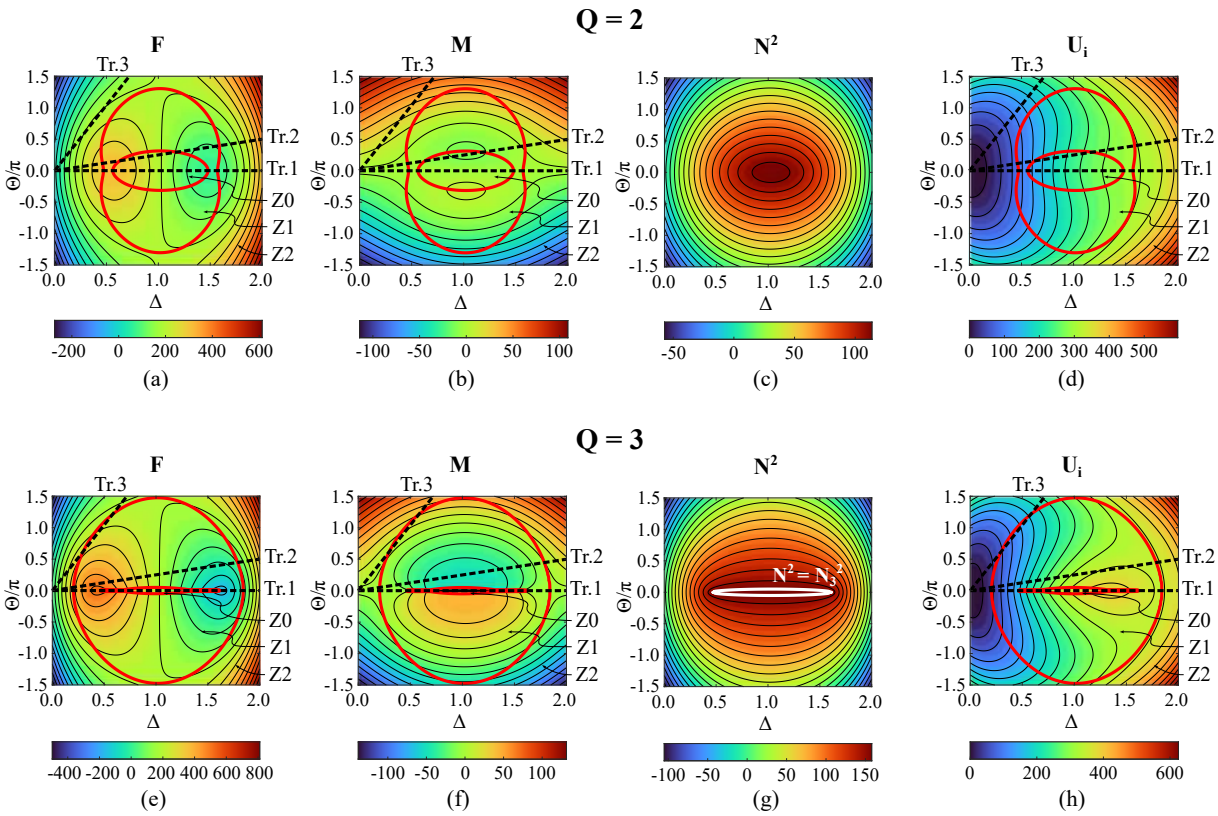


**Figura E.6:** Results of the SA model using 30 modes for $Q = 2$ and $Q = 3$. Isolevel plots for $Q = 2$: a) $F(\Delta, \Theta)$, b) $M(\Delta, \Theta)$, c) $N^2(\Delta, \Theta)$, and d) $U_i(\Delta, \Theta)$. Isolevel plots for $Q = 3$: e) $F(\Delta, \Theta)$, f) $M(\Delta, \Theta)$, g) $N^2(\Delta, \Theta)$, and h) $U_i(\Delta, \Theta)$. Three monotonous loading trajectories (Trajectory 1 (Tr1), Trajectory 2 (Tr2) and Trajectory 3 (Tr3)) are indicated in black dashed lines. Also, zones $Z0$, $Z1$, and $Z2$ are depicted in the plots.

Results obtained with high Q-values, $Q = 3 > Q^{crit}$ are depicted in Figure E.6-e to h. Also, four isolevel plots of $F$, $M$, $N^2$, and $U_i$ are shown in terms of $\Delta$ and $\Theta$.

**Discussion of results:** The white line in Figure E.6-g indicates the values $N^2 = N_3^2$ in the $\Delta - \Theta$ space. This line encloses the region whose points represent load cases satisfying the bifurcation condition. No similar region exists in the plot of Figure E.6-c.

Plots in Figure E.6-d and h depicts isolines of the strain energy, $U_i$. Such as commented above, the system's capacity for dissipating energy is intimately related to the non-convex character of the strain energy. To analyze this feature, we recognize three zones in the plots, denoted $Z0$, $Z1$, and $Z2$. These zones are distinguished according to the sign of the principal normal curvatures of the energy surface[4]. Zone $Z2$ has two principal curvatures positive, zone $Z1$ has one curvature positive and one negative, while zone $Z0$ has both curvatures negative. The borders of these regions are indicated in Figure E.6-a, b, d, e, f, and h with red lines. Region $Z0$ is the internal zone delimited by the inner red curves in the plots. Region $Z1$ is delimited by both red curves, and region $Z2$ is the external zone to the outer red curve.

As a first approximation to understand the complex behavior of the curved beam, let us consider its response under a generic monotonically increasing loading path represented by a straight segment in the space $(\Delta, \Theta)$. According to the strain energy landscape of Figure E.6-d and h, along a monotonic loading path, the strain energy can be non-convex only when this path intersects the zones $Z1$ or $Z0$. Besides, since in zone $Z1$ the energy surface has only one negative principal curvature, a beam undergoing a loading path intersecting this zone may not show energy dissipation. Paths crossing the $Z2$ regions show strictly convex strain energies. Then, along this zone, the beam can neither dissipate energy nor undergo phase transformations.

To visualize this effect, we show additional assessments in Figure E.7. This Figure plots the $F(\Delta)$, $M(\Theta)$, and $U_i(\chi)$ responses for three monotonous loading trajectories. The arc-length coordinate of the trajectory in the $(\Delta, \Theta)$ space is denoted with the symbol $\chi$. These plots are depicted for $Q = 2$ and $Q = 3$, respectively. The three assessed trajectories are plotted in Figure E.6 in the space $(\Delta, \Theta)$ in black dashed lines, and are defined as follows:

$$\begin{array}{lllllll} \text{Trajectory 1:} & \Theta & = & 0 & ; & \Delta & \text{increasing monotonously from 0 to 2} \\ \text{Trajectory 2:} & \Theta & = & 0.25\pi\Delta & ; & \Delta & \text{increasing monotonously from 0 to 2} \\ \text{Trajectory 3:} & \Theta & = & 2.08\pi\Delta & ; & \Delta & \text{increasing monotonously from 0 to 0.72} \end{array} \tag{E.46}$$

We remark that trajectory 1, with mode 2 constrained to zero ($\Theta = 0$), provides identical results to the ones reported by [102]. In the present model, the condition $\Theta = 0$ automatically nullifies the even modes.

Furthermore, for small $\Theta$, the hysteron with $Q = 3$ can reach a second stable position corresponding to the strain energy local minimum appearing in trajectories 1 and 2 of Figure E.7-f. For $Q = 2$, the system does not show a second stable position.

Of particular interest is the response along trajectory 3 crossing zone Z1 of the case $Q = 3$. The curves $F$ versus $\Delta$ and $M$ versus $\Theta$ display regions with negative slopes. However, the strain energy $U_i(\chi)$ is convex everywhere along the load trajectory. Then, along this trajectory, no spinodal zone is detected, and the beam can neither dissipate energy nor show phase transformations.

Strain energies plots in Figure E.7 indicate the magnitude of the energy dissipation $\mathcal{D}_{mech}$, such as discussed in Figure E.2. In this analysis, we assume that phase transformations happen at the limit load points[5]. Comparing the plots in Figures E.7-c and f, it is observed that when $\Theta$ increases, the phase transformation is delayed, and the limit load decreases. Furthermore, it is observed that the normalized energy dissipation capacity is notably greater for hysterons with higher values of Q.

In summary, curved beams monotonically loaded along trajectories with $\Theta \neq 0$ tend to lose the capacity for dissipating energy due to phase transformations. This conclusion agrees with the ones reported

[4]The principal normal curvatures are the eigenvalues of the Weingarten operator [213]

[5]This condition is called the maximum delay strategy in literature [98] and allows for maximum energy dissipation.

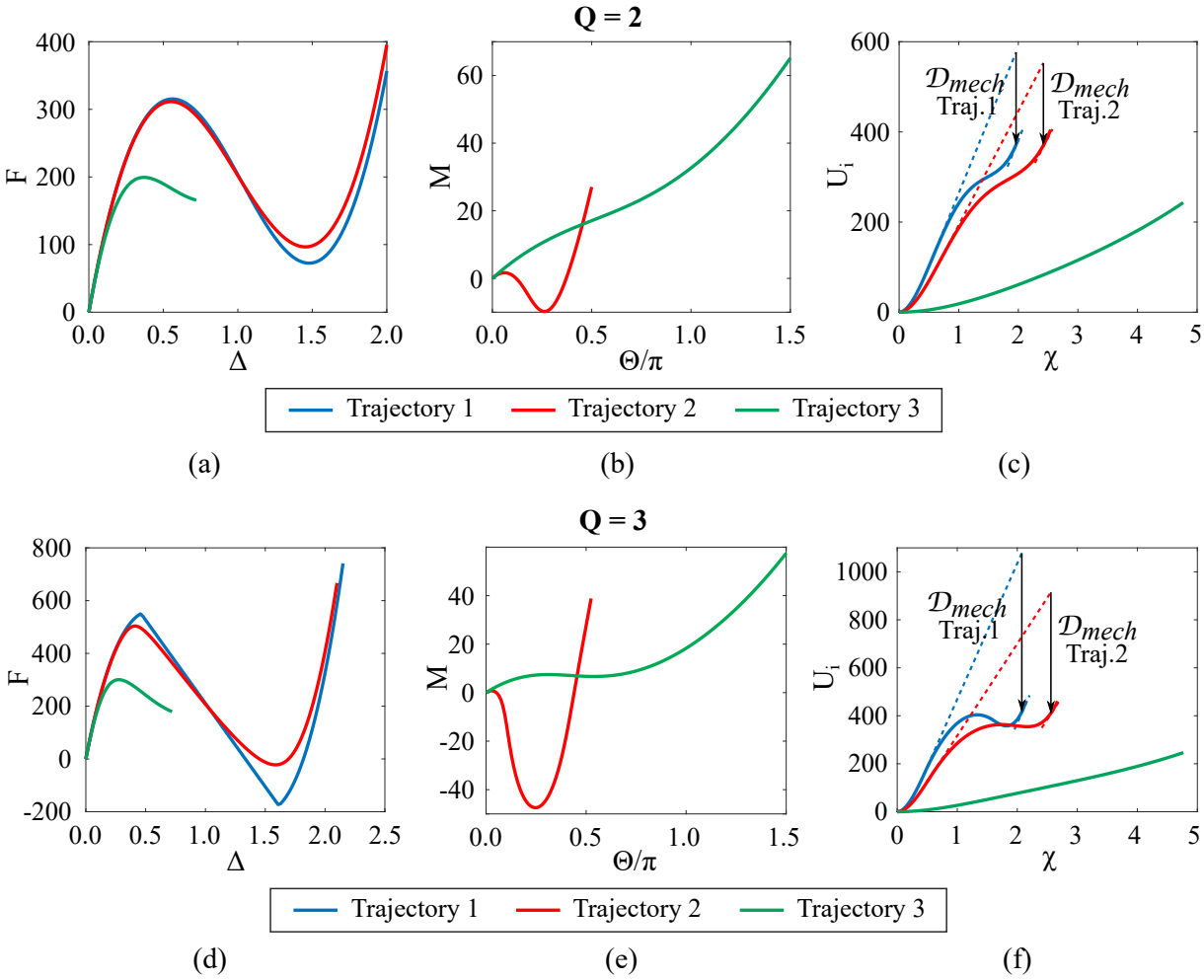


**Figura E.7:** Curved beam under monotonous load trajectories 1, 2, and 3. $Q = 2$: (a) $F$ versus $\Delta$ plot; (b) $M$ versus $\Theta$ plot; (c) Strain energy $U_i$ versus arc-length coordinates, $\chi$, of the trajectories. $Q = 3$. (d) $F$ versus $\Delta$ plot; (e) $M$ versus $\Theta$ plot; (f) Strain energy $U_i$ versus arc-length coordinates, $\chi$, of the trajectories, and energy dissipation capacity. As $\Theta = 0$ in Trajectory 1, the corresponding $M$ is excluded from the plots (b) and (e).

by [100].

### E.5.2. Surrogate model of a hysteron assembly

Elastic metamaterials designed to dissipate energy are conceived as an assembly of hysterons. When they undergo loads in more than one direction, its overall behaviour will depend on individual responses of hysterons and their topological configuration, as analyzed in the previous sub-Section E.5.1.

Following this idea, the assembly of two opposite hysterons as shown in Figure E.8-a under general loads is tested. This assembly constitutes the basic configuration of more complex microarchitectures with functionalities in two and three directions, as reported by Tan et al. [90], Zhang et al. [100], Ren et al. [107], and Ma et al. [203]. Figure E.8 also shows the geometric parameters and boundary conditions of the assembly. Boundary conditions consist of fixing the ends of the lower hysteron, while displacements are applied to the ends of the upper hysteron so that the total actions result in a vertical displacement and a rotation.

The responses of the assembly are analyzed using a high-fidelity (HF) finite element model and a SM and the results are compared. The SM of the hysteron configuration consists of two frame elements in series, such as shown in Figure E.8-b, with imposed displacements $d$ and rotations $\theta$. Although the

dimensionality reduction of the SM compared with the high fidelity model is evident, the discussion about the computational speed-ups of the SM is left for future work.

We evaluate four cases with different geometries and boundary conditions. Detailed geometric data and load conditions are presented in Table E.2. The first case, (**Case 1**), corresponds to a symmetric assembly of hysterons ($Q_1 = Q_2$) with symmetric boundary conditions in the transversal axis of the hysteron (rotations are fixed to zero). This configuration is similar to that adopted in the microarchitectures with hysterons in square or cubic arrangements described in the above-cited literature.

| Case | $t_1$ | $h_1$ | $Q_1$ | $t_2$ | $h_2$ | $Q_2$ | $L$ | $t'$ | $s$ | $d$ | $\theta$ |
|---|---|---|---|---|---|---|---|---|---|---|---|
| 1 | 0.4 | 2 | 5 | 0.4 | 2 | 5 | 30 | 1 | 5 | 8 | $0^o$ |
| 2 | 1 | 1.8 | 1.8 | 0.5 | 1.1 | 2.2 | 30 | 1.5 | 4 | 5.8 | $10^o$ |
| 3 | 0.5 | 1.5 | 3 | 0.2 | 2 | 10 | 30 | 0.5 | 4 | 7 | $5^o$ |
| 4 | 0.75 | 1.5 | 2 | 0.5 | 2 | 4 | 30 | 1.5 | 4 | 7 | $20^o$ |

**Tabla E.2:** Geometric data and load conditions of hysterons assemblies. Dimensions are in $[mm]$ and rotations are in degrees. Young modulus $E = 1000MPa$ . Notation $t_1$, $h_1$, $t_2$, $h_2$, $L$, $t'$,$s$ are indicated in Figure E.8-a.

Cases 2 to 4 correspond to arrangements of two geometrically different hysteron. Three possible combinations are chosen:

**Case 2:** both parameters Q are low ($Q_1 < Q^{crit}$ and $Q_2 < Q^{crit}$ );

**Case 3:** both parameters Q are high ($Q_1 > Q^{crit}$ and $Q_2 > Q^{crit}$), and

**Case 4:** $Q_1$ is low ($Q_1 < Q^{crit}$) and $Q_2$ is high ($Q_2 > Q^{crit}$).

Table E.3 describes the data of the high-fidelity finite element mesh models, as well as the number of frames and degrees of freedom of the SM. The results of the simulations are presented in Figure E.8. Each Case (1,2,3,4) corresponds to one column in plots (d,e,f,g) respectively.

| Case | $neleHF$ | $ndofHF$ | $neleSM$ | $ndofHF$ |
|---|---|---|---|---|
| 1 | 74500 | 155682 | 2 | 6 |
| 2 | 71900 | 148176 | 2 | 6 |
| 3 | 73664 | 154712 | 2 | 6 |
| 4 | 72600 | 150542 | 2 | 6 |

**Tabla E.3:** Discretization of the high-fidelity (HF) and surrogate (SM) models. Columns: $neleHF$ number of elements of the HF finite element mesh, $ndofHF$ number of nodes of the HF finite element mesh, $neleSM$ number of frame elements of the SM model, $ndofSM$ number of nodes of the SM model.

**Discussion of results:** Figure E.8 shows the results obtained with the HF and surrogate models. Three outcomes of the four tested cases are compared: $F(d)$, $M(\theta)$, and $U_i$ in terms of the pseudotime (load increases are proportional to the pseudotime). From these plots, we conclude that the SM with linear geometry exhibits a good predictive capability to reproduce the highly non-linear geometrical responses of the HF model. Further, the SM tends to slightly overestimate the structural stiffness. This outcome could be associated with the structural effect produced by the bar connecting both hysterons shown in Figure E.8-a, which is neglected in the SM model.

Considering that Case 1 is constrained to $\theta = 0$, see Figure E.8-a, the system shows a response similar to that of two bistable springs in series studied by Puglisi y Truskinovsky [80]. Phase transformations occur one hysteron at a time, and the energy landscape displays three wells. Therefore, in this case, exists three stable positions at zero loads.

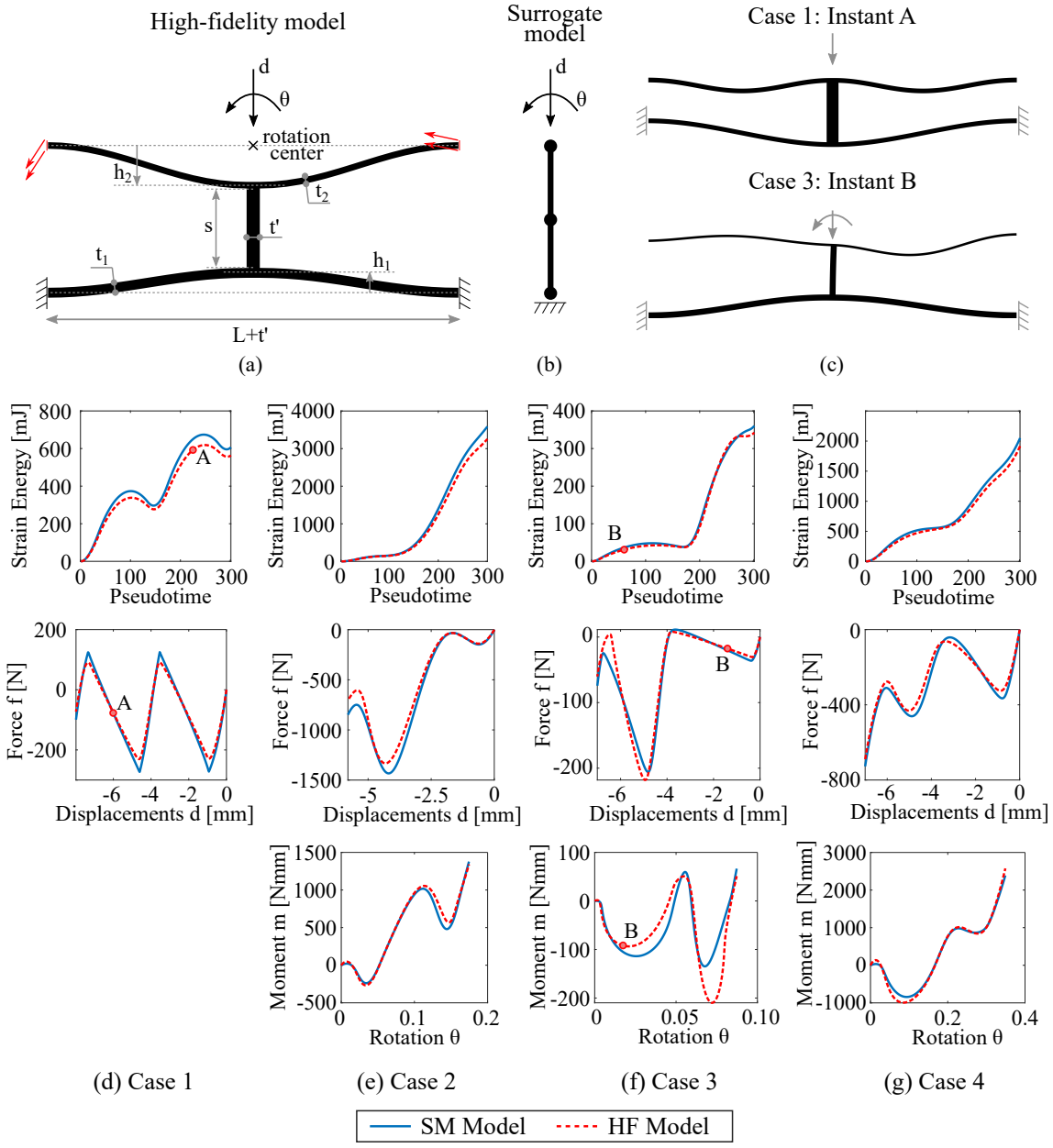


**Figura E.8:** Analysis of a basic assembly of hysterons. (a) High-fidelity finite element model with geometric parameters and notation. (b) Equivalent SM. (c) Deformed configurations of the HF models for Case 1 and Case 3 assemblies at load stages denoted: Instants A and B. The corresponding loads of A and B are signaled in plots (d) and (f). Displacements are scaled by a factor 1. Comparison of results according to the notation established in Table E.2: (d) Case 1, (e) Case 2, (f) Case 3, and (g) Case 4, in columns. Plots in rows: force $f$ vs. Displacement $d$; moment $m$ vs. rotation $\theta$, and total strain energy vs. pseudotime. HF (red curves): high-fidelity finite element model, Surrogate (blue curves): SM. Curve $m$ vs. $\theta$ is removed from plot (d) since $\theta = 0$.

In the four cases, the non-convexity of the energy means that all these systems have the capacity for dissipating energy.

Figure E.8-c shows the deformed configurations of the assemblies corresponding to Case 1 and Case 3, at Instants A and B, simulated with the HF model. The loads at both pseudotimes are indicated in Figure E.8-d and f, respectively. The configuration of Case 1, Instant A, shows that the deformed bottom hysteron is similar to the first buckling mode at phase III, and the deformed top hysteron is like the third buckling mode. In Case 3, the deformed bottom hysteron copies the first buckling mode at phase I, and the deformed top hysteron is a mixture of even buckling modes. These outcomes come from the complex non-linear geometric interactions between both hysterons and are well-captured with the SM straight frame endowed with a linear geometry and assuming small displacements and strains.

### E.5.3. Surrogate model of metamaterial that dissipates energy

We analyze a sample of periodic metamaterial composed of several unit cells using the SM. The analysis aims at reproducing the numerical results reported by Zhang et al. [100] and obtained with a high-fidelity beam finite element model and a non-linear geometrical formulation. We assess the S-type material, taken from the reference work, with a square configuration of hysterons. The unit-cell is depicted in Figure E.9-a. Each hysteron in the figure represents a double curved beam. The figure also shows the SM adopted for the analysis with hysterons modeled with one frame element. Thus, the microcell surrogate model has four frame elements and fifteen degrees of freedom.

Figure E.9-a also shows the color code used to describe the results. In this sense, we follow a similar criterion adopted by Zhang et al. [100] to report their results.

**Microarchitecture configuration:** A uniaxial, quasi-static, compressing load-unload test is performed in the S-type microarchitecture, rotated by 45deg. Since a relatively large amount of unit cells is used in this test (32 unit cells), the attained response is a coarse approximation to the metamaterial limit behavior loaded in an oblique direction. This limit behavior includes both outcomes, the hysteretic response and the pattern deformations, attained during the loading-unloading process.

**Geometric parameters and material data:** the hysteron geometric parameters, such as defined in Figure E.3, are: $l = 71.mm$, $h = 7.mm$, $t = 0.7mm$ and $b = 25.mm$. The Young modulus of the beams is $E = 2267.MPa$. To avoid convergence problems in the numerical iterative algorithm, we introduce a slight geometrical perturbation on the parameter $t$ of each frame through a random variation of $1\,\%$. Considering that Zhang et al.'s work models each hysteron as a double parallel beam and our model adopts a similar beam thickness $t$, we duplicate the generalized forces, i.e., axial and moment, of the frame element.

The numerical solutions of the balance equations are obtained through an iterative BFGS scheme together with a line search technique satisfying the Wolfe conditions. This procedure guarantees a (secant) stiffness matrix that is positive and definite. For major details see [172].

**Results:** the results of this assessment are also shown in Figure E.9.[6] The figure displays the load-displacement plots in a closed loading cycle and snapshots of the deformation pattern at different loading stages. Figure E.9-c compares the present results with the experimental and numerical ones reported by Zhang et al. [100]. Figure E.9-d compares the present results with those reported by the authors in [72]. Phase transformations are specifically detected and depicted in Figure E.9-b. In the force-displacement plot (Figure E.9-c), note the hysteresis loop generated when the sample is undergoing a closed loading cycle. The area enclosed by the hysteresis loop represents the extrinsic energy dissipation of the sample.

[6] *Aclaración para la tesis*: las referencias en la Figura están en relación a la numeración de las citas en el artículo publicado. Las mismas no coinciden con la numeración que estos trabajos tienen en esta tesis.

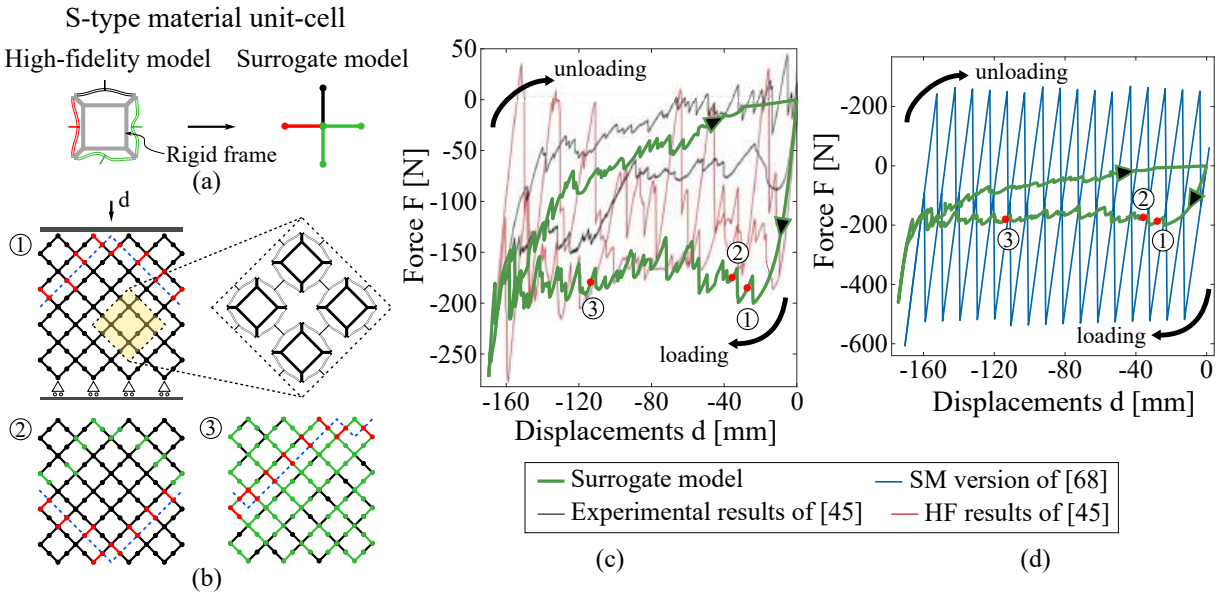


**Figura E.9:** Sample of S-type material at 45deg undergoing a compression load cycle. a) S-type material unit-cell: four hysterons are connected through a rigid frame. High-fidelity and surrogate model. Elements in black indicate that the hysteron remains in phase I. Elements in red indicate that the hysteron has previously transitioned from phase I to phase III. Elements in green indicate hysterons that perform a phase transformation. Phase switching is identified by an abrupt jump in the axial strain of the full SM. b) Deformation patterns (phase states) at several loads. c) Force $F$-displacement $d$ plots. Present results are plotted in green thick lines. The experiment reported in [100] is plotted in black thin lines. Numerical results (HF beam finite element model) reported in [100] is plotted in red thin lines. d) Force $F$ vs. displacement $d$ plots. Present results are plotted in a black thick line. Numerical results reported in [72] light blue line.

**Discussion of results:** The results presented in Figure E.9-c are comparable with those reported in Figure 4 of the paper by Zhang et al. [100] and here reproduced. In the loading process, a plateau in the force-displacement diagram is observed. The displacement interval of the plateau ranges between $24.mm$ and $170.mm$, with load values varying between $140.N$ and $200.N$ . This outcome is in very good agreement with the numerical results of [100]. During the unloading process, the load level progressively decreases, with no formation of a plateau. The response is smoother than the numerical results of [100] and qualitatively more similar to the experiment. The same work ([100]) explains the difference observed between the results obtained with the HF finite element model and the experimental reported ones.

A simpler version of the hysteron SM has been presented in a previous contribution of the authors, [72]. In this simpler version, the axial and bending effects of the hysteron are uncoupled, and the axial force is the only generalized force with a non-monotonous law. By comparing the results in Figure E.9-d with those reported for a similar case in Figure 7 of the cited paper, we conclude that the coupled semi-analytical model in the current version substantially improves the predictive capacity of the SM, mainly concerning peak load prediction.

An additional feature assessing the model performance is its ability to detect phase transformation patterns. Due to a kinematic constraint, a phase transformation occurs by generating a continuum interface of phase boundary [105]. In this case, the topology enforces a zigzagging interface that includes one transitioning element for each of the eight columns of hysterons pairs. As can be seen with the blue dashed lines in Figure E.9-b, instants (1) and (2), the SM predicts an interface with a "V"-like pattern in the initial stages of deformation, also reported by Zhang et al. [100]. At later loading times, a more complex interface pattern is captured and shown in Figure E.9-b, at instant (3).

Finally, we emphasize the dimensional reduction introduced by the SM compared with HF finite element models. The number of finite element of the meshes reported by [100] is around 250 beam elements for modeling one unit cell of the S-type design (see Figure E.9-a), while the SM only requires

four frame elements.

## E.6. Conclusions

Three contributions have been addressed in this work. A generalization of the bistable curved beam SA model, the development of a curved beam SM taking into account the generalized SA model, and the analysis of unstable metamaterials dissipating energy in the elastic regime by means of the SM.

The SA model of the bistable curved beam initially reported by Qiu et al. [102] has been generalized to admit an applied moment in the center of the beam. The attained model predicts with accuracy the response of the hysteron. The system of equations to find the equilibrium condition of the SA model is of rank 3, regardless of the number of buckling modes used as the basis of the solution expansion. Thus, its evaluation requires a relatively low computational burden making this approach computationally convenient to include additional buckling modes for accurate deformed geometry capturing.

The SM, with linear kinematics and non-linear constitutive law, describes the response of a snapping device, the hysteron, with highly non-linear geometrical effects. The success of this approach lies on the VPEE established in equation (E.35). The modeling strategy established in Section E.2, i.e., the development of a SA approach and its incorporation as a constitutive law into the bar element with linear kinematics, has focused on reducing the model dimensionality of a specific hysteron. Remarkably, this methodology may be generalized to hysterons displaying unstable responses based on alternative deformation mechanisms, such as buckling, rotational snapping, etc. In all these cases, the goal is to capture the non-convex strain energy landscape with a reduced model.

This work provides an additional methodology to understand metamaterials with unstable responses, their non-convex energy landscape as a means to extrinsically dissipate energy, as well as the role played by loads applied in different directions. In concordance with results reported in the literature, we confirm that rotations imposed to hysterons, or similarly, transversal loads, play a prominent role in decreasing this feature. Thus, the assembling direction of hysterons into the microarchitecture, relative to load directions, is relevant to achieve the best metamaterial performance.

In some cases, it has been shown that the non-convexity of the elastic energy along the load path is not ensured even for load processes involving displacements and rotations with negative stiffness in the $F$–$\Delta$ and $M$–$\Theta$ responses. In such cases, the hysteron energy dissipation capacity is not guaranteed.

Due to the computational efficiency of the SM, it is a suitable methodology for simulating the material limit response containing a large number of hysterons arranged in arbitrary topologies. This SM feature opens a route being explored in forthcoming works, i.e., the assessment of hysteron spatial configurations with several kinds of lattice symmetries aiming at the topology optimization of functionally 3D metamaterials, such as discussed in previous works of the authors ([60], [61] ,[69]).

## Appendix I: Numerical solution of the equation system (E.28)

We summarize the main steps to solve the equation system (E.28):

$$\underline{\mathbf{g}}(\Delta, \Theta, F, M, N^2) = \underline{\mathbf{0}} \tag{E.47}$$

This system is constituted by three equations $g_i$, with $i = 1, 2, 3$, determined by (E.14), (E.15), and (E.17). The coefficients $A_j$ taking place in (E.4) are defined by the equations (E.24), (E.25), and (E.26) resulting from the equilibrium conditions of the beam.

There are five variables in (E.47). Therefore, two variables, denoted $v_k$, can be chosen freely and the remaining three variables, denoted $u_j$, are implicitly determined by solving the equation system (E.47). In particular, we choose $\Delta$ and $\Theta$ as the free variables and $F(\Delta, \Theta)$, $M(\Delta, \Theta)$, and $N^2(\Delta, \Theta)$ as the

dependent terms. Also, the first derivatives: $\partial F/\partial\Delta$, $\partial F/\partial\Theta$, $\partial M/\partial\Delta$, $\partial M/\partial\Theta$ are assessed. These derivatives constitute the tangent moduli, needed to compute the tangent stiffness matrix in (E.39).

Under such conditions, the system (E.47) is solved numerically using an iterative Newton-Raphson scheme and considering that:

$$d\underline{\mathbf{g}} = \frac{\partial \underline{\mathbf{g}}}{\partial v_1} dv_1 + \frac{\partial \underline{\mathbf{g}}}{\partial v_2} dv_2 + \frac{\partial \underline{\mathbf{g}}}{\partial u_1} du_1 + \frac{\partial \underline{\mathbf{g}}}{\partial u_2} du_2 + \frac{\partial \underline{\mathbf{g}}}{\partial u_3} du_3 = \underline{\mathbf{0}} \tag{E.48}$$

which, after rearranging terms can be rewritten as follows:

$$-\underline{\underline{\mathbf{H}}} \begin{bmatrix} \delta v_1 \\ \delta v_2 \end{bmatrix} = \underline{\underline{\mathbf{J}}} \begin{bmatrix} \delta u_1 \\ \delta u_2 \\ \delta u_3 \end{bmatrix} \tag{E.49}$$

where $\underline{\underline{\mathbf{J}}}$ is the Jacobian whose components are evaluated by using the chain rule of differentiation as:

$$\frac{\partial g_i}{\partial u_j} = \left(\frac{\partial g_i}{\partial u_j}\right)_{expl} + \frac{\partial g_i}{\partial A_1}\frac{\partial A_1}{\partial u_j} + \sum_{k=5,9,13} \frac{\partial g_i}{\partial A_k}\frac{\partial A_k}{\partial u_j} + \sum_{k=2,4,6} \frac{\partial g_i}{\partial A_k}\frac{\partial A_k}{\partial u_j} \tag{E.50}$$

and $\underline{\underline{\mathbf{H}}}$ is a [3x2] matrix storing the derivatives of the balance equations respect to the independent variables, that is $H_{ij} = \partial g_i/\partial v_j$, computed respecting the chain rule. Finally, it results: $\partial u_i/\partial v_j = [-\underline{\underline{\mathbf{J}}}^{-1}\underline{\underline{\mathbf{H}}}]_{ij}$

**Remark:** A nice property of the present procedure is that the inclusion of further buckling modes (with the associated coefficients $A_j$) in the semi-analytical model approach does not imply an appreciable increase in the computational burden to solve the Newton-Raphson iterative procedure.

**Remark:** $\underline{\underline{\mathbf{J}}}$ is singular when the unknown $N^2 = N_1^2$ or $N^2 = N_2^2$, see equations: (E.24) and (E.25). This singularity is removed by minimizing the total potential energy according to (E.23) and including the condition $N^2 = N_1^2$ or $N^2 = N_2^2$. The system of equations behaves differently and the values $F$ and $M$ are calculated according to the following conditions.

**Case 1:** $N^2 = N_1^2$.

$$\begin{aligned} F &= \frac{N_1^4}{8}; \\ A_j &= \frac{4F}{N_j^2(N_1^2 - N_j^2)}, \qquad \text{for: } j = 5, 9, 13, ...; \\ A_1 &= \frac{1 - \Delta - 2\sum_{k=5,9,13} A_j}{2} \end{aligned} \tag{E.51}$$

The term $M$ is determined according to (E.31) with $N_b^2 = N_1^2$ and the even-modes coefficients following (E.25).

**Case 2:** $N^2 = N_2^2$.

$$\begin{aligned} M &= 0; \\ A_j &= \frac{2\xi_j M}{N_j^2(N^2 - N_j^2)}, \qquad \text{for: } j = 4, 6, 8, ...; \\ A_2 &= \frac{-\Theta - \sum_{j=4,6,8,...} \xi_j A_j}{\xi_2} \end{aligned} \tag{E.52}$$

In this case, $F$ is calculated using (E.30), with $N_b^2 = N_2^2$ and the odd-modes coefficients resulting from (E.24) and (E.26).

## Appendix II: Closed solutions of (E.29) when only the first three buckling modes are considered

We show the explicit expressions of the SA model when only the first three modes $A_1$, $A_2$, and $A_3$, (with $A_j = 0$; $j > 3$) are considered. This assumption results in a fairly good predictive capacity for curved beams with low Q-values.

The mode coefficients are uniquely defined by (E.14) and (E.15) as:

$$A_1 = \frac{1-\Delta}{2} \;\; ; \;\; A_2 = -\frac{\Theta}{\xi_2} \tag{E.53}$$

**Case:** $N^2 < N_3^2$ (the main path: $A_3 = 0$). From (E.17), (E.24), (E.25) and (E.53) follow the explicit expressions for $F$, $M$, and $N$:

$$\begin{aligned} F &= \frac{3Q^2N_1^2}{8}\left[\left(\frac{N_1^2}{2}+\frac{N_1^2}{3Q^2}\right)\Delta - \frac{3N_1^2}{4}\Delta^2 + \frac{N_1^2}{4}\Delta^3 - \frac{N_2^2}{\xi_2^2}\Theta^2 + \frac{N_2^2}{\xi_2^2}\Delta\Theta^2\right] \\ M &= \frac{3Q^2N_2^2}{2\xi_2^2}\left[-\frac{N_1^2}{2}\Delta\Theta + \frac{N_1^2}{4}\Delta^2\Theta + \frac{N_2^2}{3Q^2}\Theta + \frac{N_2^2}{\xi_2^2}\Theta^3\right] \\ N^2 &= \frac{3Q^2N_1^2}{2}\Delta - \frac{3Q^2N_1^2}{4}\Delta^2 - \frac{3Q^2N_2^2}{\xi_2^2}\Theta^2 \end{aligned} \tag{E.54}$$

Although $M$ is always an odd cubic function in $\Theta$, note that depending on the value $\Delta$ it is possible to obtain a negative stiffness around $\Theta = 0$. In this case, the internal energy (E.21) is[7]:

$$U_i = \frac{N_1^4}{16}\Delta^2 + \frac{N_2^4}{4{\xi_2}^2}\Theta^2 + \frac{3}{8}Q^2\left[\frac{N_1^2}{2}\Delta - \frac{N_1^2}{4}\Delta^2 - \frac{N_2^2}{\xi_2^2}\Theta^2\right]^2 \tag{E.55}$$

Figure E.10-a shows the results of this model for a beam with parameter $Q = 2$.

**Case:** $N^2 = N_3^2$. For high values of Q, this bifurcation condition may be satisfied. In this case, the SA model equations result:

$$\begin{aligned} F &= \frac{N_1^2N_3^2}{8} - \frac{N_1^2(N_3^2-N_1^2)}{8}\Delta \\ M &= -\frac{N_2^2(N_3^2-N_2^2)}{2\xi_2^2}\Theta \\ N^2 &= N_3^2 \end{aligned} \tag{E.56}$$

and both effects $\Delta$ and $\Theta$ are decoupled, i.e., $F(\Delta)$ and $M(\Theta)$ have negative stiffness. The internal energy is:

$$U_i = \frac{N_1^4}{16}\Delta^2 + \frac{N_2^4}{4{\xi_2}^2}\Theta^2 + \frac{N_3^2}{4}\left[\frac{N_1^2}{2}\Delta - \frac{N_1^2}{4}\Delta^2 - \frac{N_2^2}{\xi_2^2}\Theta^2\right] - \frac{N_3^4}{24Q^2} \tag{E.57}$$

[7]Note that these equations verify that $F = \frac{\partial U_i}{\partial \Delta}$ and $M = \frac{\partial U_i}{\partial \Theta}$

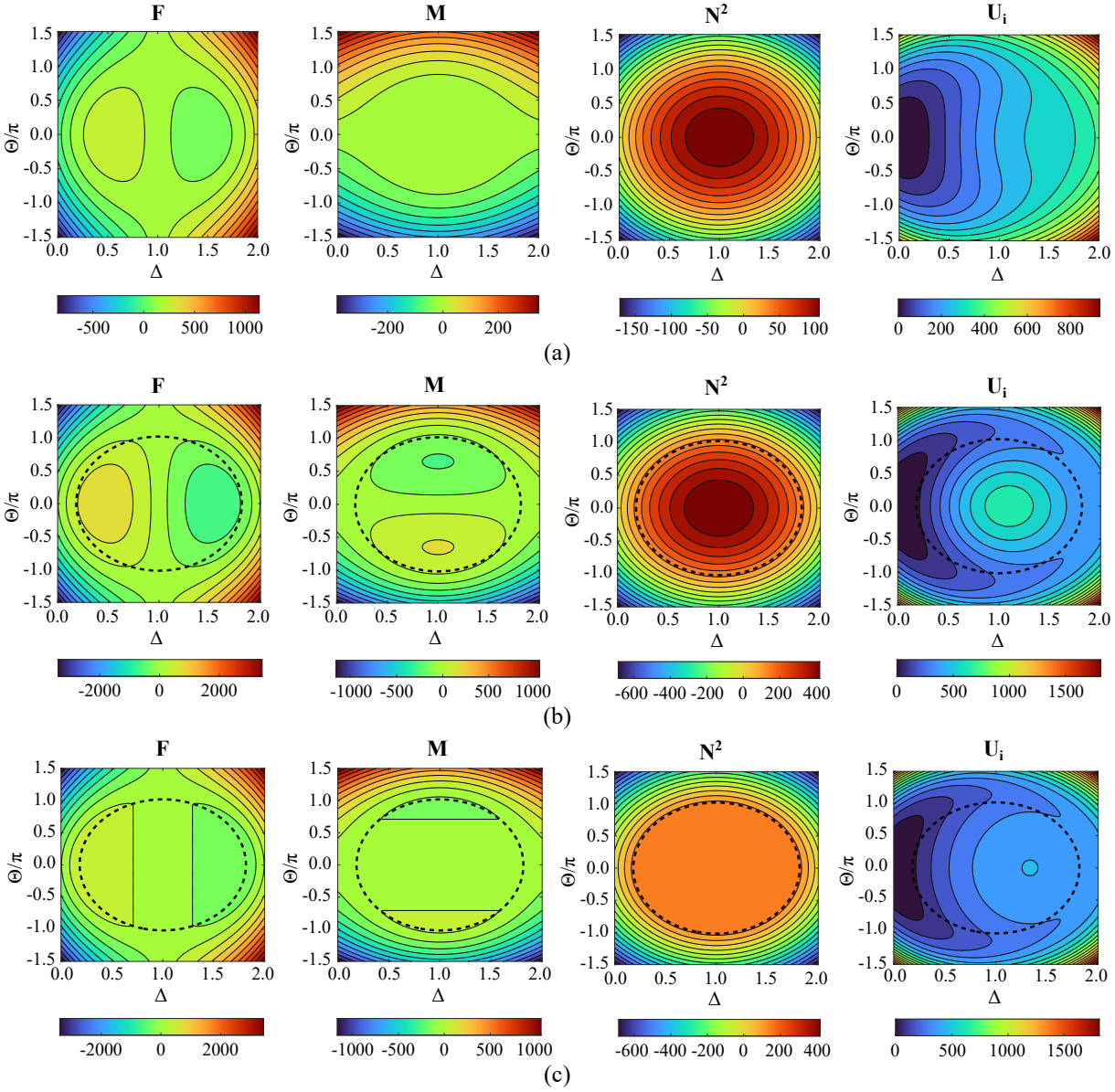


**Figura E.10:** SA model with only the first three buckling modes ($A_1$, $A_2$, and $A_3$) considered. Normalized transverse force $F(\Delta, \Theta)$, moments $M(\Delta, \Theta)$, axial force $N^2(\Delta, \Theta)$ and strain energy $U_i(\Delta, \Theta)$ for (a) a beam with parameter: $Q = 2$, (b) a beam with parameter: $Q = 4$ and the constraint $A_3 = 0$, (c) a beam with parameter: $Q = 4$ and bifurcation condition allowed ($A_3 \neq 0$). The region limited by the black dotted curve indicates the points where $N^2 \geq N_3^2$.

The last constant term enforces the continuity of the strain energy due to compression across the boundary defined by $N^2 = N_3^2$.

Figure E.10-b shows the results of this model for a beam with parameter $Q = 4$ and forcing $A_3 = 0$ (main path). Figure E.10-c shows the results of this model for a beam with parameter $Q = 4$ when the bifurcation condition is activated $A_3 \neq 0$.

## Acknowledgments

This research has been supported by grants provided by CONICET, the National University of Litoral, and funding from ANPCyT: PICT-2020-SERIEA-02793, Argentina.

# Apéndice F

# On the limit behavior of lattice-type metamaterials with bi-stable mechanisms

Rossi, N., Romero, I., and Huespe, A. E (2024). “On the limit behavior of lattice-type metamaterials with bi-stable mechanisms”. *International Journal of Mechanical Sciences*, 276, 109375.

# On the limit behavior of lattice-type metamaterials with bi-stable mechanisms

**N. Rossi**[1,2], **I. Romero** [4,5], **A.E. Huespe**[1,3]

[1]Centro de Investigación de Métodos Computacionales (CIMEC), UNL, CONICET. Santa Fe, 3000, Argentina.
[2]Computational Mechanics Laboratory (LAMEC-IMIT-CONICET), Northeast National University (UNNE), Av. Las Heras 727, 3500 Resistencia, Chaco, Argentina.
[3] Programa de Engenharía Mecânica, COPPE, Universidade Federal do Rio de Janeiro, Cidade Universitária, Rio de Janeiro, CEP 21941-972, RJ, Brazil.
[4]Department of Mechanical Engineering, Universidad Politécnica de Madrid, José Gutiérrez Abascal, 2, Madrid 29006, Spain.
[5]IMDEA Materials Institute, Eric Kandel 2, Tecnogetafe, Madrid 28906, Spain.

**Abstract.** This paper explores 2D lattice-type metamaterials featuring bi-stable unit cells and predefined symmetry configurations. Our investigation delves into the emergence of phase-transition patterns and probes the limit behavior of these lattice arrangements. We develop a macroscale generalized standard material model based on a quasi-convexified free energy framework and validate it through a specific lattice configuration—a 1D chain of bi-stable elements—where the relaxed free energy is analytically derived.

To assess the limit behavior of the analyzed lattices, we elucidate the connection between energy release and topology at the microscale. This insight aids in identifying lattice configurations yielding high extrinsic energy dissipation density. We introduce the concept of dissipation efficiency and quantify it across all examined lattices under different loading conditions. Transverse loads prevail in the studied configurations and exhibit a detrimental effect by diminishing extrinsic energy dissipation during metamaterial phase transitions. To facilitate a comprehensive numerical assessment of diverse lattice configurations, we employ a surrogate model of the bistable element. This approach enables an efficient evaluation of sampling volumes constituted by numerous unit cells.

**Keywords:** mechanical metamaterial; elastic instabilities; microstructure pattern formation; phase transitions; energy absorbing materials; extrinsic energy dissipation.

## F.1. Introduction

Elastic snap-through mechanical instabilities, triggered at the microscale, offer an avenue for designing periodic metamaterials that exhibit an unusual performance. Various applications stemming from this phenomenon have spurred substantial numerical and experimental investigations in the literature, a trend observed in the review works [17, 19, 214, 215]. To briefly highlight some recent contributions in this area, consider the work by Giri y Mailen [201], Liang et al. [216], Hua et al. [217] who describe controllable snapping sequences of bistable elements, or Tan et al. [90], Ma et al. [184], Benichou y Givli [190], Xiao et al. [218] who analyze devices with tunable vibration for shock isolation. Morris et al. [219] obtains a material damping increase by embedding inclusions depicting negative stiffness combined with elastic instabilities. Additional studies point out to understand the acoustic-mechanical response of this kind of metamaterials with elastic instabilities by incorporating the dynamical behavior of bistable chains with emphasis on soliton formation ([220, 221]), wave manipulation combined with bandgap tuning through geometrical reconfiguration ([222–224]), and the formation and propagation of domain walls [225].

Most of these works focus on structures that leverage phase transitions subjected to a single load direction. Hence, these metamaterials can be categorized as unidirectional devices. In contrast, there has

been scarce research on metamaterials with instabilities under multidirectional loads. Examples of 2D architectures can be found in [93, 100, 187], while 3D designs are proposed in [107, 202, 203].

In the context of the present work, it is of particular interest to evaluate reversible elastic phase transitions that trigger structural hysteresis in loading-unloading cycles, unveiling the metamaterial capacity for repeatable extrinsic energy dissipation, see [14, 96, 200, 226, 227]. The primary aim of this study is to obtain a deeper understanding of the macroscale behavior of lattice-type metamaterials undergoing phase transitions and multidirectional loads, as illustrated in Figure F.1[1]. We assume the metamaterial possesses negligible mass at the microscale and macroscale. Consequently, negligible inertial effects prevent waves from propagating across this medium, an assumption that does not preclude the potential utilization of the metamaterial as a shock absorber.

The focus is on elucidating the impact of the microarchitecture topology on the effective properties observed at the macroscale, specifically its effect on the energy dissipation across loading-unloading cycles. We study the limit response, defined as the asymptotic regime for a sampling volume containing a large number of unit cells.

At the microscale, our analysis provides insight into the development of microstructure patterns arising from a range of periodic microarchitecture topologies, the evolution of phase transition patterns along specific load paths, and their relationship with the metamaterial effective response. In this context, it is worth noting that the available literature dedicated to investigating deformation fields in lattice-type metamaterials with instabilities characterized by long-scale oscillations, compared to the unit cell size, is still quite limited, see [228, 229].

To link these microscale phenomena to a larger scale, we propose a macroscale constitutive response based on a generalized standard material model. This kind of material model is defined through an energy potential and a dissipation potential and has been used to describe a variety of responses, including elastoplasticity, visco-elasticity, fracture, and damage (see, among many others, [64, 230, 231]). In the framework of multiscale analysis, these two potentials are defined at the macroscale and are derived from homogenized or average values (see [232]). However, managing the conventional process of averaging to homogenize metamaterials with inherent instabilities is crucial since the unstable deformation mechanisms at the microscale determine a non-convex strain energy landscape, leading to failure of the Cauchy-Born hypothesis (Friesecke y Theil [233]).

Assessing the mechanical response of bodies characterized by a non-convex potential entails a series of difficulties, among which are strain fields with short-scale spatial oscillations, the formation of complex strain patterns, the multiplicity of energetically equivalent solutions, and the lack of an energy minimizer, in some cases. Relaxation theory has proved to be a powerful tool to achieve the bridging from micro to macroscale when these phenomena are present [234]. Following Bartels et al. [235], from a physical point of view, relaxation summarizes all relevant features of the microscale in an average material behavior at the macroscale, avoiding unnecessary details. From a mathematical point of view, relaxation theory aims to replace an ill-posed problem with a closely related, well-posed one. This approach has been used in the context of materials with multiple energy wells and single-slip plasticity (see, e.g., [75, 103, 104, 236, 237]).

In this work, we employ relaxation theory to connect the micro and macro scales using an equilibrium quasi-static formulation. Following Kohn [104], we use the strain energy relaxation at a fixed volume fraction of one of the two possible phases. Thus, the strain energy at the macroscale is described with an internal variable representing such concentration. Generalized standard material models using relaxed potentials at the macroscale have been formulated in elastoplasticity and damage by Miehe and coworkers [238–240]. A difference between our work and those proposed by Miehe is that we only have the two potentials of the standard model on the macroscale. In particular, the dissipative potential arises from the homogenization of an extrinsic energy release process arising during phase transitions at the microscale, where the microarchitecture operates at the elastic regime. The mechanisms of energy

[1]The terms effective, apparent, or limit are used as synonyms when referring to the metamaterial macroscale behavior.

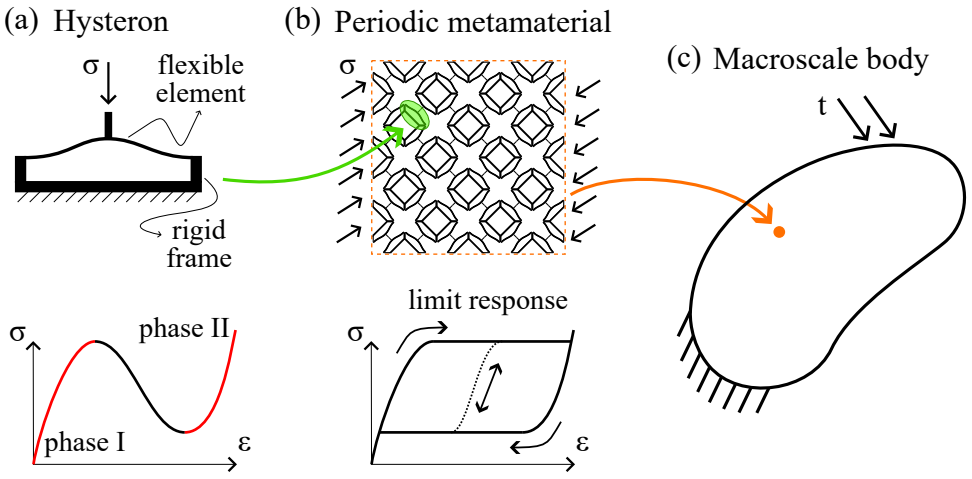


**Figura F.1:** Periodic metamaterial with phase transitions at the microscale. (a) Microscale device (hysteron) displaying a bi-stable deformation mechanism and its stress-strain response; (b) assembly of hysterons forming an (approximate) RVE and their combined stress-strain response displaying hysteresis; (c) macroscale body with a constitutive response defined by a continuum model.

release associated with phase transitions between local minima of the energy have been extensively investigated by Abeyaratne and Knowles [105, 241, 242]. The occurrence of phase transition is related to the possibility of the material surpassing internal energy barriers, which are dependent on the stress state. The energy barrier determines the phase transition rate [243] and, in the context of metamaterials, must be characterized according to the microarchitecture. In this sense, Wan et al. [244] study the minimum energy paths and the energy barriers between stable states of the sinusoidal bistable beam for symmetric and asymmetric configurations.

Much of the behavior of elastic metamaterials with phase transitions resembles similar phenomena studied in the framework of metallurgy, particularly in the field of martensitic shape memory alloys [245–248] or microstructure formation [249, 250].

The remainder of the article has the following structure. Section F.2 motivates this research by examining a simplified 1D periodic metamaterial and exploring its limit behavior. Section F.3 introduces a generalized standard material model at the macroscale. The macroscale strain energy of this model emerges as the quasiconvexification of a microscale two-well strain energy, arriving at a closed-form expression. We validate the model by describing the apparent response of a microstructure composed of 1D bi-stable springs. However, extending this quasiconvexification process to encompass complex microscale energy landscapes derived from the 2D bi-stable lattice-type systems proves challenging. In these instances, achieving relaxed strain energies necessitates the application of numerical methods. Such a task is not pursued in this work. In Section F.4, we investigate the limit response exhibited by three 2D bi-stable lattice topologies when subjected to loads applied from various directions relative to the lattice axis. We focus on examining the hysteresis phenomenon during cyclic loading and scrutinizing its dependency on the direction of the applied load. To achieve this objective, we introduce the concept of dissipation efficiency, defined as the ratio between the total energy dissipation within a load cycle and the external work required to execute that cycle. In Section F.5, we present the conclusions drawn from this study, and a final Appendix summarizes the curved-beam surrogate model.

## F.2. Motivation

We motivate the present investigation by emphasizing the effective response that exhibits a simple mechanical system characterized by non-convex strain energies. Subsection F.2.1 points out the energetic

aspects of one spring with non-convex strain energy, while subsection F.2.2 examines a simplified 1D periodic metamaterial by exploring its limit behavior. The unit cells are assembled using curved beam elements endowed with non-convex strain energies.

### F.2.1. Energy release in a bi-stable spring due to phase transition

The energy release resulting from elastic phase transitions is interpreted in the context of a simple nonlinear elastic spring, as the one sketched in Figure F.2. This spring embodies the characteristics of a bi-stable element defined by a non-convex strain energy function, $U(\delta)$, with $\delta$ denoting the displacement of the point where the force is applied. Owing to the non-convex nature of $U$, the spring exhibits a non-monotonic relationship between the force $f$ and the displacement $\delta$. At a given load $f_{RT}$, the spring undergoes a phase transition from phase I (at point $R$) to phase II (at point $T$)[2]. From a thermodynamic perspective, the mechanical energy release, $D$, throughout this process is given by:

$$D = \int_R^T (\mathcal{P}^{ext} - \dot{U})\, dt\ , \tag{F.1}$$

where $\mathcal{P}^{ext} = f_{RT}\dot{\delta}$ is the external power during the phase transition under the fixed load $f_{RT}$, and $\dot{U}(\delta) = f(\delta)\dot{\delta}$ is the strain energy rate of the spring. Considering the total potential energy function $\Pi(f,\delta) = U(\delta) - f\delta$, the energy release can be reinterpreted in terms of $\Pi$ as the difference between the total potential energies in the equilibrium states $R$ and $T$ (see Abeyaratne y Knowles [105]):

$$D = \Pi(f_{RT}, \delta_R) - \Pi(f_{RT}, \delta_T)\ . \tag{F.2}$$

The function $D$ can be graphically represented in different plots, for example, $U(\delta)$ in Figure F.2-(a), $f(\delta)$ in Figure F.2-(b), $\Pi(f_{RT}, \delta)$ in Figure F.2-(c), or $\Pi(f)$ at equilibrium conditions in Figure F.2-(d). The area $\mathcal{A}$ in Figure F.2-(b) is identified as the energy barrier in Figure F.2-(d).

It is of particular interest to appraise the maximum amount of energy that a soft device[3] can release during a phase transition. This energy release is reached when the switching between phases occurs at the limit load $f_{lim}$, i.e. when the energy barrier $\mathcal{A}$ vanishes. Alternatively, if $D = 0$ when this switch happens, the corresponding load is referred to as the Maxwell load $f_{MW}$.

### F.2.2. A chain with bi-stable elements

The behavior of a metamaterial with instabilities at the microscale is analyzed in this section. The selected metamaterial consists of a periodic assembly of unit cells connected in series. The mechanism responsible for the instabilities is a sinusoidal-shaped curved beam with lateral constraints depicted in Figure F.3-(a). We denote this element as hysteron. To form a periodic unit cell, the ends of the beam are supported by a rigid structure, as shown in Figure F.3-(b). Under compression loads transverse to the curved-beam symmetry axis, each cell exhibits a snap-through instability, and two stable states may develop [73, 102]. The states are referred to as phase I and II, and are separated by a spinodal region similar to the response shown in Figure F.1-(a). Despite being a two-dimensional structure, this metamaterial is a chain of bi-stable elements displaying phase transitions in one direction. Thus, in the present discussion, we envisage it as a one-dimensional metamaterial. The response of 1D equivalent unstable mechanical springs has been studied in the literature by Puglisi y Truskinovsky [80, 97, 98, 99].

This system is analyzed by replacing the curved beam response with a surrogate model described by Rossi et al. [73] and summarized in Appendix I. The purpose is to substitute the geometrically non-linear

[2]The occurrence of phase transitions in a soft device holds particular significant for understanding metamaterial limit behavior.

[3]The terminology soft device and hard device is taken from [80].

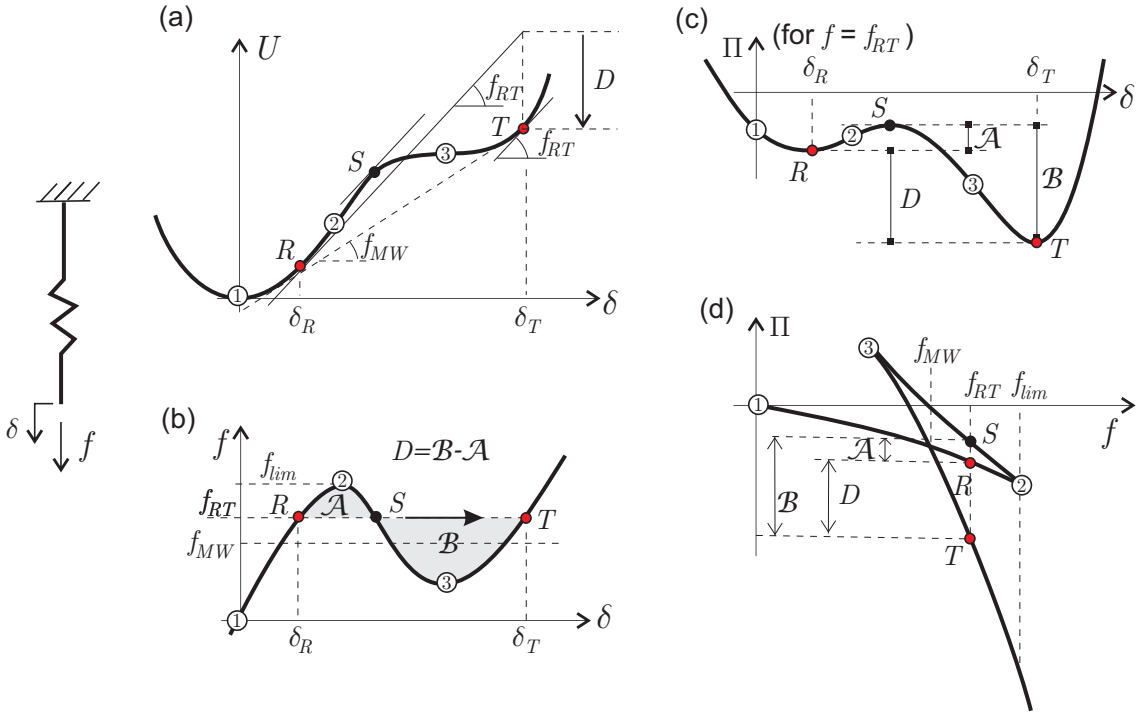


**Figura F.2:** Phase transition ($R \to T$) of a spring with a non-convex strain energy. (a) Strain energy $U(\delta)$; (b) non-monotonic load $f$ versus $\delta$; (c) total potential energy function $\Pi(f_{RT}, \delta)$ with two wells at displacements $\delta_R$ and $\delta_T$, respectively; (d) total potential energy function $\Pi(f)$ at equilibrium conditions. The mechanical energy released during the phase transition process is $D$, $\mathcal{A}$ represents the energy barrier, and $f_{MW}$ is the Maxwell load.

response of each curved beam with a geometrically linear frame element characterized by a non-convex strain energy function. With this approach, the structure depicted in Figure F.3-(b) is modeled with the simplified bar lattice schematized in Figure F.3-(c).

The response approximating the metamaterial limit behavior is assessed with a sampling volume containing an assembly of $n = 20$ unit cells in series. The number of elements in phase II is $c_{P_{II}}$ and the normalized phase II concentration is therefore $c = c_{P_{II}}/n$. This variable characterizes different mixtures of phases in the system, independently of their spatial distribution across the sampling volume.

The test applies a displacement-controlled loading-unloading cycle every time a phase transition occurs. Five instances are evaluated by introducing a slight geometrical random perturbation of 1 % to the parameters. By employing cubic unit cells of arbitrary size, specifically taken as $\ell \times \ell \times \ell$, where $\ell = 100$ mm and the length of the metamaterial sampling $L = 20\ell$, we express the results in terms of the macroscopic strains $\varepsilon = \delta/L$, the macroscopic stress $\sigma = f/\ell^2$, the phase concentrations $c$, and the macroscopic strain energy density $\hat{\psi}$. The latter is evaluated with the following expression:

$$\hat{\psi}(\varepsilon) = (1 - c)\,\psi(\varepsilon_I) + c\,\psi(\varepsilon_{II})\ , \tag{F.3}$$

where $\psi$ is the stored energy density of one individual cell, and $\varepsilon_I$, $\varepsilon_{II}$ are the strains undergoing the cells in phase I and II, respectively. The strains $\varepsilon_I$, $\varepsilon_{II}$ satisfy the kinematic and equilibrium conditions:

$$\varepsilon = (1 - c)\,\varepsilon_I + c\,\varepsilon_{II}\ , \tag{F.4}$$

$$\frac{d\psi}{d\varepsilon}(\varepsilon_I) = \frac{d\psi}{d\varepsilon}(\varepsilon_{II})\ . \tag{F.5}$$

The stable equilibrium branches as a function of $c$ are investigated. A cyclic loading-unloading process is imposed, with one cycle corresponding to each element undergoing a phase transition. The outco-

mes of the five instances are then averaged. The results are displayed in Figures F.3-(d) to (g). Plots (d) and (e) depict the equilibrium curves, $\sigma$ vs. $\varepsilon$, and $\hat{\psi}$ vs. $\varepsilon$, respectively. The red curves represent the metamaterial response undergoing a homogeneous strain, unveiling a non-convex strain energy. Additional curves in these plots are depicted with a color code that transitions from blue to green in correspondence with $c$ going from 0 to 1. These results are consistent with the analytical solution of Puglisi y Truskinovsky [80] where simpler trilinear stress-strain relationships are assumed.

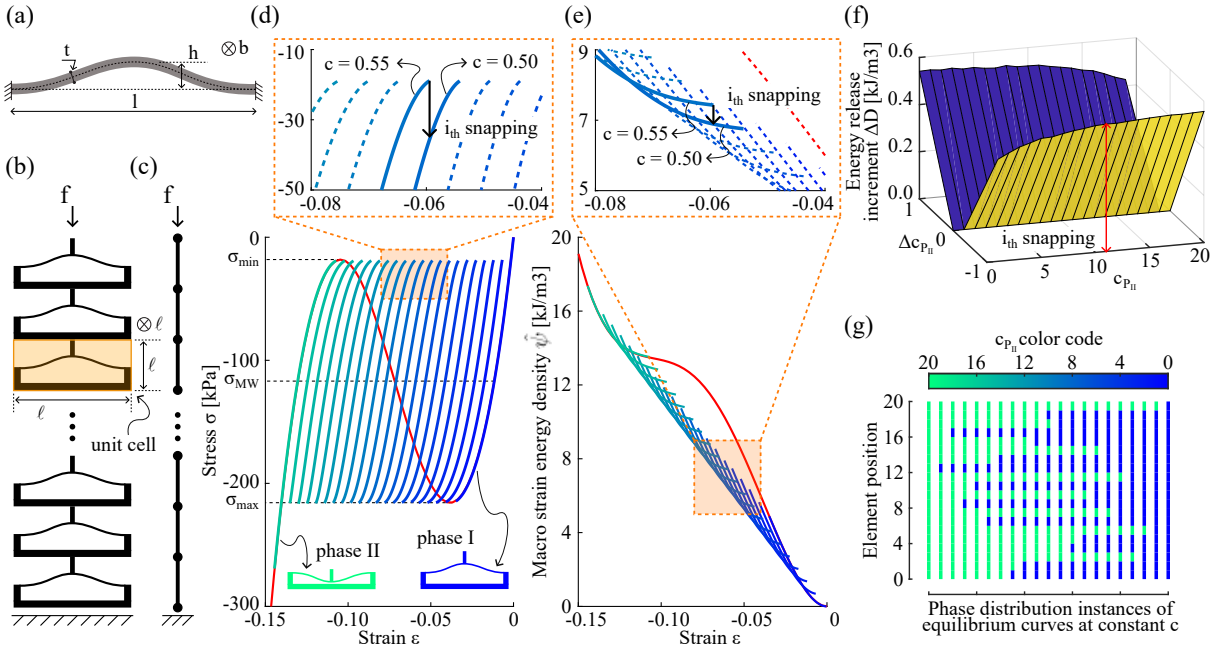


**Figura F.3:** Metamaterial consisting of unstable curved beams. (a) Curved beam geometrical parameters: $l = 71$ mm, $h = 7$ mm, $t = 3.2$ mm, $b = 50$ mm, and the beam Young modulus is $E = 2.267$ GPa. (b) Metamaterial sampling volume (SV). (c) Surrogate microarchitecture of the metamaterial. (d) Plot of $\sigma$ vs. $\varepsilon$. (e) Stored energy density, $\hat{\psi}$, vs. $\varepsilon$, color scale: blue corresponds to phase I and green to phase II, respectively. The red curves display the behavior of a single unit-cell. (f) Energy release in every snapping event as a function of $c_{P_{II}}$ and $\Delta c_{P_{II}}$. (g) Snapshots of the spatial distribution of phases during loading: elements in phase I and II are depicted in blue and green color, respectively.

The effective response of the metamaterial undergoing element phase transitions is analyzed in Figures F.3-(d) to (f). In a loading-unloading cycle, a distinctive snapping event is triggered when the load attains the threshold value of a unit cell, as shown with an arrow in the insets of Figure F.3-(d) and (e). This event determines a transition between two distinct equilibrium branches. It is accompanied by a strain energy release of the system, which is regarded as an equivalent form of extrinsic energy dissipation, as noted in sub-Section F.2.1. Figure F.3-(f) illustrates the energy release, $\Delta D$, in a snapping event as a function of $c_{P_{II}}$ and $\Delta c_{P_{II}}$ ($\Delta c_{P_{II}} = \pm 1$). Columns in Figure F.3-(g) display the spatial distribution of phases during loading (from right to left) for one instance of the five outcomes. The color scale used in sub-figures (d) and (e) is associated with the sequence of columns.

The following relevant aspects are further noted:

- The energy release during each phase transition is statistically constant, unaffected by variations in the number of elements in each phase, as well as unaffected by the specific direction of phase transition, be it from phase I to phase II or vice versa, as shown in Figure F.3-(f). This effect is related to the fact that the system, when observed from a macroscopic point of view, possesses a rate-independent response.

- The order in which the phase transition occurs is irrelevant. All elements are (statistically) equivalent. After comparing several samples of the metamaterial, it can be concluded that there is no

preferred sequence for the snapping events, as shown in Figure F.3-(g).

## F.3. Macroscale generalized standard model of materials with microscale phase transitions

We investigate the macroscale behavior of metamaterials when they undergo phase transitions at a finer length scale, similar to those motivated by the non-linear beam discussed in the preceding section. The macroscopic response of metamaterials is here described by utilizing the framework of generalized standard material models, such as reported by [64, 230, 251–253]. The mathematical formalism of this formulation can be found in the extensive literature from Mielke and coauthors, see [254], and particularly for modeling phase transitions in shape memory alloys in [255].

We begin this section by briefly stating the main ideas and equations of the generalized standard material model. Next, we specialize it to describe the problem of microscale phase transitions by discussing the connections of the macroscale model to the microscale. We close this section by validating the model to replicate (in the limit of number of unit cells $n \to \infty$) the results of Figure F.3.

### F.3.1. Summary of the generalized standard material model formulation

We study a class of generalized standard materials whose state may be described in terms of the strain $\boldsymbol{\varepsilon}$ and one dimensionless scalar internal variable $c$. The conjugate variables are the stress $\boldsymbol{\sigma}$ and $g$, and can be obtained from the free energy $\hat{\psi}(\boldsymbol{\varepsilon}, c)$ through the relations:

$$\boldsymbol{\sigma} = \frac{\partial \hat{\psi}}{\partial \boldsymbol{\varepsilon}} , \qquad g = -\frac{\partial \hat{\psi}}{\partial c} . \tag{F.6}$$

The mechanical energy dissipation rate of the material is given by:

$$\mathcal{D} = \boldsymbol{\sigma} \cdot \dot{\boldsymbol{\varepsilon}} - \dot{\hat{\psi}} , \tag{F.7}$$

which, after using the chain rule on $\hat{\psi}$ and Eq. (F.6), results in:

$$\mathcal{D} = g\, \dot{c} . \tag{F.8}$$

This type of material model assumes the existence of a dissipation potential $\phi(\dot{c}, c)$ from which the evolution of the internal variables can be derived. Since we expect a rate-independent response, we argue this potential is convex, positively homogeneous of degree one on its first argument, i.e., $\phi(\xi \dot{c}, c) = \xi \phi(\dot{c}, c)$ for $\xi > 0$, and lower semicontinuous. It determines the evolution of the force $g$ through the pseudo-kinetic relation:

$$g \in \partial_{\dot{c}} \phi , \tag{F.9}$$

where the right-hand side refers to the sub-differential of the dissipation potential. From Eqs. $(F.6)_2$ and (F.9), the Biot relation follows:

$$\frac{\partial \hat{\psi}}{\partial c} + \partial_{\dot{c}} \phi \ni 0 . \tag{F.10}$$

The dual or complementary dissipation potential $\phi^c$ can be obtained using the Legendre transform on the first argument of the potential $\phi$, that is,

$$\phi^c(g, c) = \max_{\dot{c}} \left( g\, \dot{c} - \phi(\dot{c}, c) \right) = \mathcal{I}nd_g \mathcal{P} , \tag{F.11}$$

resulting in the indicator function, $\mathcal{I}nd_g \mathcal{P}$, of the set $\mathcal{P}$ of admissible values of $g$.

### F.3.2. Model specification for a material with phase transitions

Let us now consider a material whose microscale strain energy is $\psi(\boldsymbol{\varepsilon})$. The equilibrium condition in an arbitrary microscale sampling volume, $\Omega_\mu$, is established through the minimization of the strain energy:

$$\min_{\tilde{\boldsymbol{u}}} \langle \psi(\boldsymbol{\varepsilon} + \nabla^{sym}\tilde{\boldsymbol{u}}) \rangle_{\Omega_\mu} \quad , \quad \text{with } \tilde{\boldsymbol{u}} \text{ periodic and } \langle \nabla^{sym}\tilde{\boldsymbol{u}} \rangle_{\Omega_\mu} = \mathbf{0} \, , \tag{F.12}$$

where $\boldsymbol{\varepsilon}$ is interpreted as the average strain in the sampling volume, $\tilde{\boldsymbol{u}}$ is any admissible periodic displacement field in $\Omega_\mu$, and the symbol $\langle \cdot \rangle_{\Omega_\mu}$ indicates the average integral of the argument in $\Omega_\mu$, i.e. $\langle \cdot \rangle_{\Omega_\mu} = \frac{1}{|\Omega_\mu|} \int_{\Omega_\mu} \cdot \, d\Omega_\mu$. As pointed out by Pipkin [103] and Kohn [104], when $\psi$ is not quasi-convex in the sense of Morrey [41], the minimum in Eq. (F.12) may not exist. However, a relaxed potential $\psi^{qc}(\boldsymbol{\varepsilon})$, defined as follows:

$$\psi^{qc}(\boldsymbol{\varepsilon}) = \inf_{\tilde{\boldsymbol{u}}} \langle \psi(\boldsymbol{\varepsilon} + \nabla^{sym}\tilde{\boldsymbol{u}}) \rangle_{\Omega_\mu} \, , \quad \text{with } \tilde{\boldsymbol{u}} \text{ periodic and } \langle \nabla^{sym}\tilde{\boldsymbol{u}} \rangle_{\Omega_\mu} = \mathbf{0} \, , \tag{F.13}$$

can be identified by investigating minimizing sequences of strain energies supplied by the formation of microstructures. The microstructure development furnishes an apparent strain energy function, $\psi^{qc}(\boldsymbol{\varepsilon})$, lower than that provided by a homogeneous strain distributed on the sampling volume. This feature justifies the appearance of highly oscillating strain patterns with scale lengths larger than the unit cell size. The relaxed energy $\psi^{qc}(\boldsymbol{\varepsilon})$ is, by definition, quasi-convex. After substituting $\psi(\boldsymbol{\varepsilon})$ for $\psi^{qc}(\boldsymbol{\varepsilon})$, the minimum in problem (F.12) is achieved, see Kohn [104].

According to Kohn [104], the relaxed strain energy $\psi^{qc}$ is the apparent or macroscopic strain energy that reaches the global minimizing energy. Considering that we look for minimizers of the strain energy that depend on the concentration of material with different phases, we adopt a relaxed strain energy with a fixed volume fraction concentration. In our case, the infimum in problem (F.13) is found by fixing the concentration of material in each phase, represented by the phase fraction $c$[4]. Consequently, $c$ is included as a further argument in the strain energy relaxation function, $\hat{\psi}(\boldsymbol{\varepsilon}, c)$, to emphasize that it is obtained at the fixed fraction volume $c$. This relaxed strain energy is used in the macroscale model defined by Eqs. (F.6) and (F.10). A similar methodology has been followed in [256] to model shape-memory alloys.

Solving problem (F.13) for general non-convex free energies is not a simple task since the optimal phase distribution may be non-unique (see [237]). Only a few analytical quasiconvexification expressions are known for particular energy functions [103, 104, 257, 258]. A different approach based on the numerical quasiconvexification of energy is available, which has the potential to offer, at the very least, an upper bound estimate for the relaxed energies, as demonstrated in works such as [259–261]. In this work, we develop the multiscale model for a system with two wells in strain energy. To achieve this goal without altering the microscale fundamental physics underlying the phase-transition problem, we incorporate additional assumptions that allow us to introduce a closed-form quasiconvex strain energy. First, we assume a microscale strain energy under small deformation kinematics. Second, this strain energy is modeled with an analytic function and consists of two convex quadratic branches, similar to that adopted in the works of Pipkin [103] and Kohn [104]. The minima of both branches are separated by the strain $\boldsymbol{d}$. In this way, the material may have only two possible phases, and the fraction volume $c$ is a scalar variable. The coefficients defining the convex branches, including $\boldsymbol{d}$, are characterized through a high-fidelity model of the microscale unit cell[5]. Subsequently, a closed-form solution is accessible for the quasi-convexification of such strain energy, which can be applied within the formalism outlined in Section F.3.1. Next, we show that the error induced by following these hypotheses, compared with the high-fidelity geometrically non-linear solution, does not alter the essence of the limit response of the

[4] Phase fraction $c$ is represented by a vector when several phases may coexist.

[5] Small deformation kinematics when $\boldsymbol{d}$ is small and characterization of predefined analytical non-convex strain energy coefficients through a high-fidelity model of the microcell is a procedure that has been similarly followed by [205] for determining an analytical macroscale energy function. Note that [205] does not include the strain energy relaxation in their approach.

material undergoing phase transitions at the microscale.

Following this strategy, we now consider a metamaterial with two stable phases, namely phase I and phase II, whose non-convex free energy function for a given strain $\boldsymbol{\varepsilon}^*$ at the microscale, $\psi(\boldsymbol{\varepsilon}^*)$, is defined as

$$\psi(\boldsymbol{\varepsilon}^*) = \min\{\psi_I(\boldsymbol{\varepsilon}^*), \psi_{II}(\boldsymbol{\varepsilon}^*)\} \, . \tag{F.14}$$

Here, $\psi_I$ and $\psi_{II}$ are quadratic convex functions for each phase with an identical constitutive tensor given by

$$\psi_I(\boldsymbol{\varepsilon}^*) = \frac{1}{2}\boldsymbol{\varepsilon}^* \cdot \boldsymbol{C} \cdot \boldsymbol{\varepsilon}^* + b_I \, , \qquad \psi_{II}(\boldsymbol{\varepsilon}^*) = \frac{1}{2}(\boldsymbol{\varepsilon}^* - \boldsymbol{d}) \cdot \boldsymbol{C} \cdot (\boldsymbol{\varepsilon}^* - \boldsymbol{d}) + b_{II} \, . \tag{F.15}$$

The stress-free strain tensor of phase II is defined as $\boldsymbol{d}$, whereas the stress-free strain tensor for phase I is the zero tensor. Subsequently, we shall refer to $\boldsymbol{d}$ as the transformation strain, and it represents the difference between the preferential strains, i.e., the strains associated with minimum energy for each phase.[6] The parameters $b_I$ and $b_{II}$ represent the energy levels under stress-free conditions. The functions $\psi_I$ and $\psi_{II}$ for 1D cases are depicted in Figure F.4. Strains corresponding to material in phases I and II are denoted as $\boldsymbol{\varepsilon}_I$ and $\boldsymbol{\varepsilon}_{II}$, respectively.

Motivated by the previous reasoning, we introduce a variable $c$ representing the volume ratio of phase II in the microstructure. Thus, the whole material is in phase I when $c = 0$ and, conversely, the whole material is in phase II when $c = 1$. The intermediate values of $c$ correspond to a mixture of phases in varying proportions. The rate of change of $c$, denoted as $\dot{c}$, can be either positive or negative, reflecting the phase transition pseudokinetics in the material.

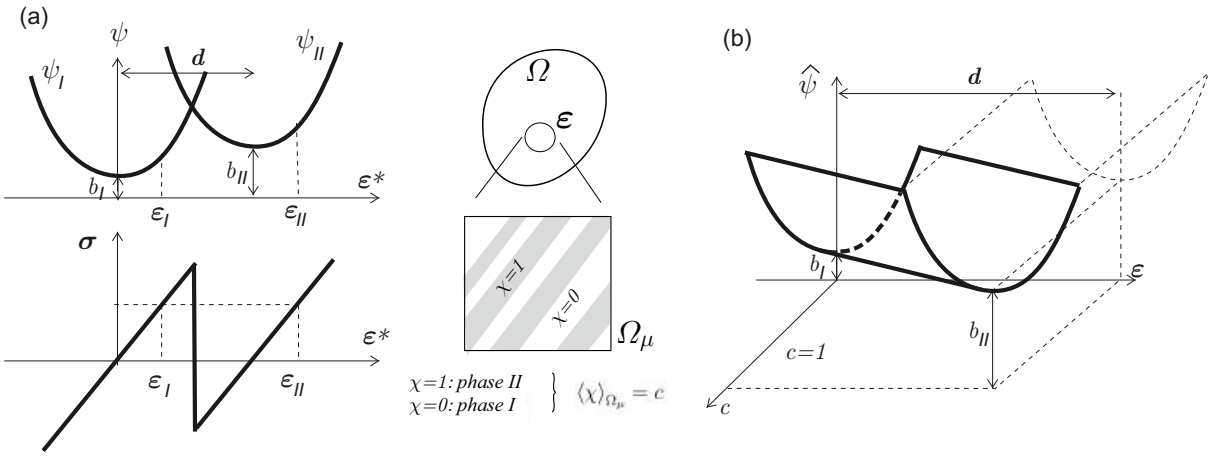


**Figura F.4:** (a) Metamaterial with phase transitions and microstructure. Under a macroscopic strain $\boldsymbol{\varepsilon}$ in the solid $\Omega$, the periodic sampling volume $\Omega_\mu$ displays a volume fraction $c$ of material in phase II ($\boldsymbol{\varepsilon}_{II}$), and a volume fraction $(1-c)$ of material in phase I ($\boldsymbol{\varepsilon}_I$). (b) Convexified free energy.

According to Abeyaratne y Knowles [105], the spinodal region is unstable and the amount of material in this state cannot increase over time within the microstructure. This result is supported by the findings of the experiment illustrated in Figure F.3 where every bi-stable element is in one of the two stable phases. The analysis of the spinodal region will prove necessary for the derivation of the dissipation potential, a point which will be discussed later.

As a general idea, the macroscale energy dissipation rate (F.7) emerges from the homogenization of

[6] This definition coincides with the one employed by Abeyaratne y Knowles [105] when $\boldsymbol{d}$ is the symmetric part of a rank-one tensor.

the microscale energy release. That is:

$$\boldsymbol{\sigma} \cdot \dot{\boldsymbol{\varepsilon}} - \dot{\hat{\psi}} = \left\langle \boldsymbol{\sigma}_\mu \cdot \dot{\boldsymbol{\varepsilon}}_\mu - \dot{\psi} \right\rangle_{\Omega_\mu} \ , \tag{F.16}$$

where the left-hand side refers to magnitudes at the macroscale, and the right-hand side to their microscale counterparts. This idea will be used later to build a dissipation potential.

**Free energy relaxation**

According to Kohn [104], for a free energy $\psi$ as defined in Eq. (F.14), if the material is capable of globally minimizing the total elastic energy, the strain energy of the volume $\Omega_\mu$ is given by:

$$\langle \psi(\boldsymbol{\varepsilon} + \nabla^{sym}\tilde{\boldsymbol{u}}) \rangle_{\Omega_\mu} = \inf_{\chi} \langle (1-\chi)\psi_I(\boldsymbol{\varepsilon} + \tilde{\boldsymbol{\varepsilon}}_I) + \chi\psi_{II}(\boldsymbol{\varepsilon} + \tilde{\boldsymbol{\varepsilon}}_{II}) \rangle_{\Omega_\mu} \ , \tag{F.17}$$

where we have introduced a characteristic function $\chi$ to indicate the distribution of the two phases in $\Omega_\mu$. Specifically, $\chi = 0$ and 1 at points with phases I and II, respectively. Also, $\tilde{\boldsymbol{\varepsilon}}_j = \nabla^{sym}\tilde{\boldsymbol{u}}$ denotes the fluctuations in the strain field corresponding to phase $j$. Inserting Eq. (F.17) in Eq. (F.13) one arrives at the relaxed energy at fixed volume fraction:

$$\hat{\psi}(\boldsymbol{\varepsilon}, c) = \inf_{\chi} \inf_{\tilde{\boldsymbol{u}}} \langle (1-\chi)\psi_I(\boldsymbol{\varepsilon} + \tilde{\boldsymbol{\varepsilon}}_I) + \chi\psi_{II}(\boldsymbol{\varepsilon} + \tilde{\boldsymbol{\varepsilon}}_{II}) \rangle_{\Omega_\mu} \ , \tag{F.18}$$

under the additional constraint:

$$c = \langle \chi \rangle_{\Omega_\mu} \ . \tag{F.19}$$

Thus, $\chi$ is determined for a given concentration $c$ and the displacement fluctuations $\tilde{\boldsymbol{u}}$ are accounted for through the strain fluctuations $\tilde{\boldsymbol{\varepsilon}}_I$ and $\tilde{\boldsymbol{\varepsilon}}_{II}$ that are compatible with $\tilde{\boldsymbol{u}}$ and consistent with stresses in equilibrium.

Assuming that the strain fluctuations have rank one, we can write

$$\begin{aligned} \boldsymbol{\varepsilon}_I &= \boldsymbol{\varepsilon} + \tilde{\boldsymbol{\varepsilon}}_I = \ \boldsymbol{\varepsilon} - c(\tilde{\boldsymbol{u}} \otimes_s \boldsymbol{n}) \ , \\ \boldsymbol{\varepsilon}_{II} &= \boldsymbol{\varepsilon} + \tilde{\boldsymbol{\varepsilon}}_{II} = \ \boldsymbol{\varepsilon} + (1-c)(\tilde{\boldsymbol{u}} \otimes_s \boldsymbol{n}) \ , \end{aligned} \tag{F.20}$$

where $\tilde{\boldsymbol{u}}$ and $\boldsymbol{n}$ are two constant vectors and $\otimes_s$ denotes the symmetrized tensor product[7]. Using the compatibility condition (F.20), the minimization problem problem (F.18) yields:

$$\hat{\psi}(\boldsymbol{\varepsilon}, c) = \frac{1}{2}(\boldsymbol{\varepsilon} - c\,\boldsymbol{d}) \cdot \boldsymbol{C} \cdot (\boldsymbol{\varepsilon} - c\,\boldsymbol{d}) + \bar{b} + c(1-c)W_m\left(\boldsymbol{d}\right) \ , \tag{F.21}$$

with $\bar{b} = (1-c)b_I + c\,b_{II}$ and

$$W_m = \min_{\tilde{\boldsymbol{u}}, \boldsymbol{n}} \left\{ \frac{1}{2} \left( \boldsymbol{d} - (\tilde{\boldsymbol{u}} \otimes_s \boldsymbol{n}) \right) \cdot \boldsymbol{C} \cdot \left( \boldsymbol{d} - (\tilde{\boldsymbol{u}} \otimes_s \boldsymbol{n}) \right) \right\} \ , \tag{F.22}$$

from where the vectors $\tilde{\boldsymbol{u}}$ and $\boldsymbol{n}$ can be determined. See [103, 104] for additional details. If the transformation strain $\boldsymbol{d}$ is the symmetric part of a rank-one tensor, then $W_m = 0$ and the relaxation of $\psi$ coincides with its convexification [104].

We conclude by noting that the relaxed free energy (F.21) has three regimes: if $c = 0$ then $\hat{\psi} = \psi_I$; if $c = 1$ then $\hat{\psi} = \psi_{II}$; if $0 < c < 1$ then $\hat{\psi}$ is a combination of the energies of both phases.

[7] Strains in $\Omega_\mu$ can be expressed as: $\boldsymbol{\varepsilon}_\mu(\boldsymbol{x}) = (1 - \chi(\boldsymbol{x}))\boldsymbol{\varepsilon}_I + \chi(\boldsymbol{x})\boldsymbol{\varepsilon}_{II}$, which leads to $\langle \boldsymbol{\varepsilon}_\mu \rangle_{\Omega_\mu} = \boldsymbol{\varepsilon}$. Moreover, the strains in Eq. (F.20) satisfy the Hadamard's compatibility condition on the interfaces.

**Generalized standard material model with relaxed free energy**

The stress tensor in the homogenized model can be obtained from Eq. (F.21) as:

$$\boldsymbol{\sigma} = \frac{\partial \hat{\psi}(\boldsymbol{\varepsilon}, c)}{\partial \boldsymbol{\varepsilon}} = \boldsymbol{C} \cdot (\boldsymbol{\varepsilon} - c\boldsymbol{d}) \ , \tag{F.23}$$

and also the conjugate force to the phase concentration

$$g = -\frac{\partial \hat{\psi}(\boldsymbol{\varepsilon}, c)}{\partial c} = \boldsymbol{d} \cdot \boldsymbol{\sigma} - \Delta b - (1 - 2c) W_m \ , \tag{F.24}$$

with $\Delta b = b_{II} - b_I$. When the transformation strain $\boldsymbol{d}$ is the symmetric part of a rank-one tensor and the phase energies are as indicated in Eq. (F.15), the macro stress $\boldsymbol{\sigma}$ is homogeneous in $\Omega_\mu$ and we can provide an alternative interpretation of $\Delta b$ in terms of the Maxwell stress $\boldsymbol{\sigma}_{MW}$. In this case, the Maxwell stress is the continuum counterpart of the Maxwell load defined in Section F.2.1 and

$$W_m = 0 \ , \qquad \frac{\partial \Delta G(\boldsymbol{\sigma})}{\partial \boldsymbol{\sigma}} = \boldsymbol{d} \ , \tag{F.25}$$

where $\Delta G(\boldsymbol{\sigma}) = G_I - G_{II}$ is the difference of the Gibbs energy between the two phases at a given stress $\boldsymbol{\sigma}$ [105]. Then:

$$\int_{\mathbf{0}}^{\boldsymbol{\sigma}_{MW}} \boldsymbol{d} \cdot d\boldsymbol{\sigma} = \Delta G(\boldsymbol{\sigma}_{MW}) - \Delta G(\mathbf{0}) = -\Delta G(\mathbf{0}) \ , \tag{F.26}$$

where, by definition, we use the identity $\Delta G(\boldsymbol{\sigma}_{MW}) = 0$. Since for $\boldsymbol{\sigma} = \mathbf{0}$ the difference in Gibbs energies between the solution for $\boldsymbol{\varepsilon}_I$ and $\boldsymbol{\varepsilon}_{II}$ coincides with the difference in the strain energies, noting that $\psi_I(\boldsymbol{\varepsilon}_I) = b_I$ and $\psi_{II}(\boldsymbol{\varepsilon}_{II}) = b_{II}$, it follows that

$$\int_{\mathbf{0}}^{\boldsymbol{\sigma}_{MW}} \boldsymbol{d} \cdot d\boldsymbol{\sigma} = \Delta b \ , \tag{F.27}$$

which in our case reduces to $\Delta b = \boldsymbol{d} \cdot \boldsymbol{\sigma}_{MW}$. Then, the conjugate force (F.24) can be rewritten as:

$$g = \boldsymbol{d} \cdot (\boldsymbol{\sigma} - \boldsymbol{\sigma}_{MW}) = \Delta G(\boldsymbol{\sigma}) \ , \tag{F.28}$$

where the last term is obtained by expression (F.26) with the lower integration limit equal to $\boldsymbol{\sigma}_{MW}$ and the upper integration limit equal to $\boldsymbol{\sigma}$.

**Homogenization of the dissipation potential**

Next, the dissipation potential is calculated for the case where the transformation strain $\boldsymbol{d}$ is the symmetric part of a rank-one tensor. Replacing the expressions of the microscale strains and elastic energy in terms of the characteristic function $\chi$ in Eq. (F.16), and considering that $\boldsymbol{\sigma}_\mu = \boldsymbol{\sigma}$ for this particular case of the transformation strain $\boldsymbol{d}$, the mechanical energy dissipation rate evaluates to:

$$\mathcal{D} = \left\langle \boldsymbol{\sigma} \cdot \frac{d}{dt}[(1-\chi)\boldsymbol{\varepsilon}_I + \chi \boldsymbol{\varepsilon}_{II}] - \frac{d}{dt}[(1-\chi)\psi_I(\boldsymbol{\varepsilon}_I) + \chi \psi_{II}(\boldsymbol{\varepsilon}_{II})] \right\rangle_{\Omega_\mu} \ . \tag{F.29}$$

Changes in the microstructure happens only through phase rearrangement, thus:

$$\mathcal{D} = \langle \boldsymbol{\sigma} \cdot [-\boldsymbol{\varepsilon}_I + \boldsymbol{\varepsilon}_{II}]\dot{\chi} + [\psi_I(\boldsymbol{\varepsilon}_I) - \psi_{II}(\boldsymbol{\varepsilon}_{II})]\dot{\chi} \rangle_{\Omega_\mu} \ . \tag{F.30}$$

Using the definition of Gibbs energy in phase $i$-th, $G_i(\boldsymbol{\sigma}) = \psi_i(\boldsymbol{\varepsilon}_i) - \boldsymbol{\sigma} \cdot \boldsymbol{\varepsilon}_i$, where $\boldsymbol{\sigma}$ and $\boldsymbol{\varepsilon}_i$ are related through the constitutive relationship at the microscale, the homogenized energy release rate (F.29) simplifies to:

$$\mathcal{D} = (G_I - G_{II}) \langle \dot{\chi} \rangle_{\Omega_\mu} = g\, \dot{c}\ . \tag{F.31}$$

In analogy to the behavior of the spring represented in Figure F.2, the difference between the Gibbs energies of the equilibrium states I and II is accounted by the energy release density when phase transitions occur. This energy release is equivalent to the driving force derived in Eq. (F.28).

Considering expression (F.31) and the constraint $c \in [0, 1]$, we define the dissipation potential $\phi(\dot{c}, c)$ as follows:

$$\phi(\dot{c}, c) = \begin{cases} k_+ \dot{c} & \text{for} \quad \dot{c} \geq 0 \\ +\infty & \text{otherwise} \end{cases} , \quad \text{for } c = 0$$
$$\phi(\dot{c}, c) = \begin{cases} k_+ \dot{c} & \text{for} \quad \dot{c} \geq 0 \\ -k_- \dot{c} & \text{for} \quad \dot{c} < 0 \end{cases} , \quad \text{for } 0 < c < 1 \quad , \tag{F.32}$$
$$\phi(\dot{c}, c) = \begin{cases} -k_- \dot{c} & \text{for} \quad \dot{c} \leq 0 \\ +\infty & \text{otherwise} \end{cases} , \quad \text{for } c = 1,$$

where convexity in the argument $\dot{c}$ is preserved. Figure F.5-(a) depicts the potential $\phi(\dot{c}, c)$.

An interpretation of the parameters $k_+$ and $k_-$ that characterize the dissipation potential can be given by arguing that they represent the maximum possible energy dissipation per unit volume during the phase transition, from $I \rightarrow II$ ($k_+$) and from $II \rightarrow I$ ($k_-$), at the stress level when the energy barrier is zero; see Figure F.2. The shape of the spinodal region plays a role in determining $k_+$ and $k_-$. As depicted in Figure F.5-(b), the spinodal response determines how much energy is dissipated according to the direction in which the phase transformation occurs. This feature of the bi-stable element also determines the Maxwell stress.

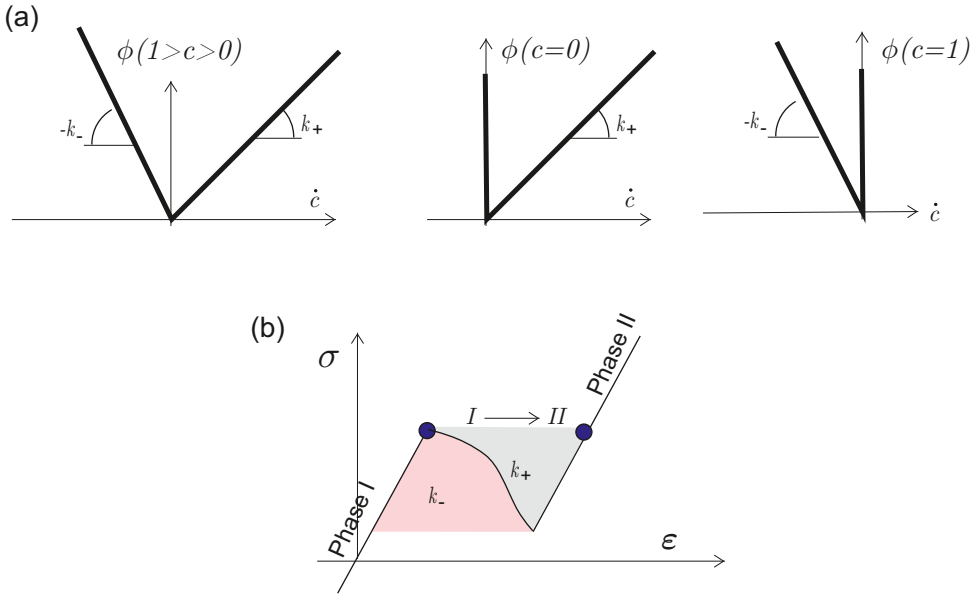


**Figura F.5:** (a) Dissipation potential function. (b) Interpretation of parameters characterizing the dissipation potential.

The Legendre transform of $\phi(\dot{c}, c)$ in the argument $\dot{c}$ is the indicator function, and hence

$$\mathcal{I}nd_g\mathcal{P} = \begin{cases} 0 & \text{for} \quad g \in \mathcal{P} \\ +\infty & \text{for} \quad g \notin \mathcal{P} \end{cases} , \tag{F.33}$$

with

$$\mathcal{P} = \begin{cases} g \leq k_+ & \text{for} \quad c = 0 \\ -k_- \leq g \leq k_+ & \text{for} \quad 0 < c < 1 \\ g \geq -k_- & \text{for} \quad c = 1 \end{cases} . \tag{F.34}$$

Additionally, the evolution equation for $c$ is determined by the subdifferential of the indicator function[8], $\dot{c} \in \partial_g \mathcal{I}nd_g\mathcal{P}$, giving the following relations:

$$\dot{c} \in \partial_g \mathcal{I}nd_g\mathcal{P} = \begin{cases} \lambda & \text{for} \quad g = k_+ \quad \wedge \quad 1 > c \geq 0 \\ -\lambda & \text{for} \quad -g = k_- \quad \wedge \quad 1 \geq c > 0 \end{cases} , \tag{F.35}$$

where $\lambda$ is a positive scalar determined to satisfy Biot's equation (F.10). Implicitly, these equations describe complementarity conditions that can be written in terms of a yield function, $f(g, c)$, as follows:

$$f(g, c) \leq 0 \qquad , \qquad f\dot{c} = 0 \, , \tag{F.36}$$

where the yield function is of the form

$$f(g, c) = \begin{cases} g - k_+ & \text{if } c = 0 \, , \\ g - k_+ & \text{if } 0 < g, \; 0 < c < 1 \, , \\ -g - k_- & \text{if } g < 0, \; 0 < c < 1 \, , \\ -g - k_- & \text{if } c = 1 \, . \end{cases} \tag{F.37}$$

### F.3.3. Macroscopic generalized standard material model validation

We validate the formulation of the macroscopic generalized standard material by characterizing the limiting response of a metamaterial composed of the chain of bi-stable elements discussed in Section F.2.2. We compare the response of this model with the one discussed in Section F.2.2 evaluated with 20 elements using the one-dimensional surrogate model.

The formulation of the generalized standard material hinges on defining both the relaxed elastic potential, based on the closed expression (F.21), and the dissipation potential. In the current one-dimensional case, the transition strain $\boldsymbol{d}$ trivially meets the condition of being compatible with the symmetric part of a rank-one tensor, which leads to canceling out the component $W_m$ of the relaxed free energy in Eq. (F.22). Consequently, $\hat{\psi}(\boldsymbol{\varepsilon}, c)$ only involves three key parameters: the elastic modulus $\boldsymbol{C}$ (assumed identical for both phases), the transformation strain $\boldsymbol{d}$, and the Maxwell stress $\boldsymbol{\sigma}_{MW}$. Thus, given these parameters together with $\boldsymbol{\varepsilon}$ and $c$, the relaxed strain energy $\hat{\psi}(\boldsymbol{\varepsilon}, c)$ can be calculated. From the latter, the stress and the conjugate force may be obtained using Eqs. (F.23) and (F.28). The dissipation potential $\phi(\dot{c}, c)$ is determined by defining the admissible domain $\mathcal{P}$ of the conjugate forces $g$ by characterizing the limits $k_+$ and $k_-$.

The five parameters of the model shown in Table F.1 are determined through the metamaterial homogenized response of the microscale model, considering a uniform strain distributed across the bi-stable elements, depicted by the red curve in Figure F.3(d). The modulus $C$ is assumed to be the secant modulus between the stresses $\sigma = 0$ and $\sigma = \sigma_{MW}$. The transformation strain $d$ is taken as the difference between the strains of both stable phases associated with $\sigma_{MW}$ through the constitutive equation. The parameters $k_+$ and $k_-$ are evaluated using the expression (F.28) with $\sigma_{max} = -215.7$ kPa and $\sigma_{min} = -18.1$ kPa (phase I to phase II, and phase II to phase I change stress values, respectively).

The procedure for validating the macroscale generalized standard material model consists of solving a series of loading-unloading tests conducted under displacement control. These tests incorporate unloading and loading stages, resulting in six distinct loading regimes represented by letters on the plots in

[8] Implicit in this assumption of the constitutive model is the Principle of Maximum Dissipation, see Carstensen et al. [236]

| $C$ [MPa] | $d$ | $\sigma_{MW}$ [kPa] | $k_+$ [kJ/m$^3$] | $k_-$ [kJ/m$^3$] |
|---|---|---|---|---|
| 10.059 38 | -0.118759 | -116.90 | 11.7334 | 11.7334 |

**Tabla F.1:** Parameters of the macroscale generalized standard material.

Figure F.6. The regimes are defined as follows[9]:

- The loading process starts at the reference stress-free configuration with a phase concentration $c = 0$, denoted as state $A$.
- Load increases until state $B$, characterized by the maximum stress $\sigma_{max}$ and $c = 0.50$.
- Upon reaching this state, the first unloading process commences until reaching state $C$, defined by the minimum stress $\sigma_{min}$ and $c = 0.10$.
- From $C$, the reloading process initiates and progresses until it reaches state $D$, characterized by the whole material remaining in phase II, i.e. $c = 1$, with a strain $\varepsilon = -0.144$.
- A new unloading process starts again until it reaches state $E$, defined by $\sigma_{min}$ and $c = 0.65$.
- A partial reloading follows until the state $F$, with $\sigma_{max}$ and $c = 0.85$, is reached.
- The unloading process follows until it reaches the state $A$.

Figure F.6 illustrates the results of this analysis. We compare the response of the macroscale model (represented in red curves) with that of the microscale surrogate model (depicted in grey). Subfigures (a), (b), and (c) plot stress vs. strain, strain energy density vs. strain and vs. phase concentration, and energy release density vs. strain, respectively. The energy release of the surrogate model is calculated by equation (F.1) (per unit volume), and the generalized standard material energy dissipation density is obtained by evaluating: $D(t) = \int_0^t \phi(\dot{c}, c)dt$. The symbols "$\times$" in the plots indicate states A to F. Points associated with the macroscale model are shown in blue, while those corresponding to the surrogate model are shown in green. Arrows are used to show the direction of loading and the progression of the internal variable $c$ at each stage of the load process.

**Discussion of results:** The macroscale generalized standard material model reproduces the key characteristics of the microscopic metamaterial limit behavior.

Figure F.6-(a) shows that the model accurately captures the stresses that induce phase transitions. Additionally, the flow rule of the standard generalized model governing $\dot{c}$ exhibits a good correlation with the phase transitions of bi-stable elements described with the microscopic surrogate model throughout both loading directions, as well as in unloading processes when no phase transition happens, and the internal variable $c$ of the generalized standard model remains constant.

Discrepancies in responses emanate from the linear elastic assumption characterizing the generalized standard model, particularly around $\sigma_{\text{max}}$ with $c = 0$ and $\sigma_{\text{min}}$ with $c = 1$, are noticeable in the stress-strain plot. In figure F.6-(b), the curves representing the microscopic response at constant $c$ extend beyond the limits defined by the macroscopic model, particularly when $c = 0$ with strains increasing and when $c = 1$ with strains decreasing. However, a remarkable agreement exists between both models in the region where $0 < c < 1$, particularly regarding the slopes of curves at constant $c$.

Figure F.6-(c) displays the dissipation overestimation of the standard generalized model compared to the surrogate model energy release. This observation aligns with the differences observed in the hysteresis cycles portrayed by both models. Nonetheless, the dissipation rate $\mathcal{D}$ is well-captured by the standard generalized model, as evinced by the matching slopes in both solutions when $\dot{c} \neq 0$.

[9] In the microscale surrogate model, phase concentrations, denoted as $c$, are computed as the ratio of the number of hysterons in phase II to the total number of hysterons, which in this case is 20.

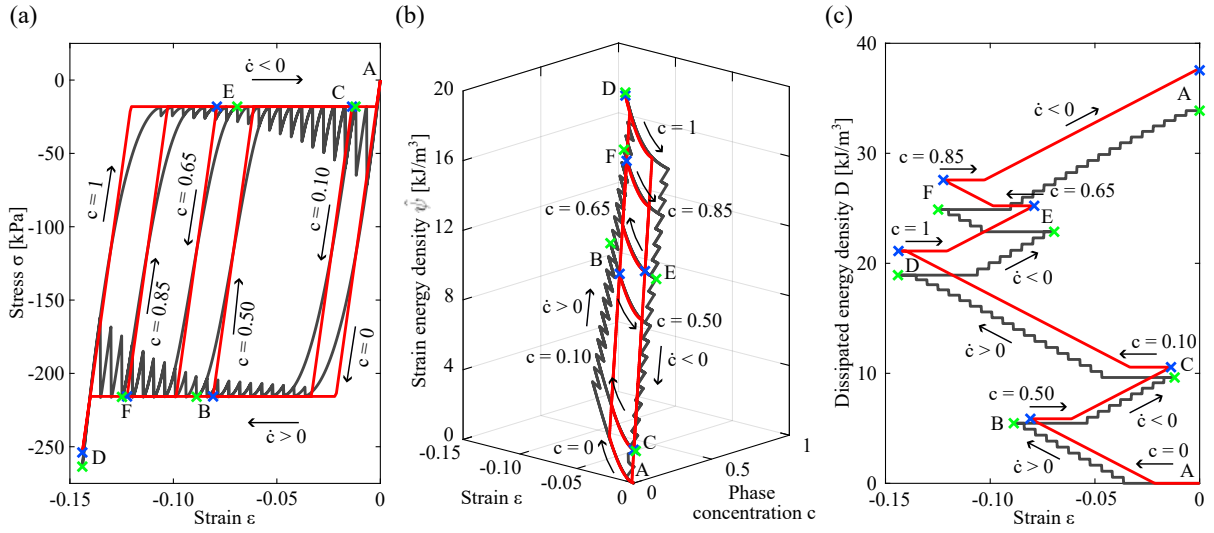


**Figura F.6:** Macroscale generalized standard material model (red curves) and microscale surrogate model of a chain with 20 bi-stable elements (grey curves): (a) stress-strain, (b) Strain energy density versus strain versus phase concentration, (c) Energy release (Dissipation) versus strain. The direction of loading is indicated by arrows. Phase concentration $c$. States A to F are depicted by blue crosses (macroscale model) and green crosses (surrogate model).

## F.4. Numerical assessments of different topologies

The next goal is to approximate the limit responses of various metamaterials considering multiple unit cells. The microstructures of these specimens have lattice-type topologies of hysterons and undergo various load conditions. In subsection F.4.1, we briefly describe the salient microarchitecture design characteristics of the studied metamaterials. In subsection F.4.2, we focus on examining four relevant features regarding their limit response; we study i) the apparent force-displacement response in terms of phase concentrations, ii) the microstructure formation ([104]) and evolution of transition patterns, and iii) the energy dissipation in closed cycles of loads. In subsection F.4.3, we assess the loading direction influence on such features. We close this Section with a summary discussion of the results.

### F.4.1. Microarchitecture design of the metamaterials

The metamaterials are composed of two-dimensional, periodic, low-connectivity lattices of hysterons arranged in various topologies. Each hysteron corresponds to a beam with a sinusoidal shape and lateral constraints, as illustrated in Figure F.7. These topologies comprise sets of opposing beams interconnected by rigid frames enforcing lateral restrictions on the curved beams. Such microarchitecture design has demonstrated its effectiveness in achieving multi-directional metamaterials with phase transitions (see, e.g., [100, 107, 202]).

Each lattice topology is classified according to the plane group symmetry of the unit cell [65], and their microarchitecture designs unveil three different features: a high-symmetry topology (p4mm), an achiral topology (p4g), and a chiral topology (p4). In the chiral topology (Figure F.7-(c)), each unit exhibits a tendency to rotate in an anticlockwise direction when the specimen is compressed. Conversely, the achiral topology of Figure F.7-(b) displays a combination of clockwise and anticlockwise rotational units. The reason for including chirality in the microarchitecture designs is that it has proven to be a remarkable feature for achieving a variety of properties within the framework of metamaterials[10]. In

[10] A comprehensive examination of chirality classification and related microarchitecture topologies can be found in the work by [262].

Figure F.7, in addition to showing the arrangements of these topologies, we also present the bar lattices of the corresponding surrogate models representing these microstructures.

Figure F.7 also depicts in blue squares equivalent points of the metamaterial constituting the underlying Bravais lattice. These points identify the unit cells (in yellow) and define the primitive vectors $\boldsymbol{a}$ and $\boldsymbol{b}$ indicating the lattice periodicity directions.

For a comparative analysis of the results presented in this section, we point to the work by Nitecki y Givli [229] who describes a comparable study of unstable microstructures involving less general lattice configurations and simpler interactions between hysterons.

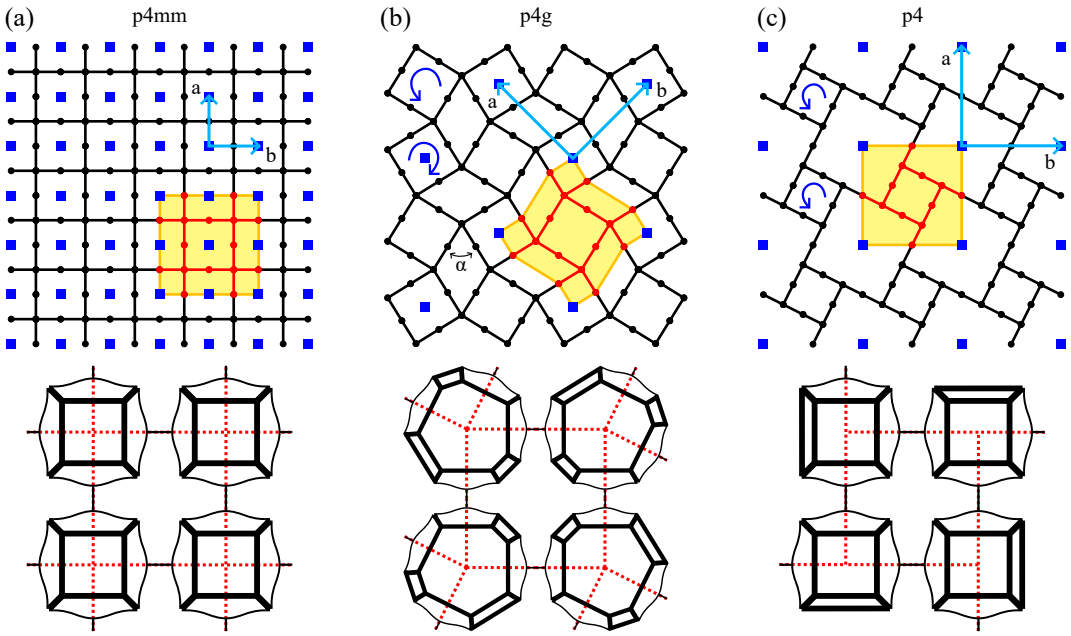


**Figura F.7:** Microarchitecture topologies and their plane group symmetries. (a) p4mm, (b) p4g (with $\alpha = arctan(2)$), (c) p4. Top row: lattice arrangement of the surrogate model according to [73]. The Bravais lattice is shown by blue squares located in equivalent points and the primitive vectors $\boldsymbol{a}$ and $\boldsymbol{b}$, indicating the periodicity directions. Bottom row: true microarchitecture topology. The dashed red lines indicate the orientation of the surrogate elements for comparison with the shadowed unit cells.

### F.4.2. Uniaxial compression tests

The limit response of the three metamaterials is analyzed via uniaxial compression tests using a surrogate model. In these tests, the sampling volumes undergo vertical loads under displacement control. The left and right lateral boundaries of the sampling volume are kept unconstrained. The sampling volumes incorporate a substantial number of unit cells, maintaining the height-to-width size ratio equal to two in all tested specimens. The analysis involves investigating two loading directions relative to the lattice axis for each metamaterial. The directions are identified by the angle between the load direction, which is always vertical, and the Bravais lattice primitive vector $\boldsymbol{a}$ depicted in Figure F.7, which is attached to the micro-architecture.

Curved beams are characterized by the same geometric and material parameters detailed in Section F.2.2, according to Figure F.3-(a), although in this case unit cells are not assigned an arbitrary cell size. We perform five instances that feature predetermined distributions of random perturbations applied to the geometric parameters. The results are averaged over five random samples. These perturbations facilitate the emergence of heterogeneous strain patterns. The maximum magnitude of these perturbations is limited to 1 % of the geometric parameters.

Considering the multiplicity of equilibrium paths, there is no guarantee that during a snapping event

the minimum amount of elements will perform the phase transition. Consequently, it is generally the case that not every equilibrium branch, characterized by a specific value of $c$, is traversed in a single simulation. Therefore, multiple instances of the same test with random geometric perturbations are employed to explore alternative equilibrium branches.

Numerical solutions of the balance equations are obtained through an iterative BFGS scheme combined with a line search technique satisfying Wolfe's optimality conditions. This procedure guarantees a (secant) stiffness matrix that is positive definite.

The results are shown in Figures F.8 through F.13. The analysis primarily focuses on investigating the influence of discrete phase concentrations on two key aspects of the problem: the force-displacement curves, as presented in subplots (a), and the progression of energy dissipation, as depicted in subplots (b). Additionally, in subplots (c), we offer insights into the microstructure formation along with the evolution of transition patterns as the phase concentration increases.

Regarding the force-displacement relations, subplots (a) present two distinct outcomes: the black line represents the metamaterial response during a complete loading cycle. This cycle encompasses the initial loading stage until all phase transitions occur, followed by a subsequent unloading stage. We refer to it as the envelope of the force-displacement curve. This loading cycle reveals the maximum energy release expected by the specimen. The outcomes from intermediate loading cycles are plotted with dashed red lines. These results provide insights into understanding the relationship between the rate of phase concentration change and its associated conjugate force, thereby characterizing the dissipation potential of the model discussed in Section F.3. The curves of subplots (a) are obtained by averaging the five instances with the same strains and phase concentration values.

In terms of energy release analysis, the results shown in subplots (b) include the energy release profile across the entire loading cycle, which is represented there by the red curves. These curves characterize the energy release rate, a crucial parameter that serves as the argument for the dissipation potential function. Also, the black curves represent the ratio between the energy release and the external work performed on the specimen during a loading process. This ratio serves as a measure to assess the efficiency of a metamaterial topology to dissipate energy.

Figures (c) depict the surrogate model lattice identifying the distributions of phases for different phase concentrations $c$, the latter being the ratio between the number of bars in phase II and the total number of bars. These pictures are shown at several intermediate load states in correspondence with the numbers in subplots (a). The color code indicates the following: blue and green represent phases I and II, respectively, while red and magenta indicate elements undergoing phase transitions in that specific load instant. Red signifies a phase transition from phase I to phase II, whereas magenta indicates a reverse phase transition from phase II to phase I. We distinguish an element as being in phase I when its curved beam central displacement is less than its initial apex height. Conversely, the element is classified as being in phase II when this displacement exceeds its initial apex height. A visual representation of phase I and II configurations is depicted in the inset of Figure F.3-(d).

The results presented here regarding the formation of microstructure patterns represent systematic outcomes observed in all instances of the same test. Thus, we can confidently assert that these features exhibit a consistent transition pattern that experiences minimal impact by the perturbations introduced in each instance.

### Topology p4mm

#### a) Case A: Direction of loading at $0^{\mathbf{o}}$

Figure F.8 displays the results obtained with the topology p4mm and with the direction of loading parallel to the lattice axis $\boldsymbol{a}$.

Initially, the complete specimen is assumed to be in phase I. Then, during the loading process, when

the initial phase transitions occur leading to a change in the phase concentration (as indicated by point 1 in Figure F.8-(a)), the elements that undergo snapping simultaneously align together along the same horizontal row of facing hysterons, as depicted in picture 1, Figure F.8-(c) ($c = 0.018$). Meanwhile, the other rows relax.

As the load increases, additional rows of hysterons undergo phase transitions, as shown in point 2 of Figure F.8-(a) and picture 2 in Figure F.8-(c) ($c = 0.179$). Ultimately, once point 8 is reached in Figure F.8-(a) and picture 8 in Figure F.8-(c) ($c = 0.5$), all vertical bars of the sampling volume are in phase II. Therefore, only half of the hysterons (the vertically aligned ones) undergo a phase transition, which is a reasonable outcome given the absence of stress orthogonal to the loading direction. This finding agrees with the results reported by Zhang et al. [100].

The sequential order of rows experiencing phase transitions during loading stages going from 1 to 8 is random. Nevertheless, this effect has a negligible impact on the overall behavior of the specimen.

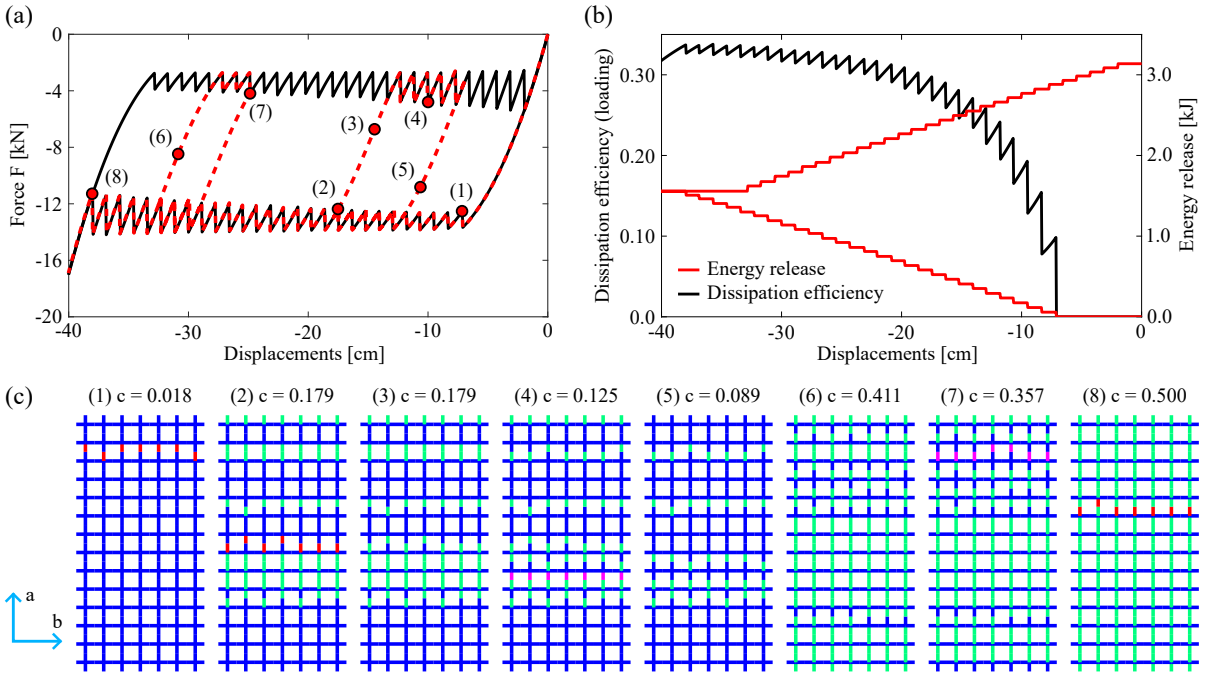


**Figura F.8:** Topology p4mm. Direction of loading at 0°, 392 hysterons. (a) Force-displacement relations during a complete loading-unloading cycle (black line) and intermediate unloading-reloading cycles (red dashed line). (b) Energy release versus imposed displacement on the specimen top and dissipation efficiency versus displacement on the specimen top. (c) Phase pattern instances corresponding to the points marked in subplot (a). The color code used is blue for phase I, green for phase II, red for transition from phase I to II, and magenta for transition from phase II to I.

Alternatively, in an unloading path from point 2 to point 3 in Figure F.8-(a), the specimen remains at constant $c$ until it reaches the conditions for opposite phase transitions. Note, for example in plots 4 and 7 of Figure F.8-(c) that the transformation pattern during unloading is the same as in loading. This particular response aligns consistently with the predictions of the generalized standard model presented in Section F.3.

The energy release rate throughout the loading cycle, i.e. the slope of the curve in Figure F.8-(b), is constant. Additionally, an equal amount of energy is released during the unloading stage. This characteristic response does not hold when this topology is subjected to load directions not aligned with the lattice axis, as is next analyzed. Moreover, the trend in dissipation efficiency consistently rises with each snapping event.

**b) Case B: Direction of loading at $45^o$**

Figure F.9 displays some features of results obtained with the topology p4mm and with loading direction at $45^{o}$ with respect to the lattice axis.

The sampling volume illustrated in Figure F.9 comprises approximately the same quantity of hysterons as those depicted in Figure F.8. However, a remarkable difference becomes apparent when the specimen is subjected to a loading angle of $45^{\circ}$ relative to the lattice axis. In this scenario, the number of snapping events increases significantly due to the fact that all the specimen hysterons undergo a phase transition.

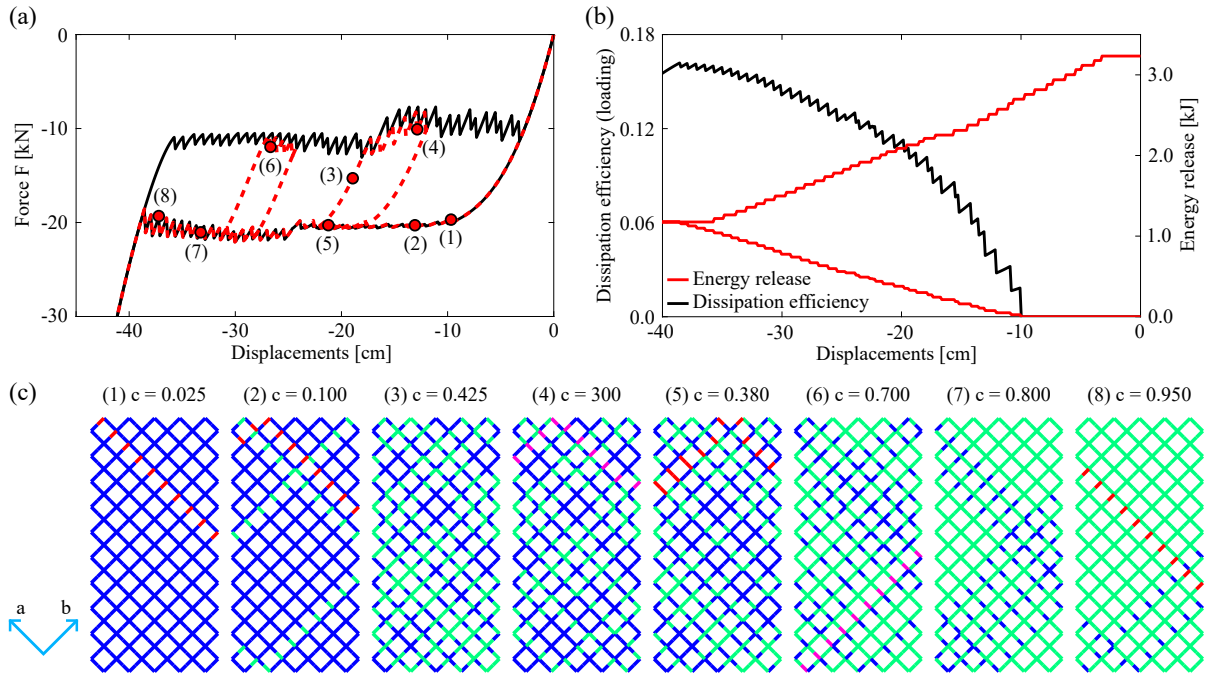


**Figura F.9:** Topology p4mm. Direction of loading at $45^{o}$, 400 hysterons. (a) Force-displacement relations during a complete loading-unloading cycle (black line) and intermediate unloading-reloading cycles (red dashed line). (b) Energy release-displacement and dissipation efficiency-displacement relations. (c) Phase pattern instances corresponding to the points marked in the subplot (a). The color code used is blue for phase I, green for phase II, red for transition from phase I to II, and magenta for transition from phase II to I.

Also, in this case, the elements undergoing simultaneous phase transition are inclined and form a diagonal pattern spanning from one specimen side to the other, as shown in pictures (c). When such diagonals intersect the specimen top or bottom boundaries, with imposed displacements, the elements that are simultaneously transitioning form a V-shaped pattern; see instances 2 and 4 in the Figure. Note the remarkable smoothness in the force-displacement plot during the initial loading stage, specifically from points 1 to 5 in Figure F.9-(a). During this stage, the snapping events display smaller drops in force. Once a relatively high value of $c$ is reached, the load levels determining phase transitions occur at a slightly increasing load, from approximately $-20$ kN to $-22$ kN. This effect is attributed to the fact that the stiffness of the elements that have previously undergone phase transition is greater than that of the ones that have not transitioned yet. A similar phenomenon is noted during unloading, where the limit load changes from approximately $-10$ kN for high $c$ values to $-8$ kN for low $c$ values.

Some incompatible phase transition patterns are observed, as revealed in plot 5 of Figure F.9, where three pairs of elements in the same diagonal undergo a simultaneous phase transition. Conversely, only one element snaps concurrently in the remaining diagonal segment. It is worth noting that such an incompatible deformation pattern does not persist in subsequent loading steps.

Analyzing the amount of energy released during a load cycle, we conclude that approximately one-third of the total energy release occurs during loading and the remainder during unloading. This notable

effect is related to the shape of the spinodal region characterizing the hysterons under compression combined with moment actions. Note in Figure F.5-(b) how the spinodal curve defines the limit values $k_+$ and $k_-$ for the conjugate force $g$, which are directly related to the energy release through equation (F.31). Additionally, the response regarding the dissipation efficiency is similar to that shown by the lattice with load at $0^o$.

In both loading cases for the p4mm topology, all the elements undergo an abrupt transition between phases I and II, or vice versa.

### Topology p4g

#### a) Case A: Direction of loading at $45^o$

We analyze the orientation depicted in Figure F.10 denoted Case A. The microarchitecture topology displays two orientations of elements relative to the load direction. These elements undergo phase transitions at different load levels, as shown in Figure F.10-(a) and evidenced in the sequence of pictures 1-8 in the Figure. A similar result has been reported by Zhang et al. [100] regarding their T-type material when loaded at $0^o$.

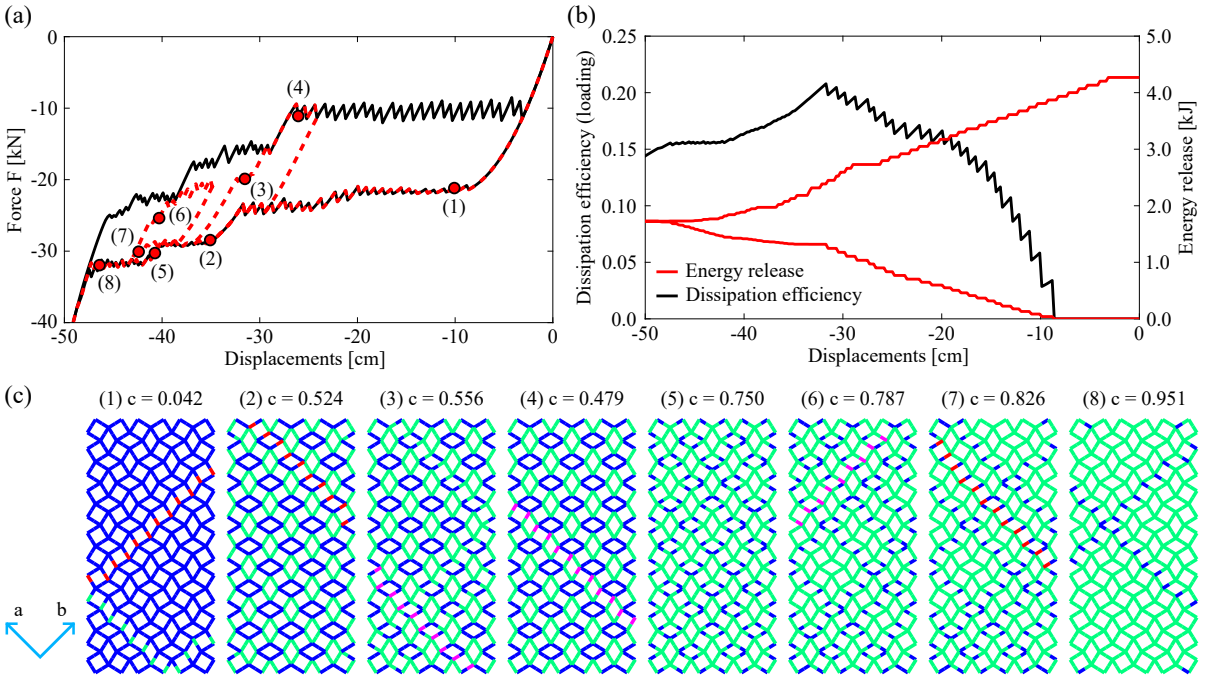


**Figura F.10:** Topology p4g. Direction of loading at $45^o$, 576 hysterons. (a) Force-displacement relations during a complete loading-unloading cycle (black line) and intermediate unloading-reloading cycles (red dashed line). (b) Energy release-displacement and dissipation efficiency-displacement relations. (c) Phase pattern instances corresponding to the points marked in the subplot (a). The color code used is blue for phase I, green for phase II, red for transition from phase I to II, and magenta for transition from phase II to I.

Phase transitions initiate in the elements most closely aligned with the direction of the applied load, leading to the formation of diagonal rows of elements transitioning into phase II. When these rows intersect the specimen top or bottom boundaries, they configure a distinctive V-shaped pattern, as illustrated in picture 1 of Figure F.10. An approximately constant load level, with forward phase transitions ranging from $-22$ kN to $-24$ kN and a backward phase transition at $-9$ kN, is observed.

Once all elements most closely aligned with the direction of the applied load have transitioned to phase II (c=0.50), a second stage starts in which the remaining elements undergo snapping. This process

occurs at a higher load, as shown in points 2, 5, and 8. In this case, the phase transition pattern consists of diagonal segments connecting the elements still in phase I. The diagonal segments intersecting the specimen boundaries no longer form the V-shaped pattern observed at lower loads, as seen in points 2 and 3. In this case, the number of elements in simultaneous transitioning is smaller, and the transitions tend to happen at a lower load if compared with a complete diagonal, as can be seen by the location of instances 3 and 6 during the first and second intermediate cycles. We attribute this outcome to a boundary effect, not necessarily tied to the topology itself.

Similar to the case of $p4mm$ topology loaded at $45^{\text{o}}$, we notice a stiffening effect in the elements that have previously undergone phase transitions. In this case, the stiffening effect occurs at concentrations $c > 0.75$, corresponding to stage 5.

We have also noted that boundary effects can lead to some elements undergoing a gradual phase transition across the spinodal region without energy release. This effect persists irrespective of the number of elements included in the sampling volume. This observation aligns with the findings reported by Nitecki y Givli [229] in the context of specific topologies.

Different landscapes of energy release during the loading and unloading stages are noted. Each critical force plateau corresponds to an energy release rate level, as shown by the slope of the red curve in Figure F.10-(b). This Figure illustrates that the dissipation efficiency reaches the peak value at approximately $0.20$ correspondingly to the end of the initial loading stage plateau. However, during the subsequent loading stage, the dissipation efficiency declines. This outcome highlights the fact that extracting the maximum dissipation capacity from the metamaterial necessitates a greater amount of external work.

**b) Case B: Direction of loading at $0^{\text{o}}$**

We analyze the orientation depicted in Figure F.11, denoted as Case B. The response closely mirrors the solution exhibited by the $p4mm$ topology with loads at a $0^{\text{o}}$ angle. This behavior is imputable to phase transitions exclusively occurring in elements oriented closely parallel to the loading direction. As a result, the outcomes presented in Figure F.11 display only two distinct force plateaus: one during loading, where the transition from phase I to phase II occurs, and another during unloading, marked by the opposite phase transition.

The elements experiencing phase transitions are arranged in rows perpendicular to the direction of the applied load, see pictures (c) of Figure F.11. It is also observed that both configurations shown in pictures 2 and 4 of Figure F.11 exhibit identical phase concentrations but differ in the spatial arrangement of phases throughout the sampling volume. Nevertheless, the response in both cases remains consistent along the same equilibrium curve. Furthermore, the energy release profile in Figure F.11-(b) shows a slight increase during unloading compared to loading. The dissipation efficiency surpasses that of the previous Case A by a significant margin, with a tendency to increase throughout the complete loading process.

**Topology p4**

**a) Case A: Direction of loading at $0^{\text{o}}$**

Similar to the $p4g$ topology oriented at an angle of $0^{\text{o}}$, the response of the $p4$ topology exhibits distinct force plateau levels, as depicted in Figure F.12-(a). Although the $p4$ topology has only two directions of elements, its response displays five plateau levels during loading and four during unloading. This effect arises due to the connectivity of the elements.

The first elements undergoing phase transitions are the ones more aligned to the load direction, i.e., elements A, B, and C depicted in the inset of Figure F.12-(a). In the first intermediate cycle, corresponding to picture 1 of Figure F.12, the first elements undergoing phase transition are elements A. In this loading stage, the pattern of elements in phase II forms rows orthogonal to the load direction. Once all

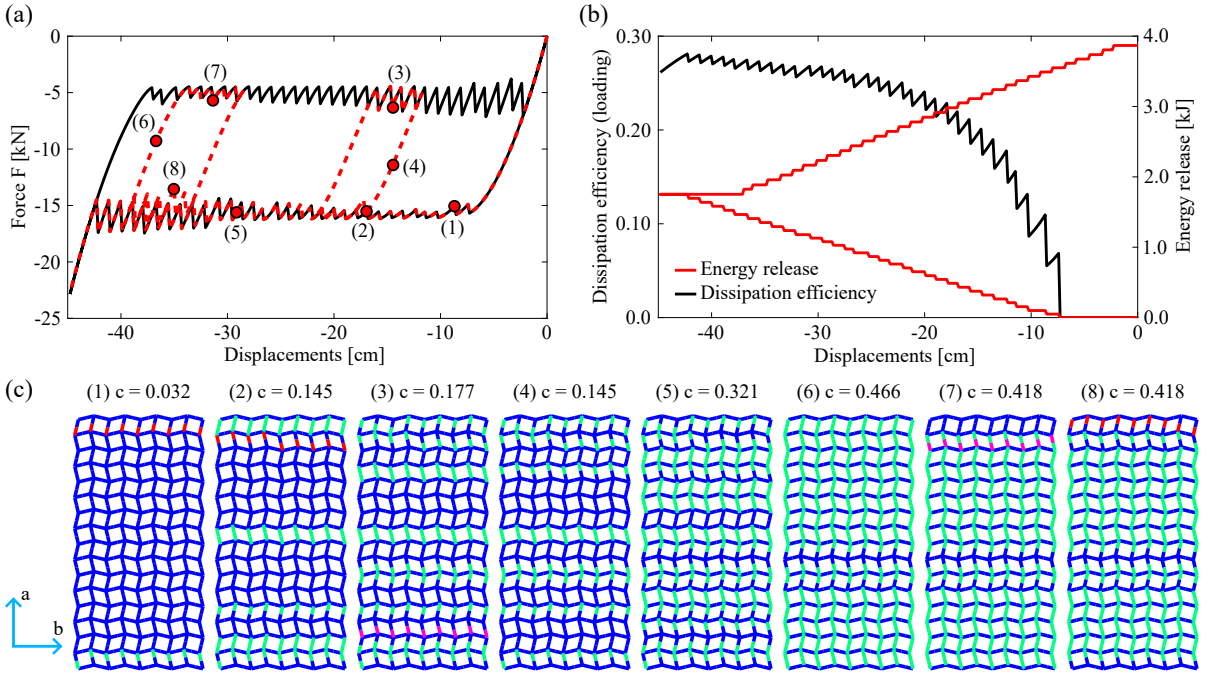


**Figura F.11:** Topology p4g. Direction of loading at 0°, 560 hysterons. (a) Force-displacement relations during a complete loading-unloading cycle (black line) and intermediate unloading-reloading cycles (red dashed line). (b) Energy release-displacement and dissipation efficiency-displacement relations. (c) Phase pattern instances corresponding to the points marked in the subplot (a). The color code used is blue for phase I, green for phase II, red for transition from phase I to II, and magenta for transition from phase II to I.

elements A are in phase II, with a phase concentration of $c = 1/6$, the subsequent phase concentration increment is promoted by elements B transitioning to phase II. Note that both elements denoted B in a unit cell are aligned horizontally, however, the transition pattern in the sampling volume corresponds to diagonal rows, as can be seen in instance 2 ($c = 0.188$). This stage lasts until until $c = 1/3$.

Subsequently, elements C distributed in diagonal rows undergo phase transitions, see picture 3. Unloading the specimen in this stage, as indicated in the second intermediate cycle with points 3 to 4 in Figure F.12-(a), the elements transitioning from phase II to I can be either B or C, both occurring at the same load level. This effect leads to a mixed pattern formation influencing the transition load during reloading.

In the following loading process, once the concentration reaches the value $c = 1/2$, all elements B and C have transitioned to phase II. Any further increase in $c$ is correlated to phase transitions of elements in the second orientation. Such transition sequence, as observed in instances 5 and 6, follows the order of elements D preceding elements E.

Notably, when the specimen is unloaded from a stage where elements E are partially in phase II, the phase transition sequence in the reverse load direction is, first elements D followed by E. This result produces an interior load-displacement cycle that does not reach the external envelope of the load-displacement curve. This phenomenon is illustrated in Figure F.12, where pictures 7 and 8 depict how elements D are the first to undergo phase transitions in both load directions. Once both types of elements, D and E, have completed their respective phase transitions during the loading process, the phase concentration reaches the value $c = 5/6$. It is worth noting that elements F do not undergo any phase transition in this loading direction.

Figure F.12-(b) represents the intricate configuration displayed in the energy release response and dissipation efficiency throughout the loading process. It highlights the shifts in these outcomes as different elements undergo phase transitions during the load cycle.

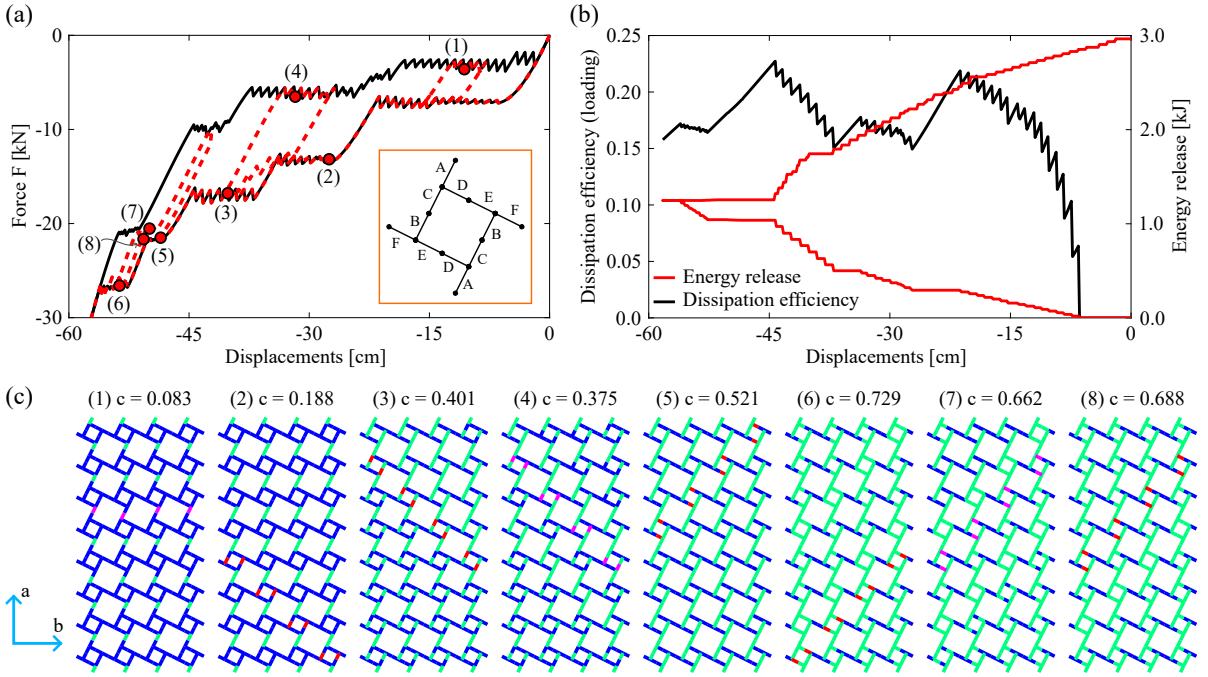


**Figura F.12:** Topology p4. Direction of loading at $0^o$, 384 hysterons. (a) Force-displacement relations during a complete loading-unloading cycle (black line) and intermediate unloading-reloading cycles (red dashed line). Inset: element classification identifying microstructure formation. (b) Energy release-displacement and dissipation efficiency-displacement relations. (c) Phase pattern instances corresponding to the points marked in the subplot (a). The color code used is blue for phase I, green for phase II, red for transition from phase I to II, and magenta for transition from phase II to I.

### b) Case B: Direction of loading at $71.6^o$

The second orientation of the topology p4 we investigate is achieved by rotating the microarchitecture axis by an angle of $71.6^o$ with reference to the load direction, as illustrated in the inset of Figure F.13-(a). Each element in this lattice orientation is inclined at angles of $\pm 45^o$ from the loading direction.

In such a particular loading scenario, no distinctive plateaus are noted in the force-displacement plot of Figure F.13-(a), neither during loading nor unloading. We attribute this response to the phenomenon that no entire rows of elements simultaneously undergo the phase transitions.

Regarding this effect, according to the nomenclature of Figure F.13-(a), pictures of instances 1, 2, and 3 display the sequence of elements A, B, and C undergoing phase transitions, even when elements A are not aligned parallel to elements B and C. This order differs from that of the previously studied case with identical topology.

After all elements A, B, and C have transitioned to phase II, the concentration $c$ reaches approximately the value $c = 0.5$. In the subsequent loading process, the following elements undergoing phase transitions are D, E, and F, as depicted in pictures 5 and 6 of Figure F.13.

In intermediate load cycles, we observe similar characteristics to those encountered in case A with the same topology. In the second load cycle, picture 4 illustrates the reverse phase transitions from phase II to I, involving a mix of elements B and C. Additionally, during the third load cycle, pictures 7 and 8 reveal that the initial elements undergoing transition are elements D, followed by elements E. Consequently, these intermediate load cycles do not reach the external force-displacement plot envelope.

As depicted in Figure F.13-(b), the specimen exhibits a relatively gradual rise in energy release, paired with modest and irregular energy efficiency. Consequently, the force-displacement plot does not feature plateaus across the entire load cycle. This outcome occurs despite all six types of elements undergoing phase transitions.

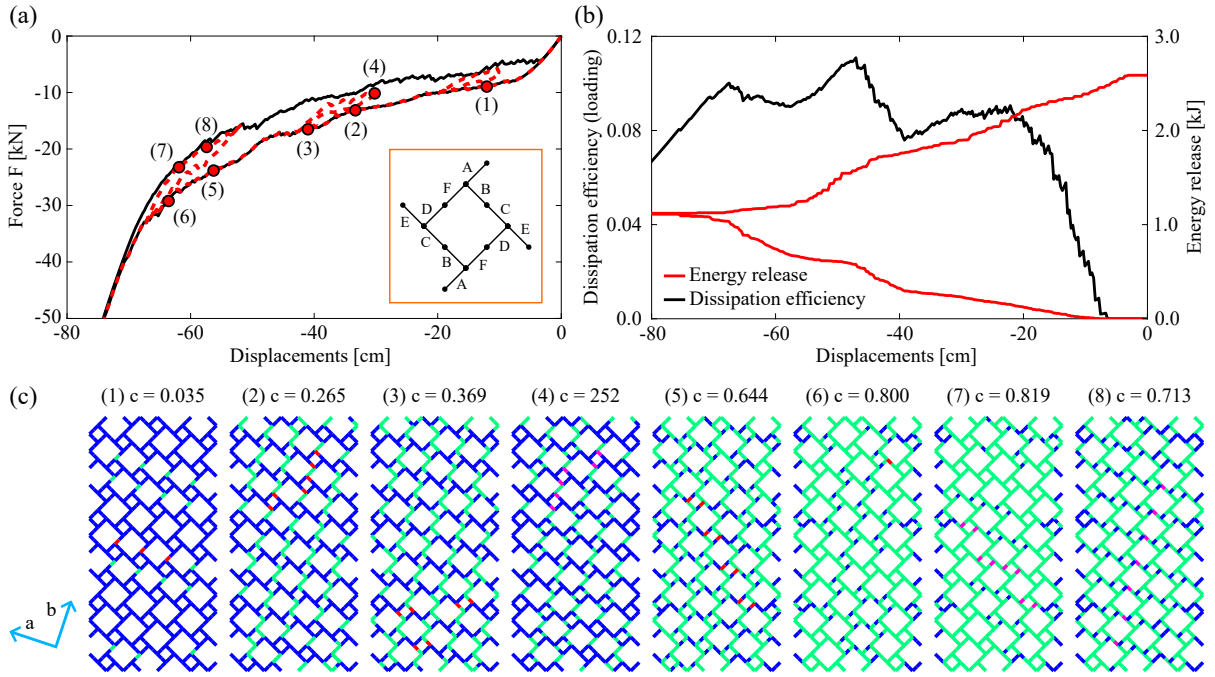


**Figura F.13:** Topology p4. Direction of loading at $71.6^{o}$, 540 hysterons. (a) Force-displacement relations during a complete loading-unloading cycle (black line) and intermediate unloading-reloading cycles (red dashed line). Inset: element classification identifying microstructure formation. (b) Energy release-displacement and dissipation efficiency-displacement relations. (c) Phase pattern instances corresponding to the points marked in the subplot (a). The color code used is blue for phase I, green for phase II, red for transition from phase I to II, and magenta for transition from phase II to I.

### F.4.3. Outline of the impact of lattice orientation

Based on the findings illustrated in the plots (b) of Figures F.8 to F.13, the analysis of two attributes in the explored topologies and their correlation to lattice orientation relative to the load direction is explored in the following. They are: i) the average energy release per hysteron, determined by dividing the total energy released by the number of hysterons within the sampling volume; ii) the dissipation efficiency. These attributes are outlined in the polar plots of Figure F.14, where the radial coordinates indicate their magnitude, and the angular coordinates correspond to the lattice orientation relative to the load direction. Due to the square symmetry of the lattice topologies, equivalent results are achieved with a lattice rotation of $90^{o}$.

Regarding the average energy released by each hysteron, as depicted in Figure F.14-(a), it is worth highlighting that the $p4mm$ and $p4g$ topologies exhibit similar values in the two examined loading directions[11]. Note also that only half of the hysterons undergo phase transitions when the lattice is oriented at an angle of $0^{o}$. Conversely, at an orientation angle of $45^{o}$, all hysterons undergo phase transitions, dissipating a smaller amount of energy because they are primarily subjected to moment-dominated actions. Additionally, the $p4$ topology in a favorable orientation ($0^{o}$) displays an average energy release similar to that of the previous two cases. However, for this lattice, the energy release decreases notably with an unfavorable orientation.

The $p4mm$ and $p4g$ topologies at an orientation angle of $0^{o}$ achieve the highest dissipation efficiency, as depicted in Figure F.14-(b). It is attributed to the fact that the $0^{o}$ orientation requires less external work to achieve the same total dissipation compared to the $45^{o}$ orientation. In contrast, the $p4$ topology, when compared to the $p4mm$ and $p4g$ topologies, exhibits lower dissipation efficiencies in both orientations.

[11] A similar result has been reported by Zhang et al. [100] for their S-type material, equivalent to the $p4mm$ topology of this work.

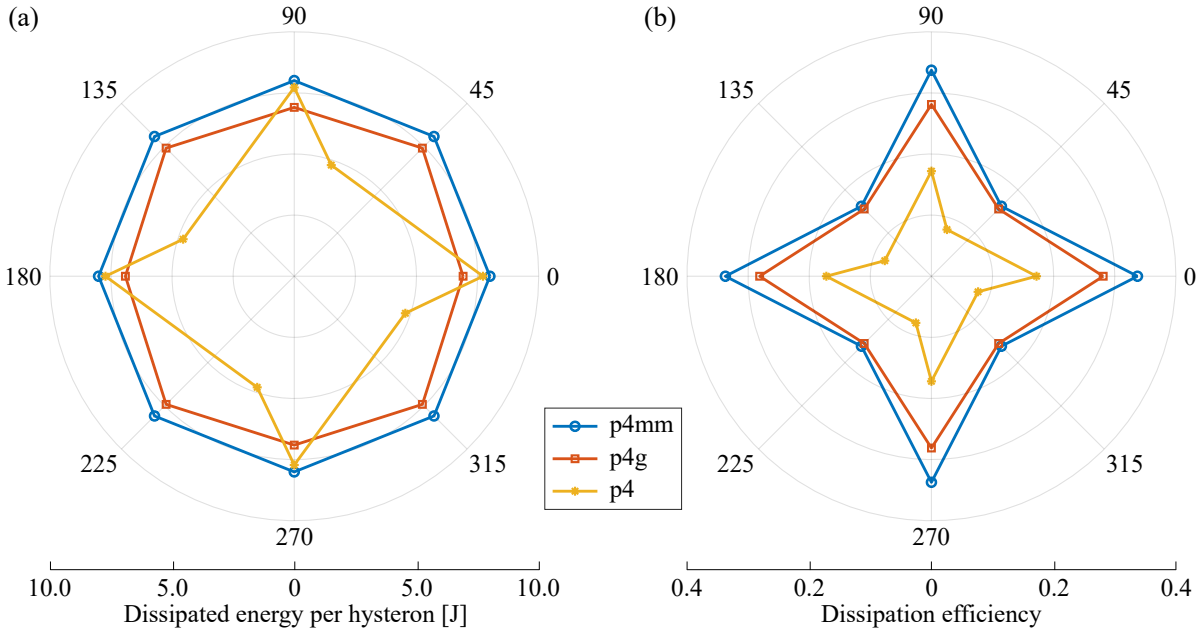


**Figura F.14:** (a) Average energy release per hysteron, and (b) dissipation efficiency analyzed as functions of the lattice orientation angle with respect to the loading direction for the three different topologies.

### F.4.4. Discussion

The three microarchitectures exhibit the ability to release energy during cyclic loading in two distinct lattice orientations. Furthermore, it is apparent that this energy release occurs during both the loading and unloading processes, but the amount in each process may not be similar.

The metamaterial energy dissipation capacity arises from a balance between the number of hysterons performing phase transitions and the efficiency with which this effect happens, i.e., depending on whether they are primarily subjected to bending or compression-dominated situations. Consequently, a trade-off emerges between the quantity of hysterons undergoing phase transition and the direction of the applied load.

The average energy release per hysteron exhibited by the three lattice topologies closely resembles one another for the $0^{\text{o}}$ orientation. However, a more comprehensive analysis of Figures F.8, F.10, and F.12, reveals differences among these cases. Such differences include: maximum achievable phase concentration $c$, number of force plateaus in the force-displacement relationship, phase transition patterns, and their evolution. This scenario offers ample flexibility to adjust multiple characteristics of the limit behavior without sacrificing energy dissipation capacity.

Contrary to the similarities observed among the three topologies mentioned in the previous paragraph, higher dissipation efficiencies are achieved when hysteron orientations align with the external load, as illustrated by examples in topologies like $p4mm$ at $0^{\text{o}}$ and $p4g$ at $45^{\text{o}}$.

The observed element phase transition patterns for a given topology may range from orthogonal to diagonal rows in reference to the loading direction. We can conclude that there is not a clear connection between the topology symmetry and the response symmetry.

## F.5. Conclusions

This article analyzes the limit behavior of periodic lattice-type microarchitectures exhibiting instabilities associated with phase transitions at small length scales.

At the microscale level, we investigate the quasi-static behavior of three 2D lattices comprising bistable curved beams. We focus on assessing the following features of sampling volumes containing a large number of unit cells: i) the force-displacement apparent response, ii) the microstructure formation and evolution of transition patterns, iii) the extrinsic energy dissipation in closed cycles of loading, and iv) the influence of the loading direction on the aforementioned features. Our analyses reveal the following facts. The three topologies studied exhibit energy dissipation when subjected to loading-unloading cycles in two different orientations, proving the effectiveness of low-connectivity lattices for building reusable dissipative metamaterials. Also, we observed that the energy dissipation density in the compared lattices is quite similar, despite the differences in their geometrical features. In addition, we showed that the dissipation of the lattices does not change much with the loading orientation, precisely due to the symmetry of the former. We observed, instead, that the main effects of the lattice geometry are the number of force plateaux, strain patterns, and the evolution of microstructures. This outcome offers the capability to adjust multiple characteristics of the limit behavior without sacrificing energy dissipation capacity.

Additionally, a homogenization procedure based on convex relaxation theory is introduced. Such formulation is a main contribution of this paper that provides a multiscale modeling framework for bistable lattice-based materials. It is shown that a generalized standard material model can be analytically constructed that captures the large-scale behavior of the lattice. The mechanical response of this material is thus described only through an effective relaxed energy and an effective dissipative potential, greatly simplifying the upscaling of material properties and providing a first step in the design of mechanical parts made of locally unstable metamaterials.

## Acknowledgments

This research has been supported by grants provided by CONICET: PIP 112202101 00455CO (2022 – 2024), the National University of Litoral, and the fund from ANPCyT: PICT 2020-SERIEA-02793, Argentina. N. Rossi gratefully acknowledges the support received by Fundación Carolina and the Argentine Ministry of Education under the program of academic mobility for Argentine faculty.

## Appendix I: Brief description of the surrogate model and its finite element approach

The elastic double-clamped curved beam illustrated in Figure F.15-(a), designated as hysteron, has been studied by Rossi et al. [73]. Its undeformed configuration copies the first buckling mode of an axially compressed beam with clamped ends. The surrogate model of this hysteron, as described in the same reference, reduces the computational complexity in the numerical simulations by avoiding detailed microarchitecture modeling, thereby facilitating the inclusion of a substantial quantity of unit cells in the analysis of each problem. This reduction in complexity, however, does not compromise the faithful representation of the inherent structural phenomena linked to the mechanical energy dissipation during phase transitions.

The surrogate model consists of a straight frame (truss+beam) element with only six degrees of freedom withstanding compression and moment loads. It follows the infinitesimal strain theory, as illustrated in Figure F.15-(b) with details of the frame finite element and degrees of freedoms. The constitutive relations of the frame element are obtained from a semi-analytical model of the curved beam behavior that it represents. Therefore, the geometrically nonlinear characteristics of the hysteron are integrated into the frame element through its non-convex strain energy, capturing the typical snap-trough behavior and the pronounced influence on the energy dissipation reduction due to moment loads. The hysteron geometry and material parameters determine the non-convex strain energy landscape.

Compression and moment loads appear naturally in two-dimensional lattice-type arrays of hysterons, as shown in [100], and their inclusion allows for idealizing complex microstructural responses if compared with the approach followed by [229] where unstable lattices with only axial forces are analyzed. Given that the alignment of hysterons within the microarchitecture relative to the load direction plays a crucial role in optimizing metamaterial performance, the last characteristic emerges as a noteworthy feature of the surrogate model.

Figures F.15-(d) to (f) compare the numerical results obtained by simulating a pair of facing hysterons, as displayed in Figure F.15-(c), undergoing three distinct cases of combined loadings. The curved-beam geometry data in the three cases are similar to those specified in Section F.2.2, i.e., $l = 71.mm$, $h = 7.mm$, $t = 3.2mm$ and $b = 50.mm$, with the dimensions of the connecting bar as $t' = 3.5mm$ and $s = 17.5mm$, and the Young modulus of the beams is $E = 2.267GPa$. The imposed generalized displacements in the three cases entail transversal compression displacements, $\delta$, and rotations, $\theta$ (Figure F.15-(c)). They increase monotonously from zero to the final values described in Table F.2. A comparative analysis between solutions obtained with a high-fidelity finite element model (with approximately 8500 2D finite elements and 18500 DoFs) and the surrogate one (two frame elements and 9 DoFs) are presented in Figure F.15. Figure F.15-(d) to (f) plots the moment $m$, force $f$, and strain energy outcomes achieved with both models. Despite the well-marked hysteron non-linear behavior, it is worth noting the strong agreement achieved with the surrogate model.

| Case | $\delta\,[mm]$ | $\theta$ |
|---|---|---|
| 1 | 30.0 | $0^o$ |
| 2 | 27.5 | $10^o$ |
| 3 | 25.0 | $30^o$ |

**Tabla F.2:** Assembly of two facing hysterons, loading data according to Figure F.15-(c).

Note further the pronounced disparity in the energy landscape between Case 1, characterized by pure compression, and Case 3, which undergoes compression combined with a significant rotation angle. Recalling the graphical representation of energy dissipation magnitude depicted in Figure F.2-(a), it becomes evident that Case 3 exhibits a notable reduction in energy dissipation capacity compared to Case 1.

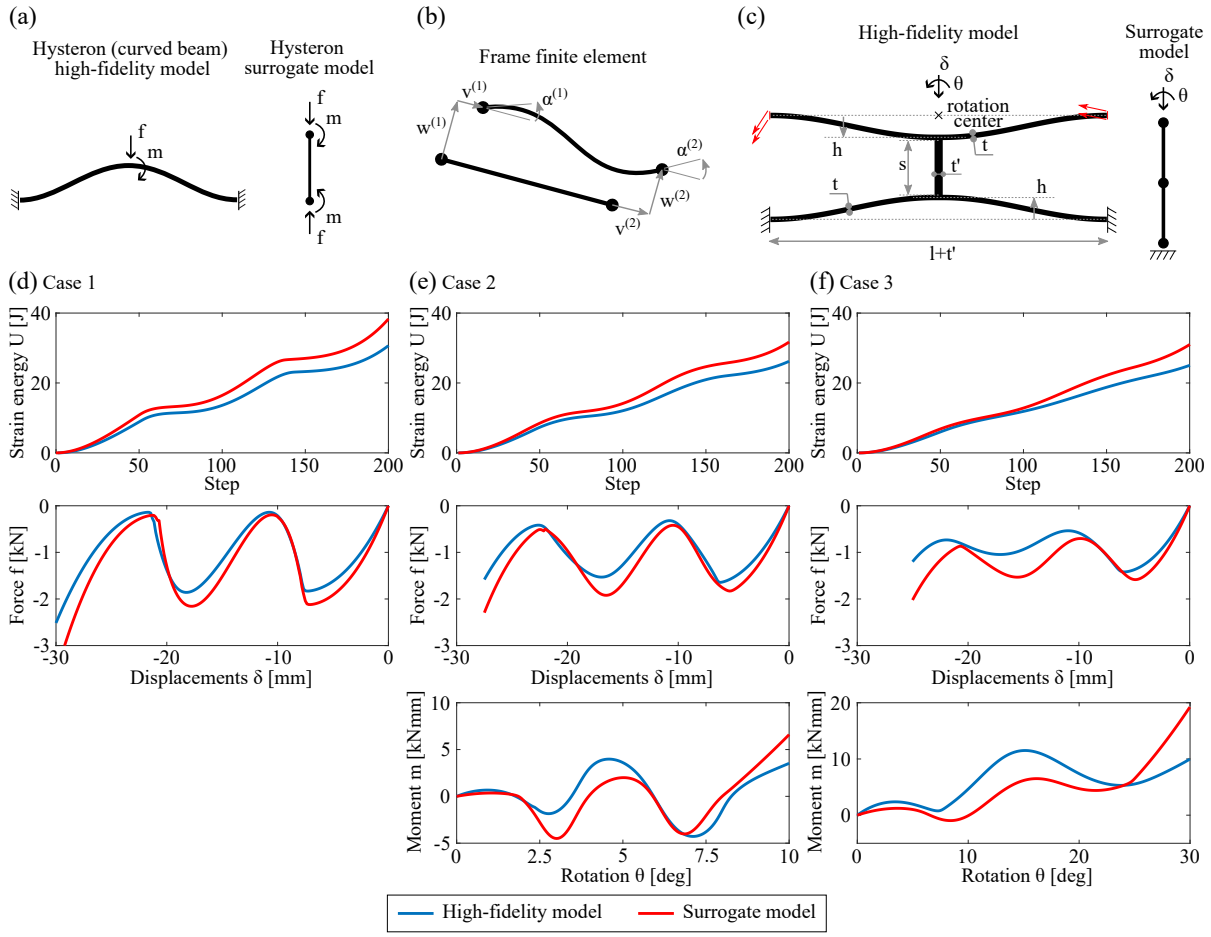


**Figura F.15:** (a) Hysteron (curved beam). High-fidelity finite element model (HF) and equivalent surrogate model (SM). (b) Frame finite element, two nodes, and six degrees of freedom. (c) Assembly of two facing hysterons. HF with geometric parameters and notation and equivalent SM. Responses of the facing hysterons for (d) Case 1, (e) Case 2, and (f) Case 3. HF: blue curves, SM: red curves.

# Bibliografía


[1] Michael F Ashby y David RH Jones. *Engineering materials 1: an introduction to properties, applications and design*, volumen 1. Elsevier, 2012.

[2] Ryan L Truby y Jennifer A Lewis. Printing soft matter in three dimensions. *Nature*, 540(7633):371–378, 2016.

[3] Muamer Kadic, Graeme W Milton, Martin van Hecke, y Martin Wegener. 3d metamaterials. *Nature Reviews Physics*, 1(3):198–210, 2019.

[4] Graeme W Milton. Composite materials with poisson's ratios close to—1. *Journal of the Mechanics and Physics of Solids*, 40(5):1105–1137, 1992.

[5] D Prall y RS Lakes. Properties of a chiral honeycomb with a poisson's ratio of—1. *International Journal of Mechanical Sciences*, 39(3):305–314, 1997.

[6] Katia Bertoldi, Pedro M Reis, Stephen Willshaw, y Tom Mullin. Negative poisson's ratio behavior induced by an elastic instability. *Advanced materials*, 2010.

[7] Muamer Kadic, Tiemo Bückmann, Nicolas Stenger, Michael Thiel, y Martin Wegener. On the practicability of pentamode mechanical metamaterials. *Applied Physics Letters*, 100(19), 2012.

[8] Carlos Gustavo Méndez, Juan Manuel Podestá, Oriol Lloberas-Valls, Sebastián Toro, Alfredo Edmundo Huespe, y Javier Oliver. Computational material design for acoustic cloaking. *International journal for numerical methods in engineering*, 112(10):1353–1380, 2017.

[9] Joseph N Grima, Daphne Attard, Roberto Caruana-Gauci, y Ruben Gatt. Negative linear compressibility of hexagonal honeycombs and related systems. *Scripta Materialia*, 65(7):565–568, 2011.

[10] Joseph N Grima, Roberto Caruana-Gauci, Daphne Attard, y Ruben Gatt. Three-dimensional cellular structures with negative poisson's ratio and negative compressibility properties. *Proceedings of the Royal Society A: Mathematical, Physical and Engineering Sciences*, 468(2146):3121–3138, 2012.

[11] Trishan Hewage, Kim Alderson, Andrew Alderson, y Fabrizio Scarpa. Double-negative mechanical metamaterials displaying simultaneous negative stiffness and negative poisson's ratio properties. *Advanced Materials*, 28(46):10323–10332, 2016.

[12] N Triantafyllidis, MD Nestorović, y MW Schraad. Failure surfaces for finitely strained two-phase periodic solids under general in-plane loading. *Journal of Applied Mechanics*, 73(3):505–515, 2005.

[13] Jean-Claude Michel, O Lopez-Pamies, P Ponte Castañeda, y N Triantafyllidis. Microscopic and macroscopic instabilities in finitely strained porous elastomers. *Journal of the Mechanics and Physics of Solids*, 55 (5):900–938, 2007.

[14] David Restrepo, Nilesh D Mankame, y Pablo D Zavattieri. Phase transforming cellular materials. *Extreme Mechanics Letters*, 4:52–60, 2015.

[15] Tobias Frenzel, Claudio Findeisen, Muamer Kadic, Peter Gumbsch, y Martin Wegener. Tailored buckling microlattices as reusable light-weight shock absorbers. *Advanced Materials*, 28(28):5865–5870, 2016.

[16] Paolo Celli, Stefano Gonella, Vahid Tajeddini, Anastasia Muliana, Saad Ahmed, y Zoubeida Ounaies. Wave control through soft microstructural curling: bandgap shifting, reconfigurable anisotropy and switchable chirality. *Smart Materials and Structures*, 26(3):035001, 2017.

[17] Dennis M Kochmann y Katia Bertoldi. Exploiting microstructural instabilities in solids and structures: from metamaterials to structural transitions. *Applied mechanics reviews*, 69(5):050801, 2017.

[18] Xianglong Yu, Ji Zhou, Haiyi Liang, Zhengyi Jiang, y Lingling Wu. Mechanical metamaterials associated with stiffness, rigidity and compressibility: A brief review. *Progress in Materials Science*, 94:114–173, 2018.

[19] Jian Li, Nitesh Arora, y Stephan Rudykh. Elastic instabilities, microstructure transformations, and pattern formations in soft materials. *Current Opinion in Solid State and Materials Science*, 25(2):100898, 2021.

[20] John Douglas Eshelby. The determination of the elastic field of an ellipsoidal inclusion, and related pro-

blems. *Proceedings of the royal society of London. Series A. Mathematical and physical sciences*, 241 (1226):376–396, 1957.

[21] Rodney Hill. Elastic properties of reinforced solids: some theoretical principles. *Journal of the Mechanics and Physics of Solids*, 11(5):357–372, 1963.

[22] Zvi Hashin y Shmuel Shtrikman. A variational approach to the theory of the elastic behaviour of multiphase materials. *Journal of the Mechanics and Physics of Solids*, 11(2):127–140, 1963.

[23] P Ponte Castañeda. The effective mechanical properties of nonlinear isotropic composites. *Journal of the Mechanics and Physics of Solids*, 39(1):45–71, 1991.

[24] Jean-Claude Michel, Hervé Moulinec, y Pierre Suquet. Effective properties of composite materials with periodic microstructure: a computational approach. *Computer methods in applied mechanics and engineering*, 172(1-4):109–143, 1999.

[25] Karel Matouš, Marc GD Geers, Varvara G Kouznetsova, y Andrew Gillman. A review of predictive nonlinear theories for multiscale modeling of heterogeneous materials. *Journal of Computational Physics*, 330: 192–220, 2017.

[26] Dana Bishara, Yuxi Xie, Wing Kam Liu, y Shaofan Li. A state-of-the-art review on machine learning-based multiscale modeling, simulation, homogenization and design of materials. *Archives of computational methods in engineering*, 30(1):191–222, 2023.

[27] Sebastian Toro, Pablo Javier Sánchez, Pablo Javier Blanco, Eduardo Alberto De Souza Neto, Alfredo Edmundo Huespe, y Raúl Antonino Feijóo. Multiscale formulation for material failure accounting for cohesive cracks at the macro and micro scales. *International Journal of Plasticity*, 76:75–110, 2016.

[28] Reinaldo A Anonis, Javier L Mroginski, y Pablo J Sánchez. Multiscale formulation for saturated porous media preserving the representative volume element size objectivity. *International Journal for Numerical Methods in Engineering*, 125(3):e7381, 2024.

[29] Martin Philip Bendsoe y Ole Sigmund. *Topology optimization: theory, methods, and applications*. Springer Science & Business Media, 2013.

[30] Ole Sigmund y Kurt Maute. Topology optimization approaches: A comparative review. *Structural and multidisciplinary optimization*, 48(6):1031–1055, 2013.

[31] Nico P Van Dijk, Kurt Maute, Matthijs Langelaar, y Fred Van Keulen. Level-set methods for structural topology optimization: a review. *Structural and Multidisciplinary Optimization*, 48:437–472, 2013.

[32] Jikai Liu, Andrew T Gaynor, Shikui Chen, Zhan Kang, Krishnan Suresh, Akihiro Takezawa, Lei Li, Junji Kato, Jinyuan Tang, Charlie CL Wang, et al. Current and future trends in topology optimization for additive manufacturing. *Structural and multidisciplinary optimization*, 57(6):2457–2483, 2018.

[33] Christian Rye Thomsen, Fengwen Wang, y Ole Sigmund. Buckling strength topology optimization of 2d periodic materials based on linearized bifurcation analysis. *Computer Methods in Applied Mechanics and Engineering*, 339:115–136, 2018.

[34] Rolando Yera, Luisina Forzani, Carlos Gustavo Méndez, y Alfredo E Huespe. A topology optimization algorithm based on topological derivative and level-set function for designing phononic crystals. *Engineering Computations*, 39(1):354–379, 2022.

[35] Anna Dalklint, Filip Sjövall, Mathias Wallin, Seth Watts, y Daniel Tortorelli. Computational design of metamaterials with self contact. *Computer Methods in Applied Mechanics and Engineering*, 417:116424, 2023.

[36] AA Romero Onco y Sebastian Miguel Giusti. A robust topological derivative-based multi-material optimization approach: Optimality condition and computational algorithm. *Computer Methods in Applied Mechanics and Engineering*, 366:113044, 2020.

[37] Raymond W Ogden. *Non-linear elastic deformations*. Courier Corporation, 1997.

[38] Klaus Hackl y Ulrich Hoppe. On the calculation of microstructures for inelastic materials using relaxed energies. En *IUTAM Symposium on Computational Mechanics of Solid Materials at Large Strains: Proceedings of the IUTAM Symposium held in Stuttgart, Germany, 20–24 August 2001*, páginas 77–86. Springer, 2003.

[39] Morton E Gurtin, Eliot Fried, y Lallit Anand. *The mechanics and thermodynamics of continua*. Cambridge university press, 2010.

[40] Philippe G Ciarlet. *Mathematical elasticity: Three-dimensional elasticity*. SIAM, 2021.

[41] Charles B Morrey. Quasi-convexity and the lower semicontinuity of multiple integrals. *Pacific Journal of Mathematics*, 2:25–53, 1952.

[42] John M Ball. Convexity conditions and existence theorems in nonlinear elasticity. *Archive for rational mechanics and Analysis*, 63:337–403, 1976.

[43] EA De Souza Neto y RA Feijóo. Variational foundations of multi-scale constitutive models of solid: small and large strain kinematical formulation. *LNCC Research & Development Report*, 16, 2006.

[44] Eduardo A De Souza Neto y Raúl A Feijóo. Variational foundations of large strain multiscale solid constitutive models: kinematical formulation. *Advanced Computational Materials Modeling: From Classical to Multi-Scale Techniques*, páginas 341–378, 2010.

[45] D Perić, EA de Souza Neto, RA Feijóo, M Partovi, y AJ Carneiro Molina. On micro-to-macro transitions for multi-scale analysis of non-linear heterogeneous materials: unified variational basis and finite element implementation. *International Journal for Numerical Methods in Engineering*, 87(1-5):149–170, 2011.

[46] Pablo Javier Sánchez, Pablo Javier Blanco, Alfredo Edmundo Huespe, y RA3043487 Feijoo. Failure-oriented multi-scale variational formulation: micro-structures with nucleation and evolution of softening bands. *Computer Methods in Applied Mechanics and Engineering*, 257:221–247, 2013.

[47] Eduardo Alberto De Souza Neto, Pablo Javier Blanco, Pablo Javier Sánchez, y Raúl Antonino Feijóo. An rve-based multiscale theory of solids with micro-scale inertia and body force effects. *Mechanics of Materials*, 80:136–144, 2015.

[48] Pablo J Blanco, Pablo J Sánchez, Eduardo A de Souza Neto, y Raúl A Feijóo. Variational foundations and generalized unified theory of rve-based multiscale models. *Archives of Computational Methods in Engineering*, 23:191–253, 2016.

[49] Edgardo O Taroco, GR Feijóo, PJ Blanco, y RA Feijóo. Introducción a la formulación variacional de la mecánica. *LNCC Internal Reports*, 2014.

[50] J Mandel. Plasticité classique et viscoplasticité (cism lecture notes, udine, italy), 1971.

[51] AV Cherkaev y LV Gibiansky. Coupled estimates for the bulk and shear moduli of a two-dimensional isotropic elastic composite. *Journal of the Mechanics and Physics of Solids*, 41(5):937–980, 1993.

[52] James G Berryman y Graeme W Milton. Microgeometry of random composites and porous media. *Journal of Physics D: Applied Physics*, 21(1):87, 1988.

[53] Carmelo Giacovazzo. *Fundamentals of crystallography*, volumen 7. Oxford university press, USA, 2002.

[54] John Frederick Nye. *Physical properties of crystals: their representation by tensors and matrices*. Oxford university press, 1985.

[55] Boris K Vainshtein. *Fundamentals of crystals: Symmetry, and methods of structural crystallography*, volumen 1. Springer Science & Business Media, 2013.

[56] Theo Hahn, Uri Shmueli, y JC Wilson Arthur. *International tables for crystallography*, volumen 1. Reidel Dordrecht, 1983.

[57] Antonio André Novotny y Jan Sokołowski. *Topological derivatives in shape optimization*. Springer Science & Business Media, 2012.

[58] Samuel Amstutz y Heiko Andrä. A new algorithm for topology optimization using a level-set method. *Journal of computational physics*, 216(2):573–588, 2006.

[59] Samuel Amstutz, Sebastian Miguel Giusti, Antonio André Novotny, y Eduardo Alberto De Souza Neto. Topological derivative for multi-scale linear elasticity models applied to the synthesis of microstructures. *International Journal for Numerical Methods in Engineering*, 84(6):733–756, 2010.

[60] Rolando Yera, N Rossi, CG Méndez, y Alfredo E Huespe. Topology design of 2d and 3d elastic material microarchitectures with crystal symmetries displaying isotropic properties close to their theoretical limits. *Applied Materials Today*, 18:100456, 2020.

[61] N Rossi, Rolando Yera, Carlos Gustavo Mendez, Sebastian Toro, y Alfredo Edmundo Huespe. Numerical technique for the 3d microarchitecture design of elastic composites inspired by crystal symmetries. *Computer Methods in Applied Mechanics and Engineering*, 359:112760, 2020.

[62] Ole Sigmund. Materials with prescribed constitutive parameters: an inverse homogenization problem. *International Journal of Solids and Structures*, 31(17):2313–2329, 1994.

[63] Habib Ammari, Pierre Calmon, y Ekaterina Iakovleva. Direct elastic imaging of a small inclusion. *SIAM Journal on Imaging Sciences*, 1(2):169–187, 2008.

[64] Quoc Son Nguyen. *Stability and nonlinear solid mechanics*. Wiley, 2000.

[65] Juan M Podestá, CM Méndez, Sebastian Toro, y Alfredo Edmundo Huespe. Symmetry considerations for topology design in the elastic inverse homogenization problem. *Journal of the Mechanics and Physics of Solids*, 128:54–78, 2019.

[66] Ole Sigmund. Tailoring materials with prescribed elastic properties. *Mechanics of materials*, 20(4):351–368, 1995.

[67] Ole Sigmund. A new class of extremal composites. *Journal of the Mechanics and Physics of Solids*, 48(2): 397–428, 2000.

[68] Robert E Newnham. *Properties of materials: anisotropy, symmetry, structure*. Oxford university press, 2005.

[69] Nestor Rossi, Juan M Podestá, Facundo Bre, Carlos G Méndez, y Alfredo E Huespe. A microarchitecture design methodology to achieve extreme isotropic elastic properties of composites based on crystal symmetries. *Structural and Multidisciplinary Optimization*, 63(5):2459–2472, 2021.

[70] Graeme W. Milton y Andrej V. Cherkaev. Which Elasticity Tensors are Realizable? *Journal of Engineering Materials and Technology*, 117(4):483–493, 10 1995. ISSN 0094-4289. doi: 10.1115/1.2804743. URL https://doi.org/10.1115/1.2804743.

[71] S Vigdergauz. Energy-minimizing inclusions in a planar elastic structure with macroisotropy. *Structural optimization*, 17:104–112, 1999.

[72] Nestor Rossi, Carlos G Mendez, y Alfredo Huespe. A new efficient methodology for the analysis of mechanical metamaterials with elastic instabilities. *WCCM-APCOM 2022*, 500, 2022.

[73] Nestor Rossi, Carlos G Méndez, y AE Huespe. Surrogate model for a mechanical metamaterial undergoing microstructure instabilities and phase transformations. *International Journal of Mechanical Sciences*, 243: 107913, 2023.

[74] Nestor Rossi, Ignacio Romero, y Alfredo E Huespe. On the limit behavior of lattice-type metamaterials with bi-stable mechanisms. *En revisión en: International Journal of Mechanical Sciences*, 2024.

[75] C Carstensen. Nonconvex energy minimization and relaxation in computational material science. En *IUTAM Symposium on Computational Mechanics of Solid Materials at Large Strains: Proceedings of the IUTAM Symposium held in Stuttgart, Germany, 20–24 August 2001*, páginas 3–20. Springer, 2003.

[76] JL Ericksen. The cauchy and born hypotheses for crystals. *Mechanics and mathematics of crystals: selected papers of JL Ericksen*, página 117, 2005.

[77] Krister Svanberg. The method of moving asymptotes—a new method for structural optimization. *International journal for numerical methods in engineering*, 24(2):359–373, 1987.

[78] Kai A James y Haim Waisman. Layout design of a bi-stable cardiovascular stent using topology optimization. *Computer Methods in Applied Mechanics and Engineering*, 305:869–890, 2016.

[79] Hao Deng, Lin Cheng, Xuan Liang, Devlin Hayduke, y Albert C To. Topology optimization for energy dissipation design of lattice structures through snap-through behavior. *Computer Methods in Applied Mechanics and Engineering*, 358:112641, 2020.

[80] G Puglisi y Lev Truskinovsky. Mechanics of a discrete chain with bi-stable elements. *Journal of the Mechanics and Physics of Solids*, 48(1):1–27, 2000.

[81] Itamar Benichou y Sefi Givli. Structures undergoing discrete phase transformation. *Journal of the Mechanics and Physics of Solids*, 61(1):94–113, 2013.

[82] Peter Wriggers y Juan C Simo. A general procedure for the direct computation of turning and bifurcation points. *International journal for numerical methods in engineering*, 30(1):155–176, 1990.

[83] Michael Anthony Crisfield. *Non-linear finite element analysis of solids and structures*. John Wiley & Sons, 1991.

[84] Esben Lindgaard y Jonas Dahl. On compliance and buckling objective functions in topology optimization of snap-through problems. *Structural and Multidisciplinary Optimization*, 47:409–421, 2013.

[85] Qi Chen, Xianmin Zhang, Hongchuan Zhang, Benliang Zhu, y Bicheng Chen. Topology optimization of bistable mechanisms with maximized differences between switching forces in forward and backward direction. *Mechanism and Machine Theory*, 139:131–143, 2019.

[86] R Kemmler, A Lipka, y E Ramm. Large deformations and stability in topology optimization. *Structural and Multidisciplinary Optimization*, 30:459–476, 2005.

[87] Fengwen Wang, Boyan Stefanov Lazarov, Ole Sigmund, y Jakob Søndergaard Jensen. Interpolation scheme for fictitious domain techniques and topology optimization of finite strain elastic problems. *Computer Methods in Applied Mechanics and Engineering*, 276:453–472, 2014.

[88] TE Bruns y Ole Sigmund. Toward the topology design of mechanisms that exhibit snap-through behavior. *Computer Methods in Applied Mechanics and Engineering*, 193(36-38):3973–4000, 2004.

[89] Jiangnan Ding y Martin van Hecke. Sequential snapping and pathways in a mechanical metamaterial. *The Journal of Chemical Physics*, 156(20), 2022.

[90] Xiaojun Tan, Bing Wang, Shaowei Zhu, Shuai Chen, Kaili Yao, Peifei Xu, Linzhi Wu, y Yuguo Sun. Novel multidirectional negative stiffness mechanical metamaterials. *Smart Materials and Structures*, 29(1): 015037, 2019.

[91] Suihan Liu, Ali Imani Azad, y Rigoberto Burgueño. Architected materials for tailorable shear behavior with energy dissipation. *Extreme Mechanics Letters*, 28:1–7, 2019.

[92] Hoon Yeub Jeong, Soo-Chan An, In Cheol Seo, Eunseo Lee, Sangho Ha, Namhun Kim, y Young Chul Jun. 3d printing of twisting and rotational bistable structures with tuning elements. *Scientific reports*, 9(1):324, 2019.

[93] Ahmad Rafsanjani y Damiano Pasini. Bistable auxetic mechanical metamaterials inspired by ancient geometric motifs. *Extreme Mechanics Letters*, 9:291–296, 2016.

[94] Sicong Shan, Sung H Kang, Jordan R Raney, Pai Wang, Lichen Fang, Francisco Candido, Jennifer A Lewis, y Katia Bertoldi. Multistable architected materials for trapping elastic strain energy. *Advanced Materials*, 27(29):4296–4301, 2015.

[95] Ahmad Rafsanjani, Abdolhamid Akbarzadeh, y Damiano Pasini. Snapping mechanical metamaterials under tension. *arXiv preprint arXiv:1612.05987*, 2016.

[96] Shuai Chen, Bing Wang, Shaowei Zhu, Xiaojun Tan, Jiqiang Hu, Xu Lian, Lianchao Wang, y Linzhi Wu. A novel composite negative stiffness structure for recoverable trapping energy. *Composites Part A: Applied science and manufacturing*, 129:105697, 2020.

[97] G Puglisi y L Truskinovsky. A mechanism of transformational plasticity. *Continuum Mechanics and Thermodynamics*, 14:437–457, 2002.

[98] G Puglisi y L Truskinovsky. Rate independent hysteresis in a bi-stable chain. *Journal of the Mechanics and Physics of Solids*, 50(2):165–187, 2002.

[99] Giovanni Puglisi y Lev Truskinovsky. Thermodynamics of rate-independent plasticity. *Journal of the Mechanics and Physics of Solids*, 53(3):655–679, 2005.

[100] Yunlan Zhang, David Restrepo, Mirian Velay-Lizancos, Nilesh D Mankame, y Pablo D Zavattieri. Energy dissipation in functionally two-dimensional phase transforming cellular materials. *Scientific reports*, 9(1): 12581, 2019.

[101] Romik Khajehtourian y Dennis M Kochmann. A continuum description of substrate-free dissipative reconfigurable metamaterials. *Journal of the Mechanics and Physics of Solids*, 147:104217, 2021.

[102] Jin Qiu, Jeffrey H Lang, y Alexander H Slocum. A curved-beam bistable mechanism. *Journal of microelectromechanical systems*, 13(2):137–146, 2004.

[103] A.C. Pipkin. Elastic materials with two preferred states. *The Quarterly Journal of Mechanics and Applied Mathematics*, 44(1):1–15, 1991.

[104] R.V. Kohn. The relaxation of a double-well energy. *Continuum Mechanics and Thermodynamics*, 3(3): 193–236, 1991.

[105] Rohan Abeyaratne y James K Knowles. *Evolution of phase transitions: a continuum theory*. Cambridge University Press, 2006.

[106] Pedro Ponte Castañeda. Soft elastic composites: Microstructure evolution, instabilities and relaxed response by domain formation. *European Journal of Mechanics-A/Solids*, 100:105033, 2023.

[107] Chenhui Ren, Deqing Yang, y Haoxing Qin. Mechanical performance of multidirectional buckling-based negative stiffness metamaterials: an analytical and numerical study. *Materials*, 11(7):1078, 2018.

[108] E. Prince; Boston ; London, editor. *International Tables for Crystallography. Volume C, Mathematical, Physical and Chemical Tables. Dordrecht*, 2004. Published for the International Union of Crystallography by Kluwer Academic Publishers.

[109] J. Sólyom. *Fundamentals of the Physics of Solids: Volume 1: Structure and Dynamics*. Springer Science & Business Media, 2007.

[110] S. Torquato. Optimal design of heterogeneous materials. *Annual Review of Materials Rresearch*, 40:101–129, 2010.

[111] M. Osanov y J.K. Guest. Topology optimization for architected materials design. *Annual Review of Materials Science*, 46:211–233, 2016.

[112] GW Milton. Stiff competition. *Nature*, 564(7734):E1, 2018.

[113] E. Andreassen y O. Lazarov, B.S.and Sigmund. Design of manufacturable 3D extremal elastic microstructure. *Mechanics of Materials*, 69(1):1–10, 2014.

[114] Juan Manuel Podestá, Carlos Gustavo Mendez, Sebastian Toro, Alfredo Edmundo Huespe, y Javier Oliver. Material design of elastic structures using voronoi cells. *International Journal for Numerical Methods in Engineering*, 115(3):269–292, 2018.

[115] C.G. Méndez, J.M. Podestá, S. Toro, A.E. Huespe, y J. Oliver. Making use of symmetries in the three-dimensional elastic inverse homogenization problem. *Journal for Multiscale Computational Engineering*, 17:261–280, 2019.

[116] R. Yera, N. Rossi, C. Méndez, y A.E. Huespe. *Three-dimensional material microstructures dataset displaying extreme isotropic elastic properties*. 2019. Mendeley Data, v1

http://dx.doi.org/10.17632/cc2hgr9kvh.2.

[117] M.F. Thorpe y I. Jasiuk. New results in the theory of elasticity for two-dimensional composites. *Proceedings of the Royal Society of London. Series A: Mathematical and Physical Sciences*, 438(1904):531–544, 1992.

[118] E. Hitzer y C. Perwass. Visualization of fundamental symmetries in nature. En *Proceedings of Fuzzy System Symposium (FSS 2009), Tsukuba, Japan, 14-16 Jul.*, 2009. http://spacegroup.info/.

[119] D.J. Eyre y G.W. Milton. A fast numerical scheme for computing the response of composites using grid refinement. *The European Physical Journal-Applied Physics*, 6(1):41–47, 1999.

[120] G.W. Milton y M. Camar-Eddine. Near optimal pentamodes as a tool for guiding stress while minimizing compliance in 3d-printed materials: A complete solution to the weak g-closure problem for 3d-printed materials. *Journal of the Mechanics and Physics of Solids*, 114:194–208, 2018.

[121] I. Ostanin, G. Ovchinnikov, D.C. Tozoni, y D. Zorin. A parametric class of composites with a large achievable range of effective elastic properties. *Journal of the Mechanics and Physics of Solids*, 118:204–217, 2018.

[122] S. Meille y E.J. Garboczi. Linear elastic properties of 2d and 3d models of porous materials made from elongated objects. *Modelling and Simulation in Materials Science and Engineering*, 9(5):371, 2001.

[123] X. Ren, R. Das, P. Tran, T.D. Ngo, y Y.M. Xie. Auxetic metamaterials and structures: A review. *Smart Materials and Structures*, 2018.

[124] D. Attard y J.N. Grima. A three-dimensional rotating rigid units network exhibiting negative poisson's ratios. *Physica Status Solidi (b)*, 249(7):1330–1338, 2012.

[125] G.W. Milton. New examples of three-dimensional dilational materials. *physica status solidi (b)*, 252(7): 1426–1430, 2015.

[126] A. Alderson, K.L. Alderson, D. Attard, K.E. Evans, R. Gatt, J.N. Grima, W. Miller, N. Ravirala, C.W. Smith, y K. Zied. Elastic constants of 3-, 4-and 6-connected chiral and anti-chiral honeycombs subject to uniaxial in-plane loading. *Composites Science and Technology*, 70(7):1042–1048, 2010.

[127] Y.J. Chen, F. Scarpa, Y.J Liu, y J.S. Leng. Elasticity of anti-tetrachiral anisotropic lattices. *International Journal of Solids and Structures*, 50(6):996–1004, 2013.

[128] M. Kadic, T. Bückmann, R. Schittny, P. Gumbsch, y M. Wegener. Pentamode metamaterials with independently tailored bulk modulus and mass density. *Physical Review Applied*, 2(5):054007, 2014.

[129] G. Allaire, F. De Gournay, F. Jouve, y A. Toader. Structural optimization using topological and shape sensitivity via a level set method. *Control and cybernetics*, 34(1):59, 2005.

[130] H. Moulinec y P. Suquet. A numerical method for computing the overall response of nonlinear composites with complex microstructure. *Computer methods in applied mechanics and engineering*, 157(1-2):69–94, 1998.

[131] I. Cohen. Simple algebraic approximations for the effective elastic moduli of cubic arrays of spheres. *Journal of the Mechanics and Physics of Solids*, 52(9):2167–2183, 2004.

[132] C.G. Lopes, R.B. dos Santos, y A.A. Novotny. Topological derivative-based topology optimization of structures subject to multiple load-cases. *Latin American Journal of Solids and Structures*, 12(5):834–860, 2015.

[133] S. Amstutz. Analysis of a level set method for topology optimization. *Optimization Methods and Software*, 26(4-5):555–573, 2011.

[134] K. K. Saxena, R. Das, y E.P. Calius. Three decades of auxetics research- materials with negative poisson's ratio: a review. *Adv. Eng. Mater.*, 18(11):1847–1870, 2016.

[135] L. Cabras y M. Brun. Auxetic two-dimensional lattices with poisson's ratio arbitrarily close to- 1. En *Proceedings of the Royal Society of London A: Mathematical, Physical and Engineering Sciences*, volumen 470, páginas 1–23, 2014.

[136] Graeme Milton, Marc Briane, y Davit Harutyunyan. On the possible effective elasticity tensors of 2-dimensional and 3-dimensional printed materials. *Mathematics and Mechanics of Complex Systems*, 5(1): 41–94, 2017. doi: 10.2140/memocs.2017.5.41.

[137] S.M. Giusti. *Análise de sensibilidade topológica em modelos constitutivos multiescalas*. PhD thesis, Laboratório Nacional de Computa cão Científica, LNCC, Brazil, 2009.

[138] S.M. Giusti. Personal communication. 2019.

[139] J.J. Moré y D.J. Thuente. Line search algorithms with guaranteed sufficient decrease. *ACM Transactions on Mathematical Software*, 20:286–307, 1994.

[140] C. Imediegwu, R. Murphy, R. Hewson, y M. Santer. Multiscale structural optimization towards three-dimensional printable structures. *Structural and Multidisciplinary Optimization*, 60(2):513–525, 2019.

[141] Z Hashin. On elastic behaviour of fibre reinforced materials of arbitrary transverse phase geometry. *Journal of the Mechanics and Physics of Solids*, 13(3):119–134, 1965.

[142] A.N. Norris. Acoustic cloaking theory. En *Proceedings of the Royal Society of London A: Mathematical, Physical and Engineering Sciences*, volumen 464, páginas 2411–2434, 2008.

[143] Y. Cheng, F. Yang, J.Y. Xu, y X.J. Liu. A multilayer structured acoustic cloak with homogeneous isotropic materials. *Appl. Phys. Lett.*, 92(15):151913, 2008.

[144] C.N. Layman, C.J. Naify, T.P. Martin, D.C. Calvo, y G.J. Orris. Highly anisotropic elements for acoustic pentamode applications. *Phys. Rev. Lett.*, 111(2):024302, 2013.

[145] G.W. Milton. Planar polycrystals with extremal bulk and shear moduli. *arXiv preprint arXiv:2002.08788*, 2020.

[146] Y. Wang y O. Sigmund. Quasiperiodic mechanical metamaterials with extreme isotropic stiffness. *Extreme Mechanics Letters*, 34:100596, 2020. doi: 10.1016/j.eml.2019.100596.

[147] Zvi Hashin. The elastic moduli of heterogeneous materials. *J. Appl. Mech.*, 29(1):143–150, 1962. doi: 10.1115/1.3636446.

[148] AN Norris. A differential scheme for the effective moduli of composites. *Mech. Mater.*, 4(1):1–16, 1985. doi: 10.1016/0167-6636(85)90002-X.

[149] GW Milton. Modelling the properties of composites by laminates. En *Homogenization and effective moduli of materials and media*, páginas 150–174. Springer, 1986. doi: 10.1007/978-1-4613-8646-9_7.

[150] Gilles A Francfort y François Murat. Homogenization and optimal bounds in linear elasticity. *Archive for Rational mechanics and Analysis*, 94:307–334, 1986.

[151] Graeme W Milton. Some open problems in the theory of composites. *arXiv preprint arXiv:2008.03394*, 2020.

[152] Sahab Babaee, Jongmin Shim, James C Weaver, Elizabeth R Chen, Nikita Patel, y Katia Bertoldi. 3d soft metamaterials with negative poisson's ratio. *Adv. Mater.*, 25(36):5044–5049, 2013. doi: 10.1002/adma.201301986.

[153] Tiemo Bückmann, Robert Schittny, Michael Thiel, Muamer Kadic, Graeme W Milton, y Martin Wegener. On three-dimensional dilational elastic metamaterials. *New J. Phys.*, 16(3):033032, 2014. doi: 10.1088/1367-2630/16/3/033032.

[154] Matthieu Rupin, Philippe Roux, Geoffroy Lerosey, y Fabrice Lemoult. Symmetry issues in the hybridization of multi-mode waves with resonators: an example with lamb waves metamaterial. *Sci. Rep.*, 5:13714, 2015. doi: 10.1038/srep13714.

[155] Zilong Wu y Yuebing Zheng. Moiré chiral metamaterials. *Adv. Opt. Mater.*, 5(16):1700034, 2017. doi: 10.1002/adom.201700034.

[156] Tobias Frenzel, Muamer Kadic, y Martin Wegener. Three-dimensional mechanical metamaterials with a twist. *Science*, 358(6366):1072–1074, 2017. doi: 10.1126/science.aao4640.

[157] Xiaoyue Ni, Xiaogang Guo, Jiahong Li, Yonggang Huang, Yihui Zhang, y John A Rogers. 2d mechanical metamaterials with widely tunable unusual modes of thermal expansion. *Adv. Mater.*, 31(48):1905405, 2019. doi: 10.1002/adma.201905405.

[158] Tobias Frenzel, Julian Köpfler, Erik Jung, Muamer Kadic, y Martin Wegener. Ultrasound experiments on acoustical activity in chiral mechanical metamaterials. *Nat. Commun.*, 10(1):1–6, 2019. doi: 10.1038/s41467-019-11366-8.

[159] L. Xia y P.r Breitkopf. Design of materials using topology optimization and energy-based homogenization approach in matlab. *Structural and Multidisciplinary Optimization*, 52(6):1229–1241, 2015.

[160] S. Amstutz. Connections between topological sensitivity analysis and material interpolation schemes in topology optimization. *Structural and Multidisciplinary Optimization*, 43(6):755–765, 2011.

[161] S. M. Giusti, Z. Mróz, A.A. Novotny, y J. Sokołowski. Topology design of thermomechanical actuators. *Structural and Multidisciplinary Optimization*, 55(5):1575–1587, 2017.

[162] K. Deb, A. Pratap, S. Agarwal, y T. Meyarivan. A fast and elitist multiobjective genetic algorithm: Nsga-ii. *IEEE Trans. Evol. Comput.*, 6(2):182–197, April 2002. ISSN 1941-0026. doi: 10.1109/4235.996017.

[163] N. Rossi, J.M. Podestá, F. Bre, C. Méndez, y A.E. Huespe. Dataset of parameterized isotropic microstructures attaining extreme properties. *Mendeley Data, v1 http://dx.doi.org/10.17632/hcpvmnwm4p.1*, 2020. doi: 10.17632/hcpvmnwm4p.1.

[164] Roderic S Lakes, T Lee, A Bersie, y Yun-Che Wang. Extreme damping in composite materials with negative-stiffness inclusions. *Nature*, 410(6828):565–567, 2001.

[165] Charles S Wojnar y Dennis M Kochmann. A negative-stiffness phase in elastic composites can produce stable extreme effective dynamic but not static stiffness. *Philosophical Magazine*, 94(6):532–555, 2014.

[166] Sicong Shan, Sung H Kang, Pai Wang, Cangyu Qu, Samuel Shian, Elizabeth R Chen, y Katia Bertoldi. Harnessing multiple folding mechanisms in soft periodic structures for tunable control of elastic waves.

*Advanced Functional Materials*, 24(31):4935–4942, 2014.

[167] David R Johnson, RL Harne, y KW Wang. A disturbance cancellation perspective on vibration control using a bistable snap-through attachment. *Journal of Vibration and Acoustics*, 136(3):031006, 2014.

[168] RL Harne y KW Wang. A bifurcation-based coupled linear-bistable system for microscale mass sensing. *Journal of Sound and Vibration*, 333(8):2241–2252, 2014.

[169] A Nuñez-Labielle, J Cante, Alfredo Edmundo Huespe, y J Oliver. Towards shock absorbing hyperelastic metamaterial design.(i) macroscopic scale: Computational shock-capturing. *Computer Methods in Applied Mechanics and Engineering*, 393:114732, 2022.

[170] Dixon M Correa, Timothy Klatt, Sergio Cortes, Michael Haberman, Desiderio Kovar, y Carolyn Seepersad. Negative stiffness honeycombs for recoverable shock isolation. *Rapid Prototyping Journal*, 21(2):193–200, 2015.

[171] Chan Soo Ha, Roderic S Lakes, y Michael E Plesha. Design, fabrication, and analysis of lattice exhibiting energy absorption via snap-through behavior. *Materials & Design*, 141:426–437, 2018.

[172] Jorge Nocedal y Stephen J Wright. *Numerical optimization*. Springer, 1999.

[173] A. Cutolo, S. Palumbo, A.R. Carotenuto, E. Sacco, y M. Fraldi. A class of periodic lattices for tuning elastic instabilities. *Extreme Mechanics Letters*, 55:101839, 2022.

[174] L. Wang, X. Tan, S. Zhu, B. Wang, S. Li, Y. Zou, y S. Chen. Directional instability-driven strain-dependent 3d auxetic metamaterials. *International Journal of Mechanical Sciences*, 199:106408, 2021.

[175] S. Rudykh y M.C. Boyce. Transforming wave propagation in layered media via instability-induced interfacial wrinkling. *Physical Review letters*, 112(3):034301, 2014.

[176] R.K. Pal, M. Ruzzene, y J.J. Rimoli. Tunable wave propagation by varying prestrain in tensegrity-based periodic media. *Extreme Mechanics Letters*, 22:149–156, 2018.

[177] Y. Liu, T. Liang, Y. Fu, Y.X. Xie, y Y.S. Wang. A novel buckling pattern in periodically porous elastomers with applications to elastic wave regulations. *Extreme Mechanics Letters*, página 101781, 2022.

[178] G. Wu, Y. Xia, y S. Yang. Buckling, symmetry breaking, and cavitation in periodically micro-structured hydrogel membranes. *Soft Matter*, 10(9):1392–1399, 2014.

[179] M. Pezzulla, S.A. Shillig, P. Nardinocchi, y D.P. Holmes. Morphing of geometric composites via residual swelling. *Soft Matter*, 11(29):5812–5820, 2015.

[180] M. Gavazzoni, S. Foletti, y D. Pasini. Cyclic response of 3d printed metamaterials with soft cellular architecture: the interplay between as-built defects, material and geometric non-linearity. *Journal of the Mechanics and Physics of Solids*, 158:104688, 2022.

[181] Z. Song, H. Liang, H. Ding, y M. Ma. Structure design and mechanical properties of a novel anti-collision system with negative poisson's ratio core. *International Journal of Mechanical Sciences*, página 107864, 2022.

[182] B. Fedelich y G. Zanzotto. Hysteresis in discrete systems of possibly interacting elements with a double-well energy. *Journal of Nonlinear Science*, 2(3):319–342, 1992.

[183] S. Pagano y R. Paroni. A simple model for phase transitions: from the discrete to the continuum problem. *Quarterly of Applied Mathematics*, 61(1):89–109, 2003.

[184] H. Ma, K. Wang, H. Zhao, W. Shi, J. Xue, Y. Zhou, Q. Li, G. Wang, y B. Yan. Energy dissipation and shock isolation using novel metamaterials. *International Journal of Mechanical Sciences*, 228:107464, 2022.

[185] S. Zhu, B. Wang, L. Chen, X. Tan, y L. Ma. Enhance the energy dissipation ability of sleeve-type negative stiffness structures via a phase-difference mechanism. *International Journal of Mechanical Sciences*, 213: 106803, 2022.

[186] Z. Wu, R.L. Harne, y K.W. Wang. Energy harvester synthesis via coupled linear-bistable system with multistable dynamics. *Journal of Applied Mechanics*, 81(6), 2014.

[187] J.E. Pechac y M.J. Frazier. Metamaterial design strategy for mechanical energy absorption under general loading. *Extreme Mechanics Letters*, 51:101580, 2022.

[188] K. Yang, R.L. Harne, K.W. Wang, y H. Huang. Dynamic stabilization of a bistable suspension system attached to a flexible host structure for operational safety enhancement. *Journal of Sound and Vibration*, 333(24):6651–6661, 2014.

[189] K. Yang, R.L. Harne, K.W. Wang, y H. Huang. Investigation of a bistable dual-stage vibration isolator under harmonic excitation. *Smart materials and structures*, 23(4):045033, 2014.

[190] I. Benichou y S. Givli. Force-sensitive metamaterials for vibration mitigation and mechanical protection. *Extreme Mechanics Letters*, 40:100932, 2020.

[191] C. Ren, Q. Li, y D. Yang. Quasi-static and sound insulation performance of a multifunctional cylindrical cellular shell with bidirectional negative-stiffness metamaterial cores. *International Journal of Mechanical*

*Sciences*, 180:105662, 2020.

[192] N. Nadkarni, C. Daraio, R. Abeyaratne, y D.M. Kochmann. Universal energy transport law for dissipative and diffusive phase transitions. *Physical Review B*, 93(10):104109, 2016.

[193] R. Khajehtourian y D.M. Kochmann. Phase transformations in substrate-free dissipative multistable metamaterials. *Extreme Mechanics Letters*, 37:100700, 2020.

[194] I. Benichou y S. Givli. Rate dependent response of nanoscale structures having a multiwell energy landscape. *Physical Review letters*, 114(9):095504, 2015.

[195] F. Xin y T.J. Lu. Modulation of acoustomechanical instability and bifurcation behavior of soft materials. *Scientific reports*, 8(1):1–10, 2018.

[196] H. Yasuda, L.M. Korpas, y J.R. Raney. Transition waves and formation of domain walls in multistable mechanical metamaterials. *Physical Review Applied*, 13(5):054067, 2020.

[197] B. Chen, L. Chen, B. Du, H. Liu, W. Li, y D. Fang. Novel multifunctional negative stiffness mechanical metamaterial structure: Tailored functions of multi-stable and compressive mono-stable. *Composites Part B: Engineering*, 204:108501, 2021.

[198] S.S. He, X. Yin, L.Y. Zhang, Z.Y. Gao, y G.K. Xu. Directional snapping instability in a bistable tensegrity under uniaxial loads. *Composite Structures*, 283:115153, 2022.

[199] K. Tan, L. Chen, S. Yang, y Q. Deng. Dynamic snap-through instability and damped oscillation of a flat arch of hard magneto-active elastomers. *International Journal of Mechanical Sciences*, 230:107523, 2022.

[200] A. Rafsanjani, A. Akbarzadeh, y D. Pasini. Snapping mechanical metamaterials under tension. *Advanced Materials*, 27(39):5931–5935, 2015.

[201] T.R. Giri y R. Mailen. Controlled snapping sequence and energy absorption in multistable mechanical metamaterial cylinders. *International Journal of Mechanical Sciences*, 204:106541, 2021.

[202] Q. Li, D. Yang, C. Ren, y X. Mao. A systematic group of multidirectional buckling-based negative stiffness metamaterials. *International Journal of Mechanical Sciences*, 232:107611, 2022.

[203] H. Ma, K. Wang, H. Zhao, R. Mu, y B. Yan. A reusable metastructure for tri-directional energy dissipation. *International Journal of Mechanical Sciences*, 214:106870, 2022.

[204] X. Shang, L. Liu, A. Rafsanjani, y D. Pasini. Durable bistable auxetics made of rigid solids. *Journal of Materials Research*, 33(3):300–308, 2018.

[205] L. Jin, R. Khajehtourian, J. Mueller, A. Rafsanjani, V. Tournat, K. Bertoldi, y D.M. Kochmann. Guided transition waves in multistable mechanical metamaterials. *Proceedings of the National Academy of Sciences*, 117(5):2319–2325, 2020.

[206] L. Herrnböck y P. Steinmann. Homogenization of fully nonlinear rod lattice structures: on the size of the rve and micro structural instabilities. *Computational Mechanics*, 69(4):947–964, 2022.

[207] M. Jamshidian, N. Boddeti, D. W Rosen, y O. Weeger. Multiscale modelling of soft lattice metamaterials: Micromechanical nonlinear buckling analysis, experimental verification, and macroscale constitutive behaviour. *International Journal of Mechanical Sciences*, 188:105956, 2020.

[208] M. Vangbo. An analytical analysis of a compressed bistable buckled beam. *Sensors and Actuators A: Physical*, 69(3):212–216, 1998.

[209] P. Cazottes, A. Fernandes, J. Pouget, y M. Hafez. Bistable buckled beam: modeling of actuating force and experimental validations. *Journal of Mechanical Design*, 131(10), 2009.

[210] B. Camescasse, A. Fernandes, y J. Pouget. Bistable buckled beam: Elastica modeling and analysis of static actuation. *International Journal of Solids and Structures*, 50(19):2881–2893, 2013.

[211] G. Chen, F. Ma, G. Hao, y W. Zhu. Modeling large deflections of initially curved beams in compliant mechanisms using chained beam constraint model. *Journal of Mechanisms and Robotics*, 11(1):011002, 2019.

[212] J.N. Reddy. *An introduction to the finite element method*, volumen 1221. McGraw-Hill New York, 2004.

[213] Manfredo P Do Carmo. *Differential geometry of curves and surfaces: revised and updated second edition*. Courier Dover Publications, 2016.

[214] L. Wu, Y. Wang, K. Chuang, F. Wu, Q. Wang, W. Lin, y H. Jiang. A brief review of dynamic mechanical metamaterials for mechanical energy manipulation. *Materials Today*, 44:168–193, 2021.

[215] R. Azulay, C. Combescure, y J. Dirrenberger. Instability-induced pattern generation in architectured materials—a review of methods. *International Journal of Solids and Structures*, página 112240, 2023.

[216] K. Liang, Y. Wang, Y. Luo, A. Takezawa, X. Zhang, y Z. Kang. Programmable and multistable metamaterials made of precisely tailored bistable cells. *Materials & Design*, 227:111810, 2023.

[217] J. Hua, Y. Zhou, y C. Q. Chen. Design and analysis of a tunable multistable mechanical metamaterial. *International Journal of Mechanical Sciences*, 272:109170, 2024.

[218] B. Xiao, Y. Liu, W. Xu, R. Wei, M. Chen, y H. Jiang. A bistable honeycomb mechanical metamaterial with transformable poisson's ratio and tunable vibration isolation properties. *Thin-Walled Structures*, página 111718, 2024.

[219] C. Morris, L. Bekker, C. Spadaccini, M. Haberman, y C. Seepersad. Tunable mechanical metamaterial with constrained negative stiffness for improved quasi-static and dynamic energy dissipation. *Advanced Engineering Materials*, 21(7):1900163, 2019.

[220] S. Katz y S. Givli. Solitary waves in a bistable lattice. *Extreme Mechanics Letters*, 22:106–111, 2018.

[221] M. Hwang y A. F. Arrieta. Topological wave energy harvesting in bistable lattices. *Smart Materials and Structures*, 31(1):015021, 2021.

[222] K. Zhang, L. Qi, P. Zhao, C. Zhao, y Z. Deng. Buckling induced negative stiffness mechanical metamaterial for bandgap tuning. *Composite Structures*, 304:116421, 2023.

[223] T. Jiang, Q. Han, y C. Li. Design and compression-induced bandgap evolution of novel polygonal negative stiffness metamaterials. *International Journal of Mechanical Sciences*, 261:108658, 2024.

[224] J. Meaud y C. Kaikai. Tuning elastic wave propagation in multistable architected materials. *International Journal of Solids and Structures*, 122:69–80, 2017.

[225] C. Wang y M. J. Frazier. Phase transitions in hierarchical, multi-stable metamaterials. *Extreme Mechanics Letters*, 64:102068, 2023.

[226] R. Gao, S. Guo, X. Tian, y S. Liu. A negative-stiffness based 1d metamaterial for bidirectional buffering and energy absorption with state recoverable characteristic. *Thin-Walled Structures*, 169:108319, 2021.

[227] A. Montalbano, G. M. Fadel, y G. Li. Design for energy absorption using snap-through bistable metamaterials. *Mechanics Based Design of Structures and Machines*, 51(3):1368–1386, 2023.

[228] E.K.H. Salje, X. Ding, Z. Zhao, T. Lookman, y A. Saxena. Thermally activated avalanches: Jamming and the progression of needle domains. *Physical Review B*, 83(10):104109, 2011.

[229] S. Nitecki y S. Givli. The mechanical behavior of 2-d lattices with bi-stable springs. *Journal of the Mechanics and Physics of Solids*, 157:104634, 2021.

[230] B. Halphen y Q. S. Nguyen. Sur les matériaux standard généralisés. *Journal de mécanique*, 14:13–63, 1975.

[231] G.A. Maugin. *The thermomechanics of plasticity and fracture*, volumen 7. Cambridge university press, 1992.

[232] C. Miehe, J. Schotte, y M. Lambrecht. Homogenization of inelastic solid materials at finite strains based on incremental minimization principles. application to the texture analysis of polycrystals. *Journal of the Mechanics and Physics of Solids*, 50(10):2123–2167, 2002.

[233] G. Friesecke y F. Theil. Validity and failure of the cauchy-born hypothesis in a two-dimensional mass-spring lattice. *Journal of Nonlinear Science*, 12:445–478, 2002.

[234] S. Müller. *Variational models for microstructure and phase transitions*, páginas 85–210. Springer Berlin Heidelberg, 1999. doi: 10.1007/BFb0092670.

[235] S. Bartels, C. Carstensen, S. Conti, K. Hackl, U. Hoppe, y A. Orlando. Relaxation and the computation of effective energies and microstructures in solid mechanics. En *Analysis, modeling and simulation of multiscale problems*, páginas 197–224. Springer, 2006.

[236] C. Carstensen, K. Hackl, y A. Mielke. Non–convex potentials and microstructures in finite–strain plasticity. *Proceedings of the royal society of London. Series A: mathematical, physical and engineering sciences*, 458 (2018):299–317, 2002.

[237] S. Bartels, C. Carstensen, K. Hackl, y U. Hoppe. Effective relaxation for microstructure simulations: algorithms and applications. *Computer Methods in Applied Mechanics and Engineering*, 193(48-51):5143–5175, 2004.

[238] C. Miehe y M. Lambrecht. Analysis of microstructure development in shearbands by energy relaxation of incremental stress potentials: Large-strain theory for standard dissipative solids. *International Journal for Numerical Methods in Engineering*, 58(1):1–41, 2003.

[239] M. Lambrecht, C. Miehe, y J. Dettmar. Energy relaxation of non-convex incremental stress potentials in a strain-softening elastic–plastic bar. *International Journal of Solids and Structures*, 40(6):1369–1391, 2003.

[240] E. Gürses y C. Miehe. On evolving deformation microstructures in non-convex partially damaged solids. *Journal of the Mechanics and Physics of Solids*, 59(6):1268–1290, 2011.

[241] R.N. Abeyaratne y J.K. Knowles. On the dissipative response due to discontinuous strains in bars of unstable elastic material. *International journal of solids and structures*, 24(10):1021–1044, 1988.

[242] R.N. Abeyaratne y J.K. Knowles. Kinetic relations and the propagation of phase boundaries in solids. *Archive for rational mechanics and analysis*, 114:119–154, 1991.

[243] A. Ghasemi y W. Gao. A method to predict energy barriers in stress modulated solid–solid phase transitions.

*Journal of the Mechanics and Physics of Solids*, 137:103857, 2020.

[244] G. Wan, S. J. Avis, Z. Wang, X. Wang, H. Kusumaatmaja, y T. Zhang. Finding transition state and minimum energy path of bistable elastic continua through energy landscape explorations. *Journal of the Mechanics and Physics of Solids*, 183:105503, 2024.

[245] A.C. Souza, E.N. Mamiya, y N. Zouain. Three-dimensional model for solids undergoing stress-induced phase transformations. *European Journal of Mechanics-A/Solids*, 17(5):789–806, 1998.

[246] F. Auricchio, R.L. Taylor, y J. Lubliner. Shape-memory alloys: macromodelling and numerical simulations of the superelastic behavior. *Computer Methods in Applied Mechanics and Engineering*, 146(3-4):281–312, 1997.

[247] K. Bhattacharya. Theory of martensitic microstructure and the shape-memory effect. *Available from author: bhatta@ co. caltech. edu*, 1998.

[248] A. Vasudevan, J. Rodríguez-Martínez, y I. Romero. Analysis and design of bistable and thermally reversible metamaterials inspired by shape-memory alloys. *International Journal of Solids and Structures*, 275 (112278), 2023. doi: 10.1016/j.ijsolstr.2023.112278.

[249] M. Ortiz y E.A. Repetto. Nonconvex energy minimization and dislocation structures in ductile single crystals. *Journal of the Mechanics and Physics of Solids*, 47(2):397–462, 1999.

[250] M. Ortiz, E.A. Repetto, y L. Stainier. A theory of subgrain dislocation structures. *Journal of the Mechanics and Physics of Solids*, 48(10):2077–2114, 2000.

[251] J. J. Moreau. Sur le lois de frottement, de plasticité et de viscosité. *Comptes Rendu de la Académie de Sciences, série A*, 271:608–611, 1970.

[252] Q. S. Nguyen. On the elastic plastic initial-boundary value problem and its numerical integration. *International Journal of Numerical Methods in Engineering*, 11:817–832, 1977.

[253] C. Miehe. Strain-driven homogenization of inelastic microstructures and composites based on an incremental variational formulation. *International Journal for Numerical Methods in Engineering*, 55(11):1285–1322, 2002.

[254] A. Mielke y F. Theil. On rate-independent hysteresis models. *Nonlinear Differential Equations and Applications NoDEA*, 11:151–189, 2004.

[255] A. Mielke, F. Theil, y V.I. Levitas. A variational formulation of rate-independent phase transformations using an extremum principle. *Archive for rational mechanics and analysis*, 162:137–177, 2002.

[256] M.S. Kuczma, A. Mielke, y E. Stein. Modelling of hysteresis in two-phase systems. *Archives of Mechanics*, 51(6):693–715, 1999.

[257] A. DeSimone y G. Dolzmann. Macroscopic response of nematic elastomers via relaxation of a class of so (3)-invariant energies. *Archive for rational mechanics and analysis*, 161:181–204, 2002.

[258] S. Conti y F. Theil. Single-slip elastoplastic microstructures. *Archive for rational mechanics and analysis*, 178:125–148, 2005.

[259] C. Carstensen, S. Conti, y A. Orlando. Mixed analytical–numerical relaxation in finite single-slip crystal plasticity. *Continuum Mechanics and Thermodynamics*, 20:275–301, 2008.

[260] S. Conti y G. Dolzmann. An adaptive relaxation algorithm for multiscale problems and application to nematic elastomers. *Journal of the Mechanics and Physics of Solids*, 113:126–143, 2018.

[261] S. Kumar, A.N. Vidyasagar, y D.M. Kochmann. An assessment of numerical techniques to find energy-minimizing microstructures associated with nonconvex potentials. *International Journal for Numerical Methods in Engineering*, 121(7):1595–1628, 2020.

[262] W. Wu, W. Hu, G. Qian, H. Liao, X. Xu, y F. Berto. Mechanical design and multifunctional applications of chiral mechanical metamaterials: A review. *Materials & design*, 180:107950, 2019.

**Doctorado en Ingeniería**
**Mención mecánica computacional**

Título de la obra:

# Diseño Computacional de Metamateriales Mecánicos en Régimen Lineal y No Lineal

Autor: Nestor Oscar Rossi Cabral

Lugar: Santa Fe, Argentina

Palabras Claves:

Mecánica computacional, metamateriales mecánicos,
homogenización inversa, optimización topológica,
simetrías cristalográficas, propiedades elásticas extremas,
G-clausura, microarquitecutras parametrizadas,
energías no convexas, transiciones de fase,
inestabilidades elásticas, pozos de energía,
histerón, modelos reducido, relajación
modelo generalizado estándar, inestabilidades volumétricas.